THE UNIVERSITY *of* EDINBURGH

The Cosmos greenstone terrane: Insights into an Archaean volcanic arc, associated with komatiite-hosted nickel sulphide mineralisation, from U-Pb dating, volcanic stratigraphy and geochemistry

Alexandra de Joux

Thesis submitted for the degree of Doctor of Philosophy

The University of Edinburgh

2014

“We are all visitors to this time, this place. We are just passing through. Our purpose here is to observe, to learn, to grow, to love…and then we return home.”

Australian Aboriginal Proverb

I declare that the work presented in this thesis is entirely my own work, except where contributions have been cited or duly acknowledged.

Alexandra de Joux

April 2nd, 2014

Lay Summary

The Cosmos nickel sulphide deposits in the Eastern Goldfields of Western Australia lie within the Yilgarn Craton, which consists of blocks of continental crust, composed of metamorphosed volcanic and sedimentary rocks and granite intrusions, formed and assembled together between ~3050 and 2620 million years ago. The Eastern Goldfields contains some of the world's most economically important nickel sulphide deposits, which are commonly found close to the base of komatiite lava flows. Komatiites are ultramafic, mantle-derived volcanic rocks, which have a low silicon and aluminium, but very high magnesium content. These lavas were erupted at very high temperatures (> 1600ºC) with a viscosity analogous to olive oil, forming vast lava flow fields. The occurrence of komatiite volcanic rocks is typically restricted to the rocks of Archaean age (> 2500 million years old) and importantly those that were erupted ~2700 million years ago contain a large proportion of the world's nickel sulphide deposits. Mineralised komatiite lavas are typically associated with volcanic rocks that are much richer in silica, such as andesites, dacites and rhyolites, and often the origin of these volcanic rocks is poorly understood. Interaction of the latter volcanic rocks with komatiite lavas is thought to be critical for the formation of nickel sulphide deposits, and the location and nickel content of the nickel ore at Cosmos appears to have been influenced by the dacitic volcanic rocks that underlie the komatiite lavas. The textures and nature of the rocks at Cosmos suggest the volcanic succession formed on land, which is unusual for late Archaean volcanism that is thought to have been largely submarine. Dating of the rocks indicates that periodic volcanic activity lasted for >50 million years. The Cosmos succession has been shown to be distinct in composition and age to nearby volcanic successions, which also contain nickel sulphide mineralisation, and thus it is considered that Cosmos may record the earliest onset of volcanic activity in the region. The rocks have a geochemistry and composition that suggests they were formed in a continental subduction zone, similar to that seen in parts of the modern Andes. The recognition of the tectonic setting of Cosmos is important as it gives evidence that plate tectonic processes were operating in this region ~2.7 billion years ago, a subject which has been debated in the scientific literature for over 30 years.

Acknowledgments

Where to start…….five years down the line from those first days when I was catapulted straight into the world of Archaean volcanism in the Australian outback, without a clue what I'd let myself in for!

First and foremost I would like to thank my supervisor Thor Thordarson for initiating this project. Thank you for your guidance throughout in all things volcanic! Thank you for encouraging me to visit Iceland whenever possible to get a grasp of modern volcanism and how this might apply to the metamorphosed rocks of the Archaean. Thank you travelling all the way to the Western Australian outback several times and teaching me how to log core, see the primary volcanic textures through the metamorphic overprint and supporting me through those testing times in 1st and 2nd year when I really didn't know how it was ever going to come together! Thank you for letting me be honest at all times, allowing me to admit to being blonde sometimes and for giving me the flexibility and freedom to tackle this PhD in my own way and on my own timeframe. Long may we debate the existence on ultramafic megasills over a few beers for years to come!

Secondly, I would like to thank my second supervisor Godfrey Fitton for his help and support over the years. Thank you for always being straight forward and honest when presented with my results. You have taught me the value of going into meetings prepared and that taking the time to proof read my work to ensure that the grammar and spelling is spot on is just as important as the scientific content! Thank you for all your help with geochemistry and for giving me confidence that I am not half bad at igneous and metamorphic geochemistry!

I think it is time to move down under….

Thank you to Xstrata Nickel Australasia and the University of Edinburgh for their financial support for this PhD. Thank you so much to Steve Vallance and Peter Langworthy for initiating this project under Jubilee Mines allowing me to move into an exciting world of research I never anticipated I would be involved in. Thank you to Don Huntly, Terry Mallinson and Graham Leaver who continued to support this research under Xstrata Nickel Australasia. Thanks to Graham for making me aware of the dangers of drop-bears in the outback, to Don for letting me be involved in an extremely memorable fieldtrip and to Terry for giving me the chance to get some fantastic experience as an exploration geologist at Cosmos.

Special thanks go to Rob Hill and Sarah Dowling; your detailed work at Alec Mairs really improved my understanding of the Cosmos Ultramafic Sequence and proved fundamental in my interpretations of the footwall volcanic sequence. Thank you for everything you taught me about komatiites and for all the delicious food and good company you provided whenever I came to visit!

And now to Cosmos! Where to start….Throughout my PhD the "darkside of the coreyard" proved to be initially a place of much confusion, frustration and disillusionment, emotions that were eventually overcome with feelings of accomplishment and excitement as the stratigraphy really started to come together and the geology actually started to make sense! So firstly I would like to thank Michael Denny for being a super brain and helping me decipher rocks in 40°C+ heat with flies trying to eat our eyeballs throughout! Thank you to Marama Garland for your enthusiasm for rocks and my PhD and the welcome distraction of your banter! Thank you to Catherine Jones for being my fellow Yorkshire lass in the core yard and being (I think) genuinely interested in the felsic rocks! Thank you to Kelly Everitt for distracting me with the promise of beers and fun trips on break when those days in the core yard seemed to stretch on forever! Thank you to Matt, Rich and Amy Carter for taking me in the early days and welcoming me into your friend group; a group of people who are now some of my closest friends and have provided a great source of support and encouragement throughout my PhD.

Thank you to all the exploration geologists that have come and gone over the years, you provided some great discussion on the Cosmos sequence amongst the copious banter, taught me a lot about the practicalities of mining and were always enthusiastic about my PhD. In no particular order – Gregor Bennett (Copy truck), Anthony Legge, Kristian Hendrikson, Alex Vukavic, Rachel Conway, Abe Schumacher, Luke Lovell, Anthony Johns, Dave Hammond, Brett Thomas, Rob Stuff, Susanna Talikowski, Derek Backhouse, Jeremy Kilner, Sam Leith, Michael Omant, Jayne Ledingham, Jeremy Lykke, Warrick Hamilton, Kathleen Patrick, Nicholas Anderson and Natasha Kirkeby. Special thanks go to Sam for the time you headbutted the fence during touch rugby, to Michael for your drilling euphenisms, to Warrick for the rig runs to 80s power ballads, to Kathleen for a never ending passion for ultimate Frisbee, to Nick for too many banterous quality times to count and for having the amazing Kathryn Anderson as your wife, to Tash for taking me trapezing and everything since and to Jayne for an amazing trip to IUGG 2011 in Melbourne and for instigating some cracking nights in the wet mess. Thank you to all the field assistants at Cosmos over the years for your help in dragging out hole after hole after hole for me to look at! In no particular order – Juck Slee, Jade Crocker, Crofty, Paul and Cara Hansford, Stiffy, Whitey, Dave Ritchie, Ian Turton and Jamie Harrington, Special thanks go to Sara Dulex, Jamie McPolin, Lisa Quirk and Andrea Lewis for providing so much more than help with the core, including some memorable nights on Awesome Ave! Thanks to Sam the Eagle for your Canadian wit and banter. Thanks to all the drillers for generally being nice blokes! Basically thank you to everyone at Cosmos; my fieldwork there was sometimes challenging, frequently confusing and hard work but your support and friendship made it a fun, successful and overall an amazing experience!

Time to head back to Edinburgh…..First and foremost I would like to thank everyone who has helped me with my sample preparation, geochemical analyses and data processing; John Craven, Richard Hinton, Chris Hayward, Valerie Olive, Mike Hall, Nicola Cazer, Margaret Hartley, Rosie Jones, Alan Hastie and Nic Odling. Special thanks go to Nic for putting up with my sometimes OCD lab habits and for helpful discussions about my samples and geochemistry over the years. Thank you to John and Richard for helping me prove that it isn't all the same age and to John for look around you. Thank you to Linda Kirstein for being my advisor and always offering help and guidance whenever I needed it. Thank you to Simon

Harley for guidance in zircon preparation and garnet-biotite geothermometry. Thank you to Mikael Attal for being the most enthusiastic geogroler I know and proving that the shell hash doesn't have to be in the limestone. Thank you to Hugh Sinclair for teaching me about geogroly and never being afraid to just got for it and bumble across a river.

And now to my support network of fellow PhD students! Thank you to my fossil friend, Rosie Jones, for being the second oldest specimen in the attic and for always being there when I was stressing a little too much about such important issues as the origin of quartz embayments. Thank for all the Noor, healthy living activities and various fun times in between the monotony of PhD write-up! Thank you to Laura Fletcher for Marvellous Wednesdays and everything since! Thanks to Simon Haunch for all the Haribo and for providing numerous non-geological quality times (beveraging) throughout our PhDs. Thank you to Gillian McCay and Tom Russon for appreciating a good shap! Thank you to Andrew Miles and Margaret Hartley for letting me share Viewforth with you and specifically to Andrew for being the King of Grant Institute gossip and to Margaret for an unforgettable summer of volcanology in Iceland! Thank you to everyone else who has been a source of support and welcome distraction in the attic over the past five years including Jamie Stewart, Jen Roberts, Matt Clarkson, Martin Hurst, Niklas Heinemann, Rudra Kapila, Rhian Meara, Tanya Jude-Eton, Grant Nicoll, Cees Van Der Land, Sophie Harland, Maddy Berg, Rachel Kilgallon and Simon King. Lastly massive thanks go to Matt Booth for being there from the beginning of this geological adventure, for understanding what it's like, for always being supportive and for memorable nights spent in ignimbrite castles.

Kaye/Greenwood/Collins/de Joux/Westaway/McColgan Family – you know who you are and how much I appreciate your support and interest over the past few years. You may not really know what I've been doing for most of that time, except for being overseas a lot, but rest assured if you're reading this I have finally finished! Thank you for understanding when I missed family occasions because the rocks required my undivided attention. Thank you to Dad for always being interested in how the PhD was coming along, even though you never really understood the answers I gave you and thank you to Little Legs (Mum) for always looking out for my wellbeing throughout. Special thanks go to Neil de Joux for asking the often pondered question "What's a Blanff?"

Thank you to all my close Skipton friends for your support and interest throughout; Special thanks go to Georgina and Kat for knowing what it's like, to Emily for always being there to listen and give advice, to Hen for sunbows and storm drains, to Viki for bunk barn banter, to Alex for providing a second home in London, to Jess for many a musical distraction, and to Heather for providing a lovely pit-stop in Bahrain on the way to Australia. To the Gubby Lee lasses – thank you for providing awesome weekends away at rugby and the races to break up the hard yaka of PhDing. Thank you to the RLWC 2013 for keeping me sane in the last month of write up!

Lastly I would like to thank Andrew for everything. I couldn't have done this without you. Thank you for being there from the beginning and for supporting me, in so many ways, right through to the end!

Abstract

The Neoarchaean Agnew-Wiluna greenstone belt (AWB) of the Kalgoorlie Terrane, within the Eastern Goldfields Superterrane (EGS) of the Yilgarn Craton, Western Australia, contains several world-class, komatiite-hosted, nickel-sulphide ore bodies. These are commonly associated with felsic volcanic successions, many of which are considered to have a tonalite-trondhjemite-dacite (TTD) affinity. The Cosmos greenstone sequence lies on the western edge of the AWB and this previously unstudied mineralised volcanic succession contrasts markedly in age, geochemistry, emplacement mechanisms and probable tectonic setting to that of the majority of the AWB and wider EGS. Detailed subsurface mapping has shown that the footwall to the Cosmos mineralised ultramafic sequence consists of an intricate succession of both fragmental and coherent extrusive lithologies, ranging from basaltic andesites through to rhyolites, plus later-formed felsic and basaltic intrusions. The occurrence of thick sequences of amygdaloidal intermediate lavas intercalated with extensive sequences of dacite lapilli tuff, coupled with the absence of marine sediments or hydrovolcanic products, indicates the succession was formed in a subaerial environment. Chemical composition of the non-ultramafic lithologies is typified by a high-K calc-alkaline to shoshonite signature, indicative of formation in a volcanic arc setting. Assimilation-fractional crystallisation modelling has shown that at least two compositionally distinct sources must be invoked to explain the observed basaltic andesite to rhyolite magma suite. High resolution U-Pb dating of several units within the succession underpins stratigraphic relationships established in the field and indicates that the emplacement of the Cosmos succession took place between ~2736 Ma and ~2653 Ma, making it significantly older and longer-lived than most other greenstone successions within the Kalgoorlie Terrane. Extrusive periodic volcanism spanned ~50 Myrs with three cycles of bimodal intermediate/felsic and ultramafic volcanism occurring between ~2736 Ma and ~2685 Ma. Periodic intrusive activity, related to the local granite plutonism, lasted for a further ~32 Myrs or until ~2653 Ma. The Cosmos succession either represents a separate, older terrane in its own right or it has an

autochthonous relationship with the AWB but volcanism initiated much earlier in this region than currently considered. Dating of the Cosmos succession has demonstrated that high-resolution geochronology within individual greenstone successions can be achieved and provides more robust platforms for interpreting the evolution of ancient mineralised volcanic successions. The geochemical affinity of the Cosmos succession indicates a subduction zone was operating in the Kalgoorlie Terrane by ~2736 Ma, much earlier than considered in current regional geodynamic models. The Cosmos volcanic succession provides further evidence that plate tectonics was in operation during the Neoarchaean, contrary to some recently proposed tectonic models.

Table of Contents

List of Figures and Tables

List of Figures

Thesis

Appendices

List of Tables

Thesis

Appendices

List of abbreviations

AFC = Assimilation-Fractional Crystallisation
AWB = Agnew-Wiluna greenstone Belt
CL = Cathodoluminescence
EGS = Eastern Goldfields Superterrane
EMPA = Electron Micro-Probe Analysis
FW = Footwall
HFSE = High Field Strength Element
HREE = Heavy Rare Earth Element
HW = Hangingwall
ICP-MS = Inductively Coupled Plasma Mass Spectroscopy
LILE = Large Ion Lithophile Element
LOI = Loss-on-ignition
LREE = Light Rare Earth Element
REE = Rare Earth Element
SEM = Scanning Electron Microscope
SIMS = Secondary Ionising Mass Spectrometry
T/S = Thin Section
TTG = Tonalite-Trondhjemite-Granodiorite
TTD = Tonalite-Trondhjemite-Dacite
XNA = Xstrata Nickel Australasia
XRF = X-Ray Fluorescence spectroscopy

Chapter 1 - Introduction

1.1 Introduction to research topic

The Neoarchaean represents a time of significant crustal growth and formation of some of the world's major base metal, nickel, gold and silver deposits within Archaean cratons. The economic significance of Neoarchaean volcanic and sedimentary successions has resulted in the geodynamic settings and petrogenesis of such sequences being the focus of much research. Detailed understanding of mineralisation mechanisms in Archaean terranes is vital to aid exploration for future deposits.

The Eastern Goldfields Superterrane (EGS) within the Yilgarn Craton of Western Australia contains some of the world's most economically important komatiite-hosted, nickel sulphide deposits. Many of these ore bodies are found close to the basal contact of ultramafic sequences, which are considered by many authors to represent preferred lava pathways where komatiite lava flowed over the country rock for a prolonged period (Barnes et al., 1988; Hill et al., 1989; 1990; 1995; 2004; Hill, 2001; Dowling et al., 2004; Naldrett, 2004; Barnes, 2006b; Lesher and Barnes, 2008). The incompatibility of sulphur during partial melting in the mantle results in komatiite melts, derived by very high (30 - ≤ 50%) degrees of partial melting, being undersaturated in sulphur when they reach the surface or subvolcanic levels (Arndt, 1977; Naldrett and Barnes, 1986; Lesher and Groves, 1986; Herzberg and O'Hara, 1985; 1998; Herzberg, 1992). Thus, external sources of sulphur are considered necessary for komatiites to reach sulphur saturation. Thermal erosion of an underlying

sulphide and/or sulphur-bearing substrate provides a mechanism for allowing the komatiite lava to become sulphur saturated (Lesher et al., 1984; Huppert and Sparks, 1985; Arndt and Jenner, 1986; Lesher and Groves, 1986; Barnes et al., 1988; Lesher and Keays, 2002; Barnes, 2006a). This results in the formation of immiscible sulphide liquid that, when concentrated and enriched in chalcophiles such as nickel, can form significant sulphide deposits (Naldrett, 2004; Hill et al., 2004; Barnes, 2006a; Arndt et al., 2008). An alternative view, that some ultramafic sequences within the Kalgoorlie Terrane of the EGS may represent large high-level sills has been presented recently (e.g., Rosengren et al., 2005; 2007; 2008; Fiorentini et al., 2007; 2012; Barnes and Fiorentini, 2012). The latter authors envisage exceptionally high fluxes of komatiite magmas, forming long-lived, high-level feeder conduits capable of assimilating crustal sulphur from the surrounding rocks. Such emplacement processes have been suggested to account for the association of nickel sulphides with thick olivine-dominated ultramafic units, particularly within the Agnew-Wiluna greenstone belt (AWB) of the Kalgoorlie Terrane of the EGS (Rosengren et al., 2005; 2008; Fiorentini et al., 2012).

Mineralised komatiite successions are often associated with, and invariably intercalated with, felsic volcanic successions within the AWB. Examples include Mount Keith (Dowling and Hill, 1992; 1993; Hill et al., 1995; Rosengren et al., 2005; 2008), Perseverance (Barnes et al., 1988; Trofimovs et al., 2003; Duuring et al., 2010) and deposits of the Cosmos region (Langworthy and Vallance, 2004). However, much of the focus of research over the past twenty years has been on developing understanding of the physical volcanology of komatiites and how the morphology of proposed flow fields could have produced the diverse range of lithologies and textures present within ultramafic sequences (Barnes et al., 1988; Hill et al., 1989; 1990; 1995; Hill, 2001; Barnes, 2006b). With debate still on-going as to whether komatiites are in fact extrusive, with several authors promoting an intrusive origin for several successions within the EGS (Cas et al. 1999; Cas and Beresford, 2001; Rosengren et al., 2005; 2008; Cas et al., 2011; Fiorentini et al., 2012), the focus is likely to remain on understanding komatiite emplacement mechanisms. Nevertheless, recent work has highlighted the common association of pre-existing crustal sources of sulphur, such as volcanogenic massive sulphide (VMS) deposits or base metal deposits and their

associated felsic volcanic centres, (e.g., Bekker et al., 2009; Fiorentini et al., 2012) with mineralised komatiite successions. Assimilation of such crustal sulphur is considered to promote the attainment of sulphur saturation of komatiite magmas, be they high-level intrusive sills or vast extrusive komatiite lava flow fields (e.g., Bekker et al., 2009; Fiorentini et al., 2012, Barnes and Fiorentini, 2012). The latter authors have emphasised that to fully understand how magmatic sulphide deposits form in komatiite systems it is important that the nature and composition of associated felsic and intermediate volcanic successions be characterised and studied in detail.

The poor preservation potential of ultramafic mineral assemblages during metamorphism often results in an interpretation of their environmental setting only being possible by consideration of the nature of associated non-ultramafic rocks (Barnes and Hill, 2000; Arndt et al., 2008). The composition and geochemical affinity of associated felsic and intermediate volcanic successions can provide an indication of their likely geodynamic setting. Given that plume generated komatiites were likely erupted in a large variety of tectonic settings (Arndt et al., 2008), the textures and geochemistry of komatiites often provides little indication of their broader geodynamic setting. Understanding the spatiotemporal association of komatiite volcanism with silicic volcanic centres has important implications for the possible geodynamic settings of Archaean volcanism. This also has broad implications for the debate as to whether plate tectonics operated in the mid to late Archaean, a subject which has recently come under renewed scrutiny (e.g., Bédard, 2006; 2013; Bédard et al., 2003; 2013; Wyman, 2013a; 2013b; Barnes et al., 2012).

The first part of this introduction will present the regional geology of the Eastern Goldfields Superterrane with an emphasis on the origin, age and occurrence of greenstone successions in the region. The geodynamic setting of Neoarchaean volcanism in this region will be discussed in the second part of the introduction, as well as a broader consideration of geodynamic settings of Archaean volcanism in general. The third part of the introduction details the theory, formation mechanisms, geological setting and occurrence of mineralisation within komatiites. Emphasis is placed on the non-ultramafic volcanic and sedimentary sequences with which komatiites are commonly associated. Finally, an introduction to the Cosmos region,

where this research is focused, will be presented to set the scene for the three papers that compose the majority of this thesis. It is intended that this introduction provides a broad overview of volcanic processes operating in the Neoarchaean and how this relates to nickel sulphide mineralisation and associated volcanism in the EGS. Each subsequent chapter provides its own more detailed introduction to the specific research topic being discussed.

1.2 Geological setting of the Eastern Goldfields Superterrane

1.2.1 Regional Geology

The Yilgarn Craton (Fig. 1.1) covers the majority of southern Western Australia and is one of three areas of crust within Western Australia to stabilise prior to 2.4 Ga (Cassidy et al., 2006). It consists of meta-volcanic and meta-sedimentary rocks, granites and granitic gneisses that formed principally between 3.05 and 2.62 Ga (Nelson 1997b; Nelson 1998; Cassidy et al., 2006). Within the EGS it consists of linear, bimodal (mafic–ultramafic and felsic) volcanic 'greenstone belt' sequences, intercalated with minor amounts of clastic sedimentary sequences and banded iron formations, which are sandwiched between voluminous elongate granitoid bodies (Nelson, 1998; Cassidy et al., 2006). These granitoids were intruded periodically between 2.76 - 2.62 Ga and coincided with Neoarchaean orogeny, which resulted in the amalgamation and assembly of several tectonic units to form the Yilgarn Craton (Cassidy et al., 2006). Individual granite greenstone successions define separate terranes within the Yilgarn Craton, which are delineated by regional scale transcurrent shear zones (Blewett et al., 2010; Czarnota et al., 2010).

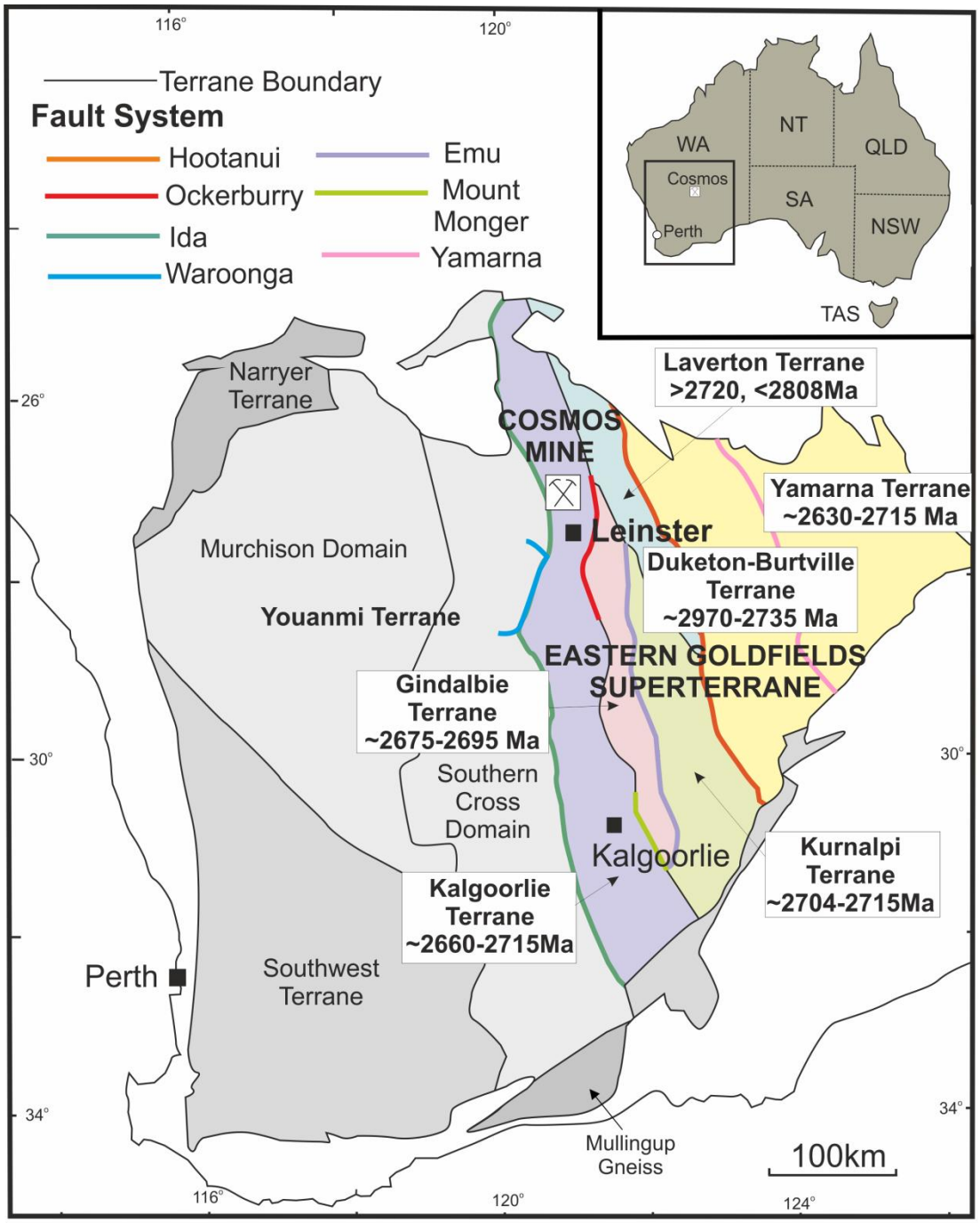

Figure 1.1. Terrane map of the Yilgarn Craton after Cassidy et al. (2006), Kositcin et al. (2008) and Pawley et al. (2012). The main terranes of the Eastern Goldfields Superterrane and age ranges of their respective greenstone successions are highlighted, as well as their bounding fault systems. The location of the Cosmos mine, where this research was focused, is also shown.

The geological framework of the Yilgarn Craton has recently been revised by Cassidy et al. (2006) and Kositcin et al. (2008). The former authors split the craton

into six different terranes (Fig. 1.1). These are the Narryer Terrane, the Southwest Terrane, the Youanmi Terrane (comprising the Murchison and Southern Cross Domains), the Kalgoorlie Terrane, the Kurnalpi Terrane and the Burtville Terrane. The latter three terranes form the EGS. Each terrane displays volcanism spanning a distinct age range, as well as distinctive stratigraphy, volcanic facies and geochemical affinities. Kositcin et al. (2008) further divided the Kurnalpi Terrane into the Kurnalpi, Gindalbie and Laverton Terranes, renamed the Burtville Terrane the Duketon-Burtville Terrane and retained the Kalgoorlie Terrane as defined by Cassidy et al. (2006). The EGS thus comprises at least five terranes that feature ~2810 to ≤2657 Ma volcanic and sedimentary sequences, which were amalgamated by ~2660 Ma (Fig. 1.1). The Kalgoorlie Terrane is considered to comprise the Kambalda Sequence, a >2715 to ~2692 Ma plume-influenced, but deep-marine, mafic-ultramafic succession overlain unconformably by the Kalgoorlie Sequence, a 2686 ± 5 to ≤2666 ± 6 Ma deep-marine felsic volcaniclastic-shale succession of tonalite-trondhjemite-diorite (TTD) affinity (Kositcin et al., 2008). The felsic volcanic sequences of the AWB and northern Yandal Belt are also included within the Kalgoorlie Terrane, based on their perceived similarity in age and geochemistry. The adjacent Gindalbie and Kurnalpi Terranes are considered to both comprise arc-related volcanic sequences, on account of their calc-alkaline geochemical affinity (Fig. 1.1; Hallberg, 1985; Morris and Witt, 1997; Barley et al., 2006; 2008; Kositcin et al., 2008) and are coeval with, but distinct from, the volcanic successions of the Kalgoorlie Terrane (Kositcin et al., 2008; Korsch et al., 2011). SHRIMP U-Pb dating has identified older volcanic sequences in the Laverton (≤2808 ± 8 Ma) and Duketon-Burtville (2805 ± 5 Ma) Terranes (Kositcin et al., 2008). Most recently, Pawley et al. (2012) reported rocks dated at ~2970 Ma from the Ulrich Range greenstone belt in the Duketon-Burtville Terrane.

Understanding the tectonostratigraphic architecture of the EGS, as well as the wider Yilgarn Craton, is continually evolving as new geochronology and geological mapping is undertaken in poorly explored domains. Pawley et al. (2012) have identified a new previously unrecognised terrane within the north-east corner of the Yilgarn Craton, which they named the Yamarna Terrane (Fig. 1.1). This newly defined terrane, dated at <2720 Ma, is much younger than the Duketon-Burtville Terrane to

which it was originally assigned. Furthermore, it is lithologically and geochronologically most similar to the Kambalda and Kalgoorlie Sequences within the Kalgoorlie Terrane. Future geological mapping, geochronology and geochemistry in little-studied domains within the EGS is likely to refine the tectonostratigraphic architecture of the region further.

1.2.2 Volcanism in the Eastern Goldfields Superterrane

Large volumes of ultramafic magma were erupted during Neoarchaean volcanism in the EGS, particularly within the Kalgoorlie Terrane. These vast komatiite flow fields, and syn-volcanic intrusive sills, are now the host for some of the world's largest nickel sulphide deposits. The modal regional emplacement age of ultramafic units within the Kalgoorlie Terrane is ~ 2707 Ma (Kositcin et al., 2008). Voluminous eruptions of komatiite lava flooded vast areas of the Archaean landscape and interacted with the topography created by previous felsic (and mafic) eruptions (Nelson, 1997b; 1998). Felsic volcanism occurred between ~2713 and ~2672 Ma from a number of volcanic centres scattered throughout the southern part of the EGS (Nelson, 1997b). Komatiites of the EGS are suggested to originate through predominantly submarine eruptions onto submerged continental platforms (Groves et al. 1984; Arndt et al., 2008). Evidence for the former includes inter-bedded pillow lavas and chert seen at Kambalda and the latter is based on geochemical data and zircon xenocrysts that indicate komatiites assimilated continental crust (Claoué-Long et al., 1988; Groves et al., 1984; Arndt et al., 2008).

As yet the majority of published data on felsic volcanic formations within the Kalgoorlie Terrane suggest it was dominated by volcanism of tonalite-trondhjemite-dacite (TTD) affinity, which is the extrusive equivalent of tonalite-trondhjemite-granodiorite (TTG) magmatism (e.g., Kositcin et al., 2008; Fiorentini et al., 2012). The petrogenesis of TTD volcanism will be discussed in Section 1.8.1. Three episodes of TTD volcanism, spanning from ~2707 to ~2665 Ma, are recognised within the Kalgoorlie Terrane (Kositcin et al., 2008). The first episode (2707 – 2692 Ma)

comprised felsic volcanism associated with komatiites at Black Swan. The second (2687 – 2676 Ma) and third (2669 – 2665 Ma) episodes comprised felsic volcanism, and associated volcaniclastic and epiclastic sedimentation, in the lower Kalgoorlie Sequence and upper Kalgoorlie Sequence respectively.

The Kurnalpi and Gindalbie Terranes, although similar in age to the adjacent Kalgoorlie Terrane, exhibit contrasting volcanic associations (Fig. 1.1; Barley et al., 2008). Within these two terranes calc-alkaline volcanism is recognised, emplaced between ~2715 - 2704 Ma in the Kurnalpi Terrane and ~2692 - 2680 Ma in the Gindalbie Terrane (Giles and Hallberg, 1982; Brown et al., 2002; Morris and Witt, 1997; Barley et al., 2006; 2008; Kositcin et al., 2008, Korsch et al., 2011). Calc-alkaline volcanism is also recognised within the Spring Well complex of the Yandal belt, in the Gindalbie Terrane (Messenger, 2000). The juvenile character of the volcanic arc rocks within these two terranes, and their similarity to modern subduction related arc systems has led several authors to suggest that a convergent plate margin was present in the eastern Yilgarn Craton during the Neoarchaean (Barley et al., 1989; Barley et al., 2006; 2008; Czarnota et al., 2010; Korsch et al., 2011). The association of plume-derived komatiites and subduction-related volcanism has led to considerable debate over the past three decades over the geodynamic setting of greenstone belts sequences within the EGS.

1.3 Origin of greenstone belts in the Eastern Goldfields Superterrane

The origin of greenstone belt sequences within the EGS has been debated for over 25 years with authors generally supporting either a plume-dominated model (e.g., Campbell and Hill, 1988; Trofimovs et al., 2004a; 2006; Fiorentini et al., 2012; Barnes et al., 2012; Van Kranendonk et al., 2012) or variants of subduction accretion models (e.g., Myers, 1993; 1997; Nelson, 1997b; Barley et al., 2006; 2008; Kositcin et al., 2008; Gee and Swager, 2008; Standing, 2008; Czarnota et al., 2010; Korsch et al.,

2011). Figure 1.2 highlights the key features and possible melt generation processes occurring within both a subduction dominated model (Fig. 1.2a) and a plume dominated model (Fig. 1.2b) in the EGS.

Campbell and Hill (1988) proposed that greenstone belts within the Kalgoorlie to Norseman region of the Kalgoorlie Terrane formed due to mantle plume and continental crust interaction. Large mantle upwellings ascended through a primitive andesitic continental crust resulting in anatexis around the plume head, resulting in formation of a felsic melt. The ultramafic/mafic plume-derived material and the associated felsic crustal melt then ascended together and were emplaced contemporaneously into the upper crust. Trofimovs et al. (2004a; 2006) considered the intercalation of komatiitic and dacitic units, including evidence of magma mingling, within the Boorara Domain of the Kalgoorlie Terrane, to have formed via this process. Fiorentini et al. (2012) hinted at a similar formation process, citing the spatial and genetic association of thick komatiite sequences with TTD-affinity felsic volcanic rocks within the AWB, as evidence that komatiites and associated felsic volcanic rocks are linked. They also suggest that the hot ascending komatiite lavas may have provided the heat to instigate melting of a mafic precursor with ultramafic and felsic melts most likely utilising the same crustal conduits (e.g., Rosengren et al., 2005; 2007; 2008). However, this model is valid only for TTD volcanic sequences, whose geochemistry can be explained by melting of a mafic crust at pressures within the garnet stability field (Drummond and Defant, 1990; Defant and Drummond, 1990; Drummond et al., 1996; Defant et al., 2001). It cannot easily account for the formation of calc-alkaline affinity felsic volcanism, recognised in the Kurnalpi and Gindalbie Terranes of the EGS (Giles and Hallberg, 1982; Hallberg, 1985; Morris and Witt, 1997; Brown et al., 2002; Barley et al., 2006; 2008), whose geochemistry is consistent with formation via partial melting of mantle above a subducting slab. Most recently Barnes et al., (2012) reiterated a mantle plume model, broadly along the lines of that proposed by Campbell and Hill (1988). A major mantle plume is envisaged to have been emplaced under the lid of the Youanmi Craton, where the plume head diverted towards the craton's eastern margin (Fig. 1.2b). This resulted in extension and continental rifting along the eastern edge of the Youanmi Terrane and emplacement of the ~2705 Ma volcanic successions

of the Kalgoorlie Terrane (Fig. 1.2b). The weakness of this model is it does not explain the nature of the contact between the Youanmi Craton and the proposed Eastern Goldfields Craton. Equally, the geodynamic setting and petrogenesis of the older volcanic sequences within the latter two proto-cratons, prior to eruption and emplacement of the volcanic successions that form the Kalgoorlie Terrane, is only discussed very briefly by Barnes et al. (2012).

Other recent geodynamic models have focused on various subduction accretion models of volcanic arc fragments to a continental margin to form the granite-greenstone succession exposed today as the eastern Yilgarn Craton (Nelson, 1997b; Myers, 1993; 1997; Gee and Swager, 2008; Barley et al., 2006; 2008; Kositcin et al., 2008; Standing et al., 2008; Czarnota et al., 2010; Korsch et al., 2011). Nelson (1997b) suggested that greenstone basins within the EGS are parts of a back-arc complex within a west-dipping subduction zone above which extension and plume-derived mafic-ultramafic volcanism developed. Subduction (>c. 2720 - 2675 Ma) ceased following collision, which resulted in D2 regional compression and transpression (Nelson, 1997b). Myers (1993; 1997) interpreted individual terranes of the EGS as strips of island arc and/or back arc, which collided and amalgamated with each other and with micro-continents during the late Archaean. Barley et al., (2008) interpreted calc-alkaline andesitic volcanic complexes in the older Kurnalpi Terrane and bimodal basalt-rhyolite, associated with coeval intermediate-silicic calc-alkaline volcanic complexes, in the younger Gindalbie Terrane as the maturation of the arc system from marginal intra-arc volcanism to mature arc-rifting phase.

Figure 1.2. (Next page) Schematic cross-sections highlighting the key features of the subduction accretion model (1.2a) and the plume-dominated model (Fig. 1.2b) for the origin of volcanism in the EGS at ~2705 Ma. Figure 1.2a is modified after Goscombe et al. (2009) and Czarnota et al. (2010). Figure 1.2b is modified after Goscombe et al. (2009) and Barnes et al. (2012)).

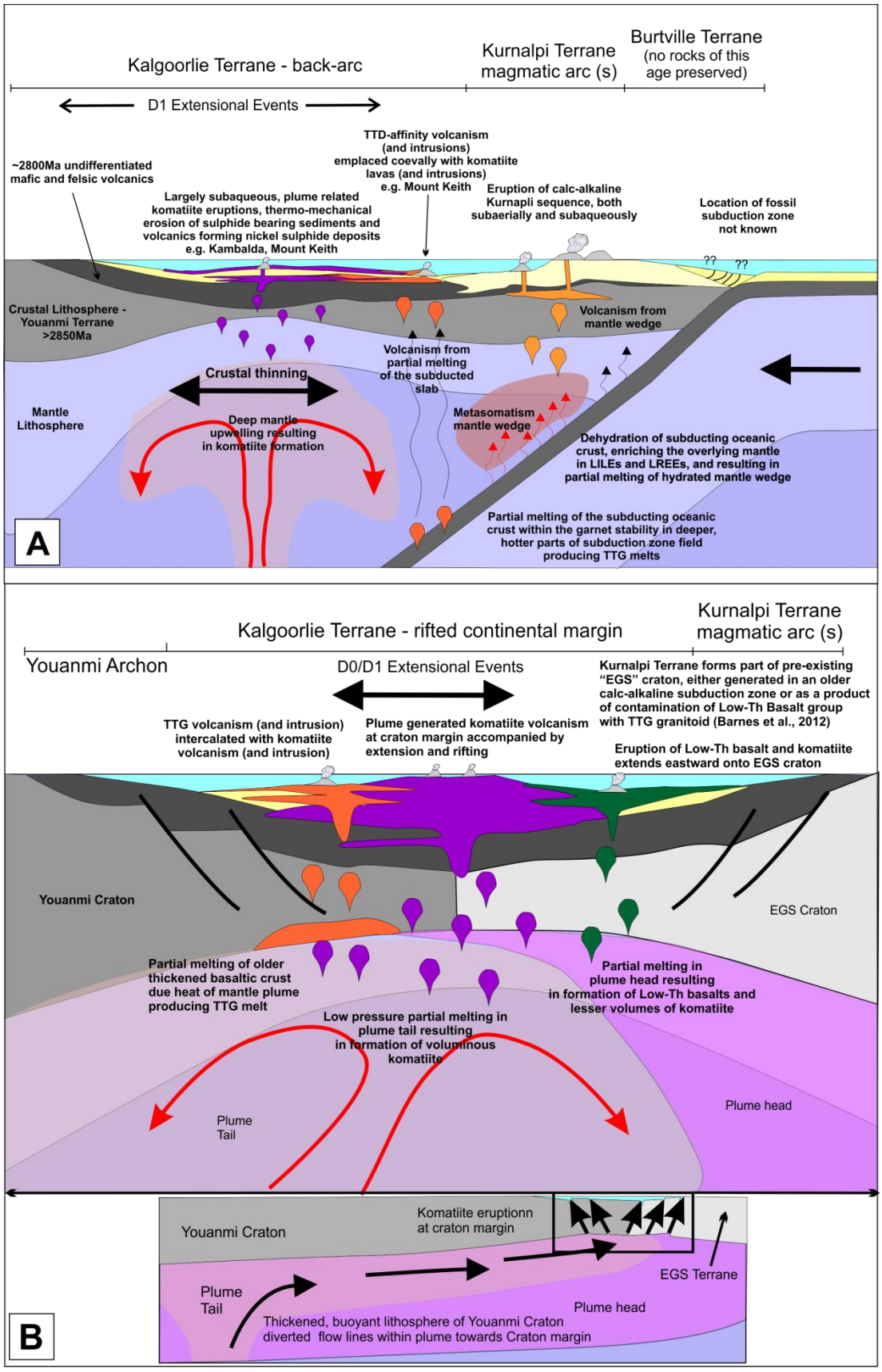
Kalgoorlie Terrane - back-arc
Kurnalpi Terrane magmatic arc (s)
Burtville Terrane (no rocks of this age preserved)
D1 Extensional Events
~2800Ma undifferentiated mafic and felsic volcanics
TTD-affinity volcanism (and intrusions) emplaced coevally with komatiite lavas (and intrusions) e.g. Mount Keith
Largely subaqueous, plume related komatiite eruptions, thermo-mechanical erosion of sulphide bearing sediments and volcanics forming nickel sulphide deposits e.g. Kambalda, Mount Keith
Eruption of calc-alkaline Kurnapli sequence, both subaerially and subaqueously
Location of fossil subduction zone not known
Crustal Lithosphere - Youanmi Terrane >2850Ma
Volcanism from mantle wedge
Volcanism from partial melting of the subducted slab
Crustal thinning
Mantle Lithosphere
Deep mantle upwelling resulting in komatiite formation
Metasomatism mantle wedge
Dehydration of subducting oceanic crust, enriching the overlying mantle in LILEs and LREEs, and resulting in partial melting of hydrated mantle wedge
Partial melting of the subducting oceanic crust within the garnet stability in deeper, hotter parts of subduction zone field producing TTG melts
A
Kalgoorlie Terrane - rifted continental margin
Kurnalpi Terrane magmatic arc (s)
Youanmi Archon
D0/D1 Extensional Events
Kurnalpi Terrane forms part of pre-existing "EGS" craton, either generated in an older calc-alkaline subduction zone or as a product of contamination of Low-Th Basalt group with TTG granitoid (Barnes et al., 2012)
TTG volcanism (and intrusion) intercalated with komatiite volcanism (and intrusion)
Plume generated komatiite volcanism at craton margin accompanied by extension and rifting
Eruption of Low-Th basalt and komatiite extends eastward onto EGS craton
Youanmi Craton
EGS Craton
Partial melting of older thickened basaltic crust due heat of mantle plume producing TTG melt
Partial melting in plume head resulting in formation of Low-Th basalts and lesser volumes of komatiite
Low pressure partial melting in plume tail resulting in formation of voluminous komatiite
Plume Tail
Plume head
Youanmi Craton
Komatiite eruptionn at craton margin
EGS Terrane
Plume Tail
Plume head
Thickened, buoyant lithosphere of Youanmi Craton diverted flow lines within plume towards Craton margin
B

Most recently Czarnota et al. (2010) undertook a holistic review of the tectonic history of the Eastern Yilgarn Craton, favouring a para-autochthonous convergent margin model that links all terranes of the EGS within a westward dipping subduction zone, with the Kalgoorlie Terrane part of a back-arc setting (Fig. 1.2a). Korsch et al. (2011) favoured a westward dipping subduction zone to the east of the Kurnalpi island arc during the period 2719 – 2702 Ma, implying that oceanic crust existed on both sides of the terrane, with a marginal sea in the back-arc region to the west. This sea separated the older continental Kalgoorlie Terrane in the west from the Kurnalpi island arc to the east (Korsch et al., 2011). After about 2685 Ma, the marginal sea to the west of the Kurnalpi island arc started to close, with subduction of the oceanic crust beneath the Kalgoorlie Terrane, producing the TTD volcanism in the Kalgoorlie continental margin arc (Korsch et al., 2011). Closure of the ocean basin between the Kalgoorlie Terrane and the Kurnalpi Terrane continued until collision between the two terranes occurred at, or shortly after, ~2658 Ma, when arc magmatism ceased (Korsch et al. 2011). The key difference between this scenario and that of Czarnota et al. (2010) (itself based on the work of Barley et al. 1989, Morris and Witt, 1997 and Nelson 1997b) is that, in the latter scenario, the back-arc to the west of the Kurnalpi Terrane is not a marginal sea but extended continental crust and the Kalgoorlie and Kurnalpi Terranes are inferred to be part of a single continuous continental crust (Czarnota et al., 2010; Korsch et al., 2011).

The majority of authors over the past decade have largely preferred a subduction setting for the EGS, due to numerous occurrences of calc-alkaline magmatism in the region, as well as juxtapositioning of different terranes with contrasting volcanic and metamorphic histories, separated by regional scale shear zones. Plume interaction with an active subduction zone in the Kalgoorlie Terrane is considered to account for the voluminous eruption of komatiite lavas in the region (e.g., Czarnota et al., 2010). However, recently Barnes et al. (2012) questioned whether the reported occurrences of calc-alkaline volcanism within the EGS are actually analogous to modern arc volcanism. They challenged whether uniformitarian models of arc accretion tectonics in the eastern Yilgarn are consistent with the geochemical characteristics of regional basalt occurrence.

1.4 Did plate tectonics operate in the Archaean?

Not only is the tectonic setting of the EGS widely debated, the operation of plate tectonics within the Archaean, particularly the Neoarchaean, has recently come under renewed scrutiny (e.g., Bédard, 2006; 2013; Wyman, 2013a; 2013b; Bédard et al., 2013). The existence of plate tectonic processes in the Archaean is debated, both on theoretical grounds and geological observations, from numerous cratons worldwide. Early studies of Archaean greenstone belts (e.g., Langford and Morin, 1976; Blackburn, 1980; Sawkins, 1984) favoured plate tectonics as the most likely tectonic regime, with plate tectonics continuing to be the favoured geodynamic regime by most workers since that time (Smithies and Champion, 2004; Moyen and Stevens, 2006; O'Neill and Wyman, 2006; Kerrich and Polat, 2006; Wyman et al., 2008; Czarnota et al., 2010; Korsch et al., 2011; Polat, 2012; Wyman, 2013a; 2013b). However, several authors have questioned whether plate tectonics operated in the Archaean, particularly in the early and mid Archaean, with some authors preferring vertical tectonic scenarios, featuring crustal diapirism, in some Archaean cratons (e.g., Hamilton, 1998; Van Kranendonk et al., 2004; Bédard et al., 2003; Bédard, 2006).

Rock types and structures that are considered to typify Phanerozoic orogens are considered to be rare and absent in the Archaean. These include blueschists, ultra high pressure rocks, paired metamorphic belts, subduction zone melanges, accretionary prisms, Atlantic style passive margins and overprinting fold and thrust belts (e.g., Bleeker, 2002; Hamilton 1998; 2003; 2007; McCall, 2003; Brown, 2006; 2007; 2008; Stern, 2005; 2008; Bédard et al., 2003; 2013a; 2013b; Bédard, 2006). Many authors attribute the rarity or absence of specific plate tectonic indicators in Archaean successions as evidence for the absence of plate tectonics (e.g., Hamilton, 1998; Bédard, 2006; Bédard et al., 2013). Opponents of plate tectonics also suggest that volcanic and intrusive rocks with geochemical signatures typical of modern arcs, such as calc-alkaline volcanic complexes, are comparatively uncommon in the Archaean (Bédard et al., 2013). Rare Archaean ophiolites also have a contested origin (e.g., Furnes et al., 2007; Zhao et al., 2007; Friend and Nutman, 2010). Some thermo-

mechanical models of the Archaean mantle suggest that the thick, hot, buoyant oceanic crust would be difficult to subduct (e.g., Davies, 1992; Sizova et al., 2010). Several of the debated constraints on the operation of plate tectonic in the Archaean, which are particularly relevant to the formation of the EGS and wider Yilgarn Craton, are discussed in greater detail below.

1.4.1 Archaean boninites

Boninites are rare, water-rich, high-Mg basaltic to andesitic rocks, which in the Phanerozoic are confined to convergent margin settings (Hickey and Frey, 1982; Crawford et al., 1989). Bédard et al. (2013) questioned whether boninites of the Archaean, described by Kerrich et al., (1998), Wyman, (1999), Smithies (2000), Manikyamba et al. (2005), and Polat et al. (2008; 2009), represented true boninites. Bédard et al. (2013) pointed out that Archaean boninites were more aluminous, less depleted in heavy rare earth elements (HREE) and contained higher concentrations of TiO_2 ($\geq$ 0.3%) than Phanerozoic boninites. However, Smithies et al. (2004) suggested these small compositional differences between modern and ancient boninites probably reflect secular changes in mantle temperatures and the existence of a more garnet-rich residual source. Many modern boninitic occurrences exhibit TiO_2 concentrations $\geq$ 0.3%, while a significant number of Archaean boninites had TiO_2 concentrations $\leq$ 0.3% (Manikyamba et al., 2005; Wyman, 2013b). Smithies et al. (2004) concluded that subduction zone processes, essentially the same as those that produce modern boninites, have operated since at least 3.12 Ga, producing the Whundo-type boninites, whose chemistry is similar to Phanerozoic boninites. However, a uniquely Archaean boninite-forming process may have occurred before then to account for Whitney-type boninites, which have very high Al_2O_3 and HREE concentrations. Wyman and Kerrich (2012) recently reported a ~2.85 Ma boninite from the Youanmi Terrane (Fig. 1.1). This is considered to be the best preserved example of an Archaean boninite on account of the low grade prehnite-pumpellyite metamorphic grade and points towards the

operation of plate tectonics within the Yilgarn Craton during the Neoarchaean (Wyman, 2013a).

1.4.2 Calc-alkaline volcanism in a non-subduction setting?

Archaean calc-alkaline volcanic successions, containing andesites, have been described from numerous cratons worldwide, including the Superior Province in Canada and the Yilgarn Craton in Western Australia (e.g., Giles and Hallberg, 1982; Hallberg, 1985; Brooks et al., 1982; Polat and Kerrich, 2001; Messenger, 2000; Brown et al., 2002; Barley et al., 2008; Korsch et al., 2011). Any alternative to plate tectonics must provide a mechanism to generate calc-alkaline mantle melts that are enriched in large ion lithophile elements (LILEs) and light rare earth elements (LREEs), but depleted in high field strength elements (HFSEs). This typical crustal signature occurs in modern subduction zones where LILEs and LREEs are preferentially partitioned into hydrous fluids during dehydration of the subducting slab, enriching the partial melt of peridotite formed in the overlying mantle wedge. HFSEs are conservative during slab dehydration and thus are relatively depleted in the mantle wedge.

Bédard et al. (2013) suggested that dehydration of delaminated crust could enrich the mantle in LILEs and LREEs and generate partial melts of the mantle with a calc-alkaline-like signature. Delamination of large volumes of meta-volcanic rock from the base of a thick basaltic crust, which consequently sinks into the mantle and melts, is suggested as a possible mechanism to produce the voluminous TTG intrusions and associated volcanic sequences that dominate many Archaean successions. It seems unlikely that partial melts of enriched mantle, with a calc-alkaline-like affinity, from dehydration of the same delaminated crust would make it to the surface without interacting with the greater volumes of TTG-affinity melt in the mantle, thus altering their composition and geochemical affinity. This model also assumes that fragments of delaminated crust sinking into the mantle have not already devolitised. This is likely to have already occurred if delamination is taking place beneath a thickened crust

subject to the higher geothermal gradients of the Archaean mantle. Bédard et al. (2013) also suggested that rare intermediate calc-alkaline magmas could result from mixing of high pressure felsic anatectic melts (with a typical TTG affinity) with tholeiitic basalts in a complex plumbing system. However, this is based upon the Abitibi volcanic stratigraphy in the Superior Province in Canada. Here there is a close spatial association of rare thin andesites with enriched LREE and HREE depleted rhyodacites, which are sandwiched between thick tholeiitic sequences (Bédard et al., 2013). The calc-alkaline volcanic sequences in the Kurnalpi Terrane of the EGS, are composed of dominantly andesite lavas and volcaniclastic rocks, contain few TTD-affinity felsic volcanic units and sparse occurrences of tholeiitic basalt (Barley et al., 2008). These calc-alkaline sequences are considered to have been derived from LILE-enriched mafic magmas by fractional crystallisation (with or without assimilation) processes (Barley et al., 2008). Thus, the mechanism described by Bédard et al. (2013) can only account for the formation of low volume andesitic melts in specific greenstone successions rather than being a viable mechanism for formation of all arc-like Archaean andesites.

1.4.3 Alternative models to plate tectonics

Opponents of the operation of modern style plate tectonics in the Archaean often prefer variants on models of convective overturn or vertical tectonics, to explain the dome and keel architecture of many greenstone granite terranes, particularly those that are older than 3 Ga (e.g., Van Kranendonk et al. 2004; 2007; 2009; 2011; Bédard et al., 2003). Broadly this model suggests that dense basaltic lavas that erupted onto less dense and ductile TTG crust resulted in the crust becoming gravitationally unstable, resulting in diapirism and rapid foundering into the mantle (e.g., Mareschal and West, 1980; Collins et al., 1998; Van Kranendonk et al., 2004; Robin and Bailey, 2009; Thébaud and Rey, 2013). The Eastern Pilbara granite-greenstone terrane in Western Australia is considered to have formed via the latter mechanism (Van Kranendonk et al., 2004). The structural, geometric, geochronological, and

metamorphic features of Eastern Pilbara are considered to be hard to explain by horizontal plate tectonic models by Van Kranendonk et al. (2004) who prefer a tectonic model involving punctuated partial convective overturn of the upper and middle crust in response to dominantly magmatic processes.

There is good evidence in Archaean Cratons for amalgamation of terranes with different geological histories (e.g., Cassidy et al., 2006; Kositcin et al., 2008; Windley and Garde, 2009; Czarnota et al., 2010). The common recognition of Archaean contractional deformation fabrics and accreted terranes is perceived by many to necessitate the operation of uniformitarian plate tectonics. Thus any alternative model to plate tectonics in the Archaean must provide a mechanism for terrane accretion and associated compression. Bédard et al. (2013) built on the delamination-driven catalytic model of Bédard (2006), itself based upon various early models of vertical tectonics, suggesting that cratonic mobilisation in response to mantle convection currents could be a driving force for compression and terrane accretion. In this scenario proto-cratons develop deep high viscosity keels, formed via large scale delamination events of eclogite restites from differentiation of basaltic plateau type crust. This contributed to the top down formation of strong and buoyant subcratonic lithospheric mantle (SCLM). The stiff SCLM keel is considered to be subject to pressure from mantle currents, allowing it to drift (Bédard et al., 2013). Immature cratons, without large keels, would be static and could be accreted and/or subcreted onto the drifting, larger protocraton. Contractional structures would develop at the leading edge of drifting Archaean cratons without the need for subduction (Bédard et al., 2013). This model has received criticism from Wyman (2013b) who suggests it narrowly avoids being a variant on plate tectonics, highlighting that shield volcanos are considered to founder into the mantle but never lead to spontaneous subduction initiation and that rifts and transform faults that develop in the wake of mobile cratons resemble ocean spreading centres. Wyman (2013b) concludes that although the Bédard et al., (2013) model is thought provoking it cannot explain the formation of cratons such as the Superior Province in Canada.

1.4.4 Initiation of plate tectonics, when did it start?

Views on plate tectonics initiation differ wildly with some authors suggesting that plate tectonics operated through much of the Archaean, especially within the Neoarchaean (e.g., de Wit et al., 1992; Daigneault et al, 2002; Polat and Kerrich, 2001, Barley et al., 2006; 2008; Czarnota et al., 2010; Wyman, 2013a; 2013b), even as far back as the Eoarchaean (Dilek and Polat, 2008; Polat et al., 2009; 2011; Friend and Nutman, 2010). Other workers suggest that different plate tectonic regimes operated in different places within the Archaean and that regional and temporal differences controlled which was the more important, with localised regions of coeval vertical tectonics and plate tectonics during the Meso and Neoarchaean (e.g., Van Kranendonk et al., 2004; 2007). Other authors suggest that plate tectonics did not begin until the Paleoproterozoic (Brown, 2008) or the Neoproterozoic (Stern, 2005; 2011) and suggest that vertical tectonics, otherwise known as partial convective overturn, as described above, dominated the tectonic regime throughout the Archaean (e.g., Bédard et al., 2003; Bédard, 2006). It is suggested that a non-plate tectonic regime gave way to more uniformitarian processes due to planetary cooling, decay of radioactive isotopes and progressively increasing lithospheric strength which permitted subduction of oceanic crust as it became less buoyant on a cooling mantle (Van Kranendonk, 2007).

In summary, the majority of authors concur that plate tectonics was in operation during the Neoarchaean, with possibly both vertical tectonics and early plate tectonics occurring during the Mesoarchaean (e.g., Van Kranendonk, 2004). The operation of plate tectonics during the Neoarchaean agrees with the dominance of subduction accretion models for the amalgamation and formation of the EGS, although the occurrence of subduction-derived versus plume-derived volcanism in this region continues to be debated (e.g., Barnes et al., 2012; Fiorentini et al., 2012).

1.5 Komatiites; a near-exclusive feature of Archaean volcanism

A key feature of the Neoarchaean is the presence of komatiites. Komatiites are ultramafic lithologies that are the crystallisation products of ultramafic melts with >18 wt. % MgO, which commonly contain spinifex texture (Hill, 2001). Komatiites account for only ~1% of the entire Archaean rock assemblage (Arndt et al., 2008). They are confined to discreet time intervals within the Archaean at ~3.5 - 3.2 Ga (e.g., Barberton komatiites, South Africa) and ~2.7 Ga (Abitibi greenstone belt, Canada and Kalgoorlie Terrane, Western Australia), and are rare in the Proterozoic (e.g., Gilmour Island, Canada) and almost unknown of in the Phanerozoic, the unusual Cretaceous Gorgona flows being the only exception (Arndt et al., 2008). What makes komatiites interesting is their unusual and unique physical and chemical characteristics and what makes them important to understand is their association with nickel sulphide mineralisation. Exploration for nickel sulphide deposits over the past 30 years has driven research into how komatiites formed, where and how were they erupted and what might control the location and metal endowment of massive and disseminated sulphide ore bodies that they commonly contain. Unlike mineralisation associated with hydrothermal systems around intrusions, such as epithermal polymetallic vein deposits, which post-date their hosting stratigraphy, nickel mineralisation is syn-eruptive. A komatiite-hosted nickel-sulphide deposit's location, size and grade are largely controlled directly by the primary volcanic processes that operated over 2.7 billion years ago. Unlike other mineralised systems mined today, there are no modern analogues to these hot, fluid, nickel and platinum group element (PGE) bearing lavas so that reconstructing their eruption and emplacement mechanisms, as well as tectonic setting, is challenging. A detailed overview of komatiite volcanism in the Archaean is beyond the scope of this introduction (see Barnes, 2006b; Arndt et al., 2008). However, the next part of this introduction will discuss the formation and nature of nickel-sulphide deposits within komatiites, their common association with felsic volcanic sequences, the likely tectonic setting(s) of such felsic-komatiite associations and

whether such felsic volcanic sequences have a vital role to play in forming world-class nickel-sulphide ore deposits.

1.5.1 Definition

Komatiites have traditionally been defined as ultramafic volcanic rocks that can be diagnosed by the presence of spinifex texture (distinctive growths of large, skeletal, platy blades of olivine or acicular needles of pyroxene found in the upper parts of komatiite flows; Arndt and Nesbitt, 1982). However, studies of komatiite flow fields in the Yilgarn Craton (e.g., Hill et al., 1995) have shown that only a small proportion of such rocks exhibit spinifex texture. This prompted Hill (2001) to more broadly define komatiites as 'ultramafic lithologies which are the crystallisation products of ultramafic melts with >18 wt. % MgO'. The mineralogy of ultramafic rocks is relatively simple comprising of dominantly olivine, minor chromite, pyroxenes (augite, pigeonite, and bronzite), volcanic glass and occasionally plagioclase and/or amphiboles (Barnes, 2006b). Olivine makes up 40 - 80% of the primary mineralogy, although in the centre of thick adcumulate sequences the olivine content may be close to 100% (Arndt et al., 2008).

1.5.2 Komatiite textures

Komatiites were erupted at ~ 1400 - 1700ºC (e.g., Green, 1975; Huppert et al., 1984; Huppert and Sparks 1985a; Nisbet et al., 1993; Arndt et al., 2008), in what are thought to be largely submarine eruptions. They are inferred to have had very low viscosities; analogous to olive oil. The conditions within rapidly flowing, very low viscosity and extremely hot magmas produce a range of unusual structures and textures during crystallisation. The range of komatiite lithofacies has been developed and extensively described by Lesher et al. (1984), Lesher (1989), Hill and Gole (1990), Hill et al., (1990; 1995), Barnes (2006b) and Arndt et al., (2008). Komatiites exhibit

many unique lithofacies, rarely seen in basaltic lava flow fields, such as spinifex-textured, orthocumulate, mesocumulate and adcumulate facies (Arndt et al., 2008). The diversity of structures and textures in komatiites results mainly from their high eruption temperature and low viscosity but equally important may be the wide temperature interval between the liquidus of olivine and the appearance of the second mineral, clinopyroxene (Arndt et al., 2008). This temperature interval is vital in facilitating the formation of spinifex textures and assists the settling out of olivine phenocrysts, which is important for the formation of adcumulate textures (Arndt et al., 2008).

Spinifex textures (Lewis, 1971; Nesbitt, 1971) are a defining characteristic of komatiites, although these are less common in the ultramafic sequences of the Kalgoorlie Terrane (Hill et al., 1995). Many thin flows exhibit the typical textural sequence of Munro-style komatiite flows (Pyke et al., 1973; Fig. 1.3). Spinifex textures were originally considered to be a quench texture formed by rapid cooling (Nesbitt, 1971) but later experiments (e.g., Donaldson 1976, 1982) suggested that spinifex textures in fact formed under conditions of strong undercooling, not necessarily rapid cooling.

Figure 1.3. (Next page). A profile through a typical komatiite lava flow lobe, illustrating the characteristic petrological textures (modified after Pyke et al. (1973), Arndt et al. (1977) and Barnes (2006b). Included are the authors own hand specimen photographs from Xstrata Nickel Australasia's regional tenements in the Kalgoorlie Terrane of the EGS and from the Pyke Hill type locality in Ontario, Canada. The upper crust of the lava flow forms under a combination of very steep thermal gradients and high cooling rates producing the random spinifex (A1 and A2) zones (Faure et al., 2006). At the base of the A2 zone the steep thermal gradients coincide with reduced cooling rates, resulting in the formation of dendritic olivine under supercooled conditions. Parallel A3 olivine plates grow rapidly roughly downwards with their c-axis perpendicular to the isotherms (Arndt et al., 2008).

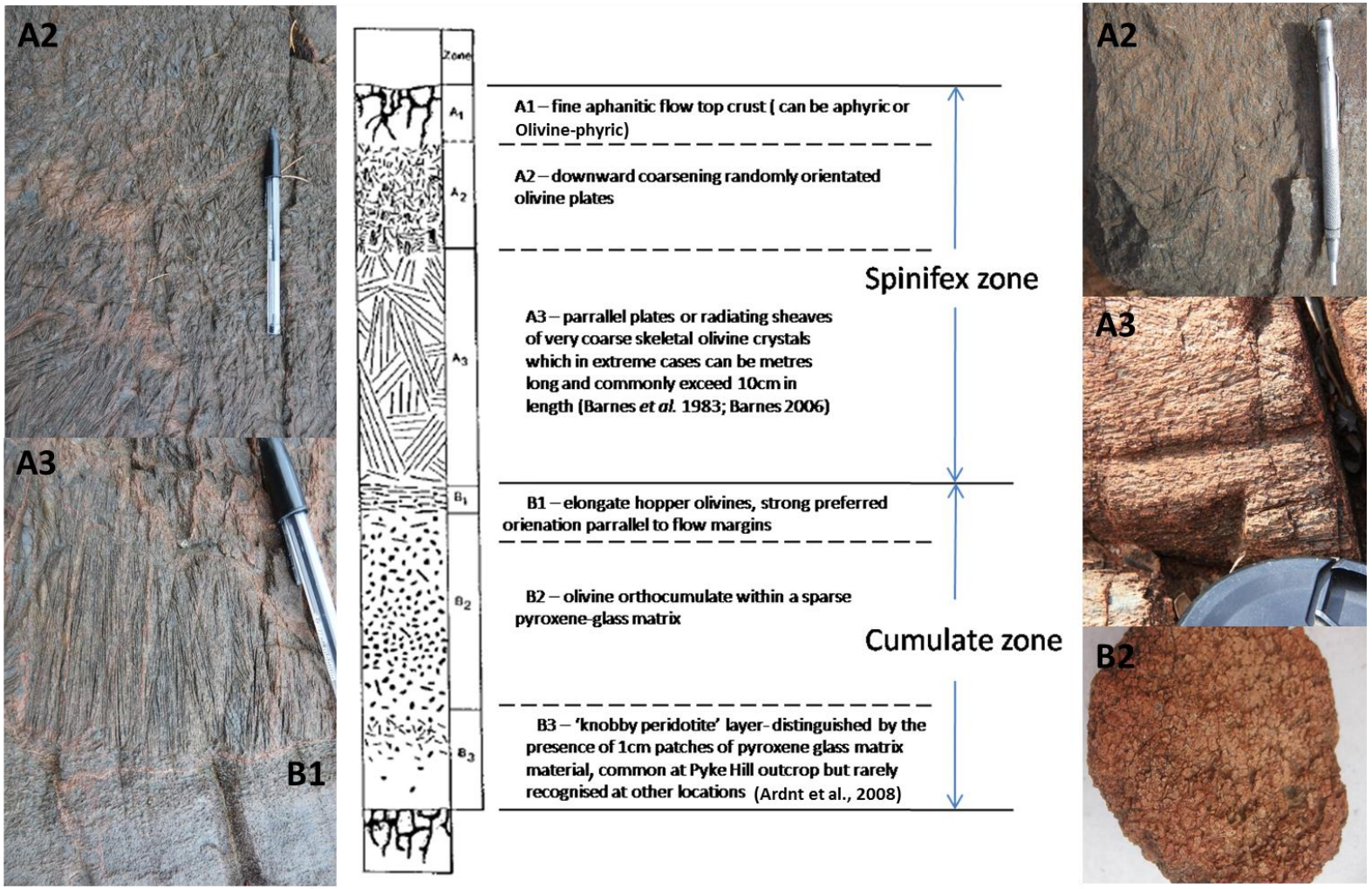
A2
A3
B1
Zone
A1
A2
A3
B1
B2
B3
A1 – fine aphanitic flow top crust (can be aphyric or Olivine-phyric)
A2 – downward coarsening randomly orientated olivine plates
Spinifex zone
A3 – parrallel plates or radiating sheaves of very coarse skeletal olivine crystals which in extreme cases can be metres long and commonly exceed 10cm in length (Barnes *et al.* 1983; Barnes 2006)
B1 – elongate hopper olivines, strong preferred orienation parrallel to flow margins
B2 – olivine orthocumulate within a sparse pyroxene-glass matrix
Cumulate zone
B3 – 'knobby peridotite' layer- distinguished by the presence of 1cm patches of pyroxene glass matrix material, common at Pyke Hill outcrop but rarely recognised at other locations (Ardnt et al., 2008)
A2
A3
B2

1.5.3 Physical volcanology

The physical volcanology of komatiites has been described by Hill et al. (1995) and Hill (2001). These latter authors proposed a composite komatiite flow field model which related all the common facies associations (spinifex through to adcumulates), based on field relationships seen in the Norseman-Wiluna and Forrestania greenstone belts of Western Australia. Hill et al. (1995) and Hill (2001) envisioned large sub-aqueous komatiite lava flow fields that had very high eruption rates. A largely subaqueous setting for the eruption of komatiites is implied by their common association with pillowed basalts, chert and banded iron formations (Groves et al., 1984; Claoué-Long et al., 1988). The full spectrum of textures seen in komatiites can be related to a lithological unit's relative position in the flow field; thick adcumulate bodies are formed in long-lived, proximal, preferred lava pathways, capable of thermal erosion of their substrate, whereas thin, differentiated and often spinifex textured flow units are episodically emplaced lava breakouts, often distal to the main rift, and originate from laterally confined lava pathways (Hill et al., 1995; Hill, 2001).

1.5.4 Formation of large adcumulate bodies

Much of the debate concerning komatiites centres around whether large thicknesses, tens to several hundreds of metres, of adcumulate-textured komatiites are extrusive or intrusively emplaced. Evidence for an extrusive origin for thinner spinifex-textured and orthocumulate ultramafic units is reasonably widespread, while evidence of an extrusive origin for mesocumulates and adcumulates units is normally inferred from their close spatial and temporal association with the former lower MgO units. Hill et al. (2004) found that many of the coarse-grained olivine orthocumulates at Black Swan, in the Kalgoorlie Terrane, exhibited vesicular textures. An extrusive origin at Black Swan is also indicated by fine-grained quench spinifex textures and the complex relationships and hybridisation that exist between the komatiite and dacitic

lavas (Hill et al., 2004). Vesicles are also described by Beresford et al. (2000) from Kambalda.

Hill et al. (1995) and Donaldson (1982) suggest that the close association of adcumulate bodies and spinifex textured rocks indicates an extrusive origin for thick adcumulate bodies. In several localities including Murrin Murrin (Barnes, 2006b) and Perseverance (Barnes et al., 1988; Dowling and Hill, 1993), olivine mesocumulates and differentiated spinifex lobes are interpreted to occur in a single continuous body of ultramafic rock. However, Trofimovs et al. (2003) suggest that in areas where there has been extensive deformation, such as Perseverance, the juxtaposition of adcumulate and spinifex-textured rocks may be entirely structural. Duuring et al. (2010) concurred with the latter authors and suggested that polyphase deformation at Perseverance could have structurally juxtaposed spinifex textured, stratigraphically higher, extrusive komatiite flows against the deeper adcumulate portions of the same extrusive flow.

Similarly, the origin of the Mount Keith ultramafic sequence has been debated for over thirty years with the thick mineralised adcumulate being alternately interpreted as a sub-volcanic sill (Naldrett and Turner, 1977; Rosengren et al. 2005; 2008; Fiorentini et al., 2012) or an extrusive lava flow(s) (Donaldson et al., 1986; Dowling and Hill, 1992; 1993; Hill et al., 1995). Rosengren et al. (2005; 2008), suggested that the mineralised Mount Keith adcumulate body was emplaced as a series of sub-volcanic sills intruded within and below an extrusive komatiite pile. The occurrence of apophyses of ultramafic material projecting into the overlying dacite, along with xenoliths of dacite within the Mount Keith ultramafic along its upper contact, as well as fine grained perceived chilled margins in the ultramafic unit at the upper contact are suggested to provide evidence for an intrusive origin for the ultramafic adcumulate unit (Rosengren et al., 2005; 2008). Fiorentini et al. (2012) suggest that the intrusive Mount Keith ultramafic unit may in fact represent part of a continuous sill along the Agnew-Wiluna greenstone belt from north of Albion Downs to Perseverance. An extrusive origin for komatiites at Mount Keith is suggested from the vertical and lateral gradation from mineralised ultramafic adcumulate into spinifex-textured komatiite flows (Hill et al., 1990; Hill and Dowling, 1992; 1993; Hill et al., 1995). Rosengren et al. (2005) however suggested that margins of the Mount Keith

Ultramafic unit are sheared and that it is in faulted contact with the spinifex bearing Cliffs ultramafic unit and therefore this contact is not conformable.

In proposed extrusive komatiite flow fields, olivine cumulates can form via two separate mechanisms at the base of long-lived lava pathways. Olivine cumulates containing predominantly lobate chromites, as seen at Perseverance and Mount Keith, are formed by in situ growth of olivine at very low degrees of undercooling at the base of flowing magma pathways. Preferred alignment of platy and elongate olivines, coupled with the occurrence of euhedral rather than lobate chromites, is indicative of formation via gravitational accumulation of transported olivine crystals within a long lived lava pathway (e.g., Black Swan; Hill et al., 2004).

1.6 Nickel sulphide formation in komatiites

1.6.1 Komatiite-hosted nickel sulphide deposits in Western Australia

Nickel sulphide ore bodies are important economic resources that are located predominantly within Archaean ultramafic successions. Ninety percent of Australia's nickel resources, derived from sulphide deposits, have been discovered within the EGS of the Yilgarn Craton, including, in the AWB, Mount Keith (~3.4 Mt global resource), Perseverance (~2.5 Mt) and Yakabindie (~1.7 Mt) (Hoatson et al., 2006). Nickel sulphide production in Australia is principally concentrated within these komatiite-hosted deposits, dated at ~ 2705 Ma, many of which are associated with felsic volcanic successions.

1.6.2 Sulphide formation

Sulphides form due to the segregation and concentration of drops of sulphide liquid from ultramafic or mafic magma, into which chalcophile elements are then partitioned (Naldrett, 2004). Komatiites are derived by very high degrees of partial melting within the mantle, approximately 30 - ≤ 50% (e.g., Arndt, 1977; Hertzberg and O'Hara, 1985; 1998; Hertzberg, 1992). Sulphur has a low concentration within the mantle (125 - 250ppm; McDonough and Sun, 1995). It is incompatible, meaning all of the sulphur is consumed at comparatively low degrees of partial melting (Naldrett and Barnes, 1986). Therefore, komatiites would have had a low sulphur content in the region of 250 - 500 ppm (Lesher and Stone, 1996; Lesher and Barnes, 2008). This is much lower than the sulphur capacity of komatiitic magmas at sulphide saturation, which is considered to be ≥ 1600 ppm (Shima and Naldrett, 1975; Barnes, 2007). Sulphur solubility in komatiite magmas is considered to exhibit strong negative dependence with respect to pressure, i.e. sulphur solubility increases with decreasing pressure (e.g., Naldrett, 2004; Barnes, 2006, Lesher and Barnes, 2008). Thus, komatiites are considered to arrive at the surface substantially undersaturated in sulphur (Lesher and Groves, 1986; Lesher and Barnes, 2008). The assimilation of continental crust, accompanied by fractionation of the magma, during a komatiitic magma's ascent to the surface has been shown by Lesher and Arndt (1995) to be insufficient to result in sulphide saturation of the magma. Therefore, it is largely considered that local contamination of komatiitic magmas, through the incorporation of sulphur-bearing country rocks, during eruption and emplacement at the surface, is the key mechanism that allows komatiite lavas to reach sulphur saturation (e.g., Lesher and Arndt, 1995; Lesher et al., 2001; Lesher and Barnes, 2008). Figure 1.4 illustrates how massive sulphide (Type 1) ore bodies are formed within erupting komatiite lavas.

Recent S and Fe isotope studies of Archaean komatiite-hosted nickel sulphide deposits on samples from the Agnew-Wiluna and Norseman-Wiluna greenstone belts of Western Australia, and the time-equivalent Abitibi greenstone belt in Canada, have indicated that sulphur in such deposits has previously been processed through the atmosphere and then accumulated on the ocean floor (Bekker et al., 2009). Such

studies indicate that externally derived sulphur had been involved in the formation of many large nickel sulphide deposits (Bekker et al., 2009; Fiorentini et al., 2012; Ripley and Li, 2013).

Komatiite ore bodies in Western Australia can either occur as primary magmatic-sulphide deposits, formed as described above, or as secondary laterite deposits developed over thick olivine cumulate units, whose occurrence is thus far limited to the Yilgarn Craton of Western Australia (Elias, 2006). Occurrences in the Archaean of the former, more common primary ore bodies can be split into two distinct types; -

- Type I deposits – Massive or net textured sulphide, which occurs at or near the basal contact of host ultramafic units, which are often localised in embayments that transgress the footwall rocks (e.g., Hill et al., 2004; Naldrett, 2004; Lesher and Barnes, 2008). Such deposits are formed through the accumulation of immiscible magmatic sulphide liquid at the basal contact of komatiite flows or perhaps in sub-volcanic ultramafic intrusions. Examples in the EGS include; The Kambalda Komatiite Formation, (Barnes, 2006b) and the Black Swan deposits (Dowling et al., 2004, Hill et al., 2004).
- Type II deposits – These occur as disseminated sulphides within olivine-rich komatiite units, typically lenticular adcumulate bodies (Arndt et al., 2008). Type II deposits dominate nickel sulphide mineralisation in the AWB (Grguric et al., 2006; Fiorentini et al., 2012). Examples of the latter include Mount Keith (Hill et al., 1995; Rosengren et al., 2005; 2007; 2008; Grguric et al., 2006) and the neighbouring Yakabindie deposits (Grguric et al. 2006; Arndt et al., 2008). Type II deposits also occur in the same belt in conjunction with Type I deposits at Perseverance (Barnes et al., 1988).

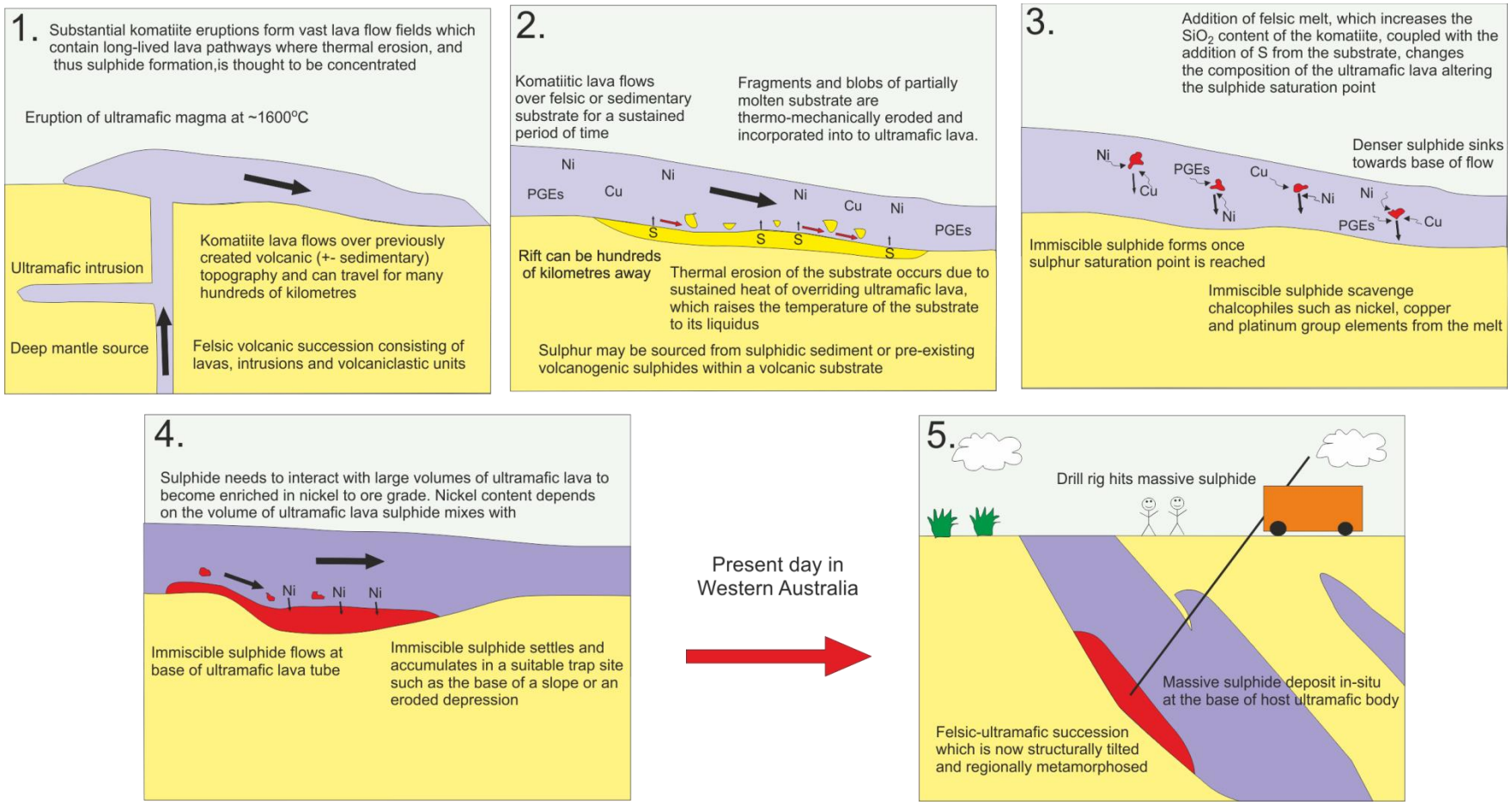

Figure 1.4. A schematic cartoon of Type 1 nickel sulphide formation in a komatiite lava flow field, based on Naldrett (2004) and Lesher and Barnes (2008).

Sulphide formation is thought to rely heavily on thermo-mechanical erosion of an underlying, often felsic, substrate that likely provides an external source of sulphur (Huppert and Sparks, 1985b; Barnes et al., 1988; Dowling et al., 2004; Naldrett, 2004; Fig. 1.4). However, Ripley and Li (2013) recently suggested that contamination and magma mixing may produce early sulphide saturation in ultramafic magmas without the addition of externally derived sulphur. Nonetheless, nickel sulphide deposits can only form in such cases from large-volume, open systems (Ripley and Li, 2013). The latter authors concluded that it was theoretically possible to form nickel sulphide deposits from the collection of cotectic proportions of sulphide but that this required large, but not unreasonable, volumes of magma (50 - >200 km^3). Sulphur isotope studies clearly indicated that externally derived sulphur had been involved in the formation of many large deposits (Ripley and Li, 2013). Key controls as to whether sulphur saturation is achieved in ultramafic lavas (or high level intrusions), is a combination of the duration and flux rate of ultramafic emplacement, the susceptibility of the substrate to thermo-mechanical erosion and the underlying substrate's sulphur content. Komatiites can achieve sulphur saturation from assimilation of a variety of crustal rocks, that contain pre-existing concentrations of sulphide, for example, by cannibalisation of VMS deposits or base metal horizons (e.g., Mount Keith; Fiorentini et al., 2012) or from thermo-mechanical erosion and incorporation of surficial or wall-rock sulphur-bearing sediments during emplacement (e.g., Kambalda; Bekker et al., 2009).

1.7 Thermal erosion

The ability of komatiite lava flows (or high-level sills) to thermally erode a sulphur-bearing substrate (or shallow level wall-rocks) over which they flow (or intrude) is considered as to be an essential mechanism for adding sulphur to ultramafic lavas (Nisbet, 1982; Huppert and Sparks, 1985b; Barnes, 2006a; Cas and Beresford, 2001; Fiorentini et al., 2012). The theory for thermal erosion developed through the

recognition that the linear hosts at Kambalda represent lava conduits and that the ore-localising embayments and adjacent sediment free zones might reflect chemical erosion (Naldrett, 2004; Arndt et al., 2008). Lava conduits at Kambalda, and Perseverance, were considered to have been emplaced as high-volume, fast, turbulent flows and that erosion and flow emplacement happened instantaneously and simultaneously (Williams et al., 1998; 2002). Williams et al. (2002) suggested that thermo-mechanical erosion becomes more effective for substrates that are unconsolidated and water rich. Geochemical analysis of komatiites at Kambalda, both mineralised and un-mineralised, have produced conflicting evidence for contamination and sediment assimilation although Lesher and Groves (1986) and Arndt and Jenner (1986), using Nd–Sm isotopic and rare earth elements (REE), suggested there was evidence in some komatiites for sediment assimilation.

Recently, Bekker et al. (2009) have inferred, from multiple S isotopes, that pyritic exhalative sulphides were the sulphur source for the komatiitic Ni-Cu-(PGE) deposits within the AWB. Ore-forming processes are considered to have involved incorporation of sulphur from pyrite-rich exhalative sulphide deposits during magma emplacement either along pre-existing fracture systems in submarine felsic volcanic successions or in lava channels (Barnes and Fiorentini, 2012). They considered that high fluxes of komatiite magma formed in long-lived high-level feeder conduits, rather than at the surface as extensive long-lived komatiite lava fields. These conduits are considered to be capable of assimilating crustal sulphur, at shallow levels within the sub-surface, with crustal sulphur derived from spatially associated felsic volcanic events (Barnes and Fiorentini, 2012). Fiorentini et al. (2012) highlight the association of felsic volcanic sequences, barren pyritic exhalative sulphides and mineralised komatiites along the axis of the AWB and conclude that the addition of crustal sulphur is a prerequisite for ore genesis in komatiite systems.

1.7.1 Thermo-mechanical erosion and sulphide formation in a bi-modal volcanic succession; examples from Black Swan and Perseverance

The Black Swan succession in the EGS shows a bimodal association of komatiitic and felsic volcanism containing a number of economically exploitable nickel sulphide deposits (Hill et al., 2004). Hill et al. (2004) suggest that the footwall succession of dacitic coherent lava and autoclastic breccias, overlain by a thick succession of olivine orthocumulates, mesocumulates and adcumulates, formed through a synchronous eruption of both dacitic and ultramafic lavas. Komatiite lava flowed over the uneven dacitic topography, resulting in thermo-mechanical erosion of the substrate, forming entrenched and long-lived lava tubes and pathways. Evidence for thermo-mechanical erosion comes from felsic inclusions within sulphide ore bodies and the preservation of a hybrid-textured basal layer beneath one of the sulphide bodies (Dowling et al., 2004). Such containment of immiscible sulphides at the base of deeply eroded channels may help to contain and concentrate the ore body. Thermo-mechanical erosion was concentrated on poorly consolidated felsic fragmental lithologies, thus the occurrence and location of thermo-mechanical erosion can be controlled by the underlying felsic substrate (Hill et al., 2004). A substrate composed of coherent lava and lacking in fragmental units may have been harder to erode in significant enough volumes, to promote sulphur saturation of the overriding komatiite lava.

However, Cas et al. (2011) questioned whether the dacitic units at Black Swan actually represent dacitic lavas and reinterpreted the Black Swan succession as an intrusive association of dacites and komatiites. They suggest the dacitic units are too thin to be lavas and that there is no evidence of autobrecciation or quench fragmentation. Therefore, the dacites are considered to be emplaced before the komatiites as part of a major sub-surface felsic sill/intrusive complex, which was then intruded by a komatiitic sill (Cas et al., 2011).

The contrasting interpretations made at the same deposit from examination of similar drill core examples, as described previously for both Black Swan and Mount

Keith is a theme throughout current literature within the EGS, particularly the AWB. For example the origin of the komatiite hosted nickel-sulphide deposits at Perseverance have also been debated. Barnes et al. (1988) suggested that the Perseverance adcumulate body (PUC) represents a very large komatiite lava river, which extensively thermally-eroded its base. The thermo-mechanical erosion down cut through several hundred metres of felsic volcanic and volcaniclastic rocks, and thermal erosion was halted by the presence of a lower komatiite unit (East Perseverance Komatiite) due to its respectively much higher melting temperature (Barnes et al., 1988). Truncation of apparent marker horizons was considered be due to thermo-mechanical erosion of the substrate (Barnes et al., 1988). This study was thought to provide strong evidence for the operation of thermo-mechanical erosion within a vast komatiite flow field. However Trofimovs et al. (2003) disputed the interpretation of Barnes et al. (1988) and argued for an intrusive origin for the PUC, citing apparent chilled contacts between the PUC and overlying felsic units, as well as the lack of unequivocal evidence for the truncation of marker horizons. Duuring et al. (2010) suggested that both an extrusive or intrusive genetic model for the Perseverance deposit was possible and that the present geometry of the Perseverance deposit is primarily controlled by volcanic processes, which included thermo-mechanical erosion of the footwall rocks and channelling of the mineralised komatiite lava. The latter authors also consider that subsequent deformation events have resulted in the physical remobilisation of massive sulphides up to 20m from their primary footwall positions. Remobilisation of sulphide was also acknowledged by Barnes et al (1988). Both Barnes et al., (1988) and Duuring et al., (2010) emphasised volcanic processes as the first order control in the formation of the Perseverance deposit.

1.8 Ultramafic-felsic successions within the EGS

Several mineralised ultramafic successions in the EGS of Western Australia are associated with felsic lithologies. Many of the examples within the EGS have been described above including Black Swan (Hill et al., 2004, Dowling et al., 2004),

Perseverance (Barnes et al. 1988; Trofimovs et al., 2003; Duuring et al., 2010), Boorara (Trofimovs et al., 2004; 2006), Mount Keith (Donaldson et al., 1986; Hill and Dowling, 1993; Hill et al., 1995; Rosengren et al., 2005; 2008), the Black Flag Group (Morris and Witt, 1997), Melita, Jeedamya and Kanowna (Morris, 1998; Brown et al., 2002) and the Cosmos region (Langworthy and Vallance, 2004). However, the majority of studies, particularly prior to the mid-2000s focused on the emplacement mechanisms of komatiites and associated mineralisation. In-depth studies that are specifically focused on the non-ultramafic volcanic centres within the EGS are growing in number as the importance of these rocks for interpreting the tectonic setting of the EGS is recognised (e.g. Czarnota et al., 2010; Barnes et al., 2012) and as the wider debate on the operation of plate tectonics in the Archaean continues (e.g., Wyman 2013; Bédard et al. 2013). Literature on felsic and intermediate volcanism in the EGSs is growing and how the location and nature of felsic volcanism may influence and facilitate nickel sulphide mineralisation within komatiites is becoming an area of increasing research (e.g., Bekker et al., 2009; Fiorentini et al., 2012).

As yet the majority of published data on the Kalgoorlie Terrane indicates that felsic volcanism in this terrane was dominated by TTD-affinity volcanism (Kositcin et al., 2008). Within the AWB, in which Cosmos lies, dacitic volcanic rocks are proposed to have a strong TTD affinity and are associated with mineralised komatiites (Fiorentini et al., 2012). The petrogenesis of TTD-affinity volcanic successions and TTG-affinity intrusions within the Archaean remains contentious and has great implications for the geodynamic settings of such successions.

1.8.1 Tonalite-trondhjemite-granodiorite intrusions and tonalite-trondhjemite-dacite volcanism in the EGS

Most Archaean felsic rocks have geochemical signatures indicative of derivation from meta-basaltic sources with a garnet-bearing residue at depths of 40-60 km (e.g., Smithies, 2000; Moyen and Stevens, 2006; Moyen, 2009; 2011; Moyen and Martin, 2012). Moyen and Stevens (2006) suggested that TTG rocks are generated by high pressure melting of basalt and that this does not necessarily imply they have to

be generated by melting of a subducting slab. Bédard (2006) suggested from mass balance calculations that the volume of TTG intrusions and volcanic rocks within the north-east Superior Province is too high to be generated in a subduction zone, unless faster rates of subduction were operating to process enough crust to generate TTG in the high volumes seen within this craton. Some geodynamic modelling (e.g., Syracuse et al., 2010) has suggested that slow thermal diffusion from the convecting wedge can only heat up the top 1 - 2 km of slab to H_2O saturated solidus conditions. Therefore, most of the slab remains subsolidus, regardless of the assumed convergent rate or the ambient mantle temperature. Consequently, Bédard (2006) suggested that early generations of Archaean TTG were in fact formed due to crustal anatexis at the base of a thick basaltic crust. Earlier TTG rocks were then subsequently re-melted by mafic-ultramafic magma pulses (Bédard, 2006). Wyman (2013a) criticised Bédard's (2006) mass balance calculations, suggesting they do not take into account the role of intra- or sub-crustal processes in generating TTG compositions. Wyman (2013a) suggests that most TTG found in long-lived terranes cannot be derived by direct slab melting and that TTG volume and genesis reflects multi-stage granitoid generation processes (e.g. Whalen et al., 2002) thus models invoking generation of TTG by slab melting alone are invalid.

In a review of forty years of TTG research, Moyen and Martin (2012) concluded that there was growing recognition of the fact that both slab melting (Fig. 1.5c) and non-subduction intra-plate models, such as melting of a delaminated crustal fragments (Fig. 1.5a) or melting at the base of thickened crust due to rising mantle plumes (Fig. 1.5b), are valid petrogenetic processes for various rocks within the TTG sodic granitoid group. Moyen and Martin (2012) conclude that the high pressure sub-group under the TTG umbrella is most likely to be subduction-related, while the low pressure sub-group is most likely to be due to crustal anatexis of thickened crust. The rest of the TTG sodic granitoids, accounting for 60% of TTG occurrence, belong to the medium-pressure group and are somewhat ambiguous. This TTG group form along a 15 – 20 °C/km geotherm that is too low for a plateau geodynamic setting but probably too hot for subduction, even taking into account hotter Archaean subduction zones (Moyen and Martin, 2012). Interaction between mantle plumes and convergent

margins could account for locally higher geothermal gradients and thus generation of these ambiguous TTG suites. The generation of compositionally variable TTG granitoids, and associated TTD volcanic successions, cannot be accounted for by one petrogenetic process and/or geodynamic setting. It is likely that TTG melts were generated in several tectonic environments, which is suggested by their compositional variability (Moyen and Martin, 2012). This is easier to explain in an Archaean in which plate tectonics existed and resulted in interaction between mantle plumes and a variety of geodynamic settings, including subduction zones. Moyen and Martin (2012) showed that there are some high pressure TTG compositions that are hard to generate in any geodynamic setting other than a hot Archaean subduction zone, which provides further evidence for the operation of uniformitarian plate tectonic scenarios within the Archaean.

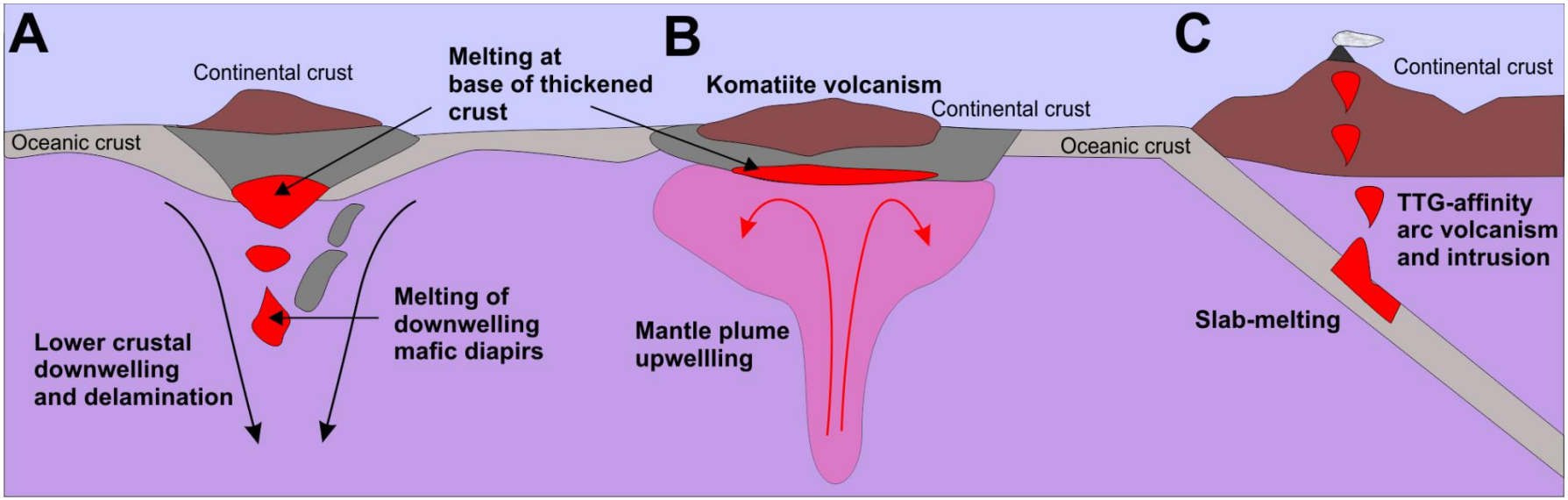

Figure 1.5. Schematic illustration showing the possible geodynamic settings and formation of TTG-affinity melts; (A) Over a down-welling zone, portions of the mafic lower crust, thickened by tectonic stacking or plume activity delaminate from the base of the crust and sink into the mantle. Mafic rocks are heated and carried into the garnet stability field forming TTG-affinity melts: (B) A mantle plume generates a thick oceanic plateau type crust. The base of the thickened crust melts within the garnet stability field to produce TTG melt: (C) Melting of a subducted slab in a hot Archaean subduction zone can produce TTG melt. Red = partially molten mafic rocks. Dark grey = mafic rocks. Brown = continental crust. Light grey = oceanic crust (modified after Moyen and Martin, 2012).

1.9 Geology of the Cosmos region, previous research and motivation for this study

1.9.1 Location

The Cosmos mine area and surrounding tenements are located 35 km north of Leinster and 370 km north of Kalgoorlie, in the Eastern Goldfields of Western Australia (Fig. 1.6). The Cosmos region straddles the Lake Miranda salt lake system, lies to the south of the historic gold mining region of Kathleen Valley and is located on the Yakabindie Pastoral Station. Geologically the Cosmos mine site lies within a western segment of the AWB, which forms part of the Kalgoorlie Terrane of the EGS (Fig. 1.1 and 1.6). The mineralised ultramafic belt within the Cosmos region is situated several tens of kilometres to the west of the main ultramafic belt within the eastern segment of the AWB. This eastern segment hosts several large nickel sulphide deposits such as Mount Keith and Perseverance (Fig. 1.6). The geology of this region has already been discussed in detail in Section 1.1.

1.9.2 History of mining in the Cosmos region

The nickel prospectivity of the Cosmos greenstone belt, which extends north-south between Kathleen Valley and Lake Miranda, was first identified by Anaconda exploration company, following the discovery of the Mt Goode (Anomaly 1) disseminated nickel sulphide deposit in the early 1970s (Stuff, 2011). Prior to this the area had only been historically explored for gold and to a lesser extent copper. Gold was discovered near Kathleen Valley Station in 1897 and mined, along with local copper finds, until the 1940s. Exploration activities from the 1940's through to the 1970's were very limited in the Kathleen Valley and surrounding area.

Xstrata Nickel Australasia (XNA), and previously Jubilee Mines, actively explored in the Kathleen Valley region from 1987. Much of this exploration concentrated on gold mineralisation centred around the historic gold workings of Yellow Aster, Nils Desperandum and Mossbecker in the Kathleen Valley (Stuff, 2011). In 1997 Jubilee Mines discovered the Cosmos massive nickel sulphide deposit on one of their tenements to the south of Kathleen Valley, resulting in a switch in focus from gold to nickel exploration (Fig. 1.7). A subsequent massive nickel sulphide deposit, Cosmos Deeps, was discovered within the sub-surface, some 300-400 metres below the Cosmos nickel sulphide deposit (Fig. 1.8). Open pit mining of the Cosmos deposit ceased in 2003, whilst underground mining of the Cosmos Deeps deposit commenced during this same period. Cosmos produced 37,177 tonnes of contained nickel metal from 427,330 tonnes of ore at an average grade of 8.70% and Cosmos Deeps produced 42,060 tonnes of contained Ni metal from 680,598 tonnes of ore at an average grade of 6.18% (Stuff, 2011). Both massive sulphide, and in the case of Cosmos Deeps, breccia sulphide, deposits were very high tenor, in comparison to other occurrences of typically low grade, disseminated nickel sulphide deposits within the AWB, such as Mount Keith (e.g., Hill et al., 1995: Rosengren et al., 2005, Beresford et al., 2004). The majority of nickel sulphide deposits in the AWB tend to have a larger tonnage of ore but at a much lower grade. These include Perseverance, Rocky's Reward and Harmony (69.8 Mt of ore at 2.2% Nickel combined) at Leinster, located approximately 40 km south of Cosmos, and the Yakabindie (270 Mt of ore at 0.53% Nickel), Cliffs (5.7 Mt of ore at 2.3% Nickel) and Mount Keith (420 Mt of ore at 0.6% Nickel) deposits to the north of the Cosmos region (Stuff, 2011; Fig. 1.7).

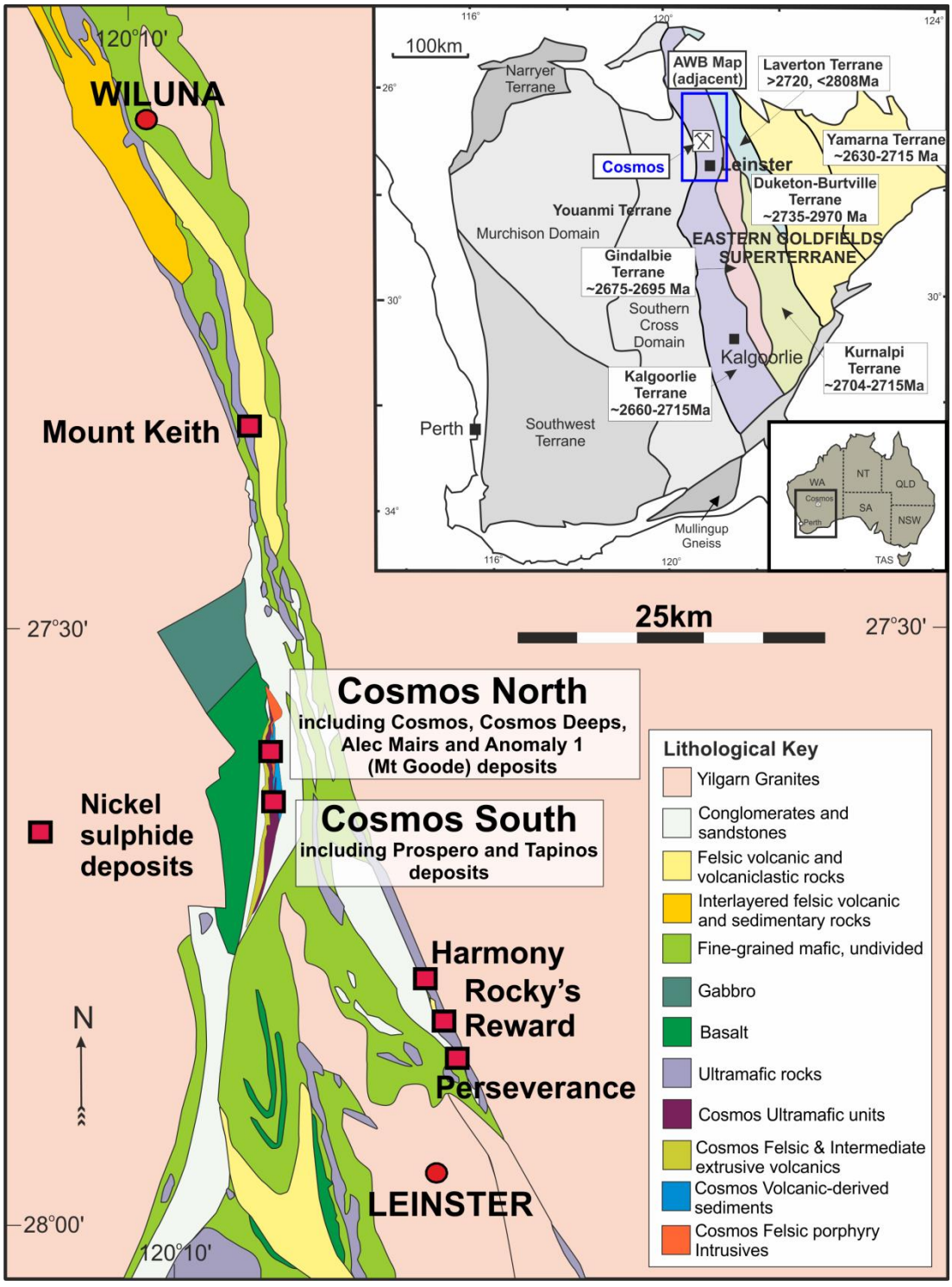

Figure 1.6. Simplified geological map of the Agnew-Wiluna Greenstone belt, showing the location of the Cosmos Mine site and other significant nickel sulphide deposits within the area (modified after GSWA (2009 and XNA in-house maps). Inset – Map showing the location of the Agnew-Wiluna greenstone belt within the Eastern Goldfields Superterrane of the Yilgarn Craton (modified after Cassidy et al. (2006), Kositcin et al. (2008) and Pawley et al. (2012).

XNA acquired the Cosmos South tenement in April 2003 to explore the southern strike extent of the Cosmos Ultramafic belt (Fig. 1.7). This resulted in the discovery of the Alec Mairs and Tapinos/Prospero massive nickel sulphide deposits. The Alec Mairs complex lies 400 - 700 m south of the Cosmos Deeps deposit and consists of several small massive, breccia and stringer nickel sulphide pods (Fig. 1.7). The Prospero and Tapinos nickel sulphide deposits are located in the Cosmos South region, 4.5 km south of Cosmos/Cosmos Deeps. Subsequent drilling in the Cosmos North region, continuing until the end of 2011, discovered several reasonably high tenor Type II disseminated nickel sulphide deposits within the Alec Mairs complex.

All deposits within the region were mined from underground apart from the Cosmos deposit that was mined by open pit. Mining operations at Tapinos and Prospero finished in January 2012 with all infrastructures removed and dewatering ceased. Cosmos Nickel mine ceased mining operations in September 2012 and was placed onto care and maintenance after a takeover of Xstrata by Glencore.

1.9.3 Geology of the Cosmos region

Cosmos mine concession comprises a package of felsic to intermediate volcanic rocks and volcaniclastic units, sediments, ultramafic units and polymictic Jones Creek Conglomerates (Stuff, 2011; Fig. 1.7). The regolith attains a maximum thickness of some 40 - 80 m of weathered material and comprises alluvial sands and gravels, transported clays and relict saprolitic clays (Stuff, 2011). Surface outcrop is sparse in the region, particularly in the vicinity of Lake Miranda. Prior to this study two ultramafic units were recognised within the Cosmos area; the Western Ultramafic and the Cosmos Ultramafic Sequence. The latter hosts all know sulphide mineralisation, whereas the Western Ultramafic unit is entirely barren. Within the tenement package the Cosmos Ultramafic Sequence reaches a maximum thickness of ~500 m towards the northern end of tenement but appears to thin to the south of Lake Miranda. The ultramafic units are underlain by a felsic volcanic footwall that prior to this study was poorly constrained. The Cosmos Ultramafic Sequence is unconformably

overlain by a volcanically derived sedimentary package. The sequence dips sub vertically but faces east.

1.9.4 Sulphide deposits of the Cosmos region

There are several Type I high grade nickel sulphide deposits within the Cosmos region, as described above, which are largely of high tenor and are considered to be originally komatiite-hosted, magmatic nickel sulphide deposits (Langworthy and Vallance , 2004; Hill and Dowling, 2008; Denny, 2010; Kaye et al., 2010; 2011; de Joux et al., 2013). Sulphide mineralisation style is variable. Massive, breccia and stringer sulphides typify the Type I deposits of Cosmos, Cosmos Deeps, Alec Mairs in the Cosmos North Region and Prospero and Tapinos in the Cosmos South region (Fig. 1.8). The majority of these Type II deposits occur along the basal contact of the Cosmos Ultramafic Sequence, although interestingly the Cosmos Deeps deposit is almost entirely encased within the footwall felsic volcanic sequence several tens of metres below the basal contact of the Cosmos Ultramafic Sequence. Hill and Dowling (2008) also noted that the Alex Mairs AM5 massive sulphide deposits protruded into the footwall felsic volcanic sequence.

Figure 1.7. (Next page). Left - Aerial photograph of the Cosmos mine showing the main nickel sulphide deposits and ultramafic units in the region, as well as the region of focus for this study. Right – Surface geology of the Cosmos region again showing the main sulphide deposits (modified from XNA in-house maps).

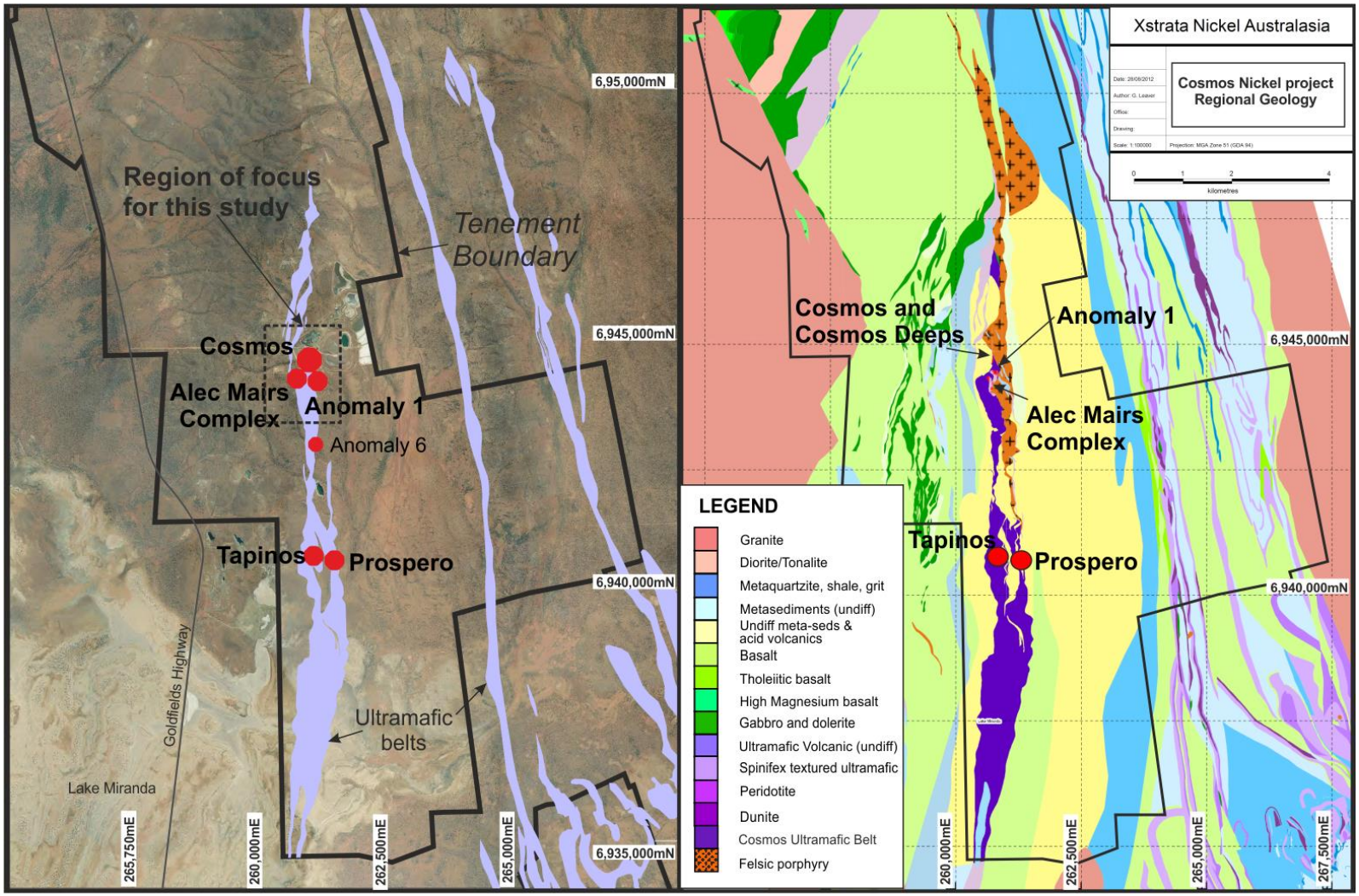
Region of focus for this study
Tenement Boundary
Cosmos
Alec Mairs Complex
Anomaly 1
Anomaly 6
Tapinos
Prospero
Ultramafic belts
Goldfields Highway
Lake Miranda
6,95,000mN
6,945,000mN
6,940,000mN
6,935,000mN
265,750mE
260,000mE
262,500mE
265,000mE
Xstrata Nickel Australasia
Cosmos Nickel project Regional Geology
Cosmos and Cosmos Deeps
Anomaly 1
Alec Mairs Complex
Tapinos
Prospero
LEGEND
Granite
Diorite/Tonalite
Metaquartzite, shale, grit
Metasediments (undiff)
Undiff meta-seds & acid volcanics
Basalt
Tholeiitic basalt
High Magnesium basalt
Gabbro and dolerite
Ultramafic Volcanic (undiff)
Spinifex textured ultramafic
Peridotite
Dunite
Cosmos Ultramafic Belt
Felsic porphyry
267,500mE

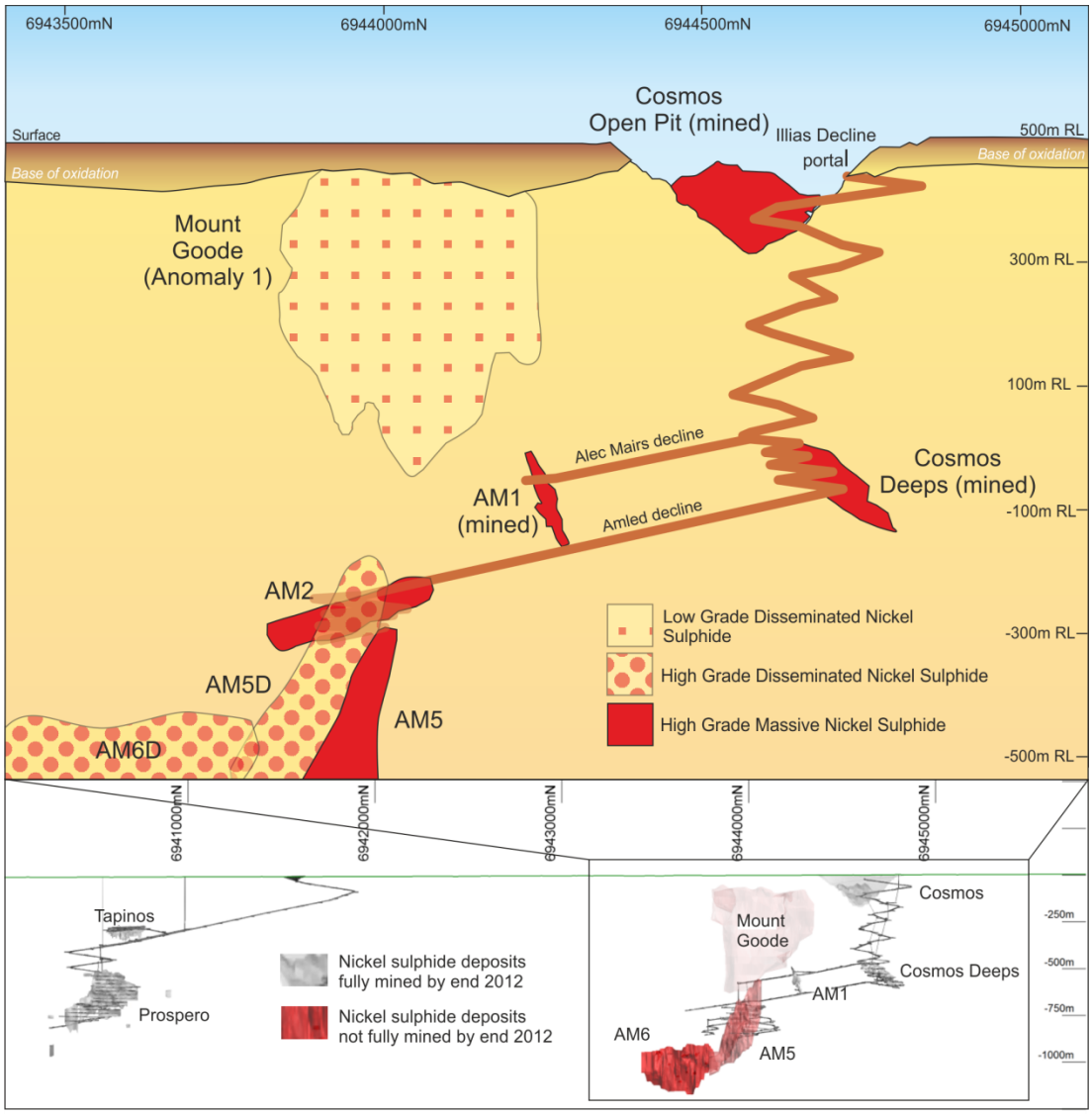

Figure 1.8. Long section through the Cosmos nickel sulphide deposits showing the deposits of both north and south Cosmos (looking west). A larger scale long section of the Cosmos North region is shown above, which was the focus of the footwall study, showing the mineralisation style of different deposits (modified after XNA in-house maps).

The association of massive and breccia sulphides hosted within the footwall volcanic rocks has led to debate over the extent of structural modification of sulphide deposits (e.g. Langworthy and Vallance, 2004; Hill and Dowling, 2008; Stuff, 2011). While some deposits are thought to be largely intact deposits at the base of host ultramafic flows (Cosmos and Tapinos) others such as Cosmos Deeps and Prospero are suggested to be strongly structurally modified and deformed (Langworthy and Vallance, 2004). Prospero represents an apparently continuous zone of structurally re-

mobilised massive-breccia-stringer Fe-Ni-Cu sulphide mineralisation, which is variably deformed and boudinaged, hosted in both felsic and ultramafic volcanic rocks (Stuff, 2011). However, Hill and Dowling (2008) suggested the association of massive sulphides within the felsic footwall at Alec Mairs represented possible primary depositional structures and that fractionated sulphide liquids percolated down into the footwall. The Cosmos Ultramafic Sequence also hosts several Type II low to moderate grade disseminated sulphide bodies (e.g., Mount Goode; AM5D, AM6D) that are hosted by meta-mesocumulates and meta-adcumulates several tens of metres above the basal contact of the Cosmos Ultramafic Sequence (Fig. 1.8).

Sulphide mineralisation is dominated by pentlandite and pyrrhotite, with lesser amounts of pyrite, chalcopyrite, millerite and heazlewoodite. Nickel arsenides are occasionally encountered, such as gersdorffite and maucherite, which provided significant challenges during ore processing. The mineralogy, texture, fabric and location of the nickel sulphides at Cosmos are the end products of a complex igneous, metamorphic and deformation history (Hill and Dowling, 2008). The mineralogy of primary Fe-Ni-Cu-S sulphides is the result of solid-state exsolution of pyrrhotite, pentlandite and chalcophyrite from monosulphide solid solution - MSS (a nickel-rich pyrrhotite phase) or solidified sulphide-oxide liquid (Naldrett, 1969; Ebel and Naldrett, 1996; Hill and Dowling, 2008).

1.9.5 Nature of the ultramafic units at Cosmos

The Cosmos Ultramafic Sequence consists of thick, dominantly mesocumulate and adcumulate ultramafic units with associated thin flow units. The Cosmos Ultramafic Sequence is underlain by a footwall volcanic sequence, whose internal architecture, prior to this study, was poorly constrained. Hill and Dowling (2008) identified spinifex-textured komatiites, olivine-pyroxene cumulates, olivine orthocumulates, olivine mesocumulates and olivine adcumulates, moving up through the stratigraphy, in the vicinity of Alec Mairs. These lithological units are encountered throughout the North Cosmos region. The igneous assemblages of olivine-pyroxene-

chromite-liquid have been metamorphosed to various proportions of metamorphic olivine, serpentine, anthophyllite, enstatite, talc, tremolite, actinolite, gedrite, cummingtonite, diopside and chlorite (Hill and Dowling, 2008). Thin low MgO units (<10 m) have been positively identified immediately adjacent to footwall contacts at Alec Mairs and have been interpreted to be spinifex-orthocumulate textured flow lobes (Hill and Dowling 2008; Denny, 2010). Although the primary spinifex-textured or olivine cumulate textures are not preserved, the A and B zones of the flows can be recognised by the relative proportions of metamorphic olivine, tremolite and chlorite and the presence of disseminated, coarse-grained skeletal chromite, along with the whole-rock composition of particular intervals (Hill and Dowling, 2008). The presence of these units immediately above the footwall contact underpins the interpretation that the Cosmos Ultramafic Sequence began as a dynamic thin flow-system that evolved into a high-volume internal pathway and/or channelised flow field (Denny, 2010). Hybrid rocks have also been identified close to the basal contact in the vicinity of the AM5 massive sulphide deposit and have been interpreted to be komatiite lava involved in thermo-mechanical erosion of the underlying felsic and intermediate substrate (Hill and Dowling, 2008).

The Western Ultramafic unit consists of olivine mesocumulates and orthocumulates, which have undergone pervasive serpentinisation and formation of metamorphic olivine obscuring the primary cumulate textures. Despite abundant exploration drilling within this unit, it has never been found to host nickel sulphide mineralisation and is thus considered to be entirely barren. Consequently, it has received little attention during in-house research projects. It lies stratigraphically below the Cosmos Ultramafic sequence, encased within the felsic and intermediate volcanic footwall to the Cosmos Ultramafic Sequence.

1.9.6 Previous research and Thesis motivation

While the mineralogy and lithological associations of the ultramafic units are relatively well understood, the footwall and hangingwall lithologies that enclose the ultramafic units are poorly constrained. All known nickel-sulphide deposits have a

stratigraphic footwall composed of felsic and intermediate volcanic lithologies. However, time constraints on logging during active drilling prior to this study, coupled with mineralisation within the footwall rarely extending beyond a few metres below the basal contact, resulted in much of the footwall succession being bulk logged as a generic felsic volcanic unit. Similarly the un-mineralised hangingwall succession had also been paid little attention, although the angle and direction of drilling meant that the hangingwall succession was seldom intersected in drilled holes.

Previous work in the Cosmos region has been largely internal and has focused on sulphide mineralogy, textures and style of mineralisation, as well as some pilot study work on the nature and likely emplacement mechanisms of the ultramafic units, as described above (Hill and Dowling, 2008; Denny, 2010). Undoubtedly these studies provided vital information on mineralisation processes and styles within the Cosmos greenstone belt and helped focus exploration strategies, as well as provide important information for mine development and ore processing. Without a detailed study of the non-ultramafic lithologies, an understanding of the likely environment of deposition, possible tectonic setting and age of the sequence, as well as the possible spatial association of massive sulphide deposits with specific footwall lithologies is not possible. Consequently, the Cosmos greenstone succession has not been placed in a regional context and its association with, or lack thereof, other nickel-sulphide deposits within the AWB has not been more than loosely speculated upon.

Limited previous in-house interpretation by Jubilee Mines prior to this study indicated that the footwall in the region of Cosmos Deeps was composed of large volumes of granodiorite intrusions (Vallance, 2003). Annual reports to the Western Australia Department of Mines and Petroleum (DMP) have described that "the project area comprises a package of felsic to intermediate volcaniclastic sediments and relict polymictic Jones Creek Conglomerates. These units interfinger with….two ultramafic komatiite flows, the Western and Central Ultramafic" (now referred to as the Western Ultramafic unit and the Cosmos Ultramafic Sequence respectively; Stuff, 2011).

An honours thesis was undertaken by Farran in 2008, which focused on an identifying the protoliths of the footwall and hangingwall volcanic successions to the

Prospero and Tapinos massive sulphide deposits, with an aim to establish the volcanic architecture in this region. Farran (2008) discovered a complex stratigraphy of interleaved ultramafic cumulates and felsic to basaltic volcanic and volcaniclastic rocks. These were considered to have formed via episodic volcanism in a convergent margin on account of apparent calc-alkaline and transitional magmatic affinities. However, the studied region is 4 - 5 km to the south of the Cosmos North region raising the possibility that there may be significant stratigraphic variations along the strike of the Cosmos ultramafic belt (Fig. 1.7). The work was never published, but did provide an initial insight into the complex nature of the non-ultramafic volcanic stratigraphy in the region that ultimately led to the instigation of this PhD focused on the Cosmos North region. There has been no peer reviewed material published on the Cosmos succession prior to this study and the mine has not taken part in regional collaborative research initiatives, such as the P710 AMIRA report (Beresford et al., 2004) so the region's position within a regional tectonic and stratigraphic framework was not known. References to Cosmos in a recent paper on the structural evolution of the AWB are vague (Duuring et al., 2012). These authors concluded that further investigation was required in the Cosmos/Kathleen Valley region to resolve how this domain relates to the rest of the AWB.

This thesis was commissioned first by Jubilee Mines, then by Xstrata Nickel Australasia (XNA) to focus on establishing the nature and composition of the footwall volcanic sequence, and to a lesser extent the hangingwall sedimentary sequence. The aim was to establish the geodynamic setting, emplacement mechanisms and geochemical affinity of the footwall volcanic sequence. A structural interpretation of the Cosmos greenstone belt and detailed geochemical analysis of the individual komatiite units was intended to be undertaken separately by consultants employed by XNA.

1.10 Thesis layout

This thesis is set out as three separate papers that have been published or are intended to be submitted for publication in due course.

The first paper, Chapter Two, is focused on development of the Cosmos footwall and hangingwall stratigraphy. This is largely based on the primary volcanic textures and mineral assemblages preserved in the mid-amphibolite metamorphosed succession and the subsequent correlation of volcanic units to build up a picture of the subsurface stratigraphy.

The second paper, Chapter Three, undertakes a detailed geochemical analysis of the footwall volcanic succession beneath the Cosmos Ultramafic Sequence and the implications the geochemical affinity of the volcanic footwall has for interpretation of the geodynamic setting of Cosmos and the wider AWB.

The third paper, Chapter Four, combines the newly developed stratigraphic framework and geochemical attributes of the succession with detailed U-Pb dating of several units from different stratigraphic levels within the succession. A detailed analysis of the temporal evolution of the Cosmos greenstone succession is provided. The paper also discusses the relationship of the Cosmos greenstone belt to adjacent mineralised volcanic sequences and how the Cosmos succession fit into current geodynamic frameworks for the EGS.

In Chapter Five, a detailed model of the evolution of the geodynamic setting of the Cosmos region, and wider AWB and EGS, between ~2755 - 2655 Ma, is provided.

Chapter Six presents a summary of the findings of this research, discusses the remaining unanswered questions and potential avenues for future studies.

Each individual paper provides a specific introduction to the geological background relevant to the topic of the chapter, as well as a brief description of the methodology. Detailed methodology can be found within the Appendices one to six.

1.11 References

Arndt, N. T., 1977. Ultrabasic magmas and high-degree melting of the mantle. Contributions to Mineralogy and Petrology 64(2), 205-221.

Arndt, N. T., Nesbit, E. G., 1982. What is a komatiite? In; Arndt, N. T., Nesbit, E. G., (Eds.). Komatiites. George Allen and Unwin, London, pp19-28.

Arndt, N. T., Jenner, G. A., 1986. Crustally contaminated komatiites and basalts from Kambalda, Western Australia. Chemical Geology 56, 229-255.

Arndt, N. J., Naldrett, A. J., Pyke, D. R. 1977. Komatiitic and iron-rich tholeiitic lavas of Munro Township, northeast Ontario. Journal of Petrology 18, 319-369.

Arndt, N. T., Lesher M. C., Barnes S. J. 2008. Komatiite. Cambridge University Press, Cambridge.

Barley, M. E., Eisenlohr, B. N., Groves, D. I., Perring, C. S., Vearncombe, J. R., 1989. Late Archean convergent margin tectonics and gold mineralisation: a new look at the Norseman-Wiluna belt, Western Australia. Geology 17, 826–829.

Barley, M. E., Brown, S. J. A., Krapež, B., 2006, Felsic volcanism in the eastern Yilgarn Craton, Western Australia: Evolution of a Late Archean convergent margin. Geochimica et Cosmochimica Acta 70, A35.

Barley, M. E., Brown, S. J., Krapež, B., Kositcin, N., 2008. Physical volcanology and geochemistry of a Late Archaean volcanic arc: Kurnalpi and Gindalbie Terranes, Eastern Goldfields Superterrane, Western Australia. Precambrian Research 161(1), 53-76.

Barnes, S. J., Gorton, M. P., Naldrett, A. J., 1983. A comparative study of olivine and clinopyroxene spinifex flows from Alexo, Abitibi greenstone belt, Ontario, Canada. Contributions to Mineralogy and Petrology 83(3-4), 293-308.

Barnes, S. J., 2006a. Komatiite-hosted nickel sulfide deposits: geology, geochemistry, and genesis. Society of Economic Geologists Special Publication 13, 51–118.

Barnes, S. J., 2006b. Komatiites: petrology, volcanology, metamorphism and geochemistry. Society of Economic Geologists Special Publication 13, 13–49.

Barnes, S. J., 2007. Cotectic precipitation of olivine and sulfide liquid from komatiite magma and the origin of komatiite-hosted disseminated nickel sulfide mineralization at Mount Keith and Yakabindie, Western Australia. Economic Geology 102(2), 299-304.

Barnes, S. J., Hill, R. E. T., 2000. Metamorphism of komatiite-hosted nickel sulfide deposits. Reviews in Economic Geology 11, 203-215.

Barnes, S. J., Fiorentini, M. L., 2012. Komatiite magmas and sulfide nickel deposits: A comparison of variably endowed Archean terranes. Economic Geology 107(5), 755-780.

Barnes, S. J., Hill, R. E. T., Gole, M. J., 1988. The Perseverance ultramafic complex, Western Australia: the product of a komatiite lava river. Journal of Petrology 29(2), 305-331.

Barnes, S. J., Van Kranendonk, M. J., Sonntag, I., 2012. Geochemistry and tectonic setting of basalts from the Eastern Goldfields Superterrane, Australian Journal of Earth Science: An International Geoscience journal of the Geological Society of Australia 59(5), 707-735.

Bédard, J. H., Brouillette, P., Madore, L., Berclaz, A., 2003. Archaean cratonization and deformation in the northern Superior Province, Canada: an evaluation of plate tectonic versus vertical tectonic models. Precambrian Research 127(1), 61-87.

Bédard, J. H., 2006. A catalytic delamination-driven model for coupled genesis of Archaean crust and sub-continental lithospheric mantle. Geochimica et Cosmochimica Acta 70(5), 1188-1214.

Bédard, J. H, Harris, L. B., Thurston, P. C. 2013. The hunting of the snArc. Precambrian Research 229, 20-48.

Bédard, J. H., 2013. How many arcs can dance on the head of a plume?: A 'Comment' on: A critical assessment of Neoarchean 'plume only' geodynamics: Evidence from the Superior province, by Derek Wyman, Precambrian Research, 2012. Precambrian Research 229, 189-197.

Bekker, A., Barley, M. E., Fiorentini, M. L., Rouxel, O.J., Rumble, D., Beresford, S.W., 2009. Atmospheric sulfur in Archean komatiite-hosted nickel deposits. Science 326 (5956), 1086-1089.

Beresford, S., Duuring, P., Fiorentini, M., Rosengren, N., Bleeker, W., Barley, M., Cas, R., Tait, M., Wallace, H. 2004. P710. The Structural and Stratigraphic Architecture of the Agnew/Wiluna Belt, WA; Final Report, AMIRA, pp75-124.

Blackburn, C. E. 1980. Towards a mobilist tectonic model for part of the Archean of north-western Ontario. Geoscience Canada, 7(2).

Bleeker, W., 2002. Archaean tectonics: a review, with illustrations from the Slave craton. Special Publication Geological Society of London 199, 151-182.

Blewett, R. S., Czarnota, P. A., Henson, 2010. Structural-event framework for the eastern Yilgarn Craton, Western Australia, and its implications for orogenic gold, Precambrian Research 183 (2), 203-229.

Brooks, C., Ludden, J., Pigeon, Y., Hubregtse, J. J. M. W., 1982. Volcanism of shoshonite to high-K andesite affinity in an Archean arc environment, Oxford Lake, Manitoba. Canadian Journal of Earth Sciences 19(1), 55-67.

Brown, M., 2006. Duality of thermal regimes is the distinctive characteristic of plate tectonics since the Neoarchean. Geology 34(11), 961-964.

Brown, M., 2007. Metamorphism, plate tectonics, and the supercontinent cycle. Earth Science Frontiers 14(1), 1-18.

Brown, M., 2008. Characteristic thermal regimes of plate tectonics and their metamorphic imprint throughout Earth history: When did Earth first adopt a plate tectonics mode of behaviour? When Did Plate Tectonics Begin on Planet Earth? The Geological Society of America Special Paper 440, 97.

Brown, S. J. A., Barley, M. E., Krapež, B., Cas, R. A. F., 2002. The Late Archaean Melita Complex, Eastern Goldfields, Western Australia: shallow submarine bimodal volcanism in a rifted arc environment. Journal of Volcanology and Geothermal Research 115(3), 303-327.

Campbell, I. H., Hill, R. I., 1988. A two-stage model for the formation of the granite-greenstone terrains of the Kalgoorlie-Norseman area, Western Australia. Earth and Planetary Science Letters 90(1), 11-25.

Cas, R. A. F., Self, S., Beresford, S. W., 1999. The behaviour of the fronts of komatiite lavas in medial to distal settings. Earth and Planetary Research Letters 72, 127-139.

Cas, R. A. F., Beresford, S. W., 2001. Field characteristics and erosional processes associated with komatiitic lavas: Implications for flow behaviour. Canadian Mineralogist 39, 505–524.

Cas, R. A. F., Marks, K., Perazzo, S., Beresford, S. W., Trofimovs, J., Rosengren, N., 2011. Were intercalated komatiites and dacites at the Black Swan nickel sulphide mine, Yilgarn Craton, Western Australia, emplaced as extrusive lavas or intrusive bodies? The significance of breccia textures and contact relationships, Precambrian Research 229, 133-149.

Cassidy, K. F., Champion, D. C., Krapež, B., Barley, M. E., Brown, S. J. A., Blewett, R. S., Groenewald P. B., Tyler, I. M., 2006. A revised geological framework for the Yilgarn Craton, Western Australia. Western Australia Geological Survey, Record 2006/8.

Claoué-Long, J. C., Compston, W., Cowden, A., 1988. The age of the Kambalda greenstones resolved by ion-microprobe: implications for Archean dating methods. Earth and Planetary Science Letters 89, 239-259.

Collins, W. J., Van Kranendonk, A. M., Teyssier, C., 1998. Partial convective overturn of Archaean crust in the east Pilbara Craton, Western Australia: driving mechanisms and tectonic implications. Journal of Structural Geology 20(9), 1405-1424.

Crawford, A. J., Falloon, T. J., Green, D. H., 1989. Classification, petrogenesis and tectonic setting of boninites. In: Crawford, A.J., (Ed.). Boninites and Related Rocks. Unwin, London. 1-49.

Czarnota, K., Champion, D. C., Goscombe, B., Blewett, R. S., Cassidy, K. F., Henson, P. A., Groenewald, P. B., 2010. Geodynamics of the eastern Yilgarn Craton. Precambrian Research 183(2), 175-202.

Daigneault, R., Mueller, W. U., Chown, E. H., 2002. Oblique Archean subduction: accretion and exhumation of an oceanic arc during dextral transpression, Southern Volcanic Zone, Abitibi Subprovince Canada. Precambrian Research 115(1), 261-290.

Davies, G. F., 1992. On the emergence of plate tectonics. Geology 20(11), 963-966.

Defant, M. J., Drummond, M. S., 1990. Derivation of some modern arc magmas by melting of young subducted lithosphere. Nature 347(6294), 662-665.

Defant, M. J., Kepezhinskas, P., 2001. Evidence suggests slab melting in arc magmas. Eos, Transactions American Geophysical Union 82(6), 65-69.

de Joux, A., Thordarson, T., Denny, M., Hinton, R. W., de Joux A. J., 2013a. U-Pb dating constraints on the felsic and intermediate volcanic sequence of the nickel-sulphide bearing Cosmos succession, Agnew-Wiluna greenstone belt, Yilgarn Craton, Western Australia. Precambrian Research, 236. 85-105.

Denny, M. 2010 AM5 Disseminated (AM5D) mineralogical model. Unpublished internal memo, Xstrata Nickel Australasia, 4-13.

de Wit, M. J., de Ronde, C. E. J., Tredoux, M., Roering, C., Hart, R. J., Armstrong, R. A., Green, R. W. E, Peberdy, E., Hart. R. A., 1992. Formation of an Archaean continent. Nature 357(6379), 553-562.

Dilek, Y., Polat, A., 2008. Suprasubduction zone ophiolites and Archean tectonics. Geology 36(5), 431-432.

Donaldson, C. H., 1976. An experimental study of olivine morphology. Contributions to Mineralogy and Petrology 57, 187-213.

Donaldson, C. H., 1982. Spinifex textured komatiites; a review of textures, mineral compositions and layering. In; Arndt, N. T., Nisbit, E. G., (Eds.). Komatiites. George Allen and Unwin, London, pp211-244.

Donaldson, M. J., Lesher, C. M., Groves, D. I., Gresham, J. J. 1986. Comparison of Archean dunites and komatiites associated with nickel mineralisation in Western Australia: Implications for dunite genesis. Mineralium Deposita 21(4), 296-305.

Dowling, S. E., Hill, R. E. T., 1992. The distribution of PGE in fractionated Archaean komatiites, western and central ultramafic units, Mt Keith region, Western Australia. Australian Journal of Earth Sciences 39(3), 349-363.

Dowling, S. E., Hill, R. E. T, 1993. The Mount Keith ultramafic complex and the Mount Keith nickel deposit. Australian Geological Survey Organisational Record 1993/54, pp165-170.

Dowling, S. E., Barnes, S. J., Hill, R. E. T., Hicks, J., 2004. Komatiites and nickel sulphide ores of the Black Swan area, Yilgarn Craton, Western Australia. 2. Geology and genesis of the ore bodies, Mineralium Deposita 39, 707-728.

Drummond, M. S., Defant, M. J., 1990. A model for trondhjemite–tonalite–dacite genesis and crustal growth via slab melting: Archaean to modern comparisons. Journal of Geophysical Research 95, 21503–21521.

Drummond, M. S., Defant, M. J., Kepezhinskas P. K., 1996. Petrogenesis of slab-derived trondhjemite-tonalite-dacite/adakite magmas. Transactions of the Royal Society of Edinburgh - Earth Sciences 87.1, 205-216.

Duuring, P., Bleeker, W., Beresford, S. W., Hayward, N., 2010. Towards a volcanic–structural balance: relative importance of volcanism, folding, and remobilisation of nickel sulphides at the Perseverance Ni–Cu–(PGE) deposit, Western Australia. Mineralium Deposita 45(3), 281-311.

Duuring, P., Bleeker, W., Beresford, S. W., Fiorentini, M. L., Rosengren, N. M. 2012. Structural evolution of the Agnew–Wiluna greenstone belt, Eastern Yilgarn Craton and implications for komatiite-hosted Ni sulfide exploration. Australian Journal of Earth Sciences 59(5), 765-791.

Ebel, D. S., Naldrett, A. J., 1996. Fractional crystallization of sulfide ore liquids at high temperature. Economic Geology 91(3), 607-621.

Elias, M., 2006. Lateritic nickel mineralisation of the Yilgarn Craton. Society of Economic Geologists Special Publication 13, 195-210.

Farran, M., 2008. Volcanic, metamorphic and structural architecture of the Prospero-Tapinos nickel sulfide host succession, Western Australia, BSc Honours Thesis, unpublished.

Faure, F., Arndt, N. T., Libourel, G., 2006. Formation of spinifex texture in komatiites; an experimental study. Journal of Petrology 47, 1591-1610.

Fiorentini, M. L., Rosengren, N., Beresford, S. W., Grguric, B., Barley, M. E., 2007. Controls on the emplacement and genesis of the MKD5 and Sarah's Find Ni–Cu–PGE deposits, Mount Keith, Agnew–Wiluna Greenstone Belt, Western Australia. Mineralium Deposita 42(8), 847-877.

Fiorentini, M. L., Beresford, S. W., Barley, M. E, Duuring, P., Bekker, A., Rosengren, N., Cas, R. A. F., Hronsky, J., 2012. District to camp controls on the genesis of komatiite-hosted nickel sulfide deposits, Agnew-Wiluna greenstone belt, Western Australia: Insights from the multiple sulfur isotopes. Economic Geology 107(5), 781-796.

Friend, C. R., Nutman, A. P., 2010. Eoarchean ophiolites? New evidence for the debate on the Isua supracrustal belt, southern West Greenland. American Journal of Science 310(9), 826-861.

Furnes, H., de Wit, M., Staudigel, H., Rosing, M., Muehlenbachs, K., 2007. A vestige of Earth's oldest ophiolite. Science 315(5819), 1704-1707.

Gee, M., Swager, C., 2008. Late Archaean volcanic arcs and their accretionary history, Eastern Goldfields Superterrane: Plate tectonic models inferred from tectonostratigraphic analysis. Precambrian Research 161(1), 1-4.

Giles, C. W., Hallberg, J.A., 1982. The genesis of the Archaean Welcome Well volcanic complex, Western Australia. Contributions to Mineralogy and Petrology 80(4), 307-318.

Goscombe, B., Blewett, R.S., Czarnota, K., Groenewald, B., Maas, R., 2009. Metamorphic evolution and integrated terrane analysis of the eastern Yilgarn Craton: Rationale, methods, outcomes and interpretation: Geoscience Australia, Record 2009/23, 270.

Groves, D. I., Lesher, C. M., Gee, R. D., 1984. Tectonic setting of the sulphide nickel deposits of Western Australian Shield. In; D. L. Buchanan, Jones, M. J., (Eds.) Sulphide deposits in Mafic and Ultramafic Rocks, Institution of Mining and Metallurgy, London.

Green, D. H., 1975. Genesis of Archean peridotitic magmas and constraints on Archean geothermal gradients and tectonics. Geology 3(1), 15-18.

Grguric, B. A., Rosengren, N. M., Fletcher, C. M., Hronsky, J. M. A., 2007. Type 2 deposits: Geology, mineralogy, and processing of the Mount Keith and Yakabindie ore bodies, Western Australia. Special Publication Society of Economic geologists 13, 119.

Geological Survey of Western Australia (GSWA), 2009. Compilation of geochronology information, 2009 update. Western Australia Geological Survey.

Hallberg, J. A., 1985. Geology and mineral deposits of the Leonora-Laverton area north-eastern Yilgarn Block, Western Australia. Hesperian Press.

Hamilton, W. B., 1998. Archean magmatism and deformation were not products of plate tectonics. Precambrian Research 91(1), 143-179.

Hamilton, W. B., 2003. An alternative earth. GSA Today 13(11), 4-12.

Hamilton, W. B. 2007. Earth's first two billion years - The era of internally mobile crust. Geological Society of America Memoirs 200, 233-296.

Hickey, R. L., Frey, F. A., 1982. Geochemical characteristics of boninite series volcanics: implications for their source. Geochimica et Cosmochimica Acta 46(11), 2099-2115.

Herzberg, C., 1992. Depth and degree of melting of komatiites. Journal of Geophysical Research: Solid Earth (1978–2012), 97(B4), 4521-4540.

Herzberg, C. T., O'Hara, M. J., 1985. Origin of mantle peridotite and komatiite by partial melting. Geophysical Research Letters 12(9), 541-544.

Herzberg, C., O'Hara, M. J., 1998. Phase equilibrium constraints on the origin of basalts, picrites, and komatiites. Earth-Science Reviews 44(1), 39-79.

Hill, R.E.T., 2001. Komatiite volcanology, volcanological setting and primary geochemical properties of komatiite-associated nickel deposits. Geochemistry: Exploration, Environment, Analysis 1, 365-381.

Hill, R. E. T., Gole, M. J., 1990. Nickel sulphide deposits of the Yilgarn Block. Geology of the mineral deposits of Australia and Papua New Guinea. Australian Institute of Mining and Metallurgy, Melbourne, 557-559.

Hill, R.E.T., Dowling, S.E., 2008. The petrology and geochemistry of mineralised komatiites intersected in three diamond drill holes (AM262B, AMD275 and BJD048A) from the AM5 Nickel Sulphide Deposit; Cosmos region, Agnew-Wiluna Greenstone Belt; A pilot study for characterising mineralised domains within the ore body. Unpublished External report, Kalapana Research Associates and Triodia Research.

Hill, R. E. T., Gole, M. J., Barnes, S. J., 1989. Olivine adcumulates in the Norseman-Wiluna greenstone belt, Western Australia; implications for the volcanology of komatiites. In; Prendergast, M. D., Jones, M. J., Jones (Eds) Magmatic sulphides - the Zimbabwe volume, Institute of Materials, Minerals and Mining, London, pp. 189-206.

Hill, R. E. T., Gole, M. J., Barnes, S. J., 1990. Physical Volcanology of Komatiites: A Field Guide to the Komatiites between Kalgoorlie and Wiluna, Eastern Goldfields Province, Yilgarn Block, Western Australia. Geological Society of Australia, WA Division.

Hill, R. E. T., Barnes, S. J., Gole, M. J., Dowling S. E., 1995. The physical volcanology of komatiites as deduced from field relationships in the Norseman-Wiluna greenstone belt, Western Australia. Lithos 34, 159-188.

Hill, R. E. T., Barnes, S. J., Dowling, S. E., Thordarson, T., 2004. Komatiites and nickel sulphide ore bodies of the Black Swan area, Yilgarn Craton, Western Australia. 1. Petrology and volcanology of host rocks. Mineralium Deposita 39(7), 684-706.

Hoatson, D. M., Jaireth, S., Lynton Jaques, A., 2006. Nickel sulfide deposits in Australia: Characteristics, resources, and potential. Ore Geology Reviews 29, 177–241.

Huppert, H. E., Sparks, R. S. J., Turner, J. S., Arndt, N. T., 1984. Emplacement and cooling of komatiite lavas. Nature 309(5963), 19-22.

Huppert, H. E., Sparks, R. S. J., 1985a. Komatiites 1: eruption and flow. Journal of Petrology 26, 694-725.

Huppert, H. E., Sparks, R. S. J., 1985b. Cooling and contamination of mafic and ultramafic magmas during ascent through continental crust. Earth and Planetary Science Letters 74(4), 371-386.

Kaye, A., Thordarson, T., Hayward, C., Denny, M., de Joux, A. J., 2010. The felsic and intermediate footwall to the Cosmos Nickel sulphide deposits, Agnew-Wiluna greenstone belt, Yilgarn Craton, Western Australia, SEG 2010 conference abstract and presentation, Colorado.

Kaye, A., Thordarson, T., Hayward, C., Fitton, G., de Joux, A. J., 2011. The felsic and intermediate footwall to the Cosmos Nickel sulphide deposits, Agnew-Wiluna greenstone belt, Yilgarn Craton, Western Australia, IUGG 2011 conference abstract and presentation, Melbourne.

Kerrich, R., Wyman, D., Fan, J., Bleeker, W., 1998. Boninite series: low Ti-tholeiite associations from the 2.7 Ga Abitibi greenstone belt. Earth and Planetary Science Letters 164(1), 303-316.

Kerrich, R., Polat, A., 2006. Archean greenstone-tonalite duality: Thermochemical mantle convection models or plate tectonics in the early Earth global dynamics? Tectonophysics 415(1), 141-165.

Korsch, R. J., Kositcin, N., Champion, D. C., 2011. Australian island arcs through time: geodynamic implications for the Archean and Proterozoic. Gondwana Research 19(3), 716-734.

Kositcin, N., Brown, S. J., Barley, M. E., Krapež, B., Cassidy, K. F., Champion, D. C., 2008. SHRIMP U-Pb zircon age constraints on the Late Archaean tectonostratigraphic architecture of the Eastern Goldfields Superterrane, Yilgarn Craton, Western Australia. Precambrian Research 161(1), 5-33.

Langford, F. F., Morin, J. A., 1976. The development of the Superior Province of north-western Ontario by merging island arcs. American Journal of Science 276(9), 1023-1034.

Langworthy, P., Vallance, S., 2004. Exploration Strategies for the discovery of the Cosmos Region nickel sulphide deposits, Western Australia. Unpublished internal memo, Xstrata Nickel Australasia.

Lesher, C. M., 1989. Komatiite-associated nickel sulfide deposits. Reviews in Economic Geology 4, 45-101.

Lesher, C. M., Groves, D. I., 1986. Controls on the formation of komatiite-associated nickel copper sulphide deposits. In; Friedrich, G.H. (Ed.) Geology and Metallogeny of Copper deposits. Springer Verlag, Berlin.

Lesher, C. M., Arndt, N. T., 1995. REE and Nd isotope geochemistry, petrogenesis and volcanic evolution of contaminated komatiites at Kambalda, Western Australia. Lithos 34(1), 127-157.

Lesher, C. M., Keays, R. R., 2002. Komatiite associated Ni-Cu-(PGE) deposits; Mineralogy, geochemistry and genesis. In: L. J. Cabri (Ed.) The Geology, Geochemistry, Mineralogy and Mineral Beneficiation of the Platinum-Group Elements, Special Montreal: Canadian Institute of Mining, Metallurgy and Petroleum, Volume 54, pp. 579-617.

Lesher, M. C., Barnes, S. J., 2008. Komatiite-associated Ni-Cu-PGE deposits. In; Arndt, N. T., Lesher M. C., Barnes S.J. 2008. Komatiite. Cambridge University Press, Cambridge, pp. 295 – 327.

Lesher, C. M., Arndt, N. T., Groves, D. I., 1984. Genesis of komatiite-associated nickel sulphide deposits at Kambalda, Western Australia: A distal volcanic model. Sulphide deposits in mafic and ultramafic rocks, Proceedings of International Geology Correlation Projects 161 and 91, Third Nickel Sulfide Field Conference, Perth, Western Australia, Institution of Mining and Metallurgy, London, pp. 70–80.

Lesher, C. M., Stone, W. E., 1996. Exploration geochemistry of komatiites. Igneous trace element geochemistry applications for massive sulfide exploration. GAC-MAC Short Course Notes, 12, 153-204.

Lesher, C. M., Burnham, O. M., Keays, R. R., Barnes, S. J., Hulbert, L., 2001. Trace-element geochemistry and petrogenesis of barren and ore-associated komatiites. The Canadian Mineralogist 39(2), 673-696.

Lewis, J. D., 1971. "Spinifex texture" in a slag, as evidence for its origin in rocks. Annual Report of the Geological Survey of Western Australia 1971, pp45-49.

Manikyamba, C., Naqvi, S. M., Subba Rao, D. V., Ram Mohan, M., Khanna, T. C., Rao, T. G., Reddy, G. L. N., 2005. Boninites from the Neoarchaean Gadwal greenstone belt, Eastern Dharwar craton, India: implications for Archaean subduction processes. Earth and Planetary Science Letters 230(1), 65-83.

Mareschal, J. C., West, G. F., 1980. A model for Archean tectonism. Part 2. Numerical models of vertical tectonism in greenstone belts. Canadian Journal of Earth Sciences 17(1), 60-71.

McCall, G. J. H., 2003. A critique of the analogy between Archaean and Phanerozoic tectonics based on regional mapping of the Mesozoic-Cenozoic plate convergent zone in the Makran, Iran. Precambrian Research 127(1), 5-17.

McDonough, W. F., Sun, S. S., 1995. The composition of the Earth. Chemical Geology 120(3), 223-253.

Messenger, P. R., 2000. Geochemistry of the Yandal belt metavolcanic rocks, Eastern Goldfields Province, Western Australia. Australian Journal of Earth Sciences 47(6), 1015-1028.

Morris, P. A., Witt, W. K., 1997. Geochemistry and tectonic setting of two contrasting Archaean felsic volcanic associations in the Eastern Goldfields, Western Australia. Precambrian Research 83(1), 83-107.

Moyen, J. F., 2009. High Sr/Y and La/Yb ratios: the meaning of the "adakitic signature". Lithos 112(3), 556-574.

Moyen, J. F., 2011. The composite Archaean grey gneisses: petrological significance, and evidence for a non-unique tectonic setting for Archaean crustal growth. Lithos 123(1), 21-36.

Moyen, J. F., Stevens, G., 2006. Experimental constraints on TTG petrogenesis: implications for Archean geodynamics. Benn, K., Mareschal, J., Condie, K. C., (Eds.), Archean geodynamics and environments, American Geophysical Union, Washington, pp.149-175.

Moyen, J. F., Martin, H., 2012. Forty years of TTG research. Lithos 48, 312-336.

Myers, J. S., 1993. Precambrian history of the West Australian Craton and adjacent orogens. Annual Reviews of Earth Planetary Science 21, 453-485.

Myers, J. S., 1997. Preface: Archaean geology of the Eastern Goldfields of Western Australia—regional overview. Precambrian Research 83(1), 1-10.

Naldrett, A. J., 1969. A portion of the system Fe-S-O and its application to sulphide ore magmas. Journal of Petrology 10, 171-202.

Naldrett, A. J., 2004. Magmatic sulphide deposits: Geology, Geochemistry and Exploration. Springer Berlin Heidelberg, New York.

Naldrett, A. J., Turner, A.R., 1977. The geology and petrogenesis of a greenstone belt and related nickel sulfide mineralization at Yakabindie, Western Australia. Precambrian Research 5(1), 43-103.

Naldrett, A. J., Barnes, S.J., 1986. The behaviour of platinum group elements during fractional crystallization and partial melting with special reference to the composition of magmatic sulfide ores. Fortschritte der Mineralogie 64(2), 113M133.

Nelson, D. R., 1997b. Evolution of the Archean granite-greenstone terranes of the Eastern Goldfields, Western Australia; SHRIMP U-Pb zircon constraints. Precambrian Research 83, 57-81.

Nelson, D. R., 1998. Granite-greenstone crust formation on the Archean earth- a consequence of 2 superimposed processes. Earth and Planetary Science Letters 158, 109-119.

Nesbitt, R. W., 1971. Skeletal crystal forms in the ultramafic rocks of the Yilgarn Craton, Western Australia; evidence for an Archaean ultramafic liquid. Geological Society of Australia Special Publication 3, 331-347.

Nisbet, E. G., 1982. The tectonic setting and petrogenesis of komatiites. In; Arndt, N.T., Nisbet, E.G., (Eds.). Komatiites. George Allen and Unwin, London, pp501-520.

Nisbet, E. G., Cheadle, M. J., Arndt, N. T., Bickle, M. J., 1993. Constraining the potential temperature of the Archaean mantle: a review of the evidence from komatiites. Lithos 30(3), 291-307.

O'Neill, C., Wyman, D. A., 2006. Geodynamic Modelling of Late Archean Subduction: Pressure-Temperature Constraints from Greenstone Belt Diamond Deposits. Archean Geodynamics and Environments, American Geophysical Union, Washington D.C., pp. 177-188.

Pawley, M. J., Wingate, M. T. D., Kirkland, C. L., Wyche, S., Hall, C. E., Romano, S. S., Doublier, M. P., 2012. Adding pieces to the puzzle: episodic crustal growth and a new terrane in the northeast Yilgarn Craton, Western Australia. Australian Journal of Earth Sciences 59(5), 603-623.

Polat, A., 2012. Growth of Archean continental crust in oceanic island arcs. Geology 40(4), 383-384.

Polat, A., Kerrich, R., 2001. Geodynamic processes, continental growth, and mantle evolution recorded in late Archean greenstone belts of the southern Superior Province, Canada. Precambrian Research 112(1), 5-25.

Polat, A., Frei, R., Appel, P. W. U., Dilek, Y., Fryer, B., Ordóñez-Calderón, J.C., Yang, Z., 2008. The origin and compositions of Mesoarchean oceanic crust: Evidence from the 3075 Ma Ivisaartoq greenstone belt, SW Greenland, Lithos 100 (1–4), 293-321.

Polat, A., Frei, R., Fryer, B., Appel, P.W., 2009. The origin of geochemical trends and Eoarchean (ca. 3700 Ma) zircons in Mesoarchean (ca. 3075Ma) ocelli-hosting pillow basalts, Ivisaartoq greenstone belt, SW Greenland: Evidence for crustal contamination versus crustal recycling. Chemical Geology 268(3), 248-271.

Polat, A., Appel, P. W., Fryer, B. J., 2011. An overview of the geochemistry of Eoarchean to Mesoarchean ultramafic to mafic volcanic rocks, SW Greenland: Implications for mantle depletion and petrogenetic processes at subduction zones in the early Earth. Gondwana Research 20(2), 255-283.

Pyke, D. R., Naldrett, A. J., Eckstrand, O. R., 1973. Archaean ultramafic flows in Munro Township, Ontario. Bulletin of the Geological Society of America 84, 955-978.

Ripley, E. M., Li, C., 2013. Sulfide Saturation in Mafic Magmas: Is External Sulfur Required for Magmatic Ni-Cu-(PGE) Ore Genesis? Economic Geology 108(1), 45-58.

Robin, C. M. I., Bailey, R.C., 2009. Simultaneous generation of Archean crust and subcratonic roots by vertical tectonics. Geology 37(6), 523-526.

Rosengren, N. M., Beresford, S. W., Grguric, B. A., Cas, R. A. F., 2005. An intrusive origin for the komatiitic dunite-hosted Mount Keith disseminated nickel sulfide deposit, Western Australia. Economic Geology 100(1), 149-156.

Rosengren, N. M., Grguric, B.A., Beresford, S.W., Fiorentini, M.L., Cas, R. A. F., 2007. Internal stratigraphic architecture of the komatiitic dunite-hosted MKD5 disseminated nickel sulfide deposit, Mount Keith Domain, Agnew-Wiluna Greenstone Belt, Western Australia. Mineralium Deposita 42(8), 821-845.

Rosengren, N. M., Cas, R. A. F., Beresford, S. W., Palich, B. M., 2008. Reconstruction of an extensive Archaean dacitic submarine volcanic complex associated with the komatiite-hosted Mt Keith nickel deposit, Agnew-Wiluna greenstone belt, Yilgarn Craton, Western Australia. Precambrian Research 161(1), 34-52.

Sawkins, F. J. 1984. Metal deposits in relation to plate tectonics (Vol. 17). Berlin: Springer-Verlag.

Shima, H., Naldrett, A. J., 1975. Solubility of sulfur in an ultramafic melt and the relevance of the system Fe-S-O. Economic Geology 70(5), 960-967.

Sizova, E., Gerya, T., Brown, M., Perchuk, L. L., 2010. Subduction styles in the Precambrian: Insight from numerical experiments. Lithos 116(3), 209-229.

Smithies, R. H., 2000. The Archaean tonalite–trondhjemite–granodiorite (TTG) series is not an analogue of Cenozoic adakite. Earth and Planetary Science Letters 182(1), 115-125.

Smithies, R. H., Champion, D. C., Sun, S. S., 2004. The case for Archaean boninites. Contributions to Mineralogy and Petrology 147(6), 705-721.

Standing, J. G., 2008. Terrane amalgamation in the Eastern Goldfields Superterrane, Yilgarn Craton: evidence from tectonostratigraphic studies of the Laverton Greenstone Belt. Precambrian Research 161(1), 114-134.

Stern, R. J., 2005. Evidence from ophiolites, blueschists, and ultrahigh-pressure metamorphic terranes that the modern episode of subduction tectonics began in Neoproterozoic time. Geology 33(7), 557-560.

Stern, R. J., 2008. Modern-style plate tectonics began in Neoproterozoic time: An alternative interpretation of Earth's tectonic history. When did plate tectonics begin on planet Earth. The Geological Society of America Special Paper 440, 265-280.

Stuff, R., 2011. Xstrata Nickel Australasia-Cosmos Nickel Project- Technical Report No: STR01126, Annual report on Cosmos Nickel Project Tenements submitted to Department of Mines and Petroleum (DMP), 12-18.

Syracuse, E. M., van Keken, P. E., Abers, G. A., 2010. The global range of subduction zone thermal models. Physics of the Earth and Planetary Interiors 183(1), 73-90.

Thébaud, N., Rey, P. F., 2013. Archean gravity-driven tectonics on hot and flooded continents: Controls on long-lived mineralised hydrothermal systems away from continental margins. Precambrian Research 229, 93-104.

Trofimovs, J., Tait, M. A., Cas, R. A. F., McArthur, A., Beresford, S.W., 2003. Can the role of thermal erosion in strongly deformed komatiite–Ni–Cu–(PGE) deposits be

determined? Perseverance, Agnew–Wiluna Belt, Western Australia. Australian Journal of Earth Sciences 50(2), 199-214.

Trofimovs, J., Davis, B. K., Cas, R. A. F., 2004. Contemporaneous ultramafic and felsic intrusive and extrusive magmatism in the Archaean Boorara Domain, Eastern Goldfields Superterrane, Western Australia, and its implications. Precambrian Research 131(3), 283-304.

Trofimovs, J., Davis, B. K., Cas, R. A. F., Barley, M. E., Tripp, G. I., 2006. Reconstructing the event stratigraphy from the complex structural–stratigraphic architecture of an Archaean volcanic–intrusive–sedimentary succession: the Boorara Domain, Eastern Goldfields Superterrane, Western Australia. Australian Journal of Earth Sciences 53(2), 303-327.

Vallance, S., 2003. Geology, mineralisation and structure of the Cosmos Deeps nickel sulphide deposit. Unpublished internal memo, Xstrata Nickel Australasia.

Van Kranendonk, M. J., 2004. Preface: Archaean tectonics 2004: a review. Precambrian Research 131(3), 143-151.

Van Kranendonk, M. J. Collins, W. J. Hickman, A., Pawley, M. J. 2004. Critical tests of vertical vs. horizontal tectonic models for the Archaean East Pilbara Granite–Greenstone Terrane, Pilbara Craton, Western Australia, Precambrian Research 131(3–4), 173-211.

Van Kranendonk, M. J., Smithies, H. R., Hickman, A. H., Champion, D.C., 2007. Review: secular tectonic evolution of Archean continental crust: interplay between horizontal and vertical processes in the formation of the Pilbara Craton, Australia. Terra Nova 19(1), 1-38.

Van Kranendonk, M. J., Kröner, A., Hegner, E., Connelly, J., 2009. Age, lithology and structural evolution of the c. 3.53 Ga Theespruit Formation in the Tjakastad area, south-western Barberton Greenstone Belt, South Africa, with implications for Archaean tectonics. Chemical Geology 261(1), 115-139.

Van Kranendonk, M. J., 2011. Cool greenstone drips and the role of partial convective overturn in Barberton greenstone belt evolution. Journal of African Earth Sciences 60(5), 346-352.

Van Kranendonk, M. J., Ivanic, T. J., Wingate, M. T., Kirkland, C. L., Wyche, S., 2012. Long-lived, autochthonous development of the Archean Murchison Domain, Implications for Yilgarn Craton tectonics. Precambrian Research 229, 49 – 92.

Whalen, J. B., Percival, J. A., McNicoll, V. J., Longstaffe, F. J., 2002. A mainly crustal origin for tonalitic granitoid rocks, Superior Province, Canada: implications for late Archean tectonomagmatic processes. Journal of Petrology 43(8), 1551-1570.

Williams D. A., Kerr, R. C., Lesher, C. M., 1998. Emplacement and erosion Archaean komatiite lava flows at Kambalda: revisited. Journal of Geophysical Research – Solid Earth 103, 27533-27549.

Williams, D. A., Kerr, R. C., Lesher, C. M., Barnes, S. J., 2002. Analytical/Numerical modelling of komatiite lava emplacement and thermal erosion at Perseverance, Western Australia. Journal of Volcanology and Geothermal Research 110(1), 27-55.

Windley, B. F., Garde, A. A., 2009. Arc-generated blocks with crustal sections in the North Atlantic craton of West Greenland: crustal growth in the Archean with modern analogues. Earth-Science Reviews 93(1), 1-30.

Wyman, D. A., 1999. A 2.7 Ga depleted tholeiite suite: evidence of plume-arc interaction in the Abitibi greenstone belt, Canada. Precambrian Research 97(1), 27-42.

Wyman, D. A., 2013a. A critical assessment of Neoarchean "plume only" geodynamics: Evidence from the Superior Province. Precambrian Research 229, 3-19.

Wyman, D. A., 2013b. A reply to "How many arcs can dance on the head of a plume?" by Jean Bédard, Precambrian Research 229, 198-202.

Wyman, D. A., Kerrich, R., 2012. Geochemical and isotopic characteristics of Youanmi terrane volcanism: the role of mantle plumes and subduction tectonics in the western Yilgarn Craton. Australian Journal of Earth Sciences 59(5), 671-694.

Wyman, D. A., O'Neill, C., Ayer, J. A., 2008. Evidence for modern-style subduction to 3.1 Ga: A plateau–adakite–gold (diamond) association. Geological Society of America Special Papers 440, 129-148.

Zhao, G., Wilde, S. A., Li, S., Sun, M., Grant, M. L., Li, X. 2007. U–Pb zircon age constraints on the Dongwanzi ultramafic–mafic body, North China, confirm it is not an Archean ophiolite. Earth and Planetary Science Letters 255(1), 85-93.

Paper 1 – Petrology and physical volcanology of the Archaean metamorphosed Cosmos volcanic succession and its relation to mineralised komatiites, Agnew-Wiluna greenstone belt, Yilgarn Craton, Western Australia

A. de Joux[1] and T. Thordarson[1,*]

[1]School of GeoSciences, University of Edinburgh, Grant Institute, The King's Buildings, West Mains Road, Edinburgh, EH9 3JW, UK

*Faculty of Science, University of Iceland, Sturlugata 7, IS101, Reykjavik, Iceland

Intended for submission to Journal of Volcanology

- A. de Joux undertook all fieldwork, subsurface mapping, sampling and sample preparation, petrography and wrote the manuscript and all earlier drafts
- T. Thordarson provided supervision plus assistance during data collection, thorough editorial comments and general guidance for accurate lithological descriptions and nomenclature

Chapter 2 – Lithostratigraphy and volcanology of the Cosmos greenstone succession

2.1 Abstract

The metamorphosed Cosmos greenstone succession within the Agnew-Wiluna belt of the Kalgoorlie Terrane of the Eastern Goldfields Superterrane, within the Yilgarn Craton, is an example of a mineralised komatiite succession associated with an intricate succession of felsic and intermediate volcanic rocks. The metamorphic mineral assemblage, combined with new garnet-biotite geothermometry, indicate the succession was exposed to peak metamorphic temperatures of ~560 - 580°C at a pressure of ~3 kbars. Despite being subjected mid-amphibolite metamorphism many of the primary volcanic textures are preserved allowing protoliths and emplacement mechanisms to be established.

Three separate komatiite units are recognised within the succession; the Western Ultramafic unit and the two units that make up the Cosmos Ultramafic Sequence; the lower UMu1 komatiite package and the upper UMu2 komatiite package, which are separated by a discontinuous felsic volcanic horizon known as the AM5 "reactivation" contact. The footwall succession to the mineralised Cosmos Ultramafic Sequence is composed of a compositionally diverse succession of basaltic andesite through to rhyolite coherent and fragmental lithologies. Six texturally and compositionally distinct volcanic units are recognised within the succession. A sequence of rhyolite lavas, overlain sequentially by a felsic tuff and an andesitic crystal

tuff sequence form the stratigraphic footwall to the barren Western Ultramafic unit. An intercalated succession of dacite lavas, dacite lapilli tuffs (and associated tuff breccias) and andesite lavas, with associated volcaniclastic units, compose the stratigraphic footwall to the UMu1 komatiite package, indicating the volcanic sequence was constructed via both effusive and explosive eruptions. The UMu1 package contains several high-grade massive nickel sulphide ore bodies along its basal contact, which often penetrate several metres into the underlying dacite lapilli tuff and tuff breccia sequence. Sulphide-footwall textural relationships and sulphide morphology indicates its occurrence within the footwall may reflect its primary depositional location. Sulphur saturation of the overriding UMu1 komatiite may have been promoted by the thermo-mechanical erosion of the fragmental dacite footwall. The Cosmos Ultramafic Sequence is overlain by the hangingwall sedimentary sequence which features conglomerates containing granitic clasts. The Cosmos footwall sequence lacks any evidence of being erupted under water and thus is considered to have erupted sub-aerially. The Cosmos volcanic succession's nature and diverse composition contrasts with other mineralised volcanic successions within the surrounding Agnew-Wiluna greenstone belt, specifically by containing abundant andesite lavas and exhibiting a distinct high-K calc-alkaline affinity.

2.2 Introduction

Whilst ultramafic sequences that host nickel sulphide deposits are commonly well characterised, mineralogically, texturally and structurally (e.g., Barnes et al., 1988; Hill et al., 1990, 1995, 2004), the lithostratigraphy of the enclosing succession is often comparatively poorly constrained. To date only a few detailed studies have been undertaken on the lithostratigraphy and chemical composition of felsic lithologies associated with mineralised ultramafic successions (e.g., Trofimovs et al., 2004; Rosengren et al., 2008). Komatiites are considered to have been emplaced in a variety of volcano-tectonic settings including oceanic plateaus (e.g., Gresham and Loftus-Hill, 1981), island arcs (Dostal and Mueller, 1997; Hollings et al., 1999; Parman et al., 2001; Trofimovs et al., 2004; Grove and Parman, 2004), submerged continental crust

(Groves et al., 1984; Bleeker et al., 2000) and in intraplate settings (McDonough and Ireland, 1993). On the basis of their primary igneous textures (when present), komatiites have been inferred to be emplaced as lavas or shallow dykes or sills (Barnes et al., 1988, 1999; Hill and Gole, 1990; Hill et al., 1989, 1990, 1995, 2004; Dowling and Hill, 1990; 1992; Perring et al., 1995; Trofimovs et al., 2003; Rosengren et al., 2005; Duuring et al., 2010; Fiorentini et al., 2012). Ultramafic units subsequently experience multi-stage metamorphism of variable grade and, given that their original olivine-dominated mineralogy and petrographic textures are unstable in near surface environments, their mineral assemblages have readily been modified by such metamorphism. In mid-grade terranes (i.e. amphibolite facies) original igneous textures, such as spinifex and cumulate textures, commonly used to infer the mode of emplacement of a komatiite, are poorly preserved and overprinted by wholesale recrystallisation (e.g., Gole et al., 1987; Gole et al., 1990; Barnes and Hill, 2000). Therefore, information on the geological environment of komatiite emplacement is best obtained from the nature of the associated lithologies (Arndt et al., 2008).

Ultramafic sequences are often associated with felsic (and to a lesser extent intermediate) volcanic, volcaniclastic and sedimentary sequences (e.g., Hallberg, 1985; Hill et al., 2004; Rosengren et al., 2008; Duuring et al., 2010; Fiorentini et al., 2012). This is the case in the Agnew-Wiluna greenstone belt (AWB) of Western Australia. Felsic lithologies in such regions contain a substantial proportion of igneous quartz and feldspar phases (e.g. Hallberg, 1985; Barley et al., 2008), which are more stable than olivine-dominated komatiites at conditions of low to mid-grade metamorphism. Thus primary igneous textures are invariably preserved or can be positively identified from pseudomorphic textures. Furthermore, the chemical composition and geochemical affinity of the felsic and intermediate volcanic successions associated with ultramafic sequences provides important clues about the likely volcano-tectonic setting for the succession, especially in mid-grade metamorphosed terranes. This has important implications for the geodynamic setting of volcanism within the late Archaean.

The Cosmos greenstone succession, within the AWB of Eastern Goldfields Superterrane (EGS) of the Yilgarn Craton, consists of several ultramafic units

intercalated with a varied sequence of intermediate and felsic volcanic lithologies. It contains several komatiite-hosted disseminated and massive nickel sulphide ore bodies. The focus of this study was to establish the volcanic stratigraphy of the footwall succession, and to a lesser extent the hangingwall sedimentary succession, to the mineralised Cosmos Ultramafic Sequence. An integrated approach utilising subsurface correlation of stratigraphy, petrology, geochemistry, geothermometry and U-Pb dating was applied to establish the overall age, timing, metamorphic grade, emplacement mechanisms and tectonic setting of the Cosmos greenstone succession. Here I present a detailed account of the volcanology and emplacement mechanisms of the Cosmos greenstone sequence, underpinned by careful documentation of the primary volcanic textures still preserved in this mid-amphibolite metamorphic grade succession. New garnet-biotite geothermometry has also provided a more detailed assessment of the metamorphic grade in the Cosmos region.

2.3 Regional geology

The Cosmos mine site is situated on the western edge of the AWB within the Kalgoorlie Terrane of the EGS (Fig. 2.1). The 2.7 Ga AWB features sequences of basaltic, intermediate and felsic volcanic and volcaniclastic rocks, as well as clastic sedimentary rocks and carbonaceous shales (e.g. Hallberg, 1985; Hill et al., 1989; Morris, 1998; Cassidy et al., 2006). These sequences are intercalated with multiple komatiite horizons of laterally variable extent, which include cumulates, thin spinifex textured units and komatiitic basalt lithologies (Hill et al., 1989, 1990, 1995; Dowling and Hill, 1990; Rosengren et al., 2005; Fiorentini et al., 2012; Fig. 2.1). This greenstone belt is the most highly nickel endowed komatiite belt in the world and contains several economic nickel deposits including Mount Keith, Perseverance and Yakabindie (e.g., Binns et al., 1976; Barnes et al., 1988; Dowling and Hill, 1990; 1992; Hill et al., 1995; Hill, 2001; Trofimovs et al., 2003; Rosengren et al., 2005; 2008; Duuring et al., 2007; 2010; 2012; Fiorentini et al., 2012). There is a the close spatial association of large nickel deposits with felsic volcanic rocks in the AWB as well as the wider Kalgoorlie Terrane (e.g., Gole et al., 1996; Trofimovs et al., 2004; Rosengren

et al., 2008, de Joux et al., 2013). This association was originally interpreted to represent the eruption of very large, prolonged submarine komatiite flows onto a felsic substrate (Barnes et al., 1988; Hill et al., 1995). Thin flow komatiites intercalated with felsic tuffs at Mount Keith were suggested to be the result of simultaneous bimodal felsic-ultramafic volcanism, which occurred prior to the major eruptive event which produced the mineralised Mount Keith complex (Dowling and Hill, 1992; Hill et al., 1995). However, Fiorentini et al. (2012) conjecture that the felsic volcanics in the Mount Keith domain (i.e. along the eastern axis of the AWB) represent an inverted palaeo-rift with intrusive and extrusive ultramafic units. The intrusive unit is suggested to represent a single continuous sill along the AWB from north of Albion Downs to Perseverance. However, as the Cosmos greenstone belt is placed within a distinctive western segment, separate and to the west of the main axis of the AWB, its origin is not directly related to and differs from that of the main-axis eastern segment (Fig. 2.1).

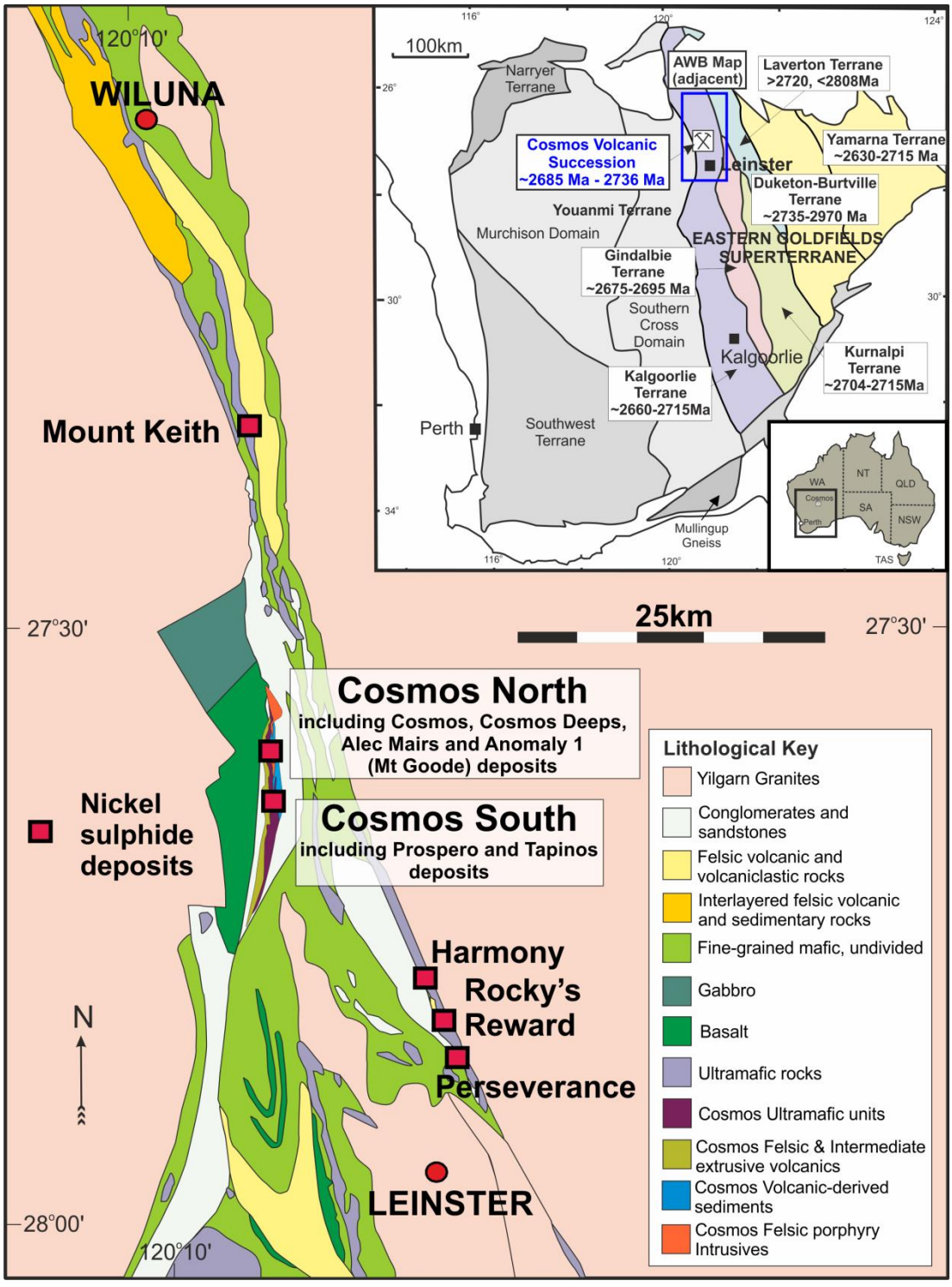

Figure 2.1. A Geological Map of the Agnew-Wiluna greenstone belt showing the location of the Cosmos mine site and its location within the wider Eastern Goldfields Superterrane and the Yilgarn Craton. Inset of the Yilgarn Craton shows the main terrane boundaries and the age ranges of individual terranes (modified after Cassidy et al. (2006) and GSWA (2009)). Age ranges for individual terranes are taken from Kositcin et al. (2008) and references therein and Pawley et al. (2012). The age range of the Cosmos volcanic succession is summarised from de Joux et al. (2013).

2.4 Alteration and deformation of the AWB and the Cosmos succession

The AWB is a section of Archaean crust that has experienced polyphase deformation and has been metamorphosed to a variable degree. The general trend in the region is low-grade prehnite-pumpelleyite facies metamorphism in the north to amphibolite facies metamorphism in the south (Binns et al., 1976; Archibald et al., 1978; Gole et al., 1987; Hill et al., 1995; Goscombe et al., 2009; Duuring et al., 2012). Consequently, preservation of primary textures within the volcanic lithologies is highly variable. Supracrustal rocks in the northern sector of the AWB (i.e., between Perseverance and Wiluna; Fig. 2.1) are characterized by NNW-trending, steeply dipping, attenuated and dismembered supracrustal strata that are now structurally juxtaposed against granitoid rocks and granitic gneisses (e.g., Duuring et al., 2012; Fiorentini et al., 2012 and references therein). Within the Cosmos succession at least four phases of regional deformation are recognised (Kositcin et al., 2008; Goscombe et al., 2009; Stuff, 2011). As a result, the succession is orientated sub-vertically, dipping and younging to the east. The age of metamorphism and deformation within the AWB has been dated to ~2.67 – 2.63 Ga (Cassidy et al., 2006). An in-depth description of the alteration mineralogy, style and textures, as well as a discussion of the local deformation history of the Cosmos succession is beyond the scope of this paper. However, I have estimated the peak metamorphic temperature for the Cosmos domain using garnet-biotite geothermometry, which is discussed in Section 2.5. A detailed regional overview of the metamorphic and deformation history of the Eastern Yilgarn Craton is given in Goscombe et al. (2009) and Czarnota et al. (2010). More recently Duuring et al. (2012) have provided a detailed account of the structural evolution of the AWB.

2.5 Ultramafic units of the Cosmos succession

The Cosmos succession consists of ultramafic, intermediate and felsic lithologies and contains several massive and disseminated high-grade, nickel-sulphide ore bodies. These ore bodies are generally located close to, or at the base of, thick olivine meso-adcumulates, commonly bounded by meta-orthocumulates and meta-spinifex-textured horizons whose primary volcanic textures have been largely obliterated by metamorphic recrystallisation (Hill and Dowling, 2008). The ultramafic sequences are considered to have formed in preferred lava pathways based on: (i) the observed spatial association of sulphide-hosting adcumulate horizons with thin, low magnesium flow units (interpreted to represent metamorphosed equivalent of orthocumulate and spinifex textured horizons), (ii) the internal local versus distal komatiite stratigraphy, and (iii) numerous complex komatiite-felsic relationships (Langworthy and Vallance, 2004; Hill and Dowling, 2008; Denny, 2010; Kaye et al., 2010, 2011; Stuff, 2011; de Joux et al., 2013). Three different ultramafic sequences are recognised within the Cosmos greenstone succession; the Western Ultramafic unit and the UMu1 and the UMu2 packages, which collectively, along with a discontinuous felsic horizon that separates the two packages, comprise the Cosmos Ultramafic Sequence (de Joux et al., 2013). All three units have undergone a pervasive metamorphic overprint. The igneous assemblages of olivine-pyroxene-chromite-liquid been metamorphosed to various proportions of metamorphic olivine, serpentine, anthophyllite, enstatite, talc, tremolite, actinolite, gedrite, cummintonite, diopside and chlorite (Hill and Dowling, 2008). Hill and Dowling (2008) indicated that the olivine-rich host rocks have suffered at least three major phases of metamorphic reconstitution; (1) early greenschist serpentinisation and talc-carbonate alteration, (2) prograde amphibolite metamorphism producing metamorphic olivine-rich rocks, (3) partial/complete retrograde serpentinisation and alteration of amphibolite facies mineral assemblages. Thus, mineral assemblages preserved within the ultramafic units vary spatially within the deposit and are controlled by H_2O and CO_2 levels during prograde and retrograde metamorphism.

The Western Ultramafic unit is interpreted to consist of meta-mesocumulates and meta-orthocumulates and ranges in thickness from 5 to >100m. This unit lies stratigraphically below the felsic and intermediate volcanic footwall to the Cosmos Ultramafic Sequence.

The Cosmos Ultramafic Sequence contains a cryptic patchy intermediate and felsic horizon, referred to as the AM5 "reactivation" contact, which defines the contact between the earlier UMu1 komatiite package and the later UMu2 komatiite package (de Joux et al., 2013; Chapter 4). This horizon is interpreted as an eroded in-situ volcanic deposit representing a significant break in komatiite lava emplacement (Denny, 2010; de Joux et al., 2013). The lower UMu1 package is 30 – 60m thick and typified by several internally-stacked units of meta-mesocumulates and meta-adcumulates that are sporadically separated by sequences of compound low-MgO meta-spinifex – meta-orthocumulate komatiite flow lobes, especially in the vicinity of the footwall contact (Hill and Dowling, 2008; Denny, 2010). Hybrid (i.e. contaminated by felsic melts) komatiites are also identified close to the basal contact of the UMu1 package (Hill and Dowling, 2008). These contaminated units are interpreted to represent komatiite lava involved in thermo-mechanical erosion of the underlying substrate (Hill and Dowling, 2008). The upper UMu2 package is comprised of meta-adcumulates and meta-mesocumulates, often with thin compound low-MgO meta-spinifex-orthocumulate komatiite flow lobes at its base. This unit attains thicknesses of >300m. Overall the Cosmos Ultramafic Sequence (UMu1+UMu2) attains a maximum thickness of 500m in the south thinning to <50 m in the northernmost sector of the study area (Fig. 2.1).

Style and occurrence of nickel sulphide mineralisation varies between the three main ultramafic sequences in the Cosmos North region. The Western Ultramafic unit is entirely barren. Massive, and to a lesser extent felsic-breccia-hosted, high tenor nickel sulphide deposits occur close to the basal contact of the UMu1 package, directly overlying the underlying volcanic footwall. In contrast, the upper part of the Cosmos Ultramafic Sequence, the UMu2 package, typically hosts high and low tenor adcumulate-hosted disseminated ore bodies that sit above the AM5 "reactivation" contact.

2.6 Methods

104 (~19,000m) diamond drill holes, between 50 - 600m in length and spread over 1km in strike length of the Cosmos north-south striking greenstone belt were logged in detail and sampled. It should be noted there is little to no surface outcrop in the Cosmos North region so assessment of the stratigraphy is based on logging of diamond drill cores and subsurface correlation. The stratigraphic logging of cores emphasised protolith identification, key contact relationships and sulphide-footwall relationships within the footwall to the Cosmos Ultramafic Sequence and the underlying Western Ultramafic unit. The hangingwall sedimentary package, which is considered to unconformably overlie the mineralised Cosmos Ultramafic Sequence, was also investigated, albeit in less detail. The subsurface footwall stratigraphy was mapped on cross-sections and long-sections, underpinned by correlations of re-logged drill cores and aided by geological constraints from existing data. Details of fieldwork methods, drill hole and sample data are given in Appendix 1.

Major and trace element compositions of all identified lithologies, in total 225 samples, were measured via X-ray Fluorescence (XRF) using a PanAnalytical PW2402 wavelength dispersive, sequential X-ray fluorescence spectrometer at the University of Edinburgh, following the analytical procedures outlined by Fitton et al. (1998). In addition, 85 samples were analysed for their rare earth element (REE) concentrations. The samples were prepared via tri-acid digestion and measured by Inductively Coupled Plasma Mass Spectrometry (ICP-MS) at Scottish Universities Environmental Research Centre (SUERC) in East Kilbride. Samples were taken from representative units and levels within the stratigraphy and throughout the Cosmos North area to assess the spatial and temporal variation in facies associations. Full details of analytical methods can be found in Appendix 2.

The effects of element mobility during deformation and metamorphism in Archaean terranes must be considered when using major and trace element geochemistry to classify volcanic rocks and discriminate their likely tectonic setting. Chapter 3 provides a detailed discussion on the geochemistry of the Cosmos footwall

volcanic succession, which demonstrates that K_2O and Na_2O were variably mobilised on a succession-wide basis during metamorphism. Consequently the Total Alkali Silica (TAS) plot (Le Bas et al., 1986; Le Bas et al., 1992) cannot be used to classify meta-volcanics. Emphasis has thus been placed on immobile element ratios, as immobile elements are considered to preserve the primary igneous signature of individual lithologies (Chapter 3). The method of Winchester and Floyd (1977) utilising Zr/TiO_2 versus Nb/Y is used to discriminate between different volcanic magma series and rock types within the Cosmos volcanic succession (Fig. 2.4) and to confirm field and petrography-based identifications of lithologies.

An interpretation of the geochemical affinity of the Cosmos volcanic succession is challenging due to its metamorphic grade. As K_2O is demonstrably mobile, the K_2O-SiO_2 diagram (Peccerillo and Taylor, 1976; Rickwood, 1989) used to subdivide subalkaline rocks cannot be confidently used to classify the succession. La can be used as a proxy for the original K_2O content because the abundance of La increases sympathetically with increasing K_2O contents of mafic rocks (Wheller et al., 1987). This relationship lead Hollings and Kerrich (2006) to calculate K_2O from La using K_2O (calc) = [La (ppm) x800]/8301. This relationship holds for felsic rocks with original K_2O content <5 wt% as the equivalent relationship between K ppm and La ppm breaks down above 5 wt % K_2O (Wheller et al., 1987; Hollings and Kerrich, 2006). A plot of K_2O (calc) vs. SiO_2 is shown on Figure 2.5 and clearly indicates that coherent Cosmos andesites and dacites have a high-K calc-alkaline (to shoshonite) affinity.

Nine zircon-bearing samples from various lithologies and stratigraphic positions (Fig. 2.2), were analysed for U-Pb by SIMS – secondary ionising mass spectrometry – on a Cameca 1270 Ion microprobe at the University of Edinburgh. A detailed account of the methods and results of U-Pb dating within the Cosmos volcanic succession is given by de Joux et al. (2013a) and discussed in detail in Chapter 4. Electron microprobe analysis (EMPA) was carried out on five garnet-biotite bearing samples from the stratigraphic footwall on the Cameca SX100 electron probe at the University of Edinburgh. Full details of EMPA methodology and garnet-biotite geothermometry results are presented in Appendix 3.

2.7 Metamorphic grade of the Cosmos Succession

The metamorphic mineral assemblages within individual lithological units indicates that the Cosmos succession has experienced mid-amphibolite metamorphism (Hill and Dowling, 2008). A felsic schist (BJD050L) analysed by EMPA contained abundant porphyroblasts of the aluminous amphibole gedrite, which is also, albeit rarely, present as a metamorphic phase replacing interstitial glass within low MgO ultramafic units (Hill and Dowling, 2008). The presence of gedrite indicates the Cosmos succession was subjected to temperatures >525^{o}C (assuming >1 kbar pressure) during metamorphism (Akella and Winkler, 1966). The ubiquitous presence of metamorphic olivine throughout the ultramafic succession also indicates that peak metamorphic conditions exceeded 485^{o}C at ~2 kbar (Deer et al., 1992). Metamorphic olivine is stable throughout the southern AWB, and in rocks as far north as the Six Mile deposit (Gole et al., 1987; Fig. 2.1). An intermediate garnet-biotite schist (AMD310Q) contained porphyroblasts of andalusite, that were wrapped by the biotite-rich fabric and thus were considered to be pre-tectonic and a prograde occurrence of the aluminosilicate polymorph. The presence of andalusite indicates maximum pressure conditions of ~4 kbar. Combining the inferred minimum temperature indicated by the presence of gedrite within the succession, and assuming an Al_2SiO_5 triple point of 504 ± 20 ^{o}C and 3.75 ± 0.25 kbar (Holdaway and Mukhopadhyay, 1993), the presence of andalusite indicates that the Cosmos succession was unlikely to have been exposed to pressure conditions >3.25 kbar. Therefore, the peak metamorphic temperature at Cosmos must exceed 525^{o}C (due to the presence of gedrite) but is unlikely to have exceeded 600^{o}C (due to the presence of prograde andalusite).

Garnet-biotite geothermometry results are shown on Figure 2.2. Full details of the results of garnet-biotite geothermometry can be found in Appendix 3. Garnet compositions within all samples were dominated by almandine. However, many of the larger garnets in individual samples exhibited normal zoning with grossular and spessartine-rich cores. Consequently garnet core-biotite matrix pairs tend to give unrealistically low temperatures due to the elevated Mn and Ca contents of the garnet cores. The composition of biotite within individual samples was found to vary little

between crystals in close proximity to garnet porphyroblasts and those that were located far from porphyroblasts. Consequently, garnet rim-biotite matrix pairs give the most reliable temperature estimates (Fig. 2.2). However, garnet-rim biotite-matrix pairs from samples that may have been affected by chlorite retrogression were discounted, as they gave unrealistic overestimates of the peak metamorphic temperatures. The data was initially processed using six different geothermometry calculations. Of these six geothermometry calibrations, those of Thompson (1976) and Lavrent'eva and Perchuk (1981) produced the most consistent results for garnet-biotite pairs within individual samples and across the dataset as a whole (see Appendix 3). Therefore, these calibrations are used to compare estimates of temperature between the three samples and were modelled at 2.5 kbar (Fig. 2.2).

Three samples analysed for garnet-biotite provided robust temperature estimates (Fig. 2.2). Collectively, the results indicate a peak metamorphic temperature of ~560 - 580^{o}C, which in conjunction with presence of andalusite porphyroblasts indicates that the succession was unlikely to be subjected to pressures > 3 kbar. These results are very similar to that obtained at the Perseverance mine site, situated ~40 km south-east of Cosmos (Fig. 2.1), where garnet-biotite geothermometry indicated peak metamorphic conditions of 550°C and maximum pressure of 3 kbar (Gole et al., 1987). It is assumed that the estimated peak metamorphic conditions represent the regional metamorphic grade within the North Cosmos region because average temperature estimates are consistent across three samples obtained from different locations and levels within the established stratigraphy. Hence, effects of localised contact metamorphism from local intrusions such as the felsic porphyry intrusions, are therefore considered to be negligible.

The metamorphic conditions estimated at Cosmos could be linked to the M2 phase of regional-contact metamorphism within the EGS, where temperatures ranged between 300 and 550^{o}C across individual greenstone belts accompanied by peak metamorphic pressures of 3.5 – 5.0 kbar (Czarnota et al., 2010). The timing of M2 is constrained to 2685 – 2665 Ma, indicating it took place during or shortly after the peak of high-Ca granite intrusion. The M2 event was dominated by the heat supplied by large volumes of high-Ca granites (Goscombe et al., 2009; Czarnota et al., 2010). The

peak metamorphic temperature indicated at Cosmos is slightly higher than typical M2 peak metamorphic temperatures. Therefore, it is possible that the M2 metamorphic event was overprinted by the later M3a phase of regional metamorphism, which is characterised by peak conditions of 500 – 580°C and 4.0 ± 1 kbar. This event is inferred to have accompanied regional sustained late basin fill events, constraining the timing of M3a to 2665 – 2650 Ma (Czarnota et al., 2010). The currently established distribution of the M3a thermal overprint is restricted to the vicinity of the Ockerburry Fault, which lies ~ 50km to the east of Cosmos (Fig. 2.1), and to the regional late basin-fill sequences. One such basin sequence fill, the Jones Creek Conglomerate uncomformably overlies the Cosmos volcanic sequence to the north (Bunting, 1979). It is difficult to discern confidently whether the M3a thermal peak is present at Cosmos as its footprint is obscured by the pre-existing M2 paragenesis. M2 metamorphism overlaps with the last phases of D1 extension, related to high-Ca granite emplacement (Czarnota et al., 2010).

Figure 2.2. (Next two pages) Garnet-biotite geothermometry from the Cosmos succession. Three samples were analysed; BJD102B, AMD310Q and BJD312HB, which represent an intermediate volcaniclastic horizon, a felsic schist and an andesitic lava respectively (a) These three panels are histograms showing the calculated temperature distribution obtained from garnet-biotite pairs within the three samples. Results from six different geothermometer calibrations are illustrated (see key); Ferry and Spear (1978; F & S), Lavrent'eva and Perchuk (1981; L & P 81), Thompson (1976; Th), Holdaway and Lee (1977; H & L), Perchuk and Lavrent'eva (1983; P & L 83A; P & L 83B). AMD310Q shows all garnet-biotite pairs, whereas BJD102B and BJD312HB show the garnet-rim, biotite-close pairs. The results of the garnet-core, biotite far pairs can be seen in Appendix 3, however as discussed above it is considered that these give unrealistic temperature estimates due to composition of the garnet cores coupled with the fact that the garnet cores are unlikely to have equilibrated with biotite crystals within the matrix. (b) Calculated temperature ranges for the three samples using the geothermometry calibrations of Thompson (1976) (Th) and Lavrent'eva and Perchuk (1981) (L&P 81). The averages temperature (± 2σ) for each are sample are shown, as well as the range between the individual garnet-biotite pairs that gave the highest and lowest temperature estimates for each sample. Also indicated are the constraints on peak metamorphic temperature as indicated by the presence of andalusite and gedrite.

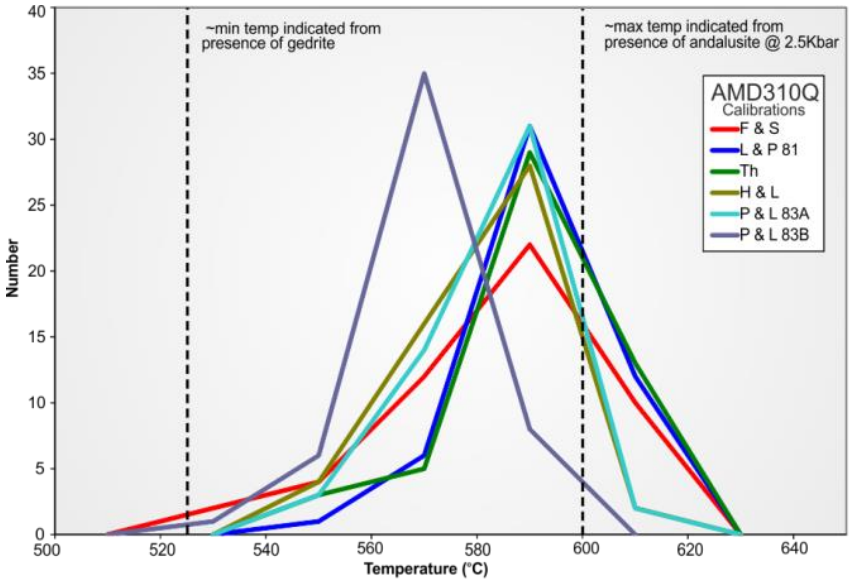
~min temp indicated from presence of gedrite
~max temp indicated from presence of andalusite @ 2.5Kbar
AMD310Q
Calibrations
F & S
L & P 81
Th
H & L
P & L 83A
P & L 83B
Number
Temperature (°C)

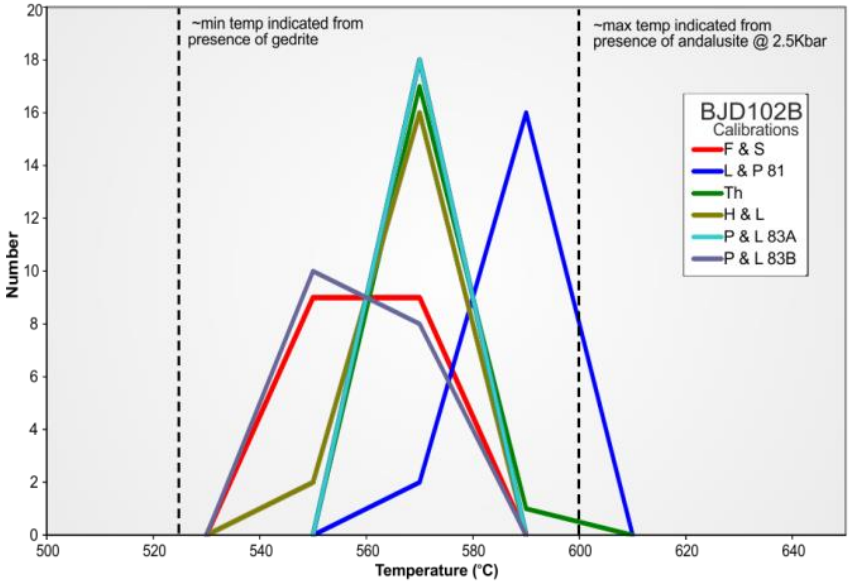
~min temp indicated from presence of gedrite
~max temp indicated from presence of andalusite @ 2.5Kbar
BJD102B
Calibrations
F & S
L & P 81
Th
H & L
P & L 83A
P & L 83B
Number
Temperature (°C)

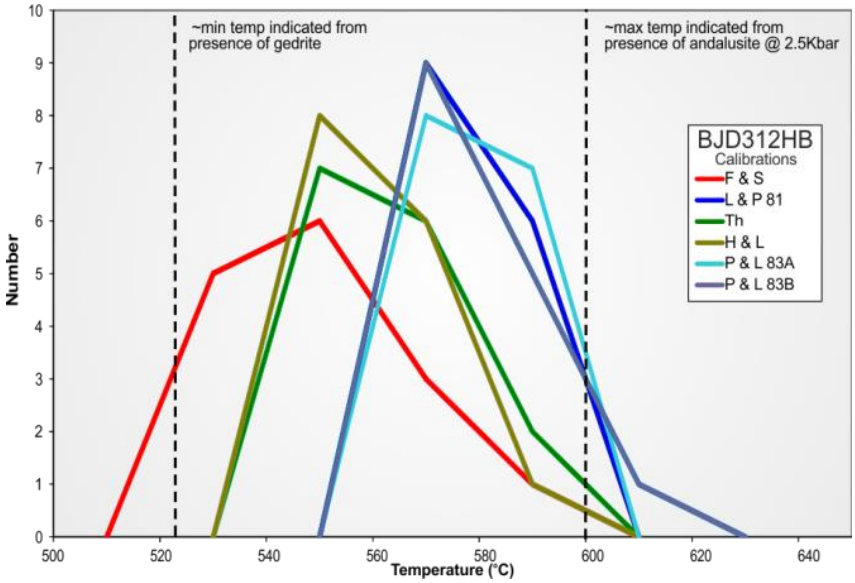
~min temp indicated from presence of gedrite
~max temp indicated from presence of andalusite @ 2.5Kbar
BJD312HB
Calibrations
F & S
L & P 81
Th
H & L
P & L 83A
P & L 83B
Number
Temperature (°C)

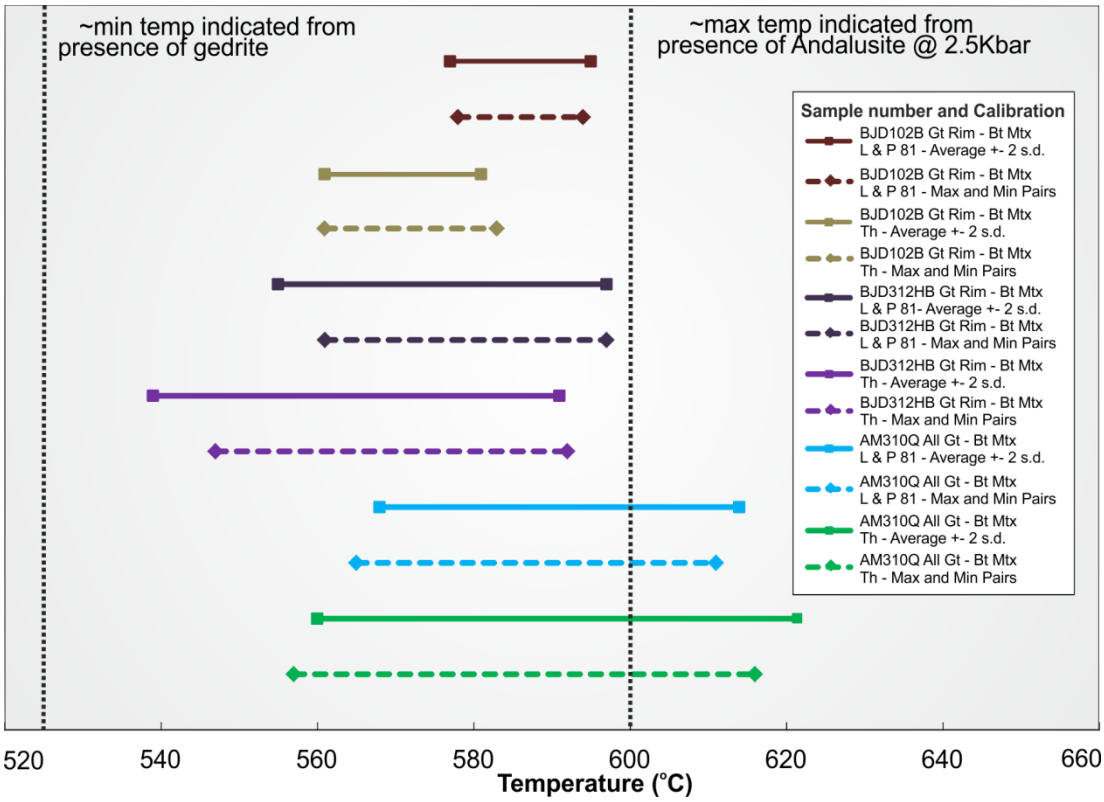

2.8 Lithologies and lithostratigraphy of the Cosmos succession

The felsic and intermediate volcanic succession at Cosmos, as well as the hangingwall sedimentary succession, exhibit a number of primary textural features, despite the fact that the region has experienced regional amphibolite facies metamorphism and several deformation events. These features include phenocrysts and amygdales in coherent units and volcaniclastic/pyroclastic (volcanic breccia, lapilli tuff) as well as sedimentary fabric (i.e., conglomerates in fragmental units). These features aid protolith identification. They also provide important information about the emplacement processes of the units that make up the succession and thus the geological history of the Cosmos region. Coherent and fragmental lithologies have experienced mid amphibolite metamorphism. Consequently, the felsic lithologies typically contain variable proportions of quartz + feldspar + biotite + sericite ± muscovite ± chlorite ± garnet ± epidote. Intermediate lithologies typically contain

varying proportions of feldspar + hornblende + biotite + chlorite ± quartz ± amphibole ± epidote ± sericite. The prefix "meta" is inferred but omitted from lithological descriptions in this study and protolith rock nomenclature is used for units where primary textures are preserved or inferred on basis of chemical composition and/or pseudomorphic mineral overprints. The classification scheme of White and Houghton (2006) is used for volcaniclastic and sedimentary rocks and the scheme of Cas et al. (2008) is used for coherent volcanic rocks (see Appendix 5). A composite vertical section and simplified level plan (Fig. 2.3) highlight the key lithological groups identified in the stratigraphy and these are described below. Additionally, the major and trace element data was used to confirm the lithological identification's based on mineralogy and petrography (Fig. 2.4).

The geochemical attributes of the individual lithological units and the geochemical affinity of the succession as a whole are covered in detail in Chapter 3. However, Figure 2.4 shows the composition of the main lithological groups used to support the interpretation of their respective compositions indicated by their metamorphic mineral assemblages. All lithologies are sub-alkaline. Figure 2.5 highlights the high-K calc-alkaline to shoshonite affinity of the coherent andesites and dacites, which will be discussed in detail in Chapter 3.

Figure 2.3. (Next page) Composite vertical section of the stratigraphy of the Cosmos greenstone succession. Thickness of individual units are approximate as many of the units vary widely in thickness along the >1km length of the studied area as can be seen in the adjacent relative level plan. Average U-Pb ages are given for zircons contained within nine different lithologies within the Cosmos succession (after de Joux et al, 2013; Chapter 4). Ages stated are the average $^{207}Pb/^{206}Pb$ age for each lithology, quoted with errors of 2σ. The adjacent level plan shows a simplified reconstruction of the interpreted geology on the -150m RL (i.e. 150m below sea level) showing how the main lithological units relate to one another and their variation in thickness along strike. Only the Alec Mairs mafic intrusion is shown on this level plan as the Cosmos Deeps mafic intrusion cross cuts the stratigraphy at a shallower relative level, above the 0mRL level.

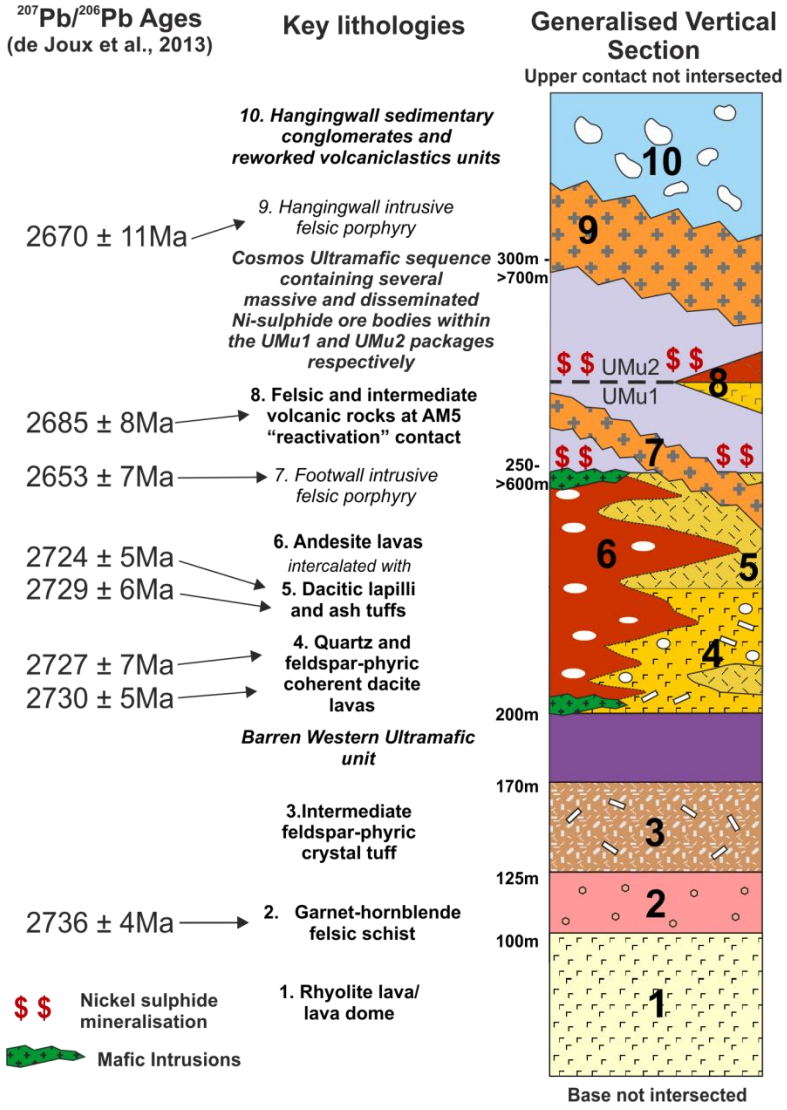
^{207}Pb/^{206}Pb Ages
(de Joux et al., 2013)
Key lithologies
Generalised Vertical Section
Upper contact not intersected
10. Hangingwall sedimentary conglomerates and reworked volcaniclastics units
9. Hangingwall intrusive felsic porphyry
2670 ± 11Ma
Cosmos Ultramafic sequence containing several massive and disseminated Ni-sulphide ore bodies within the UMu1 and UMu2 packages respectively
300m - >700m
8. Felsic and intermediate volcanic rocks at AM5 "reactivation" contact
2685 ± 8Ma
2653 ± 7Ma
7. Footwall intrusive felsic porphyry
250- >600m
6. Andesite lavas intercalated with
2724 ± 5Ma
2729 ± 6Ma
5. Dacitic lapilli and ash tuffs
2727 ± 7Ma
2730 ± 5Ma
4. Quartz and feldspar-phyric coherent dacite lavas
200m
Barren Western Ultramafic unit
170m
3.Intermediate feldspar-phyric crystal tuff
125m
2736 ± 4Ma
2. Garnet-hornblende felsic schist
100m
1. Rhyolite lava/ lava dome
$ $ Nickel sulphide mineralisation
Mafic Intrusions
UMu2
UMu1
Base not intersected

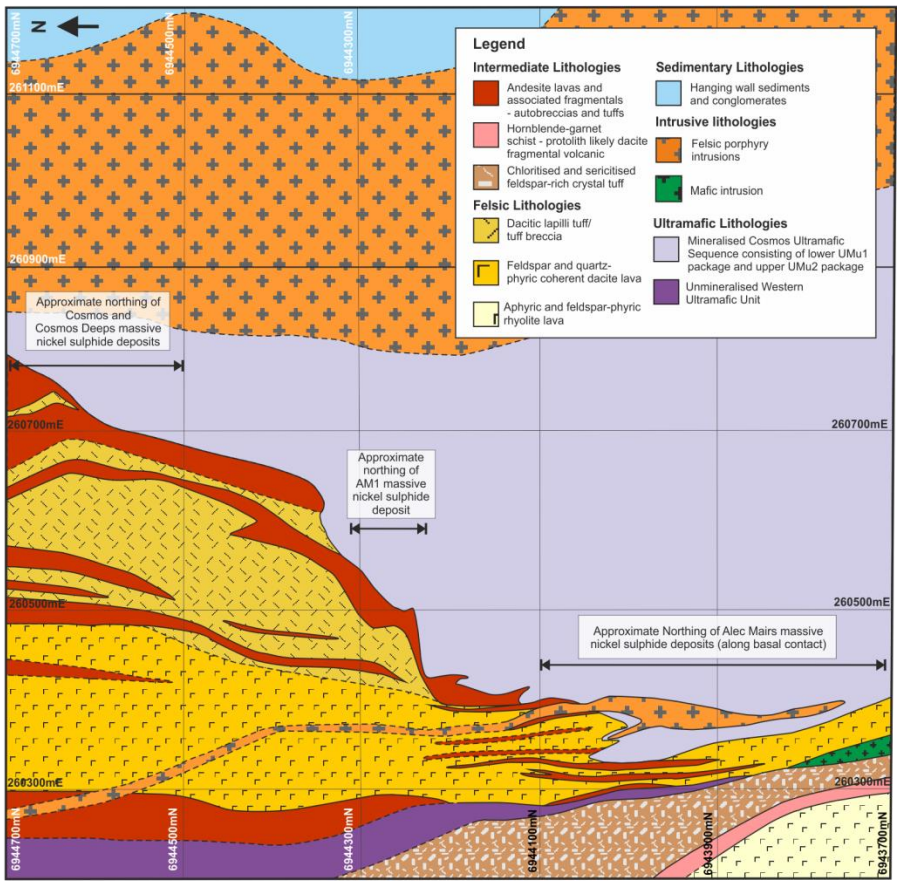
Simplified -150m (below sea level) level plan
N
Legend
Intermediate Lithologies
Andesite lavas and associated fragmentals - autobreccias and tuffs
Hornblende-garnet schist - protolith likely dacite fragmental volcanic
Chloritised and sericitised feldspar-rich crystal tuff
Felsic Lithologies
Dacitic lapilli tuff/ tuff breccia
Feldspar and quartz-phyric coherent dacite lava
Aphyric and feldspar-phyric rhyolite lava
Sedimentary Lithologies
Hanging wall sediments and conglomerates
Intrusive lithologies
Felsic porphyry intrusions
Mafic intrusion
Ultramafic Lithologies
Mineralised Cosmos Ultramafic Sequence consisting of lower UMu1 package and upper UMu2 package
Unmineralised Western Ultramafic Unit
Approximate northing of Cosmos and Cosmos Deeps massive nickel sulphide deposits
Approximate northing of AM1 massive nickel sulphide deposit
Approximate Northing of Alec Mairs massive nickel sulphide deposits (along basal contact)
6944700mN
6944500mN
6944300mN
6944100mN
6943900mN
6943700mN
261100mE
260900mE
260700mE
260500mE
260300mE

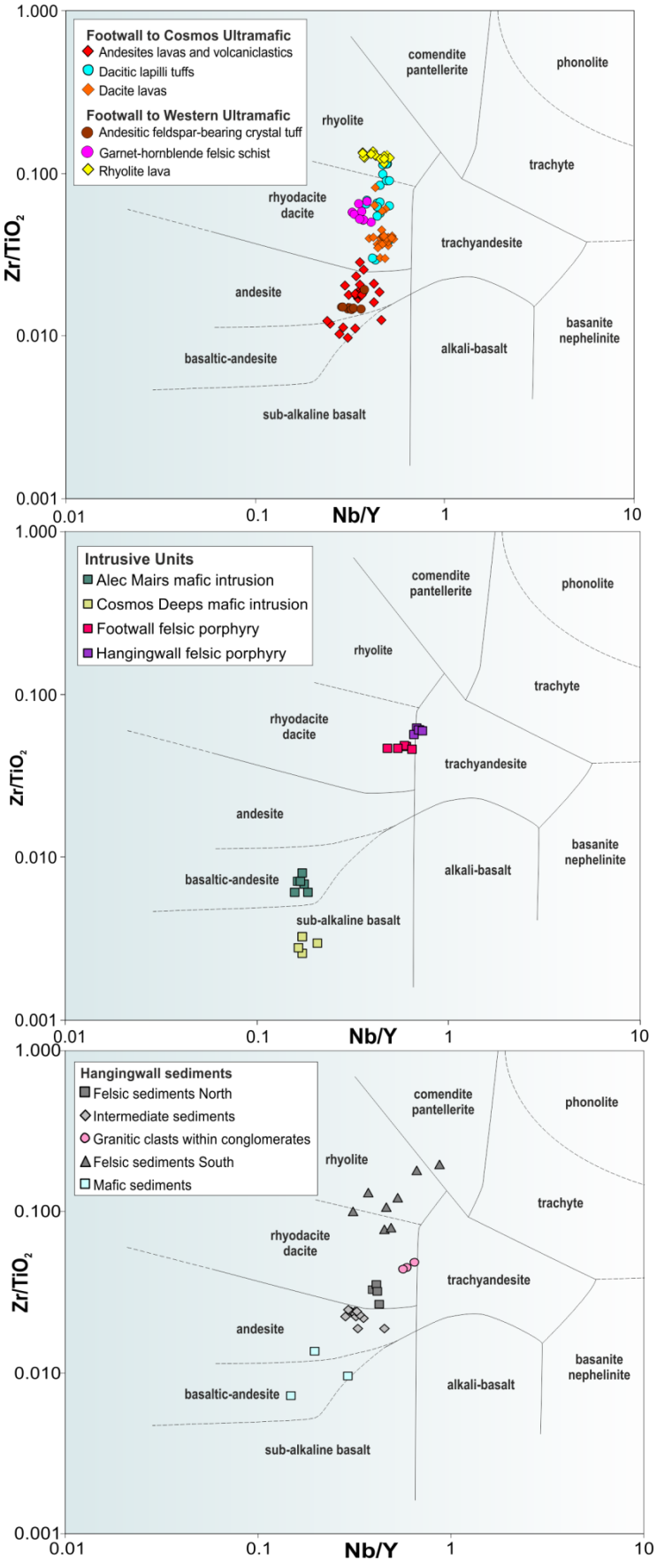
Footwall to Cosmos Ultramafic
Andesites lavas and volcaniclastics
Dacitic lapilli tuffs
Dacite lavas
Footwall to Western Ultramafic
Andesitic feldspar-bearing crystal tuff
Garnet-hornblende felsic schist
Rhyolite lava
comendite pantellerite
phonolite
rhyolite
trachyte
rhyodacite dacite
trachyandesite
andesite
basanite nephelinite
alkali-basalt
basaltic-andesite
sub-alkaline basalt
1.000
0.100
0.010
0.001
0.01
0.1
1
10
Zr/TiO2
Nb/Y
Intrusive Units
Alec Mairs mafic intrusion
Cosmos Deeps mafic intrusion
Footwall felsic porphyry
Hangingwall felsic porphyry
Hangingwall sediments
Felsic sediments North
Intermediate sediments
Granitic clasts within conglomerates
Felsic sediments South
Mafic sediments

Figure 2.4. (Previous page). Compositional plots using immobile element ratios Zr/TiO_2 versus Nb/Y (after Winchester and Floyd, 1977) for the Cosmos Succession. TOP - Composition of the extrusive volcanic footwall succession to both the Western Ultramafic unit and the Cosmos Ultramafic Sequence. MIDDLE - Composition of the four main felsic and mafic intrusions. BOTTOM - Composition of the four broad lithological groups within the hangingwall sedimentary succession.

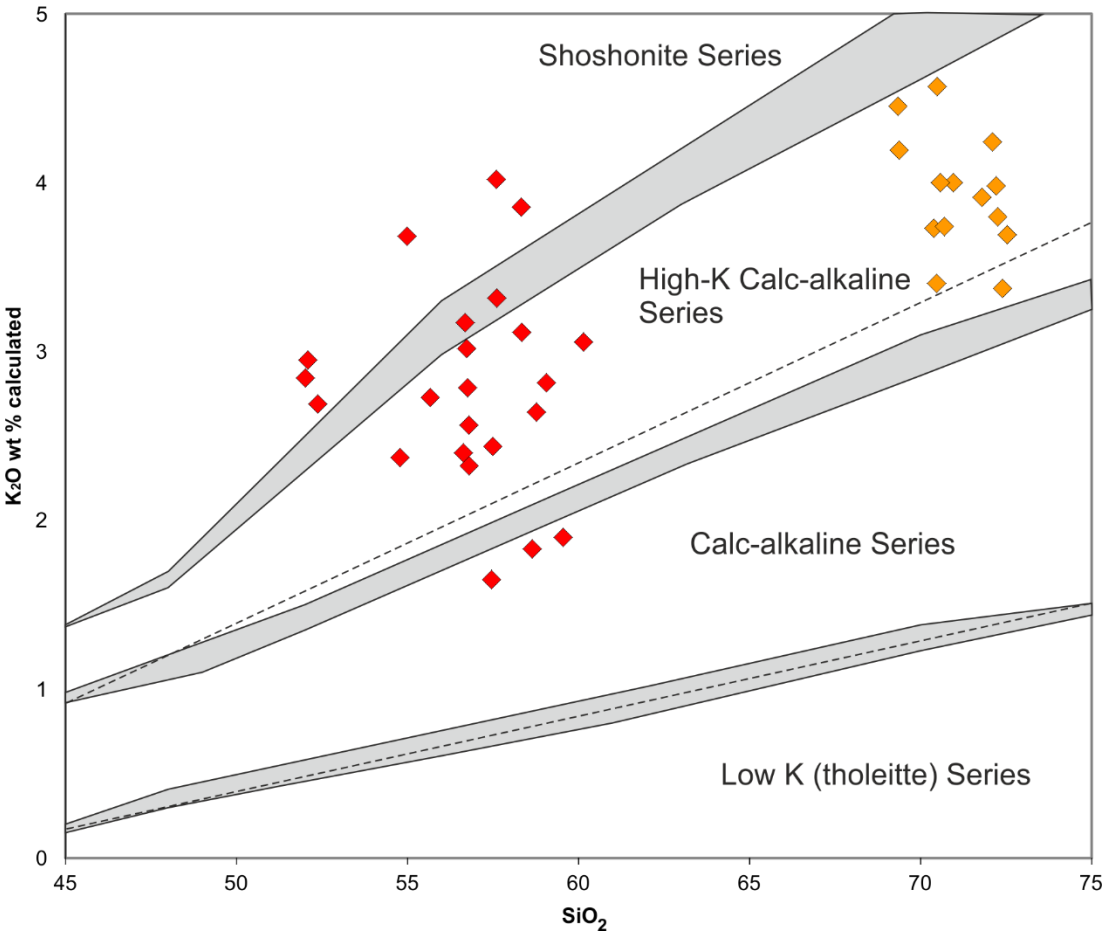

Figure 2.5. K_2O vs. SiO_2 diagrams for assessing the geochemical affinity of the coherent andesites (red diamonds) and coherent dacites (orange diamonds). K_2O (calc) vs. SiO_2, calculated after Hollings and Kerrich (2006) using K_2O (calc) = [La (ppm) x800]/8301. This plot has been used to classify coherent andesites and dacites with K_2O (calc) contents <5%, as the equivalent relationship between K ppm and La ppm breaks down above 5 wt % K_2O (Wheller et al., 1987; Hollings and Kerrich, 2006). The coherent andesites and dacites can be seen to have a high-K calc-alkaline affinity with some andesitic samples extending into the shoshonite field.

2.9 Coherent lithologies

2.9.1 Coherent rhyolite

Coherent rhyolite occurs within the deepest parts of the footwall succession to the Western Ultramafic unit. Current drilling has yet to intersect the base of this unit, which is >100m thick (Fig. 2.3). It has a sharp contact with the overlying felsic garnet-hornblende schist.

This lithology exhibits both aphyric and porphyritic varieties with feldspar as the only phenocryst phase (Fig. 2.6a and 2.7). Feldspar phenocrysts are 1 - 3mm in size and account for 4 - 6 modal% of the rock. They typically exhibit euhedral to sub-hedral tabular or stubby prismatic, and more rarely equant, forms and are often present as glomerocrystic aggregates. Individual crystals often exhibit simple twins (Fig. 2.6a) and more rarely multiple twinning, indicating they are now of albite or microcline composition. In regions least effected by metamorphism the feldspars commonly contain small inclusions of very fine-grained (<20µm in diameter) secondary muscovite and/or quartz (Fig. 2.6a). As the metamorphic overprint intensifies the feldspar phenocrysts are progressively replaced and overgrown by anhedral very fine-grained, light brown sericite (± quartz), giving the feldspars a "dusty" appearance in thin section and a more anhedral appearance in hand specimen (Fig. 2.7). Further intensification of the metamorphism, coupled with higher strain, results in pervasive replacement of the feldspar by sericite, both within the groundmass and individual phenocrysts. This process often completely obliterates the original porphyritic texture (Fig. 2.7). Fine-grained biotite is present throughout the unit but accounts for ≤1 modal% of the rock and is interpreted to be the metamorphic replacement of mafic phases, originally present in minor amounts. The groundmass is composed of a cryptocrystalline quartz-feldspar mosaic, where the feldspar is interstitial to the quartz grains. The groundmass also contains coarser grained (~200 - 1000µm) lath-shaped to bladed sericite present along grain boundaries and defining the foliation (Fig. 2.6a). With increasing degree of metamorphic overprint, the cryptocrystalline quartz groundmass is progressively overgrown by aligned lathy sericite crystals, as the

interstitial feldspar breaks down (Fig. 2.6a). At peak replacement the coarse grained sericite is aligned in distinct bands that crosscut the groundmass and define the foliation (Fig. 2.6a). This transition from weakly to strongly sericitised rhyolite is generally gradual (Fig. 2.7).

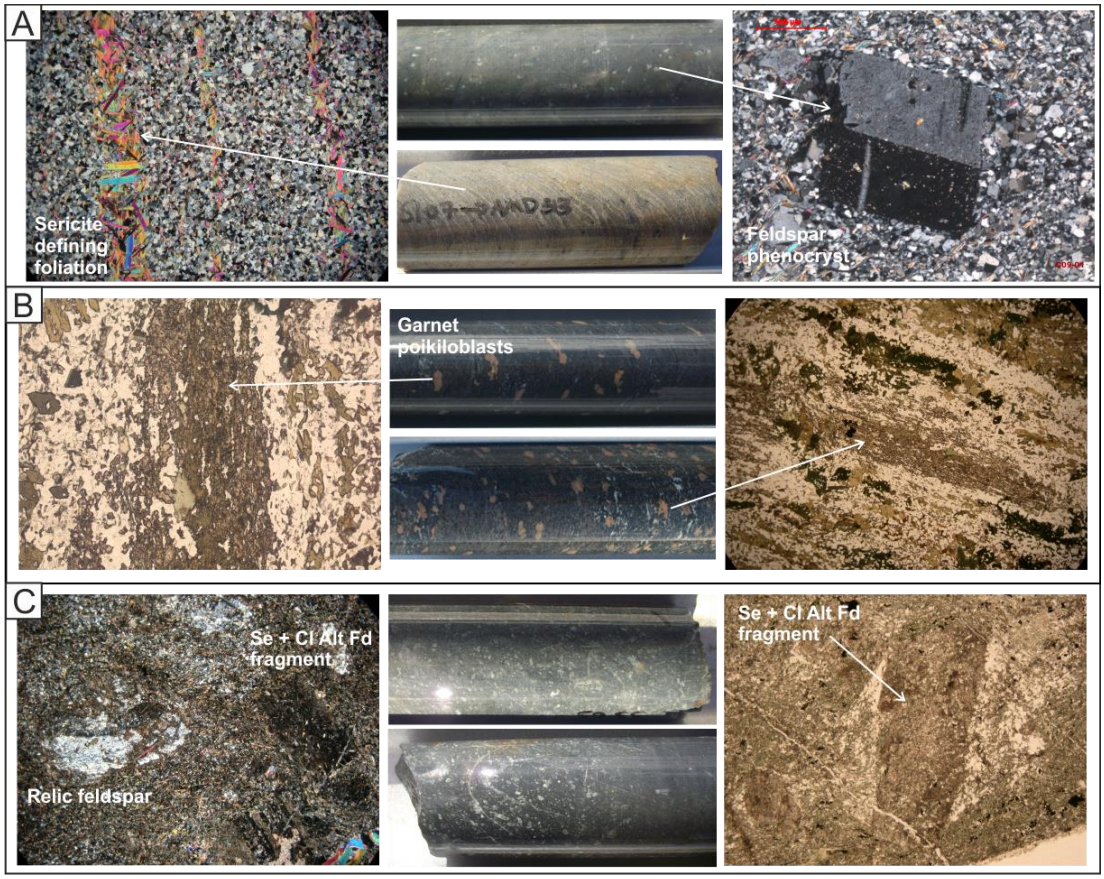

Figure 2.6. Representative core samples and photomicrographs of the lithologies from the footwall to the Western Ultramafic unit in stratigraphic order (a) Coherent rhyolite, highlighting a relic simply twinned feldspar phenocryst (right) and the typical sericite-defined foliation (left). (b) Garnet-hornblende felsic schist containing skeletal poikiloblastic garnets in a banded feldspar, hornblende and epidote groundmass (c) Intermediate feldspar-bearing crystal tuff containing feldspar crystal fragments of variable size and morphology, which are now pervasively overprinted by sericite and chlorite. Se = sericite, Cl Alt = chlorite altered. Fd = Feldspar.

The aphyric sectors of the rhyolite have a homogeneous appearance. The groundmass is now composed of cryptocrystalline quartz mosaic, with some minor interstitial feldspar and varying modal contents of sericite depending on the strength of the metamorphic overprint via recrystallisation. It is difficult to correlate, with satisfactory confidence, individual aphyric or feldspar-phyric domains between

adjacent drill holes. This, along with absence of any discernible internal contacts, suggests that this alteration between aphyric and 4 - 6 modal% feldspar phyric domains is an internal feature rather than multiple (i.e. separate and alternating) lithological units.

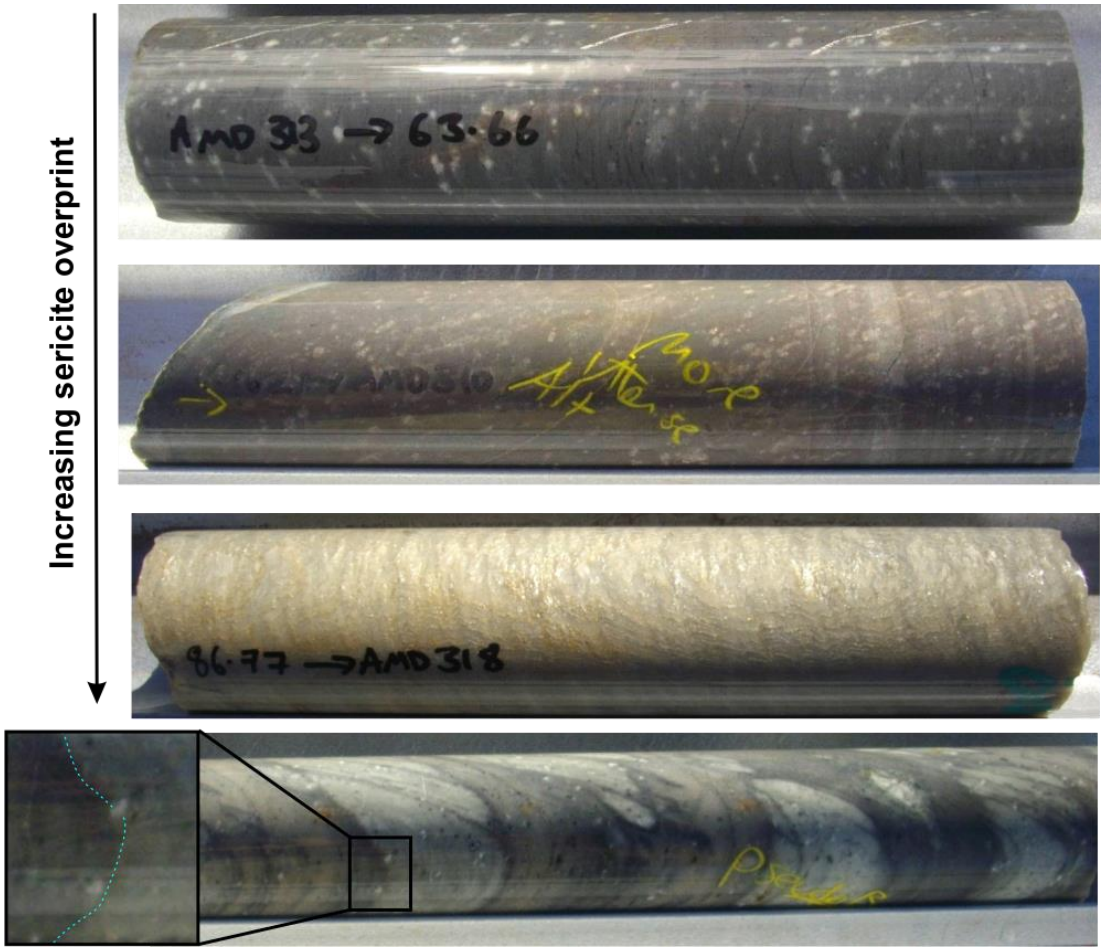

Figure 2.7. Core photos of coherent rhyolite, highlighting how progressive sericitisation obscures the original porphyritic texture. The lowest panel shows an example of the pseudobreccia texture present in the coherent rhyolites from AMD310 at ~30m depth, where feldspar phenocrysts extend across the apparent "clast" boundaries.

In a few places pseudo-breccias are discernable within the coherent rhyolites (Fig. 2.7). These are isolated 0.3 - <2m thick horizons present in the central sector of the known rhyolite extent. They have apparent clastic texture where white angular, and variably sheared 2 - 8 cm-size domains are resting in a more continuous yellow matrix-like mass (Fig. 2.7). The pseudo-breccia origin is indicated by feldspar phenocrysts extending across apparent clast-matrix boundaries coupled with the isolated and

somewhat sporadic occurrence of apparent breccia facies (Fig. 2.7). Such pseudobreccias are readily distinguished from true fragmental breccias that exhibit contrasting textural and compositional attributes between the clasts and matrix. It is thought that such pseudo-breccias are formed by decimetre-scale variation in the intensity and style of metamorphic recrystallisation (Rosengren et al., 2005; 2008). Similar pseudobreccias are present within the coherent dacites (see Section 2.9.2).

In terms of chemical composition this lithofacies is the most silicic volcanic unit within the succession and the chemical analyses define a tight cluster within the rhyolite field on Figure 2.4.

Interpretation: This coherent rhyolite unit has a dome-like geometry and contains 0 - 6 modal% feldspar phenocrysts sitting in a cryptocrystalline quartz-feldspar mosaic groundmass. This type of felsic groundmass, consisting of fine intergrowths of recrystallised quartz and feldspar, has been demonstrated to represent a range of syn-volcanic devitrification textures after volcanic glass (e.g., Lofgren, 1971; McPhie et al., 1993). Subsequent metamorphism would have promoted further recrystallisation of the groundmass. Hence, the Cosmos rhyolite is considered to be a lava flow/lava dome composed of numerous stacked lava flow lobes and potentially formed in a single eruption (Fig. 2.3).

2.9.2 Coherent dacite

This unit is present within the deeper parts of the footwall succession below the UMu1 package of the Cosmos Ultramafic Sequence and commonly directly above the Western Ultramafic Unit (Fig. 2.3).

The coherent dacites are typically porphyritic, with 5 - 20 modal % of 2-15 mm quartz phenocrysts and 5 - 15 modal% of 2 - 12mm relict feldspar phenocrysts (Fig. 2.8a). Quartz phenocrysts are sub-hedral to sub-rounded equant crystals that often exhibit undulose extinction and parallel deformation bands (Fig. 2.8b). They are

commonly broken down into subgrains, with highly sutured boundaries. A significant number of the quartz phenocrysts feature embayments filled with groundmass; a clear indication of resorption (Fig. 2.8b). The feldspar phenocrysts are most commonly present as relict crystals replaced by very fine grained (< 50µm) light brown sericite, giving them a dusty appearance (Fig. 2.8c). Less metamorphosed sections of the dacite contain 15 modal% of sub-hedral tabular or stubby prismatic feldspar phenocrysts ranging in size from 2 - 12mm. These phenocrysts commonly feature simple twinning. Importantly, the long axis of feldspar phenocrysts are typically aligned with the foliation, indicating that foliation is following an original flow fabric. Feldspar phenocrysts are often fractured in-situ, with jigsaw fit arrangement of fragments, indicating that the fracturing is deformation-induced.

In hand specimen the apparent abundance of feldspar phenocrysts is highly variable and appears significantly much less abundant in highly strained samples (Fig. 2.8a). To what extent this variation is influenced by alteration is difficult to discern because some apparently aphyric hand specimens do have relict feldspar phenocrysts in thin section while others have none. This suggests that there is an original variability in the abundance of feldspar phenocrysts throughout the coherent dacite units, although the extent of this variability is somewhat obscured by sericite overprinting (Fig. 2.8a).

The groundmass consists of fine-grained (50 - 100µm) cryptocrystalline quartz-feldspar mosaic with abundant aggregates of biotite laths (partly replaced by chlorite). These aggregates are often aligned and define a weak to moderate foliation that wraps around large quartz phenocrysts (Fig. 2.8d). In domains characterised by slightly coarser grained groundmass, distinct cross-hatched twinning is present in the feldspars suggesting it was (or is) predominantly microcline.

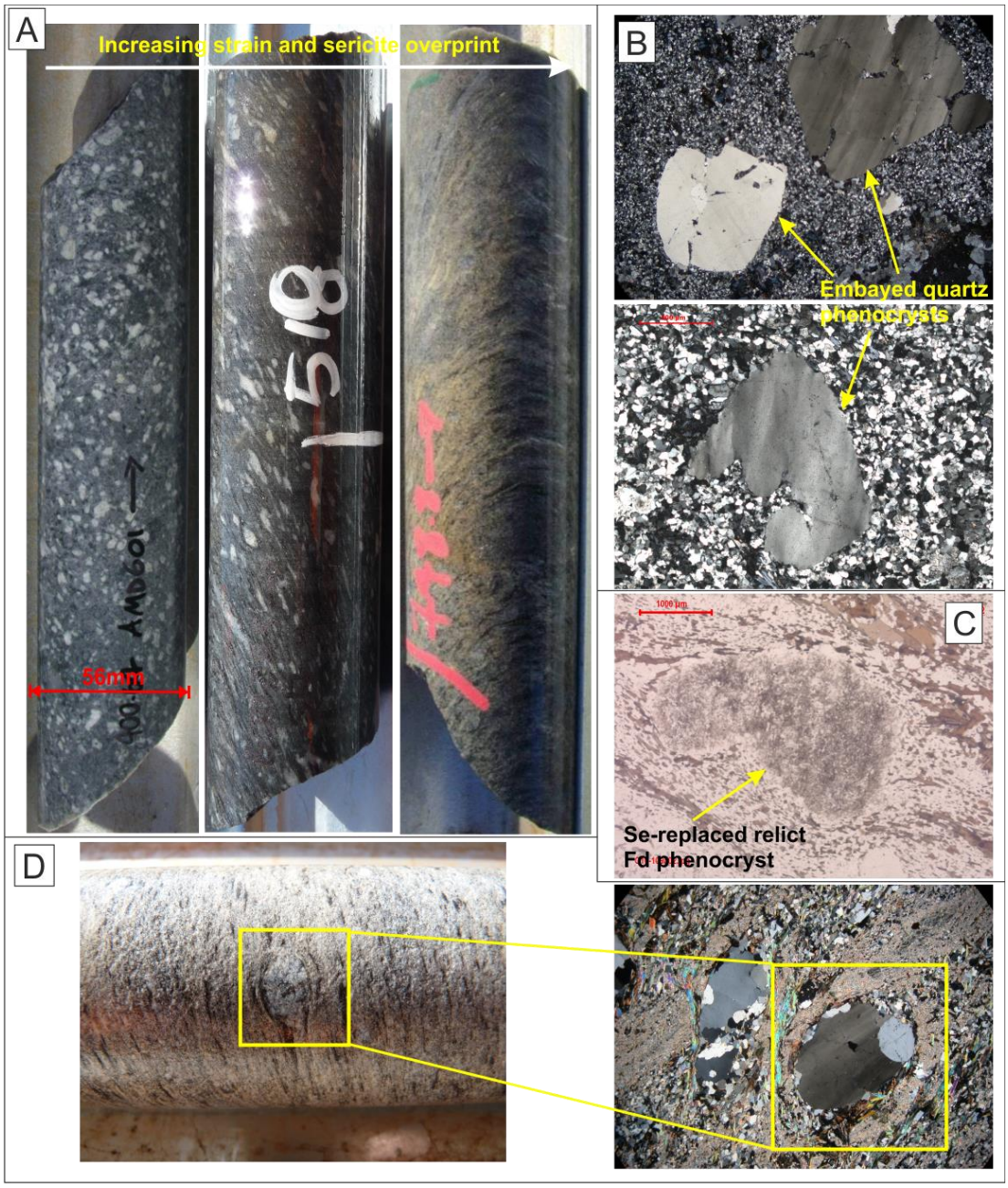

Figure 2.8. Core photos and photomicrographs of the coherent dacites. (A) Core photos of coherent dacite showing pristine porphyritic appearance (far left) as well as the effect of increasing strain and sericite overprint on the preservation of the original igneous texture; (B) Photomicrographs of quartz phenocrysts with strain-induced undulose extinction and embayments (upper panel) and a strongly embayed quartz phenocryst (lower panel). (C) A relict feldspar phenocryst pervasively replaced by very fine grained sericite, recognised only in plan polarised light by its pseudomorphed crystal habit and typical "dusty" appearance; (D) Strongly sheared coherent dacite with relict quartz phenocrysts present as quartz "eyes" wrapped by the strongly foliated groundmass (left panel, in core sample; right panel, in thin section).

Style, intensity and occurrence of the metamorphic overprint are highly variable throughout the succession with silicification, chloritisation and sericitisation common throughout. The composition and extent of the overprinting mineral assemblage is likely to be controlled by a combination of factors; such as proximity to metamorphic fluid pathways or contacts of late-stage intrusions, extent of retrogressive reactions, as well as location of any large structures within the succession. Sericitisation is common in strongly sheared samples where quartz phenocrysts present as isolated quartz "eyes" and are all that remains of the primary texture. These "eyes" are often accompanied by pressure shadows and surrounded by a strongly foliated aligned sericite and quartz groundmass (Fig. 2.8d). Strongly sericitised and chloritised samples exhibit crenulation and strong foliation. They lack the typical porphyritic texture suggesting these horizons were aphyric, although it is possible that in places the phenocrystic nature is obscured by the metamorphic overprint.

In terms of chemical composition the coherent dacites form a tight group within the rhyodacite field (Fig. 2.4) and display high-K calc-alkaline geochemical affinity (Fig. 2.5).

Interpretation: The spatiotemporal intercalation of amygdaloidal andesite lavas with coherent dacites is strongly suggestive of an extrusive origin (Fig. 2.3; Appendix 4). The stratigraphic association and shared geochemical attributes of coherent dacite and dacite lapilli tuff units (Fig. 2.4), implies common magmatic and volcanic source. The coherent dacite is typified by relict, embayed quartz phenocrysts that sit in a mosaic quartz-feldspathic matrix, which is, as indicated in section 2.9.1, derived from devitrification of glassy groundmass. Embayed quartz phenocrysts exhibit rounded corners and edges suggesting they were resorbed (Donaldson and Henderson, 1988). Embayed quartz phenocrysts are commonly present in modern dacite lava domes/lavas. Resorption of quartz phenocrysts in magma occurs when phenocrysts become unstable, typically due to an increase in the liquidus temperature of the magma, and consequently the quartz phenocrysts react to re-equilibrate with the melt. This can be caused by magma mixing of the host magma with a higher

temperature magma or induced by decompression-driven degassing of water in slowly rising magma and/or upon eruption (Gill, 2010).

2.9.3 Coherent andesite

Coherent andesites, with associated fragmental facies, are intercalated with both the coherent and fragmental dacites, and together these three lithofacies comprise the footwall between the Western Ultramafic unit and the UMu1 package of the Cosmos Ultramafic Sequence (Fig. 2.3). Individual packages of andesites range in stratigraphic thickness from less than 1m to up to ~70m.

Coherent andesites are typically aphyric and less commonly contain amphibole or biotite porphyroblasts that may be pseudomorphs after primary mafic (possibly pyroxene) phenocrysts. These porphyroblasts are typically comprised of lathy hornblende and/or biotite and occupy 5 - 10 modal% of the rock. They are <0.2 - 5mm across, and exhibit euhedral to subhedral, equant form, that give this lithology a spotted appearance in drill core (Fig. 2.9b). Aphyric andesites are similar in texture and mineralogy to the "mafic-phyric" andesites except they lack the distinctive spotted texture formed by the hornblende and biotite porphyroblasts. The groundmass is composed of <200µm crystal aggregate of hornblende, biotite and feldspar with minor amounts of chlorite and lesser amounts of quartz (Fig. 2.9b). In general, the coherent andesites are homogenous in terms of mineral assemblage and texture.

Andesites regularly contain amygdales filled with quartz aggregate, which is coarser grained than the surrounding groundmass (~200 - 400µm), as well as minor interstitial phylosillicates, such as chlorite (Fig. 2.9a). The amygdales are variable in size, occurrence and shape. Elliptical clusters of amygdales, ranging in size from <5mm to >30mm across, occur as sporadic horizons within the coherent andesite and are not evenly distributed within individual units (Fig. 2.9a). Irregular, "wispy" amygdales, 10 - 70mm across, are more common throughout andesitic horizons (Fig. 2.9a).

Breccia horizons are present at the base of the thinner (10 - 20m thick) andesitic units, and more rarely as intercalated horizons near the centre of the thicker (up to 70m thick) andesitic bodies. These horizons are recognised by their clastic appearance (including clear sub-angular clasts) in conjunction with distinctly more prominent textural and mineralogical heterogeneity and higher modal abundances of void-filling material. The clasts, when discernible, generally account for 40% of breccia horizons, ranging in size from 5 – 80mm and a modal size of 10 - 30mm.

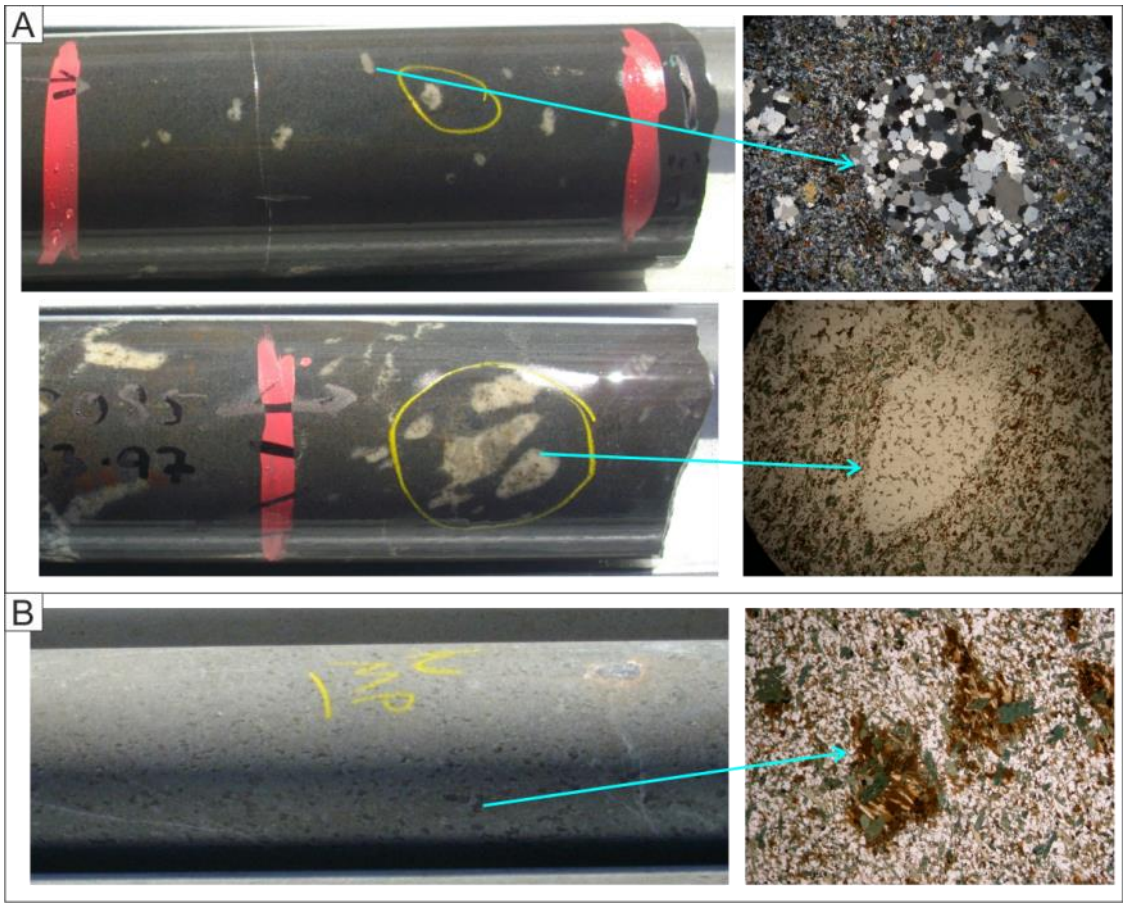

Figure 2.9. Representative core photos and photomicrographs of coherent andesites (a) Coherent andesite containing elliptical and more irregular "wispy" amygdales filled with an aggregate of quartz crystals with interstitial phylosillicates, largely biotite and chlorite (b) An example of "mafic-phyric" coherent andesite containing large biotite and hornblende porphyroblastic aggregates in a finer grained feldspar-hornblende-biotite-chlorite groundmass.

Sporadic fragmental andesitic horizons are present within the sequence and can be distinguished from the coherent units due to absence of amygdales, heterogeneous mineralogy, sporadic presence of distinctly banded/layered horizons, and the presence

of rare fractured feldspar crystals. These are distinguished from the breccia horizons by their lack of discernible clasts, although this distinction is often obscured by the variable degree of deformation, alteration and metamorphic recrystallisation. The amygdaloidal horizons typically provide the only unequivocal evidence of a coherent origin. In terms of their chemical composition these fragmental units broadly have the same composition as the coherent andesites.

Collectively, the andesite units span the entirety of the basaltic andesite to andesite field on Figure 2.4 and do not exhibit the uniform composition shown by the coherent dacites and rhyolites. They have a high K-calc-alkaline to shoshonite affinity (Fig. 2.5).

Interpretation: The presence of abundant amygdales and breccia facies underpin the emplacement of the andesites as lava flows. Breccia horizons within thick andesite packages are interpreted to represent flow top or flow base rubble (i.e., autobreccia) and thus implying that these units are composed of stacked flow lobes or flows. Elliptical rounded amygdales are indicative of a less viscous lava with unimpeded gas exsolution forming near-spherical vesicles. More common and larger irregular amygdales indicate formation in more viscous lava, such as a'a flows, where viscous shearing of the melt stretched and deformed exsolved gas bubbles. Fragmental andesites are interpreted to represent lapilli tuff horizons that are intercalated with the more dominant andesite lava sequences.

2.10 Fragmental lithologies

2.10.1 Fragmental dacites

Fragmental (= lapilli tuff) dacites are abundant within the footwall to UMu1 package of the Cosmos Ultramafic Sequence and are intercalated with andesite lavas (Fig. 2.3). The fragmental dacites are present in greater thickness towards the north (>200m in stratigraphic thickness), in the region of Cosmos Deeps, and thin towards the south. By ~6944100mN, they are sparse and generally <5m thick.

The dacite lapilli tuff units are broadly distinguished from coherent dacites by absence of large (>2 mm) quartz phenocrysts, specifically embayed quartz phenocrysts, their heterogeneous clastic fabric and the common, variably sericite-replaced and fractured feldspar crystals within the lapilli grains (Fig. 2.10b). Collectively, feldspar crystals account for ~25 – 40 modal % of the rock and range in size from 1 - 7mm. They are dominantly fragments, or more rarely shards of feldspar, and have been variably replaced by fine-grained sericite. The feldspar crystal fragments are best distinguished from the finer grained quartzo-feldspathic matrix in plane-polarised light, where the sericite replacement results in a dark, dusty appearance (Fig. 2.10b). The variability in abundance of feldspar crystals could be directly attributed to primary variation in the feldspar content of individual dacite lapilli tuff packages. However, the possible obliteration of feldspar phenocrysts due to recrystallisation and shearing of the succession is difficult to constrain and quantify. Small quartz phenocrysts (0.5 – 2mm) are also present and are typically equant and euhedral to subhedral (Fig. 2.10b).

Figure 2.10c demonstrates how the fragmental nature of the rock can be obscured by pervasive metamorphic overprinting. The two core samples on either side of the central example, which preserves the pristine clastic fabric, were taken within two metres of the central piece. These core samples demonstrate how alteration and recrystallisation, dominantly a strong sericite overprint, obliterates the original clastic texture. In samples exhibiting a less pervasive metamorphic overprint, discreet 5-20mm (up to 70 mm) lapilli-size fragments are distinguished. (Fig. 2.10a). Three different types of lapilli fragments are identified (i) Grains with abundant feldspar phenocryst fragments and shards sitting in a fine grained quartz-feldspar mosaic groundmass (Fig. 2.10a2) (ii) angular, lapilli grains with very fine-grained biotite-rich, groundmass (Fig. 2.10a3) (iii) rare aphanitic silica-rich lapilli grains. The feldspar-quartz phyric grains are most abundant representing over 90 modal% of the lapilli clast population. Angular biotite-rich lapilli grains compose much of the remaining 10 modal % (Fig. 2.10a3).

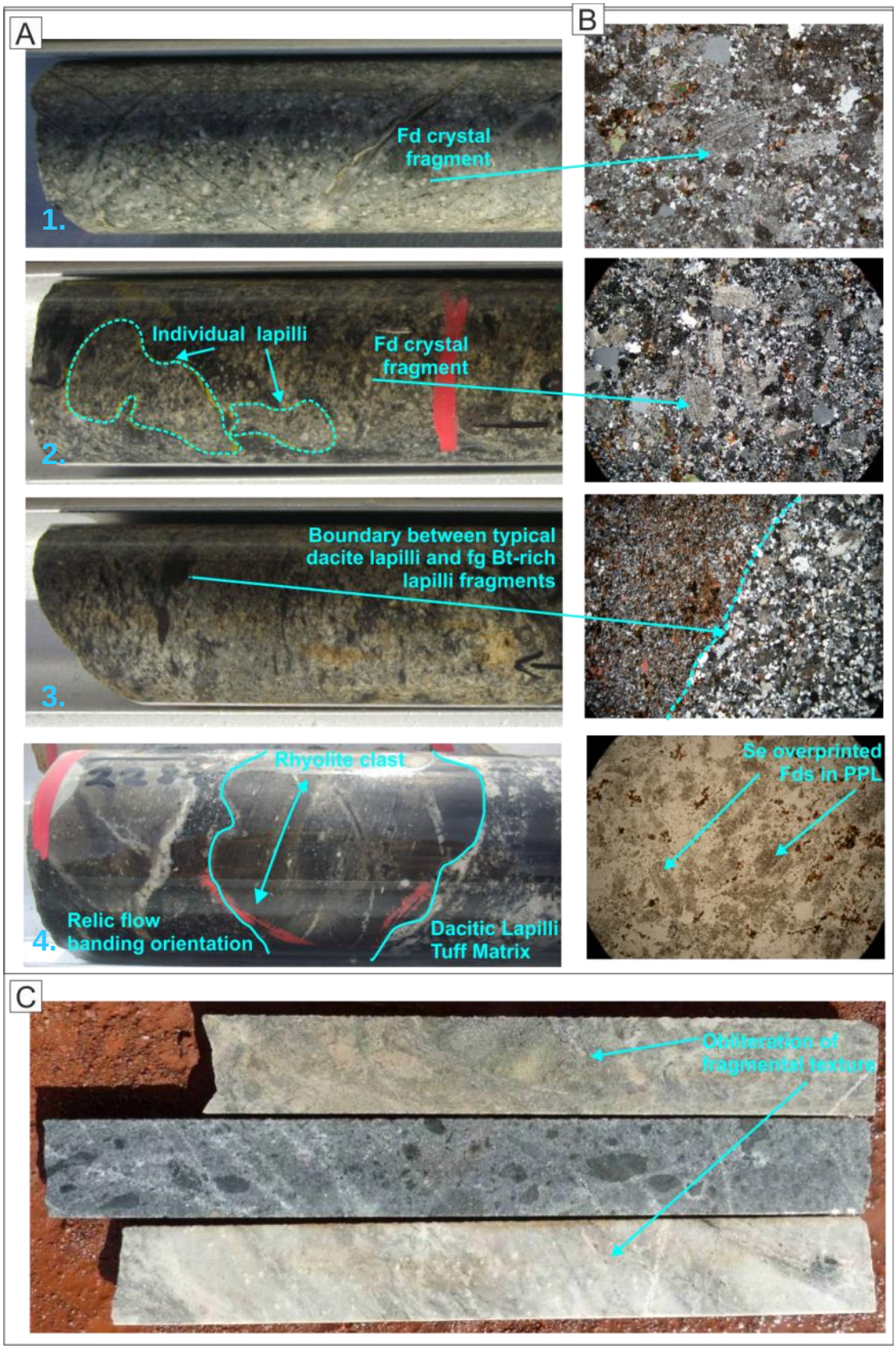
A
B
Fd crystal fragment
1.
Individual lapilli
Fd crystal fragment
2.
Boundary between typical dacite lapilli and fg Bt-rich lapilli fragments
3.
Rhyolite clast
Relic flow banding orientation
Dacitic Lapilli Tuff Matrix
4.
Se overprinted Fds in PPL
C
Obliteration of fragmental texture

Figure 2.10. (Previous page). (A) Core photos of fragmental dacite showing the typical morphology of individual lapilli clasts (highlighted). The bottom core photo (4.) gives an example of a tuff breccia with a rhyolitic clast that displays primary flow banding that is discordant to the dacite matrix fabric. (B) Photomicrographs of fragmental dacite; the top two photos highlight the typical concentration of feldspar crystal fragments within lapilli clasts in cross-polarised light (XPL). The actually concentration, abundance and morphology feldspars crystals is hard to discern in XPL and the fourth photo down highlight how the pervasive sericite overprint allows the feldspar fragments to be more easily discerned in plane polarised light (C) Example of the typical silica and sericitic overprints seen within the fragmental dacites, highlighting how both the intensity of metamorphic overprinting and alteration related to late stage silicic intrusion, pegmatites and associated quartz veining can obliterate the fragmental lapilli texture displayed by the central core piece. This type of recrystallisation often makes protolith identification of the volcanic units challenging such that detailed geochemistry is required for positive protolith identification of the most pervasively metamorphically and/or hydrothermally altered samples.

Tuff breccia horizons are common within the dacite lapilli tuff sequence, which also represent the breccia-dominated host rock to some massive sulphide deposits; e.g. Cosmos Deeps and Alec Mairs. Tuff breccia horizons are distinct from the dacite lapilli tuffs, described above, as they contain sub-angular breccia-size andesite clasts floating in a dacite tuff matrix. The size of these andesite clasts ranges from 20 - 150mm in diameter with rare clasts up to 700mm across. These clasts feature fine-grained biotite, hornblende and chlorite groundmass and minor amounts of feldspar (Fig. 2.11a). The tuff breccia horizons are matrix supported, with typical andesite clast abundance between 30 - 40%, but locally clasts can make up to 70% of individual breccia horizons. Breccia-size clast abundance and size is highly variable within individual horizons and shows no indication of systematic size grading. Individual tuff breccias horizons can be correlated over several tens of metres and often grade into typical dacite lapilli tuff horizons. The matrix is composed of fine-grained quartzo-feldspathic lapilli-ash-grade fragments with dispersed 1-3mm free-standing feldspar crystals. This matrix is demonstrably texturally, mineralogically and geochemically similar to that in the dacite lapilli tuff described above (Appendix 2, Table A2.5). A minor amount of flow-banded and feldspar-phyric rhyolitic clasts are also present and show evidence of possible primary flow banding, indicating they are incorporated lava clasts (Fig. 2.10a4).

The composition of the dacite lapilli tuffs span the rhyodacite/dacite field and extend into the rhyolite compositional field on Figure 2.4. They exhibit a greater

variability in their composition than the coherent dacite lavas. This is most likely due to their somewhat diverse clast population as well as their susceptibility to diagenetic and hydrothermal alteration and subsequent regional metamorphism. The composition of the tuff breccia matrix is similar to that of the lapilli tuffs while the intermediate clasts are andesitic in composition.

Interpretation: These fragmental lithologies are interpreted as being dacite lapilli tuffs based on the abundance of feldspar crystal fragments, as well as clear fragmental textures including occasional primary volcanic breccia horizons. The lapilli grains are considered to have formed via fragmentation of a partially crystallised porphyritic dacite magma. By the same token, the bimodal andesite clast-dacite matrix tuff breccias are considered to be primary volcanic breccias because they are stratigraphically conformable with the dacite lapilli tuff and feature the same type of matrix. Quartz veins, fault traces or fractured clasts with jigsaw fit arrangement are not present within or near these tuff breccia horizons. Hence, secondary origin via post emplacement tectonic or alteration related processes can be ruled out.

2.10.1.1 Association of dacite lapilli tuff with sulphide mineralisation

Several of the Cosmos massive sulphide deposits extend into the felsic footwall, particularly in the region of Alec Mairs and Cosmos Deeps. In these locations the dacite lapilli tuff sequence contains distinct tuff breccia horizons, predominantly comprised of andesite breccia-size clasts as described above (Fig. 2.11). These tuff breccia horizons are infiltrated by sulphide, where the massive sulphide often appears to be "bent around" andesite clasts present in the lapilli to ash-grade matrix (Fig. 2.11b). The massive sulphide may have passively filled the spaces between the breccia clasts, suggesting that these breccia horizons featured domains of open framework (i.e. clast-supported and matrix free domains). However, in places the sulphide melt appears to have made space by displacing the breccia and in other places it has interacted with and partially consumed the ash-grade dacite matrix (Fig. 2.11c). Reaction rims between the lapilli-size clasts and the molten sulphide are common (Fig.

2.11c). Pods and blebs of massive sulphide are present between individual grains in the matrix, abut andesite breccia clasts and in one instance at Cosmos Deeps infill possible relict vesicles within an andesite clast (Fig. 2.11b). Dacite lapilli tuff breccias are relatively undeformed and only exhibit minor attenuation of the lapilli- and breccia-size clasts. It is noteworthy that the unit is devoid of major fractures where the sulphide penetrates several metres into the footwall.

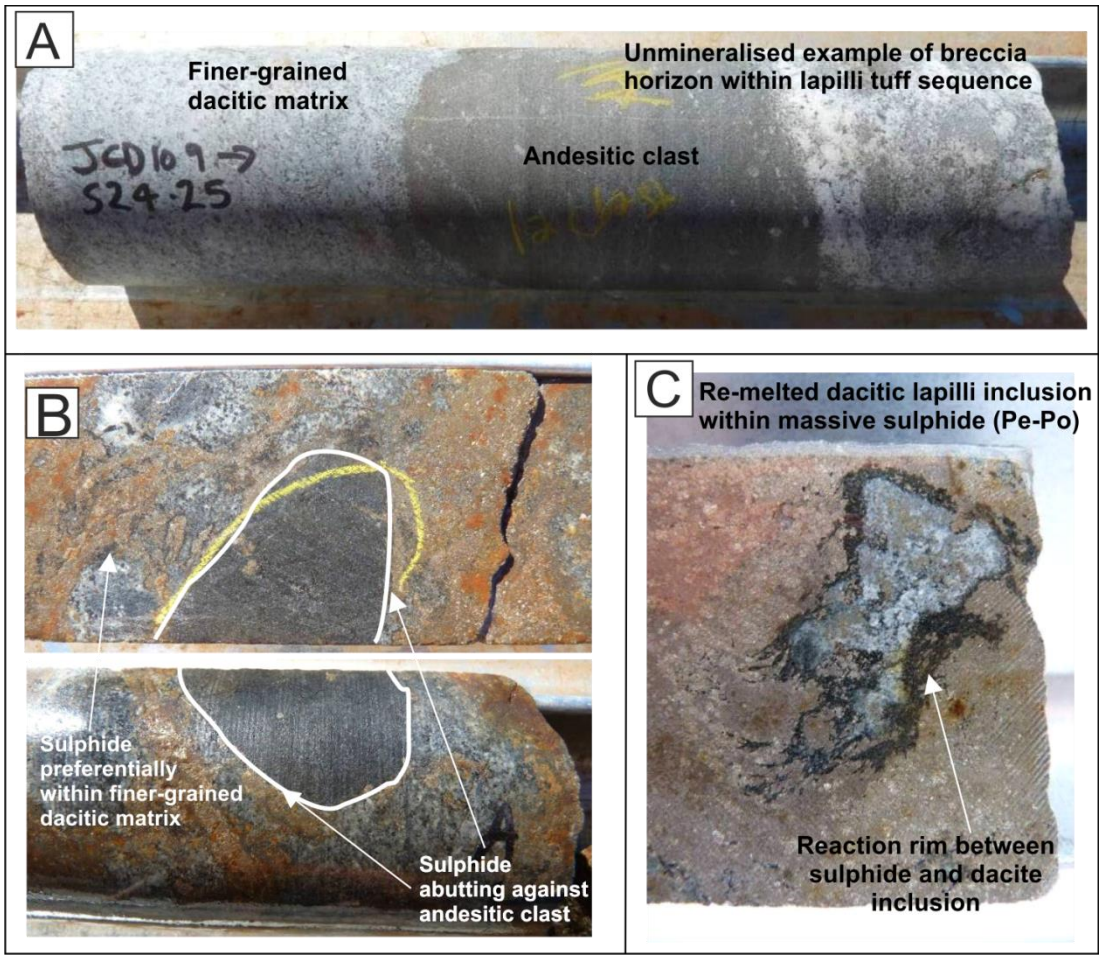

Figure 2.11. Core photographs of massive sulphide textures within the tuff breccias. (A) An unmineralised example of a typical tuff breccia lithofacies, featuring a sub-rounded andesite breccia clast resting in a dacite tuff matrix; (B) Mineralised breccia horizon with massive sulphides preferentially contained within the lapilli-ash-grade matrix and abutting against the andesite clasts; (C) Dacite lapilli tuff inclusion in a domain of massive sulphide and showing typical "wispy" biotite–rich rim indicating reaction between molten sulphide and dacite inclusion.

2.10.2 Garnet-hornblende felsic schist

This unit directly overlies the coherent rhyolite within the footwall to the Western Ultramafic unit and is the second lowest stratigraphic unit in the succession (Fig. 2.3). It ranges in thickness from 10 - 25m metres and has a sharp dominantly planar contact with the underlying rhyolite.

The unit is totally recrystallised and provides limited textural clues of its original lithology. It consists of large poikiloblastic garnets, sitting in a foliated hornblende-plagioclase matrix. The foliation is defined by alternating irregular bands of hornblende+epidote and plagioclase+quartz. The inclusion-rich garnet poikiloblasts are elongate, with longest axis ranging from ~5mm to ~20mm and aligned with the foliation (Fig. 2.6b). Their abundance, size and occurrence is highly variable throughout the unit, as is the proportion of mafic and felsic bands (Fig. 2.6b). The garnets are considered to be syn-tectonic and their salmon orange colour indicates almandine. This garnet-hornblende schist also contains rare <10mm relict feldspar phenocryst fragments that are now largely replaced by sericite and/or quartz.

Chemical analyses indicate a rhyodacite-like composition with a geochemical signature very similar to the overlying dacite lavas.

Interpretation: Protolith identification for this unit is problematic, because primary textures are largely obliterated by pervasive metamorphic recrystallisation. Its rhyodacite composition and similarity with the overlying dacites indicates this unit likely represents a strongly metamorphosed fragmental dacite lithology (Fig. 2.5). The presence of occasional fragments of feldspar phenocrysts, coupled with the units overall textural heterogeneity supports this interpretation. Feldspars can be taken to represent crystal fragments generated in an explosive eruption of a porphyritic dacite magma. During metamorphism the underlying rhyolite lava would have been relatively impermeable with respect to metamorphic fluids. The impermeable nature of the rhyolite unit could have resulted in concentration of fluid transport within the overlying fragmental dacite unit (Fig. 2.3). This could account for the high degree of

metamorphic recrystallisation, especially if the unit had a high porosity because it was fairly coarse grained and fines poor (i.e. a lapilli tuff with a low ash content.

2.10.3 Intermediate feldspar-bearing crystal tuff

The intermediate feldspar-bearing crystal tuff forms the immediate footwall to the Western Ultramafic unit. It ranges in thickness from ~15m thick in the region of Alec Mairs and >100m thick along strike in the AM1 region (Fig. 2.3).

This unit consists of strongly sericite-replaced feldspar crystal fragments within a fine-grained (~50 - 100µm) matrix that has experienced pervasive chlorite and sericite replacement during metamorphism (Fig. 2.6a). Feldspar fragments and shards range in size from 0.2 - 15mm in diameter, and make up ~30 - 40 modal% of the unit. This proportion could be higher because it is possible that the smallest fragments are obscured by the pervasive chlorite and sericite overprint (Fig. 2.6a). Feldspar morphologies are variable. They are dominated by fragments from originally tabular crystals, along with smaller irregular angular fragments, that are pervasively sericite overprinted (Fig. 2.6a). Rare well-formed tabular feldspars are also present. The feldspar crystals are overprinted by very fine-grained sericite and acicular chlorite crystals but commonly retain the geometry of their original multiple twining structure (Fig. 2.6a). The orientation of the feldspar crystals fragments appears to be random. The groundmass consists of acicular needles of chlorite with very-fine grained interstitial sericite and fine-grained feldspar (± quartz) (Fig. 2.4a). A weak foliation fabric is defined by the chloritic matrix especially where it wraps around the relict feldspar crystals. The chlorite needles also overgrow the margins of the relic feldspar phenocryst fragments. Lime-green epidote-bearing patches, commonly associated with quartz veining, are present throughout the unit. They form sub-rounded domains, 15 - 20cm in diameter that have sharp alteration boundaries. When present in abundance, these epidote-patches destructively overprint and obliterate the fragmental texture.

Chemical analyses show that this unit has composition similar to that of the overlying andesite lavas and forms a tight cluster in the andesite field on Figure. 2.4.

Interpretation: The most distinguishing feature of this unit is the high abundance (≤40 modal %) of free-standing, often broken, feldspar crystals in a recrystallised fine-grained matrix. The protolith is therefore taken to be crystal-rich feldspar tuff produced by explosive eruption of a feldspar-phyric andesite magma. The lack of evidence of any coherent textures such as amygdales or evidence of autobreccias also supports this interpretation. The groundmass may have been more susceptible to pervasive chloritised if it were a very fine-grained ash-rich tuff with a poor preservation potential.

2.11 Hangingwall sedimentary succession

The Cosmos Ultramafic Sequence is unconformably overlain by a volcaniclastic sedimentary succession that is distinct from the footwall volcanic succession in terms of its chemical composition and texture. The extent of the hangingwall succession is poorly constrained on account of sparse diamond drill hole coverage in this barren region. A felsic porphyry intrusion commonly stopes out the lower contact of the hangingwall succession with the Cosmos Ultramafic Sequence, further complicating interpretation of the hangingwall stratigraphy. Four broad groups are identified within the hangingwall succession on grounds of texture and underpinned by chemical compositions (Fig. 2.4; 2.12). These are:-

1. Resedimented rhyodacite fragmental units.
2. Banded fine to medium grained (<0.5mm) sedimentary units with an intermediate bulk chemical composition that contains dispersed rounded granitic pebbles, cobbles and more rarely small boulders , 2- >20cm in diameter.
3. A fine grained (<0.5 - 10mm) mafic sedimentary unit.
4. Fragmental units that have high-silica rhyolite composition and are confined to a small sedimentary package in the south of the studied region.

The extent and thickness of individual units is hard ascertain, due to limited drill hole coverage, and contacts between lithological groups described above are often gradational or difficult to discern. Mafic-intermediate banded sediments commonly feature 1-10 cm scale folds and are crenulated. They are comprised of alternating biotite and hornblende dominated layers, and more felsic (feldspar-dominated) layers (Fig. 2.12b, c). Banding is on scales of <1mm to >10mm (Fig. 2.12c). It is unclear whether the banding has a primary sedimentary origin, or whether banding has been produced entirely via segregation of mineral phases during metamorphic recrystallisation. Polymictic and monomictic conglomerates commonly occur as horizons within the banded sediments (Fig. 2.12a). Monomictic matrix-supported conglomerates consist of rounded to sub-rounded granitic pebbles and cobbles in an intermediate banded and foliated matrix that wraps around the clasts (Fig. 2.12a). The granitic clasts range in size from 2 - 20cm in diameter and in abundance from <5 modal % up to ~35 modal %. The polymictic conglomerates also contain more attenuated feldspar-phyric lapilli tuff clasts as well as sub-angular mafic clasts. Pebbles and cobbles are contained within a banded matrix comprised of alternating felsic and mafic bands. The felsic bands are 0.3 - 20mm thick and often contain feldspar crystal fragments and grade into mafic bands of biotite and hornblende, and vice versa (Fig. 2.12b). The mineralogy of the mafic pebbles is similar to that of the mafic matrix, suggesting they may be derived from the same source rock.

Figure 2.12. (Next page). Core examples of the main lithological groups that compose the hangingwall sedimentary succession (a) An example of a monomictic conglomerate containing rounded to sub-rounded granitic clasts in an intermediate hornblende-biotite-feldspar matrix (b) Intermediate sediment containing attenuated re-worked dacite lapilli clasts that contain feldspar crystal fragments (c) Banded mafic sediments with alternation between biotite-dominated versus hornblende-dominated bands that are typically 0.1 - 0.4mm in thickness.

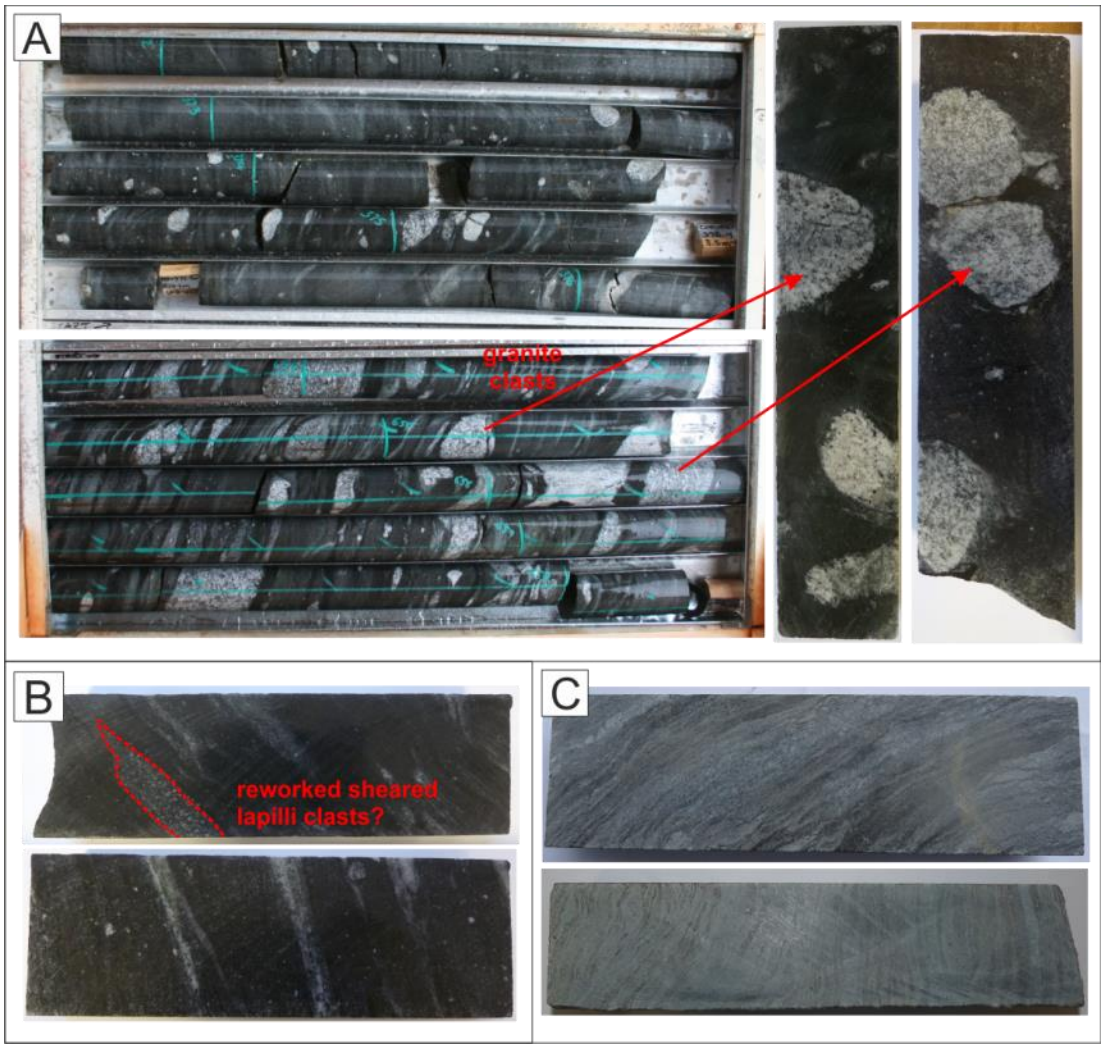

Interpretation: Although the hangingwall succession has been studied in less detail, evidence for a sedimentary origin is strong, including conglomerates containing rounded granitic pebbles and cobbles (absent in the in-situ volcanic footwall) and common occurrences of laminated and banded sedimentary units of intermediate composition. This interpretation is supported by the absence of units featuring distinct primary volcanic textures such as amygdaloidal lavas, autobreccias and lapilli tuffs. The extent and nature of individual units is poorly constrained, therefore it is not possible at this stage to put together, with desired degree of confidence, a coherent stratigraphy for the hanging wall succession.

2.12 Intrusive Lithologies

2.12.1 Granodiorite intrusions

Two felsic intrusions are present within the succession and U-Pb dating has confirmed that these units are >50 Ma younger than the extrusive Cosmos volcanic succession (de Joux et al., 2013; Chapter 4). Both intrusions were intruded approximately along stratigraphic boundaries, broadly along the hangingwall and footwall contacts of the Cosmos Ultramafic Sequence respectively (Fig. 2.3). Both intrusions cross-cut lithological contacts and are thus considered to have intruded along structural lineaments, likely focused by the rheological contrast between the ultramafic and more felsic volcanic lithologies (Fig. 2.3). Felsic intrusions exhibit sharp planar contacts and interestingly these contacts display no evidence of chilled margin, with phenocrysts and crystalline groundmass extending right to the contact. Porphyritic textures of both intrusions is sometimes obscured by bleaching associated with pervasive silicification and/or epidote/sericite alteration, both of which appear to be contemporary with episodes of quartz veining.

The two felsic porphyry intrusions are compositionally similar but intruded at different levels within the stratigraphy (Fig. 2.3). The hangingwall felsic porphyry intrusion cross-cuts and largely stopes out the contact between the Cosmos Ultramafic Sequence and the overlying hangingwall sedimentary succession (Fig. 2.3). This intrusion ranges from 150 - >250m in stratigraphic thickness. It is mineralogically uniform throughout. It is feldspar and quartz-phyric, with 1 - 2.5mm phenocrysts resting in a quartzo-feldspathic groundmass that contains minor amounts (<5 modal %) of mica and biotite (Fig. 2.13a). The feldspar phenocrysts are euhedral and dominantly stubby prismatic with lamellar twinning. They commonly exhibit patchy mild to moderate sericite recrystallisation, particularly in the crystal cores, which also contain numerous inclusions of fine grained muscovite. Quartz phenocrysts are sub-equant and sub-rounded. They are often show breakdown into sub-grains. The lower contact of this intrusion is often obscured by a large granite pegmatite swarm, as well

as dense arrays of quartz veins with associated sillicification, sericitisation and epidote recrystallisation selvages.

The footwall felsic porphyry intrusion is focused along the basal contact of the Cosmos Ultramafic Sequence in the region of Alec Mairs (Fig 2.3). It contains feldspar phenocrysts sitting in a fine-grained (<50 - 200µm) quartz-feldspar mosaic groundmass that also features later formed 100 - 300µm mm laths of biotite aligned along pre-existing grain contacts (Fig. 2.13b). Feldspar phenocrysts are euhedral tabular, equant or stubby prismatic and exhibit moderately strained simple twins and more rarely discontinuous multiple twining (Fig. 2.13b). Feldspar is the only phenocryst phase, present as 1 - 5mm crystals that typically make up 15 - 18 modal % of the rock, although horizons with up to 25 modal% phenocrysts are present (Fig. 2.13b).

Both felsic intrusions have a rhyodacite composition (Fig. 2.4). In contrast to the volcanic footwall succession, which displays a strong high-K calc-alkaline to shoshonite island-arc affinity (Fig. 2.5; Chapter 3; de Joux et al., 2013), the felsic porphyry intrusions have a strong tonalite–trondhjemite–granodiorite (TTG) geochemical affinity. The significance of this will be discussed in Chapter 3.

Interpretation: The felsic porphyries are distinctively less deformed than the country rock into which they intrude, implying that their emplacement post-dates some of the main deformation events within the Cosmos region. Absence of chilled margins indicates that they intruded hot country rocks. The country-rock side of the contacts contains elevated abundances of biotite formed by localised contact metamorphism. This contact metamorphic halo is particularly well developed within ultramafic lithologies (Hill and Dowling, 2008). Felsic intrusions cross cut lithological contacts, both the upper and lower contact of the Cosmos Ultramafic Sequence, as well as sulphide mineralisation, and thus post-date emplacement of the Cosmos volcanic sequence.

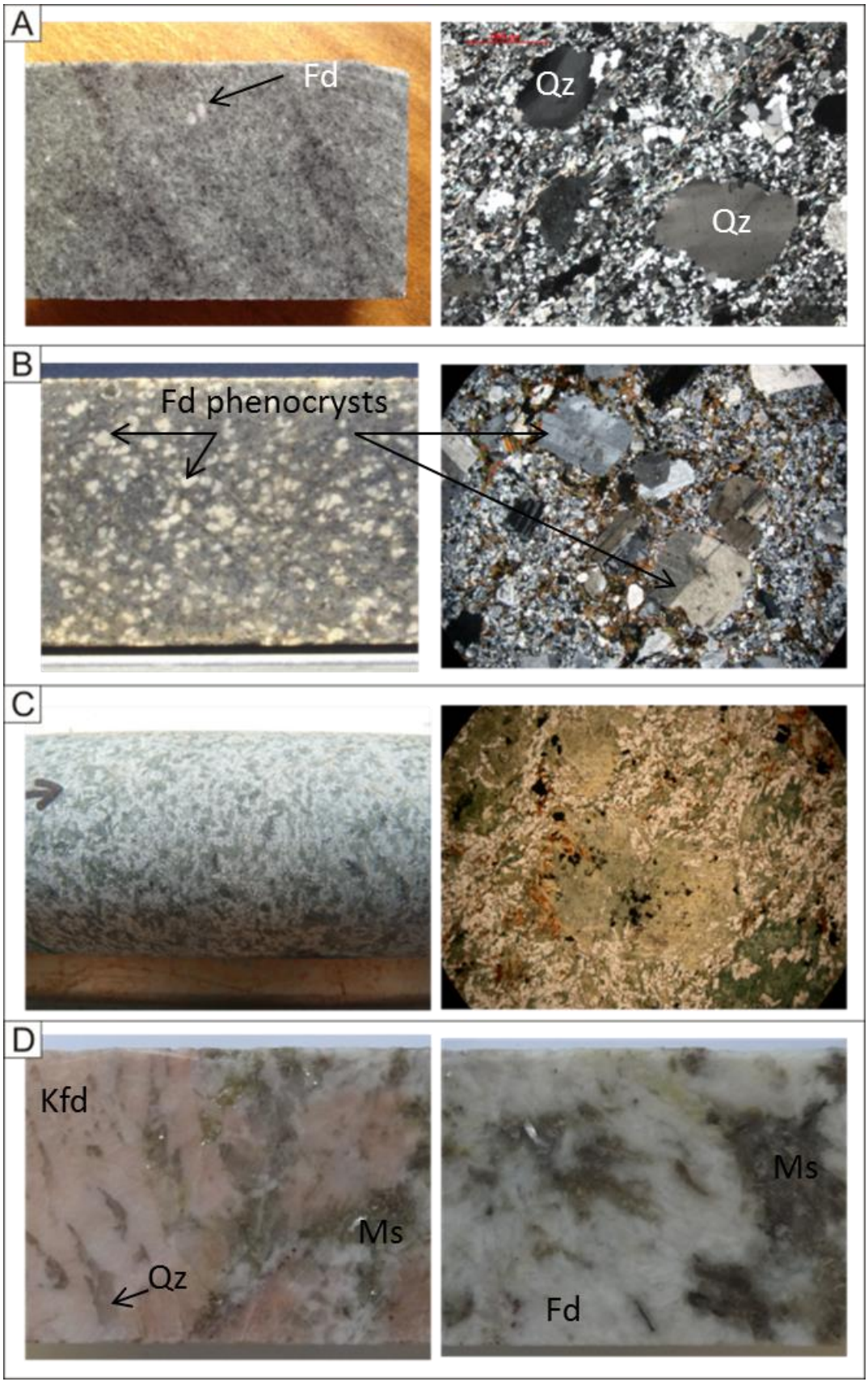
A
Fd
Qz
Qz
B
Fd phenocrysts
C
D
Kfd
Ms
Qz
Ms
Fd

Figure 2.13. (Previous page) Representative core photos (left) and photo micrographs (right) of intrusions within the Cosmos succession (a) The hangingwall felsic porphyry intrusion, highlighting the quartz (Qz) and feldspar (Fd) -phyric nature of the unit. The quartz phenocrysts exhibit undulose extinction and are wrapped by a indistinct swarm of finer-grained metamorphic biotite crystals that that define a weak foliation (b) The footwall felsic porphyry intrusion, which contains only feldspar phenocrysts. They are euhedral tabular to stubby prismatic crystals that exhibit multiple twinning (c) The AM5 mafic intrusion highlighting the typical hornblende and chlorite porphyroblasts (right) that give the rock a distinct spotted texture in hand specimen (left) (d) Examples of a light pink K-feldspar-rich (Kfd) pegmatite (left), which also contains quartz (Qz) and muscovite (Ms), and a plagioclase-rich pegmatite (right), which also contains abundant quartz and lesser muscovite. Pegmatites commonly also contain variable concentrations, but generally < 5 - 8 modal %, of garnet, muscovite, epidote and tourmaline as along with rare molybdenite.

2.12.2 Mafic intrusions

Two mafic intrusions are present within the Cosmos succession; one emplaced approximately stratiformly to the basal contact of the Cosmos Ultramafic Sequence in the region of Cosmos Deeps and the other intruded sub-parallel to the stratigraphy at relatively shallow levels within the footwall at the Alec Mairs, in the proximity of the AM5 deposit (Fig. 2.3). The Cosmos Deeps mafic intrusion ranges in thickness from <5m to ~35m and was emplaced approximately along the basal contact of the Cosmos Ultramafic Sequence, displacing the footwall succession several tens of metres away from the base of the Cosmos Ultramafic Sequence. The Alec Mairs (AM5) mafic intrusion is much less well delineated due to its location within the footwall several tens of metres to the east of the Alec Mairs ore deposits (Fig. 2.3). It is >50m thick and approximately stratiform. It is not possible to ascertain if these intrusions represent sills or dykes, as the exact timing of their intrusion relative to tilting of the volcanic stratigraphy is not currently resolvable.

In hand specimen the intrusions have a distinct “spotted” texture formed by subhedral to anhedral, equant hornblende and chlorite porphyroblasts (Fig. 2.13c). These are 2 - 10mm across and typically compose 25 - 30 modal % of the rock. The porphyroblasts sit in a finer-grained (50 - 200µm) feldspar (variably altered to sericite), amphibole ± biotite groundmass, with abundant opaque phases. Sporadically, aligned fibrous tremolite and actinolite appear to be overgrown by the hornblende porphyroblasts, indicative of multi-phase amphibole recrystallisation during

metamorphism. In other samples hornblende has been overgrown by a secondary acicular hornblende phase which is ubiquitous throughout the groundmass. Relict lamellar-twinned feldspar phenocrysts are present in minor amounts and are broken down into an aggregate of quartz and feldspar. Overall these mafic intrusions are mineralogically and texturally uniform. However, the grain size increases from coarse crystals (~5mm) up to very large crystals (~10mm) towards the centre of the thicker AM5 intrusion where it is equigranular and exhibits gabbro-like appearance.

Compositionally the intrusions are distinct; the Cosmos Deeps intrusion is a dolerite while the AM5 intrusion exhibits a more evolved diorite composition (Fig. 2.4). Both intrusions are more primitive than the coherent andesites.

Interpretation: The lithological uniformity of the intrusions, their distinct geochemical attributes (Fig. 2.4; Chapter 3), sharp contacts with the surrounding stratigraphy and lack of any extrusive features, such as amygdales, fragmental textures or autobreccia facies, strongly suggests they are not part of the conformable volcanic stratigraphy. The intrusions are also less foliated than the surrounding stratigraphy in to which they were emplaced and thus, like the felsic porphyries, are likely to have been intruded after the Cosmos volcanic succession had undergone deformation. The regional significance and timing of these small, minor mafic intrusions is not known.

2.12.3 Granitic pegmatites

Granitic pegmatites are ubiquitous throughout the Cosmos succession and represent the youngest rocks of the succession, cross-cutting all other lithologies. They range in thickness from <1m to > 200m and cross-cut the succession at a variety of angles, although the dominant orientation is sub-horizontal and approximately perpendicular to the stratigraphy. Multi-stage intrusion of the pegmatites is indicated by variable chemical composition and mineralogy of individual domains as well as cross-cutting pegmatite to pegmatite relationships. The pegmatites often exploit the

rheological contrast across lithological boundaries and regularly stope out the upper and basal contact of the Cosmos Ultramafic Sequence.

The dominant mineralogy is composed >5 - 50mm euhedral feldspar, quartz and muscovite, with lesser occurrence of K-feldspar, garnet, sericite, tourmaline and chlorite (Fig. 2.13d). Individual quartz and muscovite grains are up to 5cm across. Grain size is variable within individual intrusions, often with sharp contacts between domains of different crystal sizes, perhaps reflecting growth by sequential intrusion. Pegmatite veins cross-cutting the ultramafic units are surrounded by distinct localised metamorphic contact haloes, with the distal-to-proximal zonation of lizardite → antigorite → talc ± chlorite → chlorite + biotite → pegmatite. The association of antigorite and talc is indicative of carbon dioxide-rich fluids from the late-stage pegmatite intrusions penetrating the surrounding country rock (Hill and Dowling, 2008). Where pegmatites have intruded the felsic footwall or the felsic porphyry the host experienced silicification and bleaching, that is possibly related to the leaching of mafic phases.

Compositionally the granite pegmatites are alkalic, plotting in the trachyte field on Figure. 2.4 (see Appendix 2). At least three different pegmatite compositions are discernable from their REE concentrations (Appendix 2).

Interpretation: The granite pegmatites represent the youngest units within the stratigraphy as they cross cut all extrusive and intrusive lithologies within the succession, including the footwall felsic porphyritic intrusion. Thus the granitic pegmatites are younger than ~2653Ma and are considered to be the late-stage expression of neighbouring regional granite intrusion that took place at ~2650Ma (Lui et al., 2002; Black et al., 2002; de Joux et al., 2013).

2.13 Discussion: lateral and vertical facies associations in the footwall volcanic succession and location of sulphide ore bodies

This section describes the accurate reconstruction of the architecture of the felsic and intermediate volcanic footwall in the North Cosmos region established via an integrated approach combining drill core correlation, U-Pb dating and geochemical analyses (Fig. 2.14, 2.15). Earlier preliminary investigations at the Prospero-Tapinos deposits in the South Cosmos region, which is part of the same ultramafic belt (Fig. 2.1), identified similar lithofacies and facies association as present at North Cosmos (Farran, 2008). The Prospero-Tapinos succession is comprised of intercalated coherent andesites and coherent and schistose felsic units with similar compositional affinities similar to those of the North Cosmos succession (Farran, 2008). This is taken to indicate that the broad volcanic footwall stratigraphy, as established in this study, may persist along strike for at least ~ 4 km within the Cosmos greenstone belt.

Figure 2.14 shows a level plan through the succession, at the -200 metres below sea level (looking down), highlighting the three main ore hosting regions of Cosmos North; Alec Mairs, AM1 and Cosmos/Cosmos Deeps. It shows a north to south cross section through the original volcanic stratigraphy. Figure 2.15 shows five separate east-west (looking north) cross-sections perpendicular to the level plan and spread across the area between Alec Mairs and Cosmos/Cosmos Deeps. The sections represent east-west cross sections through the original volcanic stratigraphy.

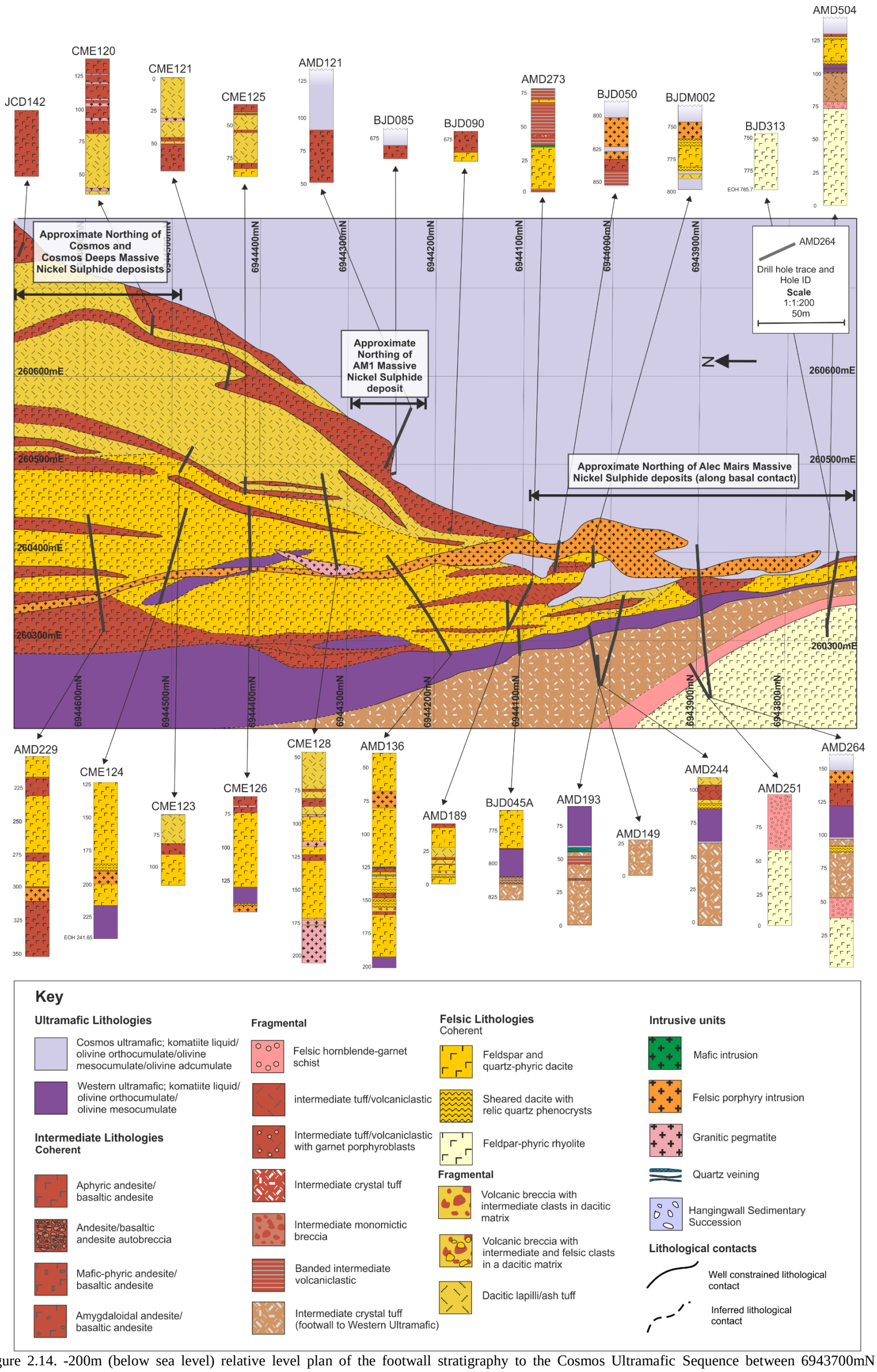

Figure 2.14. -200m (below sea level) relative level plan of the footwall stratigraphy to the Cosmos Ultramafic Sequence between 6943700mN – 6944700mN, highlighting the main core logs that underpin the correlation of the stratigraphy. Drill hole lithologies are projected onto the level plan plane over a 50m window (i.e., ± 25m above and below the -200m level plan) to allow lithologies to be correlated along strike. As the Cosmos stratigraphy is now orientated sub-vertically a level plan in this orientation represents a cross section through the original stratigraphy. Neither of the mafic intrusions are shown on the level plan as they do not intersect the -200mRL; the Cosmos Deeps intrusion only extends to the ~0mRL, the reader is referred to Figure 2.15e for its location and Appendix 4. The Alec Mairs (AM5) mafic intrusion is not intersected by drilling on the -200mRL, but its location can be seen on the -150mRL level plan in Figure 2.3, Figure 2.15a and in Appendix 4.


Cross Section
6943750mN
+- 12.5m
(Scale 1:2000)
400RL
200RL
0RL
-400RL
-600RL
260400mE
260600mE
260800mE
261000mE
BJD313
AMD278
AMD321
AMD504
A
Cross Section
6944025mN
+- 12.5m
(Scale 1:2000)
BJDM002
AMD193
AMD149
AMD275
AMD274
AMD273
AMD365
B
Cross Section
6944300mN
+- 12.5m
(Scale 1:2000)
AMD071
BJD061A
AMD116
CME128
BJD030
C

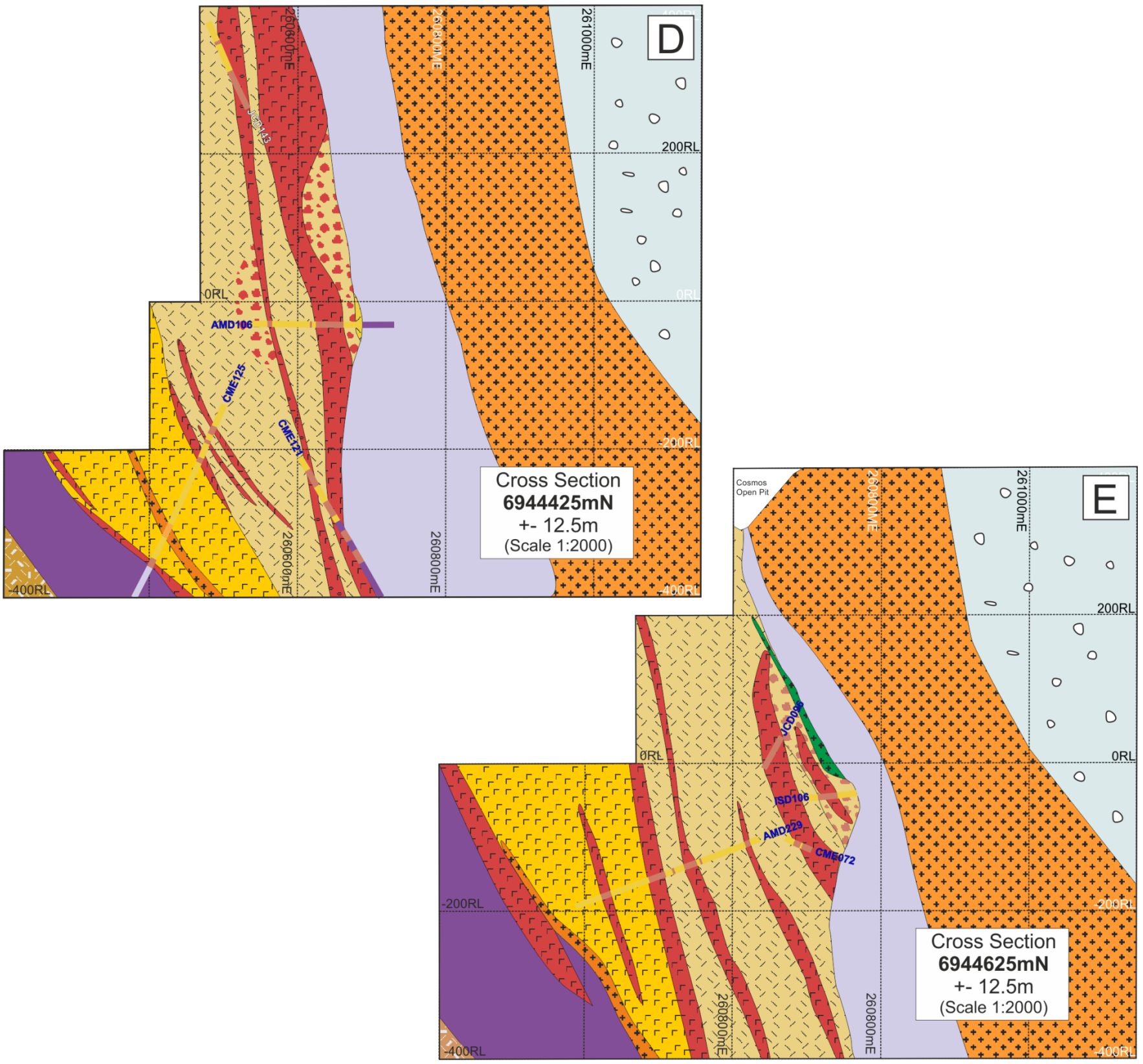

Figure 2.15. Five cross-sections through the Cosmos footwall succession. A and B are in the Alec Mairs area, C and D are in the Anomaly 1 area and E is in the Cosmos Deeps area. Position of these cross sections relative to the level plan on Figure 2.14 can be obtained via reference to the northing of the cross-section plane. Lithological key is identical to that of Figure 2.14. Portions of drill holes are projected onto the central reference plane if they occur within ±12.5m of the plane's northing. Cross-section planes along the strike of the Cosmos Ultramafic belt were constructed at 25m intervals between 6943700mN and 6944700mN, ensuring interpretations were consistent with adjacent cross sections. Drill hole traces and hole IDs are shown and lithologically colour coded; purple = ultramafic; yellow = felsic volcanic; lightest yellow = rhyolite; brown = intermediate volcanic pink = pegmatite; green = mafic intrusion; orange = felsic porphyry. All drill hole logs and full sets of cross section and level plan interpretations are provided in Appendix 4.

The rhyolite lava/lava dome is in the deepest parts of the footwall succession to the Western Ultramafic unit in the region of Alec Mairs (6943700 – 6944100mN; Fig. 2.14). Current drilling has yet to intersect the base of this unit, but indicates that the stratigraphic thickness of this unit is >100m. The reconstructed level plan suggests a steep-sided dome-like geometry for this unit, tapering out rapidly to the north as it is yet to be discovered beneath the intermediate feldspar-phyric crystal tuff beyond 6944000mN (Fig. 2.14).

The garnet-hornblende felsic schist exhibits a relatively uniform thickness. It sits conformably on the underlying rhyolite dome and the contact between the two is sharp and planar. The upper contact of the garnet-hornblende felsic schist with the overlying intermediate crystal tuff is commonly gradational in nature and difficult to discern.

The intermediate feldspar-bearing crystal tuff thickens to the north substantially in this region, reaching an approximate stratigraphic thickness of over 125m at ~6944100mN compared to <15m at 6943800mN (Fig. 2.14, 2.15a; Appendix 4). Isolated deep drilling through the basal contact of the Western Ultramafic unit confirms that the intermediate feldspar-bearing crystal tuff still forms the immediate footwall lithology to this unit in the Cosmos Deeps region.

The Western Ultramafic unit is generally less than 20m thick at Alec Mairs, thickening along strike to the north to ~50 - 70m at AM1. It's up dip occurrence is confined to levels below -50m relative level (RL; 0m = sea level: Fig. 2.14, 2.15a, b). Deep drilling into the footwall has shown that the Western Ultramafic unit is still present within the subsurface at Cosmos Deeps and reaches >150m in stratigraphic thickness (Fig. 2.14, Fig. 2.15e).

The footwall succession to the Cosmos Ultramafic Sequence is relatively thin at Alec Mairs (~25-100m; Fig. 2.15a) on the southern sector of the level plan, thickening along strike to the north, reaching thicknesses of ~150m at Anomaly 1 (Fig. 2.15c) and in excess of 400m beneath Cosmos Deeps at ~6944700mN (Fig. 2.14; Fig. 2.15e). The footwall succession is composed of andesites lavas, and associated volcaniclastic facies, intercalated with both dacite lavas and dacite lapilli tuffs.

Andesitic units typically range from less than 1m to up to ~70m in stratigraphic thickness. The transition from dacite lava packages to dacite lapilli tuff packages is relatively sharp, with the dacite lavas occurring at deeper levels within the footwall as the thickness of the dacite lapilli tuff sequence increases moving along strike to the north. The dacite lapilli tuff packages also contain monomictic and polymictic tuff breccia horizons close to the basal contact of the Cosmos Ultramafic Sequence (Fig. 2.15c). Dacite lapilli tuffs are thickest towards the north of the studied area (6944500mN – 6944700mN), where the footwall succession of intercalated dacite lapilli tuffs and lesser amounts of andesite lavas, reaches 200m in stratigraphic thickness (Fig. 2.14, 2.15e). Dacite lavas are still present within the deep footwall to the Cosmos Ultramafic Sequence, with the footwall succession reaching >350m in thickness beneath Cosmos Deeps.

At Alec Mairs dacite lava packages dominate the immediate footwall succession and dacite lapilli tuff is sparse and generally <5 - 10m thick. In this context, it is interesting that the largest massive sulphide deposit in the area (AM5) is hosted by and partly overlies the footwall containing the thin dacite lapilli tuff units. Sulphide ore bodies at Alec Mairs were further modified by the late-stage intrusion of the footwall felsic porphyry. This porphyry splits the Alec Mairs 4 sulphide deposit into several smaller domains. It clearly displaced them for several tens of metres from their original position on and within the dacite lapilli tuffs and associated tuff breccias. In the Alec Mairs region the footwall felsic porphyry intrudes approximately along and parallel to the Cosmos Ultramafic Sequence-felsic footwall contact. It pinches, swells and branches and in doing so attains a maximum stratigraphic thickness of ~50 - 60m (Fig. 2. 14, 2.15b).

Dacite lapilli tuff dominates the immediate footwall to the Cosmos Ultramafic Sequence in the Cosmos Deeps region and massive sulphide mineralisation extends into and is hosted by tuff breccia horizons within the dacite lapilli tuff sequence forming the Cosmos Deeps ore body. The hosting tuff breccia horizons contain abundant sub-angular to sub-rounded andesitic clasts hosted in a dacite lapilli-ash grade matrix. This unit is very similar in composition and appearance to other tuff breccias within the footwall succession (e.g. AM5 at Alec Mairs; Fig. 2.15c). The

Cosmos Deeps deposit has been considered by previous authors to be a structurally re-mobilised massive and breccia nickel sulphide deposit hosted entirely within a felsic to mafic breccia/volcaniclastic unit (Langworthy and Vallance, 2004). However, Kaye et al. (2010) considered that the lack of attenuation of clasts or sulphide present within large scale secondary fractures indicated a more primary origin for the location of massive sulphide within the dacite lapilli tuff footwall. The Cosmos Deeps mafic intrusion intrudes along the basal contact between the Cosmos Ultramafic Sequence and the dacite tuff footwall (Fig. 2.15e), further complicating interpretation of the paragenesis of the Cosmos Deeps ore body.

Unlike similar units at Cosmos Deeps and Alec Mairs, breccia horizons are un-mineralised at Anomaly 1 (Fig. 2.15c). The only pod of massive sulphide in the Anomaly 1 region is the AM1 ore body, which sits directly on the basal contact of the Cosmos Ultramafic Sequence, which is ~125m thick. Here the immediate footwall lithology is andesite lava. Sulphide mineralisation here does not extend into the footwall, possibly reflecting the rheological contrast of the coherent andesite lavas versus the fragmental dacite lapilli tuffs during primary nickel sulphide deposition and/or secondary sulphide remobilisation.

The Cosmos Ultramafic Sequence is over 250m thick in the region of Alec Mairs and is divided by the AM5 "reactivation" contact into two sub-units (see Chapter 4 for further details), the massive-sulphide-dominated UMu1 package and disseminated-sulphide-bearing UMu2 package (de Joux et al., 2013). Beyond 6944100mN the AM5 "reactivation" contact has not been detected within the Cosmos Ultramafic Sequence and it is unclear whether this horizon is present within the sequence. It is therefore difficult to delineate the UMu1 package from the UMu2 package when moving to the north along strike. The Cosmos Ultramafic Sequence thins substantially to the north being <10m thick up dip at the Cosmos ore body and thickening down dip to ~100m thickness in the region of Cosmos Deeps (Fig. 2.15e). However, its upper contact is stoped out by the hangingwall felsic porphyry intrusion so that the actual thickness of the Cosmos Ultramafic Sequence is hard to ascertain.

The upper contact of the Cosmos Ultramafic Sequence is almost always stoped out by the hangingwall felsic porphyry complicating interpretation of the nature of the contact relationship between the Cosmos Ultramafic Sequence and hangingwall sedimentary succession (Fig. 2.15). In the south of the region the hangingwall succession is underrepresented in drill hole coverage. However in the region of Cosmos Deeps the hangingwall succession is >350m thick.

2.14 Mode of emplacement for the volcanic units of the Cosmos footwall

In comparison to the footwall successions to other nickel-sulphide deposits within the Agnew-Wiluna greenstone belt (e.g., Beresford et al., 2004; Duuring et al., 2007; Rosengren et al., 2008), the Cosmos succession exhibits much more compositional variability, whilst also having a high-K calc-alkaline to shoshonite geochemical affinity that is unique within the AWB, as well as the wider EGS (Czarnota et al., 2010; Fiorentini et al., 2012; Chapter 3 and 4).

2.14.1 Emplacement of the footwall to the Western Ultramafic unit

The footwall to the Western Ultramafic unit is compositionally distinct to that of the footwall to the Cosmos Ultramafic Sequence, as well as being significantly older (Fig. 2.3; de Joux et al. 2013; Chapter 4). The rhyolite lava/lava dome is considered to have extruded slowly and essentially right above its vent due to its high silica content and hence high viscosity. The rhyolite was then overlain by the explosive eruption and emplacement of the intermediate crystal tuff. The marked thinning of this unit over the rhyolite dome in the region of Alec Mairs suggests that the rhyolite dome could have been a topographical high (Fig. 2.14). The garnet-hornblende felsic schist between these two units may represent an earlier phase of more evolved explosive volcanism prior to the emplacement of the less evolved intermediate feldspar-bearing crystal tuff. The garnet-hornblende felsic schist's relatively uniform thickness suggests that it

mantled the pre-existing topography created by the rhyolite lava. It is considered that the Western Ultramafic unit represents an earlier phase of komatiite volcanism that overrode a compositionally distinct volcanic footwall, and is barren as it never reached sulphur saturation. The composite felsic-intermediate volcanic sequence could represent a topographic high that focused and channelised komatiite lava flow fields in the region. This is indicated from the thickening of the Western Ultramafic unit towards the north away from the domal morphology of the rhyolite. The Western Ultramafic unit may be barren due to its andesite footwall having a higher melting temperature than the dacite lapilli tuffs that form the footwall to the Cosmos Ultramafic Sequence. The substrate beneath the Western Ultramafic unit was therefore more resistant to thermo-mechanical erosion. Alternatively the Western Ultramafic komatiite may have been a smaller, short-lived flow field that never became sufficiently channelised to erode and assimilate sufficient quantities of the andesitic substrate to reach sulphur saturation. Dating of the stratigraphy that encloses the Western Ultramafic unit indicates it was emplaced between ~2736 and ~2730 Ma, indicating it represents a much earlier phase of komatiite volcanism than the modal regional emplacement age of ultramafic sequences of ~2707 Ma within the Kalgoorlie Terrane (Kositcin et al., 2008).

2.14.2 Emplacement of the footwall to Cosmos Ultramafic Sequence

The immediate footwall to the Cosmos succession is considered to have formed through the construction of a volcanic pile via both explosive and effusive eruptions of dacite magma and dominantly effusive eruptions of basaltic andesite to andesite lavas. The deepest, and stratigraphically oldest, parts of the Cosmos footwall succession are dominated by porphyritic dacite lavas intercalated with amygdaloidal andesite lavas, indicating effusive eruptions were dominant in the initial stages of felsic eruptive phase (Fig. 2.14, 2.15). A transition to explosive dacite eruptions is seen moving up through the stratigraphy towards the basal contact of the Cosmos Ultramafic Sequence, with the emplacement of 20 - 200m thick dacite lapilli tuff

(Figure 2.14, 2.15). It is not possible to constrain the emplacement mechanisms of the tuffs as internal structures, such as stratification and grading, have not been persevered. It is likely that the lapilli tuffs and tuff breccias were emplaced via a combination of airfall and pyroclastic density currents. Tuff breccia horizons within the dacite lapilli tuff sequences exhibit a bimodal compositional nature of dacite matrix versus andesite clasts. Such horizons may have been emplaced as talus lobes proximal to the volcanic vent or may represent breccia horizons within ignimbrites. Dacite lapilli tuffs are still intercalated with andesite lavas indicating that effusive eruption of intermediate lava was on-going throughout the dacite eruptive phase.

The andesite lavas and both the dacite lavas and dacite lapilli tuffs contrast in their geochemical attributes; the dacite lavas and dacite lapilli tuffs exhibiting greater enrichment in large ion lithophile elements and light REEs as well as contrasting high field strength element concentrations (Chapter 3). Assimilation-fractional crystallisation (AFC) modelling has also indicated that the andesites and dacites are not co-genetically related (Chapter 3) and thus it is considered that the andesite and dacite eruptive products are not from the same volcanic source. Their intercalation throughout the succession, both spatially and temporally indicates that they may have been sourced from two separate volcanic centres that were active over the same time period.

The Cosmos Ultramafic Sequence is considered to have been emplaced as a dynamic thin-flow system before evolving into a high-volume channelised flow (Hill and Dowling 2008; Denny, 2010). It reached sulphur saturation via thermo-mechanical erosion of the fragmental dacite footwall, which may account for some of the possible "embayments" seen within the mapped footwall stratigraphy at Alec Mairs (Fig. 2.14, 2.15b). The presence of contaminated komatiite (hybrids) along the basal contact of the UMu1 package indicates that thermo-mechanical erosion did occur (Hill and Dowling, 2008). Thermo-mechanical erosion would have been promoted in regions where the immediate substrate comprised dacite lapilli tuff sequences due to their significantly lower melting point than the associated andesite lavas (e.g., Hill et al., 2004). Such fragmental horizons may also have been easier to mechanically entrain. The presence of massive sulphide within primary volcanic tuff breccia horizons

indicates that such horizons could have promoted sulphide deposition by providing a suitable depositional trap (e.g., Naldrett, 2004). It is not possible to quantify the amount of thermo-mechanical erosion the dacite footwall may have undergone nor the timing of emplacement of the andesitic and dacitic footwall compared to the timing of emplacement of the Cosmos UMu1 package beyond emplacement between ~2724 Ma and ~2685 Ma (de Joux et al., 2013; Chapter 4).

2.15 Footwall lithologies and location and style of sulphide mineralisation

Understanding the mechanism that transported sulphide from the ultramafic basal contact down into the felsic footwall is important for exploration targeting. At Cosmos, two possible scenarios are considered: (a) the sulphide may have been physically or chemically remobilised from its original komatiite-footwall contact position, possibly related to the late-stage felsic intrusions and/or regional deformation and metamorphism; (b) it may have migrated into the footwall during deposition via molten percolation into a fractured and/or porous substrate. Dacite lapilli tuff inclusions within massive sulphide have an irregular wispy "fluidised" texture indicating the tuffaceous substrate was partially re-melted during the deposition (or remobilisation) of molten sulphide (Fig. 2.11c).

Remobilisation of massive sulphides occurs by both physical and chemical processes. Physical mechanisms tend to dominate under most conditions because massive sulphides have a high ductility and plasticity compared with most silicate rocks (Duuring et al., 2007). Deformation processes include brittle failure, solution-precipitation creep, diffusion creep and dislocation creep (Cox, 1984; Duuring et al., 2007). The latter is the most common deformation mechanism; however the composition of the sulphide, as well as the pressure-temperature conditions and presence, or absence, of metamorphic fluids affects their susceptibility to remobilisation (Plimer, 1984; Duuring et al., 2007). At mid-amphibolite grades, such

as those experienced at Cosmos, massive Ni ores are likely to have reverted to monosulfide solid solution (MSS) during peak metamorphism (McQueen, 1979; Dowling and Hill, 2008). Common evidence for physical remobilisation includes the presence of pentlandite–pyrrhotite banding, local heterogeneous redistribution of pyrrhotite, pentlandite and chalcopyrite into fractures and country rock clasts that are mechanically granulated (e.g., Durchbewegung textures; Duuring et al., 2007; 2009; 2010).

Chemical remobilisation has been described for footwall and hangingwall mineralisation at Kambalda (Lesher and Keays, 1984). At Kambalda, cited evidence for chemical remobilisation includes (1) the presence of hydrothermal quartz ± albite ± carbonate at the tips of some piercement structures in footwall lithological units (Lesher and Keays, 1984) and (2) Cu-Pt-Pd–rich massive sulphides that have very low Ir contents and high Pd/Ir ratios compared with primary magmatic sulphides (Lesher and Keays, 1984). Chemically remobilised massive sulphides are enriched in Cu, Pt, and Pd relative to Ir, Ru, and Os due to the higher relative solubilities of the former metals under most metamorphic and hydrothermal fluid conditions (Bavinton and Keays, 1978; Duuring et al., 2007).

Duuring et al. (2007) considered that massive sulphides at Harmony in the AWB (Fig. 2.1) were physically remobilised up to 10m from their magmatic position, along the footwall contact or into shear zones and faults that intersect the footwall contact. At Perseverance massive sulphide was remobilised no more than 5m in 1A ore body and up to 20m in Felsic Nose area (Duuring et al., 2009). Duuring et al. (2007) suggested that massive sulphides are commonly remobilised less than 50 m from primary magmatic ore positions. Therefore, in the AWB, in regions such as Perseverance and Harmony that experienced similar peak metamorphic conditions to Cosmos, massive sulphide is typically physically remobilised less than 20m (Duuring et al., 2007; 2009; 2010). The latter authors suggest that the thermo-mechanical erosion of footwall rocks and the channelling of the mineralised komatiitic magma are the first-order controls on the geometry of nickel sulphide deposits such as those of the Perseverance region. Sulphide remobilisation is a second or third order control.

Therefore a deposits location is largely controlled by primary magmatic processes (Duuring et al., 2010).

It is not easy to positively discriminate between remobilised sulphides versus primary sulphides at Cosmos due to the absence of a detailed structural interpretation of the region and only limited modelling of local structures and faults. However massive sulphide deposits within the footwall exhibit several features that are suggestive of emplacement into the footwall via primary magmatic processes. These include; (1) the observation that intra-felsic sulphides commonly reside in spaces between clasts in the relatively undeformed dacite lapilli tuff and their associated breccia horizons; (2) massive sulphide pods and blebs can be seen to penetrate between individual ash/lapilli fragments, bend around andesitic clasts terminating at their clast boundaries, as well as infilling possible original vesicles within the andesitic clasts; (3) where the immediate footwall is andesite lava (e.g., AM1; Fig.2.3; 2.14), massive sulphide sits directly on the contact, indicating that massive sulphide may have been unable to penetrate into this coherent substrate; (4) lack of large scale faults within the sulphide hosting footwall sequence; (5) absence of veining and hydrothermal quartz ± albite ± carbonate assemblages in the vicinity of footwall hosted mineralisation. However, some late-stage sulphide mobility is evident from chalcophyrite-rich sulphide assemblages along micro-fractures and along cleavage planes in the meta-phylosillicates within the lapilli tuff.

The presence of occasional iron and base metal sulphide veins within the dacite footwall indicates that thermo-mechanical erosion of pre-existing sulphide deposits within the footwall, possibly related to hydrothermal activity within the volcanic sequence, may also have contributed to the achievement of sulphur saturation of the overriding Cosmos UMu1 package (Mark Styles, pers comm; Chapter 5). This concurs with the Fiorentini et al. (2012) who concluded that country rock sulphur addition is crucial to ore genesis and that the specific sulphur source in the AWB may be the pyritic exhalative sulphides of inferred VMS origin in the region. In the case of Cosmos an active sulphide-bearing hydrothermal system may have provided a source of sulphur and/or sulphides to the overriding Cosmos komatiite sequence, promoting sulphur saturation of the flow. This will be discussed further in Chapter 5.

The felsic footwall porphyry intrusion cross-cuts massive sulphide deposits in the region of Alec Mairs, displacing the pods of massive sulphide for several tens of metres. Latest stage granitic pegmatites (<2653 Ma) also terminate against and are deflected by massive sulphide loads indicating that massive sulphide pods were in place prior to intrusion of the pegmatites. This indicates massive sulphide deposits can be displaced by late-stage intrusions from their primary depositional location as well as themselves acting as a rheology barrier influencing the emplacement orientation and propagation of late stage intrusions.

2.16 Environment of deposition

The presence of abundant thicknesses of dacite lapilli tuff, coupled with the lack of hydrovolcanic products within the dacite and andesite lavas, such a hyaloclastite, is indicative of formation in a subaerial environment. The footwall to the Cosmos Ultramafic Sequence also contains no discernible marine sedimentary deposits, such as banded iron formations or black shales. The lack of hydrovolcanic products or distinguishable marine sediments, which would be expected volcanic arc succession that persisted for ~12 Ma if it were submarine, indicates that a large proportion of the volcanic succession was emplaced subaerially (de Joux et al., 2013; Fig. 2.3). Lack of discernable pillow textures within the least evolved basaltic andesites also supports this interpretation.

This lack of evidence for marine deposition contrasts with similar successions within the Kalgoorlie Terrane, such as Mount Keith and Boorara (Trofimovs et al., 2004; Rosengren et al., 2005; 2008). Rosengren et al. (2008) concluded that the dacite lava succession associated with the Mount Keith mineralised ultramafic sequence were erupted into a deep subaqueous environment were water pressure retarded explosivity. The latter authors cite the occurrence of coherent lavas and hyaloclastite and the presence of black shales as evidence of a subaqueous environment. Trofimovs et al. (2004) concluded that the majority of volcanism in the Boorara Domain occurred in a deep submarine setting due to the presence of fine-grained, laminated, carbonatious

metapelites as well as pillow structures and hyaloclastites within basaltic units. Turbidites are also recognised within the stratigraphy, although rounded porphyry clasts are considered to have been derived from a subaerial to shallow marine tractional environment, likely an emergent felsic dome complex within the basin. Therefore, the Boorara succession was emplaced and derived from a wide range of sedimentary and volcanic environments, which included emergent volcanic edifices (Trofimovs et al., 2004). Subaerial volcanic island-arc successions have been described within the Welcome Well complex (Giles and Hallberg, 1982) and andesites within the Kurnalpi Terrane are described as being erupted on subaqueous to emergent volcanic edifices by Barley et al. (2008).

Given that the volcanic footwall to the Cosmos Ultramafic Sequence is considered to be formed subaerially, the lower part of the Cosmos Ultramafic Sequence, UMu1, may have been erupted subaerially also. This would be in contrast to evidence that the majority of komatiites within the Kalgoorlie Terrane were erupted subaqueously onto submerged continental platforms. Komatiites in the Kalgoorlie Terrane are associated with pillowed basalts, immature chert and banded iron formations (e.g., Groves et al., 1984; Claoué-Long et al., 1988; Gresham and Loftus-Hills, 1991; Rosengren et al., 2008; Arndt et al., 2008). Komatiites could have erupted onto to dry land as by the Neoarchaean large areas of continental crust already existed, the Cosmos volcanic succession being an example of this. Arndt et al., (2008) suggest that subaerial komatiites almost certainly did exist but that there are no convincingly documented examples presented from the Archaean record. There are little unambiguous criteria that might be used to identify komatiites that erupted onto land and not under water in the Archaean (Arndt et al., 2008). However the association of komatiites with the emergent island-arc volcanic sequence at Cosmos, that contains no evidence of being emplaced subaqueously, provides evidence that the mineralised komatiites may have been erupted onto land. However, given that dating of the units enclosing the UMu1 package cannot delineate its emplacement more precisely than after ~2724 Ma and before ~2685 Ma, it is hard to speculate on the environment of emplacement of the Cosmos Ultramafic Sequence itself with confidence.

2.17 Tectonic setting

The high-K calc-alkaline to shoshonite affinity of the majority of the volcanic succession and the range of non-ultramafic rock types, spanning from basaltic-andesites through to rhyolites, with notably large volumes of andesitic lavas, distinguishes the Cosmos rock suite from the conspicuously bimodal ultramafic/mafic-felsic association of the "Archaean mafic plains" that typify the majority of komatiite occurrences within the Kalgoorlie Terrane (e.g. Gresham and Loftus-Hills 1981; Arndt et al., 2008) as well as the largely bimodal dacite associations in the AWB (Rosengren et al., 2005; 2008; Fiorentini et al., 2012). The wide variety of rock types and compositions present within the Cosmos succession, coupled with their distinctly enriched geochemical affinity, indicates that they were formed in a subduction environment, at an island arc or convergent margin (de Joux et al., 2013; Chapter 3). The intricate association of felsic and intermediate volcanism at Cosmos, with three distinct komatiite units, two of which are mineralised, indicates eruption of contemporaneous ultramafic volcanism within an island-arc setting also. This concurs with Farran (2008) who concluded that the volcanic succession in the South Cosmos region formed by episodic volcanism in an island arc setting. Thus, the Cosmos succession is an example of ultramafic volcanism associated with active subduction zone. The significance of this and a more detailed description of the geochemical attributes of the footwall volcanic sequence is discussed in Chapter 3.

2.18 Conclusions

The Cosmos greenstone succession hosts several high grade massive and disseminated nickel sulphide deposits hosted within a thick ultramafic succession considered to represent preferred lava pathways within a komatiite flow field. The Cosmos komatiites preserve no primary volcanic textures, but the intermediate and felsic volcanic rocks with which they are associated preserve primary volcanic textures, despite the amphibolite metamorphic grade experienced by the succession.

The emplacement mechanisms of the Cosmos volcanic sequence have been inferred from the relict primary volcanic textures and show that the volcanic sequences was constructed via both explosive and effusive eruptions. The succession is compositionally diverse, composing basaltic andesite through to rhyolite volcanic products, with significant volumes of andesite lavas, likely representing an emergent volcanic sequence within an island-arc setting. Associated ultramafic volcanism is interpreted to have been erupted within this tectonic setting also. Nickel sulphide mineralisation penetrates up to several tens of metres into the dacite lapilli tuff footwall, which may represent its primary depositional location, rather than being wholly attributable to remobilisation during deformation and metamorphism. A lack of indicators of a submarine setting for the succession indicates it was likely emplaced subaerially. In contrast to the majority of the ultramafic-felsic associations in the east of the AWB, the Cosmos volcanic succession is composed of more compositionally diverse volcanic products, has a distinct high-K calc-alkaline affinity and was emplaced in a subaerial environment. This contrasts Fiorentini et al. (2012) who proposed that dacites from the AWB, associated with mineralised komatiites, display a strong tonalite–trondhjemite–granodiorite (TTD) and were formed in subaqueous environment in a rift or back-arc rift. Understanding of komatiite emplacement mechanisms and their tectonic setting in the Archaean is key to improving understanding of volcanism during this period and utilising this during future exploration for nickel deposits.

2.19 References

Akella, J., Winkler, H. G. F., 1966. Orthorhombic amphibole in some metamorphic reactions. Contributions to Mineral Petrology 12, 1-12.

Archibald, N. J., Bettenay, L. F., Binns, R. A., Groves, D. I., Gunthorpe, R. J. 1978. The evolution of Archaean greenstone terrains, Eastern Goldfields Province, Western Australia. Precambrian Research 6(2), 103-131.

Arndt, N. T., Lesher M. C., Barnes S. J. 2008. Komatiite. Cambridge University Press, Cambridge.

Barley, M. E., Brown, S. J., Krapež, B., Kositcin, N., 2008. Physical volcanology and geochemistry of a Late Archaean volcanic arc: Kurnalpi and Gindalbie Terranes, Eastern Goldfields Superterrane, Western Australia. Precambrian Research 161(1), 53-76.

Barnes, S. J., Hill, R. E., Gole, M. J., 1988. The Perseverance ultramafic complex, Western Australia: the product of a komatiite lava river. Journal of Petrology 29(2), 305-331.

Barnes, S. J., Brand, N. W., 1999. The distribution Cr, Ni, and chromite in komatiites, and application to exploration for komatiite-hosted nickel sulfide deposits. Economic Geology 94(1), 129-132.

Barnes, S. J., Hill, R. E. T., 2000. Metamorphism of komatiite-hosted nickel sulfide deposits. Reviews in Economic Geology 11, 203-215.

Bavinton, O. A., Keays, R. R., 1978. Precious metal values from interflow sedimentary rocks from the komatiite sequence at Kambalda, Western Australia. Geochimica et Cosmochimica Acta 42(8), 1151-1163.

Beresford, S., Duuring, P., Fiorentini, M., Rosengren, N., Bleeker, W., Barley, M., Cas, R., Tait, M., Wallace, H. 2004. P710. The Structural and Stratigraphic Architecture of the Agnew/Wiluna Belt, WA; Final Report, AMIRA, 75-124.

Binns R. A, Groves, D. I., 1976. Iron-nickel partition in metamorphosed olivine-sulfide assemblages from Perseverance, Western Australia. American Mineralogist 61, 782-787.

Black, L. P., Champion, D. C., Cassidy, K. F., 2002. Compilation of SHRIMP U-Pb geochronology data, Yilgarn Craton, Western Australia, 1997-2000. Unpublished Geoscience Australia, analytical data available from http://www.ga.gov.au/oracle/ozchron/frames.html.

Bleeker, W., Stern, R., Sircombe, K., 2000. Why the Slave Province, Northwest Territories, got a little bigger. Geological Survey of Canada, Current Research, Canadian Shield, C2.

Bunting, J. A., Williams, S. J. 1979. Sir Samuel, W.A. (1st edition): Western Australia Geological Survey, 1:250 000 Geological Series Explanatory Notes, 40p.

Cas, R., Porritt, L., Pittari, A., Hayman, P., 2008. A new approach to kimberlite facies terminology using a revised general approach to the nomenclature of all volcanic rocks and deposits: descriptive to genetic. Journal of Volcanology and Geothermal Research 174(1), 226-240.

Cassidy, K. F., Champion, D. C., Krapež, B., Barley, M. E., Brown, S. J. A., Blewett, R. S., Groenewald P. B., Tyler, I. M., 2006. A revised geological framework for the Yilgarn Craton, Western Australia. Western Australia Geological Survey, Record 2006/8, 8 pp.

Claoué-Long, J. C., Compston, W., Cowden, A. 1988. The age of the Kambalda greenstones resolved by ion-microprobe: implications for Archaean dating methods. Earth and Planetary Science Letters 89, 239-259.

Cox, S.F., 1984, Controls on the strength and mechanical behaviour of sulphides during regional metamorphism and deformation: Australian Geological Convention, 7th, Sydney, Short Course on the mechanical and chemical (re)mobilization of metalliferous mineralization, p. 91–98.

Czarnota, K., Champion, D. C., Goscombe, B., Blewett, R. S., Cassidy, K. F., Henson, P. A., Groenewald, P. B., 2010. Geodynamics of the eastern Yilgarn Craton. Precambrian Research 183(2), 175-202.

Deer, W. A., Howie, R. A., Zussman, J. 1992. An introduction to the rock-forming minerals. Second Edition. Longman Scientific and Technical, Harlow, UK, pp. 12.

Denny, M. 2010. AM5 Disseminated (AM5D) mineralogical model. Unpublished internal memo, Xstrata Nickel Australasia, 4-13.

de Joux, A., Thordarson, T., Denny, M., Hinton, R. W., de Joux A. J., 2013a. U-Pb dating constraints on the felsic and intermediate volcanic sequence of the nickel-sulphide bearing Cosmos succession, Agnew-Wiluna greenstone belt, Yilgarn Craton, Western Australia. Precambrian Research 236. 85-105.

Denny, M. 2010 AM5 Disseminated (AM5D) mineralogical model. Unpublished internal memo, Xstrata Nickel Australasia, 4-13.

Donaldson, C., Henderson, C., 1988. A new interpretation of round embayments in quartz crystals. Mineralogical Magazine 52(1), 27-33.

Dostal, J., Mueller, W. U., 1997. Komatiite flooding of a rifted Archean rhyolitic arc complex: geochemical signature and tectonic significance of the Stoughton-Roquemaure Group, Abitibi greenstone belt, Canada. The Journal of Geology, 105(5), 545-564.

Dowling, S. E., Hill, R. E. T. 1990. Rivers of fire: the physical volcanology of komatiites in the Mount Keith region, Norseman-Wiluna greenstone belt, Western Australia. CSIRO Exploration Geoscience Restricted Report 103, 170.

Dowling, S. E., Hill, R. E. T., 1992. The distribution of PGE in fractionated Archaean komatiites, western and central ultramafic units, Mt Keith region, Western Australia. Australian Journal of Earth Sciences 39(3), 349-363.

Duuring, P., Bleeker, W., Beresford, S. W., 2007. Structural modification of the komatiite-associated Harmony nickel sulfide deposit, Leinster, Western Australia. Economic Geology 102(2), 277-297.

Duuring, P., Bleeker, W., Beresford, S. W., Hayward, N., 2010. Towards a volcanic–structural balance: relative importance of volcanism, folding, and remobilisation of nickel sulphides at the Perseverance Ni–Cu–(PGE) deposit, Western Australia. Mineralium Deposita 45(3), 281-311.

Duuring, P., Bleeker, W., Beresford, S. W., Fiorentini, M. L., Rosengren, N. M., 2012. Structural evolution of the Agnew–Wiluna greenstone belt, Eastern Yilgarn Craton and implications for komatiite-hosted Ni sulfide exploration. Australian Journal of Earth Sciences 59(5), 765-791.

Farran, M., 2008. Volcanic, metamorphic and structural architecture of the Prospero-Tapinos nickel sulfide host succession, Western Australia, BSc Honours Thesis, unpublished.

Ferry, J. M., Spear, F. S., 1978, Experimental calibration of the partitioning of Fe and Mg between biotite and garnet: Contributions to Mineralogy and Petrolology 66, 113-117.

Fiorentini, M., Beresford, S., Barley, M., Duuring, P., Bekker, A., Rosengren, N., Cas, R., Hronsky, J., 2012. District to camp controls on the genesis of komatiite-hosted nickel sulfide deposits, Agnew-Wiluna greenstone belt, Western Australia: Insights from the multiple sulfur isotopes. Economic Geology 107(5), 781-796.

Fitton, J. G., Saunders, A. D., Larsen, L. M., Hardarson, B. S., Norry, M. J., 1998. Volcanic rocks from the southeast Greenland margin at 63°N: composition, petrogenesis and mantle sources. In: Saunders, A.D., Larsen, H.C., Wise, S.H. (Eds) Proceedings of the Ocean Drilling Program Scientific Results, 152. College Station, TX: Ocean Drilling Program, pp. 331–350.

Geological Survey of Western Australia (GSWA), 2009. Compilation of geochronology information, 2009 update. Western Australia Geological Survey.

Giles, C. W., Hallberg, J. A., 1982. The genesis of the Archaean Welcome Well volcanic complex, Western Australia. Contributions to Mineralogy and Petrology 80(4), 307-318.

Gill, R., 2010. Igneous rocks and processes: a practical guide. John Wiley & Sons, Chichester.

Gole, M. J., Barnes, S. J., Hill, R. E., 1987. The role of fluids in the metamorphism of komatiites, Agnew nickel deposit, Western Australia. Contributions to Mineralogy and Petrology 96(2), 151-162.

Gole, M. J., Barnes, S. J., Hill, R. E. T., 1990. Partial melting and recrystallization of Archaean komatiites by residual heat from rapidly accumulated flows. Contributions to Mineralogy and Petrology 105(6), 704-714.

Gole, M. J., Andrews, D. L., Drew, G. J., Woodhouse, M., 1996. Komatiite-hosted nickel sulphide deposits, Honeymoon Well, Western Australia. Nickel, 96, 97-102.

Goscombe, B., Blewett, R. S., Czarnota, K., Groenewald, B., Maas, R., 2009 Metamorphic evolution and integrated terrane analysis of the eastern Yilgarn Craton: Rationale, methods, outcomes and interpretation: Geoscience Australia, Record 2009/23, 270.

Gresham, J. J., Loftus-Hills, G. D., 1981. The geology of the Kambalda nickel field, Western Australia. Economic Geology 76(6), 1373-1416.

Grove, T. L., Parman, S. W., (2004). Thermal evolution of the Earth as recorded by komatiites, Earth and Planetary Science Letters 219 (3–4), 173-187.

Groves, D. I., Lesher, C. M., Gee, R. D., 1984. Tectonic setting of the sulphide nickel deposits of Western Australian Shield. In; Buchanan, D. L., Jones, M.J. (Eds) Sulphide deposits in Mafic and Ultramafic Rocks, Institution of Mining and Metallurgy, London.

Hallberg, J. A., 1985. Geology and mineral deposits of the Leonora-Laverton area north-eastern Yilgarn Block, Western Australia. Hesperian Press.

Hill, R. E. T., Gole, M. J., Barnes, S. J., 1989. Olivine adcumulates in the Norseman-Wiluna greenstone belt, Western Australia; implications for the volcanology of komatiites. In; Prendergast, M. D., Jones, M. J., Jones (Eds) Magmatic sulphides - the Zimbabwe volume, Institute of Materials, Minerals and Mining, London, pp. 189-206.

Hill, R. E. T., Gole, M. J., 1990. Nickel sulphide deposits of the Yilgarn Block. Geology of the mineral deposits of Australia and Papua New Guinea. Australian Institute of Mining and Metallurgy, Melbourne, 557-559.

Hill, R. E. T., Gole, M. J., Barnes, S. J., 1990. Physical Volcanology of Komatiites: A Field Guide to the Komatiites between Kalgoorlie and Wiluna, Eastern Goldfields Province, Yilgarn Block, Western Australia. Geological Society of Australia, WA Division.

Hill, R. E. T., Barnes, S. J., Gole, M. J., Dowling S. E., 1995. The physical volcanology of komatiites as deduced from field relationships in the Norseman-Wiluna greenstone belt, Western Australia. Lithos 34, 159-188.

Hill, R. E. T., 2001. Komatiite volcanology, volcanological setting and primary geochemical properties of komatiite-associated nickel deposits. Geochemistry: Exploration, Environment, Analysis 1(4), 365-381.

Hill, R. E. T., Barnes, S. J., Dowling, S. E., Thordarson, T. 2004. Komatiites and nickel sulphide ore bodies of the Black Swan area, Yilgarn Craton, Western Australia. 1. Petrology and volcanology of host rocks. Mineralium Deposita 39(7), 684-706.

Hill, R. E. T., Dowling, S. E., 2008. The petrology and geochemistry of mineralised komatiites intersected in three diamond drill holes (AM262B, AMD275 and BJD048A) from the AM5 Nickel Sulphide Deposit; Cosmos region, Agnew-Wiluna Greenstone Belt; A pilot study for characterising mineralised domains within the ore body. Unpublished External report, Kalapana Research Associates and Triodia Research.

Holdaway, M. J., Lee, S. M., 1977, Fe-Mg cordierite stability in high grade pelitic rocks based on experimental, theoretical, and natural observations: Contributions to Mineralogy and Petrology 63, 175- 198.

Holdaway M. J., Mukhopadhyay, B. 1993. A re-evaluation of the stability relations of andalusite; Thermochemical data and phase diagram form the aluminium silicates. American Mineralogist 78, 298-315.

Hollings, P., Wyman, D., Kerrich, R., 1999. Komatiite–basalt–rhyolite volcanic associations in Northern Superior Province greenstone belts: significance of plume-arc interaction in the generation of the proto continental Superior Province. Lithos 46(1), 137-161.

Hollings, P., Kerrich, R., 2006. Light rare earth element depleted to enriched basaltic flows from 2.8 to 2.7 Ga greenstone belts of the Uchi Subprovince, Ontario, Canada. Chemical Geology 227(3), 133-153.

Kaye, A., Thordarson, T., Hayward, C., Denny, M., de Joux, A.J., 2010. The felsic and intermediate footwall to the Cosmos Nickel sulphide deposits, Agnew-Wiluna greenstone belt, Yilgarn Craton, Western Australia, SEG 2010 conference abstract and presentation, Colorado.

Kaye, A., Thordarson, T., Hayward, C., Fitton, G., de Joux, A.J., 2011. The felsic and intermediate footwall to the Cosmos Nickel sulphide deposits, Agnew-Wiluna greenstone belt, Yilgarn Craton, Western Australia, IUGG 2011 conference abstract and presentation, Melbourne.

Kositcin, N., Brown, S. J., Barley, M. E., Krapež, B., Cassidy, K. F., Champion, D. C., 2008. SHRIMP U-Pb zircon age constraints on the Late Archaean tectonostratigraphic architecture of the Eastern Goldfields Superterrane, Yilgarn Craton, Western Australia. Precambrian Research 161(1), 5-33.

Langworthy, P., Vallance, S., 2004. Exploration Strategies for the discovery of the Cosmos Region nickel sulphide deposits, Western Australia. Unpublished internal memo, Xstrata Nickel Australasia.

Langworthy, P., Vallance, S., 2004. Exploration Strategies for the discovery of the Cosmos Region nickel sulphide deposits, Western Australia. Unpublished internal memo, Xstrata Nickel Australasia.

Lavrent'eva, I. V., Perchuk, L. L., 1981. Phase correspondence in the system biotite-garnet: Experimental data. In Dokl. Akad. Nauk USSR 260, 731-734).

Le Bas, M. J., Le Maitre, R. W., Streckeisen, A., Zanettin, B., 1986. A chemical classification of volcanic rocks based on the total alkali-silica diagram. Journal of Petrology 27(3), 745-750.

Le Bas, M. J., Le Maitre, R. W., Woolley, A. R., 1992. The construction of the total alkali-silica chemical classification of volcanic rocks. Mineralogy and Petrology 46(1), 1-22.

Lesher, C. M., Keays, R. R., 1984. Metamorphically and hydrothermally mobilized Fe-Ni-Cu sulphides at Kambalda, Western Australia. Sulphide deposits in mafic and ultramafic rocks. Institute of Mining and Metallurgy, London, 62-69.

Liu, S. F., Champion, D. C., Cassidy K. F., 2002. Geology of the Sir Samuel 1:250,000 sheet area, Western Australia Geoscience Australia Record 14.

Lofgren, G., 1971. Spherulitic textures in glassy and crystalline rocks. Journal of Geophysical Research 76(23), 5635-5648.

McDonough, W. F., Ireland, T.R., 1993. Intraplate origin of komatiites inferred from trace-elements in glass inclusions. Nature 365, 432–434.

McPhie, J., Doyle, M., Allen, R., Allen, R. L., 1993. Volcanic textures: a guide to the interpretation of textures in volcanic rocks. CODES-University of Tasmania.

McQueen, K. G., 1979. Experimental heating and diffusion effects in Fe-Ni sulfide ore from Redross, Western Australia. Economic Geology 74(1), 140-148.

Morris, P. A., 1998. Archaean felsic volcanism in parts of the Eastern Goldfields region, Western Australia (No. 55). Geological Survey of Western Australia.

Naldrett, A. J., 2004. Magmatic sulfide deposits: geology, geochemistry and exploration. Springer, Berlin.

Parman, S. W., T. L Grove, T. L., Dann, J. C., 2001. The production of Barberton komatiites in an Archaean subduction zone. Geophysical Research Letters 28, 2513–2516.

Pawley, M. J., Wingate, M. T. D., Kirkland, C. L., Wyche, S., Hall, C. E., Romano, S. S., Doublier, M. P., 2012. Adding pieces to the puzzle: episodic crustal growth and a new terrane in the northeast Yilgarn Craton, Western Australia. Australian Journal of Earth Sciences 59(5), 603-623.

Peccerillo, A., Taylor, S. R., 1976. Geochemistry of Eocene calc-alkaline volcanic rocks from the Kastamonu area, northern Turkey. Contributions to Mineralogy and Petrology 58(1), 63-81.

Perchuk L. L., Lavrent'eva I. V., 1983. Experimental investigation of exchange equilibria in the system cordierite-garnet-biotite. In; Saxena SK (Eds) Kinetics and equilibrium in mineral reactions. Springer, Berlin Heidelberg New York, 199-239.

Perring, C. S., Barnes, S. J., Hill, R. E. T., 1995. The physical volcanology of Archaean komatiite sequences from Forrestania, Southern Cross Province, Western Australia. Lithos 34(1), 189-207.

Plimer, I., 1984. Remobilization in high grade metamorphic environments: Australian Geological Convention, 7th, Sydney, Short Course on the mechanical and chemical (re)mobilization of metalliferous mineralization, 119–128.

Rickwood, P. C., 1989. Boundary lines within petrologic diagrams which use oxides of major and minor elements. Lithos 22(4), 247-263.

Rosengren, N. M., Beresford, S. W., Grguric, B. A., Cas, R. A. F., 2005. An intrusive origin for the komatiitic dunite-hosted Mount Keith disseminated nickel sulfide deposit, Western Australia. Economic Geology 100(1), 149-156.

Rosengren, N. M., Cas, R. A. F., Beresford, S. W., Palich, B. M., 2008. Reconstruction of an extensive Archaean dacite submarine volcanic complex associated with the komatiite-hosted Mt Keith nickel deposit, Agnew-Wiluna greenstone belt, Yilgarn Craton, Western Australia. Precambrian Research 161(1), 34-52.

Stuff, R., 2011. Xstrata Nickel Australasia-Cosmos Nickel Project- Technical Report No: STR01126, Annual report on Cosmos Nickel Project Tenements submitted to DMP, 12-18.

Thompson, A. B., 1976. Mineral reactions in pelitic rocks; II, Calculation of some PTX (Fe-Mg) phase relations. American Journal of Science 276(4), 425-454.

Trofimovs, J., Tait, M. A., Cas, R. A. F., McArthur, A., Beresford, S. W., 2003. Can the role of thermal erosion in strongly deformed komatiite–Ni–Cu–(PGE) deposits be determined? Perseverance, Agnew–Wiluna Belt, Western Australia. Australian Journal of Earth Sciences 50(2), 199-214.

Trofimovs, J., Davis, B. K., Cas, R. A. F., 2004. Contemporaneous ultramafic and felsic intrusive and extrusive magmatism in the Archaean Boorara Domain, Eastern Goldfields Superterrane, Western Australia, and its implications. Precambrian Research 131(3), 283-304.

Wheller, G. E., Varne, R., Foden, J. D., Abbott, M. J., 1987. Geochemistry of Quaternary volcanism in the Sunda-Banda arc, Indonesia, and three-component genesis of island-arc basaltic magmas. Journal of Volcanology and Geothermal Research 32(1), 137-160.

White, J. D. L., Houghton, B. F., 2006. Primary volcaniclastic rocks. Geology 34(8), 677-680.

Winchester, J. A., Floyd, P. A., 1977. Geochemical discrimination of different magma series and their differentiation products using immobile elements. Chemical Geology 20, 325-343.

Paper 2 - The Cosmos Greenstone succession, Agnew-Wiluna greenstone belt, Yilgarn Craton, Western Australia: Geochemistry of an enriched Late Archaean island-arc succession

A. de Joux[1], T. Thordarson[1*], G.Fitton[1] and A. Hastie[1]

[1]School of GeoSciences, University of Edinburgh, Grant Institute, The King's Buildings, West Mains Road, Edinburgh, EH9 3JW, UK

*Faculty of Science, University of Iceland, Sturlugata 7, IS101, Reykjavik, Iceland

In revision for Lithos

- A. de Joux undertook all fieldwork, sampling and sample preparation, data processing and wrote the manuscript and all earlier drafts
- T. Thordarson provided supervision plus editorial comments and general guidance during data processing
- G. Fitton provided editorial comments and suggestions on how to make the paper more concise
- A. Hastie provided guidance on suitable discrimination plots to use, guidance on assimilation-fractional-crystallisation (AFC) modelling and editorial comments

Chapter 3 - The Cosmos Greenstone succession, Agnew-Wiluna greenstone belt, Yilgarn Craton, Western Australia: Geochemistry of an enriched Neoarchaean island-arc succession

3.1 Abstract

The composition and geochemical affinity of the volcanic stratigraphic footwall succession to the Cosmos komatiite-hosted nickel-sulphide deposits contrasts with the majority of felsic volcanism within the Agnew-Wiluna greenstone belt and also the wider Kalgoorlie Terrane. Volcanism in this Kalgoorlie Terrane is considered to have a tonalite-trondhjemite-dacite (TTD) geochemical affinity. The Cosmos footwall consists of an intercalated succession of both fragmental and coherent basaltic andesites through to rhyolites, which all exhibit a strong crustal signature that is geochemically most similar to modern high-K calc-alkaline to shoshonite continental island-arc successions. Light rare earth elements (LREEs) and large ion-lithophile

elements (LILEs) are strongly enriched relative to high field strength elements (HFSEs) and volcanic lithologies display strong positive Pb and negative Nb anomalies. Contrasting REE, LILE and HFSE concentrations, coupled with assimilation-fractional crystallisation (AFC) modelling, has shown that intercalated dacitic and andesitic volcanic rocks within the footwall succession are not co-genetic. Xenocrystic zircons within the felsic volcanic lithologies indicate assimilation of older continental crust contributed to the generation of the footwall volcanic sequence. The geochemical characteristics of the Cosmos volcanic succession indicates the most likely tectonic setting was a subduction zone, with parental melts derived via partial melting of enriched peridotite that had been contaminated by subducted crustal material within the mantle wedge. In contrast, two younger felsic porphyry intrusions that cross-cut the volcanic succession have a distinct TTD affinity. REEs are strongly fractionated compared to those of the volcanic lithologies, exhibiting strong heavy rare earth element (HREE) depletion. Therefore these intrusions are considered to be generated via partial melting of the subducted slab itself and are related to local high-Ca granite intrusion. The Cosmos volcanic succession represents the first extrusive high-K calc-alkaline to shoshonite island-arc volcanic sequence described in the Kalgoorlie Terrane and, coupled with age dating of the stratigraphy, is indicative of formation in a long-lived volcanic arc setting active from 2736 Ma to beyond 2724 Ma. The age and geochemical affinity of the Cosmos footwall volcanic succession shows that the overall architecture of the Agnew-Wiluna greenstone belt and wider Kalgoorlie terrane is more complex than currently accepted. The island-arc affinity of the Cosmos volcanic succession, containing abundant calc-alkaline andesite lavas, also provides further support for the operation of plate tectonics in the Neoarchaean.

3.2 Introduction

Discussions of the evolution of greenstone belt sequences within Archaean cratons, such as the Canadian Superior Craton and the Australian Yilgarn Craton are relevant to the wider debate on the existence of plate tectonics during the Archaean (e.g., Czarnota et al., 2010; Korsch et al., 2011; Barnes et al., 2012; Bédard, 2006; Bédard et al., 2013; Wyman, 2013a). The origin of greenstone belt sequences within the Eastern Goldfields Superterrane (EGS) of the Yilgarn Craton of Western Australia, which are commonly associated with komatiite-hosted nickel sulphide deposits, has been debated for over 25 years. Workers generally support either a plume-dominated model (e.g., Campbell and Hill, 1988; Trofimovs et al., 2004, 2006; Fiorentini et al., 2012; Barnes et al., 2012) or variants on subduction accretion models (Nelson, 1997b; Myers, 1993; Gee and Swager, 2008; Barley et al., 2008; Kositcin et al., 2008; Standing, 2008; Czarnota et al., 2010; Korsch et al., 2011). Most recently Barnes et al. (2012) reiterated a mantle plume model based on the composition of basalts throughout the EGS, broadly along the lines of that proposed by Campbell and Hill (1988). This model largely precludes the possibility of arc development and subsequent terrane accretion within the EGS. In contrast Czarnota et al. (2010) recently provided a holistic review of the tectonic history of the EGS which built on the models of Barley et al. (2008) and favoured a para-authochtonous convergent margin model linking all terranes of the EGS within a westward dipping subduction zone.

The tectonic setting and petrogenesis of greenstone successions within the Yilgarn Craton and beyond is in no way resolved, with certain authors still questioning whether modern style plate tectonics even operated in the late Archaean (e.g., Hamilton, 2003; Bédard, 2006; Bédard et al., 2013). Understanding the tectonic setting of mineralised greenstone belt sequences has important implications both for future exploration and for understanding of the geodynamics of Archaean volcanism. Detailed geochemical analysis of individual Archaean greenstone terranes to discern a likely tectonic setting is often challenging: within a single terrane there are often several tens of greenstone belt sequences which are to varying degrees poorly

outcropping, deeply weathered, highly metamorphosed and strongly deformed. A detailed description of the major, trace and REE geochemical trends exhibited by the Cosmos volcanic sequence is undertaken here in an attempt to resolve the relative contribution and interaction of fractional crystallisation, crustal assimilation and source composition in the formation of the Cosmos volcanic succession, and ultimately to derive its likely tectonic setting.

3.3 Regional geology and debate over the formation of greenstone belt sequences in the EGS

The EGS comprises the eastern part of the Yilgarn Craton and features linear, bimodal (mafic–ultramafic and felsic), volcanic 'greenstone belt' sequences, with minor clastic sedimentary sequences and banded iron formations. These are sandwiched between voluminous elongate granitoid plutons intruded between 2760 and 2620 Ma (Nelson, 1998; Cassidy et al., 2006; Fig. 3.1). SHRIMP U-Pb zircon data indicates a major peak in volcanism between 2720 and 2650 Ma, with lesser peaks at 2950 Ma and 2810 Ma (Nelson, 1997b; Cassidy et al., 2006; Fig. 3.1).

The Cosmos mine is situated on the western edge of the Agnew-Wiluna greenstone belt (AWB), on the north-western edge of the Kalgoorlie Terrane, which forms the western most terrane of the EGS. The AWB contains some of the world's most economically significant nickel sulphide deposits including Mount Keith, Perseverance and Yakabindie (Fig. 3.1). Mineralised ultramafic successions within the Kalgoorlie Terrane have a modal emplacement age of ~2707 Ma (Kositcin et al., 2008) and are commonly associated and intercalated with felsic and intermediate volcanic packages. Examples include Black Swan (Hill et al., 2004), Perseverance (Barnes et al., 1988; Trofimovs et al., 2003), Boorara (Trofimovs et al., 2004, 2006) and Mount Keith (Dowling and Hill, 1990; Hill et al., 1995; Rosengren et al., 2005, 2008; Fiorentini et al., 2012). Dacite is, volumetrically, the dominant volcanic rock type within the AWB, although non-ultramafic lithologies range from basaltic andesites to

more rare rhyolites (Rosengren et al., 2008; Fiorentini et al., 2012). The felsic volcanic rocks within the AWB are considered by Fiorentini et al. (2012) to exhibit a TTD geochemical affinity. They are thus considered to be geochemically similar to felsic volcanic sequences in the south of the Kalgoorlie Terrane, such as the Kalgoorlie Sequence, which includes the Black Flag Group (Morris and Witt, 1997; Krapež and Hand, 2008) and the Boorara Domain (Trofimovs et al. 2004; 2006).

The volcanic footwall succession to mineralised komatiite units at Cosmos does not display a TTD affinity. Volcanic lithologies exhibit a distinct island-arc character, with a trace element geochemistry most similar to those found in modern continental island-arc settings. Calc-alkaline island-arc volcanic packages, rarely described within the Kalgoorlie Terrane, are recognised within the adjacent Kurnalpi and Gindalbie Terranes of the EGS (Fig. 3.1), which most likely represents the evolution and maturation of the same Neoarchaean volcanic arc (Morris and Witt, 1997; Barley et al., 2008; Korsch et al., 2011). However, Barnes et al. (2012) questioned whether the reported occurrences of calc-alkaline volcanism within the EGS (e.g., Kurnalpi Terrane) are actually analogous to modern arc volcanism, arguing that uniformitarian models of arc accretion tectonics in the eastern Yilgarn are inconsistent with geochemical characteristics of regional basalt occurrence.

The recognition of a distinct island-arc volcanic sequence at Cosmos, within the AWB, not only indicates this greenstone belt, and therefore the wider Kalgoorlie Terrane, is tectonically more complex than currently considered, but also has consequences for recent models of the tectonic evolution of the Eastern Goldfields Superterrane (e.g., Czarnota et al., 2010; Korsch et al., 2011; Barnes et al., 2012). I present a detailed geochemical analysis of the Neoarchaean Cosmos greenstone succession showing that melt generation processes and tectonic evolution can be resolved even in a relatively small greenstone sequence. My conclusions also have consequences for the re-ignited debate on the operation of plate tectonics locally within the EGS, and during the late Archaean in general (e.g., Bédard et al., 2013; Barnes et al., 2012; Wyman, 2013a).

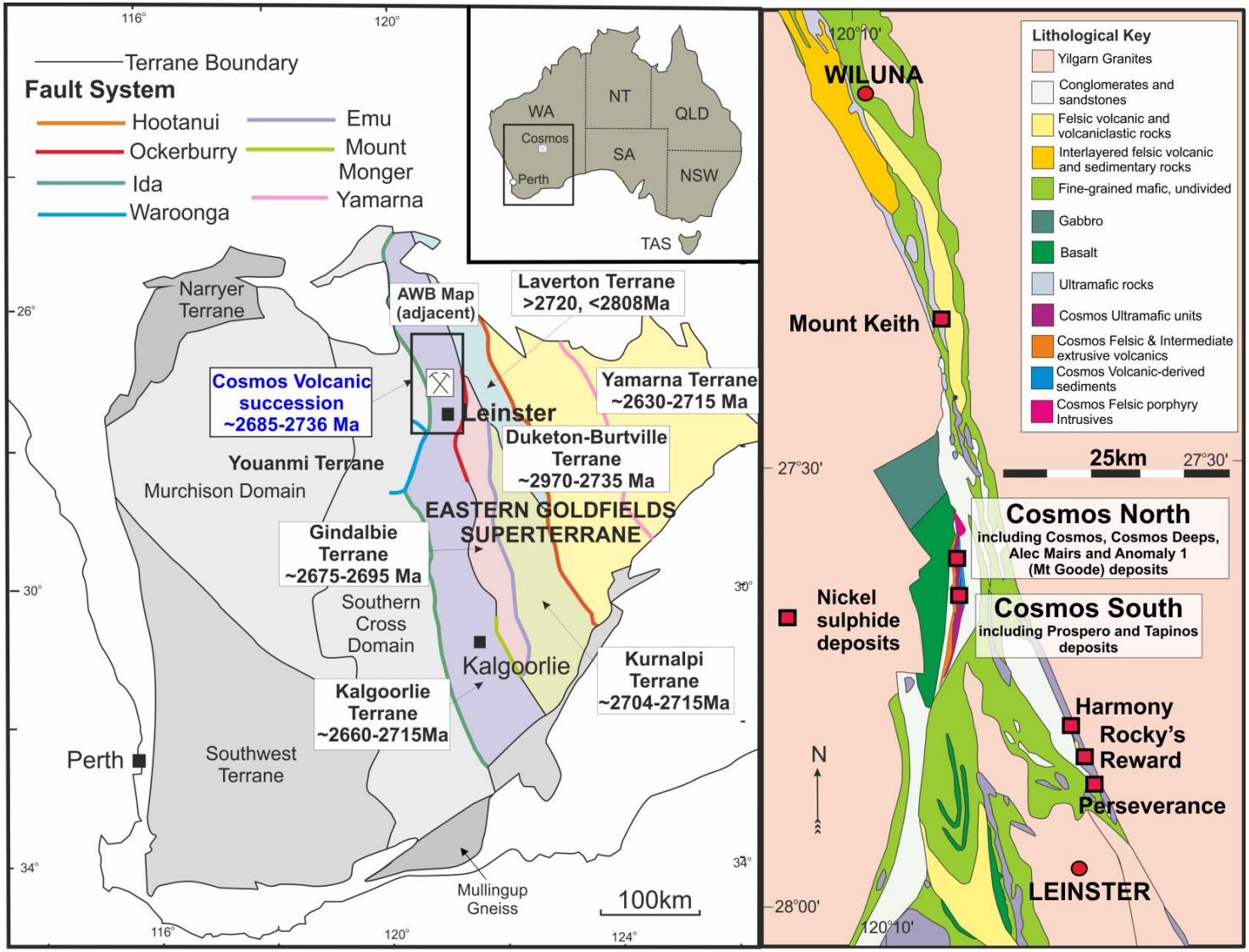

Figure 3.1. Location maps of the Cosmos mine site within the AWB and its position within the EGS of the Yilgarn Craton, highlighting terrane boundaries and the approximate ages of the different terranes (modified after Cassidy et al., 2006 and de Joux et al., 2013. U-Pb ages from Kositcin et al., (2008) and Pawley et al., (2012).

3.4 Geology of the Cosmos region

The Cosmos greenstone succession contains several komatiite-hosted massive and disseminated nickel-sulphide ore bodies (Hill and Dowling, 2008; Stuff, 2011; de Joux et al., 2013; Fig. 3.2). The stratigraphic footwall volcanic succession to these ore deposits consists of a complex succession of both fragmental and coherent extrusive lithologies ranging from basaltic andesites through to rhyolites, as well as later-formed felsic and basaltic intrusions (Fig. 3.2, 3.3; Chapter 2). The stratigraphic hangingwall succession consists largely of volcanically-derived sedimentary rocks (Fig. 3.2). The key aspects of the stratigraphy, including direct and inferred U-Pb ages, are described in Table 3.1 and Figure 3.2. A detailed description of the lithostratigraphy at Cosmos is provided in Chapter 2.

The succession has undergone several phases of regional deformation (Stuff, 2011), resulting in a subvertical succession that dips and youngs to the east. Figure 3.3 shows a 200m below sea level plan through the succession, which a north-south cross-section through the primary volcanic stratigraphy may have resembled. Garnet-biotite geothermometry and metamorphic mineral assemblages indicate maximum metamorphic temperatures of 560 - 580^{o}C at ~3 kbar (Hill and Dowling, 2008; de Joux et al., 2013; Chapter 2). Despite experiencing amphibolite metamorphism and several deformation events, many of the stratigraphic footwall lithologies to the ultramafic lava sequences preserve primary igneous textures, thereby enabling protoliths to be established. A more detailed description of the stratigraphy, in particular the U-Pb dating constraints, is given by de Joux et al. (2013) and discussed in Chapters 2 and 4.

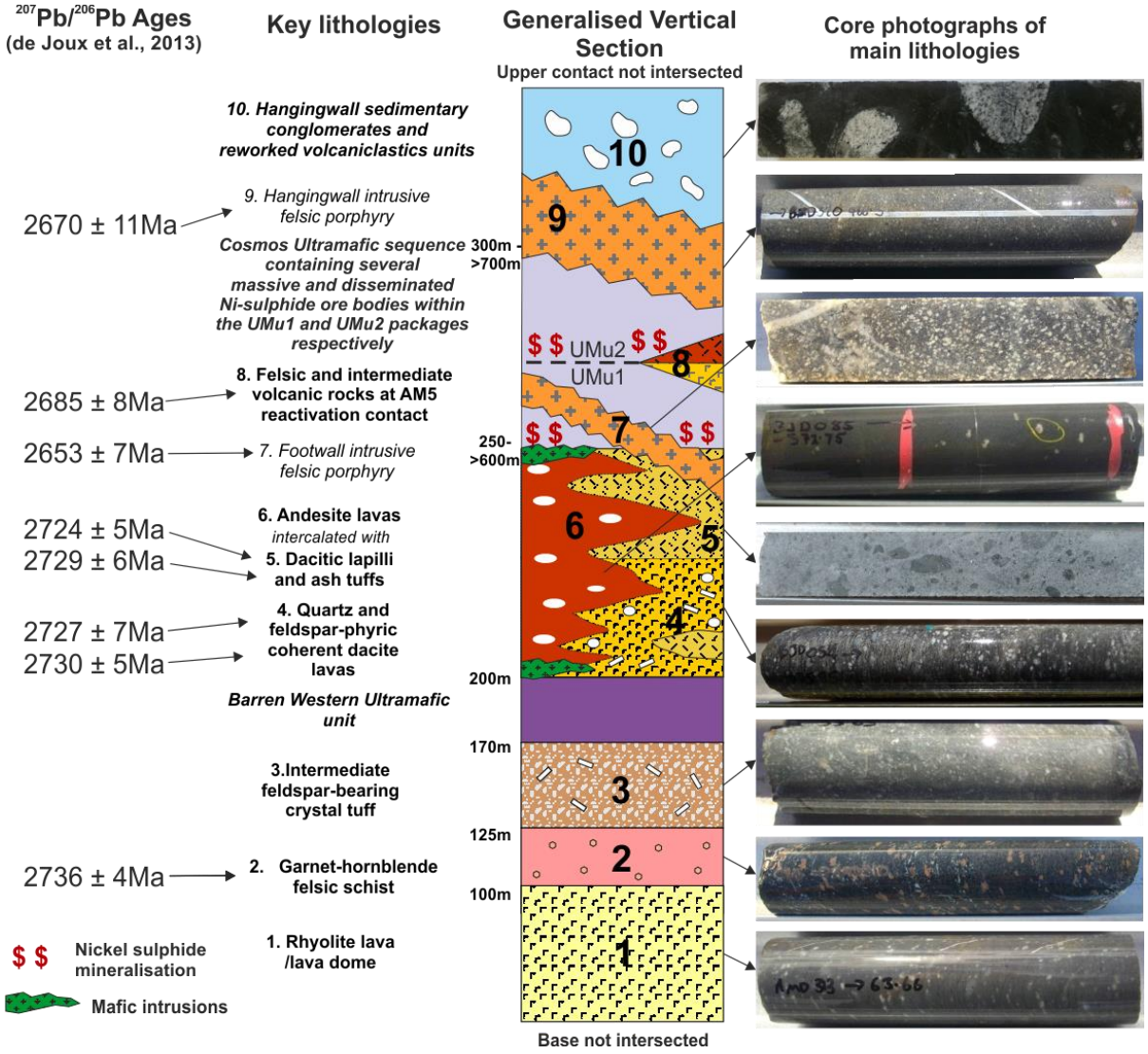

Figure 3.2. Generalised vertical section of the Cosmos greenstone stratigraphy including representative core photos and U-Pb ages (modified after de Joux et al., 2013).

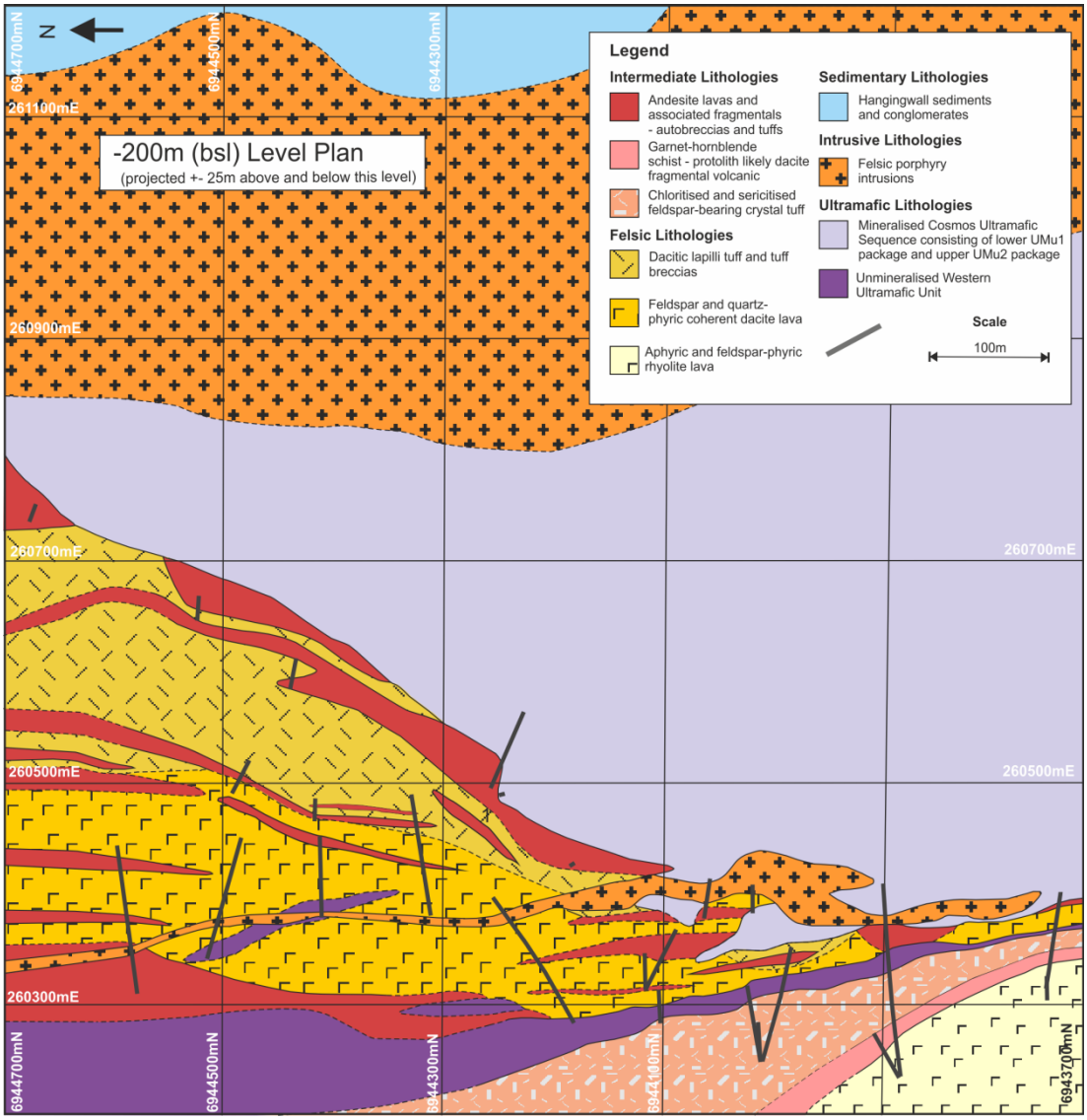

Figure 3.3. A -200m (below sea level) level plan through the succession, which given the subvertical dip of the succession, may represent what a north-south cross-section through the primary volcanic stratigraphy resembled.

Table 3.1 showing the age, mineralogy, volcanic facies and typical alteration styles of the main lithological groups within the Cosmos Succession

Stratigraphic unit	Age	Mineralogy	Volcanic Facies	Typical alteration type
Coherent rhyolite lava	> 2736Ma ± 4 Ma	Quartz + feldspar + sericite + biotite ± muscovite ± chlorite	Coherent porphyritic and aphyric rhyolite lava flow/dome. Feldspar phenocrysts in a cryptocrystalline quartz-feldspar groundmass	Sericitic, Silicic
Garnet-hornblende felsic schist	2736Ma ± 4 Ma	Feldspar + garnet + hornblende + epidote ± chlorite	Recrystallised fragmental unit typified by skeletal porphyroblastic garnets in a hornblende and plagioclase-rich banded matrix. Occasional relic feldspar phenocryst fragments suggest the protolith is likely a crystal-rich felsic tuff	Sericitic
Intermediate feldspar-bearing crystal tuff	< 2736 ± 4 Ma	Feldspar + sericite + chlorite ± epidote	Andesitic crystal-rich tuff with abundant feldspar fragments and shards. Forms the immediate footwall unit to the Western Ultramafic unit	Sericitic, Chloritic, Epidote
Western Ultramafic unit	< 2736 ± 4 Ma, > 2730 ± 5 Ma	Lizardite + antigorite + tremolite actinolite + magnetite	Barren olivine mesocumulates and orthocumulates that have been pervasively serpentinised and overprinted by metamorphic olivine, destroying primary cumulate and spinifex textures	Serpentinisation, metamorphic olivine
Coherent dacite lava	2730-2727 ± 7 Ma	Quartz + feldspar + sericite + biotite ± muscovite ± chlorite	Quartz and feldspar-phyric dacite lava package with occasional intermediate xenoliths. Embayed quartz phenocrysts common. Intercalated with andesitic lavas and associated volcaniclastic horizons	Sericitic, Silicic
Dacitic lapilli tuff	2729-2724 ± 6 Ma	Quartz + feldspar + sericite + biotite ± muscovite ± chlorite	Dacitic lapilli tuff with abundant relic feldspar phenocryst fragments and shards. Features tuff breccias with intermediate clasts. Intercalated with andesitic lavas and associated volcaniclastic horizons. Along with andesite lavas forms the footwall to the Cosmos Ultramafic Sequence	Sericitic, Silicic
Andesite lavas and associated volcaniclastic horizons	2730-2724 ± 7 Ma	Feldspar + hornblende + biotite + chlorite ± quartz ± sericite	Variably amygdaloidal basaltic andesite to andesite lavas with autobreccias discernible in places. Associated volcaniclastic deposits. Intercalated with dacitic lavas and tuffs. Along with dacitic tuffs forms the footwall to the Cosmos Ultramafic Sequence	Chloritic, Silicic,
Cosmos Ultramafic Sequence	< 2724 Ma	Lizardite + antigorite + tremolite actinolite + magnetite ± olivine ± chlorite ± Ni-sulphide	Dominantly olivine mesocumulates and olivine adcumulates and features spinifex-textured komatiites, olivine-pyroxene cumulates, olivine orthocumulates towards the unit's margin, although pervasive serpentinisation and overprinting by metamorphic olivine has destroyed primary volcanic textures. Contains numerous disseminated and massive high-tenor nickel sulphides	Serpentinisation, metamorphic olivine

Stratigraphic unit	Age	Mineralogy	Volcanic Facies	Typical alteration type
Mafic Intrusions	<2724 Ma	Hornblende + feldspar + chlorite ± biotite	Two main mafic intrusions cross-cut the Cosmos volcanic succession at a shallow angle, notably the Cosmos Deeps Dolerite and the AM5 Diorite that both feature large distinct poikiloblasts of chlorite and hornblende	Chloritic
Hangingwall felsic porphyry intrusion	2670 ± 11 Ma	Quartz + feldspar + sericite + biotite ± muscovite ± epidote	Porphyritic felsic intrusion with small quartz and feldspar phenocrysts that crosscuts the upper contact of the Cosmos Ultramafic Sequence and the overlying hangingwall sedimentary package	Chloritic, Silicic, Epidote
Footwall felsic porphyry intrusion	2653 ± 7 Ma	Quartz + feldspar + sericite + biotite ± muscovite ± epidote	Porphyritic felsic intrusion with large feldspar phenocrysts that cross cuts the basal contact of the Cosmos Ultramafic Sequence	Chloritic, Silicic, Epidote
Hangingwall sedimentary package	<2685 ± 8 Ma, >2670 Ma ± 11 Ma	Feldspar + amphibole + chlorite + biotite + quartz + sericite + muscovite + pyrite + garnet	Package of intercalated polymictic and monomictic conglomerates and reworked volcaniclastic sandstones and siltstones. Conglomerates feature granitic clasts in a more intermediate matrix	Chloritic, Silicic

3.5 Analytical techniques

104 diamond drill holes, covering a 1 km strike length of the Cosmos greenstone belt sequence, were re-logged in detail with focus on lithological identification of individual felsic and intermediate units within the footwall packages to the Cosmos Ultramafic Sequence, and also the underlying older barren Western Ultramafic unit (Fig. 3.2). There is little to no surface outcrop in the Cosmos North region: assessment of sub-surface stratigraphy was undertaken via diamond drill core logging and sampling, thereby correlating and consolidating the stratigraphy. Lithological names were initially assigned based on textures and mineralogical assemblages of hand specimens. Subsequently, rock types were confirmed using geochemical attributes established via X-ray Fluorescence (XRF) and Inductively Coupled Plasma Mass Spectrometry (ICP-MS) in combination with petrography. Rock protolith nomenclature is used in this paper for units where primary textures are preserved or can be inferred from metamorphic mineral assemblages and/or geochemical attributes.

Core samples were crushed in a jaw-crusher and then powdered in a ring mill. These powders were used for major and trace elemental analysis. Major and trace elements were analysed on 225 samples using a PanAnalytical PW2402 wavelength dispersive sequential XRF spectrometer at the University of Edinburgh. Major element oxide totals were generally within +/- 2% of 100% and have been recalculated to a 100% volatile free basis. Of the samples analysed via XRF, 85 samples, which are representative of samples from each volcanic group, were analysed using ICP-MS to establish their REE concentrations, as well as selected samples for U, Th, Pb and Hf. REE analysis samples were prepared via tri-acid digest and analysed via ICP-MS at the Scottish Universities Environmental Research Centre (SUERC) in East Kilbride. Detailed XRF and ICP-MS methods are given in Appendix 2.

3.6 Alteration

Element mobility during metamorphism in Archaean terranes must be considered when using major and trace element geochemistry to classify volcanic rocks and assess likely tectonic settings. Given the mid-amphibolite metamorphic grade of the Cosmos succession, it is particularly important to assess the likely extent of element mobility during alteration.

The majority of major elements within different lithological groups show typical correlations with respect to TiO_2, with different volcanic units being reasonably tightly grouped (Fig. 3.4). The andesite lavas and dacitic tuffs, however, exhibit a wider spread of data (Fig. 3.4). Al_2O_3, Fe_2O_3, MgO show a typical positive correlation with TiO_2 across all lithological groups (Fig. 3.4b, c, d), implying TiO_2 generally decreases as rocks become more evolved. SiO_2 shows a negative correlation with TiO_2, with some vertical scatter within individual lithological groups, notably in the rhyolites lavas (Fig. 3.4a). This indicates SiO_2 may have been weakly mobile during metamorphism. Zr shows a negative correlation with TiO_2 with relatively tight clustering of individual lithological groups (Fig. 3.4f). K_2O and Na_2O display a very weak negative correlation with TiO_2, exhibiting a large scatter across the data set as a whole and to variable degrees within individual lithological groups, indicating these elements were probably mobile during subsolidus alteration (Fig. 3.4g, h). This is most apparent within the dacitic lavas, with K_2O and Na_2O contents ranging from ~0.5 wt. % to ~5.5 wt. % and <0.2 wt. % to >6 wt. % respectively, forming a broad vertical array with little variation in TiO_2 content (Fig. 3.4g, h).

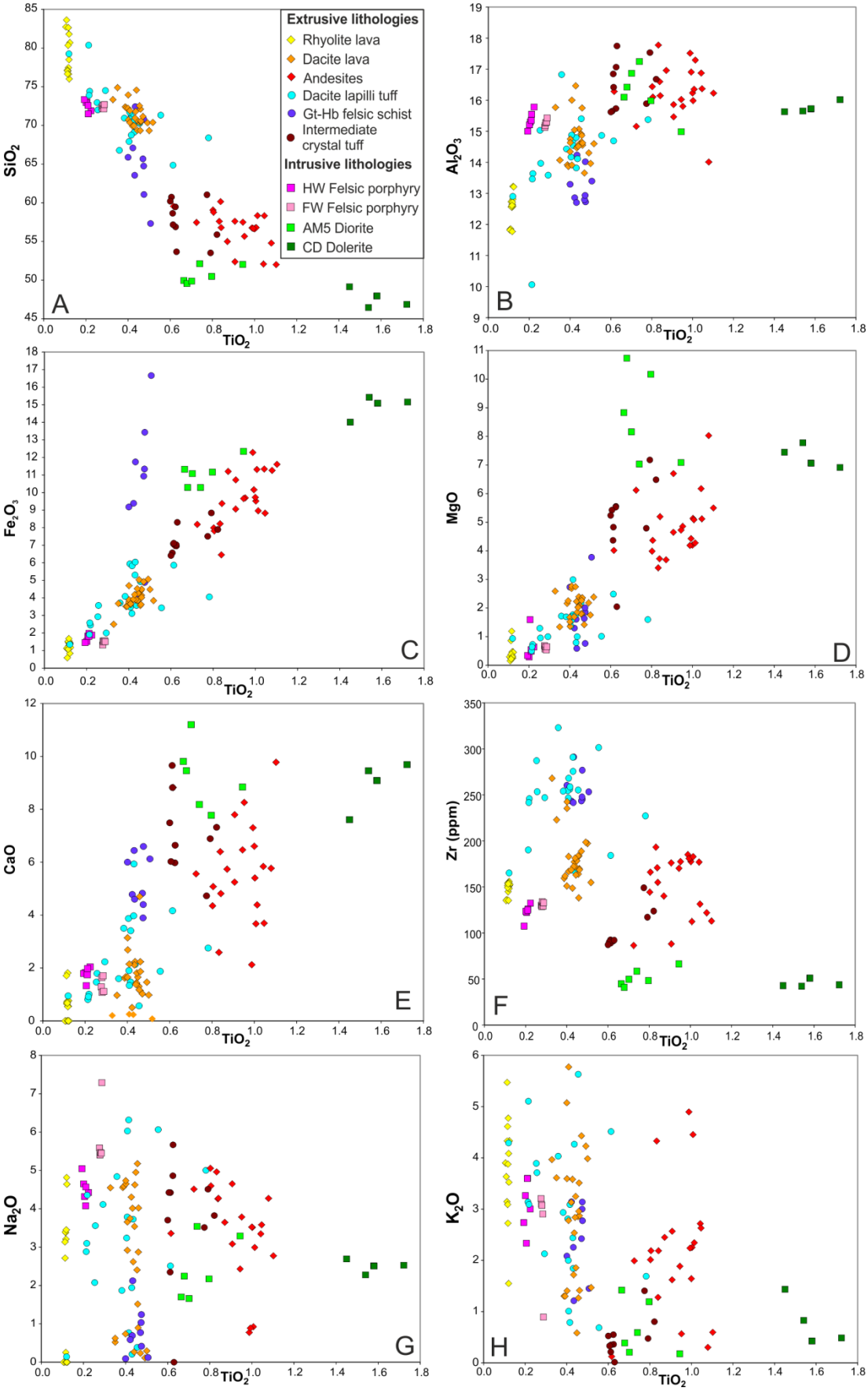
Extrusive lithologies
Rhyolite lava
Dacite lava
Andesites
Dacite lapilli tuff
Gt-Hb felsic schist
Intermediate crystal tuff
Intrusive lithologies
HW Felsic porphyry
FW Felsic porphyry
AM5 Diorite
CD Dolerite
A
B
C
D
E
F
G
H
SiO2
Al2O3
Fe2O3
MgO
CaO
Zr (ppm)
Na2O
K2O
TiO2

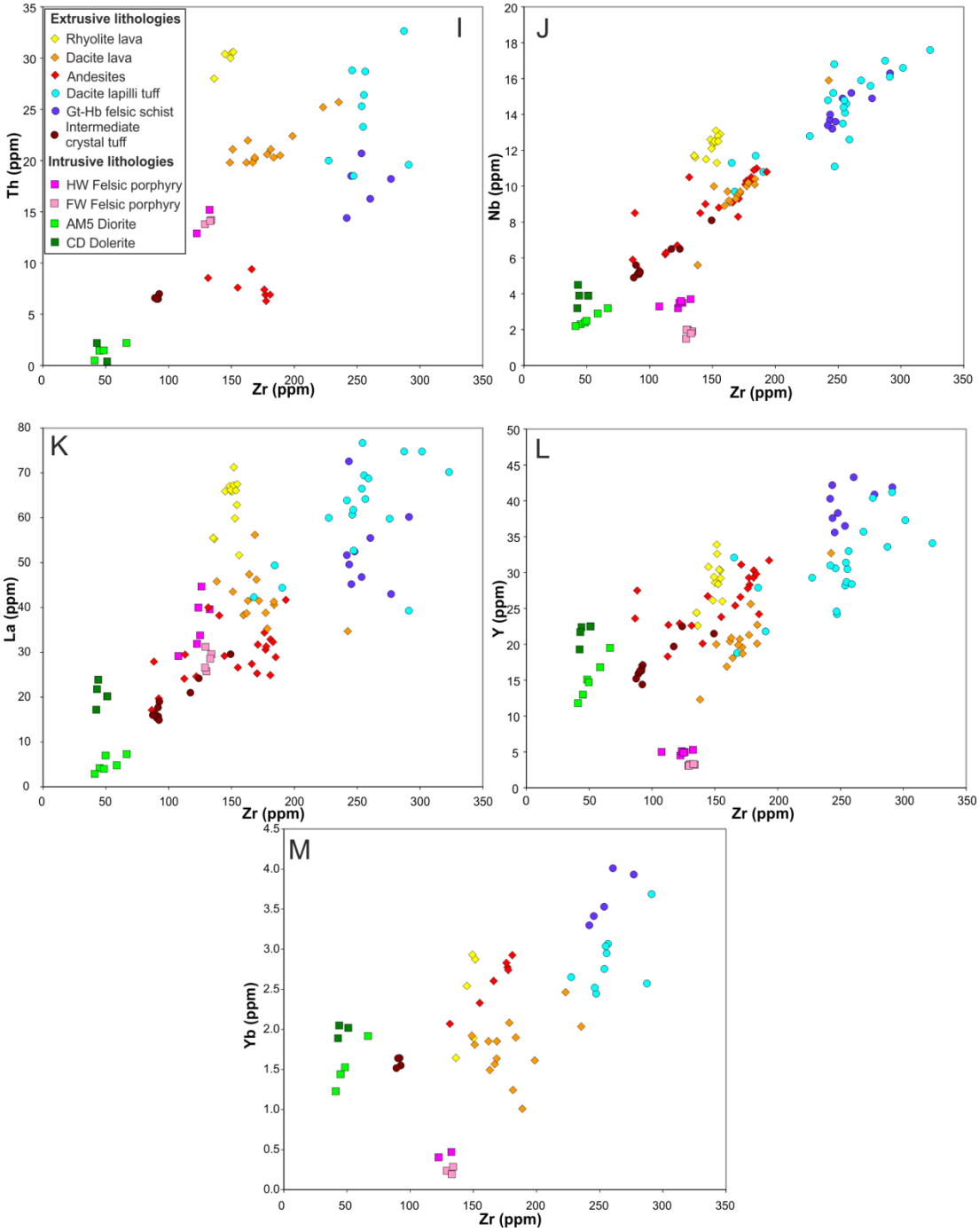

Figure 3.4. (A-H; Previous page). Variation plots against TiO_2 of major elements for different lithological units within the stratigraphy. Individual analyses have been recalculated to 100% on a volatile-free basis. (I-M) Incompatible element plots against Zr to highlight trace element immobility.

When characterising the Cosmos succession, emphasis is consequently placed on those elements regarded as being least mobile during weathering, hydrothermal alteration and regional metamorphism, including Th, high field strength elements

(HFSEs) and REEs. The REE content of alteration fluids has been shown to be extremely low (e.g., Bau 1991), so that the modification of whole-rock REE patterns during diagenetic, hydrothermal or metamorphic fluid rock interaction is minimal. The exception is when infiltration metasomatism is severe, very large fluid-rock ratios exist, or an extensive hydrothermal system is present (e.g., Ludden et al., 1982; Michard and Albarede, 1986; Whitford et al., 1988; Bau, 1991). Selected HFSEs, utilised in subsequent discrimination diagrams, form strong positive correlations with respect to Zr content (Fig. 3.4i-m). Individual lithological units are reasonably tightly grouped with only minor scatter (Fig. 3.4i-m). Some scatter would be expected, even in unaltered successions, reflecting primary spatiotemporal compositional variability within individual volcanic lithologies. REE and incompatible element composition within the Cosmos volcanic succession are therefore considered to represent primary volcanic abundances that are unlikely to be significantly affected by metasomatism.

The Total Alkali Silica (TAS) plot (Le Bas et al., 1986; Le Bas et al., 1992 etc.) was not used to classify the Cosmos volcanic succession as alkalis have been shown to be mobile (Fig. 3.4g, h). Consequently the Zr/TiO_2 vs. Nb/Y plot of Winchester and Floyd (1977) is used to discriminate between volcanic rock types (Fig. 3.5), as the latter elements are considered to be immobile during secondary alteration processes (Winchester and Floyd, 1977; Floyd and Winchester, 1978). Zr/TiO_2 can be used as an approximate measure of the degree of magmatic differentiation. Negative Ti anomalies become increasingly pronounced during continuing fractional crystallisation, whereas Zr is incompatible up until very high degrees of fractional crystallisation. Nb/Y has been shown to reflect the alkalinity of a magma series (Winchester and Floyd, 1977).

As K_2O is demonstrably mobile within the Cosmos volcanic succession (Fig. 3.4g), the K_2O-SiO_2 subalkaline discriminatory plot (Peccerillo and Taylor, 1976; Rickwood, 1989) cannot be used. Consequently, the Th/Yb vs. Nb/Yb discrimination diagram of Pearce (2008), and also the Sr/Y vs. Y (Defant and Drummond 1990; Drummond and Defant 1990) and $(La/Yb)_N$ vs. Yb diagrams (Martin 1986; 1999) have been used.

3.7 Results

Table 3.2 shows representative geochemical compositions of the main lithological groups within the Cosmos succession. Detailed geochemical data can be found in Appendix 2.

3.7.1 Rhyolite lava

Rhyolite samples are tightly grouped in the rhyolite field on Figure 3.5. Several of the most altered samples appear to have lost most of their Na_2O (Fig. 3.4g). Alteration also significantly affects K_2O content (Fig. 3.4h), which is likely to have been offset by a proportional increase in the concentration of the other major elements. Rhyolites are enriched in LREEs with pronounced negative Eu anomalies and have flat to slightly concave upwards HREE patterns (Fig. 3.6a). N-MORB-normalised trace element plots show elevated LILEs (Rb, Ba, Th, U, K) relative to HFSEs (Nb, Hf, Zr, Ti, Y). The rhyolite exhibits strong pronounced negative anomalies for Nb, Sr, P and Ti and a strong positive Pb anomaly (Fig. 3.6b).

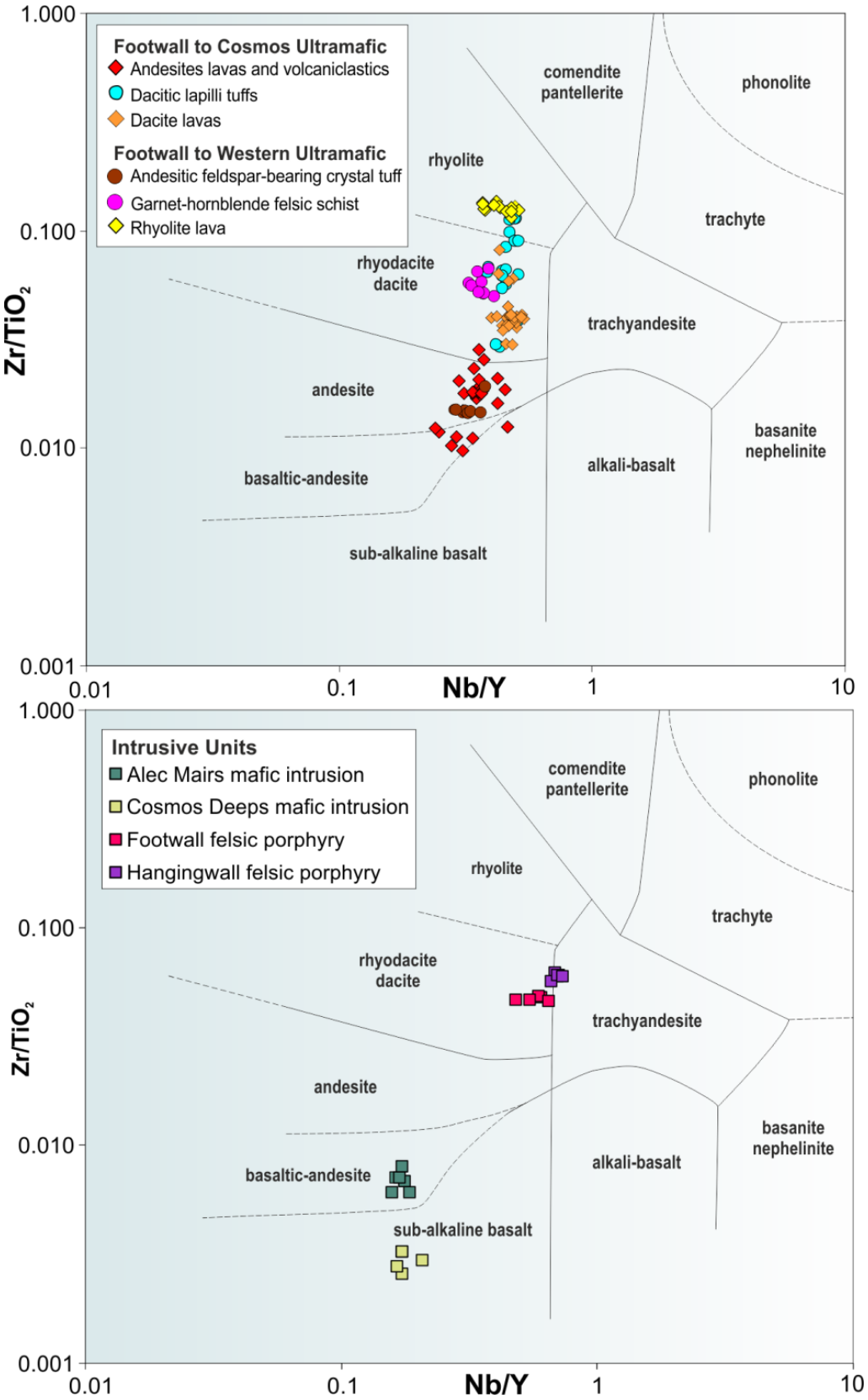

Figure 3.5. Compositional diagrams (after Winchester and Floyd, 1977) showing the composition of the main lithological groups.

Table 3.2 Representative samples from the main lithological groups within the Cosmos succession. Major element concentrations in wt. %, trace elements in ppm, n.d denotes below detection limit; – denotes not analysed. Trace elements reported to 1 decimal place were analysed by XRF, elements reported to 2 decimal places were analysed by ICP-MS. Gt-Hb = garnet-hornblende.

Lithology	**Rhyolite lava**	**Felsic Gt-Hb Schist**	**Intermediate crystal tuff**	**Dacite lava**	**Strongly sericitised Dacite lava**	**Dacitic lapilli tuff**	**Andesite Lava**	**Hangingwall felsic intrusion**	**Footwall felsic intrusion**	**Cosmos Deeps mafic intrusion**	**AM5 mafic intrusion**
Sample name	**C09-03**	**C10-95**	**C09-61**	**C10-109**	**C09-17**	**C10-126**	**C09-48**	**CO9-23**	**C10-155**	**C10-148**	**C10-122**
SiO_2	75.43	64.20	55.40	69.47	73.52	67.35	57.11	72.13	71.42	47.47	49.03
Al_2O_3	12.29	12.95	16.62	14.39	14.83	15.14	15.72	15.12	15.03	15.56	15.80
Fe_2O_3	1.25	8.94	6.78	4.42	4.46	4.00	8.98	1.81	1.48	14.93	11.12
MnO	0.02	0.25	0.11	0.08	0.04	0.07	0.14	0.03	0.02	0.18	0.14
MgO	0.24	2.66	5.41	2.32	1.67	1.58	4.61	1.58	0.63	7.00	8.67
CaO	0.72	5.85	6.47	1.84	0.50	2.72	5.20	1.32	1.07	9.00	9.63
Na_2O	3.31	0.09	5.52	3.96	0.23	4.93	4.61	4.27	5.38	2.49	1.67
K_2O	4.52	2.03	0.35	1.39	2.80	1.66	1.61	2.31	3.02	0.42	1.40
TiO_2	0.11	0.39	0.61	0.45	0.43	0.77	0.90	0.20	0.28	1.56	0.65
P_2O_5	0.01	0.07	0.12	0.10	0.11	0.25	0.26	0.06	0.07	0.37	0.04
LOI	2.06	2.26	1.86	1.42	1.66	1.23	0.63	1.36	0.65	0.47	1.60
Total Majors	**99.96**	**99.70**	**99.24**	**99.85**	**100.25**	**99.69**	**99.76**	**100.18**	**99.06**	**99.46**	**99.75**
Zn	8.0	181.9	88.6	32.8	59.5	40.3	73.5	16.9	47.4	115.2	102.1
Cu	5.3	11.2	24.1	11.4	3.6	22.2	27.4	6.0	9.1	74.3	95.5
Ni	n.d	7.5	100.5	16.6	14.4	24.4	59.3	4.4	0.1	135.9	166.4
V	15.3	n.d	144.9	51.4	65.5	51.2	148.1	32.7	20.0	265.0	218.8
Ba	886.7	205.9	56.4	712.4	464.5	416.8	498.6	820.0	863.7	232.4	239.0
Sc	3.1	15.5	27.9	9.7	16.7	13.5	23.0	n.d	2.5	33.4	36.1
Nb	11.5	15.2	5.1	9.3	10.3	12.8	10.1	3.2	1.9	3.9	2.3
Zr	144.9	260.4	91.6	168.6	181.3	227.3	176.2	122.5	133.9	51.0	44.9
Y	30.8	43.3	16.6	19.9	21.6	29.3	27.8	4.5	3.2	22.5	13.0
Sr	63.1	55.5	140.4	107.8	15.6	145.9	198.3	348.2	351.1	341.3	71.1
Rb	114.6	84.7	19.0	47.4	72.5	65.5	54.3	68.8	99.4	25.7	40.7
Hf	-	6.3	-	4.8	-	6.3	-	-	3.3	1.3	1.5
U	8.4	4.9	1.5	5.5	5.5	5.2	1.9	2.8	4.7	0.9	0.4
Th	30.4	16.3	6.5	20.1	21.1	20.0	7.4	12.9	14.2	0.4	1.5
Pb	16.0	30.6	11.2	18.3	25.4	15.3	10.9	23.0	37.2	4.8	8.1
La	58.92	50.88	17.22	38.76	41.93	54.74	31.80	30.52	25.86	22.49	5.47
Ce	101.65	95.78	34.01	66.46	69.63	102.14	60.61	54.32	47.28	48.11	11.63
Pr	9.93	10.81	3.82	6.67	6.85	11.00	6.86	5.46	4.82	5.84	1.47
Nd	31.20	38.66	13.94	22.13	21.78	38.79	25.44	16.85	16.34	23.44	6.27
Sm	5.18	7.31	2.97	3.76	3.69	6.58	5.34	2.38	2.57	4.51	1.58
Eu	0.80	1.65	0.67	0.99	0.92	1.61	1.55	0.64	0.75	1.58	0.70
Gd	5.00	7.18	2.87	3.65	3.59	6.04	5.30	1.86	1.83	4.37	1.78
Tb	0.68	1.08	0.46	0.51	0.46	0.86	0.83	0.19	0.19	0.66	0.32
Dy	3.76	6.51	2.78	3.01	2.31	4.87	4.91	0.86	0.77	3.87	2.15
Ho	0.80	1.34	0.58	0.60	0.44	0.96	1.04	0.14	0.12	0.77	0.46
Er	2.31	4.00	1.63	1.78	1.17	2.78	2.91	0.42	0.28	2.17	1.41
Tm	0.36	0.64	0.25	0.29	0.17	0.43	0.45	0.05	0.04	0.33	0.23
Yb	2.54	4.01	1.64	1.85	1.24	2.65	2.83	0.40	0.29	2.02	1.44
Lu	0.37	0.63	0.24	0.29	0.19	0.40	0.42	0.05	0.04	0.30	0.22
Total Majors +Traces	**100.12**	**99.82**	**99.35**	**99.98**	**100.37**	**99.83**	**99.92**	**100.34**	**99.23**	**99.62**	**99.88**

3.7.2 Dacite lavas and lapilli tuffs

Dacite lavas and lapilli tuffs compose a significant amount of the footwall succession to the mineralised Cosmos Ultramafic Sequence (Fig. 3.2, 3.3). Their similar mineralogy, intercalation with andesite lavas (Fig. 3.3), and overlapping U-Pb ages (Table 3.1; Fig. 3.2) suggest they are genetically related and represent the explosive and effusive components of the same magma source (de Joux et al., 2013; Chapter 4). Geochemically they are very similar (Fig. 3.6c-f); however while dacitic lavas are tightly grouped on Figure 3.5, the dacitic tuffs show a wider scatter. This is not surprising given that the dacitic lapilli tuffs comprise volcanic fragments that have been subsequently metamorphosed. Both the dacitic lapilli tuffs and the lavas have experienced silica enrichment during alteration and show a corresponding reduction in Na_2O and K_2O (Fig. 3.4a, g, h). Both show enriched LREEs patterns and exhibit flat HREE patterns (Fig. 3.6c, e). Moderate negative Eu anomalies are present in both lavas tuffs but are less pronounced than those exhibited by rhyolites (Fig. 3.6c, e). N-MORB-normalised trace element plots for both lavas and tuffs are very similar (Fig. 3.6.d, f), each showing elevated LILEs relative to HFSEs with pronounced negative anomalies exhibited for Nb, Sr, P and Ti, and a strong positive anomaly exhibited for Pb. These anomalies are less pronounced than those within the rhyolite samples.

Figure 3.6. (Next page) REE and multi-element plots for each of the six main extrusive footwall lithologies as well as the mafic and felsic intrusions. REE plots are normalised to the chondrite values of Boynton (1984). Multi-element plots are normalised to the N-MORB values of Sun and McDonough (1989). The darkest shaded region shows the Black Flag rhyolites, with the medium and lightest shaded regions showing respectively the dacite and andesite volcanic rocks of the Black Flag Group (data from Morris and Witt, 1997). The shaded region on Figure 3.6O is the field of the Black Flag dacites also.

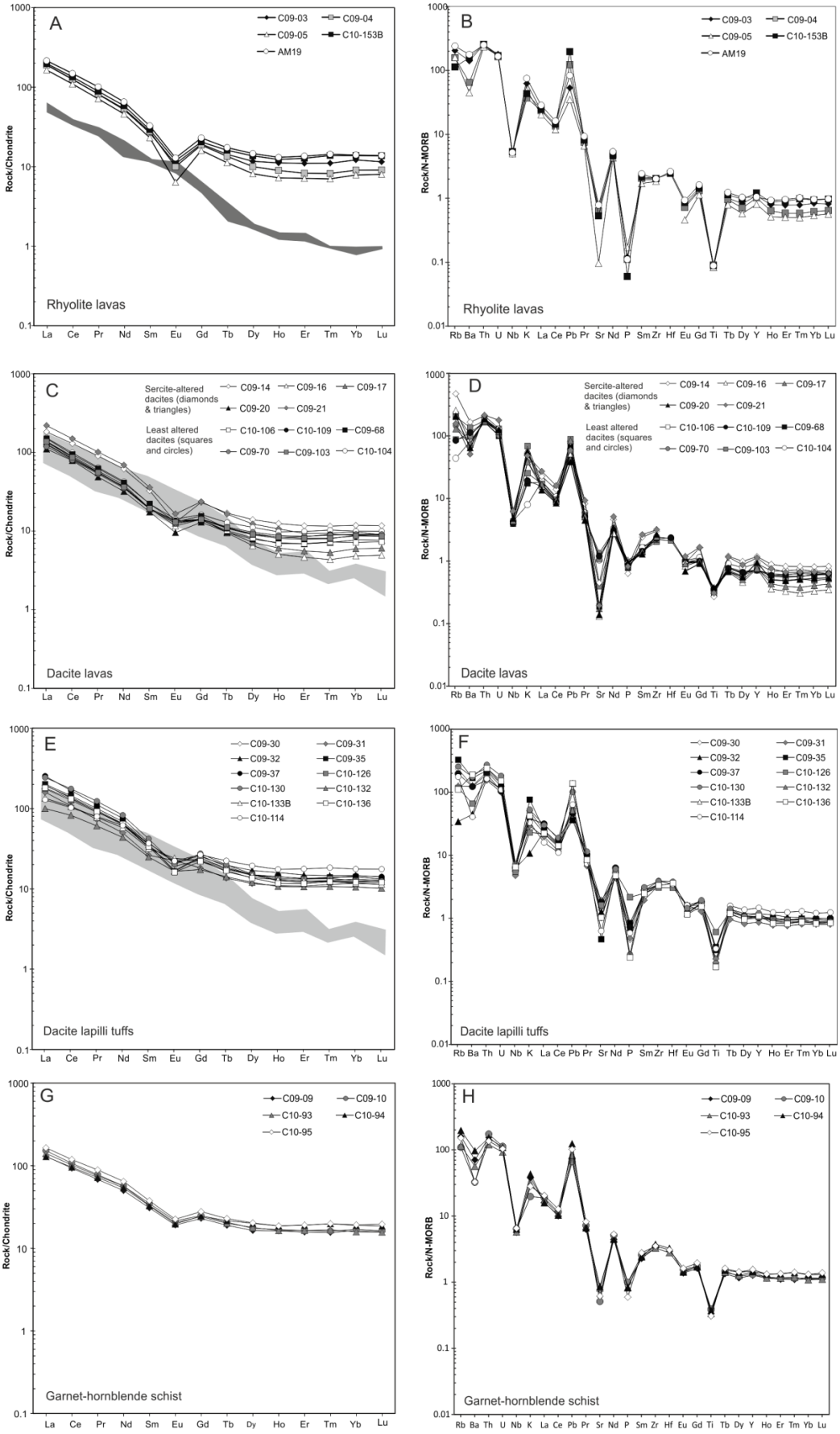
A
C09-03
C09-04
C09-05
C10-153B
AM19
Rock/Chondrite
Rhyolite lavas
La Ce Pr Nd Sm Eu Gd Tb Dy Ho Er Tm Yb Lu
B
C09-03
C09-04
C09-05
C10-153B
AM19
Rock/N-MORB
Rhyolite lavas
Rb Ba Th U Nb K La Ce Pb Pr Sr Nd P Sm Zr Hf Eu Gd Ti Tb Dy Y Ho Er Tm Yb Lu
C
Sercite-altered dacites (diamonds & triangles)
C09-14
C09-16
C09-17
C09-20
C09-21
Least altered dacites (squares and circles)
C10-106
C10-109
C09-68
C09-70
C09-103
C10-104
Rock/Chondrite
Dacite lavas
La Ce Pr Nd Sm Eu Gd Tb Dy Ho Er Tm Yb Lu
D
Sercite-altered dacites (diamonds & triangles)
C09-14
C09-16
C09-17
C09-20
C09-21
Least altered dacites (squares and circles)
C10-106
C10-109
C09-68
C09-70
C09-103
C10-104
Rock/N-MORB
Dacite lavas
Rb Ba Th U Nb K La Ce Pb Pr Sr Nd P Sm Zr Hf Eu Gd Ti Tb Dy Y Ho Er Tm Yb Lu
E
C09-30
C09-31
C09-32
C09-35
C09-37
C10-126
C10-130
C10-132
C10-133B
C10-136
C10-114
Rock/Chondrite
Dacite lapilli tuffs
La Ce Pr Nd Sm Eu Gd Tb Dy Ho Er Tm Yb Lu
F
C09-30
C09-31
C09-32
C09-35
C09-37
C10-126
C10-130
C10-132
C10-133B
C10-136
C10-114
Rock/N-MORB
Dacite lapilli tuffs
Rb Ba Th U Nb K La Ce Pb Pr Sr Nd P Sm Zr Hf Eu Gd Ti Tb Dy Y Ho Er Tm Yb Lu
G
C09-09
C09-10
C10-93
C10-94
C10-95
Rock/Chondrite
Garnet-hornblende schist
La Ce Pr Nd Sm Eu Gd Tb Dy Ho Er Tm Yb Lu
H
C09-09
C09-10
C10-93
C10-94
C10-95
Rock/N-MORB
Garnet-hornblende schist
Rb Ba Th U Nb K La Ce Pb Pr Sr Nd P Sm Zr Hf Eu Gd Ti Tb Dy Y Ho Er Tm Yb Lu

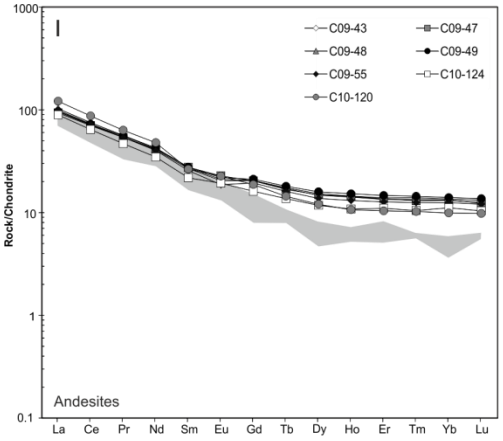
I
C09-43
C09-47
C09-48
C09-49
C09-55
C10-124
C10-120
Rock/Chondrite
Andesites
La Ce Pr Nd Sm Eu Gd Tb Dy Ho Er Tm Yb Lu

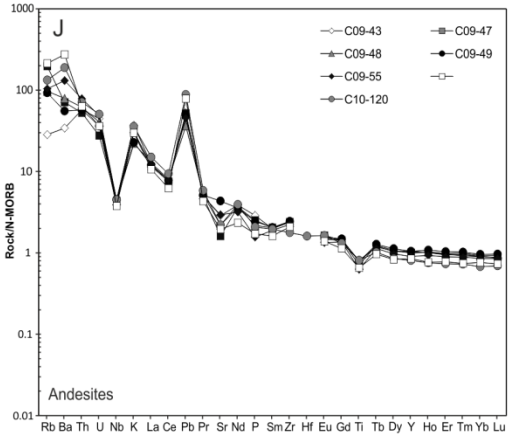
J
C09-43
C09-47
C09-48
C09-49
C09-55
C10-120
Rock/N-MORB
Andesites
Rb Ba Th U Nb K La Ce Pb Pr Sr Nd P Sm Zr Hf Eu Gd Ti Tb Dy Y Ho Er Tm Yb Lu

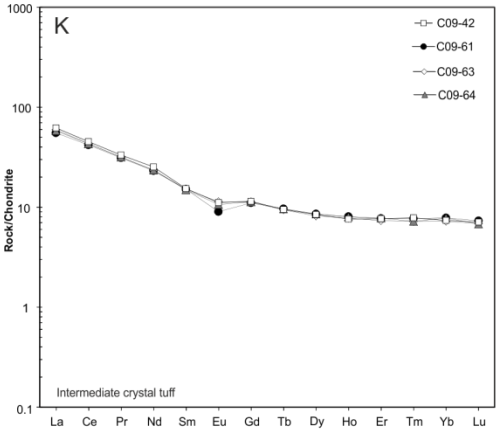
K
C09-42
C09-61
C09-63
C09-64
Rock/Chondrite
Intermediate crystal tuff
La Ce Pr Nd Sm Eu Gd Tb Dy Ho Er Tm Yb Lu

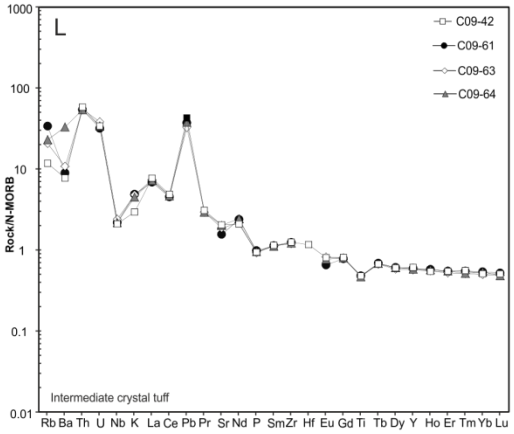
L
C09-42
C09-61
C09-63
C09-64
Rock/N-MORB
Intermediate crystal tuff
Rb Ba Th U Nb K La Ce Pb Pr Sr Nd P Sm Zr Hf Eu Gd Ti Tb Dy Y Ho Er Tm Yb Lu

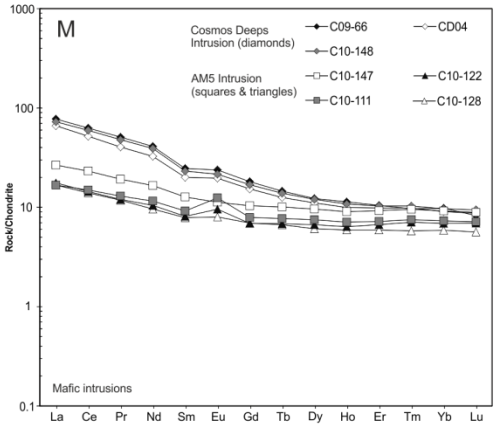
M
Cosmos Deeps Intrusion (diamonds)
C09-66
CD04
C10-148
AM5 Intrusion (squares & triangles)
C10-147
C10-122
C10-111
C10-128
Rock/Chondrite
Mafic intrusions
La Ce Pr Nd Sm Eu Gd Tb Dy Ho Er Tm Yb Lu

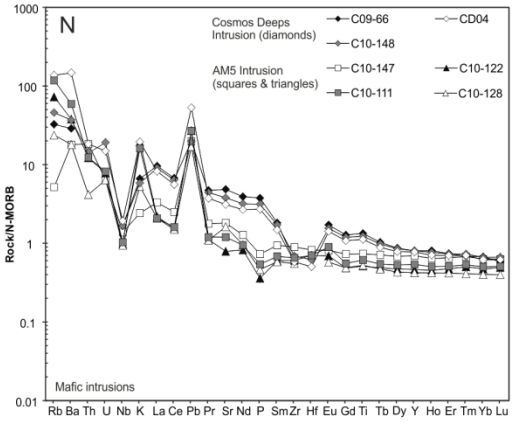
N
Cosmos Deeps Intrusion (diamonds)
C09-66
CD04
C10-148
AM5 Intrusion (squares & triangles)
C10-147
C10-122
C10-111
C10-128
Rock/N-MORB
Mafic intrusions
Rb Ba Th U Nb K La Ce Pb Pr Sr Nd P Sm Zr Hf Eu Gd Ti Tb Dy Y Ho Er Tm Yb Lu

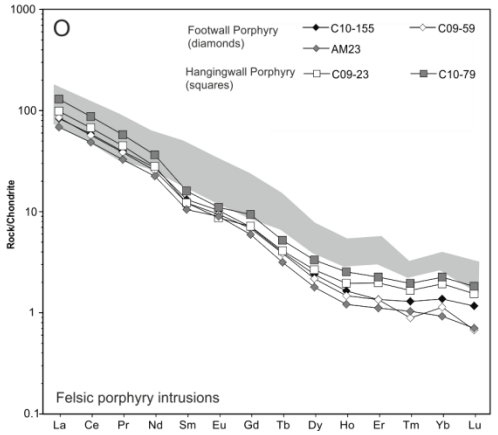
O
Footwall Porphyry (diamonds)
C10-155
C09-59
AM23
Hangingwall Porphyry (squares)
C09-23
C10-79
Rock/Chondrite
Felsic porphyry intrusions
La Ce Pr Nd Sm Eu Gd Tb Dy Ho Er Tm Yb Lu

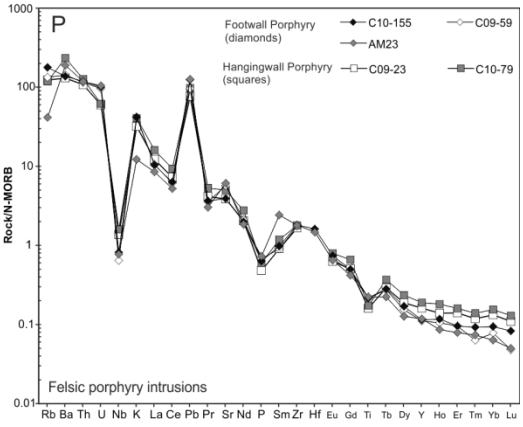
P
Footwall Porphyry (diamonds)
C10-155
C09-59
AM23
Hangingwall Porphyry (squares)
C09-23
C10-79
Rock/N-MORB
Felsic porphyry intrusions
Rb Ba Th U Nb K La Ce Pb Pr Sr Nd P Sm Zr Hf Eu Gd Ti Tb Dy Y Ho Er Tm Yb Lu

3.7.3 Garnet-hornblende felsic schist

Poor primary textural preservation within this unit renders protolith assignment difficult (Section 2.11). The primary mineralogy has been almost entirely overprinted by abundant garnet porphyroblasts in a strongly banded hornblende-plagioclase matrix (Table 3.1). Garnet abundance, size and occurrence is highly variable throughout the unit, as is the proportion of mafic and felsic domains. This heterogeneity is mirrored in the geochemistry with SiO_2 between 56 - 71 wt. %, giving it a broadly andesitic/dacitic composition. However the data points are tightly grouped in the rhyodacite-dacite field of Figure 3.5, suggesting that this variability in silica is largely controlled by metamorphic recrystallisation. The schist exhibits enriched LREEs, flat HREEs patterns and a weak negative Eu anomaly (Fig. 3.6g). Multi-element plots for this unit are markedly similar to those of the dacitic lavas and lapilli tuffs, with enrichment in LILEs and strong negative anomalies for Nb, Sr, P, and Ti, and a strong positive Pb anomaly(Fig. 3.6h). This suggests a volcaniclastic dacite as the most likely protolith.

3.7.4 Andesites and associated volcaniclastic units

Despite their relatively constant Nb/Y ration, intermediate lavas and associated volcaniclastic rocks range from basaltic andesites to andesites and span the entirety of the basaltic andesite and andesite fields. In comparison to the felsic volcanic rocks, these andesite lavas show less LREE enrichment with much flatter trends towards the HREEs and no perceptible Eu anomaly (Fig. 3.6i). Multi-element plots also show less enrichment in LILEs and lack the distinct anomalies seen within the dacitic and rhyolitic units, although small negative Ti and P anomalies are still present (Fig. 3.6j). However, negative Nb and positive Pb anomalies are distinct.

3.7.5 Intermediate crystal tuff

This unit is andesitic in composition with all data points showing a tight grouping on Figure 3.5; it is very geochemically similar to the overlying younger andesitic lavas. This unit shows the least LREE enrichment of all the Cosmos footwall volcanic rock units, exhibits a small negative Eu anomaly and has a flat HREE pattern (Fig. 3.6k). N-MORB-normalised plots are very similar to those of the andesites and show a strong positive Pb anomaly, although the negative Nb and Ti anomalies are less pronounced (Fig. 3.6l).

3.7.6 Mafic intrusions

Multiple mafic intrusions crosscut the Cosmos volcanic succession. The two largest of these are the Cosmos Deeps and AM5 mafic intrusions, which intrude largely parallel to the now subvertical stratigraphy (Fig. 3.2). The morphology and extent of the AM5 intrusion is poorly constrained due to drilling paucity. These two main intrusions are compositionally distinct, forming distinct clusters on Figure 3.5; the Cosmos Deeps intrusion as a dolerite and the AM5 intrusion as a more evolved diorite. The REE patterns are shallow, with flat HREE traces and slight positive Eu anomalies. The Cosmos Deeps dolerite is more enriched in LREEs than the AM5 diorite, but neither intrusion displays the level of enrichment seen within the majority of extrusive volcanic units (Fig. 3.6m). The intrusions show enrichment in Rb and Ba but respective depletion in Th and U compared to the extrusive volcanic units. Both intrusions exhibit a negative Nb anomaly and positive Pb anomaly (Fig. 3.6n). HFSEs patterns are generally flat patterns with the AM5 diorite displaying only a weak P anomaly. The Cosmos Deeps dolerite displays distinct negative Hf and Zr anomalies (Fig. 3.6n).

3.7.7 Felsic porphyry intrusions

The two felsic porphyry intrusions crosscutting the volcanic succession contrast in age and mineralogy, with the older hangingwall intrusion dated at ~2670 Ma while the younger footwall intrusion is dated at ~2653 Ma (Fig. 3.2; de Joux et al., 2013; Chapter 4). Thus, the footwall and hangingwall felsic porphyries are respectively ~71 Ma and ~54 Ma younger than the youngest age of 2724 Ma obtained for the dacitic footwall volcanic sequence (Fig.2; de Joux et al., 2013; Chapter 4). Despite their age difference the two intrusions are geochemically similar, with high Al_2O_3 (>~15 wt. %) (Fig. 3.4b), high Sr (~350 -550 ppm; Table 3.3; Appendix 2) and low Y concentrations (<5 ppm; Fig. 3.4l; Table 3.3; Appendix 2). They have a distinct geochemical affinity with REE concentrations that are strongly fractionated compared to those of the Cosmos extrusive volcanic lithologies. Both intrusions are enriched in LREEs but strongly depleted in HREEs, with HREE values for the older footwall intrusion approaching chondrite values between Ho – Lu (Fig. 3.6o). The two felsic intrusions are LILE-enriched and show large negative Nb and positive Pb anomalies (Fig. 3.6p). They also exhibit steeply dipping multi-element plots with HFSEs and HREEs strongly depleted with respect to N-MORB (Fig. 3.6o,p).

3.8 Discussion

3.8.1 Trends in trace and rare earth element geochemistry

All extrusive volcanic units exhibit LREE and LILE enrichment compared to HREEs and HFSEs. Multi-element plots show strong negative anomalies for Nb, Sr, P, Eu and Ti within the rhyolites, dacitic lavas and tuffs and the hornblende-garnet schist (Fig. 3.6). Low overall Ti, Sr, P and Eu abundances with respect to their adjacent elements and N-MORB are indicative of the formation of restite phases in the source

region or fractional crystallisation involving phases that are compatible, or a combination of these processes. Negative Eu anomalies are typical of continental rocks produced by intra-crustal partial melting where granitic melts are separated from residues containing feldspar, which is the major host of Eu^{2+}. The negative Sr anomaly is also controlled by residual plagioclase in the source region and/or by plagioclase crystallisation during fractional crystallisation. The negative Ti anomaly is likely related to crystallisation of a Ti-bearing oxide such as ilmenite. The amplitude of the Ti anomaly increases as the units become more evolved, reflecting the abundance of Ti-bearing phases progressively removing Ti from the melt during fractional crystallisation. The large negative P anomalies are controlled by residual apatite in the source region and/or during fractional crystallisation (e.g., Campbell McCuaig et al., 1994).

The intermediate volcanic units show less LILE enrichment (Fig. 3.6). They also lack the distinct negative anomalies seen within the dacitic and rhyolitic lithologies, which are related to fractional crystallisation and/or residual phases in the source region. Both the andesite lavas and intermediate crystal tuff show small negative Ti anomalies indicative of minor Ti-retention in restite phases in the source region and/or crystallisation of a Ti-bearing phase. They also lack a significant Eu anomaly.

On Figure 3.5 the Cosmos dolerite and AM5 diorite form two distinct clusters, also plotting away from the andesite lavas. The AM5 diorite lacks the appreciable LREE enrichment seen in the andesite lavas and thus is unlikely to be a sub-volcanic expression of the andesite volcanism. The Cosmos Deeps dolerite is the only unit to display a distinct negative Hf and Zr anomaly. These intrusions' contrasting trace element contents indicate they are not genetically related.

The two felsic intrusions also have incompatible element concentrations distinct to those of the Cosmos extrusive volcanic succession (Fig. 3.4j, l, m) and have depleted HREE concentrations. These characteristics, along with high SiO_2, Al_2O_5 > 15wt. %, average Sr > 420ppm, Y < 5ppm and no perceptible Eu anomaly, indicate they have a strong tonalite–trondhjemite–granodiorite (TTG) affinity (Table 3.3).

REEs in TTGs are strongly fractionated; the average $(La/Yb)_{cn}$ of the footwall and hangingwall intrusion is ~70 and ~54 respectively compared with the TTG average $(La/Yb)_{cn}$ of ~ 38 (Martin, 1994).

Negative Nb and positive Pb anomalies are distinct across all extrusive and intrusive lithological groups. These anomalies are characteristic of the involvement of continental crust and, along with the enrichment in LILEs relative to HFSEs, reflect assimilation-fractional crystallisation (AFC) processes and/or subduction processes in the generation of parental melts.

3.8.2 Crustal signature displayed by the Cosmos volcanic sequence

The Cosmos volcanic footwall sequence displays a strong crustal signature as indicated by the overall enrichment in in LILEs and LREEs as well as strong positive Pb anomalies and strong negative Nb anomalies. The extrusive volcanic succession's trace and REE geochemistry indicates that parental melts were most likely generated in a subduction zone. Crustal material from subducted sediments and oceanic crust are transferred by either dehydration or melting to the overlying mantle wedge (Pearce and Peate, 1995; Johnson and Plank, 1999). LILEs and LREEs are preferentially partitioned into hydrous fluids during dehydration of the subducting slab, thereby enriching partial melts of peridotite formed in the overlying mantle wedge. HFSEs are conservative during slab dehydration and thus are not enriched relative to N-MORB source regions in the mantle wedge. Addition of crustal material from melting of subducted sediment may also enrich the mantle wedge. The absence of depleted HREEs signatures in any unit but the two felsic intrusions rules out contribution from melting of the subducting oceanic crust itself, where amphibolite or eclogite would be the stable form of subducted oceanic crust at the likely depths of melt generation. The Nb depletion exhibited by all lithologies within the succession is likely related to Nb retention in the dehydrating slab (likely within residual rutile), which could be further

enhanced by assimilation of Nb-depleted crustal rocks during magma ascent through the crust.

Generation of the Cosmos volcanic sequence via assimilation of a crustal component and/or crustal anatexis, rather than by partial melting of peridotite contaminated by subducted crustal material, could in theory produce the geochemical characteristics of the volcanic sequence. However, this would require an extremely enriched crustal component, more enriched in LILEs and LREEs than estimates either modern or Archaean continental crust (e.g., Rudnick and Fountain, 1995; Taylor and McLennan, 1985) or of average TTG (e.g. Drummond et al., 1996; Smithies, 2000). Contamination by average TTG crust would result in strongly fractionated REE concentrations, which is not exhibited by the extrusive volcanic sequence. The presence of xenocrystic zircons within the dacitic volcanic rocks indicates that assimilation of pre-existing crustal components, which are dated at ~2750 Ma, contributed to the Cosmos volcanic succession (de Joux et al., 2013; Chapter 4). However as only two xenocrystic zircons were found in 52 concordant analyses from numerous felsic volcanic lithologies within the succession, the contribution of assimilated crustal material is likely to have been relatively minor (de Joux et al., 2013). It is not possible to further quantify the contribution of crustal assimilation during magma ascent within the volcanic succession further without the use of isotope ratios such as Nd. Additionally no older, suitably enriched potential crustal contaminant has been described within the local region. It is therefore considered that the geochemical characteristics of the Cosmos extrusive volcanic succession are largely derived from convergent margin processes.

The similarities in multi-element plots and REE patterns between the felsic volcanic lithologies are striking (Fig. 3.6a-f). This suggests they share a similar petrological evolution and/or source region. The intermediate units, while having similar LILE concentrations to the felsic units, show markedly different HFSE patterns lacking the strong Sr, Eu and P negative anomalies seen within the felsic volcanic units. Whether these trace element distinctions can be explained by fractional crystallisation alone or whether different source regions and/or contrasting AFC paths

are required to account for the compositional distinction between the intermediate and felsic volcanic units as a whole is discussed in Section 3.8.6.

The two felsic intrusions have a distinct TTG affinity exhibiting a trace element and REE geochemistry indicative of partial melting of a plagioclase-poor source at pressures high enough to leave residual garnet ± amphibole (Drummond and Defant, 1990). HREEs would be strongly partitioned into residual garnet, which would be left as a restite mineral in the source region following efficient melt segregation and ascent of the HREE-depleted melt. This requires partial melting of a thickened crust or of a subducting slab (e.g., Drummond and Defant 1990). The footwall felsic intrusion contains two xenocrystic zircons dated at ~2720Ma and ~2830Ma, indicating some crustal assimilation occurred during genesis of the parental melt. Assimilation and/or crustal anatexis of an earlier TTG-affinity crustal component could have played a part in the genesis of the felsic porphyry intrusions, although a greater abundance of xenocrystic zircons might be expected if this process played a large role in melt generation. Given the strong TTG affinity of the felsic intrusions, the melt generation processes and possible tectonic regime during intrusion of the felsic porphyries emplaced after 2670Ma was likely to be markedly different than those that generated the felsic and intermediate volcanic sequence emplaced between 2736 and 2724 Ma (de Joux et al., 2013; Chapter 4). This will be explored further in Section 3.8.3.

3.8.3 TTD and TTG affinity in the Eastern Goldfields Superterrane

Adakites were recognised by Defant and Drummond (1990) as a unique type of modern arc lava. Although controversial (e.g., Macpherson et al., 2006), present-day adakites are considered by many to be generated via melting of young (<25 Myrs) subducting crust (e.g., Drummond et al., 1996; Martin et al., 2005). They show significant similarities to some Archaean TTG granitoids and therefore they may be regarded as possible modern equivalents (Martin et al., 2005). However, Moyen and Martin (2012) have recently suggested that Archaean TTGs show a wider compositional variation than modern adakites and that Archaean TTGs may be

generated by both slab melting and crustal anatexis. Tonalite-trondhjemite-dacite (TTD) volcanic packages are the extrusive equivalent of the Archaean TTG intrusions that comprise much of the EGS. TTD volcanic packages are volumetrically less significant than TTG batholiths but it is the common association of TTD volcanic packages with mineralised komatiites that makes the understanding of TTD formation, emplacement mechanisms and possible tectonic setting important (e.g., Fiorentini et al., 2012). The typical features of modern adakite volcanic rocks, characteristics that also distinguish Archaean TTD/TTG units, are shown in Table 3.3. It should be noted that every aspect of the description as shown in Table 3.3 is an integral part of the distinction and that no rock should be called an adakite or TTD/TTG if it doesn't match the whole description (Moyen and Martin, 2012).

The majority of currently published data on the Kalgoorlie Terrane indicates the terrane was dominated by TTD volcanism. Within the AWB dacitic volcanic rocks are proposed to have a strong TTD affinity (Fiorentini et al., 2012). Three episodes of TTD-affinity volcanism, spanning ~2710 to ~2665 Ma, are recognised within the Kalgoorlie Terrane (Kositcin et al., 2008). The first episode (2707 – 2692 Ma) comprised felsic volcanism associated with komatiites at Black Swan. The second (2687 – 2676 Ma) and third (2669 – 2665 Ma) episodes comprised felsic volcanism, with associated volcaniclastic and epiclastic sedimentation, in the lower Kalgoorlie Sequence, including the Black Flag Group, and upper Kalgoorlie Sequence respectively.

Table 3.3 Comparison of the geochemical attributes of typical TTD-affinity volcanic rocks with the average compositions of the Cosmos dacitic volcanic lavas, dacitic lapilli tuffs, felsic porphyry intrusions and the TTD-affinity Black Flag dacites (data from Morris and Witt, 1997).

	Typical TTD affinity rocks	**Average Cosmos dacite lavas**	**Average Cosmos dacite lapilli tuffs**	**Average Cosmos Hangingwall felsic intrusion**	**Average Cosmos Footwall felsic intrusion**	**Average Black Flag Dacite**
Al_2O_3	**≥ 15 wt. %**	14.34	14.22	15.87	14.98	16.00
Sr(ppm)	**300 - >2000**	88	102	463	434	635
Y(ppm)	**<18**	21	31	4.9	3.2	6.0
LREE	**Enriched**	Yes	Yes	Yes	Yes	Yes
HREE	**Depleted**	No	No	Yes	Yes	Yes
EU Anomaly	**None or positive**	Negative	Negative	None	None	None
K_2O/Na_2O	**Commonly <1**	Highly variable due to mobility of alkaline phases	Highly variable due to mobility of alkaline phases	0.58	0.45	0.55

The rhyolitic and dacitic volcanic rocks at Cosmos are distinct in being significantly older (respectively >2736 Ma and 2730-2724 Ma; Table 3.1) than the majority of felsic rocks within the Kalgoorlie Terrane (Fig. 3.1). They are geochemically distinct, particularly in comparison to the Black Flag Group, which has a strong TTD-affinity geochemical signature (Morris and Witt, 1997; Krapež and Hand, 2008). The Black Flag Group has been used for comparison with the Cosmos volcanic sequence as there is comprehensive published geochemistry on the Black Flag succession. This group exhibits a similar compositional suite of basaltic lavas through to rhyolitic lavas and volcaniclastic rocks, which are largely considered to be unrelated via fractional crystallisation (Morris and Witt, 1997). The Black Flag Group is considered to have formed via partial melting of amphibolite whose likely source is subducted ocean crust (Morris and Witt, 1997). Consequently, the felsic lavas of the Black Flag Group are depleted in HREEs and less enriched in LREEs relative to the Cosmos felsic volcanic rocks. They exhibit no, or a slight positive, Eu anomaly contrasting the negative Eu anomaly exhibited by the Cosmos felsic volcanic rocks (Fig. 3.6). The Cosmos dacite lavas and tuffs lack many of the geochemical attributes considered to indicate a TTD affinity in volcanic rocks, whereas both the Cosmos felsic porphyry intrusions have a strong TTD affinity and are geochemically similar to the Black Flag dacitic rocks (Table 3.3; Fig. 3.6 o, p). Thus the extrusive volcanic sequence within the Cosmos sequence shows no TTD affinity whereas the later cross-cutting felsic porphyry intrusions show a strong TTD affinity.

This can be seen on Figure 3.7a where Sr/Y vs. Y ratio has been used to define the modern day adakite field and typical island-arc volcanic rocks (after Drummond and Defant (1990) and Defant and Drummond (1990)). The extrusive Cosmos volcanic lithologies and mafic intrusions fall within the island-arc field whereas the felsic intrusions and the Black Flag Group plot in the adakite field, exhibiting much higher Sr/Y ratios and lower Y concentrations (Fig. 3.7a). Given the potential mobility of Sr during metamorphism it is also useful to also utilise discrimination diagrams whose element ratios are considered to be immobile during metamorphism. Martin (1986) presented a way to define TTG-affinity rocks using La/Yb and Yb (Fig. 3.7b). TTG rocks typically exhibit high La/Yb ratios and low HREE contents whereas modern

continental crust (equivalent geochemically to the products of basaltic-andesite-dacite-rhyolite (BADR) island-arc volcanism) have higher HREE concentrations and lower La/Yb ratios. The Cosmos extrusive volcanic lithologies plot entirely within the field of modern continental crust confirming their dominantly island-arc signature whereas the felsic intrusions exhibit a much more typical TTG affinity.

3.8.4 Felsic porphyry intrusions and their relation to regional granite plutons

The TTG affinity of the felsic intrusions indicates the melt generation processes and possible tectonic regime in the Cosmos region had shifted prior to 2670Ma. Dating of an in-situ volcanic horizon within the Cosmos ultramafic sequence, referred to as the AM5 "reactivation" contact (Fig. 3.2), indicates komatiite volcanism continued in the region after ~2685 Ma (de Joux et al., 2013; Chapter 4). The hangingwall felsic intrusion crosscuts the Cosmos Ultramafic Sequence's upper contact with the overlying hangingwall sedimentary succession (Fig. 3.2). Thus this transition in geodynamic regime likely occurred post 2685 Ma and prior to 2670 Ma. The age of this transition is consistent with that suggested for the extensional D1 phase of deformation within the Norseman-Wiluna belt, which was accompanied by a change from volcanic-dominated to plutonic-dominated magmatic between ~2685 and 2675 Ma (Weinberg et al., 2003). The slight difference in composition between the two porphyries, coupled with their contrasting ages, indicates they are the product of two separate episodes of felsic intrusive activity and are likely related to regional granite emplacement.

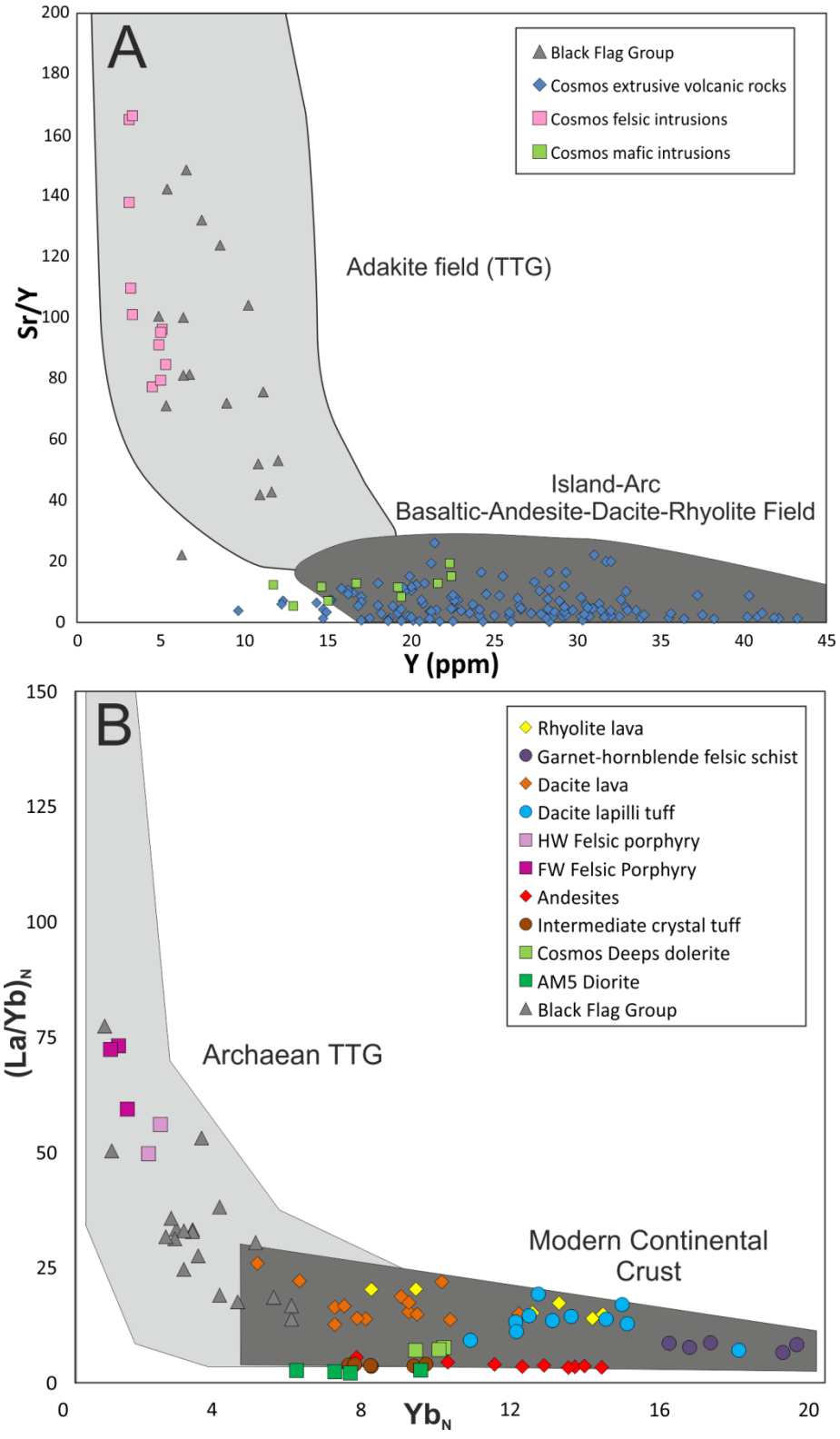

Figure 3.7. (A) Sr/Y vs. Y diagram (after Defant and Drummond (1990) and Drummond and Defant (1990)) modified after de Joux et al. (2013). (B) $(La/Yb)_N$ vs. Yb_N after Martin (1986). La/Yb_N is chondrite normalised using the values from Masuda et al. (1973) divided by 1.2, after Moyen and Martin (2012). Black Flag Group data from Morris and Witt (1997).

Champion and Sheraton (1997) divided the granites and granite gneisses of the EGS into five groups; high-Ca, low-Ca, high-HFSE, mafic and syenitic. The high-Ca and low-Ca groups comprise over 80% of the granite occurrence within the EGS (Champion and Sheraton, 1997). Figure 3.8 shows the Cosmos felsic intrusions are geochemically most similar to the high-Ca granites and are thus likely related to the local emplacement of high-Ca granite plutons. The felsic porphyry intrusions also show LILE enrichment, appreciable negative Nb anomalies and high Sr, which is typical of high-Ca granites (Fig. 3.6o). This granite group shares many features with the typical Archaean TTG suites. Their derivation is considered to have occurred at high pressures within a thickened crust or by crustally-contaminated slab-derived melts (Champion and Sheraton, 1997). High-Ca granitoids occur immediately west of the AWB and are by far the most abundant granite type in the region, followed by the low-Ca plutons that dominate the central granitoid region between the Agnew-Wiluna and Yandal greenstone belts (Liu et al., 2002). The high-Ca granitoids in this region were emplaced between ~2720 - 2655Ma whereas low-Ca and syentitic granitoids were emplaced after 2660 Ma (Liu et al., 2002). This change in granite composition has been interpreted to represent a fundamental change in the tectonic environment post ~2660 - 2655Ma, from crustal shortening and voluminous high-Ca granitoids to a tensional environment favouring low-Ca and syentitic magmatism (Smithies and Champion, 1999).

Figure 3.8. (Next page).Yilgarn Granite discrimination diagrams (after Champion and Sheraton, 1997) showing the geochemical composition of the footwall and hangingwall felsic porphyry intrusions. Sr/Sr* is primordial mantle-normalised Sr abundance divided by the interpolated value obtained by averaging the normalised Ce and Nd concentrations (Primordial mantle normalising values from Sun and McDonough, 1989)

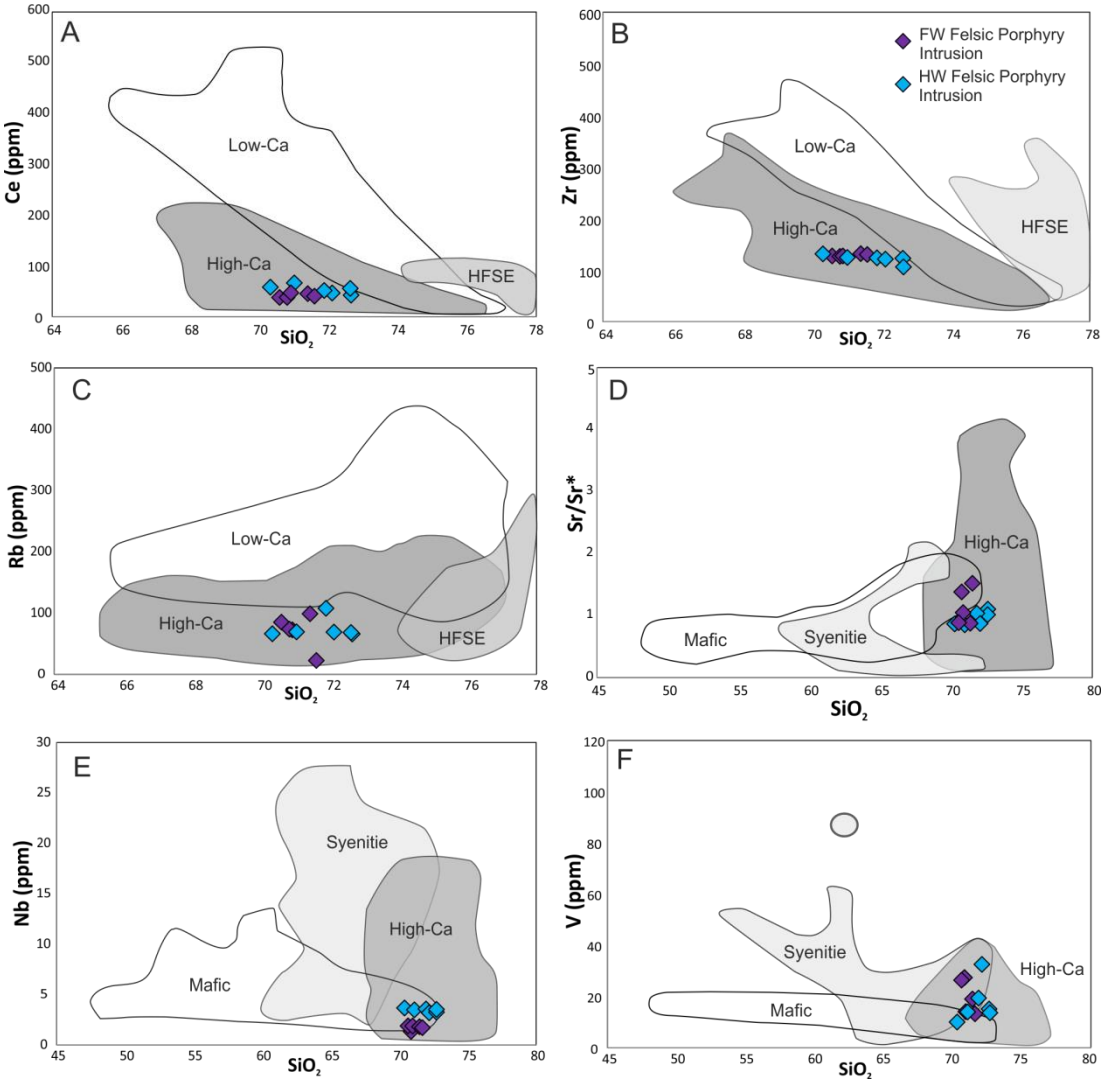

3.8.5 The intermediate to felsic Cosmos volcanic succession – a high-K calc-alkaline to shoshonite continental island arc

The Cosmos extrusive volcanic succession has been shown to have a strong island-arc affinity (Fig. 3.7). The succession appears to be strongly enriched compared to the majority of modern and ancient arc successions (Fig. 3.6) and volcanic lithologies plot within the continental margin array on Figure 3.9. The less enriched andesites straddle the calc-alkaline-shoshonite boundary, with the more felsic volcanic units plotting distinctly in the shoshonite field (as defined by Manikyamba et al., 2012;

Fig. 3.9). The modern shoshonite rock association is characterised by high Na_2O and K_2O, high LILEs content, high but variable Al_2O_3, high Fe_2O_3/FeO and low TiO_2 (Morrison, 1980). Given that this diagram does not define high-K calc-alkaline affinity, and that the volcanic units are grouped relatively close to the shoshonite-calc-alkaline boundary, the Cosmos volcanic sequence is likely to have a high-K calc-alkaline to shoshonite affinity. In modern continental margins, and some island arc settings, there is often a complete gradation between calc-alkaline, high-K calc-alkaline and shoshonitic suites (Morrison, 1980). Therefore it is not unusual that the Cosmos volcanic sequence straddles the calc-alkaline and shoshonite boundary between (Fig. 3.9).

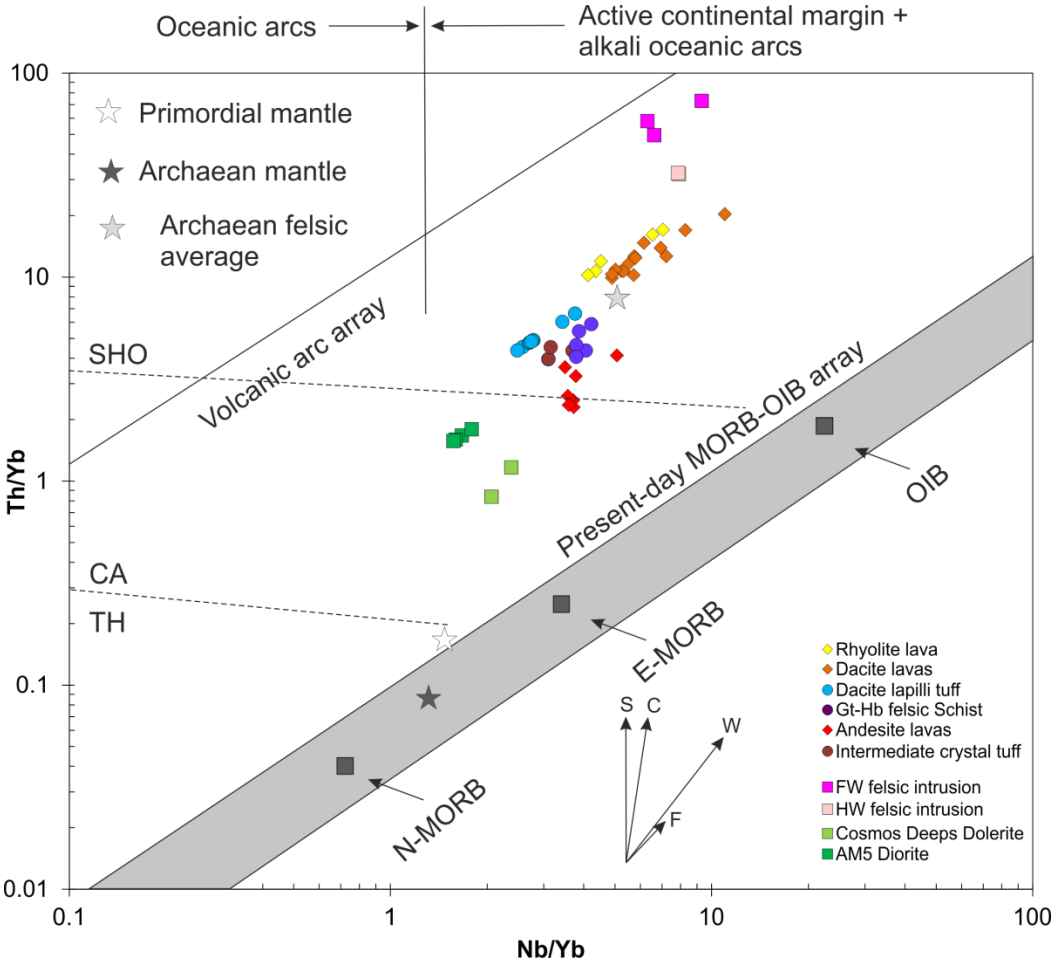

Figure 3.9. Th/Yb vs. Nb/Yb discrimination diagram after Pearce (2008) and Manikyamba et al. (2012). Shoshonite (SHO), calc-alkaline (CA) and tholeiite (TH) are shown after Manikyamba et al. (2012). S, subduction component vector; C, crustal contamination vector; W, within plate variation; F, fractional crystallization (after Manikyamba et al. 2012). Primordial mantle, Archaean mantle and Archaean felsic average are taken from Pearce (2008) and references therein. FW = Footwall, HW = Hangingwall, Gt-Hb = garnet-hornblende

3.8.6 Can the intercalated andesite and dacite volcanic units be related by AFC processes?

The intercalated nature of the andesitic units with the dacitic units might superficially indicate they may be the less evolved and more evolved products respectively of the same magma source (Fig. 3.3). However differing REE concentrations, as well as distinct variations on multi-element plots (Fig. 3.6) indicate the andesitic and dacitic units are unlikely to have a co-genetic relationship. Assimilation-fractional crystallisation (AFC) modelling further indicates that the andesite lavas cannot be related to the dacite lavas via AFC processes. A crystallising gabbroic assemblage from the northern Marianas Islands, with an average composition of PLAG:CPX:MAG:OLIV = 60:25:10:5 (Woodhead, 1988), was used for AFC modelling. The AFC model of De Paolo (1981) was utilised to assess whether a similar composition to the dacite lavas can be achieved, from the least evolved basaltic andesite, when assimilation of crust is included. Modelling also included variable proportions of apatite as a crystallising phase, with a proportional reduction in the other four phases. The Archaean felsic average from Rudnick and Fountain (1995) was used as the contaminant. However, even at high r factors (rate of assimilation relative to the rate of crystallisation), enriched compositions such as those exhibited by the dacite lavas cannot be achieved via AFC processes from the least evolved basaltic andesite lava (Fig. 3.10b, c). The Archaean felsic average volcanic itself has a lower Th/Yb ratio than the enriched dacite lavas (Fig. 3.9). Therefore to generate an enriched dacite composition from a basaltic andesite parent melt, the composition of the contaminating crust would have to be substantially more enriched than the Archaean felsic average.

Czarnota et al. (2010) proposed that the Youanmi Terrane may form the basement to the Kalgoorlie Terrane. Consequently a felsic volcanic rock from the Greensleeves Formation of the Pollelle Group within the Youanmi Terrane has also been tested as a potential contaminant (Wyman and Kerrick, 2012). This group is dated at ~2760 Ma (Wyman and Kerrich 2012), which is similar in age to the two xenocrystic zircons dated within the felsic footwall (~2750 - 2760 Ma), making it a feasible crustal

contaminant for generation of the Cosmos felsic volcanic sequence. However, AFC processes cannot produce compositions with high enough Th/Yb from the least evolved basaltic andesite, even in the presence of apatite, (Fig. 3.10d, e). The same is also true when average TTG is used as a crustal contaminant (Drummond and Defant 1996; Fig. 3.10f).

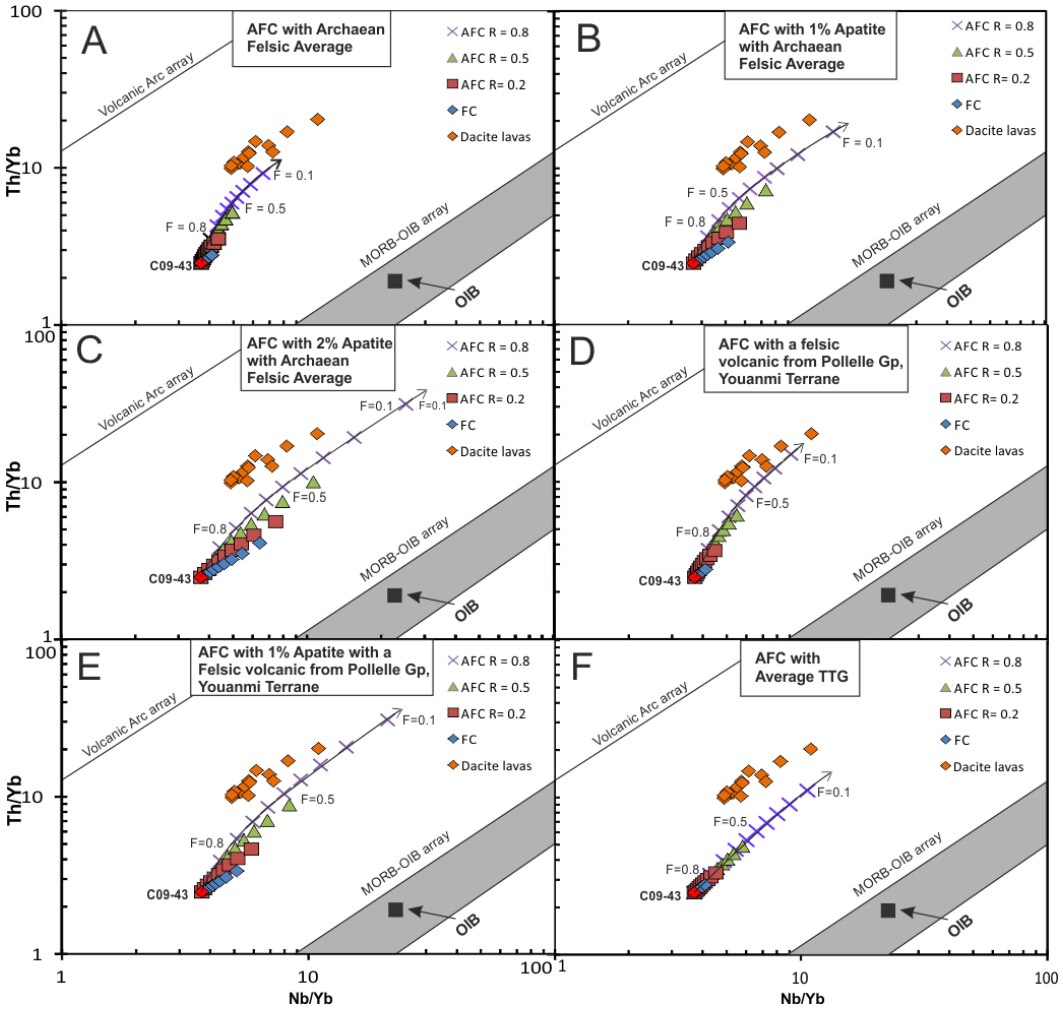

Figure 3.10. AFC modelling of the least evolved basaltic andesite to assess if a composition close to that of the dacite lavas can be achieved by AFC processes. Fractional crystallisation modelling was carried out using a crystallising gabbroic assemblage with the average composition of PLAG:CPX:MAG:OLIV = 60:25:10:5 (after Woodhead, 1988). Modelling including apatite as a crystallising phase was also used (10.b, c, e). **(A-C)** AFC modelling of De Paolo (1981) used Archaean felsic average (Rudnick and Fountain, 1995), **(D, E)** AFC modelling using, CUE-21, an evolved felsic volcanic from the Youanmi Terrane (Wyman and Kerrick, 2012). **(F)** AFC modelling using Average TTG (Rudnick and Fountain, 1995). Distribution coefficients for crystallising phases were obtained from McKenzie and O'Nions (1991; plagioclase, clinopyroxene and olivine), Mahood and Stimac (1983; apatite – Th, Yb), Pearce and Norry (1979; apatite - Nb), Lemarchand et al. (1987; magnetite – Th, Yb) and Schock (1979; magnetite - Nb).

The combined effect of fractional crystallisation in the presence of apatite with contamination by either the Archaean felsic average or a felsic volcanic from the Pollelle group increases both the Th/Yb and Nb/Yb ratios but requires both high r factors and fractional crystallisation including ≥2% apatite. This still does not reproduce the high Th/Yb ratios exhibited by the dacite lavas, although contamination by a more enriched source lithology cannot be ruled out. However given the large proportion of assimilation required, and the requirement for ≥2% apatite as a crystallising phase, it is considered more likely that the dacitic lavas are unrelated to the andesites via AFC processes. The dacites are considered to be derived from a compositionally distinct source region with a more enriched slab component. Thus, the intercalated andesite and dacite lavas appear to have been formed from at least two separate but coeval volcanic centres. These tapped different mantle sources that had experienced contrasting sediment and/or slab-derived fluid input from the subducting slab.

3.9 Tectonic setting of the Cosmos volcanic succession

3.9.1 Archaean shoshonites

In both modern and ancient geological settings, shoshonitic volcanic rocks are characterised by high LILE abundances relative to HFSEs. As modern shoshonitic and calc-alkaline affinity volcanism occurs largely in convergent plate margin tectonic settings with active subduction of oceanic crust or a past history of subduction (Morrison, 1980) modern-style subduction processes have been inferred in the genesis of the equivalent Archaean rock suites (e.g., Giles and Hallberg, 1982; Dostal and Mueller, 1992; Hollings and Kerrich, 2006; Manikyamba et al., 2012). Late Archaean shoshonites are described in the North America's Superior Province including the Timiskaming Group in Ontario (Corfu et al., 1991 and references therein), the Oxford

Lake Group (Brooks et al., 1982), the Opemisca Group in Quebec (Dostal and Mueller, 1992), and the 2.7-2.8 Ga greenstone terranes of the Uchi greenstone-granite subprovince in Ontario (Hollings and Kerrich, 2006). Late Archaean shoshonites have also been recognised in Indian's western Dharwar Craton (Manikyamba et al., 2012). It has been argued that the Superior Province shoshonites represent late or last-stage magmatic products in volcanic arc settings and, based on geochemical analogy to modern shoshonites, they were derived from mantle sources metasomatised by subduction-related fluids rich in LILEs (e.g., Brookes et al., 1982; Dostal and Mueller, 1992; Hollings and Kerrich, 2006). No extrusive shoshonites are recognised within the Yilgarn Craton, with strongly enriched rocks only represented by shoshonitic lamprophyre dykes in the EGS (Taylor et al., 1994). Shoshonitic magmatism manifested as sub-volcanic lamprophyres is spatiotemporally associated with mesothermal gold mineralisation whose emplacement is confined to ~2.6 Ma (Taylor et al., 1994).). Calc-alkaline volcanism is recognised within the Kurnalpi and Gindalbie Terranes of the EGS, dated respectively between ~2715 - 2704 Ma and ~2692 - 2680 Ma (e.g., Giles and Hallberg, 1982; Barley et al., 2008), and also within the Spring Well complex of the Yandal belt (Messenger, 2000). However TTD-affinity volcanic products are much more voluminous throughout the EGS. Thus although calc-alkaline volcanism has been described in the EGS, the Cosmos volcanic succession is the first recorded strongly enriched high-K calc-alkaline to shoshonite island-arc sequence within the Kalgoorlie Terrane and is unique in being significantly older and more enriched than other island-arc successions within adjacent terranes of the EGS.

3.9.2 Island-arc and TTD-affinity volcanism within the Kalgoorlie Terrane

The relative rarity of typical arc-derived volcanic successions within the Kalgoorlie Terrane could be a function of hotter subduction zones within the Archaean (e.g., Kerrich and Polat, 2006). If the Late Archaean oceanic lithosphere was generally

young, this would result in slow, shallow subduction, and, coupled with higher geothermal gradients in the Archaean mantle (e.g., Martin 1986), would result in hot subduction zones. Moyen and Stevens (2006) considered high pressure TTGs to be the product of melting of fluid-absent metabasite under P/T conditions only likely to be achieved in significantly hotter subduction zones than modern counterparts. Thus, in hot late Archaean subduction zones, partial melting of the subducted oceanic crust, generating typical TTG melts, may have been a dominant melt-forming process in active arc settings. However calc-alkaline BADR volcanic sequences resembling Phanerozoic counterparts and considered to represent extensive intra-oceanic arc systems exist within the Archaean, indicating partial melting in the mantle wedge also contributed to late Archaean volcanism (e.g., Kerrich and Polat, 2006).

This paper demonstrates the Cosmos extrusive volcanic footwall succession has geochemical characteristics much more typical of partial melting of peridotite, which had been enriched in the mantle wedge by slab-derived fluids and/or sediment melt. Fiorentini et al. (2012) proposed that TTD-affinity volcanic successions within the AWB formed via partial melting of the mafic lower crust, with ascending komatiitic mantle plumes possibly providing the heat source in a rift or back-arc rift environment. If a back-arc was the tectonic setting of the AWB, an outside heat source, such as a rising mantle plume, would not be required because melting of the down-going slab could occur regardless in a hotter subduction zone. Mantle plume impingement on an active subduction zone could also sufficiently increase the geothermal gradient to result in a switch from partial melting of the mantle wedge to melting of the slab itself. Thus, the Cosmos volcanic succession, and TTD-affinity volcanic successions of the Kalgoorlie Terrane, could be formed in the same arc setting.

The trace element concentrations of individual volcanic units within the Cosmos succession suggest derivation from at least two distinct mantle sources that were influenced by either one or a combination of the following: different mantle sources, or sources which experienced contrasting sediment and/or slab-derived fluid input from the subducting slab. A later switch to more partial melts derived via melting of the subducting oceanic crust, potentially at greater depths within the subduction

zone or under the influence of a higher geothermal gradient, could have formed the typical TTD-melts seen regionally within the Kalgoorlie Terrane. More detailed geochemical examination of the TTD affinity of felsic volcanic sequences within the Agnew-Wiluna Belt and the wider Kalgoorlie Terrane needs to be undertaken to discern what proportion of TTD volcanism shows characteristics of the high pressure TTD sub-group that can only be attributed to derivation via slab melting in a subduction setting (Moyen and Martin, 2012). The ~15 - 20Ma age difference between the Cosmos volcanic arc succession and the neighbouring Mount Keith and Perseverance successions leaves abundant time for the evolution of an arc system and a transition from mantle derived partial-melts above the subducting slab, to partial melting of the down-going slab itself. Defant and Kepezkinkas (2001) showed that the transition from arc basalts to adakites in modern arcs settings may occur in only a few million years.

Defant and Drummond (1993) recognised that both partial melting of the oceanic crust and flux melting of the mantle wedge can contribute "simultaneously" to active volcanism in a subduction zone, forming the arc volcanoes of Mount St Helens and Mount Adams respectively. Mount St. Helens is associated with the subduction of young crust and has erupted dacites that are similar in composition to adakites (Defant and Drummond, 1993). The geographical positions and geochemistry of these two arc volcanoes is thus controlled by the dominant melt generating processes occurring within or above the down-going slab. Similar processes may have operated within Archaean arcs. Czarnota et al. (2010) linked the Kalgoorlie, Kurnalpi and Burtville Terranes within a westward-dipping subduction zone active between ~2715 and 2690 Ma. The Kalgoorlie Terrane is considered to represent a back-arc setting where minor calc-alkaline volcanism within the Kalgoorlie sequence, generated by partial melting of the mantle wedge is suggested to have occurred contemporaneously with slab-melting producing the high-Ca granite magmatism between 2690 and 2670 Ma (Czarnota et al., 2010). Given that the Cosmos succession is ~10 - 20 Ma older than the volcanic sequences within the Kalgoorlie Terrane, it either represents an earlier phase of arc volcanism within the EGS arc-system or may be a separate arc-fragment that became accreted onto the Kalgoorlie Terrane prior to

voluminous high-Ca granite intrusion between 2690 and 2670 Ma (Czarnota et al., 2010).

3.10 Conclusions

The Cosmos volcanic succession represents the first extrusive, high-K calc-alkaline to shoshonitic island-arc volcanic sequence described in the Kalgoorlie Terrane, if not the entirety of the Eastern Goldfields Superterrane. The only units present within the Cosmos succession to show a TTD affinity are the significantly younger felsic porphyry intrusions that are linked to local high-Ca granite intrusion. Thus, the AWB is not wholly composed of intermediate and felsic volcanic sequences with a TTD-affinity as suggested by Fiorentini et al. (2012). Given that the Cosmos volcanic succession is ~15 - 25 Ma older than the majority of felsic rocks within the AWB (de Joux et al., 2013) and has a different and distinct geochemical affinity, it may represent a separate arc terrane in its own right that experienced subsequent accretion with the Kalgoorlie Terrane. Alternatively, the geochemical affinity and thus potential tectonic setting of the AWB itself may be more complex than currently considered, suggesting that surrounding felsic successions require further detailed geochemical assessment to establish if they do in fact all exhibit TTD affinity. Unravelling the apparent tectonic complexity of the region is particularly important given the recent re-ignition of the plume-dominated versus subduction accretion models for the origin for the Eastern Goldfields Superterrane (Barnes et al., 2012). Recognition of this distinct high-K calc-alkaline to shoshonite island-arc sequence gives further evidence that modern style plate tectonics were operating during the late Archaean, contrary to the assertion by Bédard et al. (2013) that evidence for Archaean island arcs is sparse because they did not exist.

3.11 References

Barley, M. E., Brown, S J., Krapež, B., Kositcin, N., 2008. Physical volcanology and geochemistry of a Late Archaean volcanic arc: Kurnalpi and Gindalbie Terranes, Eastern Goldfields Superterrane, Western Australia. Precambrian Research 161(1), 53-76.

Barnes, S. J., Hill, R. E., Gole, M. J., 1988. The Perseverance ultramafic complex, Western Australia: the product of a komatiite lava river. Journal of Petrology 29(2), 305-331.

Barnes, S. J., Van Kranendonk, M. J., Sonntag, I., 2012. Geochemistry and tectonic setting of basalts from the Eastern Goldfields Superterrane, Australian Journal of Earth Science: An International Geoscience journal of the Geological Society of Australia 59(5), 707-735.

Bau, M., 1991. Rare-earth element mobility during hydrothermal and metamorphic fluid-rock interaction and the significance of the oxidation state of europium. Chemical Geology 93(3), 219-230.

Bédard, J. H., 2006. A catalytic delamination-driven model for coupled genesis of Archaean crust and sub-continental lithospheric mantle. Geochimica et Cosmochimica Acta 70(5), 1188-1214.

Bédard, J. H, Harris, L. B., Thurston, P. C. 2013. The hunting of the snArc. Precambrian Research 229, 20-48.

Boynton, N. L., 1984. Geochemistry of the rare earth elements: meteorite studies. In: Rare Earth Element Geochemistry, Elsevier, 63 - 114.

Brooks, C., Ludden, J., Pigeon, Y., Hubregtse, J. J. M. W., 1982. Volcanism of shoshonite to high-K andesite affinity in an Archaean arc environment, Oxford Lake, Manitoba. Canadian Journal of Earth Sciences 19(1), 55-67.

Campbell, I. H., Hill, R. I., 1988. A two-stage model for the formation of the granite-greenstone terrains of the Kalgoorlie-Norseman area, Western Australia. Earth and Planetary Science Letters 90(1), 11-25.

Campbell McCuaig, T., Kerrich, R., Xie, Q., 1994. Phosphorus and high field strength element anomalies in Archean high-magnesian magmas as possible indicators of source mineralogy and depth. Earth and Planetary Science Letters 124 (1), 221-239.

Cassidy, K. F., Champion, D. C., Krapež, B., Barley, M. E., Brown, S. J. A., Blewett, R.S., Groenewald P. B., Tyler, I. M., 2006. A revised geological framework for the Yilgarn Craton, Western Australia. Western Australia Geological Survey, Record 2006/8, 8 pp.

Champion, D. C., Sheraton, J. W., 1997. Geochemistry and Nd isotope systematics of Archaean granites of the Eastern Goldfields, Yilgarn Craton, Australia: implications for crustal growth processes. Precambrian Research 83(1), 109-132.

Corfu, F., Jackson, S. L., Sutcliffe, R. H. 1991. U-Pb ages and tectonic significance of late Archean alkalic magmatism and nonmarine sedimentation: Timiskaming Group, southern Abitibi belt, Ontario. Canadian Journal of Earth Sciences, 28(4), 489-503.

Czarnota, K., Champion, D. C., Goscombe, B., Blewett, R. S., Cassidy, K. F., Henson, P. A., Groenewald, P.B., 2010. Geodynamics of the eastern Yilgarn Craton. Precambrian Research 183(2), 175-202.

Defant, M. J., Drummond, M. S., 1990. Derivation of some modern arc magmas by melting of young subducted lithosphere. Nature 347(6294), 662-665.

Defant, M. J., Kepezhinskas, P., 2001. Evidence suggests slab melting in arc magmas. Eos, Transactions American Geophysical Union 82(6), 65-69.

de Joux, A., Thordarson, T., Denny, M., Hinton, R. W., de Joux A. J., 2013. U-Pb dating constraints on the felsic and intermediate volcanic sequence of the nickel-sulphide bearing Cosmos succession, Agnew-Wiluna greenstone belt, Yilgarn Craton, Western Australia. Precambrian Research 236, 86-105.

De Paolo, D. J., 1981. Trace element and isotopic effects of combined wallrock assimilation and fractional crystallization. Earth and Planetary Science Letters 53(2), 189-202.

Dowling, S. E. Hill, R. E. T., 1990. Rivers of fire: the physical volcanology of komatiites of the Mt. Keith region, Norseman-Wiluna belt, Western Australia. CSIRO Exploration Geoscience Restricted Report, 103R, 170.

Dostal, J., Mueller, W., 1992. Archaean shoshonites from the Abitibi greenstone belt, Chibougamau (Québec, Canada): geochemistry and tectonic setting. Journal of Volcanology and Geothermal Research 53(1), 145-165.

Drummond, M. S., Defant, M. J., 1990. A model for trondhjemite–tonalite–dacite genesis and crustal growth via slab melting: Archaean to modern comparisons. Journal of Geophysical Research 95, 21503–21521.

Drummond, M. S., Defant, M. J., Kepezhinskas P. K., 1996. Petrogenesis of slab-derived trondhjemite-tonalite-dacite/adakite magmas. Transactions of the Royal Society of Edinburgh-Earth Sciences 87 (1), 205-216.

Fiorentini, M., Beresford, S., Barley, M., Duuring, P., Bekker, A., Rosengren, N., Cas, R., Hronsky, J., 2012. District to camp controls on the genesis of komatiite-hosted nickel sulfide deposits, Agnew-Wiluna greenstone belt, Western Australia: Insights from the multiple sulfur isotopes. Economic Geology 107(5), 781-796.

Floyd, P. A., Winchester, J. A., 1978. Identification and discrimination of altered and metamorphosed volcanic rocks using immobile elements. Chemical Geology 21(3), 291-306.

Gee, M., Swager, C., 2008. Late Archaean volcanic arcs and their accretionary history, Eastern Goldfields Superterrane: Plate tectonic models inferred from tectonostratigraphic analysis. Precambrian Research 161(1), 1-4.

Giles, C. W., Hallberg, J. A., 1982. The genesis of the Archaean Welcome Well volcanic complex, Western Australia. Contributions to Mineralogy and Petrology 80(4), 307-318.

Hamilton, W. B., 2003. An alternative earth. GSA Today 13(11), 4-12.

Hill, R. E. T. Barnes, S. J. Gole, M. J. Dowling, S. E., 1995. The volcanology of komatiites as deduced from field relationships in the Norseman-Wiluna greenstone belt, Western Australia. Lithos 34 (1-3), 159-188

Hill, R. E. T., Barnes, S. J., Dowling, S. E., Thordarson, T., 2004. Komatiites and nickel sulphide ore bodies of the Black Swan area, Yilgarn Craton, Western Australia. 1. Petrology and volcanology of host rocks. Mineralium Deposita 39(7), 684-706.

Hill, R. E. T., Dowling, S. E., 2008. The petrology and geochemistry of mineralised komatiites intersected in three diamond drill holes (AM262B, AMD275 and BJD048A) from the AM5 Nickel Sulphide Deposit; Cosmos region, Agnew-Wiluna Greenstone Belt; A pilot study for characterising mineralised domains within the ore body. Unpublished External report, Kalapana Research Associates and Triodia Research.

Hollings, P., Kerrich, R., 2006. Light rare earth element depleted to enriched basaltic flows from 2.8 to 2.7 Ga greenstone belts of the Uchi Subprovince, Ontario, Canada. Chemical Geology 227(3), 133-153.

Johnson, M. C., Plank, T., 1999. Dehydration and melting experiments constrain the fate of subducted sediments. Geochemistry Geophysics Geosystems, 1 GC000014.

Kerrich, R., Polat, A., 2006. Archean greenstone-tonalite duality: Thermochemical mantle convection models or plate tectonics in the early Earth global dynamics? Tectonophysics 415(1), 141-165.

Korsch, R. J., Kositcin, N., Champion, D. C., 2011. Australian island arcs through time: geodynamic implications for the Archaean and Proterozoic. Gondwana Research 19(3), 716-734.

Kositcin, N., Brown, S. J., Barley, M. E., Krapež, B., Cassidy, K. F., Champion, D. C., 2008. SHRIMP U-Pb zircon age constraints on the Late Archaean tectonostratigraphic architecture of the Eastern Goldfields Superterrane, Yilgarn Craton, Western Australia. Precambrian Research 161(1), 5-33.

Krapež, B., Hand, J. L. 2008. Late Archaean deep-marine volcaniclastic sedimentation in an arc-related basin: the Kalgoorlie Sequence of the Eastern Goldfields Superterrane, Yilgarn Craton, Western Australia. Precambrian Research 161(1), 89-113.

Le Bas, M. J., Le Maitre, R. W., Streckeisen, A., Zanettin, B., 1986. A chemical classification of volcanic rocks based on the total alkali-silica diagram. Journal of Petrology 27(3), 745-750.

Le Bas, M. J., Le Maitre, R. W., Woolley, A. R., 1992. The construction of the total alkali-silica chemical classification of volcanic rocks. Mineralogy and Petrology 46(1), 1-22.

Lemarchand, F., Villemant, B., Calas, G. 1987. Trace element distribution coefficients in alkaline series. Geochimica et Cosmochimica Acta 51(5), 1071-1081.

Ludden, J., Gélinas, L., Trudel, P., 1982. Archaean metavolcanics from the Rouyn-Noranda district, Abitibi Greenstone Belt, Quebec. 2. Mobility of trace elements and petrogenetic constraints. Canadian Journal of Earth Sciences 19(12), 2276-2287.

Liu, S. F., Champion, D.C., Cassidy K. F., 2002. Geology of the Sir Samuel 1:250,000 sheet area, Western Australia Geoscience Australia Record 14.

Macpherson, C. G., Dreher, S. T., Thirlwall, M. F. 2006. Adakites without slab melting: high pressure differentiation of island arc magma, Mindanao, the Philippines. Earth and Planetary Science Letters 243(3), 581-593.

Mahood, G. A., Stimac, J. A. 1990. Trace-element partitioning in pantellerites and trachytes. Geochimica et Cosmochimica Acta 54(8), 2257-2276.

Manikyamba, C., Kerrich, R., Polat, A., Raju, K., Satyanarayanan, M., Krishna, A.K., 2012. Arc Picrite-Potassic Adakitic-Shoshonitic Volcanic Association of the NeoArchaean Sigegudda Greenstone Terrane, Western Dharwar Craton: Transition from Arc Wedge to Lithosphere Melting. Precambrian Research 212, 207-224.

Martin, H., 1986. Effect of steeper Archaean geothermal gradient on geochemistry of subduction-zone magmas. Geology 14, 753–756.

Martin, H., 1994. The Archaean grey gneisses and the genesis of continental crust. In: Condie, K. C. (ed.) Archaean Crustal Evolution. Amsterdam: Elsevier, pp.205–259.

Martin, H., 1999. Adakitic magmas: modern analogues of Archaean granitoids. Lithos 46, 411-429.

Martin, H., Smithies, R. H., Rapp, R., Moyen, J. F., Champion, D. 2005. An overview of adakite, tonalite–trondhjemite–granodiorite (TTG), and sanukitoid: relationships and some implications for crustal evolution. Lithos 79(1), 1-24.

Masuda, A., Nakamura, N., Tanaka, T., 1973. Fine structures of mutually normalized rare-earth patterns of chondrites. Geochimica et Cosmochimica Acta 37(2), 239-248.

McKenzie, D. A. N., O'nions, R. K. 1991. Partial melt distributions from inversion of rare earth element concentrations. Journal of Petrology 32(5), 1021-1091.

Messenger, P. R., 2000. Geochemistry of the Yandal belt metavolcanic rocks, Eastern Goldfields Province, Western Australia. Australian Journal of Earth Sciences 47(6), 1015-1028.

Michard, A., Albarède, F., 1986. The REE content of some hydrothermal fluids. Chemical Geology 55(1), 51-60.

Morris, P. A., Witt, W. K., 1997. Geochemistry and tectonic setting of two contrasting Archaean felsic volcanic associations in the Eastern Goldfields, Western Australia. Precambrian Research 83(1), 83-107.

Morrison, W., 1980. Characteristics and tectonic setting of the shoshonite rock association. Lithos 13 (1), 97-108.

Moyen, J. F., Martin, H., 2012. Forty years of TTG research. Lithos 48, 312-336.

Moyen, J. F., Stevens, G., 2006. Experimental constraints on TTG petrogenesis: implications for Archaean geodynamics. Benn, K., Mareschal, J., Condie, K. C., (Eds.), Archaean geodynamics and environments, American Geophysical Union, Washington, pp. 149-175.

Myers, J. S., 1993. Precambrian history of the West Australian Craton and adjacent orogens. Annual Reviews Earth Planetary Science 21, 453-485.

Nelson, D. R., 1997b. Evolution of the Archaean granite-greenstone terranes of the Eastern Goldfields, Western Australia: SHRIMP U-Pb zircon constraints. Precambrian Research 83(1), 57-81.

Nelson, D.R., 1998. Granite–greenstone crust formation on the Archaean Earth: a consequence of two superimposed processes. Earth and Planetary Science Letters 158(3), 109-119.

Pawley, M. J., Wingate, M. T. D., Kirkland, C. L., Wyche, S., Hall, C.E., Romano, S. S., Doublier, M. P., 2012. Adding pieces to the puzzle: episodic crustal growth and a new terrane in the northeast Yilgarn Craton, Western Australia. Australian Journal of Earth Sciences 59(5), 603-623.

Pearce, J. A., 2008. Geochemical fingerprinting of oceanic basalts with applications to ophiolite classification and the search for Archaean oceanic crust. Lithos 100(1), 14-48.

Pearce, J. A., Peate, D. W., 1995. Tectonic implications of the composition of volcanic arc magmas. Annual Reviews in Earth Planetary Science 23, 251–285.

Pearce, J. A., Norry, M. J. 1979. Petrogenetic implications of Ti, Zr, Y, and Nb variations in volcanic rocks. Contributions to Mineralogy and Petrology 69(1), 33-47.

Peccerillo, A., Taylor, S. R., 1976. Geochemistry of Eocene calc-alkaline volcanic rocks from the Kastamonu area, northern Turkey. Contributions to Mineralogy and Petrology 58(1), 63-81.

Rickwood, P. C., 1989. Boundary lines within petrologic diagrams which use oxides of major and minor elements. Lithos 22(4), 247-263.

Rosengren, N. M., Beresford, S. W., Grguric, B. A., Cas, R. A. F., 2005. An intrusive origin for the komatiitic dunite-hosted Mount Keith disseminated nickel sulfide deposit, Western Australia. Economic Geology 100(1), 149-156.

Rosengren, N. M., Cas, R. A. F., Beresford, S. W., Palich, B.M., 2008. Reconstruction of an extensive Archaean dacitic submarine volcanic complex associated with the komatiite-hosted Mt Keith nickel deposit, Agnew-Wiluna greenstone belt, Yilgarn Craton, Western Australia. Precambrian Research 161(1), 34-52.

Rudnick, R. L., Fountain, D. M., 1995. Nature and composition of the continental crust: a lower crustal perspective. Reviews of Geophysics 33(3), 267-309.

Schock, H. H. 1979. Distribution of rare-earth and other trace elements in magnetites. Chemical Geology 26(1), 119-133.

Smithies, R. H., 2000. The Archaean tonalite–trondhjemite–granodiorite (TTG) series is not an analogue of Cenozoic adakite. Earth and Planetary Science Letters 182(1), 115-125.

Smithies, R. H., Champion, D. C. 1999. Late Archaean felsic alkaline igneous rocks in the Eastern Goldfields, Yilgarn Craton, Western Australia: a result of lower crustal delamination? Journal of the Geological Society 156(3), 561-576.

Standing, J. G., 2008. Terrane amalgamation in the Eastern Goldfields Superterrane, Yilgarn Craton: evidence from tectonostratigraphic studies of the Laverton Greenstone Belt. Precambrian Research 161(1), 114-134.

Stuff, R., 2011. Xstrata Nickel Australasia-Cosmos Nickel Project- Technical Report No: STR01126, Annual report on Cosmos Nickel Project Tenements submitted to DMP, 12-18.

Sun, S. S., McDonough, W., 1989. Chemical and isotopic systematics of oceanic basalts: implications for mantle composition and processes. Geological Society, London, Special Publications 42(1), 313-345.

Taylor, S. R., McLennan, S. M., 1985. The continental crust: its composition and evolution. Reviews of Geophysics 33(2), 241-265.

Taylor, W. R., Rock, N., Groves, D. I., Perring, C. S., Golding, S. D., 1994. Geochemistry of Archaean shoshonitic lamprophyres from the Yilgarn Block, Western Australia: Au abundance and association with gold mineralization. Applied Geochemistry 9(2), 197-222.

Trofimovs, J., Tait, M. A., Cas, R. A. F., McArthur, A., Beresford, S.W. 2003. Can the role of thermal erosion in strongly deformed komatiite–Ni–Cu–(PGE) deposits be determined? Perseverance, Agnew–Wiluna Belt, Western Australia. Australian Journal of Earth Sciences 50(2), 199-214.

Trofimovs, J., Davis, B. K., Cas, R. A. F., 2004. Contemporaneous ultramafic and felsic intrusive and extrusive magmatism in the Archaean Boorara Domain, Eastern Goldfields Superterrane, Western Australia, and its implications. Precambrian Research 131(3), 283-304.

Trofimovs, J., Davis, B. K., Cas, R. A. F., Barley, M. E., Tripp, G. I., 2006. Reconstructing the event stratigraphy from the complex structural–stratigraphic architecture of an Archaean volcanic–intrusive–sedimentary succession: the Boorara

Domain, Eastern Goldfields Superterrane, Western Australia. Australian Journal of Earth Sciences 53(2), 303-327.

Weinberg, R. F., Moresi, L., van der Borgh, P., 2003. Timing of deformation in the Norseman-Wiluna belt, Yilgarn Craton, Western Australia. Precambrian Research 120(3), 219-239.

Whitford, D. J., Korsch, M. J., Porritt, P. M., Craven, S. J., 1988. Rare-earth element mobility around the volcanogenic polymetallic massive sulfide deposit at Que River, Tasmania, Australia. Chemical Geology 68(1), 105-119.

Winchester, J. A., Floyd, P. A., 1977. Geochemical discrimination of different magma series and their differentiation products using immobile elements. Chemical Geology 20, 325-343.

Woodhead, J. D., 1988. The origin of geochemical variations in Mariana lavas: a general model for petrogenesis in intra-oceanic island arcs? Journal of Petrology 29(4), 805-830.

Wyman, D. A., 2013a. A critical assessment of Neoarchean "plume only" geodynamics: Evidence from the Superior Province. Precambrian Research 229, 3-19.

Wyman, D. A., Kerrich, R., 2012. Geochemical and isotopic characteristics of Youanmi terrane volcanism: the role of mantle plumes and subduction tectonics in the western Yilgarn Craton. Australian Journal of Earth Sciences 59(5), 671-694.

Paper 3 – U-Pb dating constraints on the felsic and intermediate volcanic sequence of the nickel-sulphide bearing Cosmos succession, Agnew-Wiluna greenstone belt, Yilgarn Craton, Western Australia

A. de Joux[1], T. Thordarson[1*], M. Denny[2**], R. W. Hinton[1], and A. J. de Joux[2***]

[1]School of GeoSciences, University of Edinburgh, Grant Institute, The King's Buildings, West Mains Road, Edinburgh, EH9 3JW, UK

[2]Xstrata Nickel Australasia, 24 Outram Street, Level 3, West Perth, Western Australia 6005, Australia

*Faculty of Science, University of Iceland, Sturlugata 7, IS101, Reykjavik, Iceland

**Phosphate Australia, PO Box 1235, West Perth, WA 6872, Australia

***Deno Gold Mining Company, 4 Gortsaranayin Street, Kapan, Armenia

Published in Precambrian Research v236, pp85–105.

- T. Thordarson provided supervision plus editorial comments and guidance on how to structure the paper
- M. Denny provided editorial comments and contributed ideas and discussion on the AM5 "reactivation" contact
- R.W. Hinton helped run the SIMS analyses and provided help with the methods section and during data processing
- A.J. de Joux provided editorial comments

Chapter 4 - U-Pb dating constraints on the felsic and intermediate volcanic sequence of the nickel-sulphide bearing Cosmos succession, Agnew-Wiluna greenstone belt, Yilgarn Craton, Western Australia

4.1 Abstract

The Cosmos succession, within the Agnew-Wiluna greenstone belt of the Yilgarn Craton, consists of ultramafic, intermediate and felsic volcanic lithologies, and contains several komatiite-hosted nickel sulphide ore bodies. The volcanic succession that forms the stratigraphic footwall to the mineralised komatiite lavas consists of an intercalated sequence of fragmental and coherent extrusive lithologies, ranging from basaltic andesites through to rhyolites. It also contains cross cutting felsic intrusions. The stratigraphic hangingwall consists largely of reworked volcanic-derived sedimentary rocks that include polymictic conglomerates containing granitic clasts.

SIMS U–Pb dating was undertaken on zircons from nine felsic lithologies spanning the established stratigraphy. The footwall succession gives emplacement ages ranging from 2736 ± 4 to 2724 ± 5 Ma. The overlying Cosmos Ultramafic Sequence consists of two units; the basal ultramafic UMu1 package and the upper ultramafic UMu2 package, which are separated by a discontinuous felsic volcanic horizon that sits approximately 30 – 60 m above the basal contact of the Cosmos Ultramafic Sequence. This discontinuous felsic horizon is dated at 2685 ± 8 Ma and represents a break in accumulation of komatiite lavas and may be associated with a major hiatus. The succession also features two felsic intrusions emplaced at 2653 ± 7 Ma and 2670 ± 6 Ma, where the latter cross-cuts the upper contact of the UMu2 package. These results bracket the age of UMu1 package between 2724 ± 5 Ma and 2685 ± 8 Ma and that of UMu2 package between 2685 ± 8 Ma and 2670 ± 11 Ma. This stratigraphic division of the Cosmos ultramafic is further strengthened by the contrasting styles of mineralisation above and below the discontinuous felsic horizon and associated unconformity; UMu1 hosts several massive nickel sulphide deposits situated at the contact with the footwall volcanic succession, while UMu2 is typified by high-tenor disseminated nickel sulphide deposits situated just above the discontinuous felsic horizon. This data indicates that the Cosmos volcanic succession was accumulated via punctuated volcanism spanning ~50 Ma that was followed by intrusive activity lasting for at least a further 32 Ma. The results also imply that construction of this relatively small, mineralised greenstone succession lasted longer than anticipated on stratigraphic considerations alone, an outcome that may have implications for the timing of emplacement of other bimodal volcanic successions in similar greenstone terranes.

4.2 Introduction

SHRIMP U–Pb ion-probe analysis of zircons has been used extensively over the last 20 years to establish the geological and metamorphic framework for the Yilgarn Craton of Western Australia (e.g., Nelson, 1997a, Nelson, 1997b, Cassidy et al., 2006, Kositcin et al., 2008, Goscombe et al., 2009 and Czarnota et al., 2010). As a result, the large-scale volcanic and tectonic evolution of the Yilgarn Craton is relatively well understood (e.g., Kositcin et al., 2008; Fig. 4.1). However, high-resolution dating of individual successions is necessary for evaluating the timing and longevity of volcanism on the terrane scale. Hitherto, such high-resolution dating has not been attempted, in part because surface outcrops are geographically sparse, often deeply weathered or difficult to access due to issues related to mining tenures. Consequently, it has been difficult to reconstruct in detail the evolution of specific greenstone successions (Liu et al., 2002). The potential zircon yield of individual volcanic successions is an added concern, because zircon is not ubiquitous within crustal rocks and is most common as a crystalizing phase in andesites to low-silica rhyolites (Watson, 1979, Watson and Harrison, 1983; Hoskin and Schaltegger, 2003).

The purpose of this study is to present new age constraints for the Cosmos volcanic succession in the Agnew-Wiluna greenstone belt (AWB), within the Kalgoorlie Terrane of the Eastern Goldfields Superterrane (EGS) (Fig. 4.1 and Fig. 4.2). Nine different zircon-bearing lithologies within the succession have been U–Pb dated, representing the volcanic stratigraphic footwall and sedimentary stratigraphic hangingwall, along with two felsic porphyry intrusions. The results indicate that the construction of the Cosmos succession took at least 80 million years, featuring episodic extrusive volcanism separated by periods of non-deposition, including three distinct phases of komatiite eruption. This has important implications for geological interpretation of the sulphide-hosting Cosmos ultramafic system. I discuss the implications of my results for constraining the Archaean volcanic environment that produced the Cosmos succession, as well as other bimodal felsic-ultramafic successions within the Yilgarn Craton. To the best of my knowledge this is the first

time that the age of a continuous volcanic succession has been constrained in this manner within this region.

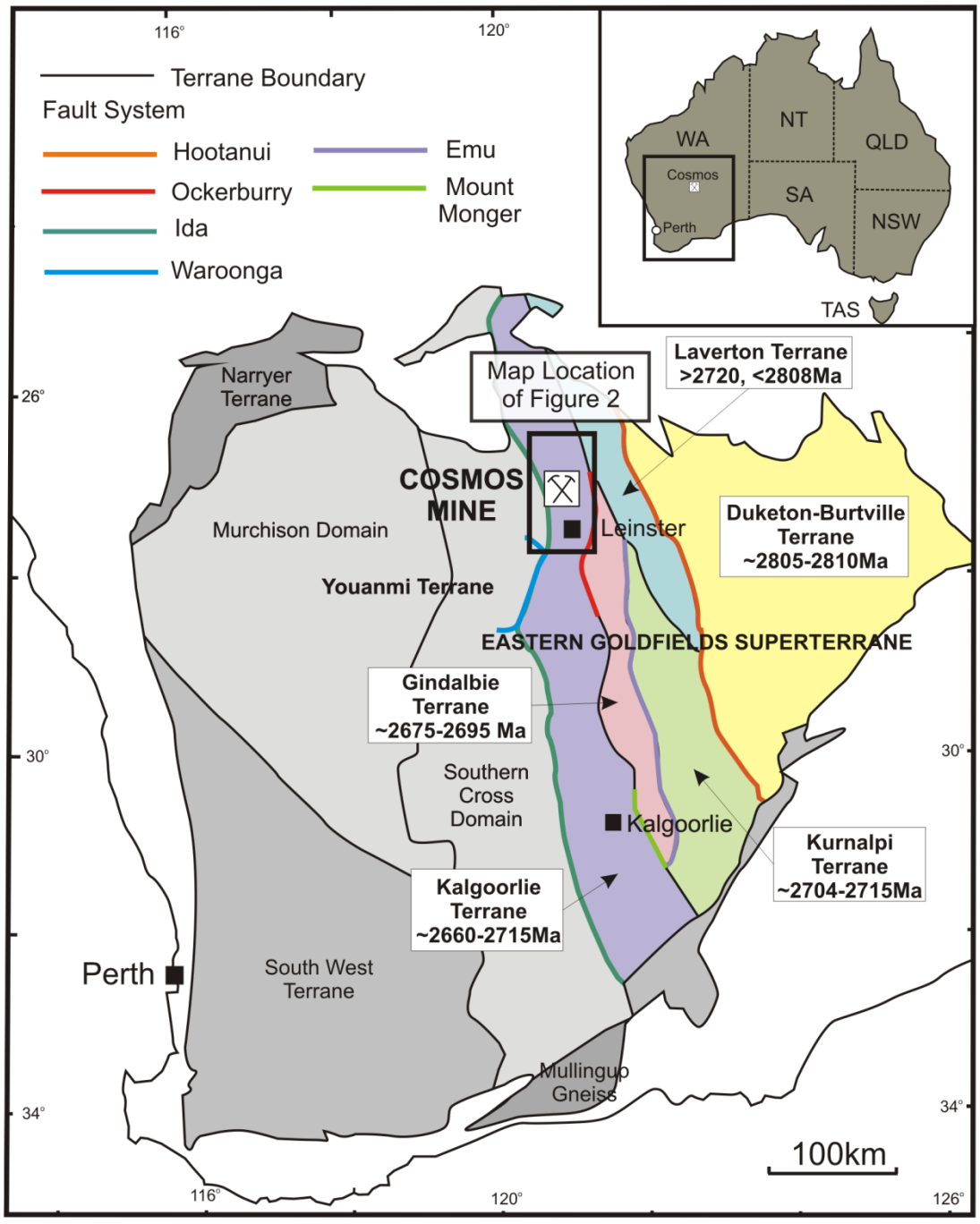

Figure. 4.1. Simplified terrane map of the Yilgarn Craton showing the location of the Cosmos Nickel Mine on the western edge of the Eastern Goldfields Superterrane (modified after Cassidy et al., 2006). Approximate age ranges are shown for the main terranes that make up the EGS (Kositcin et al., 2008 and references therein).

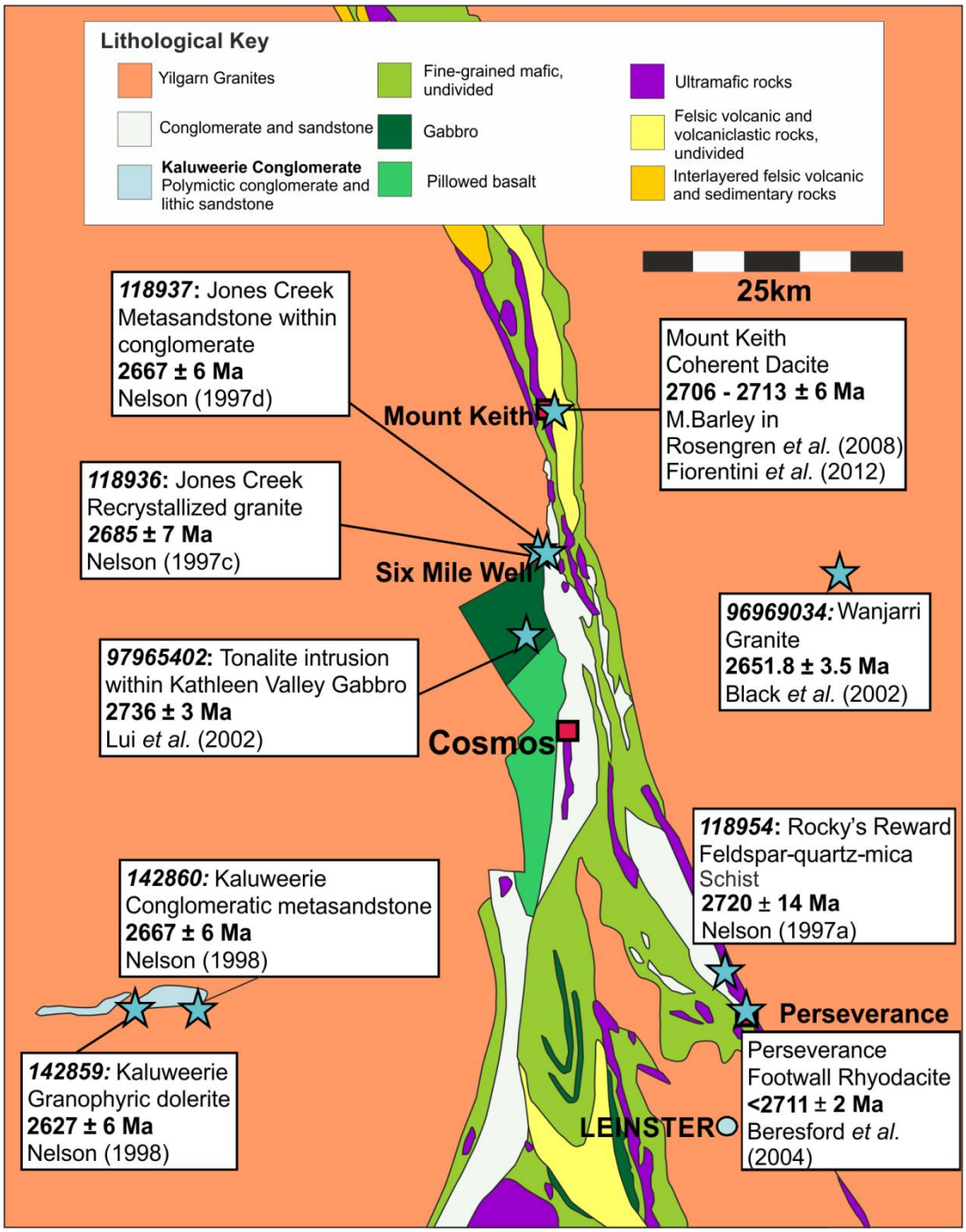

Figure 4.2. Simplified Geological Map of the Agnew-Wiluna Greenstone belt (covering the Sir Samuel sheet area 1:250,000) showing the location of current dates obtained for various lithologies in the region and the major nickel sulphide mines in the region (modified from Geological Survey of Western Australia, Compilation of geochronology data, 2009 update).

4.3 Background

4.3.1 Regional geology and dating

The Archaean Yilgarn Craton of Western Australia (Fig. 4.1) contains some of the World's most economic nickel sulphide deposits including Mount Keith, Perseverance and Yakabindie in the AWB (Fig. 4.2). The majority of these are hosted by thick ultramafic units interpreted to represent preferred lava pathways within large komatiite flow fields constructed by endogenous growth and flow inflation (Hill et al., 1995; 2004; Barnes, 1998, Barnes, 2006; Hill, 2001, Dowling et al., 2004; Arndt et al., 2008). In extrusive settings the komatiite lava is considered to reach sulphur saturation by the thermal and mechanical erosion of an underlying, often felsic substrate, promoting formation of immiscible sulphides that, when concentrated and enriched in chalcophiles such as nickel, form significant sulphide deposits (Naldrett, 2004, Hill et al., 2004, Barnes, 2006; Arndt et al., 2008). Alternative views have recently been presented, suggesting that significant proportions of the ultramafic units within the Kalgoorlie Terrane were emplaced as sills (Fiorentini et al., 2007; 2012; Rosengren et al., 2007; 2008). However this is of little concern here as it has no bearing on the dominantly extrusive volcanic Cosmos succession under consideration.

The Yilgarn Craton consists of metavolcanic and metasedimentary rocks, granites and granitic gneisses formed between 3050 and 2620 Ma (Fig. 4.1). The EGS, which comprises the eastern part of the Craton, features linear, bimodal (mafic–ultramafic and felsic) volcanic greenstone belt sequences, with clastic sedimentary sequences and banded iron formations forming minor components (Nelson, 1998). The greenstone belts are sandwiched between voluminous elongate granitoid bodies, which were intruded between 2760 and 2620 Ma (Cassidy et al., 2006; Fig. 4.1). SHRIMP U–Pb zircon data indicates a major peak in volcanism between 2720 and 2650 Ma, with second-order peaks at 2950 Ma and 2810 Ma (Nelson, 1997b, Cassidy et al., 2006; Kositcin et al., 2008). Ore-hosting ultramafic units within the Kalgoorlie terrane of the EGS have a modal emplacement age of ~2707 Ma (Kositcin et al., 2008).

4.3.2 Current dating constraints within the Agnew-Wiluna greenstone belt

The Cosmos mine site is situated in the eastern part of the Yilgarn Craton, within the AWB of the Kalgoorlie Terrane (Fig. 4.1 and Fig. 4.2). Prior to this study no dates existed for the Cosmos volcanic succession. Geochronology in the surrounding AWB is confined to a few isolated dates that do not allow for effective correlation between terranes and thus the age range of the greenstone belts within the surrounding Sir Samuel area is poorly constrained (Liu et al., 2002; Fig. 4.2). Reassessment of Archaean tectonostratigraphic architecture in the EGS by Kositcin et al. (2008) combined new U–Pb dating with existing age data. The compiled data confirmed an age range of 2715 – 2660 Ma for the felsic volcanic suites, which in the Kalgoorlie Terrane are commonly associated with mineralised ultramafic sequences (Fig. 4.1). Older terranes and domains (>2720 Ma) are identified in the Northern part of the Kalgoorlie Terrane, including the Yakabindie Domain and the Agnew Complex (Kositcin et al., 2008). A tonalite intrusion within the Kathleen Valley Gabbro in the Yakabindie Domain, just to the north of the Cosmos succession, has an age of 2736 ± 3 Ma (Liu et al., 2002; Black et al., 2002; Fig. 4.2). The Yakabindie Domain is regarded as a separate structural terrane that is faulted against the Cosmos succession (Kositcin et al., 2008; Andrew de Joux, pers comm., 2012). Deformed felsic volcanic schist in the Agnew Domain, present deep within the footwall to the ultramafic unit at Rocky's Reward has a poorly constrained SHRIMP $^{207}Pb/^{206}Pb$ age of 2720 ± 14 Ma (Nelson, 1997a; Fig. 4.2). Dating of a footwall rhyodacite at the adjacent Perseverance mine produced individual zircon ages ranging from 2742 to 2711 Ma (Beresford et al., 2004; Duuring et al., 2012), which led the authors to conclude that 2711 Ma is the minimum age for the Perseverance footwall. However, only four individual zircons were measured in this study, giving contrasting age estimates, and thus the results should be viewed with caution. The mineralised ultramafic sequence, along with the footwall and hangingwall dacites, at Mount Keith yielded Re/Os isotopic ages and

SHRIMP U–Pb ages in the range of 2706 and 2713 Ma, indicating that it was part of the '2707 Ma modal-age' volcanism (Foster et al., 1996, Rosengren et al., 2008; Fiorentini et al., 2012). Granitic rocks in the area are generally younger than the greenstones, ranging from ~2685 to 2650 Ma (Champion and Sheraton, 1997; Nelson, 1997c; Nelson, 1998; Fig. 4.2).

4.4 Geology of the Cosmos Succession

The Cosmos succession consists of ultramafic, intermediate and felsic lithologies, and contains several massive and disseminated high-grade, nickel-sulphide ore bodies (Fig. 4.3 and 4.4). These ore bodies are generally located close to, or at the base of, thick olivine meso-adcumulates, commonly bounded by orthocumulates and spinifex-textured horizons that have been pervasively serpentinised and overprinted by metamorphic olivine (Hill and Dowling, 2008). The ultramafic sequences are considered to have formed in preferred lava pathways based on: (i) the observed spatial association of sulphide-hosting adcumulate bodies with thin, low magnesium flow units (interpreted to represent metamorphosed equivalent of orthocumulate and spinifex textured horizons), (ii) internal and distal komatiite stratigraphy, and (iii) numerous complex komatiite-felsic relationships (Langworthy and Vallance, 2004; Hill and Dowling, 2008; Kaye et al., 2010; 2011; Stuff, 2011).

The succession has undergone at least four phases of regional deformation (Kositcin et al., 2008, Goscombe et al., 2009; Stuff, 2011), resulting in the succession being orientated sub-vertically, dipping and younging to the east. New garnet-biotite geothermometry, coupled with metamorphic mineral assemblage, indicates a peak metamorphic temperature of 560 – 580 °C at a pressure of ~3 kbar (Hill and Dowling, 2008; Chapter 3). Despite this regional amphibolite metamorphism, many of the stratigraphic footwall lithologies exhibit primary igneous textures enabling protolith identification. For this reason, protolith rock nomenclature is used here for stratigraphic units where primary textures are preserved. However, more subtle

structures such as internal bedding/laminations and textures of fine grained fragmental rocks are generally obscured by the metamorphism, making the exact mode of emplacement or assessment of possible re-sedimentation hard to ascertain. Thus, for fragmental deposits with clear indication of primary volcanic origin, I use the volcaniclastic nomenclature of Fisher (1961) without the prefix 'meta-' (see Appendix 5). Volcaniclastic is used for fragmental units containing identifiable fragments of volcanic rocks but of uncertain origin while units suspected to be clastic in origin are simply referred to as fragmental rocks. It should be noted that there is little to no outcrop within the Cosmos North area and interpretation of the stratigraphy has been established by sub-surface correlation and interpretation of over 100 diamond drill holes.

The footwall to the Cosmos nickel sulphide deposits comprises an intricate succession of fragmental and coherent extrusive lithologies, ranging in composition from basaltic andesites to rhyolites, as well as later-formed felsic intrusions. The key aspects of the stratigraphy are outlined below and illustrated in Fig. 4.3 and Fig. 4.4. The stratigraphic thickness of the volcanic footwall succession to the Cosmos nickel-sulphide deposits is more than 300 m (Fig. 4.3). However, in the southern part of the study area its thickness is reduced to ~100 m although in this area drilling rarely extended more than 100 m beyond the target basal contact of the mineralised Cosmos Ultramafic Sequence. Consequently, the footwall succession could be considerably thicker (Fig. 4.3). The hangingwall succession consists largely of reworked volcanic-derived sedimentary rocks and is over 300 m in stratigraphic thickness (Fig. 4.3). Although the area studied in detail here was focussed over 1 km of strike, in the vicinity of major ore bodies, the Cosmos greenstone belt itself has a strike length of over 5 km.

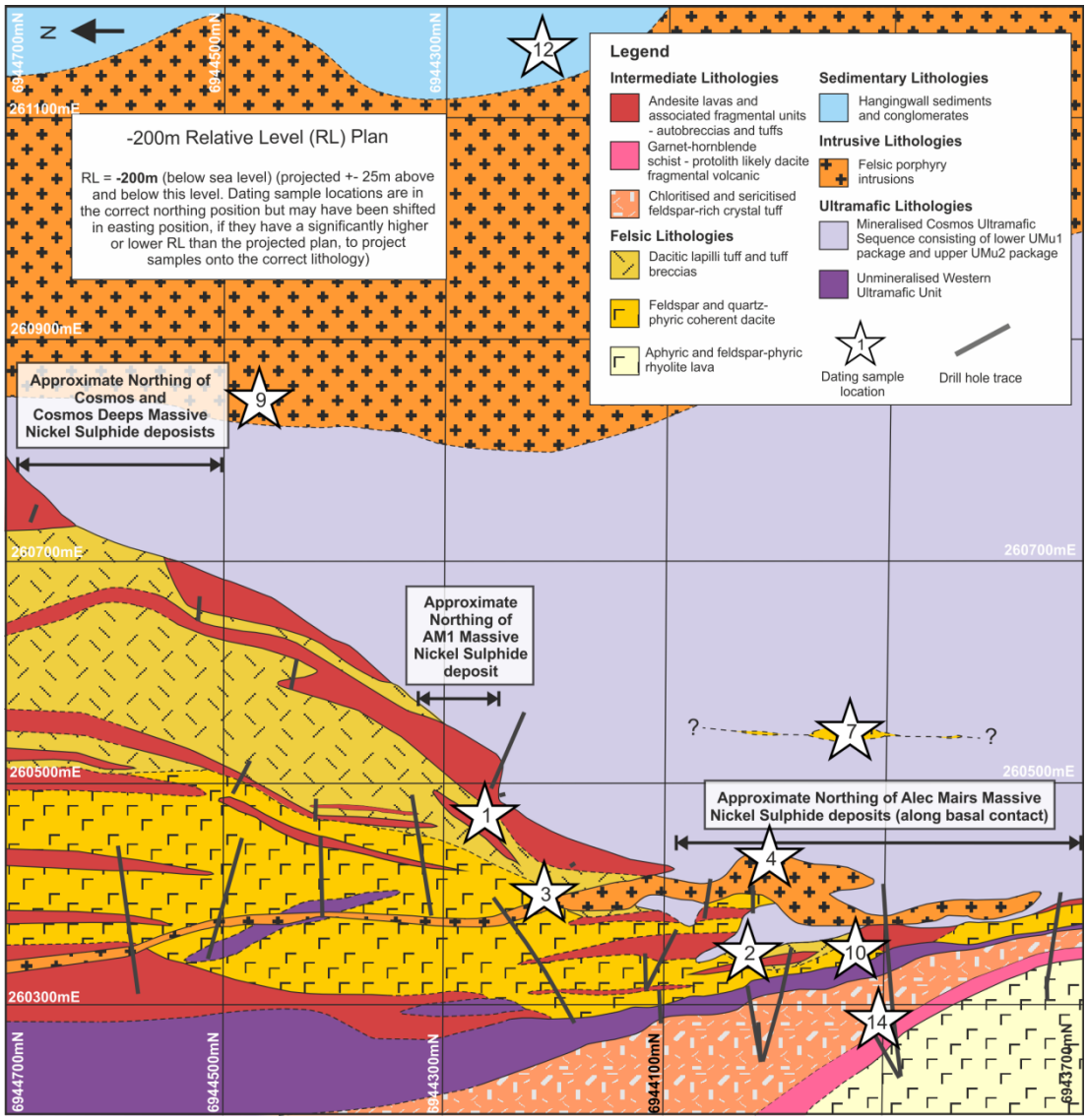

Figure 4.3. Level Plan at -200m (±25m) BSL (below sea level) through the Cosmos succession showing the mapped lithologies interpreted from diamond drillhole logging and the approximate projection of the stratigraphic location of successfully dated samples. As the Cosmos succession is orientated sub-vertically, dipping steeply to the east, a level plan in this orientation represents what an east-west cross section through the originally stratigraphy may have resembled.

Figure 4.4. (Next Page). Generalised Vertical Section through the Cosmos succession showing the stratigraphic location of the successfully dated samples, along with hand specimen examples of each lithology. The basal contact of the rhyolite has not yet been intersected by current drilling. Thickness of each unit is variable along the strike of the greenstone belt so approximate depths have been used.

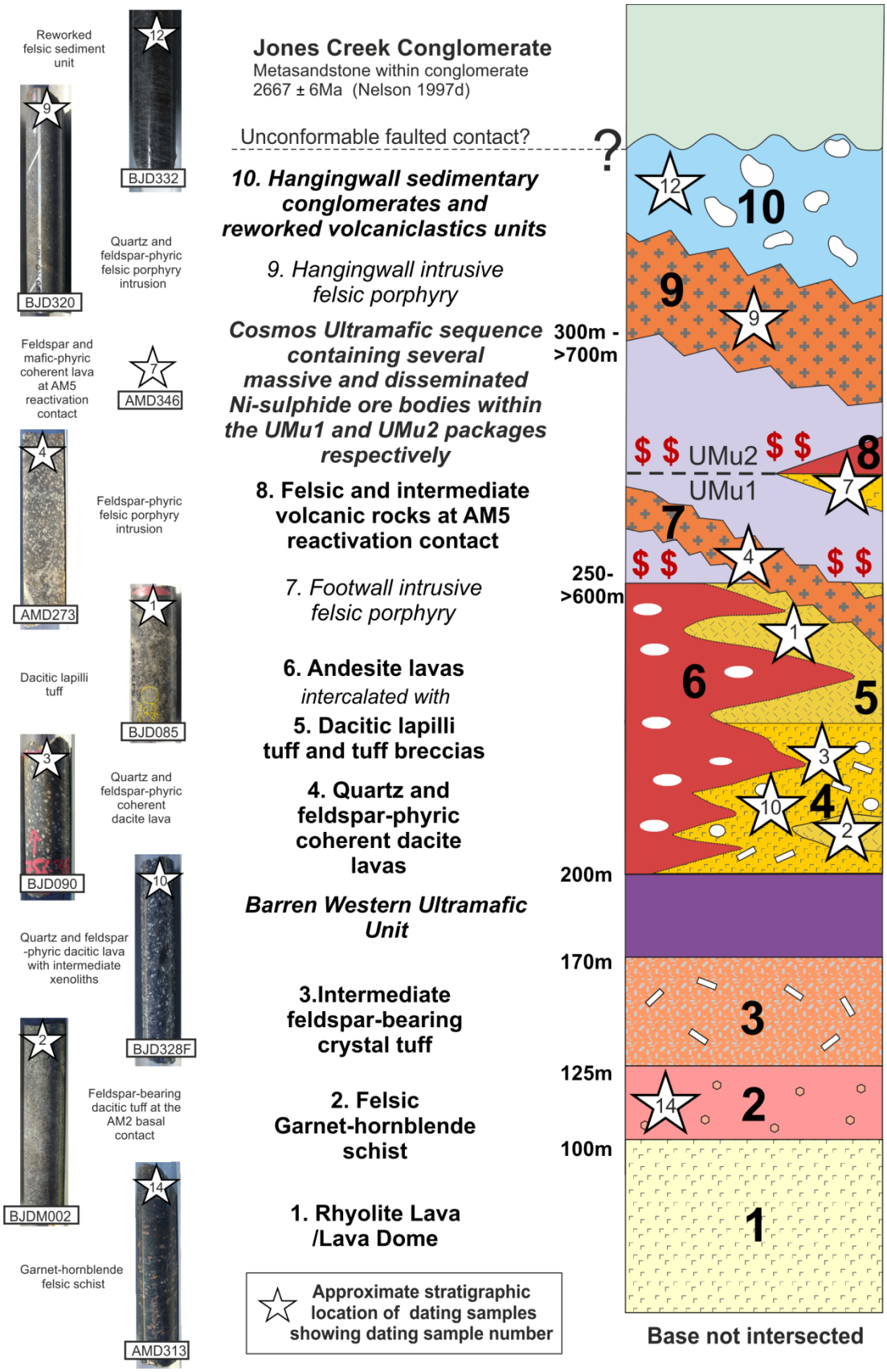
Reworked felsic sediment unit
BJD332
Quartz and feldspar-phyric felsic porphyry intrusion
BJD320
Feldspar and mafic-phyric coherent lava at AM5 reactivation contact
AMD346
Feldspar-phyric felsic porphyry intrusion
AMD273
Dacitic lapilli tuff
BJD085
Quartz and feldspar-phyric coherent dacite lava
BJD090
Quartz and feldspar -phyric dacitic lava with intermediate xenoliths
BJD328F
Feldspar-bearing dacitic tuff at the AM2 basal contact
BJDM002
Garnet-hornblende felsic schist
AMD313
Jones Creek Conglomerate
Metasandstone within conglomerate
2667 ± 6Ma (Nelson 1997d)
Unconformable faulted contact?
10. Hangingwall sedimentary conglomerates and reworked volcaniclastics units
9. Hangingwall intrusive felsic porphyry
Cosmos Ultramafic sequence containing several massive and disseminated Ni-sulphide ore bodies within the UMu1 and UMu2 packages respectively
300m - >700m
8. Felsic and intermediate volcanic rocks at AM5 reactivation contact
7. Footwall intrusive felsic porphyry
6. Andesite lavas
intercalated with
5. Dacitic lapilli tuff and tuff breccias
250- >600m
4. Quartz and feldspar-phyric coherent dacite lavas
Barren Western Ultramafic Unit
200m
170m
3.Intermediate feldspar-bearing crystal tuff
125m
2. Felsic Garnet-hornblende schist
100m
1. Rhyolite Lava /Lava Dome
Approximate stratigraphic location of dating samples showing dating sample number
UMu2
UMu1
Base not intersected

4.4.1 Footwall to the Western Ultramafic Unit

Lowest in the stratigraphy is a feldspar-phyric coherent rhyolite containing 1–3 mm feldspar phenocrysts within a fine-grained groundmass (Fig. 4.3 and Fig. 4.4). Textural properties of the groundmass are consistent with devitrification and subsequent metamorphism of silicic glass, indicating that this unit was emplaced as lava.

Overlying the feldspar-phyric rhyolite is a garnet-hornblende felsic schist with no primary volcanic textures preserved, making texture-based protolith determination challenging. The schist has rhyodacite-like composition with a geochemical signature very similar to the overlying dacites (Fig. 4.5) therefore this unit likely represents a strongly metamorphosed fragmental volcanic sequence. Overlying the garnet-hornblende schist is a strongly chloritised, intermediate, crystal tuff featuring abundant broken feldspar crystals. This unit is interpreted as being the product of an explosive eruption of feldspar-phyric andesite and is overlain by the barren Western Ultramafic Unit. This unit consists of olivine mesocumulates and orthocumulates, which have undergone pervasive serpentinisation obscuring the primary cumulate textures. This unit ranges in thickness from 5 to >100 m. The stratigraphic thickness of the footwall succession beneath the Western Ultramafic Unit is at least 100 m (Fig. 4.3).

Figure 4.5 (Next page). Discrimination diagrams showing the compositional fields of the extrusive footwall lithologies. (A) Immobile elements Zr/TiO_2 and Nb/Y discrimination diagram showing the composition of the six main footwall lithologies along with the two felsic porphyry intrusions and the volcanic rocks along the AM5 reactivation contact (after Winchester and Floyd, 1977). The total alkali vs. silica (TAS) diagram cannot be used for classifying rocks within the succession due to major element mobility during metamorphism and deformation. (B) Sr/Y vs. Y diagram of Defant and Drummond (1990) to highlight the island-arc affinity of the volcanic footwall rocks underlying the Western and Cosmos Ultramafic sequences as well as the volcanic rocks along the AM5 reactivation contact. Moyen and Martin (2012) recently reviewed 40 years of (tonalite–trondhjemite–granodiorite) TTG research and concluded that modern adakite arc lavas are reasonably close equivalents to Archaean TTGs thus the Adakite field, as originally defined by Defant and Drummond (1990), is also applicable to distinguish Archaean rock with a TTG affinity, such as the two felsic porphyry intrusions, which are demonstrably distinct from the rest of the volcanic footwall succession.

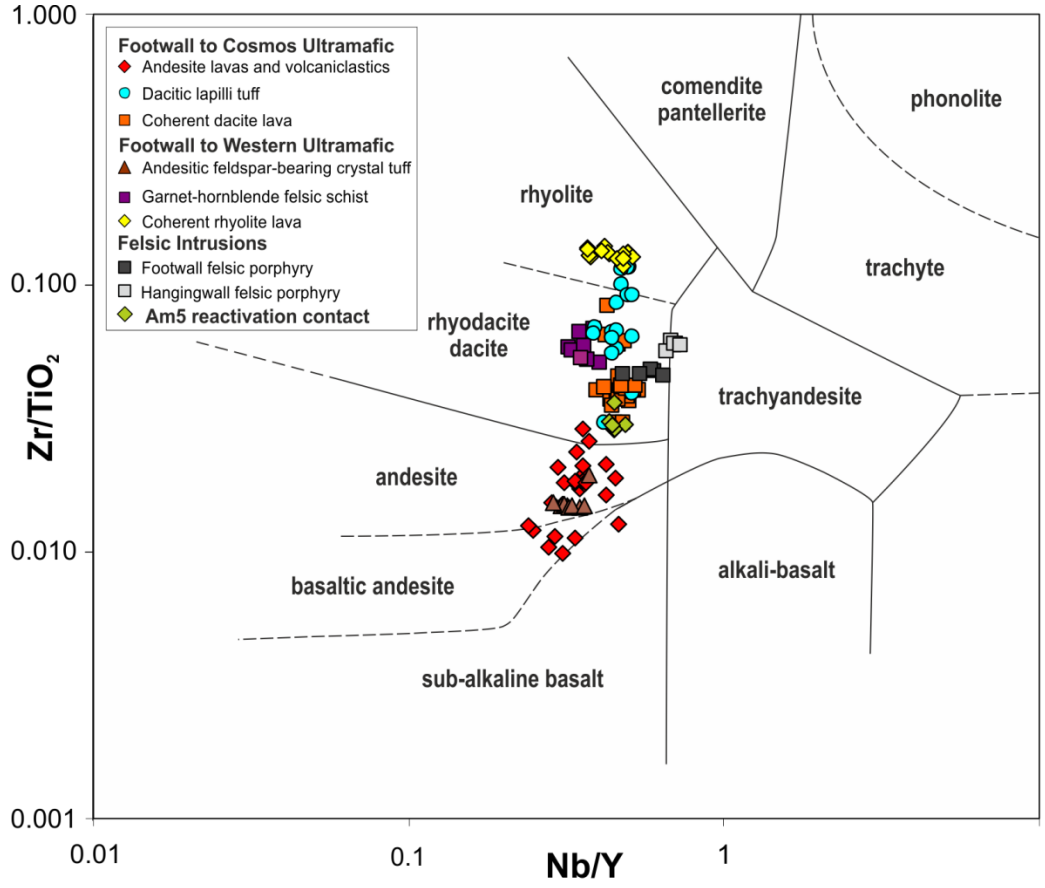
Footwall to Cosmos Ultramafic
Andesite lavas and volcaniclastics
Dacitic lapilli tuff
Coherent dacite lava
Footwall to Western Ultramafic
Andesitic feldspar-bearing crystal tuff
Garnet-hornblende felsic schist
Coherent rhyolite lava
Felsic Intrusions
Footwall felsic porphyry
Hangingwall felsic porphyry
Am5 reactivation contact
comendite
pantellerite
phonolite
rhyolite
trachyte
rhyodacite
dacite
trachyandesite
andesite
alkali-basalt
basaltic andesite
sub-alkaline basalt
Zr/TiO2
Nb/Y
1.000
0.100
0.010
0.001
0.01
0.1
1

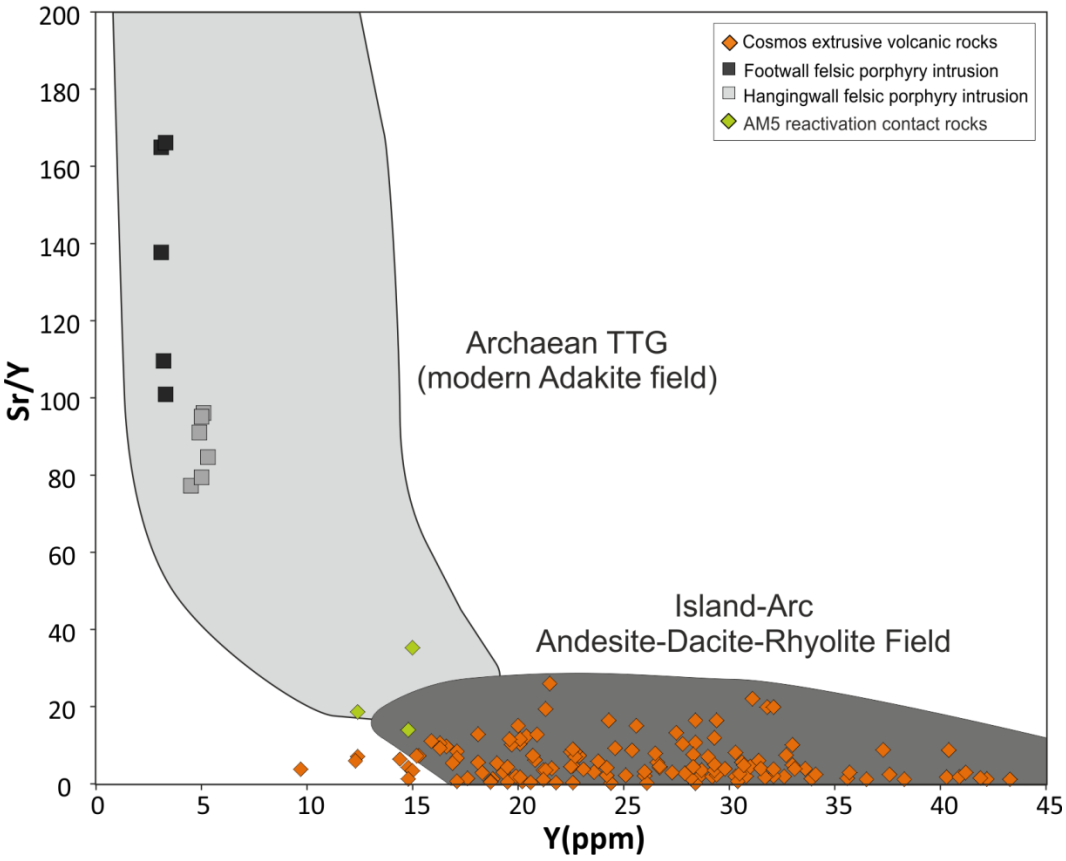
Cosmos extrusive volcanic rocks
Footwall felsic porphyry intrusion
Hangingwall felsic porphyry intrusion
AM5 reactivation contact rocks
Archaean TTG
(modern Adakite field)
Island-Arc
Andesite-Dacite-Rhyolite Field
Sr/Y
Y(ppm)
200
180
160
140
120
100
80
60
40
20
0
0
5
10
15
20
25
30
35
40
45

4.4.2 Footwall to the Cosmos Ultramafic Sequence

Above the barren Western Ultramafic unit is a sequence of coherent, quartz- and feldspar-phyric dacites intercalated with variably amygdaloidal andesite lavas and minor volcaniclastic andesite horizons. The presence of embayed quartz in the dacite indicates lava as the most likely protolith. Moving upward through the stratigraphy, this dacite lava sequence grades sharply into dacite tuff, commonly with well-preserved fragmental textures and still intercalated with andesite lavas (Fig. 4.3). This association implies an initial phase of near-coeval eruption of dacite and andesite lavas followed by a transition to alternating explosive dacite and effusive andesite volcanism. In terms of major, trace and rare earth element compositions, the dacites and andesites have sufficiently contrasting geochemical signatures that they are considered to be derived from separate sources and not related to one another by fractional crystallisation (Chapter 3; Fig. 4.5). This bi-modal andesite lava and dacitic tuff succession forms the immediate footwall to the Cosmos Ultramafic Sequence. It ranges in stratigraphic thickness from 30 m in the south to >250 m in the north part of the study area (Fig. 4.3 and Fig. 4.4).

The footwall volcanic successions to both the Cosmos and Western Ultramafic sequences exhibit a distinct island-arc affinity (Fig. 4.5b). Evidence of a submarine depositional environment, such as hydrovolcanic products (e.g., hyaloclastite) or marine sediments (e.g., black shales), commonly observed in adjacent greenstone terranes (e.g., Rosengren et al., 2008) is ubiquitously absent within the Cosmos footwall volcanic succession pointing towards eruption in a subaerial environment.

4.4.3 The mineralised Cosmos Ultramafic Sequence

The Cosmos Ultramafic Sequence attains a maximum thickness of 500 m in the south, thinning to <50 m in the northernmost sector of the study area (Fig. 4.3). In the Alec Mairs region (Fig. 4.3), Hill and Dowling (2008) identified an up-section

sequence of spinifex-textured komatiites, olivine-pyroxene cumulates, olivine orthocumulates, olivine mesocumulates and olivine adcumulates. The igneous assemblages of olivine-pyroxene-chromite-liquid have been metamorphosed to various proportions of metamorphic olivine, serpentines, amphiboles, pyroxene and chlorite. Thin units (<10 m) of spinifex-orthocumulate textured flow lobes have been positively identified immediately adjacent to footwall contacts at Alec Mairs (Fig. 4.3) underpinning the interpretation that the formation of the Cosmos Ultramafic Sequence began as a dynamic system of thin flows that, through continued eruption, evolved into a high-volume internal pathway and/or channelized flow field (Hill and Dowling, 2008; Denny, 2010). Hybrid rocks have also been identified close to the basal contact in the vicinity of the Alec Mairs (Hill and Dowling, 2008). These contaminated units are interpreted to represent komatiite lava involved in thermo-mechanical erosion of the underlying substrate (Hill and Dowling, 2008).

The AM5 "reactivation" contact defines two separate ultramafic units within the Cosmos Ultramafic Sequence, referred to here as the UMu1 and UMu2 ultramafic packages. The lower UMu1 package is 30 – 60m thick and typified by multiple units of serpenitinised mesocumulates and adcumulates that are sporadically intercalated with and often underlain by compound low-MgO spinifex-orthocumulate komatiite flow lobes in the vicinity of the footwall contact (Hill and Dowling, 2008; Denny, 2010). The upper UMu2 package consists of serpentinised olivine adcumulates and mesocumulates, commonly with compound low-MgO spinifex-orthocumulate komatiite flow lobes at its base. It attains thicknesses of >300 m.

4.4.4 The AM5 "reactivation" contact

A cryptic patchy intermediate and felsic horizon, referred to as the AM5 "reactivation" contact, is present within the Cosmos Ultramafic Sequence. It defines the contact between the earlier UMu1 komatiite package and the later UMu2 komatiite package and is interpreted as an in situ volcanic deposit representing a significant break in komatiite lava emplacement (Denny, 2010; Stuff, 2011). The volcanic rocks

along the AM5 "reactivation" contact are composed of feldspar-phyric coherent dacites as well as heterogeneous andesite–dacite crystal tuffs. Although the occurrence of felsic lithologies is patchy along the AM5 "reactivation" contact they are up to 6–10 m thick when present. The base of the UMu2 package in direct contact with the felsic lithologies at the "reactivation" contact is invariably comprised of low MgO spinifex-orthocumulate komatiite flow lobes. Where felsic lithologies are not present at the AM5 "reactivation" contact, the low MgO horizons are in sharp contact with the underlying high MgO mesocumulates and adcumulates (35 – 50 wt% MgO) of the UMu1 package. This demonstrates that the AM5 "reactivation" contact is expressed within the ultramafic sequence itself, even when felsic lithologies are absent. Locally the low MgO komatiites contain euhedral plagioclase phenocrysts and are interpreted to represent contaminated ultramafic lava that has thermally and mechanically eroded the heterogeneous andesitic and dacitic substrate, producing a hybrid melt along the basal contact (Denny, 2010).

Collectively the above features are consistent with the concept of the felsic horizon at the AM5 "reactivation" contact being a remnant of a concordant sequence and argues against an intrusive origin. This conclusion is further supported by the discontinuous and patchy nature of the felsic and intermediate volcanic rocks along the AM5 "reactivation" contact as well as the overall appearance, geochemical heterogeneity and architecture of these rocks. They markedly contrast the continuous, relatively un-deformed nature of the geochemically uniform hangingwall and footwall felsic porphyritic intrusions. Furthermore, the felsic volcanic rocks along the contact exhibit more of an island-arc affinity, similar to the rest of the extrusive volcanic footwall to the Cosmos and Western Ultramafic sequence, contrasting the two felsic porphyry intrusions that have a distinct tonalite–trondhjemite–granodiorite (TTG) affinity (Fig. 4.5b). Thus the patchy felsic horizon along the AM5 "reactivation contact" is taken here to be the remnant of a felsic volcanic package that was deposited after emplacement of the underlying UMu1 komatiite (Denny, 2010).

4.4.5 Nickel sulphide mineralisation within the Cosmos Ultramafic Sequence

Nickel sulphide mineralisation within the Cosmos Ultramafic Sequence occurs in three main areas between 6,943,700 mN and 6,944,700 mN, the approximate locations of which have been projected onto Fig. 4.3: (i) Cosmos and Cosmos Deeps, (ii) AM1 and Anomaly 1 (Mount Goode) (iii) the Alec Mairs complex. Massive and to a lesser extent felsic-breccia hosted nickel sulphide deposits occur close to the basal contact of the UMu1 package directly overlying the underlying dacitic and andesitic footwall. In contrast, the upper part of the Cosmos Ultramafic sequence, the UMu2 package, typically hosts high and low tenor disseminated ore bodies that sit above the AM5 "reactivation" contact. The most northerly deposit, Cosmos, is a typical komatiite-associated nickel sulphide deposit, with massive nickel sulphides accumulated within preferred pathway near the basal contact of the UMu1 package. Although compositionally and mineralogically similar and adjacent to the Cosmos deposit, the Cosmos Deeps deposit is unusual in being hosted entirely within a dacitic tuff breccia sequence, several tens of metres below the Cosmos UMu1 basal contact (Langworthy and Vallance, 2004; Stuff, 2011). AM1 is a relatively small pod of massive sulphide mineralization that sits directly on the basal contact of the UMu1 package. The Alec Mairs complex in the south of the studied region consists of several massive, breccia and stringer sulphide lenses situated on and below (within the dacitic tuffaceous footwall) the basal contact of the UMu1 package. The Alec Mairs complex also includes two high-tenor disseminated ore bodies hosted within the UMu2 package above the AM5 "reactivation" contact.

4.4.6 The sedimentary hangingwall succession

The Cosmos Ultramafic Sequence is overlain by a volcanic-derived sedimentary succession that includes polymictic conglomerates composed of sub-rounded granitic, felsic and intermediate clasts in an intermediate fine-grained matrix.

The evidence for a sedimentary origin is strong, including conglomerates containing rounded granitic clasts (which are entirely absent in the footwall) and common occurrences of laminated and banded sediments of intermediate composition. Furthermore, units featuring primary volcanic textures such as amygdaloidal lavas, autobreccias and lapilli tuffs have not been identified in the hangingwall sequence. The basal contact of this sedimentary package is commonly stoped out by the hangingwall felsic porphyry intrusion, but most likely has an unconformable contact with the underlying Cosmos Ultramafic Sequence (Fig. 4.3 and 4.4).

4.4.7 Felsic intrusions

The Cosmos volcanic and sedimentary succession is cross-cut by two felsic porphyry intrusions that climb through the volcanic sequence at a low angle. The upper intrusive 'hangingwall unit' is 100 – 300m thick and as mentioned above stopes out the contact between the hangingwall sequence and the UMu2 package (Fig. 4.3). The lower footwall intrusion is tens of metres thick and cross-cuts the basal contact of the UMu1 package in the region of Alec Mairs, where it splits massive sulphide mineralisation and displaces it for several tens of metres.

4.5 Methods

4.5.1 Sample locations

U–Pb zircon dating has been undertaken on samples collected from various lithologies and stratigraphic positions within the Cosmos succession. Details of their location, lithology and zircon yield can be seen in Table 4.1 and their projected stratigraphic position can be seen on Fig. 4.3 and Fig. 4.4. Overall fourteen samples were selected for analysis; five had no or very poor zircon yield and thus were excluded from the study. The nine remaining zircon-bearing samples were analysed for U–Pb.

These consisted of two dacitic tuffs (1.BJD085 and 2.BJDM002), two dacitic lavas (3.BJD090 and 10.BJD328F), two felsic porphyritic intrusions (4.AMD273 and 9.BJD320), a felsic schist (14.AMD313), a hangingwall volcanically-derived sediment (12.BJD332) and a coherent dacite from the AM5 "reactivation" contact (7.AMD346). Detailed U-Pb methodology can be found in Appendix 6.

Table 4.1. Summary of zircon separates returned with an appreciable zircon yield, correlating sample number with borehole ID and position, sample depth and zircon yields. Nine out of fourteen samples gave a suitable zircon yield for U-Pb analysis, the other five contained very little to no zircon and were excluded from the study.

Sample number	Hole ID	Sample Depth (m)	Easting (m)	Northing (m)	RL (m)	Description	Zircon yield
1	BJD085	452.3	260480	6944273	31	Dacitic lapilli tuff	Excellent
2	BJDM002	834.0	260365	6944018	-257	Dacitic lapilli tuff, immediate footwall to AM2 massive sulphide	Excellent
3	BJD090	756.4	260431	6944178	-269	Coherent dacitic feldspar and quartz-phyric lava	Excellent
4	AMD273	218.5	260477	6944029	-300	AM5 footwall felsic porphyry intrusion	Few Small with abundant titanite
7	AMD346	148.6	260537	6943930	-251	Feldspar phyric coherent lava at AM5 "reactivation" contact	Good
9	BJD320	467.7	260628	6944882	63	Hangingwall felsic porphyry intrusion	Some zircon
10	BJD328F	1142.5	260630	6943924	-660	Coherent feldspar and quartz phyric dacite with intermediate xenoliths	Excellent
12	BJD332	406.2	260950	6943015	118	Hangingwall re-worked felsic volcaniclastic sediments	Good - small
14	AMD313	77.2	260292	6943885	-268	Garnet-hornblende felsic schist (Footwall to Western Ultramafic Unit)	Very few, with abundant titanite

4.5.2 Sample preparation

Fourteen diamond drill core samples from a variety of locations and drill holes were sent to Geotrack International in Melbourne for zircon separation. Approximately 2 kg of each sample was crushed and milled with fine material then removed prior to heavy mineral separation. Frantz isodynamic magnetic separators and heavy liquid mineral separations were used to separate mineral grains by gravity and magnetic susceptibility. Table 4.1 details the concentration of zircons obtained from each sample.

Zircons from each sample separate were hand-picked and mounted in epoxy, sequentially in rows around a central row of the zircon standards of either 91500 ($^{206}Pb/^{238}U$ age −1062.5 Ma (Wiedenbeck et al., 1995) or GJ-1 ($^{206}Pb/^{238}U$ age – 600.4 Ma (Jackson et al., 2004). The mount was then polished to expose the zircon interiors.

4.5.3 Analytical methods

The characteristic features of individual zircons were mapped using backscattered electrons on a Philips XL30CP SEM as zircons were only weakly luminescent under cathodoluminescence. These mineral-maps were utilised to select zircons of a suitable size and morphology for analysis. Zircon mounts were gold-coated and selected zircons were analysed by SIMS (secondary ionising mass spectrometry) on a Cameca 1270 Ion microprobe for U–Pb.

Individual sessions lasted 5 to >24 h, depending on the beam conditions and analyses required in each session. Analysis of an individual zircon grain took ~30 minutes. In each session, standards were analysed at the beginning and the end, as well as between every third to fifth analysis of unknowns. Only standards analysed in a specific session were used when correcting the data obtained from the unknowns. Pb yield was enhanced by flooding the surface with oxygen (resulting in a factor of two increase in Pb intensity). A primary beam of ~5 nA $^{16}O_2^-$ created a beam diameter at

~30 μm. The surface was pre-cleaned using a 15 μm^2 raster for 2 minutes prior to starting each analysis.

Processing of raw data is as follows. A correction was applied for common Pb, ^{204}Pb. A correction for dead time was applied (electronically set 51 ns). 20 analytical cycles were taken for each sample, although the first five were not used in any subsequent data processing. The analysed Uranium content for each sample is based on the Uranium content of 91500, which is taken to be 81 ppm. The Uranium content was based on the UO_2/Zr_2O_2 ratio, measured in 91500. One mount contained only GJ1 and no 91500 thus the standard Uranium analysis was measured off mount on 91500, prior to the start of the session. The precise U/Pb ratio was corrected for changes in instrumental conditions using $\ln(^{206}Pb/^{238}U)$ vs. $\ln(^{238}UO_2/^{238}UO)$ and a slope factor of 2.6 (Kelly et al., 2008) and either 91500 or GJ-1 standards to derive the U/Pb ion yields.

4.6 Zircon morphology

The majority of zircons have prismatic or stubby prismatic forms with corroded pyramidal termination (Fig. 4.6a-d). Size varies between samples with lengths from <100 μm to 500 μm. Most of the zircon crystals exhibit concentric growth zoning and are strongly fractured on a variety of scales. Fractures originate at the interface with the more metamict domains, or higher uranium zones, or from high-U inclusions and develop radially outward across the low-U bands. Fractures were likely caused by differential metamictization (e.g., McLaren et al., 1994, Lee and Tromp, 1995; Corfu et al., 2003; Fig. 4.6). Fracturing also radiates outward to crystal edges more randomly from inclusions of apatite and biotite as well as radiating outwards from abrupt terminations in growth zones (Fig. 4.6d). As discussed in the following section the abundance and nature of fracturing (both aerially and with depth) made analysis by micro-beam essential. Even using a microbeam a number of analyses encountered fractures (indicated by detection of high common lead).

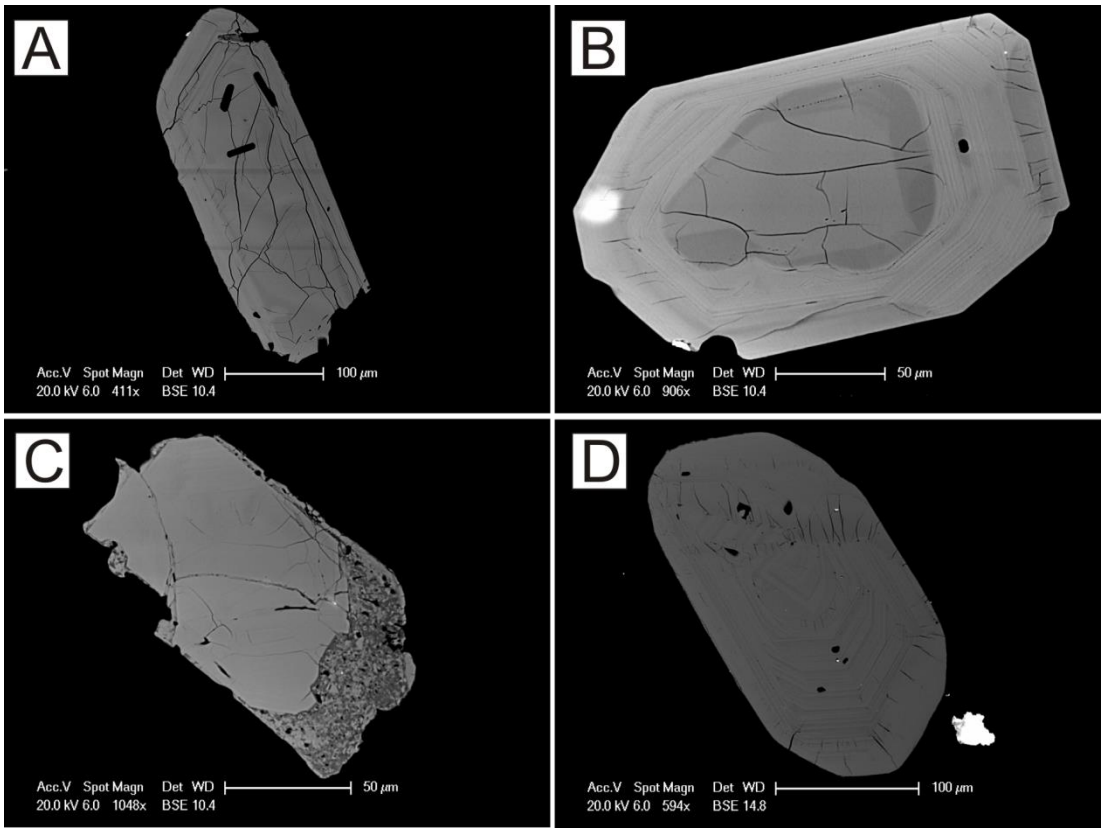

Figure. 4.6. Examples of zircon textures seen within dated samples: (A) strongly fractured euhedral zircon showing pervasive fractures radiating from elongate apatite inclusions (sample 7.AMD346); (B) Possible xenocrystic core within concentrically zoned stubby prismatic zircon. The central core is much darker, indicating it may have a higher uranium content, and also exhibits pervasive fractures that emanate/terminate at the boundary between the irregular, possibly magmatically resorbed core and the more uniformally zoned euhedral rim (sample 10.BJD328F); (C) Zircon exhibiting strongly metamict high uranium rim around a more uniform, fractured core (sample 12.BJD332); (D) stubby prismatic zircon showing clear fine concentric zoning with some abrupt zonation truncations and terminations indicative of multiple phases of crystal growth (sample 7.AMD346).

Zoning in several zircons is indistinct, suggesting there is only a small compositional difference between trace element rich and trace element poor bands (Corfu et al., 2003). Regular growth zoning can be seen to abruptly terminate in several crystals, which is indicative of multiple phases of crystal growth (Fig. 4.6d). Some zircons appear to have xenocrystic cores as implied by their difference in back scattered electron intensity and fracture abundance (McLaren et al., 1994). Their irregular sub-rounded outlines are also indicative of some resorbtion prior to growth of the outer zones, with later stage oscillatory zoning truncating zoning within the core (Fig. 4.6d). Half of the zircons in sample 12.BJD332 had highly distorted rims, with

sharp boundaries around concentrically zoned prismatic zircons (Fig. 4.6c). The alteration is probably related to the presence of high Uranium outer zones, which became metamict during diagenetic fluid ingress and subsequent metamorphism. Overall zircons within all samples exhibited primary magmatic prismatic forms with typical oscillatory growth zoning and lacked evidence of appreciable metamictisation and thus were suitable for U–Pb dating to establish magmatic formation ages for the Cosmos volcanic rocks.

4.7 Results

Zircon dating was performed on just under 150 zircons obtained from nine separate felsic units within the Cosmos succession. For samples with a low zircon yield, a relatively small fraction of the mounted zircons (~10 - 20 grains) were suitable for analysis due to abundant fracturing. Despite careful selection of the least fractured zircons approximately a third of the measured crystals had high common lead concentrations, due to undetected internal fractures. Invariably grains with high common lead were discordant. Zircons with common lead concentrations >8 ppb ^{204}Pb were not used in age calculations or accompanying concordancy plots and are thus not reported in Table 2. Analytical points deviating from concordia by greater than ± 3% (based on ^{206}Pb/^{238}U) were classed as discordant and not used in average age calculations, but are included on concordancy plots and appear in italics in Table 2. The analytical results in Table 4.2 report all concordant (non-italicised) and discordant (italicised) ages obtained from each sample.

Despite these difficulties, concordant dates were obtained for each of the nine analysed samples. Concordant ages obtained are interpreted to represent the time of crystallisation of the felsic volcanic units and felsic intrusions except for sample 12.BJD332, from the hangingwall sedimentary sequence, whose age is interpreted as a detrital age signature. The average population dates for each sample are summarised in Table 3, where they are listed in stratigraphic order. Three of the nine samples

yielded concordant ages that are not statistically robust. Hence, conclusions drawn from samples with less than five concordant ages should be given due caution. All population errors are given at 2σ within the text and on concordia plots, while for individual isotope ratios and ages in Table 2 the errors are reported at 1σ level. Fig. 4.7 shows the concordia plots for all samples.

The $^{207}Pb/^{206}Pb$ age for the Cosmos data set has average 2σ errors in the range of ~4 – 12 Ma, while errors are much larger on the $^{206}Pb/^{238}U$ ages, ranging from ~46 to ~68 Ma. The majority of the zircons are very slightly discordant, with arrays trending towards the present day rather than a distinct metamorphic event, resulting in almost all zircons within the succession lying just below concordia. The majority of the data line up parallel to this single recent Pb loss line and thus high precision $^{207}Pb/^{206}Pb$ ages where obtained by extrapolation to concordia. The $^{207}Pb/^{206}Pb$ ages are therefore more precise age determinations so these shall be referred to within the discussion.

The oldest rock within the succession, dated at 2736 ± 4 Ma (14.AMD313) is the garnet-hornblende felsic schist that sits within the footwall to the Western Ultramafic Unit (Fig. 4.3 and Fig. 4.4). Four dates were obtained from the footwall succession to the Cosmos Ultramafic UMu1 package; two from dacitic lavas (3.BJD090 and 10.BJD328F) giving ages of 2727 ± 7 Ma and 2729 ± 6 Ma, respectively, and two from dacitic tuffs (1.BJD085 and 2.BJDM002) with ages of 2724 ± 5 and 2730 ± 5 Ma, respectively. Concordant age determinations were obtained for a total of 15 zircons from Sample 10.BJD328F. Thus this sample's 2729 ± 6 Ma age represents the most statistically robust age and underpins the 2724 – 2730 ± 7 Ma age range for the dacitic sequence of the footwall succession. The overlying Cosmos Ultramafic Sequence is thus younger than 2724 ± 7 Ma, while the age of the Western Ultramafic Unit is between 2730 and 2736 Ma.

Table 4.2. – Ion probe analytical results for individual zircon analyses within samples 4.AMD273, 9.BJD320, 7.AMD346, 12.BJD332, 1.BJD085, 3.BJD090, 10.BJD328F, 2.BJDM002 and 14.AMD313, displayed in stratigraphic order from average youngest to oldest. Samples in italics are considered discordant and not included in the average age population calculations in Table 3. (R) in a sample name denotes zircon rim analysis, (C) denotes zircon core analysis.

Sample number	U (ppm)	Th (ppm)	Pb (ppm)	^{204}Pb (ppb)	^{207}Pb/^{206}Pb	± 1σ	^{208}Pb/^{206}Pb	± 1σ	^{207}Pb/^{235}U	± 1σ	^{206}Pb/^{238}U	± 1σ	^{206}Pb/^{238}U	± 1σ	^{207}Pb/^{235}U	± 1σ	^{207}Pb/^{206}Pb	± 1σ	% Concordance
4.AMD273																			
AMD273z7	274.7	87.6	154.0	3.8	0.17982	0.00038	0.08998	0.00039	12.6453	0.15588	0.51003	0.00619	2656.8	26.4	2653.6	11.5	**2651.0**	**3**	100.2
AMD273z4	373.5	139.9	213.5	3.9	0.18033	0.00043	0.10574	0.00030	12.7711	0.15561	0.51365	0.00613	2672.2	26.1	2662.9	11.4	**2655.0**	**4**	100.6
AMD273z10	745.0	88.5	400.8	5.5	0.18015	0.00041	0.03299	0.00009	12.7213	0.15696	0.51216	0.00621	2665.8	26.4	2659.2	11.5	**2654.0**	**3**	100.4
9.BJD320																			
BJD320z7	154.7	144.2	98.5	0.2	0.18192	0.00057	0.27861	0.00091	12.7723	0.16524	0.50919	0.00639	2653.2	27.3	2663.0	12.1	**2670.0**	**5**	99.4
BJD320z5	103.7	75.2	63.4	0.3	0.18125	0.00056	0.21620	0.00087	12.7455	0.17944	0.51000	0.00701	2656.6	29.8	2661.0	13.2	**2664.0**	**5**	99.7
BJD320z9	115.7	61.4	68.1	0.4	0.18088	0.00047	0.15302	0.00112	12.7539	0.21455	0.51138	0.00850	2662.5	36.2	2661.6	15.7	**2660.0**	**5**	100.1
BJD320z1	79.1	52.5	47.2	0.4	0.18177	0.00067	0.19452	0.00113	12.6126	0.19594	0.50323	0.00759	2627.7	32.5	2651.2	14.5	**2669.0**	**6**	98.5
BJD320zG	85.8	91.3	56.1	0.4	0.18175	0.00061	0.30192	0.00129	12.7645	0.20415	0.50935	0.00796	2653.9	33.9	2662.4	14.9	**2668.0**	**6**	99.5
BJD320zH	158.1	119.6	97.6	0.5	0.18173	0.00048	0.21389	0.00073	12.8011	0.20294	0.51087	0.00798	2660.3	34.0	2665.1	14.8	**2668.0**	**5**	99.7
BJD320zD	174.8	148.4	106.8	0.7	0.18122	0.00045	0.23862	0.00121	12.3999	0.19333	0.49626	0.00764	2597.7	32.8	2635.2	14.5	**2664.0**	**4**	97.5
BJD320z3	104.4	54.3	62.2	0.8	0.18472	0.00058	0.14638	0.00109	13.1690	0.16619	0.51705	0.00632	2686.7	26.8	2691.8	11.8	**2695.0**	**5**	99.7
BJD320z9	114.1	89.1	70.8	0.9	0.18207	0.00071	0.21878	0.00089	12.8283	0.16625	0.51101	0.00632	2660.9	26.9	2667.1	12.1	**2671.0**	**7**	99.6
BJD320z10	165.4	118.7	100.7	1.7	0.18190	0.00087	0.20319	0.00059	12.7411	0.16528	0.50801	0.00613	2648.1	26.1	2660.7	12.1	**2670.0**	**8**	99.2
BJD320z2	268.5	150.1	165.6	1.1	0.18744	0.00045	0.15524	0.00046	13.6979	0.17077	0.53001	0.00648	2741.5	27.3	2729.0	11.7	**2719.0**	**4**	100.8
BJD320z1a(C)	214.8	131.7	139.6	2.1	0.20117	0.00079	0.17041	0.00061	15.1733	0.19579	0.54705	0.00672	2812.9	27.9	2826.2	12.2	**2835.0**	**7**	99.2
BJD320z1b(R)	125.1	80.8	82.2	3.5	0.20012	0.00074	0.17967	0.00072	15.1807	0.19407	0.55016	0.00674	2825.8	27.9	2826.6	12.1	**2827.0**	**6**	100.0
BJD320zGb	*75.9*	*73.6*	*47.3*	*0.1*	*0.18179*	*0.00040*	*0.27421*	*0.00097*	*12.3837*	*0.19987*	*0.49405*	*0.00790*	*2588.2*	*34.0*	*2633.9*	*15.1*	***2669.0***	***3***	*97.0*
BJD320zI	*97.2*	*99.8*	*59.1*	*0.8*	*0.18075*	*0.00050*	*0.23188*	*0.00075*	*11.8753*	*0.18758*	*0.47650*	*0.00741*	*2512.0*	*32.3*	*2594.6*	*14.7*	***2659.0***	***5***	*94.5*
BJD320z6	*487.1*	*300.9*	*225.6*	*2.2*	*0.16679*	*0.00330*	*0.15977*	*0.00162*	*9.1401*	*0.56313*	*0.39745*	*0.02319*	*2157.3*	*106.1*	*2352.1*	*54.9*	***2525.0***	***33***	*85.4*
BJD320z7	*750.6*	*344.2*	*179.7*	*3.0*	*0.12887*	*0.00067*	*0.13419*	*0.00055*	*3.8721*	*0.05585*	*0.21793*	*0.00293*	*1270.9*	*15.5*	*1607.9*	*11.6*	***2082.0***	***9***	*61.0*
7.AMD346																			
AMD346z2	203.1	81.0	115.4	0.3	0.18487	0.00094	0.12003	0.00226	12.8883	0.30387	0.50563	0.01164	2637.9	49.7	2671.5	22.0	**2697.0**	**8**	97.8
AMD346z7	232.1	51.3	126.5	0.5	0.18441	0.00030	0.06570	0.00024	12.8457	0.15717	0.50520	0.00613	2636.1	26.2	2668.4	11.5	**2692.0**	**3**	97.9

Sample Number	U (ppm)	Th (ppm)	Pb (ppm)	^{204}Pb (ppb)	^{207}Pb/^{206}Pb	± 1σ	^{208}Pb/^{206}Pb	± 1σ	^{207}Pb/^{235}U	± 1σ	^{206}Pb/^{238}U	± 1σ	^{206}Pb/^{238}U	± 1σ	^{207}Pb/^{235}U	± 1σ	^{207}Pb/^{206}Pb	± 1σ	% Concor-dance
AMD346z5	199.3	65.6	112.0	0.6	0.18398	0.00055	0.09695	0.00050	12.8955	0.16340	0.50835	0.00626	2649.6	26.7	2672.0	11.9	**2689.0**	**5**	98.5
AMD346z4	309.2	164.5	180.7	1.7	0.18411	0.00030	0.15333	0.00033	12.8393	0.21471	0.50578	0.00842	2638.6	35.9	2667.9	15.6	**2690.0**	**2**	98.1
AMD346z6	505.6	488.3	332.9	1.9	0.18443	0.00041	0.27185	0.00057	13.2819	0.16267	0.52230	0.00629	2708.9	26.6	2699.9	11.5	**2693.0**	**3**	100.6
AMD346z3	307.8	132.1	175.1	2.9	0.18285	0.00040	0.12743	0.00077	12.7019	0.14889	0.50382	0.00580	2630.2	24.8	2657.8	11.0	**2678.0**	**4**	98.2
AMD346z19	635.7	441.9	395.1	3.3	0.18432	0.00047	0.19333	0.00189	13.2209	0.19556	0.52021	0.00758	2700.1	32.1	2695.6	13.9	**2692.0**	**4**	100.3
AMD346z3	537.4	373.7	324.1	5.9	0.17979	0.00045	0.19377	0.00067	12.5491	0.15431	0.50622	0.00610	2640.5	26.0	2646.4	11.5	**2650.0**	**5**	99.6
AMD346z6	*65.1*	*45.0*	*37.4*	*0.6*	*0.18670*	*0.00102*	*0.20854*	*0.00246*	*12.3563*	*0.23428*	*0.48000*	*0.00871*	*2527.3*	*37.8*	*2631.9*	*17.7*	***2713.0***	***9***	*93.2*
AMD346-z23	*823.0*	*1275.5*	*502.4*	*5.4*	*0.16441*	*0.00096*	*0.42658*	*0.00123*	*9.9292*	*0.13921*	*0.43802*	*0.00558*	*2341.8*	*25.0*	*2428.2*	*12.9*	***2501.0***	***10***	*93.6*
12.BJD332																			
BJD332z1	425.5	284.6	260.3	1.1	0.18799	0.00030	0.19943	0.00055	13.3050	0.19928	0.51331	0.00764	2670.8	32.5	2701.5	14.0	2724.0	3	98.0
BJD332z8	391.6	164.6	228.0	1.2	0.18880	0.00031	0.12362	0.00042	13.3920	0.16151	0.51444	0.00615	2675.6	26.1	2707.7	11.3	2731.0	3	98.0
BJD332z5b	322.4	122.6	186.3	1.2	0.18755	0.00027	0.11218	0.00033	13.3351	0.17661	0.51568	0.00679	2680.8	28.8	2703.7	12.4	2720.0	3	98.6
BJD332z16	477.7	229.2	287.5	1.4	0.18788	0.00031	0.13979	0.00028	13.6142	0.16062	0.52556	0.00614	2722.7	25.9	2723.3	11.1	2723.0	3	100.0
BJD332z7	447.3	237.6	266.0	1.8	0.18832	0.00027	0.15441	0.00022	13.3315	0.16188	0.51343	0.00619	2671.3	26.3	2703.4	11.4	2727.0	2	98.0
BJD332z6	304.9	129.1	181.8	2.1	0.18843	0.00037	0.12453	0.00034	13.6881	0.16897	0.52685	0.00642	2728.2	27.1	2728.4	11.6	2728.0	3	100.0
BJD332z12	580.8	314.7	350.2	4.7	0.18719	0.00041	0.15518	0.00038	13.4188	0.16807	0.51990	0.00641	2698.8	27.1	2709.6	11.8	2717.0	4	99.3
BJD332z13	*735.9*	*444.0*	*153.2*	*1.3*	*0.10964*	*0.00032*	*0.18323*	*0.00068*	*2.8059*	*0.03833*	*0.18560*	*0.00248*	*1097.5*	*13.4*	*1357.1*	*10.2*	*1793.0*	*5*	*61.2*
BJD332z10	*480.4*	*193.0*	*230.8*	*2.8*	*0.17512*	*0.00057*	*0.12603*	*0.00051*	*10.3819*	*0.15315*	*0.42996*	*0.00619*	*2305.5*	*27.8*	*2469.4*	*13.6*	*2607.0*	*5*	*88.4*
BJD332z21	*439.0*	*224.9*	*234.7*	*6.0*	*0.17871*	*0.00083*	*0.16070*	*0.00146*	*11.4849*	*0.21054*	*0.46609*	*0.00827*	*2466.4*	*36.3*	*2563.4*	*17.0*	*2640.0*	*8*	*93.4*
BJD332z19	*814.4*	*499.1*	*204.1*	*6.2*	*0.11772*	*0.00111*	*0.18759*	*0.00104*	*3.6024*	*0.07174*	*0.22195*	*0.00389*	*1292.2*	*20.5*	*1550.1*	*15.7*	*1921.0*	*17*	*67.3*
BJD332z3	*379.3*	*193.7*	*214.8*	*7.0*	*0.18556*	*0.00036*	*0.15274*	*0.00102*	*12.5781*	*0.22688*	*0.49162*	*0.00882*	*2577.7*	*38.0*	*2648.6*	*16.8*	*2703.0*	*3*	*95.4*
BJD332z20	*850.5*	*607.9*	*309.0*	*7.1*	*0.13831*	*0.00030*	*0.21908*	*0.00054*	*5.9255*	*0.09285*	*0.31073*	*0.00482*	*1744.3*	*23.7*	*1965.0*	*13.5*	*2206.0*	*3*	*79.1*
1.BJD085																			
BJD085zL4	540.6	318.9	327.3	0.6	0.18859	0.00019	0.16654	0.00025	13.4207	0.14257	0.51613	0.00546	2682.7	23.2	2709.7	10.0	**2729.0**	**2**	98.3
BJD085z4	522.3	308.5	320.2	1.0	0.18949	0.00024	0.16676	0.00030	13.6507	0.19152	0.52247	0.00730	2709.6	30.8	2725.8	13.2	**2737.0**	**2**	99.0
BJD085zL1	583.4	286.7	351.1	1.3	0.18731	0.00035	0.13688	0.00015	13.5443	0.14332	0.52443	0.00546	2717.9	23.1	2718.4	10.0	**2718.0**	**3**	100.0
BJD085z6	474.7	286.6	283.7	2.9	0.18672	0.00030	0.17218	0.00033	13.0961	0.18760	0.50867	0.00724	2651.0	30.9	2686.6	13.4	**2713.0**	**3**	97.7

Sample Number	U (ppm)	Th (ppm)	Pb (ppm)	^{204}Pb (ppb)	^{207}Pb/^{206}Pb	± 1σ	^{208}Pb/^{206}Pb	± 1σ	^{207}Pb/^{235}U	± 1σ	^{206}Pb/^{238}U	± 1σ	^{206}Pb/^{238}U	± 1σ	^{207}Pb/^{235}U	± 1σ	^{207}Pb/^{206}Pb	± 1σ	% Concor-dance
BJD085zL2	*409.1*	*221.4*	*232.1*	*3.7*	*0.18830*	*0.00041*	*0.15518*	*0.00325*	*12.6792*	*0.13354*	*0.48836*	*0.00503*	*2563.6*	*21.8*	*2656.1*	*9.9*	***2727.0***	***3***	*94.0*
BJD085zL3	*722.0*	*450.9*	*296.2*	*5.4*	*0.16179*	*0.00092*	*0.17991*	*0.00050*	*7.8580*	*0.12760*	*0.35225*	*0.00535*	*1945.3*	*25.5*	*2214.9*	*14.5*	***2474.0***	***10***	*78.6*
3.BJD090																			
BJD090-8	483.1	167.8	281.8	1.4	0.18847	0.00067	0.09797	0.00055	13.6151	0.17501	0.52394	0.00647	2715.9	27.3	2723.3	12.1	2728.0	6	99.6
BJD090z12(R)	491.5	207.9	293.3	1.2	0.18806	0.00033	0.11935	0.00017	13.6803	0.15071	0.52758	0.00574	2731.2	24.2	2727.8	10.4	2725.0	3	100.2
BJD090zL5	621.0	254.1	367.2	1.9	0.18859	0.00019	0.11609	0.00012	13.6247	0.14261	0.52397	0.00546	2716.0	23.0	2724.0	9.9	2729.0	2	99.5
BJD090z4	649.5	335.5	399.4	4.3	0.18848	0.00034	0.14404	0.00043	13.8428	0.16657	0.53268	0.00634	2752.7	26.6	2739.0	11.3	2728.0	3	100.9
BJD090z1	509.6	212.2	303.2	4.5	0.18823	0.00041	0.11513	0.00052	13.6679	0.17166	0.52663	0.00651	2727.3	27.4	2727.0	11.8	2726.0	4	100.0
BJD090zL3	*913.9*	*443.4*	*521.1*	*3.6*	*0.18593*	*0.00024*	*0.13485*	*0.00048*	*12.7617*	*0.13048*	*0.49780*	*0.00505*	*2604.3*	*21.7*	*2662.2*	*9.6*	*2706.0*	*2*	*96.2*
BJD090z28	*419.5*	*183.5*	*240.6*	*5.2*	*0.18817*	*0.00036*	*0.12419*	*0.00023*	*13.1027*	*0.14523*	*0.50503*	*0.00551*	*2635.4*	*23.6*	*2687.1*	*10.4*	*2726.0*	*3*	*96.7*
BJD090zL6	*792.5*	*391.7*	*414.9*	*5.5*	*0.17757*	*0.00144*	*0.14119*	*0.00129*	*11.2266*	*0.22218*	*0.45853*	*0.00828*	*2433.1*	*36.5*	*2542.1*	*18.3*	*2630.0*	*13*	*92.5*
BJD090z3a	*701.4*	*323.0*	*374.1*	*6.4*	*0.17886*	*0.00027*	*0.12679*	*0.00069*	*11.5998*	*0.14074*	*0.47036*	*0.00566*	*2485.1*	*24.8*	*2572.7*	*11.3*	*2642.0*	*2*	*94.1*
BJD090z7	*586.9*	*230.9*	*322.9*	*8.0*	*0.18327*	*0.00055*	*0.11095*	*0.00048*	*12.4062*	*0.15577*	*0.49097*	*0.00599*	*2574.9*	*25.8*	*2635.6*	*11.7*	*2682.0*	*5*	*96.0*
BJD090z27	*553.2*	*202.1*	*241.0*	*10.0*	*0.16595*	*0.00029*	*0.10180*	*0.00032*	*9.0522*	*0.10131*	*0.39562*	*0.00437*	*2148.8*	*20.2*	*2343.3*	*10.2*	*2517.0*	*3*	*85.4*
10.BJD328F																			
BJD328Fz19	455.4	251.0	279.1	0.4	0.18880	0.00027	0.15617	0.00042	13.7178	0.20685	0.52695	0.00791	2728.6	33.3	2730.4	14.2	2731.0	3	99.9
BJD328FzL5(R)	660.8	252.0	386.6	0.6	0.18810	0.00023	0.10744	0.00018	13.5319	0.14157	0.52174	0.00542	2706.6	22.9	2717.5	9.8	2725.0	2	99.3
BJD328Fz21	574.2	272.0	348.0	0.7	0.18886	0.00020	0.13628	0.00321	13.7904	0.19900	0.52958	0.00762	2739.7	32.0	2735.4	13.6	2732.0	2	100.3
BJD328FzL5(C)	341.9	216.5	212.7	0.9	0.18909	0.00064	0.17924	0.00202	13.7043	0.24981	0.52564	0.00941	2723.0	39.7	2729.5	17.1	2734.0	5	99.6
BJD328FzL1	449.7	167.0	262.9	1.0	0.18838	0.00027	0.10590	0.00019	13.5673	0.15037	0.52235	0.00574	2709.1	24.3	2720.0	10.4	2728.0	2	99.3
BJD328FzL2	526.3	223.7	311.8	1.3	0.18920	0.00030	0.12113	0.00133	13.6402	0.14775	0.52287	0.00560	2711.3	23.7	2725.1	10.2	2735.0	2	99.1
BJD328Fz15	573.0	293.6	349.7	1.4	0.18731	0.00021	0.14595	0.00167	13.6781	0.18911	0.52962	0.00730	2739.9	30.7	2727.7	13.0	2718.0	2	100.8
BJD328Fz14	514.4	267.6	312.8	1.5	0.18918	0.00025	0.14683	0.00048	13.7226	0.18954	0.52610	0.00723	2725.0	30.5	2730.8	13.0	2735.0	2	99.6
BJD328Fz-22	827.8	583.0	527.5	1.5	0.18946	0.00031	0.20060	0.00068	13.8621	0.19222	0.53064	0.00731	2744.1	30.7	2740.3	13.0	2737.0	3	100.3
BJD328FzU	507.4	223.9	307.4	2.1	0.18853	0.00035	0.12392	0.00029	13.8601	0.15272	0.53321	0.00579	2754.9	24.3	2740.2	10.4	2729.0	3	101.0
BJD328Fz16	501.0	255.6	310.9	2.3	0.18900	0.00067	0.14260	0.00098	14.0264	0.21584	0.53825	0.00806	2776.1	33.7	2751.5	14.5	2733.0	6	101.6

Sample Number	U (ppm)	Th (ppm)	Pb (ppm)	^{204}Pb (ppb)	^{207}Pb/^{206}Pb	± 1σ	^{208}Pb/^{206}Pb	± 1σ	^{207}Pb/^{235}U	± 1σ	^{206}Pb/^{238}U	± 1σ	^{206}Pb/^{238}U	± 1σ	^{207}Pb/^{235}U	± 1σ	^{207}Pb/^{206}Pb	± 1σ	% Concord-ance
BJD328FzL7	543.5	279.1	333.9	2.5	0.18904	0.00033	0.14642	0.00171	13.8738	0.17961	0.53228	0.00683	2751.1	28.7	2741.1	12.2	2733.0	3	100.7
BJD328FzU2	318.5	95.7	184.4	2.9	0.18838	0.00036	0.08557	0.00019	13.6493	0.15066	0.52551	0.00571	2722.5	24.1	2725.7	10.4	2728.0	3	99.8
BJD328Fz6	618.4	270.7	374.3	3.1	0.18840	0.00029	0.12408	0.00029	13.8516	0.19669	0.53323	0.00753	2755.1	31.6	2739.6	13.4	2728.0	2	101.0
BJD328FzL3	575.9	302.8	361.7	3.7	0.19109	0.00038	0.15074	0.00157	14.2847	0.16800	0.54217	0.00628	2792.5	26.2	2768.8	11.1	2751.0	3	101.5
BJD328FzL4(R)	544.0	222.0	324.8	5.0	0.18793	0.00021	0.11592	0.00035	13.7211	0.15125	0.52952	0.00581	2739.4	24.4	2730.7	10.4	2724.0	2	100.6
BJD328Fz3	982.1	1144.6	687.3	6.4	0.18787	0.00060	0.31170	0.00154	13.8227	0.24677	0.53363	0.00937	2756.7	39.3	2737.6	16.8	2723.0	5	101.2
BJD328Fz11	545.6	230.0	323.7	6.5	0.18800	0.00029	0.14185	0.00221	13.6002	0.19200	0.52467	0.00736	2718.9	31.1	2722.3	13.3	2724.0	3	99.8
2.BJDM002																			
BJDM002zL5	439.5	282.1	273.4	0.5	0.18901	0.00024	0.18145	0.00064	13.6726	0.14078	0.52465	0.00536	2718.9	22.6	2727.3	9.7	2733.0	2	99.5
BJDM002zL2	505.3	246.5	305.9	0.8	0.18873	0.00027	0.13852	0.00036	13.7232	0.14911	0.52736	0.00568	2730.3	23.9	2730.8	10.2	2731.0	2	100.0
BJDM002z22	347.3	137.0	208.7	1.0	0.18796	0.00041	0.11051	0.00024	13.8552	0.15429	0.53462	0.00584	2760.9	24.5	2739.9	10.5	2724.0	4	101.4
BJDM002zL5b	452.9	289.9	281.2	1.0	0.18900	0.00024	0.18064	0.00066	13.6499	0.14122	0.52380	0.00538	2715.3	22.7	2725.7	9.7	2733.0	2	99.4
BJDM002zL13	236.1	148.0	145.9	1.8	0.18873	0.00038	0.17782	0.00105	13.6082	0.15065	0.52294	0.00569	2711.6	24.1	2722.8	10.4	2731.0	3	99.3
BJDM002z20	398.8	216.3	242.8	2.1	0.18771	0.00034	0.15306	0.00031	13.5855	0.15295	0.52490	0.00583	2719.9	24.6	2721.3	10.6	2722.0	3	99.9
BJDM002zL16	379.7	268.5	237.7	3.8	0.18885	0.00026	0.20084	0.00057	13.5698	0.14448	0.52114	0.00550	2704.0	23.3	2720.2	10.0	2732.0	2	99.0
BJDM002zL17	508.2	352.5	311.1	4.2	0.18895	0.00042	0.19730	0.00126	13.3035	0.14415	0.51065	0.00541	2659.4	23.1	2701.4	10.2	2733.0	3	97.3
BJDM002z2	*378.3*	*190.2*	*221.4*	*0.6*	*0.18920*	*0.00072*	*0.14196*	*0.00169*	*13.2529*	*0.19362*	*0.50802*	*0.00716*	*2648.2*	*30.6*	*2697.8*	*13.7*	*2735.0*	*6*	*96.8*
BJDM002z21	*766.0*	*540.6*	*336.3*	*0.9*	*0.18139*	*0.00506*	*0.19318*	*0.00519*	*9.1395*	*0.39268*	*0.36543*	*0.01195*	*2007.9*	*56.2*	*2352.1*	*38.6*	*2665.0*	*46*	*75.3*
BJDM002z13	*823.0*	*699.2*	*413.9*	*3.2*	*0.15913*	*0.00120*	*0.24445*	*0.00124*	*9.0730*	*0.14454*	*0.41352*	*0.00581*	*2231.0*	*26.4*	*2345.4*	*14.5*	*2446.0*	*13*	*91.2*
BJDM002zL19	*628.8*	*462.2*	*324.1*	*4.0*	*0.17351*	*0.00065*	*0.20906*	*0.00182*	*10.2836*	*0.15185*	*0.42986*	*0.00614*	*2305.1*	*27.6*	*2460.6*	*13.6*	*2591.0*	*7*	*89.0*
BJDM002z23	*483.9*	*326.5*	*284.2*	*4.5*	*0.18224*	*0.00055*	*0.18908*	*0.00108*	*12.4138*	*0.14024*	*0.49402*	*0.00538*	*2588.1*	*23.2*	*2636.2*	*10.6*	*2673.0*	*5*	*96.8*
BJDM002zL12	*658.4*	*463.3*	*363.8*	*8.0*	*0.17779*	*0.00087*	*0.20229*	*0.00200*	*11.3477*	*0.23194*	*0.46292*	*0.00919*	*2452.5*	*40.4*	*2552.1*	*18.9*	*2632.0*	*8*	*93.2*
14.AMD313																			
AMD313z5	596.2	313.3	361.9	0.3	0.18943	0.00020	0.15441	0.00021	13.6952	0.21099	0.52435	0.00806	2717.6	34.0	2728.9	14.5	**2737.0**	**1**	99.3
AMD313z3	563.1	289.0	343.9	0.4	0.18882	0.00018	0.15072	0.00074	13.7773	0.21216	0.52920	0.00813	2738.1	34.2	2734.5	14.5	**2731.0**	**2**	100.3
AMD313z2	712.8	399.4	448.7	1.6	0.19156	0.00029	0.16370	0.00023	14.2411	0.21569	0.53918	0.00812	2780.0	33.9	2765.9	14.3	**2755.0**	**3**	100.9
AMD313z6	651.4	358.4	396.5	1.6	0.18957	0.00023	0.15922	0.00028	13.6724	0.20845	0.52308	0.00795	2712.2	33.6	2727.3	14.3	**2738.0**	**2**	99.1
AMD313z1	555.8	302.3	334.2	2.2	0.18944	0.00030	0.15671	0.00032	13.5107	0.21089	0.51725	0.00803	2687.5	34.0	2716.0	14.7	**2737.0**	**2**	98.2
AMD313z7	*1266.0*	*676.4*	*706.6*	*3.2*	*0.17578*	*0.00070*	*0.15627*	*0.00060*	*11.7721*	*0.18475*	*0.48571*	*0.00737*	*2552.1*	*31.9*	*2586.4*	*14.6*	***2613.0***	***7***	*97.7*

Table 4.3. Summary of the concordant dates (in millions of years) obtained from 9 different felsic units within the Cosmos succession. Note these samples are arranged in order of stratigraphic position (age), with the youngest at the top. The age for sample 12.BJD332 is considered to represent the magmatic age of the source volcanic rocks from which this sedimentary rock is derived, and not the depositional age of the unit. This established stratigraphic order is confirmed by the obtained age determinations. The late stage intrusions listed at the top of the table are appreciably younger than the extrusive volcanic succession. The calculated concordancy age, calculated from the concordancy plots, has been included in the table and concurs well with the $^{207}Pb/^{206}Pb$ age. The errors quoted are 2σ.

Sample No. & Hole ID	High Common Lead Analyses	Discordant Analyses	Concordant Analyses	Average 206/238 Age (Ma)	Average 207/235 Age (Ma)	Average 207/206 Age (Ma)	Calculated Concordancy Age (Ma)
4.AMD273	3	0	3	2664.9 (± 52.3)	2658.6 (± 23)	**2653.3 (± 6.6)**	2654.1 (± 6.5)
9.BJD320	1	4	12 (10 magmatic, 2 older inherited)	2650.8 (± 61.2)	2661.9 (± 27.2	**2669.9 (± 11.2)**	2667.5 (± 8.7)
7.AMD346	4	2	8	2655.2 (± 62)	2672.4 (± 27.2)	**2685.1 (± 8.4)**	2687.6 (± 8.9)
12.BJD332	3	6	7	2692.6 (± 55.4)	2711.1 (± 24)	**2724.3 (±6)**	2722.7 (± 8.7)
1.BJD085	2	2	4	2690.3 (± 54)	2710.1 (± 23.2)	**2724.3 (± 5)**	*Not calculated – too few overlapping data points*
3.BJD090	15	6	5	2728.6 (± 51.4)	2728.2 (± 22.2)	**2727.2 (± 7.2)**	2728.5 (± 5.5)
10.BJD328F	3	0	16 (15 magmatic, 1 older inherited)	2735.4 (± 59.4)	2732.1 (± 25.4)	**2729.2 (± 5.8)**	*Not calculated – large dataset with some non-overlapping data points*
2.BJDM002	14	7	7	2715.0 (± 47.2)	2723.7 (± 20.4)	**2729.9 (± 5.2)**	2729 (± 7.6)
14.AMD313	0	1	5 (4 magmatic, 1 older inherited)	2713.9 (± 67.8)	2726.7 (± 29)	**2735.8 (± 3.6)**	2734.9 (± 8.4)

The age obtained for the felsic horizon along the AM5 "reactivation" contact, is 2685 ± 8 Ma (7.AMD346). This result indicates that the age of lower UMu1 package of the Cosmos Ultramafic Sequence is in the range of 2724 ± 7 Ma to 2685 ± 8 Ma, while the upper UMu2 package is somewhat younger. It also demonstrates that the volcanism that formed the patchy felsic horizon is separated from the volcanism that

constructed the footwall by up to 40 Ma. This wide time-gap implies that at least one major unconformity must be present between the footwall volcanic sequence and the volcanic rocks that define the AM5 "reactivation" contact.

The measured age of detrital zircons obtained from the hangingwall sample (12.BJD332) is 2724 ± 6 Ma and is taken here to represent the time of crystallisation for the felsic volcanic sequence that provided the erosional detritus that supplied the sedimentary succession. This age puts an absolute upper limit on the emplacement age of the hangingwall sequence.

The youngest rocks dated within the succession are the hangingwall and footwall felsic porphyry intrusions emplaced at ~2670 ± 11 Ma and ~2653 ± 7 Ma, respectively (Fig. 4.3). The data from the footwall felsic porphyry intrusion must be treated with caution as only three concordant analyses were obtained from this sample, due to the low zircon abundance coupled with the small size and fractured nature of individual grains. However the obtained age is consistent with observed stratigraphic field relationships and the age of local granitic plutonism to which the two felsic porphyry intrusions are likely related (Champion and Sheraton, 1997).

Figure 4.7. Concordancy plot for all samples ordered from youngest to oldest. Blue ellipses represent each data point including a 2σ error. Green ellipses represent calculated concordia ages from concordant data points at 95% confidence with decay constant errors included. The pink and purple ellipses for Sample 9.BJD320 are considered to be inherited zircons from older crustal rocks. Purple ellipses in Sample 10.BJD328F and 14.AMD313 also indicate inherited zircons.

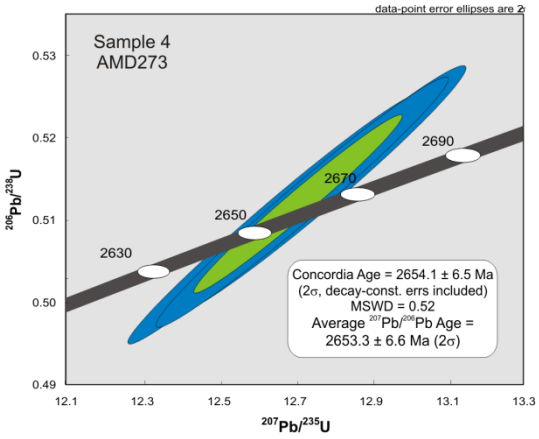
data-point error ellipses are 2
Sample 4
AMD273
2690
2670
2650
2630
Concordia Age = 2654.1 ± 6.5 Ma
(2σ, decay-const. errs included)
MSWD = 0.52
Average 207Pb/206Pb Age =
2653.3 ± 6.6 Ma (2σ)
206Pb/238U
207Pb/235U

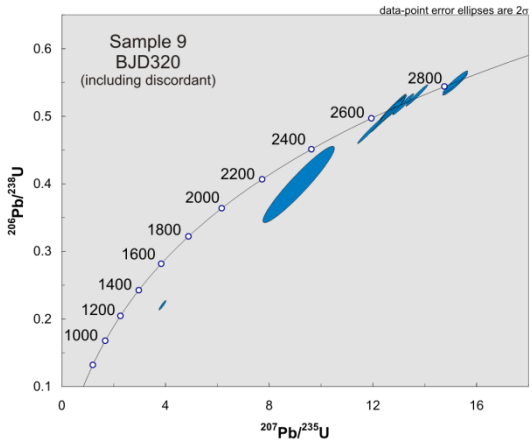
data-point error ellipses are 2σ
Sample 9
BJD320
(including discordant)
2800
2600
2400
2200
2000
1800
1600
1400
1200
1000
206Pb/238U
207Pb/235U

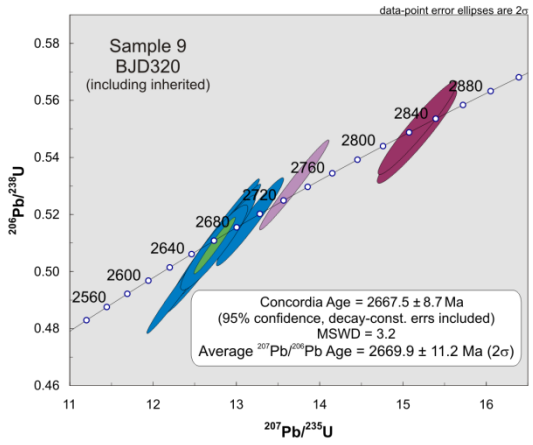
data-point error ellipses are 2σ
Sample 9
BJD320
(including inherited)
2880
2840
2800
2760
2720
2680
2640
2600
2560
Concordia Age = 2667.5 ± 8.7 Ma
(95% confidence, decay-const. errs included)
MSWD = 3.2
Average 207Pb/206Pb Age = 2669.9 ± 11.2 Ma (2σ)
206Pb/238U
207Pb/235U

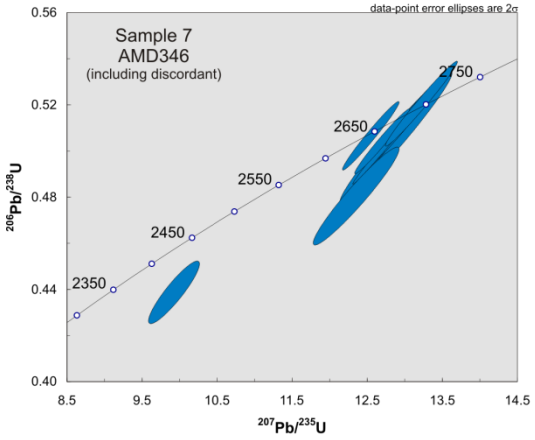
data-point error ellipses are 2σ
Sample 7
AMD346
(including discordant)
2750
2650
2550
2450
2350
206Pb/238U
207Pb/235U

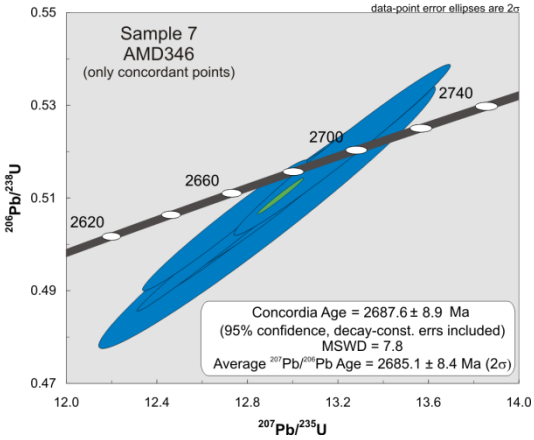
data-point error ellipses are 2σ
Sample 7
AMD346
(only concordant points)
2740
2700
2660
2620
Concordia Age = 2687.6 ± 8.9 Ma
(95% confidence, decay-const. errs included)
MSWD = 7.8
Average 207Pb/206Pb Age = 2685.1 ± 8.4 Ma (2σ)
206Pb/238U
207Pb/235U

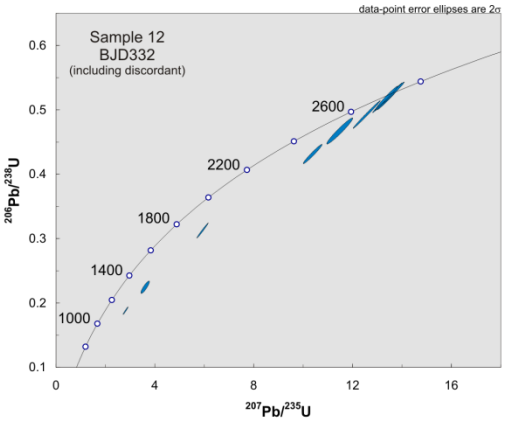
data-point error ellipses are 2σ
Sample 12
BJD332
(including discordant)
2600
2200
1800
1400
1000
$^{206}Pb/^{238}U$
$^{207}Pb/^{235}U$

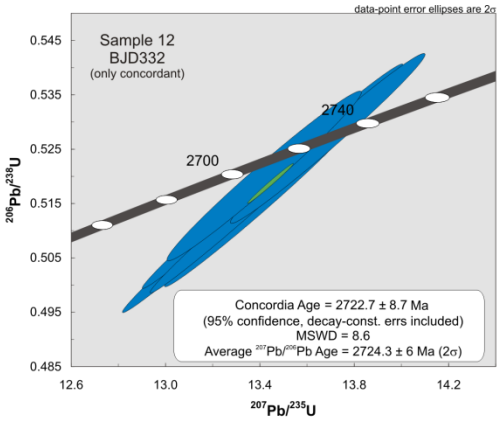
data-point error ellipses are 2σ
Sample 12
BJD332
(only concordant)
2740
2700
Concordia Age = 2722.7 ± 8.7 Ma
(95% confidence, decay-const. errs included)
MSWD = 8.6
Average $^{207}Pb/^{206}Pb$ Age = 2724.3 ± 6 Ma (2σ)
$^{206}Pb/^{238}U$
$^{207}Pb/^{235}U$

7

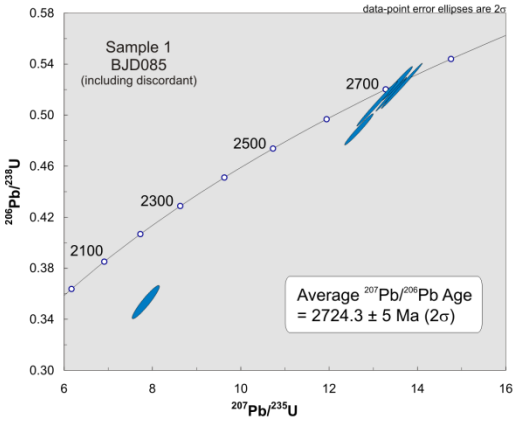
data-point error ellipses are 2σ
Sample 1
BJD085
(including discordant)
2700
2500
2300
2100
Average $^{207}Pb/^{206}Pb$ Age
= 2724.3 ± 5 Ma (2σ)
$^{206}Pb/^{238}U$
$^{207}Pb/^{235}U$

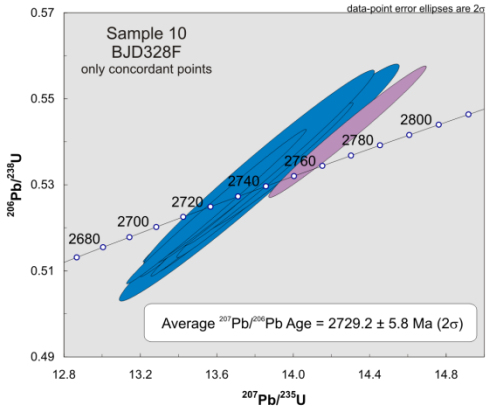
data-point error ellipses are 2σ
Sample 10
BJD328F
only concordant points
2800
2780
2760
2740
2720
2700
2680
Average $^{207}Pb/^{206}Pb$ Age = 2729.2 ± 5.8 Ma (2σ)
$^{206}Pb/^{238}U$
$^{207}Pb/^{235}U$

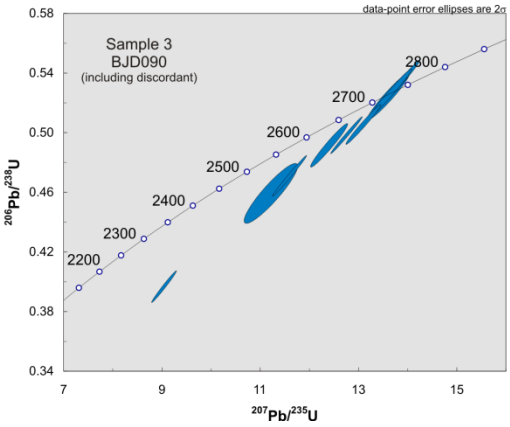
data-point error ellipses are 2σ
Sample 3
BJD090
(including discordant)
2800
2700
2600
2500
2400
2300
2200
$^{206}Pb/^{238}U$
$^{207}Pb/^{235}U$

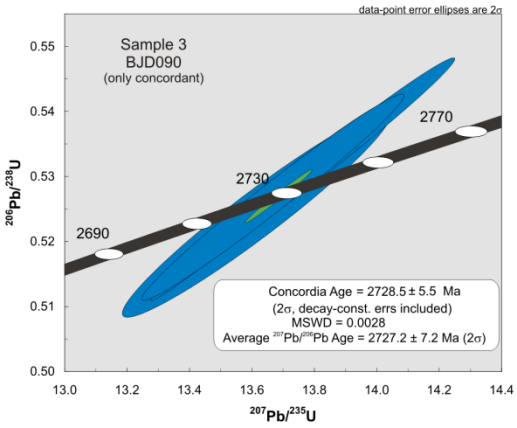
data-point error ellipses are 2σ
Sample 3
BJD090
(only concordant)
2770
2730
2690
Concordia Age = 2728.5 ± 5.5 Ma
(2σ, decay-const. errs included)
MSWD = 0.0028
Average $^{207}Pb/^{206}Pb$ Age = 2727.2 ± 7.2 Ma (2σ)
$^{206}Pb/^{238}U$
$^{207}Pb/^{235}U$

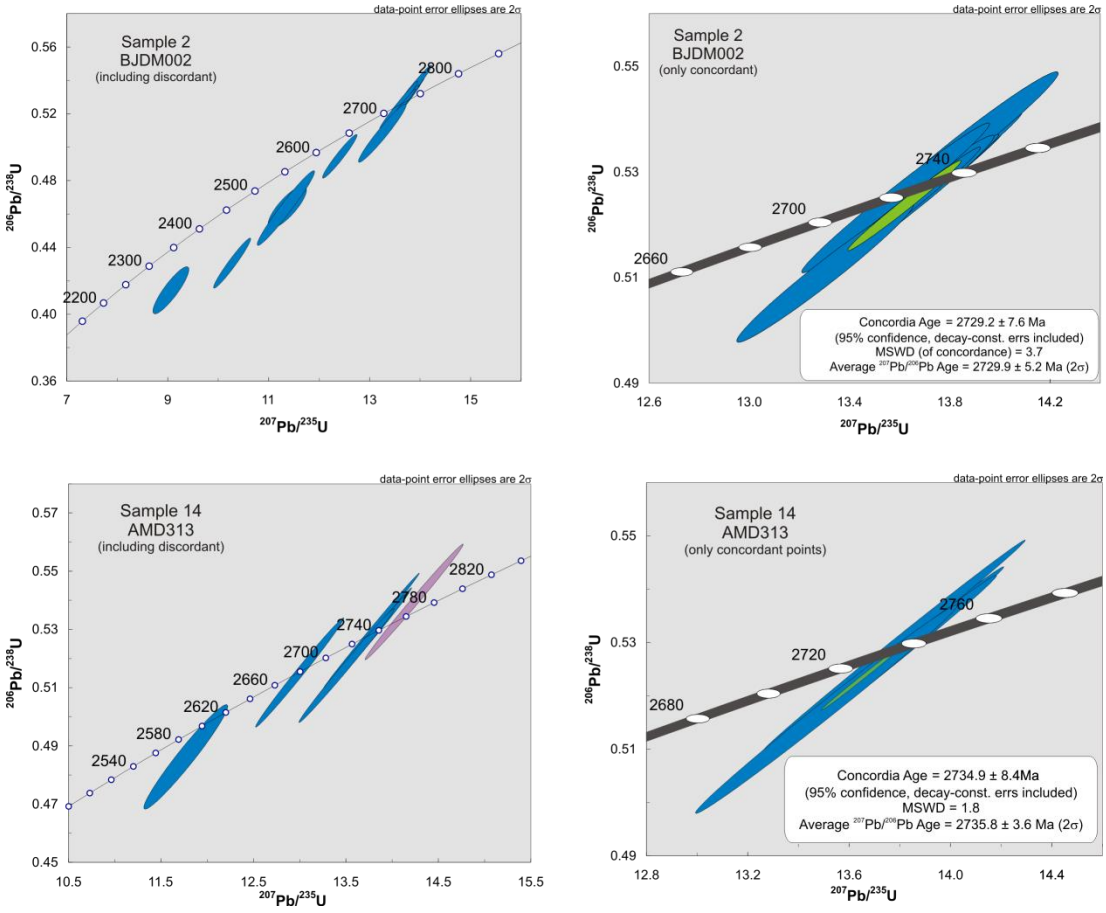

4.8 Discussion

Despite the small size, fractured and disturbed nature of a number of the zircons, SIMS microanalysis has demonstrated that there are clear age differences present within the Cosmos succession and that the formation of the succession spans a surprisingly long time period. The overall implications of these age determination for the formation of the Cosmos volcanic succession is discussed below.

4.8.1 Age and emplacement of the footwall to the Western Ultramafic Unit

The age of 2736 ± 4 Ma for the garnet-hornblende schist (14.AMD313), part of the volcanic footwall to the Western Ultramafic Unit, indicates that it is about 6 Ma older than the 2724 – 2730 Ma dacitic lava and tuff sequence that overlies the Western Ultramafic Unit. Thus the Western Ultramafic Unit was itself emplaced at some point between ~2736 and ~2730 Ma. This age difference, in conjunction with the lithological and compositional differences between rocks over and underlying the Western Ultramafic Unit indicate that it represents the earliest formed komatiite flow field in the Cosmos greenstone succession. This komatiite lava overrode an older volcanic succession that is compositionally distinct from the stratigraphically higher footwall succession to the Cosmos Ultramafic Sequence.

4.8.2 Age and emplacement of the footwall to the Cosmos Ultramafic Sequence

The age determinations of the footwall dacitic lavas and lapilli tuffs below the Cosmos Ultramafic UMu1 package indicate that this sequence was emplaced in the period from 2730 to 2724 Ma. The reconstructed stratigraphy (Fig. 4.3) demonstrates that the dacitic tuffs and dacitic lavas are intercalated with the andesitic lavas and associated volcaniclastic units. However, the chemical affinities of these volcanic rocks strongly suggest that the magmas that formed them originated from separate sources (Chapter 3). Therefore, the intercalated nature of the succession implies that the sequence was formed via multiple eruptions from two different and simultaneously active volcanic centres, whose activity persisted over a substantial time period.

The most statistically robust age at 2729 ± 6 Ma (sample 10.BJD328F) indicates that the footwall to the Cosmos Ultramafic lava sequence is significantly older than the dacite footwall succession to the neighbouring Mount Keith and

Perseverance nickel sulphide-bearing ultramafic sequences, which are dated at ~2706 – 2013 Ma (Fiorentini et al., 2012) and ≥ 2711 Ma (Beresford et al., 2004; Duuring et al., 2012), respectively. The footwall to the Cosmos Ultramafic UMu1 package also appears to be slightly older than the felsic footwall to the Rocky's Reward deposit, which is dated at 2720 ± 14 Ma (Nelson, 1997a; Fig. 4.2). However, it may be time equivalent because the average age for the Rocky's Reward felsic footwall is based on three concordant zircon crystal ages with a large uncertainty (Nelson, 1997a). Furthermore, our results indicate that the Cosmos domain of the Agnew-Wiluna greenstone belt may be a separate and older terrane (Fig. 4.2) and therefore not a structural repeat of an eastern segment of the belt. This notion is further supported by the differences in the lithostratigraphy and chemical composition of the felsic and intermediate volcanic units comprising the Cosmos succession compared to that of the Mount Keith region, as well as by the difference in style and tenor of sulphide mineralisation. In a more regional context the Cosmos footwall volcanic succession is not only older than the majority of felsic volcanism in the Kalgoorlie Terrane but also older than felsic volcanic centres present within the adjacent Gindalbie and Kurnalpi Terranes (Barley et al., 2008; Fig. 4.1). Within the EGS there is little evidence of felsic and intermediate volcanism of a similar age to the Cosmos footwall volcanic succession (2736 – 2724 Ma), further indicating that the Cosmos domain is a separate terrane in its own right or that it represents the initiation of volcanism in the Kalgoorlie Terrane.

4.8.3 Significance of the AM5 “reactivation” contact

U-Pb age data obtained here (Table 4.3) indicates that the patchy felsic horizon, the AM5 “reactivation” contact, which is fully contained within the Cosmos Ultramafic sequence in the North Cosmos region, is ~40 Ma younger than the underlying footwall sequence. Furthermore, it is significantly older than the hangingwall and footwall porphyry intrusions predating them by ~15 Ma and ~32 Ma, respectively. As described in Section 4.4, the AM5 “reactivation” contact is considered

to represent a period of volcanism featuring eruption of dacitic lavas and andesite–dacite volcaniclastic deposits (e.g., Denny, 2010). Consequently, the AM5 "reactivation" contact signifies a break in the accumulation of ultramafic lavas and confirms that the Cosmos Ultramafic Sequence is in fact comprised of two distinct ultramafic lava sequences here referred to as the UMu1 and UMu2 packages. Ages obtained in this study for the felsic horizon at the AM5 "reactivation" contact are consistent with Denny's (2010) interpretation. The horizon's heterogeneity, geochemistry and patchy nature, as discussed in Section 4.4.4, strongly suggests the felsic and intermediate volcanic rocks along this contact are of extrusive origin and not a later intrusion into the succession. The 2685 ± 8 Ma age of the felsic volcanic rocks along the AM5 "reactivation" contact imply that it may be linked with a second episode of regional felsic volcanism identified within the southern part Kalgoorlie Terrane between 2687 and 2676 Ma (Kositcin et al., 2008).

The eruption of the UMu1 package must have occurred at some point after ~2724 Ma and prior to ~2685 Ma, whereas the eruption and emplacement of the UMu2 package must post-date ~2685 Ma but predate ~2670 Ma. A maximum break of up to 40 Ma is implied between the eruptions that formed these two komatiite flow fields, but the duration of this break may be much less. However, at this stage, it is not possible to further constrain the timing for the emplacement of the UMu1 and UMu2 packages or the time that may have passed between the emplacements of these two ultramafic sequences. However, dating of the AM5 "reactivation" contact unequivocally implies that there is at least one major unconformity/period of non-deposition within the Cosmos succession, something that would have been overlooked without detailed U–Pb dating of the key stratigraphic components.

The evidence presented here that the Cosmos Ultramafic Sequence comprises at least two distinct komatiite lava packages produced by separate eruptions may explain the contrasting mineralisation styles observed within it. Pods of high-tenor massive nickel-sulphide tens of metres across characterise the mineralisation in the earlier UMu1 komatiite package, while larger lenses, tens to hundreds of metres across, of disseminated nickel-sulphides above the AM5 "reactivation" contact characterise the later UMu2 komatiite package.

The age span of punctuated komatiite volcanism within the Cosmos succession is greater than 45 Ma. It features at least three distinct episodes of komatiite volcanism where the first episode formed the Western Ultramafic Unit, the second the UMu1 package and the third the UMu2 package. The latter and youngest komatiite flow sequence postdates 2685 ± 8 Ma and thus may extend the minimum age of komatiite volcanism within the Kalgoorlie Terrane beyond the 2692 ± 4 Ma given by Claoué-Long et al. (1988). Our data also implies that komatiite volcanism, along with intermediate and dacitic volcanism in individual locations is distinctly cyclic and takes place as discreet events separated by significant time and that the style of mineralisation of individual komatiite flow fields differs between cycles.

4.8.4 Emplacement of the hangingwall sedimentary succession

Deposition of the overlying volcaniclastic-dominated sediments that form the hangingwall sequence postdates 2724 ± 6 Ma, which is the age of their constituent detrital zircons, and in fact it must postdate the formation of the AM5 "reactivation" contact at 2685 Ma. It predates ~2670 Ma when the felsic porphyry was intruded, cross cutting the contact between the hangingwall succession and the underlying UMu2 package. The age obtained from the detrital zircons within the hangingwall succession are interpreted as the time of crystallisation for the felsic volcanic rocks that, via erosion, supplied the sedimentary succession. Thus, the formation of the hangingwall sedimentary sequence involved erosion of rocks similar in age to that of the footwall succession to the UMu1 package. The younger felsic horizon along the AM5 "reactivation" contact indicates that the ultramafic eruption and emplacement continued beyond 2685 ± 4 Ma. This is consistent with the interpretation that the ca. 2724 Ma date obtained for the hanging wall succession zircons cannot represent the depositional age of these sedimentary rocks.

Sub-rounded granitic clasts contained within conglomerates in the hangingwall sedimentary sequence also argue for a younger emplacement age than 2724 Ma. The emplacement age of granitic intrusions within the EGS is well constrained, ranging

from 2685 Ma to 2640 Ma (Nelson, 1998) with local granites pluton ages ranging from 2685 to 2652 Ma (Nelson, 1997b, Nelson, 1997c; Black et al., 2002; Fig. 4.2) Dating of the Jones Creek Conglomerate, just to the north of Kathleen Valley provides a maximum age of deposition of 2667 ± 6 Ma (Fig. 4.2). Nelson (1997d) considers the zircons obtained from this metasandstone to be derived from nearby granitic rocks of these ages. Thus, the true age of deposition of the Cosmos sedimentary hangingwall succession is most likely similar to that obtained for the Jones Creek Conglomerate sequence. This unit is similar in composition to the Cosmos hangingwall conglomerates, composed of rounded granitic clasts in an arkosic or mafic matrix. Furthermore, it unconformably overlies the underlying greenstone rocks of the Kathleen Valley (Durney, 1972). The Cosmos hangingwall sediments may represent the along strike continuation of this style of sedimentation, which is considered to be formed in a subaerial fluvial environment with the conglomerate sourced in a rapidly eroding upland area composed of exhumed granite as well as mafic, intermediate and felsic volcanic rocks (Durney, 1972; Bunting and Williams, 1979).

4.8.5 Timing of intrusive units

The youngest rocks dated within the succession are the two intrusive felsic porphyries, which were emplaced >15 Ma apart. They represent two separate occurrences of late-stage magma intrusion. Given their TTG affinity and geochemical similarity to high-Ca granitoids within the Kalgoorlie Terrane, in contrast to the strong island arc affinity of the footwall volcanic sequence (Fig. 4.5; Chapter 3), it is considered that these intrusions to be related to the local granite plutonism. The whole succession, including the late stage felsic porphyry intrusions, is cross cut by multiple granitic pegmatite intrusions, ranging in thickness from a few centimetres to several tens of metres. Given that the pegmatite dykes cross cut the footwall felsic porphyry, their formation postdates ~2653 Ma.

The ages obtained here are consistent with the age suggested for the extensional D1 phase of deformation within the Norseman-Wiluna belt. This D1 phase was

accompanied by a change from volcanic-dominated to plutonic-dominated magmatism at approximately 2685 – 2675 Ma (Weinberg et al., 2003). Within the Cosmos region itself the dating presented here constrains this switch to pluton-dominated magmatism to between 2685 ± 4 Ma and 2670 ± 11 Ma, when the first felsic intrusion cross-cut the Cosmos succession.

4.8.6 Inherited zircons

Only four inherited, concordant zircons were detected across all samples from the Cosmos succession. The core of a distinctively larger (>200 μm across) single zircon crystal within the hangingwall intrusive felsic porphyry (1.BJD320z1, Table 4.2) yielded two ages of 2835 ± 7 Ma (core) and 2827 ± 6 Ma (rim). These ages indicate that this is an inherited zircon most likely incorporated via assimilation of pre-existing crustal rock during passage of magma through the crust. It is possible that this zircon comes from extrusive units produced by the >2810 Ma volcanic phase that predates the main 2720 – 2650 Ma episode of volcanism within the EGS (Nelson, 1997b and Cassidy et al., 2006). The hangingwall felsic porphyry also contained a younger inherited zircon (BJD320z22, Table 4.2) dated at 2719 ± 8 Ma, which may have been sourced through crustal assimilation of the time-equivalent dacitic footwall to the Cosmos Ultramafic Sequence. The third inherited zircon came from the dacitic footwall giving an age of 2751 ± 6 Ma (BJD328FzL3, Table 4.2), while the fourth inherited zircon was found in the garnet-hornblende schist within the footwall to the Western Ultramafic sequence giving an age of 2755 ± 6 Ma (AMD313z2, Table 4.2). The source of these two time-equivalent zircons is not known but the presence of inherited zircons indicates that crustal assimilation played a role in magma generation of the Cosmos volcanic sequence.

4.9 Synthesis

My results strongly indicate that the Cosmos succession was produced via three cycles of bi-modal felsic/intermediate and komatiite volcanism, occurring episodically over a time span of at least 50 Ma and possibly up to 65 Ma. This volcanic succession was later subjected to at least two periods of felsic intrusion, at ~2670 Ma and ~2653 Ma, respectively. As the oldest rocks dated within the succession are ~2736 Ma, the construction of the Cosmos succession as seen today took more than 80 Myrs. However, significant periods of non-deposition must exist within the Cosmos succession, given that its total stratigraphic thickness in this area is ~1000 m.

Late Archaean island-arc volcanic rocks occur in the Kurnalpi Terrane to the east of the Kalgoorlie Terrane and span ~2715 – 2704 Ma, while the volcanic succession of the adjacent Gindalbie Terrane spans ~2692 – 2680 Ma (Barley et al., 2008) These two terranes are considered to represent the evolution of the same volcanic arc but represent different tectonic fragments that were later welded together (Barley et al., 2008). Within the Abitibi Greenstone Belt in Canada, which exhibits volcanism of a similar age to that of the Kalgoorlie Terrane, individual volcanic episodes, occurring between 2734 and 2695 Ma, typically exhibit a duration of 2 – 10 Ma (Thurston et al., 2008). Thus the age range of the footwall volcanic rocks to the Western and Cosmos Ultramafic Sequences at ~12 Ma is consistent with the age span of similar Late Archaean arc-derived volcanic successions. The footwall volcanic rocks to both the Western and Cosmos ultramafic sequences have very similar geochemical attributes (Fig. 4.5; Chapter 3) indicating the entirety of the Cosmos footwall sequence is part of the same arc sequence. The maximum thickness of this package is >400 m from current drill coverage. This relatively thin package of rocks formed over <12 Ma could be explained by the Cosmos North region being distal to the main volcanic centre, where accumulation rates are likely to be lower. Consequently if the succession was formed in sub-marine setting, then marine sediments would be expected to feature within the volcanic sequence, especially in times of volcanic quiescence. Absence of marine sediments, in conjunction with other

stratigraphic evidence outlined in Section 4.4.2, strongly suggest that the Cosmos succession was emplaced in a sub-aerial setting.

The absence of large scale outcrop and pervasive alteration make recognition of an unconformity within a volcanic succession mapped only in the sub-surface through drill core correlation challenging. Evidence of sub-aerial truncation or exposure is unlikely to be preserved on the small scale of drill core samples. Thus unconformable relationships within the Cosmos volcanic succession can only be inferred by the age relationships of individual units, coupled with geochemical variations. Clearly periods of non-deposition or unconformities must exist between the footwall succession to the Cosmos Ultramafic Sequence and the felsic volcanic rocks along the AM5 "reactivation" contact, given the ~40 Ma difference in age between these units. However, recognition of this time-gap is hampered by being unable to further constrain the eruption age of the UMu1 package beyond the dates provided by the enclosing stratigraphy, coupled with pervasive and destructive serpentisation. Additional unconformities could exist between the footwall volcanic rocks to the Western Ultramafic Unit and the footwall volcanic rocks to the UMu1 ultramafic package. It is also hard to quantify the possible extent of removal of parts of the non-ultramafic stratigraphy via thermo-mechanical erosion by the overriding komatiite lavas. Our data does, however, highlight that the longevity of the Cosmos succession, and recognition of the existence of distinct periods of non-deposition, would not have been detected had dating of individual units not been undertaken.

Age results combined with the established stratigraphic relationships strongly support the following framework for the evolution of the Cosmos succession:

- **Stage 1:** Footwall to the Western Ultramafic Unit was emplaced beginning with the oldest unit identified, a coherent rhyolite lava/lava dome that was followed by emplacement of the cryptic garnet-hornblende schist (probably with a fragmental dacitic protolith) at ~2736 Ma. This was followed by eruption and emplacement of the intermediate feldspar-bearing crystal tuff post 2736 Ma and prior to 2730 Ma.

- **Stage 2:** At some point between 2736 and 2730 Ma the Western Ultramafic Unit was emplaced via effusive komatiite eruption.
- **Stage 3:** The period from 2730 to 2724 Ma featured eruption and emplacement of dacite lavas and compositionally similar lapilli tuffs and tuff breccias, as well as coeval andesitic lavas and associated volcaniclastic units.
- **Stage 4:** Eruption and emplacement of the UMu1 komatiite package and associated massive nickel sulphide ore bodies took place at some stage between 2724 and 2685 Ma. Komatiite lithologies immediately adjacent to the footwall contact indicate that emplacement of the UMu1 ultramafic began as a dynamic thin-flow system before evolving into high-volume pathway-confined flows (Hill and Dowling, 2008; Denny, 2010). A substantial period of non-deposition and/or an unconformity are inferred by the 40 Ma difference in age between the Cosmos UMu1 footwall volcanic rocks and the discontinuous volcanic rocks along the AM5 "reactivation" contact below UMu2 komatiite package.
- **Stage 5:** Emplacement of the patchy felsic volcanic sequence of the AM5 "reactivation" contact, took place at ~2685 Ma. This felsic horizon is inferred to have been subjected to substantial thermo-mechanical erosion during emplacement of the overlying UMu2 komatiite lava (Denny, 2010) resulting in only disjointed remnants of this felsic volcanic horizon being preserved.
- **Stage 6:** Eruption and emplacement of the UMu2 komatiite package and associated disseminated nickel-sulphide ore deposits took place sometime between 2685 Ma and 2670 Ma because it post-dates the felsic volcanic rocks along the AM5 "reactivation" contact and pre-dates 2670 Ma, when the felsic porphyry intrusion cross cut its upper contact.
- **Stage 7:** Sometime prior to 2670 Ma the emplacement of UMu2 was followed by the deposition of the overlying volcanogenic sedimentary hangingwall succession.
- **Stage 8:** First phase of intrusive activity is represented by the formation of the hangingwall felsic porphyry intrusion at ~2670 Ma, which was emplaced along the contact between the UMu2 package and the hangingwall volcanogenic sedimentary sequence.

- **Stage 9:** Second phase of felsic intrusion is represented by the ~2653 Ma footwall felsic porphyry, which was emplaced roughly along the footwall contact of the UMu1 package where it cross cuts and displaces massive sulphide ore bodies in the vicinity of the footwall contact.
- **Stage 10:** Intrusion of voluminous granite bodies in the vicinity of the Agnew-Wiluna greenstone belt between ~2685 Ma and ~2652 Ma (Nelson, 1997a, Nelson, 1997b, Nelson, 1997c, Nelson, 1997d; Black et al., 2002). The similarity in the ages and chemical composition between the granites and the felsic porphyry intrusions suggest that the latter are related to this regional plutonism. A late stage expression of the regional granitic plutonism is also present within the Cosmos succession as pervasive granitic pegmatite dykes that cross cut all other lithological units and thus represent the youngest formations of the Cosmos succession.

4.10 Conclusions

U–Pb dating of nine different lithological units representing the stratigraphic range of the Cosmos succession shows that it was constructed by episodic magmatic activity spanning at least ~80 Ma. It also reveals that the succession features three intermediate-felsic-ultramafic sequences formed in distinct volcanic episodes between 2736 Ma and <2670 Ma. Periods of non-deposition and unconformities, undetectable from drill core samples and contact relationships alone, are inferred to exist within the succession from the established geochronology.

In a regional context, the dating undertaken in this study strongly indicates that the Cosmos domain is separate from the AWB and is not simply a structural repeat of this adjacent domain. The age of the Cosmos footwall succession at 2736 –2724 Ma is ~15 – 25 Myrs older than the established age-span (~2710 – 2665 Ma) for felsic volcanism elsewhere within the Kalgoorlie Terrane (Kositcin et al., 2008). Therefore, the Cosmos felsic succession is appreciably older than the majority of the felsic

volcanism within the Kalgoorlie Terrane and notably at least 10 – 15 Myrs older than volcanism within the Agnew-Wiluna greenstone belt itself (Fig. 4.2). In fact the felsic and intermediate Cosmos footwall succession, dated at 2736 – 2724 Ma, is more similar in age to late stage calc-alkaline felsic volcanism, dated at 2730 Ma, in the Southern Cross Domain, in the eastern part of the Youanmi Terrane (Van Kranendonk et al., 2012). This lies to the west of and is faulted against the Kalgoorlie Terrane by the long-lived Ida fault (Fig. 4.1). It is therefore likely that onset of felsic volcanism in the AWB predates that of the Kalgoorlie Terrane, which has important implications for tectonostratigraphical correlations between individual greenstone belts within the Kalgoorlie Terrane and the wider Yilgarn Craton.

The dating of the Cosmos succession presented here demonstrates that high-resolution geochronology within individual greenstone successions can be achieved. It also creates new avenues for understanding and reconstructing any bi-modal Archaean volcanic succession and helps identify possible/critical hiatuses or unconformities that might not be immediately obvious in sub-surface, altered and deformed successions. High resolution dating of Archaean sequences provides more robust platforms for interpreting the evolution of mineralized volcanic successions.

4.11 References

Arndt, N. T., Lesher M. C., Barnes S. J. 2008. Komatiite. Cambridge University Press, Cambridge, pp. 295-327.

Barley, M. E., Brown, S. J. A., Krapez, B., Kositcin, N. 2008 Physical volcanology and geochemistry of a Late Archaean volcanic arc: Kurnalpi and Gindalbie Terranes, Eastern Goldfields Superterrane, Western Australia, Precambrian Research 161(1), 53-76.

Barnes, S. J., 1998. Chromites in komatiites, 1. Magmatic controls on crystallisation and composition. Journal of Petrology 39, 1689-1720.

Barnes, S. J., 2006. Komatiite-hosted nickel sulphide deposits; geology, geochemistry and genesis. Society for Economic Geologists Special Publication 13, 51-118.

Beresford, S., Duuring, P., Fiorentini, M., Rosengren, N., Bleeker, W., Barley, M., Cas, R., Tait, M., Wallace, H. 2004. P710. The Structural and Stratigraphic Architecture of the Agnew/Wiluna Belt, WA; Final Report, AMIRA, 75-124.

Black, L. P., Champion, D. C., Cassidy, K. F., 2002. Compilation of SHRIMP U-Pb geochronology data, Yilgarn Craton, Western Australia, 1997-2000. Unpublished Geoscience Australia, analytical data available from http://www.ga.gov.au/oracle/ozchron/frames.html.

Bunting J. A., Williams, S. J. 1979. Sir Samuel, W.A. (1st edition): Western Australia Geological Survey,1:250 000 Geological Series Explanatory Notes, 40p.

Cassidy, K. F., Champion, D. C., Krapez, B., Barley, M. E., Brown, S. J. A., Blewett, R.S., Groenewald, P.B., Tyler, I.M., 2006. A revised geological framework for the Yilgarn Craton, Western Australia: Western Australia Geological Survey, Record 2006/8, 8p.

Champion, D. C., Sheraton, J. W., 1997, Geochemistry and Nd isotope systematics of Archaean granites of the Eastern Goldfields, Yilgarn Craton, Australia: implications for crustal growth processes. Precambrian Research 83, 109–132.

Claoué-Long, J. C., Compston, W., Cowden, A. 1988. The age of the Kambalda greenstones resolved by ion-microprobe: implications for Archaean dating methods. Earth and Planetary Science Letters 89, 239-259.

Corfu F., Hanchar J. M., Hoskin P. W. O, Kinny P, 2003. Atlas of zircon textures. Reviews in Mineralogy and Geochemistry 53, 469-500.

Czarnota, K., D. C. Champion, B. Goscombe, R. S. Blewett, K. F. Cassidy, P. A. Henson, P.B. Groenewald 2010. Geodynamics of the eastern Yilgarn Craton. Precambrian Research 183 (2) 175–202.

Defant, M. J. and Drummond, M. S. 1990. Derivation of some modern arc magmas by melting of young subducted lithosphere. Nature, 347(6294), 662-665.

Denny, M. 2010 AM5 Disseminated (AM5D) mineralogical model. Unpublished internal memo, Xstrata Nickel Australasia, 4-13.

Dowling, S. E., Barnes S .J., Hill, R. E. T., Hicks, J., 2004. Komatiites and nickel sulphide ores of the Black Swan area, Yilgarn Craton, Western Australia. 2. Geology and genesis of the ore bodies. Mineralium Deposita 39, 707-728.

Durney, D. W., 1972. A major unconformity in the Archaen, Jones Creek, Western Australia. Journal of the Geological Society of Australia 19(2), 251-259.

Duuring, P., Bleeker, W., Beresford, S. W., Fiorentini, M. L., Rosengren, N. M. 2012. Structural evolution of the Agnew–Wiluna greenstone belt, Eastern Yilgarn Craton and implications for komatiite-hosted Ni sulfide exploration. Australian Journal of Earth Sciences 59(5), 765-791.

Fisher, R. V. 1961. Proposed classification of volcaniclastic sediments and rocks. Geological Society of America Bulletin 72, 1409-1414.

Fiorentini, M. L., Rosengren, N., Beresford, S. W., Grguric, B., Barley, M. E. 2007. Controls on the emplacement and genesis of the MKD5 and Sarah's Find Ni–Cu–PGE deposits, Mount Keith, Agnew–Wiluna Greenstone Belt, Western Australia. Mineralium Deposita, 42(8), 847-877

Fiorentini, M., Beresford, S., Barley, M., Duuring, P., Bekker, A., Rosengren, N., Cas, R., Hronsky, J. 2012. District to Camp Controls on the Genesis of Komatiite-Hosted Nickel Sulfide Deposits, Agnew-Wiluna Greenstone Belt, Western Australia: Insights from the Multiple Sulfur Isotopes. Economic Geology 107, 781-796.

Foster, J. G., Lambert, D. D., Frick, L. R. and Maas, R. 1996, Re-Os isotopic evidence for genesis of Archaean nickel ores from uncontaminated komatiites. Nature 382, 703-705.

Geological Survey of Western Australia, 2009. Compilation of geochronology information, 2009 update. Western Australia Geological Survey.

Goscombe, B., Blewett, R. S., Czarnota, K., Groenewald, B., Maas, R. (2009) Metamorphic evolution and integrated terrane analysis of the eastern Yilgarn Craton: Rationale, methods, outcomes and interpretation: Geoscience Australia, Record 2009/23, 270.

Hill, R.E.T. 2001. Komatiite volcanology, volcanological setting and primary geochemical properties of komatiite-associated nickel deposits. Geochemistry: Exploration, Environment, Analysis 1, 365-381.

Hill, R. E. T., Dowling, S. E., 2008. The petrology and geochemistry of mineralised komatiites intersected in three diamond drill holes (AM262B, AMD275 and BJD048A) from the AM5 Nickel Sulphide Deposit; Cosmos region, Agnew-Wiluna Greenstone Belt; A pilot study for characterising mineralised domains within the ore body. Unpublished External report, Kalapana Research Associates and Triodia Research.

Hill, R. E. T., Barnes, S. J., Gole, M. J., Dowling S. E., 1995. The physical volcanology of komatiites as deduced from field relationships in the Norseman-Wiluna greenstone belt, Western Australia. Lithos 34, 159-188.

Hill, R. E. T., Barnes, S. J., Dowling, S. E., Thordarson, T., 2004. Komatiites and nickel sulphide ore bodies of the Black Swan area, Yilgarn Craton, Western Australia. 1. Petrology and volcanology of host rocks. Mineralium Deposita 39, 684-706.

Hoskin, P, Schaltegger U., 2003. The composition of zircon and igneous and metamorphic petrogenesis. Reviews in mineralogy and geochemistry 53.1, 27-62.

Jackson, S. E, Pearson, N. J., Griffin, W. L., Belousova, E. A., 2004. The application of laser ablation-inductively coupled plasma-mass spectrometry to in situ U–Pb zircon geochronology. Chemical Geology 211, 47–69.

Kaye, A., Thordarson, T., Hayward, C., Denny, M., de Joux, A. J., 2010. The felsic and intermediate footwall to the Cosmos Nickel sulphide deposits, Agnew-Wiluna greenstone belt, Yilgarn Craton, Western Australia, SEG 2010 conference abstract and presentation, Colorado.

Kaye, A., Thordarson, T., Hayward, C., Fitton, G., de Joux, A. J., 2011. The felsic and intermediate footwall to the Cosmos Nickel sulphide deposits, Agnew-Wiluna greenstone belt, Yilgarn Craton, Western Australia, IUGG 2011 conference abstract and presentation, Melbourne.

Kelly, N. M., Hinton, R. W., Harley, S. L., Appleby, S. K., 2008. New SIMS U Pb zircon ages from the Langavat Belt, South Harris, NW Scotland: implications for the Lewisian Terrane mode. Journal of the Geological Society, 165, 967-981.

Kositcin, N., Brown, S. J. A., Barley, M. E., Krapez, B., Cassidy, K. F., Champion, D. C., 2008. SHRIMP U-Pb zircon age constraints on the Late Archaeantectonostratigraphic architecture of the Eastern Goldfields Superterrane, Yilgarn Craton, Western Australia. Precambrian Research 161, 5-33.

Langworthy, P., Vallance, S., 2004. Exploration Strategies for the discovery of the Cosmos Region nickel sulphide deposits, Western Australia. Unpublished internal memo, Xstrata Nickel Australasia.

Lee, J. K., Tromp, J., 1995. Self-induced fracture generation in zircon. Journal of Geophysical Research 100(B9), 17753-17.

Liu, S.F., Champion, D.C., Cassidy, K.F., 2002. Geology of the Sir Samuel 1:250 000 sheet area, Western Australia. Geoscience Australia, Record 2002/14, 57p.

McLaren, A. C., Gerald, J. D., Williams, I. S., 1994. The microstructure of zircon and its influence on the age determination from Pb/U isotopic ratios measured by ion microprobe. Geochimica et Cosmochimica Acta 58(2), 993-1005.

Moyen, J. F., Martin, H., 2012. Forty years of TTG research. Lithos 48, 312-336.

Naldrett, A .J., 2004. Magmatic sulphide deposits: Geology, Geochemistry and Exploration. Springer Berlin Heidelberg, New York.

Nelson, D. R., 1997a. 118954: feldspar-quartz-mica schist, Rocky's Reward; in Compilation of SHRIMP U–Pb zircon geochronology data, 1996: Western Australia Geological Survey, Record 1997/2, 65–69.

Nelson, D. R., 1997b. Evolution of the Archaean granite-greenstone terranes of the Eastern Goldfields, Western Australia; SHRIMP U-Pb zircon constraints. Precambrian Research 83, 57-81.

Nelson, D. R., 1997c, 118936: recrystallized granite, Jones Creek; Geochronology dataset 463; in Compilation of geochronology data, June 2006 update: Western Australia Geological Survey.

Nelson, D. R., 1997d, 118937: metasandstone, Jones Creek; Geochronology dataset 464; in Compilation of geochronology data, June 2006 update: Western Australia Geological Survey.

Nelson, D. R., 1998. Granite-greenstone crust formation on the Archaean earth- a consequence of 2 superimposed processes. Earth and Planetary Science Letters 158, 109-119.

Rosengren, N. M., Grguric, B. A., Beresford, S. W., Fiorentini, M. L., Cas, R. A., 2007. Internal stratigraphic architecture of the komatiitic dunite-hosted MKD5 disseminated nickel sulfide deposit, Mount Keith Domain, Agnew-Wiluna Greenstone Belt, Western Australia. Mineralium Deposita 42(8), 821-845.

Rosengren N. M., Cas R. A. F., Beresford S. W., Palich, B. M., 2008. Reconstruction of an extensive Archaean dacitic submarine volcanic complex associated with the komatiite-hosted Mt Keith nickel deposit, Agnew-Wiluna Greenstone Belt, Yilgarn Craton, Western Australia. Precambrian Research 161, 34–52.

Stuff, R., 2011. Xstrata Nickel Australasia-Cosmos Nickel Project- Technical Report No: STR01126, Annual report on Cosmos Nickel Project Tenements submitted to DMP, 12-18.

Thurston, P. C., Ayer, J. A., Goutier, J., Hamilton, M. A., 2008. Depositional gaps in Abitibi greenstone belt stratigraphy: a key to exploration for syngenetic mineralization. Economic Geology, 103(6), 1097-1134.

Van Kranendonk, M. J., Ivanic, T. J., Wingate, M. T., Kirkland, C. L., Wyche, S., 2012. Long-lived, autochthonous development of the Archean Murchison Domain, Implications for Yilgarn Craton tectonics. Precambrian Research 229, 49 – 92Watson E.B. 1979 Zircon saturation in felsic liquids: experimental results and applications to trace element geochemistry. Contributions in Mineral Petrology 70, 407-419.

Watson E. B., Harrison T. M. 1983. Zircon saturation revisited: temperature and composition effects in a variety of crustal magma types. Earth and Planetary Science Letters 64, 295-304.

Wiedenbeck, M., Alle, P., Corfu, F., Griffin, W.L, Meier, M., Oberli, F, Von Quadt, A., Roddick, J.C., Spiegel, W., 1995. Three natural zircon standards for U–Th–Pb, Lu–Hf, trace element and REE analyses, Geostandards Newsletter 19, 1–24.

Weinberg, R. F., Moresi, L., van der Borgh, P., 2003. Timing of deformation in the Norseman-Wiluna Belt, Yilgarn Craton, Western Australia. Precambrian Research 120(3), 219-239.

Winchester, J. A., Floyd, P. A., 1977. Geochemical discrimination of different magma series and their differentiation products using immobile elements. Chemical Geology 20, 325-343.

Chapter 5 - The geodynamic setting of the Cosmos region

5.1 Introduction

Detailed subsurface mapping via drill hole correlation has shown that the Cosmos greenstone succession was constructed by a combination of punctuated felsic, intermediate and ultramafic volcanism, accompanied by later-stage felsic and mafic intrusive activity and deposition of a volcanically derived sedimentary sequence (Chapter 2). Detailed U-Pb dating of the newly developed stratigraphy has shown that emplacement of the entire Cosmos greenstone succession, as seen today, spanned >80 Ma (Chapter 4). Therefore it records volcanic and intrusive activity and deposition of sedimentary sequences that covers a large portion of the geological history of the Kalgoorlie Terrane and wider EGS.

Geodynamic models of the setting of the EGS centre on either plume-dominated or subduction accretion models, or a combination of two (e.g., Campbell and Hill, 1988; Barley et al., 1989; 2006; 2008; Lesher and Arndt, 1995; Myers, 1993; 1997; Gee and Swager, 2008; Czarnota et al., 2010; Korsch et al., 2011; Barnes et al., 2012). The Cosmos volcanic sequence displays geochemical characteristics most similar to that of modern island-arc sequences (Chapter 3). Therefore, it is considered highly unlikely that the Cosmos greenstone succession could be attributed to derivation via a plume-only scenario. Komatiite volcanism in the Kalgoorlie Terrane is attributed to a large mantle plume (Campbell et al., 1988; Lesher and Arndt, 1995; Barnes et al., 2012). Arndt et al. (2008) suggest that the association of komatiites and calc-alkaline felsic volcanic rocks records the “conquest” of part of the subduction

zone by a rising mantle plume. Therefore, where ultramafic and calc-alkaline felsic rocks are intercalated, the two magma types must come from separate sources, from a plume and nearby subduction zone respectively. The association of komatiites with high-K calc-alkaline volcanic sequences at Cosmos requires that the geodynamic setting of the region feature both subduction and plume-derived volcanism. The following discussion will focus on how the Cosmos greenstone sequence relates to current subduction-accretion models for the geodynamic setting of the Kalgoorlie Terrane and wider EGS.

5.2 Arc volcanism and an early phase of komatiite volcanism - 2736 – 2730 Ma

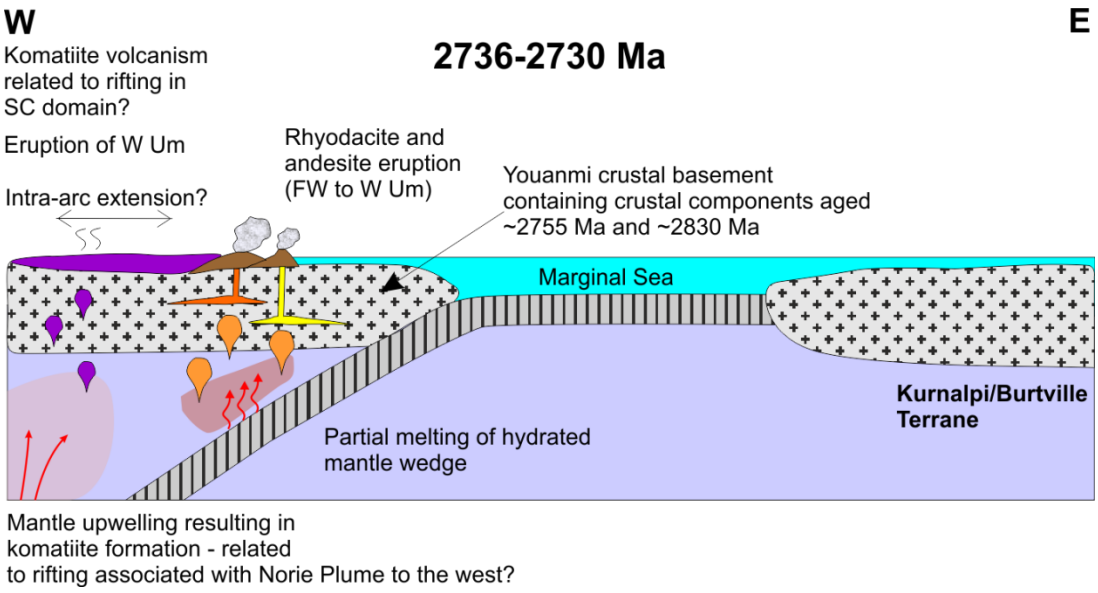

Figure 5.1 Schematic geodynamic setting for the Cosmos region, and wider Agnew-Wiluna greenstone belt between 2736Ma and 2730 Ma. SC = Southern Cross domain. FW = footwall. W Um = Western Ultramafic Unit

U-Pb dating of the Cosmos stratigraphy has shown that the emplacement of the oldest volcanic units at Cosmos took place between ~2736 Ma and ~2730 Ma (Chapter

4; de Joux et al., 2013). Both high-K calc-alkaline and komatiite volcanism occurred during this time period, indicating that subduction was active in the region along with plume activity that generated komatiite volcanism (Fig. 5.1). From the current dating constraints it is not possible to determine whether this bimodal volcanism was coeval, or separated by a hiatus of up to ~6 Ma. Czarnota et al. (2010) considered that the Kalgoorlie Terrane was underlain by Youanmi Terrane crustal basement. The occurrence of inherited zircons within the Cosmos succession, dated at ~2830 Ma and ~2755 Ma, concurs with this interpretation.

The high-K calc-alkaline affinity of the footwall volcanic sequence to the Western Ultramafic unit indicates it was most likely produced from partial melting of an enriched mantle wedge. This suggests a subduction zone was active in the region by ~2736 Ma. Hence, westwards dipping subduction beneath the proto-Kalgoorlie Terrane began earlier than has been suggested by most current subduction-accretion geodynamic models (e.g., Kositcin et al., 2008; Czarnota et al., 2010; Korsch et al., 2011). Furthermore, the Cosmos succession may represent the earliest phase of volcanism in the Kalgoorlie Terrane. The genetic relationship between the Cosmos sequence and the adjacent ~2736 Ma Kathleen Valley gabbro and associated Mt Goode basalt are currently unknown due to paucity of surface outcrop and limited drilling in the region to the north-west of Cosmos (Liu et al., 2002; Black et al., 2002; Duuring et al., 2012).

A mafic-ultramafic plume, the Norie plume, under the Southern Cross domain in the Youanmi Terrane, which lies to the west of Cosmos (Fig. 1.1), is considered to have moved eastwards between 2825 Ma and 2740 Ma (Wyman and Kerrich, 2012). This resulted in rifting along the eastern margin of the Yilgarn proto-craton, which could have produced the multiple fragments that correspond to the precursors of the six terranes that now comprise the EGS (Wyman and Kerrich, 2012). Therefore the Western Ultramafic unit could be a distal expression of plume-related magmatism between the Youanmi Terrane to the west and the proto-Kalgoorlie Terrane to the east. Equally, the magmatism that produced the Western Ultramafic unit could also be related to the Glen Group komatiite-basalt sequence in Southern Cross domain, which was emplaced between 2735 and 2700 Ma (Van Kranendonk et al., 2012). The

Western Ultramafic unit represents a phase of komatiite volcanism that significantly predates the modal ca. 2707 Ma komatiite volcanism in the Kalgoorlie Terrane (Kositcin et al., 2008). It could be suggested that the Western Ultramafic unit may represent a high level intrusion. If that were the case it would be younger than the dating constraints imposed by its enclosing stratigraphy and thus could be related to emplacement of the Cosmos UMu1 unit after ~2724 Ma. However, low-MgO horizons present within the Western Ultramafic unit are interpreted to represent meta-spinifex and meta-orthocumulate units (Hill and Dowling, 2008). The volcanic stratigraphic sequences directly under and over-lying the Western Ultramafic unit are compositionally and texturally distinct and also contrast in age. Collectively, the above evidence strongly suggests that the Western Ultramafic unit represents an older komatiite flow field and is thus a conformable part of the stratigraphy.

The Western Ultramafic unit is un-mineralised, suggesting it never reached sulphur saturation. The melting temperature of the underlying andesitic tuffaceous substrate is higher than that of a more siliceous substrate. Consequently the substrate may have been more resistant to thermo-mechanical erosion. Alternatively its barren nature may be due to a lack of pre-existing iron-sulphides in the substrate rocks, which recent workers have considered key to the formation of nickel sulphide deposits in the AWB (Bekker et al., 2009; Fiorentini et al., 2012).

It is not possible to comment upon the geodynamic regime to the east of Cosmos during the 2736 - 2730 Ma time interval (i.e., the Kurnalpi or Gindalbie Terranes) as no volcanic successions of this age occur within these terranes.

5.3 Continuation of arc volcanism - 2730 – 2724 Ma

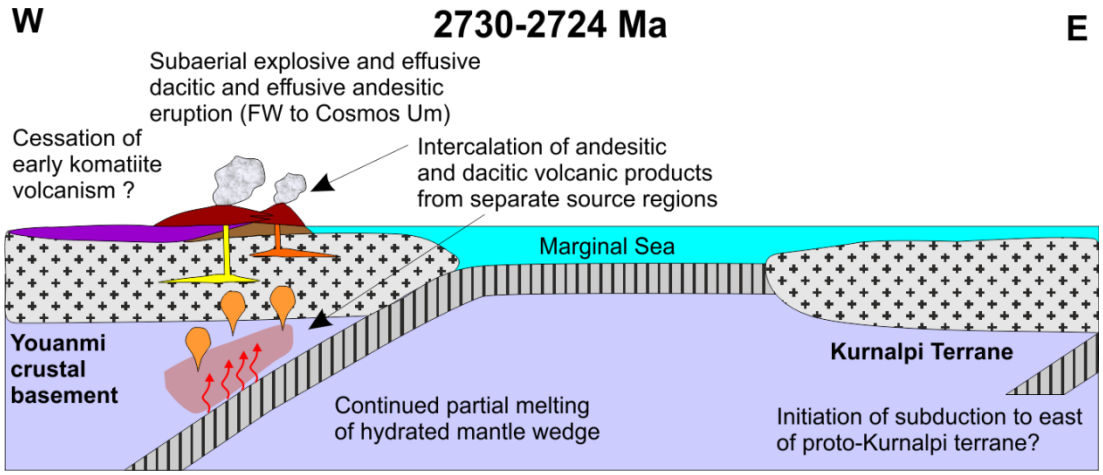

Figure 5.2. Schematic geodynamic setting for the Cosmos region, and wider Eastern Goldfields Superterrane, between 2730 and 2724 Ma. Modified after Korsch et al. (2011). FW = footwall. Cosmos Um = Cosmos Ultramafic Sequence, UMu1 package.

U-Pb dating has shown that the footwall to the Cosmos Ultramafic sequence was emplaced between 2730 and 2724 Ma (Chapter 4; de Joux et al., 2013). Geochemical analyses, along with AFC modelling, has shown that the dacitic and andesitic units, whilst both having a high-K to shoshonite calc-alkaline affinity, are not genetically related (Chapter 3). The intercalation of the dacitic and andesitic volcanic units indicate they were, however, coeval and emplaced in a subaerial setting, as indicated by their structures and textures, over several million years (Fig. 5.2; Chapter 2). Intermittent as well as post-emplacement subaerial erosion of this part of the Cosmos volcanic arc succession throughout its ~6 million years of construction may explain its relatively small thickness (~400m). Hence, periodic volcanism with substantial breaks between eruptions, combined with syn-volcanic and post-volcanic erosion of the succession, can explain the volcanic sequence's limited thickness.

A poorly constrained age of 2720 ± 14 Ma for the felsic footwall succession at Rocky's Reward suggests volcanism may have been occurring along the eastern segment of the AWB during this timeframe (Nelson, 1997a). Duuring et al. (2012) showed that the various stratigraphic components of the AWB largely display (para)

autochthonous relationships and attributed complexities to primary stratigraphic facies variations combined with the effects of polyphase deformation. Consequently, although the Cosmos succession may represent a separate accreted terrane, it is more likely that it signifies the initiation of volcanism in the AWB. The geochemical affinity of the Cosmos succession contrasts with the apparent TTD affinity of the AWB and implies different magma petrogenesis for the two successions. However, the available geochemical data on the rhyodacites at Perseverance and Mount Keith is inconclusive regarding the exact geochemical affinities of the volcanism in the eastern segment of the AWB (see Section 5.5 for further details.

The Wattagee formation of the Glen Group within the Southern Cross domain to the west of Cosmos is dated at 2725 ± 4 Ma (Wingate et al., 2009; Van Kranendonk et al., 2012) and thus is age equivalent to this part of the Cosmos succession. The Cosmos succession is also similar in age to the Marda complex in the Southern Cross domain (Van Kranendonk et al., 2012). These age relationships imply that the Youanmi Terrane accreted to the EGS proto-craton prior to ~ 2725 Ma, which is consistent with the notion that the Cosmos succession is underlain by Youanmi Terrane crustal basement. Van Kranendonk et al. (2012) consider, on the basis of plume-related komatiite volcanism in both the Youanmi Terrane and EGS between ~2720 - 2690 Ma, that accretion of the Youanmi Terrane with at least parts of the EGS occurred by ca. 2720 Ma.

5.4 Hiatus in arc volcanism in the Cosmos region and initiation of subduction in the Kurnalpi Terrane - 2724 – 2713 Ma

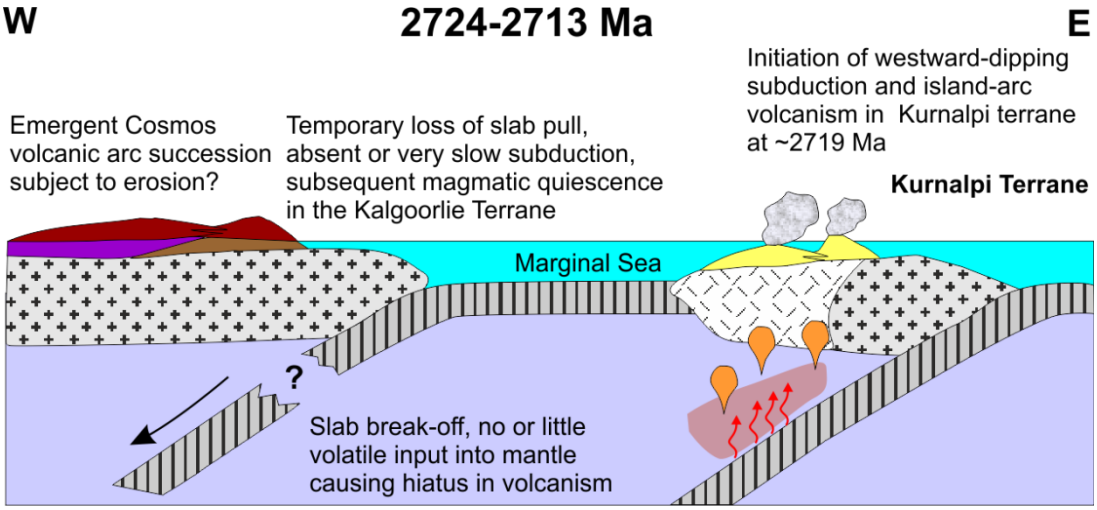

Figure 5.3. Schematic geodynamic setting for the Cosmos region, and wider Eastern Goldfields Superterrane between 2724 and 2713 Ma. Modified after Korsch et al. (2011) and Czarnota et al. (2010).

At present, the current dating constraints on the emplacement of the lower part of the Cosmos Ultramafic Sequence, UMu1, are bracketed by the ~2724 Ma age of the underlying and ~2685 Ma age of the overlying felsic volcanic sequences. Emplacement of the UMu1 package could have occurred at any point within this timeframe. de Joux et al. (2013) discussed the possibility that the contact between the UMu1 and its underlying footwall volcanic sequence may represent a significant unconformity, representing a major hiatus in volcanism in the region (Chapter 4). Ultramafic volcanism at Cosmos could be coeval with ultramafic volcanism in the eastern segment of the AWB. The only direct age dating of ultramafic units in the region is from the Mount Keith Ultramafic, where Re/Os ages indicate an emplacement age of 2706 ± 36 Ma (Foster et al., 1996). This is consistent with U-Pb dating obtained from the enclosing felsic stratigraphy at Mount Keith (Rosengren et al., 2008; Fiorentini et al., 2012; Duuring et al., 2012). These data can be taken to indicate that komatiite volcanism within the AWB is part of the ca. 2705 Ma komatiite

volcanism recorded elsewhere in the EGS (Fiorentini et al., 2012). Without direct dating of the UMu1 package, via U-Pb dating of baddeleyite or xenocrystic zircon within the ultramafic sequence, it is not possible to further constrain the timing of its emplacement. Isotopic analyses such as Re-Os could be attempted, but significant post-crystallisation Re and/or Os mobility has been observed in the sulphide deposits of the Yilgarn Craton (Lambert et al., 1998). Disturbance of the Re-Os system by hydrothermal alteration, sulfide recrystallisation during metamorphism and deformation and/or metasomatism associated with mesothermal lode-gold mineralisation potentially limit the use of this isotopic system (Lambert et al., 1998; Arndt et al., 2008). Its usefulness is limited further by the large uncertainty on Re-Os ages, such as the ± 36 Ma analytical uncertainty on the 2706 Ma Re-Os age of from Mount Keith (Foster et al., 1996; Lambert et al., 1998), especially in comparison to U-Pb dating of zircons (typically ± 5 - 10 Ma on $^{207}Pb/^{206}Pb$ ages). Therefore, the best available approach with best resolution for establishing the age of a komatiite is to date associated zircon-bearing felsic volcanic sequences using U-Pb (Arndt et al., 2008). Given the regional nature of ultramafic volcanism within the Kalgoorlie Terrane it is suggested that the emplacement of the Cosmos UMu1 package is related to the main Kalgoorlie komatiite plume event (Campbell and Hill, 1988; Lesher and Arndt 1995; Barnes et al., 2012). Consequently, the most likely emplacement age is at ca. 2705 Ma, although emplacement up to ~20 Ma before or after this date cannot be ruled out.

Felsic volcanism in the eastern segment of the AWB is dated at ~2713 - 2707 Ma at Mount Keith (Fiorentini et al., 2012), while the emplacement ages of the Rocky's Reward and Perseverance deposits are poorly constrained (e.g., de Joux et al., 2013; Chapter 4). Felsic volcanism at Rocky's Reward, dated at ~2720 Ma, could be co-eval with felsic and intermediate volcanism at Cosmos (Nelson 1997a; Duuring et al., 2012), although the statistical robustness of this date is questionable (de Joux et al., 2013; Chapter 4). Available dating, although limited in terms of coverage, suggests that the Perseverance footwall dacite is approximately the same age as the dacitic footwall at Mount Keith (~2711 Ma; Duuring et al., 2012).

The above dating constraints suggest there is little evidence of significant felsic or intermediate volcanism between ~2724 and ~2713 Ma within the AWB. Hence, this

may represent a period of volcanic quiescence and can be explained by slab breakoff within the AWB subduction zone and a consequent cessation of partial melting in the mantle above the slab. Moyen and van Hunen (2012) used numerical modelling to suggest that in these times of early plate tectonics, rather than being continuous, subducting slabs experienced frequent slab breakoff because plates were weaker and more buoyant than modern plates. Slab breakoff is one mechanism that has been proposed to explain the punctuated nature of volcanism within the Superior Province of Canada (Moyen and van Hunen, 2012). A similar slab break-off event could explain the ~10 Ma age gap between felsic volcanism in the Cosmos region and the ages obtained for felsic volcanism in the eastern segment of the AWB (Fig. 5.3).

Subduction was initiated in the Kurnalpi Terrane by ~2719 Ma (Fig. 5.3; Czarnota et al., 2010). This terrane is considered to be either part of the same subduction zone as the Kalgoorlie Terrane, that includes the AWB (Barley et al., 2008; Czarnota et al., 2010) or a separate island-arc setting (Korsch et al., 2011). The latter authors argue, based on Nd isotopes and an absence of earlier crustal components in parts of the Kurnalpi sequence, that the Kurnalpi volcanism took place in an oceanic island arc setting rather than a continental island arc. Evidence for a volcanic source for the TTD Kalgoorlie Sequence detritus that was emplaced between 2690 and >2658 Ma, has yet to be found in the Kurnalpi and Gindalbie Terranes (Krapež and Hand, 2008). This led Krapež and Hand (2008) to suggest that the boundary between the Gindalbie-Kurnalpi and the Kalgoorlie Terranes is a terrane suture and that these three terranes may not be part of the same subduction zone. Irrespective of whether these three terranes were part of the same arc, or represent different arc fragments that were later amalgamated, the similarity of volcanic sequences within all three terranes to modern subduction-related arc systems, indicate that a convergent plate margin was present in the eastern Yilgarn Craton in the Neoarchaean (Barley et al., 1989; 2006; 2008; Myers, 1993; 1997; Nelson, 1998; Morris and Witt, 1997; Czarnota et al., 2010; Korsch et al., 2011).

5.5 Arc volcanism in the eastern AWB, komatiite volcanism and continuation of subduction in the Kurnalpi Terrane - 2713 - 2700Ma

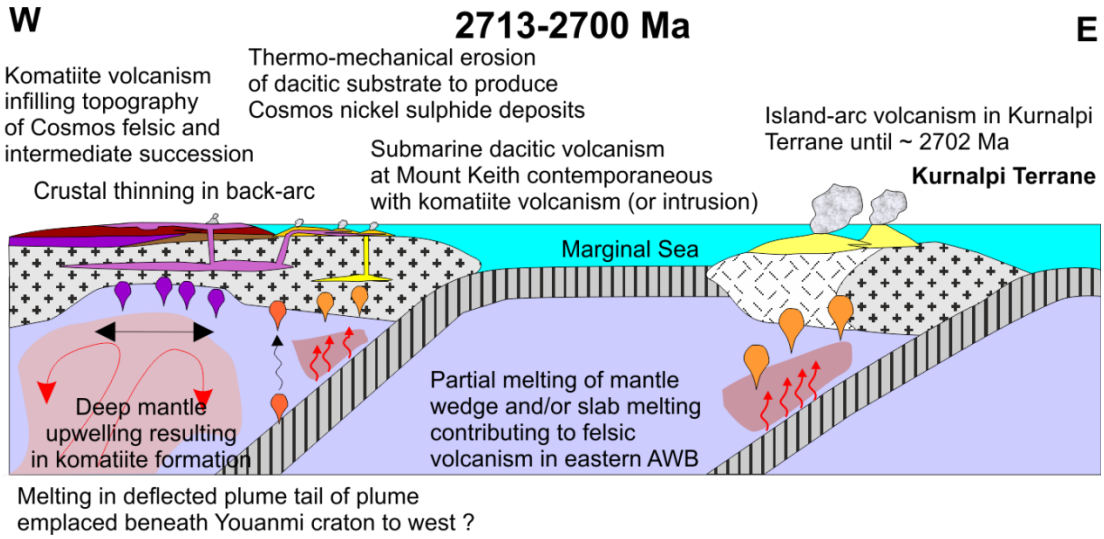

Figure 5.4 Schematic geodynamic setting for the Cosmos region, and wider Eastern Goldfields Superterrane between 2713 and 2700 Ma. Modified after Korsch et al. (2011) and Czarnota et al. (2010).

The Mount Keith and Perseverance felsic and ultramafic sequences in the eastern segment of the AWB were emplaced between ~ 2713 - 2700 Ma (Rosengren et al., 2005; 2008; Fiorentini et al., 2012; Duuring et al., 2012). The felsic units in the east of the AWB are considered to have a TTD affinity (Fiorentini et al., 2012) indicating they were formed via partial melting of a mafic precursor within the stability field of garnet. This either requires partial melting at the base of a thickened mafic crust or partial melting of a subducting slab. If volcanism in the AWB was derived via the latter mechanism, re-initiation of subduction could account for the TTD affinity of volcanism in AWB, provided that the subduction zone was subject to a higher geothermal gradient than prior to slab break-off. The presence of a plume in the back arc region of the subduction zone, as suggested by Czarnota et al. (2010), would have raised the geothermal gradient of the subduction zone and promoted slab melting, rather than partial melting in the mantle wedge.

However, the TTD affinity of volcanism in the eastern AWB has not been convincingly demonstrated. The Mount Keith dacites exhibit similar REE concentrations to those of the Cosmos dacites and other calc-alkaline suites (Fig. 5.5). Critically, they do not show the HREE depletion typical of TTD affinity felsic rocks, such as the Black Flag Group, in the Kalgoorlie Terrane (Morris and Witt, 1997; Krapež et al., 2000; Fig. 5.5). Perseverance dacites are less enriched in LREE than the Cosmos dacites but again do not show the HREE depletion typical of TTD volcanic suites (Fig. 5.5). Table 5.1 also highlights the fact that the Perseverance dacites do not meet all the criteria of TTD affinity. When plotted alongside the high-K calc-alkaline to shoshonite Cosmos dacitic tuffs and lavas, as well as the TTD-affinity Cosmos felsic intrusive porphyries and Black Flag dacites, the Perseverance felsic porphyry samples are more similar to the products of basalt-andesite-dacite-rhyolite (BADR) island arc volcanism (Fig. 5.6). The majority of samples fall into the BADR/modern continental crust fields although a few extend into the lower part of the Archaean TTG/modern Adakite fields (Fig. 5.6). Therefore, it is concluded that the Perseverance felsic porphyry do not convincingly exhibit TTD affinity. The data presented here suggests that both the Mount Keith and Perseverance dacites are geochemically more similar to the island-arc Cosmos dacitic units than TTD-affinity volcanic rock in the southern parts of the Kalgoorlie Terrane (Morris and Witt, 1997; Krapež and Hand, 2008). A more detailed investigation of the regional geochemical affinity of non-ultramafic volcanism within the AWB is required to further constrain petrogenesis of the Mount Keith and Perseverance felsic successions. Evidence presented here certainly contradicts Fiorentini et al's (2012) assertion that dacites within the AWB display a TTD affinity. Regardless, TTD-affinity volcanism cannot be used to argue against a subduction zone setting for the AWB because TTD-affinity magmas can be formed via melting of a subducting slab (Moyen and Martin, 2012). Consequently AWB volcanism could all be subduction related, with parental melt inputs from both slab melting and partial melting in the mantle wedge. Constraining the possible petrogenesis of regional felsic and intermediate volcanism in the AWB is beyond the scope of this discussion but certainly presents an avenue for future research aimed at providing better constraints on the palaeo-tectonic setting of the AWB.

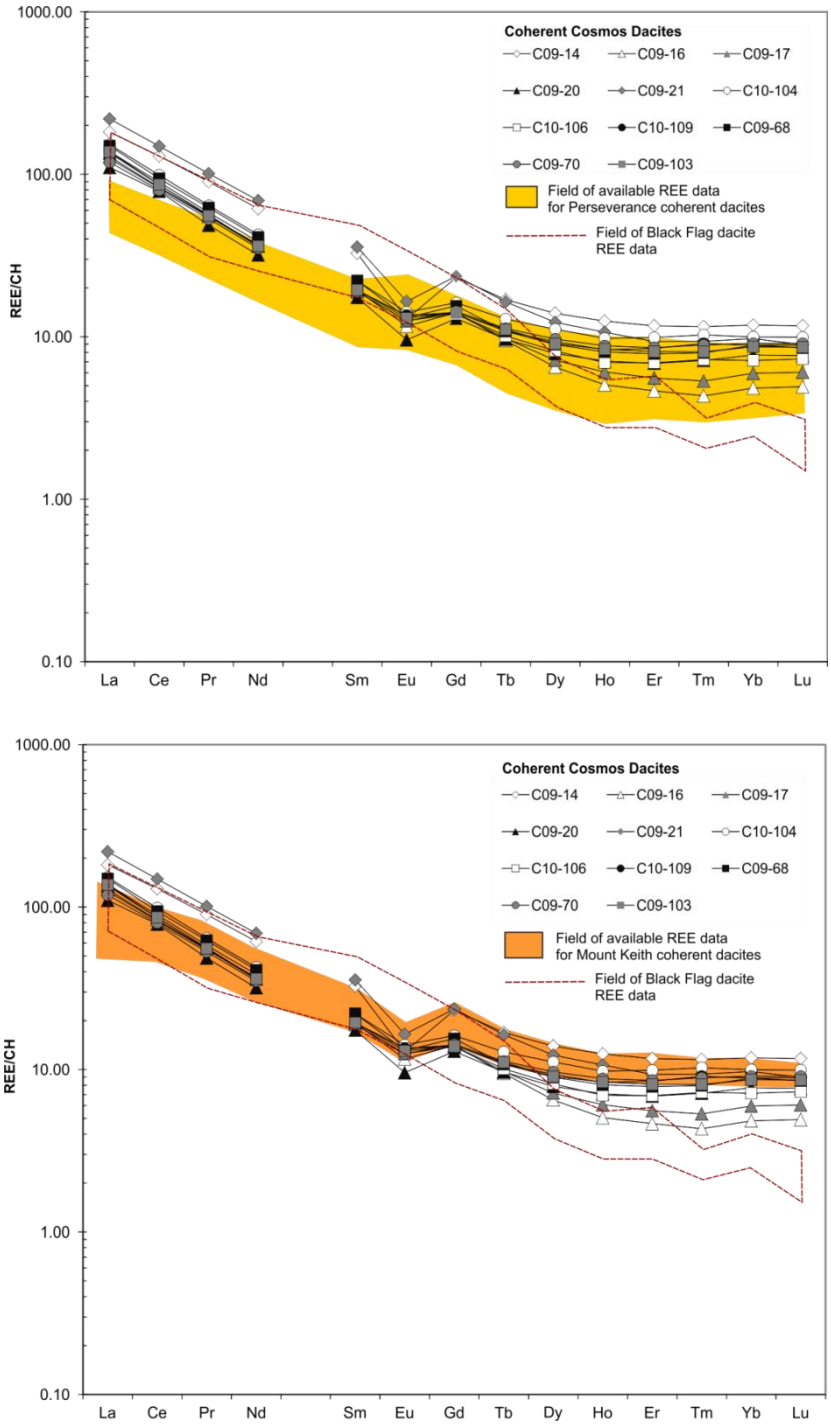

Figure 5.5. Comparison of the chondrite-normalised REE concentrations of the Cosmos, Perseverance, Black Flag and Mount Keith dacites highlighting the broad similarities between dacitic volcanic units at Cosmos, Perseverance and Mount Keith in comparison to those of the TTD-affinity Black Flag group. Black Flag data from Morris and Witt (1997), Mount Keith data from Rosengren et al. (2008), Perseverance data from Duuring et al. (2012). Note there is no detailed published geochemical data available for Mount Keith so the field of the REE field has been copied directly from Rosengren et al. (2008). The fields for Black Flag and Perseverance have been constrained using the published geochemical data sets, plotted alongside the Cosmos geochemical data. CH = chondrite.

Table 5.1. Comparison of the felsic rocks of Cosmos and those of Perseverance and Black Flag. The Cosmos felsic extrusive volcanic units display no TTD affinity, while the Cosmos intrusive porphyries and the Dacites of Black Flag are strongly TTD. The characteristics of the felsic porphyry units at Perseverance are ambiguous, suggesting that are not true TTD-affinity volcanic units as they do not meet all criteria required for a TTD affinity (Moyen and Martin, 2012). Black Flag data from Morris and Witt (1997) and Perseverance data from Duuring et al. (2012). HW = Hangingwall, FW = Footwall

	Typical TTD affinity rocks	Average Cosmos dacite lavas	Average Cosmos dacite lapilli tuffs	Average Cosmos HW felsic porphyry intrusion	Average Cosmos FW felsic porphyry intrusion	Average Black Flag dacites	Average Perseverance rhyodacite
Al_2O_3	≥ 15 wt %	14.34	14.22	15.87	14.98	16.00	14.83
Sr(ppm)	300 - >2000	88	102	463	434	635	240.8
Y(ppm)	<18	21	31	4.9	3.2	6.0	13.4
LREE	Enriched	Yes	Yes	Yes	Yes	Yes	Yes
HREE	Depleted	No	No	Yes	Yes	Yes	No
EU Anomaly	None or positive	Negative	Negative	None	None	None	None
K_2O/Na_2O	Commonly <1	Highly variable due to mobility of alkaline phases		0.58	0.45	0.55	0.48

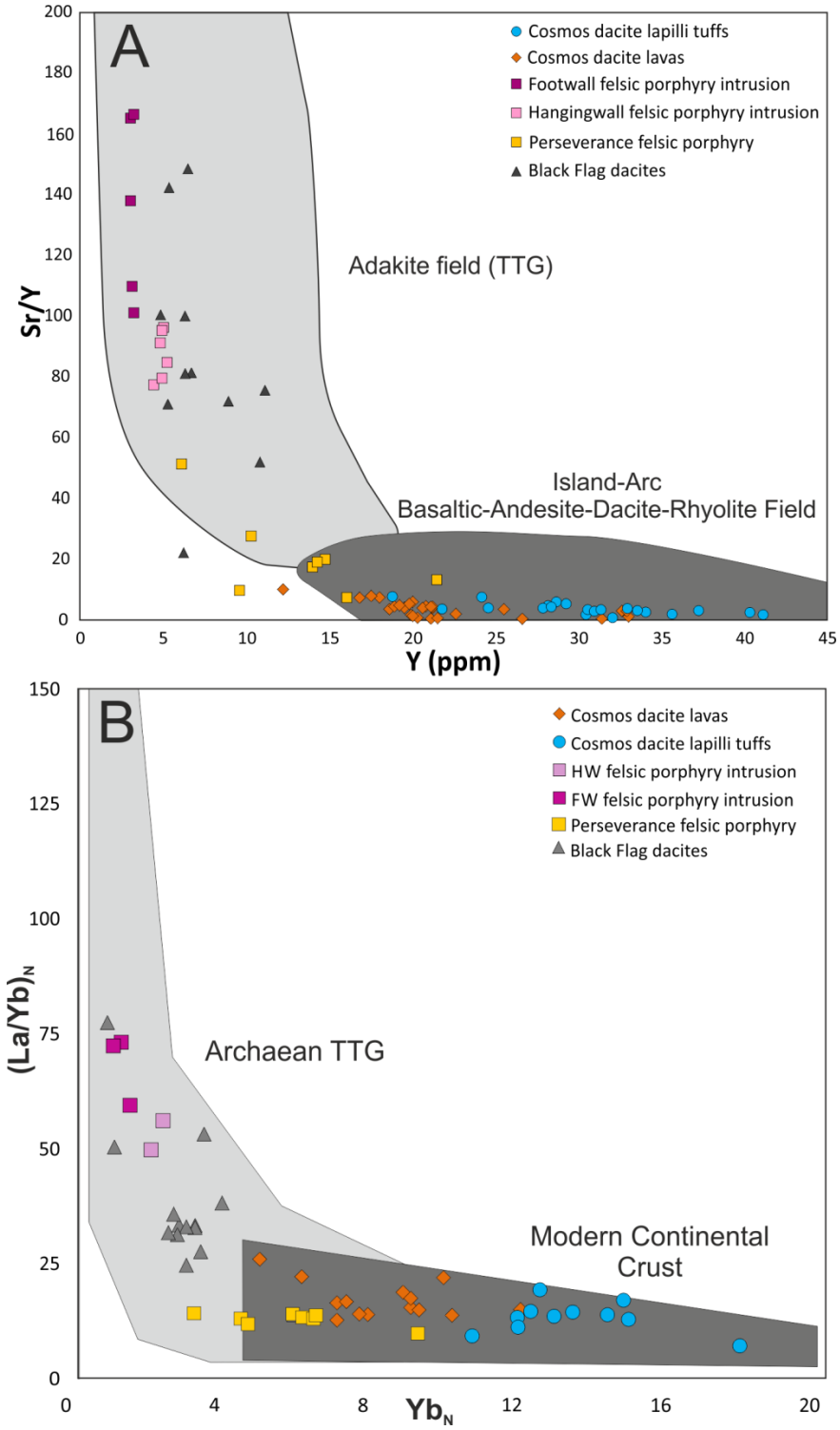

Figure 5.6. **(A)** Sr/Y vs. Y diagram (after Defant and Drummond (1990) and Drummond and Defant (1990)) modified after de Joux et al. (2013) showing the Cosmos felsic volcanic units and intrusions as well as the TTD affinity Black Flag dacites and the Perseverance felsic porphyry units **(B)** $(La/Yb)_N$ vs. Yb_N after Martin (1986). La/Yb_N is chondrite normalised using the values from Masuda *et al.* (1973) divided by 1.2, after Moyen and Martin (2012). Black Flag Group data from Morris and Witt (1997) while Perseverance data is from Duuring et al. (2012).

Komatiite volcanism throughout the AWB, and wider Kalgoorlie Terrane, is considered to result from either a plume within a back-arc region (e.g., Czarnota et al., 2010), or a larger plume head that was deflected from beneath the Youanmi Terrane to the west (Barnes et al., 2012). If the latter were the case, the Western Ultramafic unit volcanism may represent the earliest phase of komatiite volcanism in the west of the AWB, followed by the UMu1 komatiite at least 6 Ma later. Subsequent komatiite volcanism at Mount Keith and Perseverance in the eastern segment of the AWB could reflect the relative movement of the ultramafic plume to the east. If, however, UMu1 komatiite volcanism at Cosmos was contemporaneous with komatiite volcanism in the eastern segment of the AWB at ca. 2705 Ma, this implies the subaerial Cosmos succession was subjected to considerable erosion during the possible 20 Ma hiatus in volcanic activity.

Emplacement of the UMu1 komatiite resulted in thermo-mechanical erosion of the underlying substrate, where dacitic tuffaceous horizons were most susceptible to thermo-mechanical erosion. Presence of base-metal and iron sulphides within the dacitic lapilli tuff and tuff breccia units of the footwall have been noted (this study and Mark Styles, pers comm., 2013) and are indicative of a mineralised fossil hydrothermal system within the arc sequence (Fig. 5.7). The dacite footwall may have acted as a source of silica to the overriding komatiite lavas during thermo-mechanical erosion, which resulted in lowering of the sulphur saturation point, promoting the formation of immiscible sulphides. Pre-existing sulphides within the volcanic substrate may also have contributed sulphur/sulphides directly to the over-riding komatiite lavas. Fiorentini et al. (2012) considered that pre-existing sulphides, derived from VMS-like deposits, in the immediate vicinity of the AWB felsic volcanic centres, may have been crucial to the formation of nickel sulphide deposits within the region's komatiites.

During this timeframe subduction beneath both the Kalgoorlie Terrane and the Kurnalpi Terrane resulted in the continuing closure of the marginal sea between these two terranes (Fig. 5.4). Calc-alkaline volcanism in the Kurnalpi Terrane continued until ~2702 Ma (Korsch et al., 2011).

Figure 5.7. Top. Example of iron and base metal sulphides occurring within finely laminated and crenulated felsic volcanic units and associated with quartz veins. Sulphide assemblages consist of varying amounts of fine-grained sphalerite and pyrrhotite with minor galena and chalcopyrite. Sulphide grains are often folded along laminations indicating some syn-depositional emplacement. There is no evidence of pentlandite. Bottom: 6 cm vein of massive sphalerite, which may be related to primary hydrothermal activity within the volcanic edifice.

5.6 TTD-affinity volcanism and sedimentation, cessation of komatiite volcanism and initiation of high-Ca granite intrusion - 2690 – 2675 Ma

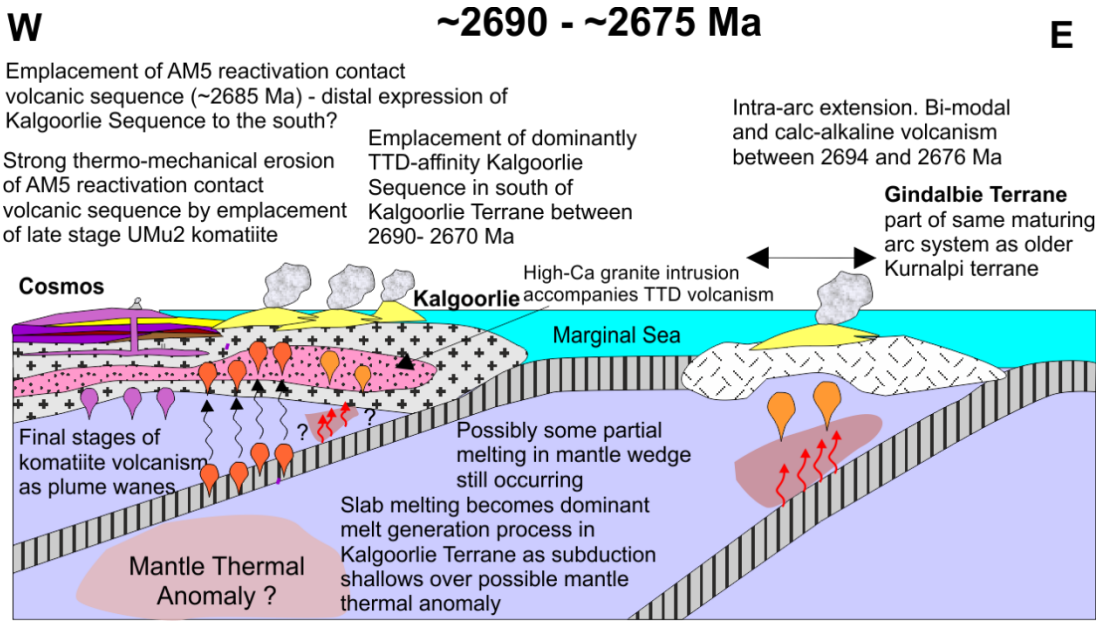

Figure 5.8. Schematic geodynamic setting for the Cosmos region, and wider Eastern Goldfields Superterrane between 2690 and 2670 Ma. Modified after Korsch et al. (2011) and Czarnota et al. (2010).

There is little volcanic stratigraphy of this age within the Cosmos succession. A felsic volcanic rock from the AM5 "reactivation" contact is dated at ~2685 Ma, underpinning the interpretation that the Cosmos Ultramafic Sequence is composed of two separate flow fields, the UMu1 package, emplaced prior to 2685 Ma, and the UMu2 package, emplaced after 2685 Ma (de Joux et al., 2013; Chapter 4). I suggest that the UMu2 ultramafic package corresponds to latest stage komatiite volcanism in the Kalgoorlie Terrane before ultramafic volcanism ceased. At present, the minimum age of komatiitic volcanism within the terrane is considered to be 2692 ± 4 Ma (Claoué-Long et al., 1988). This is based on SHRIMP U-Pb zircon dating of the Kapai Slate, which overlies the komatiite succession at Kambalda. Thus, the UMu2 package, which was emplaced after 2685 ± 8 Ma, is possibly significantly younger than the

currently assumed minimum age of komatiite volcanism in the Kalgoorlie Terrane. However, the uncertainty of this age determination overlaps with that established for the Kapai Slate. Therefore, a near-contemporaneous emplacement of the UMu2 unit with the youngest komatiites at Kambalda cannot be ruled out.

The ~2685 Ma age of the volcanic sequence along the AM5 "reactivation" contact suggests it may be a distal expression of the Kalgoorlie Sequence volcanism, which had its focus in the south of the Kalgoorlie Terrane between ~ <2690 to >2658 Ma (Krapež and Hand, 2008). This sequence is a >3000m-thick succession of volcaniclastic sedimentary rocks with subordinate rhyolite, dacite, andesite and basalt. It includes the Black Flag Group, which exhibits a strong TTD-affinity (Fig. 5.6; Morris and Witt 1997; Krapež and Hand, 2008, Kositcin et al, 2008; Czarnota et al., 2010). Limited geochemical data on volcanic units along the AM5 "reactivation" contact implies that their geochemical affinity is distinct and differs from both the 2730 Ma – 2724 Ma Cosmos footwall volcanic sequence and the 2670 Ma and 2653 Ma felsic porphyry intrusions. The AM5 "reactivation" contact felsic volcanic rocks fall close to the TTG – island-arc field boundary, exhibiting a weak TTG-affinity (Fig. 5.9) comparable to the low Sr/Y units of the Black Flag Group. However, they do not show the same span in Sr/Y values as the felsic volcanic rocks of the Black Flag Group (Fig. 5.9). The effect of element mobility on the AM5 "reactivation" sequence during metamorphism may have been substantial. Also, field relations indicate that it underwent substantial thermo-mechanical erosion during emplacement of the UMu2 komatiite, possibly forming hybrid layers (Denny, 2010; Chapter 4). Collectively, these processes have affected the major and trace element geochemistry of the AM5 volcanic sequence. Without more detailed geochemical study aimed at ascertaining the REE concentrations of volcanic units along this contact it is not possible to probe further into its petrogenesis. Therefore, given their similarity in age, I propose that volcanism along the AM5 "reactivation" contact is related to the ~2690 – 2670 Ma TTD-affinity volcanism within the Kalgoorlie Terrane.

The principal stratigraphic component of the Kalgoorlie Sequence is dominantly volcanogenic-sedimentary rocks, as well as subordinate volcanic rocks and re-sedimented syn-eruptive volcaniclastic rocks (Krapež and Hand, 2008).

Recycling of older felsic supracrustal rocks is evident from zircon provenance, with some zircon populations dated at ~2730 Ma (Krapež et al., 2000; Krapež and Hand, 2008). Prior to this study, rocks of this age were unknown in the EGS (Krapež et al., 2000; Krapež and Hand, 2008). Recycling of volcanic rocks similar in age to those of the Cosmos region could account for the provenance of ca. 2730 Ma zircons in younger Kalgoorlie volcanic sequences. Given the Cosmos sequence is now geographically separated from the Kalgoorlie sequence by ~ 400 kilometres, it raises the possibility that volcanic arc sequences aged 2730 - 2725 Ma may have been more widespread throughout the Kalgoorlie Terrane but are poorly preserved.

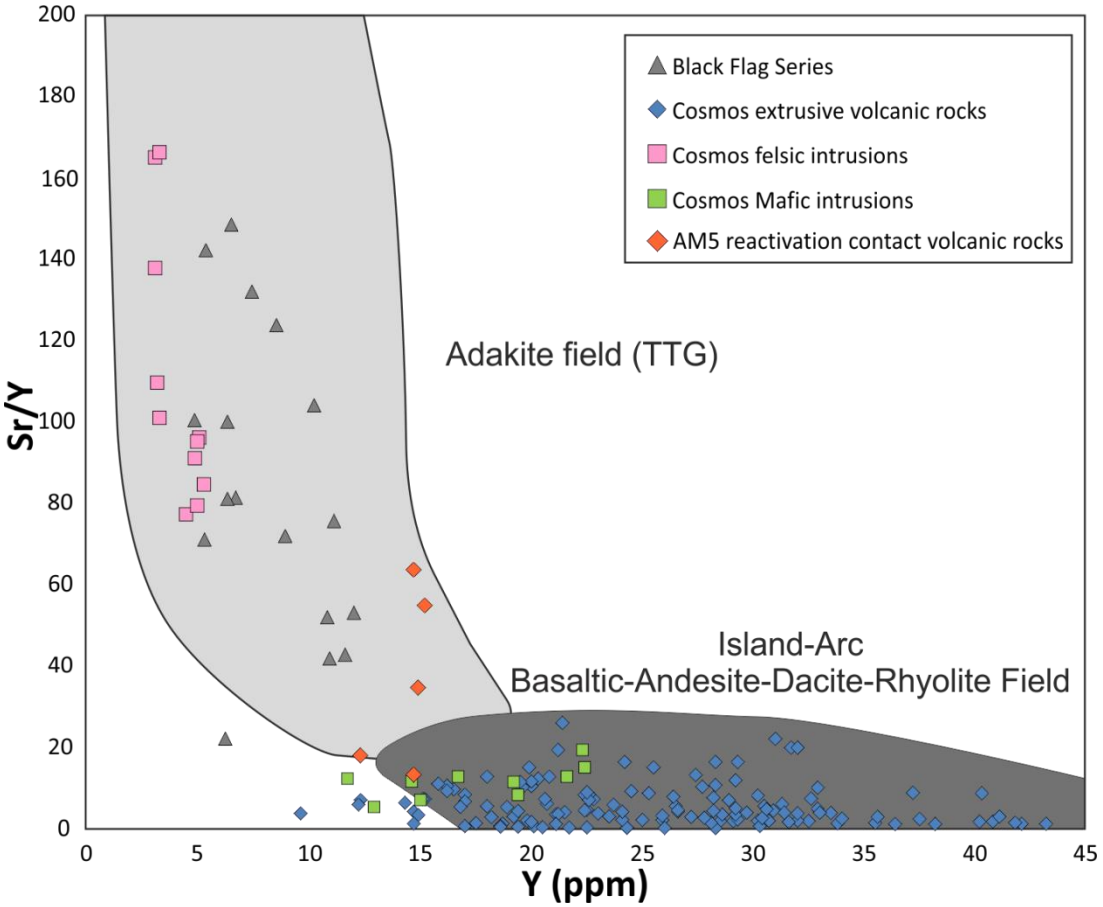

Figure 5.9. Sr/Y vs. Y diagram (after Defant and Drummond (1990) and Drummond and Defant (1990)) modified after de Joux et al. (2013) showing the Cosmos footwall volcanic units and intrusions as well as the TTD affinity Black Flag group and the volcanic units along the AM5 "reactivation" contact (after de Joux et al., 2013; Black Flag data from Morris and Witt, 1997).

Coeval basaltic-felsic TTD-affinity volcanism within the Kalgoorlie Terrane between ~2690 – 2665 Ma is considered by many authors to have occurred due to melting of the subducting slab beneath the Kalgoorlie Terrane (Fig, 5.8; Morris and Witt, 1997; Krapež and Hand, 2008; Czarnota et al., 2010). Similar TTD affinity volcanic rocks are found in modern convergent margins where slab melting is considered to taking place in response to shallow subduction of young and hot lithosphere, rather than melting of the overlying mantle wedge (Drummond and Defant, 1990). Consequently a switch from partial melting of the mantle wedge to melt generation via slab melting, and production of TTD/TTG melts in the Kalgoorlie Terrane is attributed to a shallowing of the subducting slab (e.g., Morris and Witt, 1997; Krapež and Hand, 2008; Czarnota et al., 2010). Shallowing of subducting slab is also associated with voluminous high-Ca granite magmatism, resulting in emplacement of voluminous granitoids into the upper crust with associated magmatic crustal thickening in an overall extensional regime (Fig. 5.8; Champion and Sheraton, 1997; Champion and Cassidy, 2007; Krapež and Hand; 2008; Czarnota et al., 2010). Czarnota et al. (2010) proposed that interaction of the subducting slab with hot mantle up-welling beneath the Kalgoorlie Terrane could facilitate the melting of the subducting slab. This also suggests that buoyancy effects of the plume could account for the proposed extensional regime within the Kalgoorlie Terrane in this time frame.

Volcanism was taking place in the Gindalbie Terrane in the east of the EGS between ~2694 and 2676 Ma (Fig. 5.4). Bimodal (basalt–rhyolite) complexes (Melita) and calc-alkaline intermediate-silicic volcanic complexes (Spring Well and Jeedamya) were emplaced between 2694 ± 4 and 2676 ± 5 Ma (Morris and Witt, 1997; Brown et al., 2002; Barley et al., 2008). Rhyolites from the bimodal Melita Complex are distinctive in the EGS (Brown et al, 2002), whereas felsic rocks from the calc-alkaline complexes are considered to be arc-related and chemically similar to andesites and rhyodacites from the Kurnalpi Terrane (Morris and Witt, 1997; Barley et al., 2008). The latter authors thus consider the Kurnalpi and Gindalbie Terranes represent to evolution of the same maturing arc with a change from marginal intra-arc volcanism in the Kurnalpi Terrane to a mature arc-rifting in the Gindalbie Terrane (Morris and Witt, 1997; Barley et al., 2006; 2008). Parts of the Gindalbie Terrane, such as the

Melita succession, are broadly coeval with the Black Flag Group. Both successions have been attributed, by several authors, to formation in convergent plate margin settings (e.g. Morris and Witt, 1997; Brown et al, 2002; Barley et al., 2008, Krapež and Hand, 2008; Czarnota et al., 2010; Korsch et al., 2011). However, Brown et al., (2002) brought attention to the contrasts in their volcanic and sedimentary facies, composition and petrogenesis. Therefore, they suggested that the Black Flag Group and Melita Complex represent separate arc-rift systems. This concurs with interpretation of Krapež and Hand (2008) and Korsch et al., (2011) presented in Figures 5.3 - 5.5. Brown et al. (2002) also suggested that the Gindalbie and Kalgoorlie successions may have developed upon the same complex margin and subsequently been accreted laterally.

In comparison to the Cosmos dacite lavas, the rhyodacite units from Spring Well and Jeedamya in the Gindalbie Terrane and Bore Well in the Kurnalpi Terrane are slightly less enriched in LREEs and less depleted in HREEs (Fig. 5.10). This likely reflects a higher degree of source enrichment and increased amount of garnet and/or amphibole in the source region of the Cosmos dacites. However the chondrite-normalised REE concentrations of the Gindalbie, Kurnalpi and Cosmos regions are very similar, indicative of their shared calc-alkaline (high-K calc-alkaline in the case of Cosmos) geochemical affinity and island-arc tectonic setting.

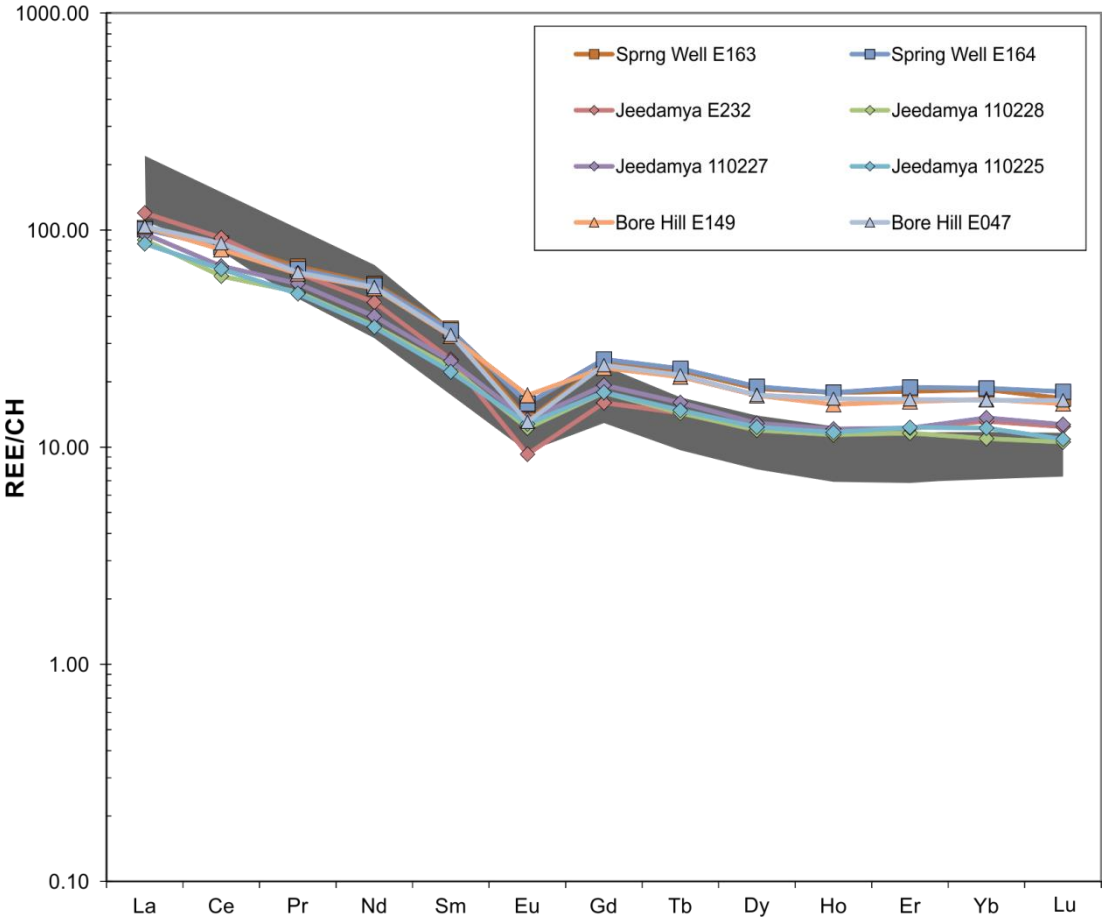

Figure 5.10. REE traces normalised to chondrite values of Boynton (1985) for selected rhyodacite samples from Spring Well and Jeedamya in the Gindalbie Terrane and Bore Hill in the Kurnalpi Terrane. The shaded region represents the field of values for dacitic lavas within the Cosmos succession. The similarity between the calc-alkaline rocks of these three regions is apparent, although the Cosmos dacites are slightly more enriched in LREE and depleted in HREE than the Gindalbie and Kurnalpi rhyodacites. The Cosmos dacites appear to be most similar to the Jeedamya rhyodacites depicted by diamond data points. Spring Well, Jeedamya and Bore Hill data is from Barley et al. (2008) and Giles (1982). CH = Chondrite

5.7 Granite intrusion, formation of late sedimentary basins and cessation of arc volcanism - 2675-2650 Ma

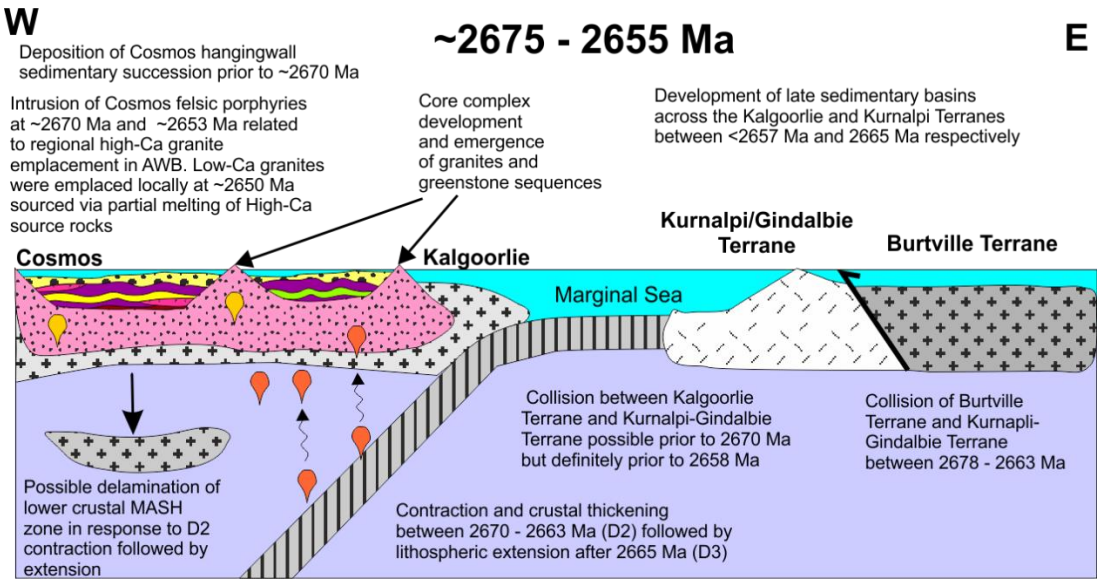

Figure 5.11 Schematic geodynamic setting for the Cosmos region, and wider Eastern Goldfields Superterrane between 2675 and 2655 Ma. Modified after Korsch et al. (2011) and Czarnota et al. (2010).

Early in this time period (~2670 Ma) diachronous, but short lived (~5 Ma), D2 contraction occurred, along with minor crustal thickening (Czarnota et al., 2010). This may have triggered delamination of an eclogite restite layer at the base of the crust (Czarnota et al., 2010). This event was followed by lithospheric extension (D3), possibly coupled with the aforementioned delamination of eclogite, which resulted in the development of metamorphic core complexes with granite centres (Czarnota et al., 2010). This led to uplift and exhumation of granites and high pressure-temperature metamorphic rocks and their subsequent erosion, resulting in the deposition of detritus in late sedimentary basins (Krapež et al., 2000; Czarnota et al., 2010). This timeframe saw many changes in the complex geodynamic setting of the EGS that are largely beyond the scope of this discussion and are covered in detail by other workers (e.g., Kositcin et al., 2008; Czarnota et al., 2010). However, it is relevant to discuss how the Cosmos stratigraphy fits into the geodynamic setting of the EGS during this time frame.

Formation of the late basins within the EGS is constrained to 2665 Ma within the Kurnalpi Terrane and <2657Ma in the Kalgoorlie Terrane, based on SHRIMP U–Pb detrital zircon in sediments and dating of zircons within intrusions (Krapež et al., 2000; Kositcin et al., 2008; Czarnota et al., 2010). The maximum age of deposition for the Jones Creek Conglomerate, a late basin sequence in the west of AWB, is constrained at ~ 2667 ± 6 Ma from contained detrital zircons (Nelson, 1997d). This led Krapež et al., (2000) to suggest that the Jones Creek Conglomerate was deposited at ~2665 ± 5 Ma.

The hangingwall sedimentary succession at Cosmos may represent the along-strike continuation of the Jones Creek Conglomerate style of sedimentation (de Joux et al., 2013; Chapter 4). Dating constraints imposed by the cross-cutting hangingwall felsic porphyry intrusion indicate that this sedimentary sequence must have been emplaced prior to 2670 Ma. Thus, late basin sedimentation in the AWB initiated ~ 10 - 15 Myr before those in the south of the Kalgoorlie Terrane, such as the Kurrawang and Merougil late basins (Czarnota et al., 2010). Initiation of late basin deposition marks a change from volcanic-dominated sedimentation to clastic-dominated sedimentation characterised by extensive recycling of older volcanic and intrusive sequences, with no new input of volcanic detritus (Czarnota et al., 2010). Late basins are coarse siliciclastic successions, with granite detritus, which overlie, unconformably or in fault contact with, older volcanic-dominated successions (Durney, 1972; Bunting and Williams, 1979; Krapež, 1997; Czarnota et al., 2010). The latter successions may have been folded prior to late basin deposition (Blewett et al., 2004). Both fluvial and turbiditic facies are recognised, with fluvial facies possibly representing an earlier stage of basin fill (Krapež, 1997; Krapež et al, 2000). Provenance studies of U-Pb dated detrital zircons indicate multiple older sources but largely corresponding to known ages of greenstones and granites in the EGS (Krapež et al., 2000; Barley et al., 2002).

The hangingwall sedimentary succession at Cosmos contains detrital zircons dated at ~ 2724 Ma indicating that erosion and transport of the local Cosmos footwall succession may have contributed to sedimentation. This is also indicated by the geochemical similarity between the felsic and intermediate volcanically-derived

sediments in the hangingwall and the dacite and andesite volcanic lavas and tuffs in the Cosmos footwall respectively. The occurrence of rounded granitic clasts within common monomictic and polymictic conglomerates indicates that older volcanic sequences were not the only source of sediments. Therefore hangingwall sedimentation must post-date granite intrusion, as well as their uplift and exhumation. Local granites to the east of Cosmos were emplaced at ~2650 Ma (Lui et al., 2002). Therefore the source of the granitic clasts is likely to be older high-Ca granites, possibly those to the west of Cosmos, such as Six Mile Well, dated at ~2685 Ma (Nelson, 1997a). Highly evolved felsic sediments in the south of the Cosmos region show little geochemical similarity to any of the volcanic rocks within the footwall. Thus the hangingwall sedimentary sequence appears to have been partially derived from erosion of volcanic units similar in age and composition to that of the Cosmos footwall volcanic sequence suggesting a proximal sediment source (de Joux et al., 2013). The hangingwall sequence also contains an evolved felsic sedimentary component of unknown provenance, as well as sub-rounded granitic clasts derived from an uplifted distal granitic source (de Joux et al. 2013). This is consistent with the interpretation that the nearby Jones Creek conglomerate was formed in a subaerial high-discharge fluvial environment and sourced in rapidly eroding, high relief areas composed of exhumed granite as well as mafic, intermediate and felsic volcanic rocks. (Durney, 1972; Bunting and Williams, 1979; Krapež and Hand, 2008). Fluvial environments identified within the Jones Creek conglomerate are considered to be proximal to medial braid-plains (Krapež and Barley, 2008). Sparse palaeocurrent data indicates axial transport was to the south or southeast, implying north-to-south palaeoslopes (Krapež and Barley, 2008). Similar depositional architecture and provenance variations for the Jones Creek, Scotty Creek, and Yandal basin fill sequences has been used to imply they were part of the same basin (Krapež and Barley, 2008). This implies that the Kalgoorlie and Gindalbie Terranes were close to their present-day geometry when basin filling initiated at ~2665 Ma (Nelson, 1997d). Thus, terrane amalgamation in this area must have occurred prior to initiation of basin deposition in the northern parts of the Kalgoorlie and Gindalbie Terranes. This notion contradicts the model put forth by Korsch et al., (2011), which suggested that the Kurnalpi-Gindalbie-Burtville amalgamated terrane did not collide with the Kalgoorlie

Terrane until 2658-2655 Ma. The results of Blewett et al. (2010) indicate that all three terranes of the EGS display a common structural history post -2670 Ma based on a study of structural overprinting relationships across the central and northern Yilgarn. If correct, this places constraints on any allochthonous model for the development of the EGS, such as that suggested by Korsch et al., (2011), because it implies that all terranes had amalgamated by 2670 Ma.

The geodynamic model for late basin deposition is debated with authors suggesting either strike-slip influences on basin filling, with each basin in the EGS representing a linear zone of subsidence adjacent to or between intra-terrane strike faults (Krapež and Barley, 2008) or late basins deposition in narrow extensional grabens (Hallberg, 1985; Czarnota et al., 2010). Czarnota et al., (2010) concluded that the timing and architectural relationships of the late basins with respect to large granite domes and extensional shear zones are more consistent with an extensional geodynamic setting. On the other hand, Krapež and Barley (2008) proposed that, in each terrane, late-stage basins developed within fault-bound compartments within a tectonic corridor bounded to the west by a dextral strike-slip fault and to the east by a sinistral strike-slip fault. They also suggested that north or northwest convergence between the Burtville Terrane to the east and an ancestral Yilgarn continent to the northwest produced a south-propagating orogen, with the Kalgoorlie, Gindalbie, and Kurnalpi Terranes trapped in a tectonic-escape corridor. Unfortunately the Cosmos hangingwall succession itself provides little information to aid the debate on late basin deposition as its link to the Jones Creek Conglomerate is not fully understood. Further geochemical and detrital zircon analyses are needed to assess its provenance more vigorously.

The latest stage events within the Cosmos stratigraphy are the felsic porphyry intrusions. As previously discussed in Chapters 3 and 4, these are considered to be related to local high-Ca granite intrusion. The TTG affinity of high-Ca granites is consistent with derivation from partial melting of a plagioclase-poor basaltic precursor, within the garnet stability field, either within a thickened mafic crust or melting of subducted oceanic crust (Champion and Cassidy, 2002; 2007). The M2 phase of metamorphism in the EGS occurred between 2685 – 2665 Ma, prior to the

deposition of late basins (Goscombe et al., 2009; Czarnota et al., 2010). This regional-contact type of metamorphism was dominated by conductive heat transfer associated with large volumes of high-Ca granites (Czarnota et al., 2010). The M2 event corresponded to temperatures of 300 - 550ºC and peak metamorphic pressures of 3.5 – 5.0 kbar across greenstone belts (Goscombe et al., 2009: Czarnota et al., 2010). As discussed in Chapter 2, this is likely to be the metamorphic event detected by garnet-biotite geothermometry within the Cosmos succession of ~3 kbar and 560-580ºC. Alternatively the higher indicated temperatures at Cosmos may represent the peak conditions, at 500 – 580ºC and 4.0 ± 1 kbar, of the M3a event, whose PT conditions are indicative of lithospheric extensional settings (Czarnota et al., 2010). M3a metamorphism is interpreted to have accompanied ongoing late basin fill between 2665 – 2650 Ma, and immediately afterwards (Czarnota et al, 2010). As the currently known distribution of the M3a thermal overprint is restricted to within late basins (Czarnota et al., 2010), it is expected to be present in the Cosmos succession because it is directly overlain by a hangingwall sedimentary succession similar in character to the Jones Creek late basin fill sequence.

Overall detailed investigation and interpretation of the Cosmos greenstone succession has contributed to a better understanding of early volcanism (>2700 Ma) within the AWB and wider EGS. The Cosmos footwall volcanic sequence is significantly older than rocks within the eastern segment of the AWB and also appears to be compositionally distinct when compared to these apparent TTD-affinity rocks (Fiorentini et al., 2012). This challenges the suggestion that supracrustal rocks, located along the eastern margin of the Kathleen Valley-Yakabindie district, which includes the Cosmos greenstone succession, are compositionally similar to those described in the Leinster district, such as Perseverance and Rocky's Reward (Duuring et al., 2012). Comparison, using the available published geochemical data, of the geochemical affinity of felsic and intermediate volcanism in the east of the AWB to that of Cosmos suggests that they share some common geochemical characteristics, and importantly do not exhibit a distinct TTD-affinity. Further detailed geochemical analysis of the volcanic sequences in the east of the AWB is required to better assess the possible

petrogenetic link between that of Cosmos and eastern AWB volcanic successions. Stratigraphic components of the Cosmos succession younger than ~2685 Ma can be linked to regional magmatic and tectonic events in the EGS and indicates that Cosmos has a shared history with the rest of the wider Kalgoorlie Terrane after this point in time.

5.8 References

Arndt, N. T., Lesher M. C., Barnes S. J., 2008. Komatiite. Cambridge University Press, Cambridge.

Barley, M. E., Eisenlohr, B. N., Groves, D. I., Perring, C. S., Vearncombe, J. R., 1989. Late Archean convergent margin tectonics and gold mineralisation: a new look at the Norseman-Wiluna belt, Western Australia. Geology 17, 826–829.

Barley, M. E., Brown, S. J. A., Krapež, B., 2006, Felsic volcanism in the eastern Yilgarn Craton, Western Australia: Evolution of a Late Archean convergent margin. Geochimica et Cosmochimica Acta 70, A35.

Barley, M. E., Brown, S. J., Krapež, B., Kositcin, N., 2008. Physical volcanology and geochemistry of a Late Archaean volcanic arc: Kurnalpi and Gindalbie Terranes, Eastern Goldfields Superterrane, Western Australia. Precambrian Research 161(1), 53-76.

Barnes, S. J., Van Kranendonk, M. J., Sonntag, I., 2012. Geochemistry and tectonic setting of basalts from the Eastern Goldfields Superterrane, Australian Journal of Earth Science: An International Geoscience journal of the Geological Society of Australia 59(5), 707-735.

Bekker, A., Barley, M. E., Fiorentini, M. L., Rouxel, O. J., Rumble, D., Beresford, S. W. 2009. Atmospheric sulfur in Archean komatiite-hosted nickel deposits. Science 326 (5956), 1086-1089.

Black, L. P., Champion, D. C., Cassidy, K. F., 2002. Compilation of SHRIMP U-Pb geochronology data, Yilgarn Craton, Western Australia, 1997-2000. Unpublished Geoscience Australia, analytical data available from http://www.ga.gov.au/oracle/ozchron/frames.html.

Blewett, R. S., Cassidy, K. F., Champion, D. C., Henson, P. A., Goleby, B. S., Jones, L., Groenewald, P. B., 2004. The Wangkathaa Orogeny: an example of episodic regional 'D2' in the late Archaean Eastern Goldfields Province, Western Australia. Precambrian Research 130(1), 139-159.

Blewett, R. S., Czarnota, K., Henson, P. A., 2010. Structural-event framework for the eastern Yilgarn Craton, Western Australia, and its implications for orogenic gold. Precambrian Research 183(2), 203-229.

Brown, S. J. A., Barley, M. E., Krapež, B., Cas, R. A. F., 2002. The Late Archaean Melita Complex, Eastern Goldfields, Western Australia: shallow submarine bimodal volcanism in a rifted arc environment. Journal of Volcanology and Geothermal Research 115(3), 303-327.

Bunting J. A., Williams, S. J., 1979. Sir Samuel, W.A. (1st edition): Western Australia Geological Survey, 1:250 000 Geological Series Explanatory Notes, 40p.

Campbell, I. H., Hill, R. I., 1988. A two-stage model for the formation of the granite-greenstone terrains of the Kalgoorlie-Norseman area, Western Australia. Earth and Planetary Science Letters 90(1), 11-25.

Champion, D. C., Cassidy, K. F., 2002. Granites in the Leonora-Laverton transect area, north eastern Yilgarn Craton. Geology, Geochronology and Geophysics of the North Eastern Yilgarn Craton, with an Emphasis on the Leonora–Laverton Transect Area 2002, 13-35.

Champion, D. C., Cassidy, K. F., 2007. An overview of the Yilgarn Craton and its crustal evolution. Geoscience Australia Record 2007/14, 8-12.

Champion, D. C., Sheraton, J. W., 1997. Geochemistry and Nd isotope systematics of Archaean granites of the Eastern Goldfields, Yilgarn Craton, Australia: implications for crustal growth processes. Precambrian Research 83(1), 109-132.

Claoué-Long, J. C., Compston, W., Cowden, A., 1988. The age of the Kambalda greenstones resolved by ion-microprobe: implications for Archean dating methods. Earth and Planetary Science Letters 89, 239-259.

Czarnota, K., Champion, D. C., Goscombe, B., Blewett, R. S., Cassidy, K. F., Henson, P. A., Groenewald, P. B., 2010. Geodynamics of the eastern Yilgarn Craton. Precambrian Research 183(2), 175-202.

Defant, M. J., Drummond, M. S., 1990. Derivation of some modern arc magmas by melting of young subducted lithosphere. Nature 347(6294), 662-665.

de Joux, A., Thordarson, T., Denny, M., Hinton, R.W., de Joux A.J., 2013. U-Pb dating constraints on the felsic and intermediate volcanic sequence of the nickel-sulphide bearing Cosmos succession, Agnew-Wiluna greenstone belt, Yilgarn Craton, Western Australia. Precambrian Research 236, 85-105.

Denny, M. 2010 AM5 Disseminated (AM5D) mineralogical model. Unpublished internal memo, Xstrata Nickel Australasia, 4-13.

Drummond, M. S., Defant, M. J., 1990. A model for trondhjemite–tonalite–dacite genesis and crustal growth via slab melting: Archaean to modern comparisons. Journal of Geophysical Research 95, 21503–21521.

Durney, D. W., 1972. A major unconformity in the Archaean, Jones Creek, Western Australia. Journal of the Geological Society of Australia 19(2), 251-259.

Duuring, P., Bleeker, W., Beresford, S. W., Fiorentini, M. L., Rosengren, N. M., 2012. Structural evolution of the Agnew–Wiluna greenstone belt, Eastern Yilgarn Craton and implications for komatiite-hosted Ni sulfide exploration. Australian Journal of Earth Sciences 59(5), 765-791.

Fiorentini, M. L., Beresford, S. W., Barley, M. E, Duuring, P., Bekker, A., Rosengren, N., Cas, R. A. F., Hronsky, J., 2012. District to camp controls on the genesis of komatiite-hosted nickel sulfide deposits, Agnew-Wiluna greenstone belt, Western Australia: Insights from the multiple sulfur isotopes. Economic Geology 107(5), 781-796.

Foster, J. G., Lambert, D. D., Frick, L. R., Maas, R., 1996. Re–Os isotopic evidence for genesis of Archaean nickel ores from uncontaminated komatiites. Nature 382, 703-706.

Gee, M., Swager, C., 2008. Late Archaean volcanic arcs and their accretionary history, Eastern Goldfields Superterrane: Plate tectonic models inferred from tectonostratigraphic analysis. Precambrian Research 161(1), 1-4.

Giles, C. W., 1982. The geology and geochemistry of the Archaean Spring Well felsic volcanic complex, Western Australia. Journal of the Geological Society of Australia 29(1-2), 205-220.

Goscombe, B., Blewett, R. S, Czarnota, K., Maas, R., Groenewald, B. A., 2007. Broad thermo-barometric evolution of the Eastern Goldfields Superterrane. In; Bierlein, F.P., Knox-Robinson, C.M., (Eds.), 2007. Proceedings of Geoconferences (WA) Inc. Kalgoorlie ’07 Conference. Geoscience Australia Record 2007/14, p33–38.

Hallberg, J. A. 1985. Geology and mineral deposits of the Leonora-Laverton area northeastern Yilgarn Block, Western Australia. Hesperian Press.

Hill, R. E. T., Dowling, S.E., 2008. The petrology and geochemistry of mineralised komatiites intersected in three diamond drill holes (AM262B, AMD275 and BJD048A) from the AM5 Nickel Sulphide Deposit; Cosmos region, Agnew-Wiluna Greenstone Belt; A pilot study for characterising mineralised domains within the ore body. Unpublished external report, Kalapana Research Associates and Triodia Research.

Korsch, R. J., Kositcin, N., Champion, D. C., 2011. Australian island arcs through time: geodynamic implications for the Archean and Proterozoic. Gondwana Research 19(3), 716-734.

Kositcin, N., Brown, S. J., Barley, M. E., Krapež, B., Cassidy, K. F., Champion, D. C., 2008. SHRIMP U-Pb zircon age constraints on the Late Archaean tectonostratigraphic architecture of the Eastern Goldfields Superterrane, Yilgarn Craton, Western Australia. Precambrian Research 161(1), 5-33.

Krapež, B., 1997. Sequence-stratigraphic concepts applied to the identification of depositional basins and global tectonic cycles. Australian Journal of Earth Sciences 44(1), 1-36.

Krapež, B., Brown, S. J. A., Hand, J., Barley, M. E., Cas, R. A. F., 2000. Age constraints on recycled crustal and supracrustal sources of Archaean metasedimentary sequences, Eastern Goldfields Province, Western Australia: evidence from SHRIMP zircon dating. Tectonophysics 322, 89–133.

Krapež, B., Hand, J. L., 2008. Late Archaean deep-marine volcaniclastic sedimentation in an arc-related basin: the Kalgoorlie Sequence of the Eastern Goldfields Superterrane, Yilgarn Craton, Western Australia. Precambrian Research 161(1), 89-113.

Krapež, B., Barley, M. E. 2008. Late Archaean synorogenic basins of the Eastern Goldfields Superterrane, Yilgarn Craton, Western Australia: Part III. Signatures of tectonic escape in an arc-continent collision zone. Precambrian Research, 161(1), 183-199.

Lambert, D. D., Foster, J. G., Frick, L. R., Hoatson, D. M., Purvis, A. C., 1998. Application of the Re-Os isotopic system to the study of Precambrian magmatic sulfide deposits of Western Australia. Australian Journal of Earth Sciences 45(2), 265-284.

Lesher, C. M., Arndt, N. T., 1995. REE and Nd isotope geochemistry, petrogenesis and volcanic evolution of contaminated komatiites at Kambalda, Western Australia. Lithos 34(1), 127-157.

Liu, S. F., Champion, D. C., Cassidy, K. F., 2002. Geology of the Sir Samuel 1:250 000 sheet area, Western Australia. Geoscience Australia, Record 2002/14, 57p.

Morris, P. A., Witt, W. K., 1997. Geochemistry and tectonic setting of two contrasting Archaean felsic volcanic associations in the Eastern Goldfields, Western Australia. Precambrian Research 83(1), 83-107.

Moyen, J. F., Martin, H., 2012. Forty years of TTG research. Lithos 48, 312-336.

Moyen, J. F., Van Hunen, J. 2012. Short-term episodicity of Archaean plate tectonics. Geology 40(5), 451-454.

Myers, J. S., 1993. Precambrian history of the West Australian Craton and adjacent orogens. Annual Reviews of Earth Planetary Science 21, 453-485.

Myers, J. S. 1997. Preface: Archaean geology of the Eastern Goldfields of Western Australia—regional overview. Precambrian Research 83(1), 1-10.

Nelson, D. R., 1997a. 118954: feldspar-quartz-mica schist, Rocky's Reward; in Compilation of SHRIMP U–Pb zircon geochronology data, 1996: Western Australia Geological Survey, Record 1997/2, 65–69.

Nelson, D. R., 1997d, 118937: metasandstone, Jones Creek; Geochronology dataset 464; in Compilation of geochronology data, June 2006 update: Western Australia Geological Survey.

Nelson, D. R., 1998. Granite-greenstone crust formation on the Archean earth- a consequence of 2 superimposed processes. Earth and Planetary Science Letters 158, 109-119.

Rosengren, N. M., Beresford, S. W., Grguric, B. A., Cas, R. A. F., 2005. An intrusive origin for the komatiitic dunite-hosted Mount Keith disseminated nickel sulfide deposit, Western Australia. Economic Geology 100(1), 149-156.

Rosengren, N. M., Cas, R. A. F., Beresford, S. W., Palich, B. M., 2008. Reconstruction of an extensive Archaean dacitic submarine volcanic complex associated with the komatiite-hosted Mt Keith nickel deposit, Agnew-Wiluna greenstone belt, Yilgarn Craton, Western Australia. Precambrian Research 161(1), 34-52.

Van Kranendonk, M. J., Ivanic, T. J., Wingate, M. T., Kirkland, C. L., Wyche, S., 2012. Long-lived, autochthonous development of the Archean Murchison Domain, and implications for Yilgarn Craton tectonics. Precambrian Research 229, 49-92.

Wingate, M. T. D., Bodorkos, S., Kirkland, C. L., (2009) 183975: metarhyolite, Wattagee Hill; Geochronology Dataset 785, in Compilation of Geochronology Information, 2009 Update, Geological Survey of Western Australia.

Wyman, D. A., Kerrich, R., 2012. Geochemical and isotopic characteristics of Youanmi terrane volcanism: the role of mantle plumes and subduction tectonics in the western Yilgarn Craton. Australian Journal of Earth Sciences 59(5), 671-694.

Chapter 6 – Summary and further work

6.1 Conclusions

The Cosmos succession, within the Agnew-Wiluna greenstone belt of the Yilgarn Craton, consists of ultramafic, intermediate and felsic volcanic lithologies, and contains several komatiite-hosted nickel sulphide ore bodies. These high grade massive and disseminated nickel sulphide deposits are hosted within thick ultramafic successions, which represent preferred lava pathways within a komatiite flow field(s). The Cosmos komatiites preserve no primary volcanic textures, but the intermediate and felsic volcanic rocks with which they are associated preserve a number of primary volcanic textures. This is in spite of the succession being exposed to peak metamorphic conditions of ~560 - 580ºC at ~3kbar. The stratigraphic footwall succession to the Cosmos Ultramafic Sequence is composed of a sequence of intercalated basaltic andesite through to rhyolite volcanic products, with significant volumes of andesite lavas, dacitic lavas and dacitic lapilli tuffs. The footwall volcanic sequence was constructed via punctuated explosive and effusive eruptions, spanning from 2736 Ma to 2724 Ma. Detailed subsurface mapping, via drillhole correlation, has established a footwall volcanic stratigraphy that composes six texturally and compositionally distinct volcanic units, which can be correlated throughout the Cosmos North area. In contrast, the stratigraphic hangingwall succession consists largely of reworked volcanic-derived sedimentary rocks that include polymictic conglomerates containing granitic clasts. It is demonstrably texturally and largely compositionally distinct from the footwall volcanic sequence. The sequence also contains a number of cross cutting

felsic and mafic intrusion. An absence of indicators of a submarine setting for the footwall volcanic succession indicates it, and by association the Western Ultramafic unit and the UMu1 komatiite package, may have been emplaced subaerially.

Several nickel sulphide ore deposits (e.g. Cosmos Deeps; Alec Mairs 5) penetrate several tens of metres into the dacitic tuffaceous footwall, typically where the footwall comprises dacitic tuffaceous breccia horizons containing abundant andesite clasts. This association may represent the massive sulphide's primary depositional location, rather than being wholly attributable to physical remobilisation during deformation and metamorphism. Therefore, such horizons may have not only provided a substrate that was readily thermo-mechanically eroded by the overriding komatiite, promoting attainment of sulphur saturation of the lava, such locations may also have acted as a suitable trap site for subsequent massive sulphide deposition. Pre-existing base metal sulphides within the dacitic substrate, possibly part of a hydrothermal/epithermal system, could have provided an external source of sulphur/sulphides that further promoted sulphur saturation of the UMu1 komatiite.

The Cosmos volcanic succession is compositionally diverse and has a distinct island-arc affinity, and contrasts the typically bimodal ultramafic-felsic associations in the eastern segment of the AWB (Duuring et al., 2007; Rosengren et al., 2008; Fiorentini et al., 2012). LREEs and LILEs are strongly enriched relative to HFSEs and volcanic lithologies display strong positive Pb and negative Nb anomalies. In comparison, the two felsic porphyry intrusions that cross-cut the volcanic succession exhibit strong HREE depletion and have a distinct TTD affinity. All volcanic lithologies exhibit a strong crustal signature that is geochemically most similar to modern high-K calc-alkaline to shoshonite continental island-arc successions. The geochemical characteristics of the Cosmos volcanic succession indicates the most likely tectonic setting was a subduction zone, with parental melts derived via partial melting of enriched peridotite within the mantle wedge that had been contaminated by subducted crustal material. Contrasting REE, LILE and HFSE concentrations, coupled with AFC modelling, has shown that intercalated dacitic and andesitic volcanic rocks within the footwall succession are not co-genetic. Thus, the andesites and dacites are considered to have tapped different mantle sources that had experienced contrasting

sediment and/or slab-derived fluid input from the subducting slab. The younger felsic porphyry intrusions are considered to have been generated via partial melting of the subducted slab itself and are related to local high-Ca granite intrusion. The presence of four inherited zircons, in three different lithological groups, indicates that crustal assimilation contributed to the Cosmos succession, although its contribution was relatively minor.

Detailed SIMS U–Pb dating of nine different lithological units representing the stratigraphic range of the Cosmos succession has shown that it was constructed by episodic magmatic activity spanning at least ~80 Ma. The Cosmos volcanic succession was accumulated via punctuated volcanism spanning at least 50 Ma, which was followed by intrusive activity lasting for at least a further 32 Ma. The succession features three intermediate-felsic-ultramafic sequences formed in distinct volcanic episodes between 2736 Ma and 2670 Ma. Emplacement of the Western Ultramafic unit and its felsic-intermediate footwall volcanic sequence occurred between ~2736 - 2730 Ma. This was followed by emplacement of the footwall volcanic sequence to the UMu1 package of the Cosmos Ultramafic Sequence between ~2730 and ~2724 Ma. The exact age of the Umu1 package is only bracketed by its underlying and overlying stratigraphy and thus it was emplaced at some point between ~2724 Ma and ~2685 Ma. The AM5 "reactivation" contact dated at 2685 ± 8 Ma, represents a break in accumulation of komatiite lavas and may be associated with a major hiatus. Dating of this discontinuous felsic horizon has confirmed that the Cosmos Ultramafic Sequence is composed of two separate komatiite sequences, the UMu1 and UMu2 packages. The latter was erupted post ~2685 Ma and thus may represent one of the youngest komatiite sequences in the Kalgoorlie Terrane (Claoué-Long et al., 1984). The intercalation of three distinct komatiites with a diverse and long-lived sequence of continental island-arc volcanic rocks at Cosmos necessitates that the geodynamic setting of the region feature both subduction-derived and plume-derived volcanism, concurring with recent geodynamic models of the EGS (Czarnota et al., 2010; Korsch et al., 2011).

The Cosmos volcanic succession represents the first extrusive high-K calc-alkaline to shoshonite island-arc volcanic sequence described in the Kalgoorlie

Terrane, if not the entirety of the EGS. It, when coupled with age dating, is indicative of formation in a long-lived volcanic arc setting active from 2736 Ma to beyond 2724. In contrast, the significantly younger felsic porphyry intrusions exhibit a TTD-affinity and these are related to late-stage local high-Ca granite intrusion. Thus the Cosmos succession demonstrates that the AWB is not wholly composed of felsic volcanic sequences with a TTD affinity as suggested by Fiorentini et al. (2012). However, I have also demonstrated that the felsic volcanism within the wider AWB does not exhibit a convincing TTD affinity and may have taken place in an arc setting. The Cosmos volcanic succession is ~15 - 25 Ma older than the majority of felsic rocks within the AWB and has a different and distinct stratigraphy and geochemical affinity. The Cosmos region may represent a separate arc terrane that experienced subsequent accretion with the Kalgoorlie Terrane. Alternatively, Cosmos could preserve the onset of felsic volcanism in the AWB, with volcanism subsequently migrating to the east of the domain during evolution of the island-arc setting. The tectonostratigraphy of the AWB is therefore more complex than currently considered. Further detailed geochemical analysis of the volcanic sequences in the eastern segment of the AWB is required to better assess the possible petrogenetic link between that of Cosmos and eastern AWB felsic volcanic complexes. Dating of the footwall sequence to the Western Ultramafic unit suggests a subduction zone was active in the Cosmos region by ~2736 Ma. This is ~20 Ma earlier than the suggested age (~2715 Ma) of establishment of a west-dipping subduction zone, beneath the Kalgoorlie Terrane (Czarnota et al., 2010). The age and geochemical affinity of the Cosmos succession has important implications for tectono-stratigraphical correlations between individual greenstone belts within the Kalgoorlie Terrane and the wider Yilgarn Craton. Unravelling the tectonic complexity of the region is particularly important given the recent re-ignition of the plume-dominated versus subduction accretion models for the origin for the EGS (Czarnota et al., 2010; Korsch et al., 2011;Barnes et al., 2012).

This work demonstrates that high-resolution geochronology within individual Archaean greenstone successions can be achieved, providing more robust platforms for interpreting the evolution of mineralised volcanic successions, particularly those

with little surface outcrop. Overall detailed investigation and interpretation of the Cosmos greenstone succession has contributed to a better understanding of early volcanism (>2700 Ma) within the AWB and wider EGS. Stratigraphic components of the Cosmos succession younger than ~2685 Ma can be linked to regional magmatic and tectonic events in the EGS and indicates that Cosmos has a shared history with the rest of the wider Kalgoorlie Terrane by this time. Of broader significance, recognition of this distinct high-K calc-alkaline to shoshonite island-arc sequence gives further evidence that modern style plate tectonics were operating within the EGS, and critically during the Neoarchaean, contrary to the suggestion that Archaean island arcs did not exist (Bédard et al., 2013).

6.2 Unanswered questions and future studies

The data presented within this thesis has raised many important questions about the tectonic setting of volcanism, including komatiite volcanism, with the EGS during the Neoarchaean. Interpretations and conclusions could be strengthened by further research at Cosmos and within the wider AWB, which is detailed below.

Further sampling, analysis and correlation along the entire length of the Cosmos greenstone belt would delineate the lateral extent of the established stratigraphy and highlight any facies associations along the length of the belt. Preliminary data from Prospero and Tapinos, ~4km, to the south of the Alec Mairs region, indicates that the same stratigraphic sequence as observed at Cosmos is present there (Farran, 2008), indicating the lateral continuation to the south of the newly established stratigraphy. A detailed structural interpretation of the Cosmos region, which has not yet been consolidated or documented, would aid assessment of the spatial occurrence of any large scale structures in the region. It would also enable a more quantitative assessment of the extent of potential sulphide remobilisation in and around the basal contact of the UMu1 package.

More detailed sampling and geochemical analysis of the three komatiite sequences present within the Cosmos region would enable their compositions, and any variability between these, to be ascertained. This would promote a better understanding of their petrogenesis and establish if all three komatiite units are co-genetically related. Equally, subsurface mapping of the komatiites' individual facies associations would contribute to a better understanding of their internal architecture and may help to delineate the morphology of possible preferred lava pathways within the sequence. This could aid nickel future exploration in the region. Given that over 100 holes required detail relogging to determine the footwall succession's internal architecture, a comprehensive understanding of the internal architecture of the komatiite units would likely require a similar level of systematic sampling and analyses.

A more in depth understanding of sulphide composition and variability could be obtained by systematic ore petrography and microprobe studies. S and Fe isotopes analyses of the massive sulphide deposits could be undertaken to ascertain if the sulphide deposits at Cosmos have experienced contribution from pre-existing sulphide deposits within or upon the substrate, such as the base metal sulphides present within the dacitic lapilli tuff sequences.

Nd isotope analysis of the volcanic lithologies could provide more information on the magmatic source (s) of footwall volcanic sequence and highlight any variability in source composition among the lithological groups. Sm-Nd and/or Re-Os isotope analysis could also potentially provide emplacement ages for the ultramafic units, which would be particularly useful for the UMu1 package, which is currently only delineated to emplacement within a ~40 Ma timeframe. However, as discussed in Chapter five the typical uncertainties associated with these two techniques are in the order of 20 - 50 Myr. Consequently, U-Pb dating already undertaken on felsic units within the succession likely provides more precise dating constraints on the Cosmos komatiites than direct dating of the ultramafic units may deliver.

On regional scale, a detailed assessment of the geochemical affinity of the felsic and intermediate volcanic centres throughout the AWB would promote a better

understanding of petrogenesis of volcanism, particularly the felsic volcanism, in the region. This could be achieved from existing data when combined with further coverage of little sampled domains. This would provide more in depth understanding of the geodynamic setting of the region and enable more rigorous assessment of whether individual domains have allochthonous or autochthonous relationships. Considering the AWB contains some of the world's largest nickel sulphide deposits, and in the case of Cosmos some of the highest grade Type 1 massive sulphide deposits, future work in this region is vital to ascertain how the primary volcanic features of its greenstone sequences controlled and promoted its high nickel endowment.

Appendix 1 – Fieldwork methods and sample data

A1.1 Data collection in the field

Drilling at the Cosmos mine site began in 1998, after the Cosmos nickel sulphide ore body was found. Since then, over 5000 holes have been drilled into the greenstone sequence. Surface and underground drilling at Cosmos was undertaken by diamond drill rigs, which produced drilled rock core for the whole length of a hole. Drilling occurred both from the surface and from underground workings. Multi-purpose UDR1000, 1200 and 1500 rigs drilled exploration holes from surface, often a distance away from known deposits, while LM75, LM90 and LM110 rigs drilled holes from underground drill pads, focused on near-mine exploration and resource modelling.

Drill core was collected from the drill rigs and then measured, marked up and orientated. It was sampled and logged by XNA geologists according to their logging programme and lithology codes. This core was then stacked in core trays and stored in a core yard. Three different drill core thicknesses were commonly used at the mine site – BQ (36.5mm diameter), NQ2 (50.6mm diameter) and HQ (63.5mm diameter) dependant on the stability of the ground and the purpose and target of the drill hole. The majority of drill holes re-logged for this project were of NQ2 or HQ size.

Drill hole selection for re-logging was initially decided by the following parameters;

1. Holes that drilled a substantial depth below the Cosmos Ultramafic Sequence, deep into the footwall, so that lithological variations in the footwall could be easily studied

2. Holes that intersected the mineralised basal contact of the Cosmos Ultramafic Sequence to study massive sulphide-footwall relationships

3. Holes that intersected ultramafic units whose basal contacts were barren.

Subsequent holes were chosen to fill "gaps" in the interpreted cross-sections and level plans and to allow better sub-surface correlation of the stratigraphy.

Holes were re-logged by hand onto A4 logging sheets, focusing on the nature, mineralogy and contact relationships of footwall lithologies. Attention was also paid to the basal parts of ultramafic units, specifically the nature of the contact with the underlying footwall volcanic sequence. Original logs, already complete by XNA geologists, were also used to aid geological interpretation. These were either from the logging programme Field Marshall or Excel spreadsheets for older holes. Logs were completed on a variety of scales depending on the complexity of the stratigraphy, the variety of different footwall lithologies encountered and the understanding and coverage already attained in the surrounding area.

The subsurface footwall stratigraphy was then mapped via drillhole correlations for a 1km strike length of the Cosmos greenstone belt utilising the mine planning program Micromine. Detailed field logs were interpreted and each hole re-coded according to their lithological composition. These were then plotted on drill hole traces on Micromine to allow units to be correlated by hand on A3 cross sections and level plans (Appendix 4). Lithological data from existing drillholes was also utilised where possible to further constrain the extent and morphology of individual lithological units and to discern contact relationships.

A1.2 Sampling

Half or quarter core samples were taken from NQ2, HQ, and BQ holes depending on the grain size of the sample and the amount of core remaining from the drill hole. Approximately 250g - 1000g were taken for each sample. Samples were

taken of unknown lithologies, drill core that showed interesting features such as footwall-sulphide interaction and across lithological contacts. Samples taken at a later stage were selected to aid correlation and consolidation of stratigraphy. Samples were cut by diamond saws at the mine site and then returned to the UK via airmail.

Table A1.1. Hole data for all holes re-logged and sampled at Cosmos during this study. UGDDH – Underground Diamond Drill Hole; DDH – Diamond Drill Hole. RC/DDH – Reverse Circulation precollar/Diamond Drill Hole tail. RL = Relative level above sea level. MD – Michael Denny re-logged as part of AM5 study. ? in azimuth or parent hole column denotes missing data from hole files. n.a = not applicable. All holes were drilled in AMG84_51 grid.

Hole ID	Hole Type	Easting (mE)	Northing (mN)	RL (mRL)	Dip	Azimuth	Parent Hole	Parent hole depth	Max Depth (m)	Tenement	Project	Prospect	Drilling Start Date	Drilling End Date	Date Relogged	ADJ Relogged?
AMD007	UGDDH	260419	6944259	-58	13	?	-	n.a	53.7	M36/127	Cosmos South	Alec Mairs	15/01/2005	15/01/2005	13/06/2009	Y
AMD014	UGDDH	260420	6944258	-58	27	?	-	n.a	65.7	M36/127	Cosmos South	Alec Mairs	19/01/2005	19/01/2005	13/06/2009	Y
AMD028	UGDDH	260419	6944258	-60	-14	?	-	n.a	65.2	M36/127	Cosmos South	Alec Mairs	27/01/2005	27/01/2005	25/06/2009	Y
AMD030	UGDDH	260419	6944257	-60	-15	?	-	n.a	77.1	M36/127	Cosmos South	Alec Mairs	29/01/2005	29/01/2005	24/06/2009	Y
AMD076	UGDDH	260456	6944341	-44	16	?	-	n.a	107.5	M36/127	Cosmos South	Alec Mairs	01/04/2005	05/04/2005	25/06/2009	Y
AMD100	UGDDH	260459	6944346	-45	1	?	-	n.a	305.0	M36/127	Cosmos South	Alec Mairs	30/06/2005	09/07/2005	15/06/2009	Y
AMD106	UGDDH	260534	6944418	-29	?	?	-	n.a	194.5	M36/127	Cosmos South	Alec Mairs	18/10/2006	21/10/2006	17/05/2009	Y
AMD116	UGDDH	260440	6944287	-157	2	?	-	n.a	131.4	M36/127	Cosmos South	Alec Mairs	21/01/2006	27/01/2006	15/06/2009	Y
AMD121	UGDDH	260439	6944286	-157	-18	?	-	n.a	141.9	M36/127	Cosmos South	Alec Mairs	10/02/2006	13/02/2006	27/06/2009	Y
AMD136	UGDDH	260434	6944284	-157	-21	232	-	n.a	350.3	M36/127	Cosmos South	Alec Mairs	29/03/2006	11/04/2006	23/05/2010	Y
AMD139	UGDDH	260657	6944547	-4	-17	?	-	n.a	107.3	M36/127	Cosmos South	Alec Mairs	08/03/2006	11/03/2006	27/06/2009	Y
AMD143	UGDDH	260656	6944548	-4	-9	43	-	n.a	95.7	M36/127	Cosmos South	Alec Mairs	21/05/2006	22/05/2006	05/06/2010	Y
AMD149	UGDDH	260247	6944014	-198	32	?	-	n.a	250.6	M36/127	Cosmos South	Alec Mairs	23/04/2006	03/05/2006	17/06/2009	Y
AMD189	UGDDH	260316	6944118	-186	88	20	-	n.a	180.0	M36/127	Cosmos South	Alec Mairs	10/07/2006	19/07/2006	24/05/2010	Y
AMD193	UGDDH	260247	6944014	-201	-20	?	-	n.a	234.0	M36/127	Cosmos South	Alec Mairs	22/07/2006	26/07/2006	28/05/2009	Y
AMD229	DDH	260636	6944622	-103	-20	260	-	n.a	560.8	M36/127	Cosmos South	Alec Mairs Footwall lodes	26/09/2006	23/05/2010	n.a	Recoded from core photos and XNA geology logs
AMD233	UGDDH	260607	6944492	-14	?	?	-	n.a	170.8	M36/127	Cosmos South	Alec Mairs	06/11/2006	14/11/2006	28/05/2009	Y
AMD244	UGDDH	260247	6944012	-200	-9	106	-	n.a	168.2	M36/127	Cosmos South	Alec Mairs	27/01/2007	01/02/2007	28/04/2010	Y
AMD251	UGDDH	260232	6943886	-220	-30	?	-	n.a	441.1	M36/127	Cosmos South	Alec Mairs	19/03/2007	07/04/2007	20/11/2008	Y
AMD264	UGDDH	260232	6943886	-219	-2	82	-	n.a	300.0	M36/127	Cosmos South	Alec Mairs	02/10/2007	13/10/2007	08/06/2009	Y
AMD268	UGDDH	260311	6943950	-237	-32	99	-	n.a	83.9	M36/127	Cosmos South	AM5	12/08/2007	15/08/2007	05/05/2010	Y
AMD273	UGDDH	260312	6944119	-187	-32	119	-	n.a	458.9	M36/127	Cosmos South	AM5	20/08/2007	14/09/2007	22/05/2009	Y
AMD274	UGDDH	260362	6944062	-245	-42	115	-	n.a	450.0	M36/127	Cosmos South	Alec Mairs	18/09/2007	01/10/2007	01/06/2009	Y
AMD275	UGDDH	260362	6944062	-245	-20	114	-	n.a	296.0	M36/127	Cosmos South	Alec Mairs	04/10/2007	10/10/2007	20/11/2008	Y
AMD295	UGDDH	260362	6944062	-245	-5	121	-	n.a	230.8	M36/127	Cosmos South	AM5	10/10/2007	15/10/2007	25/11/2008	Y
AMD310	UGDDH	260248	6943827	-229	-37	90	-	n.a	382.0	M36/127	Cosmos South	Alec Mairs	11/11/2007	21/11/2007	09/06/2009	Y
AMD310A	UGDDH	260248	6943827	-229	-37	90	AMD310	350	558.7	M36/127	Cosmos South	Alec Mairs	23/11/2007	14/12/2007	19/05/2009	MD Relog
AMD313	UGDDH	260232	6943884	-220	-39	89	-	n.a	411.0	M36/127	Cosmos South	Alec Mairs	02/12/2007	12/01/2008	04/06/2009	Y
AMD318	UGDDH	260268	6943762	-238	-47	95	-	n.a	501.0	M36/127	Cosmos South	AM6	05/05/2008	11/06/2008	12/06/2009	Y
AMD321	UGDDH	260268	6943762	-238	-24	80	-	n.a	389.7	M36/127	Cosmos South	AM5	31/07/2008	12/08/2008	20/05/2010	Y
AMD344	UGDDH	260396	6943883	-333	-23	70	-	n.a	254.6	M36/127	Cosmos South	Alec Mairs	16/03/2008	20/03/2008	13/05/2009	Y
AMD346	UGDDH	260397	6943883	-234	-7	68	-	n.a	161.0	M36/127	Cosmos South	Alec Mairs	21/03/2008	22/03/2008	26/05/2009	MD Relog

Hole ID	Hole Type	Easting (mE)	Northing (mN)	RL (mRL)	Dip	Azimuth	Parent Hole	Parent hole depth	Max Depth (m)	Tenement	Project	Prospect	Drilling Start Date	Drilling End Date	Date Relogged	ADJ Relogged?
AMD365	UGDDH	260404	6944039	-294	-17	107	-	n.a	243.1	M36/127	Cosmos South	Alec Mairs	01/04/2008	05/04/2008	13/04/2010	Y
AMD460	UGDDH	260403	6944040	-293	16	30	-	n.a	239.5	M36/127	Cosmos South	AM5	13/08/2008	16/08/2008	10/06/2010	Y
AMD464	UGDDH	260404	6944039	-292	-44	67	-	n.a	319.2	M36/127	Cosmos South	Cosmos Deeps	15/06/2008	21/06/2008	08/05/2010	Y
AMD504	UGDDH	260268	6943760	-238	15	96	-	n.a	192.4	M36/127	Cosmos South	Alec Mairs	20/08/2008	25/08/2008	10/05/2010	Y
AMD508	UGDDH	260420	6944011	-320	-3	91	-	n.a	144.0	M36/127	Cosmos South	Alec Mairs	28/10/2008	01/11/2008	16/06/2009	MD Relog
AMD544	UGDDH	260394	6943990	-319	-10	90	-	n.a	164.8	M36/127	Cosmos South	AM5	03/12/2008	05/12/2008	22/04/2010	Y
AMD552	UGDDH	260394	6943990	-319	-2	90	-	n.a	142.0	M36/127	Cosmos South	Alec Mairs	05/12/2008	07/12/2008	10/06/2009	Y
AMD601	UGDDH	260340	6943944	-312	-40	81	-	n.a	450.3	M36/127	Cosmos South	Alec Mairs	31/05/2009	11/06/2009	12/06/2009	Y
AMD626	UGDDH	260268	6943762	-238	-24	80	-	n.a	389.7	M36/127	Cosmos South	AM5	31/07/2008	12/08/2008	20/05/2010	Y
AMD640	UGDDH	260354	6943812	-352	-38	65	-	n.a	553.7	M36/127	Cosmos South	AM5 Massive	01/10/2009	21/10/2009	10/05/2010	Y
AMD641	DDH	260232	6943887	-218	43	58	-	n.a	215.5	M36/127	Cosmos South	Down dip AM2	07/04/2010	16/04/2010	13/04/2010	Y
BJD017B	DDH	260820	6943860	479	-62	270	BJD017	156.9	1026.6	M36/127	Cosmos South	Anomaly 1/Alec Mairs	06/11/2006	10/12/2006	09/05/2010	Y
BJD030	RC/DDH	261058	6944300	475	-62	274	-	n.a	990.5	M36/127	Bellevue	Anomaly 1DM	18/09/2003	06/10/2003	26/05/2010	Y
BJD045A	DDH	260704	6944100	479	-60	270	BJD045	518.9	856.3	M36/127	Cosmos South	Anomaly 1	29/08/2006	06/09/2006	05/05/2009	Y
BJD048A	RC/DDH	260865	6943900	478	-61	270	BJD048	210.5	1113.2	M36/127	Cosmos South	Anomaly 1	03/08/2006	23/08/2006	26/04/2009	Y
BJD048B	DDH	260865	6943900	442	-61	270	BJD048	447.4	966.3	M36/127	Cosmos South	Anomaly 1	09/09/2006	28/09/2006	25/04/2009	Y
BJD050	RC/DDH	260855	6944060	477	-60	270	BJD015	167	960.7	M36/127	Bellevue	Anomaly 1DM	17/02/2004	30/04/2005	29/04/2009	Y
BJD054	DDH	260443	6944051	350	56	270	-	n.a	1212.5	M36/127	Cosmos South	Anomaly 2	04/05/2005	27/05/2005	07/05/2010	Y
BJD057B	DDH	260991	6943940	476	-60	270	BJD057	440	1115.8	M36/127	Cosmos South	Anomaly 1	29/06/2006	30/07/2006	19/11/2008	Y
BJD059	DDH	260712	6944181	479	-60	270	BJD032	100	729.8	M36/127	Bellevue	Anomaly 1DM	17/03/2004	25/02/2005	26/05/2009	Y
BJD061A	DDH	260780	6944220	477	-60	270	BJD061	350.4	723.7	M36/127	Bellevue	Alec Mairs	13/03/2004	03/06/2004	25/05/2009	Y
BJD061K	DDH	260780	6944220	477	-60	270	BJD061J	453	738.3	M36/127	Cosmos South	Alec Mairs	12/10/2004	18/10/2004	09/06/2010	Y
BJD062	RC/DDH	260660	6944220	480	-60	270	-	n.a	575.0	M36/127	Bellevue	Anomaly 1DM	31/03/2004	08/04/2004	20/05/2009	Y
BJD085	RC/DDH	260454	6944314	480	-84	138	-	n.a	711.6	M36/127	Bellevue	Alec Mairs	16/07/2004	01/08/2004	15/05/2009	Y
BJD090	DDH	260371	6944256	482	-83	136	-	132	768.8	M36/127	Cosmos South	Alec Mairs	15/09/2004	29/09/2004	07/05/2009	Y
BJD102	DDH	260635	6944140	479	-60	268	-	n.a	678.3	M36/127	Cosmos South	AM5	02/10/2004	10/11/2004	06/05/2009	Y
BJD192	DDH	260500	6944060	481	-75	270	-	n.a	717.5	M36/127	Cosmos South	Anomaly 1	07/11/2005	29/11/2005	11/05/2010	Y
BJD198	RR/DDH	260500	6943900	484	-60	313	-	n.a	555.9	M26/127	Cosmos South	Anomaly 1	01/12/2005	13/12/2005	12/05/2010	Y
BJD207	DDH	260706	6944209	476	-60	313	-	n.a	480.2	M36/127	Cosmos South	Anomaly 1	10/12/2005	05/01/2006	24/05/2009	Y
BJD263	DDH	260960	6940250	463	-61	270	-	n.a	435.4	M36/127	Cosmos South	Anomaly 3	14/08/2006	19/08/2006	17/12/2008	Y
BJD282	RC/DDH	260500	6943790	479	-60	270	-	n.a	387.4	M36/127	Cosmos South	Anomaly 1	12/07/2007	19/07/2007	06/05/2010	Y
BJD283	RC/DDH	260560	6943790	479	-60	270	-	n.a	561.8	M36/127	Cosmos South	Anomaly 1	09/03/2007	21/07/2007	06/05/2010	Y
BJD289	RC/DDH	260710	6943400	475	-57	270	-	n.a	806.9	M36/127	Cosmos South	Anomaly 1	24/09/2007	08/10/2007	03/12/2008	Y
BJD312	RR/DDH	260355	6944330	478	-54	90	-	n.a	372.6	M36/127	Cosmos South	Cosmos Pit South	27/05/2007	02/06/2007	27/05/2009	Y
BJD313	RR/DDH	260623	6943750	479	-65	270	-	n.a	785.7	M36/127	Cosmos South	Anomaly 1	27/06/2007	12/07/2007	22/05/2010	Y
BJD316B	UGDDH	260383	6944244	475	-80	270	BJD316	560.4	1129.3	M36/127	Cosmos South	Alec Mairs	31/08/2007	24/09/2007	05/05/2010	Y
BJD320	RR/DDH	260420	6944900	480	-66	90	-	n.a	894.6	M36/127	Kathleen Valley	Cosmos North	14/10/2007	31/10/2007	17/06/2009	Y
BJD322A	DDH	260674	6944150	475	-87	270	BJD322	397.5	1009.4	M36/127	Cosmos South	Alec Mairs	06/12/2007	16/01/2008	10/06/2010	Y
BJD328F	DDH	260685	6943980	479	-87	268	BJD328	529.5	1143.0	M36/127	Cosmos South	Alec Mairs	22/06/2008	18/07/2008	25/06/2009	Y

Hole ID	Hole Type	Easting (mE)	Northing (mN)	RL (mRL)	Dip	Azimuth	Parent Hole	Parent hole depth	Max Depth (m)	Tenement	Project	Prospect	Drilling Start Date	Drilling End Date	Date Relogged	ADJ Relogged?
BJD332	RR/DDH	261147	6943000	472	-60	270	-	n.a	1401.2	M36/127	Cosmos South	Anomaly 6	28/03/2008	22/05/2008	24/10/2009	Y
BJD363	DDH	261335	6941050	465	-60	270	-	n.a	1039.3	M36/127	Cosmos South	N.Prospero	07/11/2008	24/11/2008	10/12/2008	Y
BJD365A	DDH	260600	6943500	478	-87	270	BJD365	497.8	1148.1	M36/127	Cosmos South	Alec Mairs	29/11/2008	09/02/2009	24/04/2010	Y
BJD383	RC/DDH	260800	6943125	475	-60	270	-	n.a	1229.1	M36/127	Cosmos South	Anomaly6	05/04/2009	25/05/2009	10/04/2010	Y
BJD393B	RR/DDH	261048	6943399	476	-60	270	BJD393	498.3	1272.7	M36/127	Cosmos South	Alec Mairs	25/01/2010	07/03/2010	28/04/2010	Y
BJD406	RC/DDH	261063	6943000	472	-65	270	-	n.a	1514.6	M36/127	Cosmos South	Alec Mairs	10/07/2009	19/08/2009	25/10/2009	Y
BJD420	RR/DDH	261094	6943300	474	-59	267	-	n.a	674.6	M36/127	Cosmos South	Alec Mairs	12/03/2010	06/04/2010	14/04/2010	Y
BJDM002	RC/DDH	260760	6944020	478	-60	270	-	n.a	972.5	M36/127	Bellevue	Anomaly 1DM	17/06/2003	18/06/2005	28/04/2009	Y
CME0121	UGDDH	260561	6944445	-129	-60	99	-	n.a	725.5	M36/371	Cosmos South	Cosmos Ultradeeps	01/12/2009	10/01/2010	07/06/2010	Y
CME070	UGDDH	260667	6944622	-99	-3	182	-	n.a	333.0	M36/371	Cosmos Underground	Cosmos Deeps	16/11/2004	30/11/2004	27/05/2010	Y
CME072	UGDDH	260672	6944627	-100	-25	?	-	n.a	137.5	M36/371	Kathleen Valley	Cosmos Deeps	07/12/2004	14/12/2004	23/04/2009	Y
CME074	UGDDH	260671	6944626	-100	-27	182	-	n.a	185.5	M36/371	Cosmos Underground	Cosmos Deeps	29/05/2005	02/06/2005	24/10/2009	Y
CME090	UGDDH	260734	6944714	-112	-35	?	-	n.a	110.5	M36/371	Kathleen Valley	Cosmos Deeps	19/08/2005	21/08/2005	16/04/2009	Y
CME119A	UGDDH	260647	6944615	-104	-66	99	CME119	463.6	675.0	M36/371	Cosmos South	Cosmos Ultradeeps	27/03/2010	20/04/2010	21/04/2010	Y
CME120	DDH	260618	6944528	-116	-64	95	-	n.a	776.7	M36/371	Cosmos South	Cosmos Ultradeeps	04/02/2010	01/03/2010	04/06/2010	Y
CME123	UGDDH	260544	6944461	-130	-53	300	-	n.a	250.8	M36/371	Cosmos South	Cosmos Footwall lodes	13/02/2010	18/02/2010	n.a	Recoded from core photos and XNA geology logs
CME124	UGDDH	260542	6944460	-130	-24	284	-	n.a	241.7	M36/371	Cosmos South	Cosmos Footwall lodes	18/02/2010	22/02/2010	n.a	Recoded from core photos and XNA geology logs
CME125	DDH	260501	6944414	-140	-66	273	-	n.a	456.5	M36/127	Cosmos South	Cosmos Footwall lodes	28/03/2010	05/04/2010	n.a	Recoded from core photos and XNA geology logs
CME126	DDH	260502	6944413	-140	-34	268	-	n.a	398.1	M36/127	Cosmos South	Cosmos Footwall lodes	21/03/2010	27/03/2010	n.a	Recoded from core photos and XNA geology logs
CME128	UGDDH	260539	6944336	-153	-22	260	-	n.a	381.0	M36/127	Cosmos South	Alec Mairs	24/02/2010	05/03/2010	06/06/2010	Y
ISD030	UGDDH	260629	6944674	-24	-22	?	-	n.a	116.4	M36/371	Kathleen Valley	Cosmos Deeps	08/10/2003	10/10/2003	08/12/2008	Y
ISD038	UGDDH	260627	6944675	-23	-16	?	-	n.a	100.6	M36/371	Kathleen Valley	Cosmos Deeps	23/10/2003	24/10/2003	06/12/2008	Y
ISD070	UGDDH	260753	6944710	-28	-55	?	-	n.a	110.4	M36/371	Kathleen Valley	Cosmos Deeps	11/01/2004	12/01/2004	05/12/2008	Y
ISD080	UGDDH	260751	6944710	-28	-52	?	-	n.a	119.1	M36/371	Kathleen Valley	Cosmos Deeps	29/01/2004	30/01/2004	07/12/2008	Y
ISD106	UGDDH	260679	6944639	-47	5	94	-	n.a	92.1	M36/371	Cosmos Underground	Cosmos Deeps	05/03/2004	08/03/2004	05/06/2010	Y
JCD072	RC/DDH	260694	6944540	476	-60	265	-	n.a	231.5	M36/371	Cosmos South	Cosmos	16/01/1998	16/01/1998	08/06/2010	Y
JCD096	RC/DDH	260902	6944616	477	-58	267	-	n.a	550.0	M36/371	Kathleen Valley	Cosmos Deeps	08/10/1999	26/10/1999	25/05/2010	Y
JCD106	RC/DDH	260960	6944660	477	-58	266	-	n.a	647.0	M36/127	Kathleen Valley	Cosmos Deeps	12/03/2000	23/03/2000	24/04/2010	Y
JCD109	RC/DDH	260930	6944659	477	-55	270	-	n.a	690.0	M36/127	Kathleen Valley	Cosmos Deeps	09/04/2000	20/04/2000	23/04/2010	Y
JCD120A	RC/DDH	261049	6944665	477	-58	?	JCD120	474.3	754.0	M36/371	Kathleen Valley	Cosmos Deeps	29/03/2000	29/07/2000	15/04/2009	Y
JCD125	DDH	260960	6944660	477	-58	266	JCD106	?	646.9	M36/127	Kathleen Valley	Cosmos Deeps	12/03/2000	09/08/2000	24/04/2010	Y

Hole ID	Hole Type	Easting (mE)	Northing (mN)	RL (mRL)	Dip	Azimuth	Parent Hole	Parent hole depth	Max Depth (m)	Tenement	Project	Prospect	Drilling Start Date	Drilling End Date	Date Relogged	ADJ Relogged?
JCD130	RC/DDH	261003	6944701	478	-58	?	-	n.a	673.0	M36/371	Kathleen Valley	Cosmos Deeps	04/06/2000	31/08/2000	14/04/2009	Y
JCD138	RC/DDH	260930	6944659	477	-55	?	JCD109	198	625.4	M36/371	Kathleen Valley	Cosmos Deeps	09/04/2000	25/09/2000	13/04/2009	Y
JCD142	RC/DDH	260400	6944720	479	-60	?	JCD123	410	889.0	M36/371	Kathleen Valley	Cosmos Deeps	26/07/2000	22/11/2000	24/04/2009	Y
JCD143	RC/DDH	260439	6944402	479	-66	69	-	n.a	1026.0	M36/371	Kathleen Valley	Cosmos Deeps	17/11/2000	17/11/2000	02/06/2009	Y
JCD155	DDH	261215	6944335	474	-62	295	JCD152	454	1128.7	M36/371	Bellevue	Cosmos Ultra Deeps	03/09/2003	22/09/2003	25/05/2010	Y

Table A1.2. Spatial data for all analysed samples. mRL = relative level compared to sea level (0m). REE = ICP-MS analyses for rare earth elements undertaken. XRF = Major and trace element analyses by X-ray fluorescence undertaken. T/S = Thin section prepared. U-Pb Dating – Sample sent for zircon separation for U-Pb analysis, samples in bold were successfully dated via SIMS, those in italics did not have sufficient zircon yield for SIMS analysis

Hole ID	Field Sample number	Lab number	From (m)	To (m)	Mid-point (m)	Easting (mE)	Northing (mN)	mRL	REE	XRF	T/S	U-Pb Dating
AMD030	AMD030-C	C09-47	66.70	66.80	66.75	260472.06	6944220.03	-76.37	Y	Y	Y	N
AMD100	AMD100-K	C09-44	175.32	175.72	175.52	260633.72	6944330.13	-44.42	Y	Y	Y	N
AMD106	AMD106-E	C09-33	59.91	60.13	60.02	260594.16	6944417.53	-29.31	N	Y	Y	N
AMD106	AMD106-K	C09-45	120.10	120.33	120.22	260654.34	6944416.45	-29.98	N	Y	N	N
AMD116	AMD116-A	C09-34	7.88	8.22	8.05	260448.06	6944287.50	-156.47	N	Y	N	N
AMD116	AMD116-G	C09-86	79.65	79.8	79.73	260519.56	6944286.95	-151.64	N	Y	N	N
AMD136	AMD136-H	C10-112	312.60	312.80	312.70	260184.84	6944129.09	-262.32	Y	Y	N	N
AMD136	AMD136-I	C10-144	322.10	322.44	322.27	260176.64	6944125.15	-265.309	N	Y	N	N
AMD136	AMD136-I	C10-145	322.10	322.44	322.27	260176.64	6944125.15	-265.31	N	Y	N	N
AMD143	AMD143-A	C10-139	49.23	49.48	49.36	260689.85	6944582.76	-10.49	Y	Y	N	N
AMD149	AMD149-I	C09-22	122.00	122.16	122.08	260349.96	6944019.59	-133.69	N	Y	N	N
AMD149	AMD149-E	C09-53	64.75	64.90	64.83	260301.17	6944017.47	-163.57	N	N	N	N
AMD149	AMD149-B	C09-62	25.50	25.77	25.64	260268.13	6944015.38	-184.54	N	Y	Y	N
AMD193	AMD193-A	C09-61	23.65	23.89	23.77	260268.77	6944018.11	-208.53	Y	Y	Y	N
AMD251	AMD251-Q	AM5-04	146.55	146.85	146.70	260357.82	6943904.56	-292.57	N	N	Y	N
AMD251	AMD251-Q	AM5-05	146.55	146.85	146.70	260357.82	6943904.56	-292.57	N	N	Y	N
AMD251	AMD251-B	AM5-08	14.63	14.85	14.74	260244.37	6943887.98	-227.26	N	Y	Y	N
AMD251	AMD251-AA	AM5-11	224.15	224.50	224.33	260424.93	6943915.45	-330.01	N	N	Y	N
AMD251	AMD251-AA	AM5-12	224.15	224.50	224.33	260424.93	6943915.45	-330.01	N	Y	Y	N

Hole ID	Field Sample number	Lab number	From (m)	To (m)	Mid-point (m)	Easting (mE)	Northing (mN)	mRL	REE	XRF	T/S	U-Pb Dating
AMD251	AMD251-H	AM5-13	69.10	69.50	69.30	260291.02	6943895.29	-254.59	N	N	Y	N
AMD251	AMD251-H	AM5-14	69.10	69.50	69.30	260291.02	6943895.29	-254.59	N	N	Y	N
AMD251	AMD251-U	AM5-16	168.40	168.80	168.60	260376.71	6943907.66	-303.20	N	Y	Y	N
AMD251	AMD251-E	AM5-19	45.35	45.60	45.48	260270.62	6943892.25	-242.65	Y	Y	Y	N
AMD251	AMD251-L	AM5-25	110.65	110.90	110.78	260326.72	6943900.32	-275.09	N	Y	Y	N
AMD251	AMD251-J	AM5-26	90.62	91.00	90.81	260309.48	6943897.94	-265.31	N	Y	Y	N
AMD251	AMD251-R	C10-152	151.00	151.40	151.20	260361.70	6943905.13	-294.76	N	Y	N	N
AMD264	AMD264Z	AMD264Z	6.20	6.80	6.50	260238.52	6943886.70	-219.24	N	N	N	*Y*
AMD264	AMD264-A	C09-4	4.67	4.95	4.81	260236.85	6943886.46	-219.20	Y	Y	N	N
AMD264	AMD264-C	C09-8	16.93	17.11	17.02	260248.94	6943888.16	-219.48	N	Y	N	N
AMD273	AMD273Z	AMD273Z	218.05	219.00	218.53	260476.60	6944029.33	-300.34	N	N	N	**Y**
AMD273	AMD273-S	C09-32	159.93	160.28	160.11	260433.29	6944054.88	-270.61	Y	Y	Y	N
AMD273	AMD273-C	C09-38	11.33	11.53	11.43	260321.13	6944114.32	-193.24	N	Y	N	N
AMD273	AMD273-G	C09-56	52.00	52.37	52.19	260352.17	6944098.58	-214.44	N	N	N	N
AMD273	AMD273-EE	C09-60	201.00	201.13	201.07	260463.73	6944037.14	-291.50	N	Y	N	N
AMD274	AMD274-J	C09-87	270.35	270.70	270.53	260536.22	6943973.30	-430.91	N	Y	N	N
AMD275	AMD275-L	AM5-09	90.85	91.25	91.05	260442.89	6944033.51	-274.17	N	Y	Y	N
AMD275	AMD275-DD	AM5-15	7.40	7.60	7.50	260368.45	6944058.72	-245.84	N	Y	Y	N
AMD275	AMD275-C	AM5-21	125.07	125.5	125.29	260473.11	6944022.62	-286.01	N	Y	Y	N
AMD275	AMD275-C	AM5-22	125.07	125.5	125.29	260473.11	6944022.62	-286.01	N	Y	Y	N
AMD275	AMD275-C	AM5-23	125.07	125.5	125.29	260473.11	6944022.62	-286.01	Y	Y	Y	N
AMD275	AMD275-G	AM5-24	117.25	117.50	117.38	260466.16	6944025.18	-283.24	N	N	Y	N
AMD275	AMD275-T	AM5-27	52.80	53.05	52.93	260408.95	6944045.16	-261.30	N	Y	Y	N
AMD295	AMD295-O	AM5-01	72.80	73.00	72.90	260424.31	6944023.41	-248.44	N	Y	Y	N
AMD295	AMD295-J	AM5-03	48.10	48.25	48.18	260403.19	6944036.13	-246.60	N	Y	Y	N
AMD295	AMD295-P	AM5-06A	77.50	77.80	77.65	260428.34	6944020.92	-248.77	N	Y	Y	N
AMD295	AMD295-P	AM5-06B	77.50	77.80	77.65	260428.34	6944020.92	-248.77	N	Y	Y	N
AMD295	AMD295-G	AM5-07	37.30	37.80	37.55	260394.03	6944041.46	-245.76	N	Y	Y	N
AMD295	AMD295-S	AM5-10A	85.50	85.75	85.63	260435.08	6944016.70	-249.31	N	N	Y	N

Hole ID	Field Sample number	Lab number	From (m)	To (m)	Mid-point (m)	Easting (mE)	Northing (mN)	mRL	REE	XRF	T/S	U-Pb Dating
AMD295	AMD295-S	AM5-10B	85.50	85.75	85.63	260435.08	6944016.70	-249.31	N	N	Y	N
AMD295	AMD295-Z	AM5-18	96.50	96.80	96.65	260444.38	6944010.81	-250.02	N	Y	Y	N
AMD310	AMD310-O	C09-17	174.43	174.62	174.53	260386.49	6943821.55	-334.44	Y	Y	N	N
AMD310	AMD310-E	C09-3	66.62	66.86	66.74	260300.92	6943825.90	-269.07	Y	Y	N	N
AMD310	AMD310-V	C09-58	251.20	251.45	251.33	260447.72	6943815.58	-380.40	N	Y	N	N
AMD310	AMD310-D	C09-7	51.07	51.20	51.14	260288.49	6943826.15	-259.63	Y	Y	Y	N
AMD310	AMD310-I	C09-9	98.16	98.38	98.27	260326.06	6943825.22	-288.09	Y	Y	Y	N
AMD310	AMD310-H	C10-153	90.98	91.41	91.20	260320.42	6943825.40	-283.81	N	Y	N	N
AMD310	AMD310-H	C10-153B	90.98	91.41	91.20	260320.42	6943825.40	-283.81	Y	Y	N	N
AMD310A	AMD310A-A	C09-18	377.80	377.95	377.88	260550.02	6943805.21	-454.17	N	Y	N	N
AMD313	AMD313Z	AMD313Z	77.00	77.43	77.22	260292.24	6943884.53	-268.27	N	N	N	**Y**
AMD313	AMD313-G	C09-11	77.00	77.30	77.15	260292.19	6943884.53	-268.23	N	Y	N	N
AMD313	AMD313-M	C09-15	93.00	93.24	93.12	260304.67	6943884.20	-278.19	N	Y	N	N
AMD313	AMD313-B	C09-2	14.35	14.65	14.50	260243.23	6943884.58	-229.15	N	Y	Y	N
AMD313	AMD313-C	C09-6	34.28	34.51	34.40	260258.79	6943884.82	-241.55	N	Y	Y	N
AMD313	AMD313-K	C09-63	125.70	126.09	125.90	260330.50	6943883.13	-298.33	Y	Y	N	N
AMD318	AMD318-E	C09-1	95.91	96.17	96.04	260333.63	6943752.38	-308.27	N	Y	Y	N
AMD318	AMD318-G	C09-10	146.94	147.07	147.01	260369.54	6943747.80	-344.15	Y	Y	N	N
AMD318	AMD318-D	C09-5	86.77	87.00	86.89	260327.26	6943753.18	-301.74	Y	Y	N	N
AMD318	AMD318-Q	C09-84	230.17	230.64	230.41	260430.31	6943739.32	-400.62	N	Y	N	N
AMD344	AMD344-D	AMD344-D	139.26	139.4	139.33	260517.56	6943910.14	-391.39	N	Y	N	**N**
AMD344	AMD344-E	AMD344-E	141	141.25	141.13	260519.16	6943911.43	-392.15	N	Y	N	**N**
AMD344	AMD344-F	AMD344-F	141.97	142.15	142.06	260519.99	6943911.58	-392.54	N	Y	N	**N**
AMD344	AMD344-G	AMD344-G	143.35	143.45	143.40	260521.19	6943911.80	-393.11	N	Y	N	**N**
AMD344	AMD344-H	AMD344-H	145.85	146.1	145.98	260523.50	6943912.20	-394.19	N	Y	N	**N**
AMD344	AMD344-I	AMD344-I	147.4	147.55	147.48	260524.84	6943912.43	-394.82	N	Y	N	**N**
AMD346	AMD346Z	AMD346Z	148.10	149.00	148.55	260537.29	6943929.75	-250.91	N	N	N	**Y**
AMD346	AMD346-A	C09-19	149.10	149.45	149.28	260537.98	6943929.94	-250.99	N	Y	Y	N
AMD464	AMD464-C	C10-96	223.00	233.40	228.20	260563.18	6944089.26	-447.61	N	Y	Y	N
AMD504	AMD504-A	C10-90	2.7.00	2.86	2.78.00	260270.85	6943759.49	-236.82	N	Y	Y	N

Hole ID	Field Sample number	Lab number	From (m)	To (m)	Mid-point (m)	Easting (mE)	Northing (mN)	mRL	REE	XRF	T/S	U-Pb Dating
AMD504	AMD504-B	C10-94	72.90	73.12	73.01	260338.05	6943751.54	-218.02	Y	Y	Y	N
AMD508	AMD508-A	C09-46	85.13	85.33	85.23	260505.53	6944012.09	-322.27	N	Y	N	N
AMD601	AMD601-A	C09-14	54.73	54.93	54.83	260382.29	6943950.68	-349.04	Y	Y	Y	N
AMD601	AMD601-K	C09-25	400.64	400.86	400.75	260635.01	6943969.41	-584.34	N	Y	Y	N
AMD601	AMD601-Q	C09-27	449.28	449.60	449.44	260670.39	6943970.14	-617.78	N	Y	N	N
AMD601	AMD601-E	C09-72	90.03	90.13	90.08	260408.02	6943954.44	-372.83	N	Y	N	N
AMD640	AMD640-G	C10-140	172.7	172.86	172.78	260476.68	6943862.08	-463.89	N	Y	N	N
AMD641	AMD641-B	C10-114	68.30	68.50	68.40	260276.31	6943911.95	-170.55	Y	Y	N	N
AMD641	AMD641-A	C10-93	44.50	44.70	44.60	260260.84	6943903.19	-186.38	Y	Y	N	N
AMD641	AMD641-C	C10-95	73.40	73.55	73.48	260279.65	6943913.79	-167.21	Y	Y	N	N
BJD017B	BJD017B-C	C10-110	1013.80	1013.93	1013.87	260357.64	6943858.24	-420.13	N	Y	N	N
BJD045A	BJD045A-M	C09-64	835.05	835.30	835.18	260274.56	6944101.34	-237.04	Y	Y	N	N
BJD045A	BJD045A-K	C09-85	810.10	810.30	810.20	260287.75	6944101.92	-215.84	N	Y	N	N
BJD048A	BJD048AZ	BJD048AZ	1077.40	1078.20	1077.80	260366.27	6943969.08	-473.60	N	N	N	*Y*
BJD048A	BJD048A-N	C09-65	1077.30	1077.50	1077.40	260366.45	6943969.03	-473.25	N	N	N	N
BJD048A	BJD048A-G	C09-71	970.30	970.50	970.40	260415.14	6943954.48	-379.09	N	Y	N	N
BJD048A	BJD048A-M	C09-88	1063.20	1063.30	1063.25	260372.90	6943967.06	-460.81	N	N	N	N
BJD048B	BJD048B-G	C09-16	944.65	944.85	944.75	260371.98	6943904.28	-325.06	Y	Y	N	N
BJD048B	BJD048B-F	C09-57	931.80	931.95	931.88	260379.49	6943904.15	-314.60	N	N	N	N
BJD050	BJD050-J	C09-20	918.60	918.90	918.75	260330.63	6944070.12	-273.47	Y	Y	Y	N
BJD054	BJD054-B	C10-106	980.40	980.77	980.59	260437.48	6944074.59	-336.26	Y	Y	Y	N
BJD054	BJD054-D	C10-107	1037.55	1038.00	1037.78	260402.56	6944088.53	-379.34	N	Y	Y	N
BJD057B	BJD057B-N	AM5-17	1096.00	1096.23	1096.12	260571.50	6944008.64	-524.95	N	Y	Y	N
BJD057B	BJD057B-H	AM5-20	1067.00	1067.17	1067.09	260578.94	6944004.94	-497.14	N	Y	Y	N
BJD057B	BJD057B-Q	AM5-28A	1105.80	1106.10	1105.95	260568.98	6944009.90	-534.38	N	N	Y	N
BJD057B	BJD057B-Q	AM5-28B	1105.80	1106.10	1105.95	260568.98	6944009.90	-534.38	N	N	Y	N
BJD057B	BJD057B-K	C10-155	1077.92	1078.08	1078.00	260576.14	6944006.33	-507.59	Y	Y	N	N
BJD085	BJD085Z	BJD085Z	451.80	452.70	452.25	260480.20	6944272.73	30.87	N	N	N	**Y**
BJD085	BJD085Z	BJD085Z	480.60	481.50	481.05	260481.59	6944269.63	2.28	N	N	N	*Y*
BJD085	BJD085Z	BJD085Z	632.60	632.85	632.73	260488.36	6944254.03	-148.44	N	N	N	*Y*

Hole ID	Field Sample number	Lab number	From (m)	To (m)	Mid-point (m)	Easting (mE)	Northing (mN)	mRL	REE	XRF	T/S	U-Pb Dating
BJD085	BJD085-J	C09-30	483.60	483.85	483.73	260481.71	6944269.34	-0.38	Y	Y	Y	N
BJD085	BJD085-Z	C09-41	273.30	273.50	273.40	260471.10	6944290.80	208.58	N	Y	N	N
BJD085	BJD085-C	C09-43	663.60	663.85	663.73	260489.57	6944250.74	-179.24	Y	Y	Y	N
BJD085	BJD085-U	C09-51	319.40	319.60	319.50	260473.56	6944286.30	162.76	Y	N	Y	N
BJD085	BJD085-R	C09-52	353.85	353.95	353.90	260475.37	6944282.83	128.59	N	N	Y	N
BJD090	BJD090Z	BJD090Z	755.80	757.00	756.40	260431.02	6944177.55	-268.72	N	N	N	**Y**
BJD090	BJD090-F	C09-48	649.55	649.70	649.63	260424.19	6944188.29	-162.71	Y	Y	N	N
BJD090	BJD090-M	C09-59	763.20	763.30	763.25	260431.40	6944176.85	-275.52	Y	Y	N	N
BJD090	BJD090-N	C09-67	766.45	766.60	766.53	260431.58	6944176.51	-278.78	N	Y	Y	N
BJD090	BJD090-O	C09-68	748.80	749.00	748.90	260430.59	6944178.33	-261.27	Y	Y	N	N
BJD090	BJD090-K	C09-69	738.55	738.80	738.68	260429.99	6944179.38	-251.12	N	Y	N	N
BJD090	BJD090-L	C09-70	756.30	756.40	756.35	260431.01	6944177.56	-268.67	Y	Y	N	N
BJD102	BJD102-K	C09-21	657.00	657.30	657.15	260294.56	6944137.93	-81.62	Y	Y	N	N
BJD102	BJD102-A	C09-89	559.10	559.30	559.20	260348.84	6944134.01	-0.20	N	N	N	N
BJD192	BJD192-A	C10-149	594.95	595.20	595.08	260350.70	6944064.35	-95.27	N	Y	N	N
BJD198	BJD198-I	C10-122	555.70	555.90	555.80	260231.52	6943871.57	-2.05	Y	Y	N	N
BJD198	BJD198-G	C10-127	526.63	526.90	526.77	260245.34	6943873.76	23.40	N	Y	N	N
BJD198	BJD198-H	C10-128	544.70	545.00	544.85	260236.73	6943872.40	7.55	Y	Y	Y	N
BJD198	BJD198-F	C10-147	501.60	501.80	501.70	260257.26	6943875.62	45.36	Y	Y	N	N
BJD283	BJD283-C	C10-105	517.90	518.10	518.00	260346.23	6943812.48	13.30	N	Y	Y	N
BJD312	BJD312-F	C09-12	184.70	184.86	184.78	260456.01	6944327.46	327.92	Y	Y	Y	N
BJD312	BJD312-C	C09-35	140.40	140.64	140.52	260430.73	6944329.21	364.21	Y	Y	N	N
BJD312	BJD312-I	C09-49	195.16	195.42	195.29	260462.04	6944326.90	319.33	Y	Y	N	N
BJD313	BJD313-F	C10-108	618.63	619.00	618.82	260367.78	6943752.18	-81.71	N	Y	Y	N
BJD313	BJD313-A	C10-111	716.60	716.83	716.72	260328.31	6943750.92	-171.29	Y	Y	N	N
BJD313	BJD313-C	C10-129	683.95	684.15	684.05	260341.61	6943751.22	-141.46	N	Y	Y	N
BJD316B	BJD316B-C	C10-99A	1097.40	1097.70	1097.55	260673.17	6944234.90	-604.15	Y	Y	N	N
BJD316B	BJD316B-C	C10-99B	1097.40	1097.70	1097.55	260673.17	6944234.90	-604.15	Y	Y	N	N
BJD320	BJD320Z	BJD320Z	467.30	468.00	467.65	260628.20	6944882.09	62.51	N	N	N	**Y**
BJD320	BJD320-A	C09-23	466.30	466.67	466.49	260627.61	6944882.18	63.51	Y	Y	Y	N

Hole ID	Field Sample number	Lab number	From (m)	To (m)	Mid-point (m)	Easting (mE)	Northing (mN)	mRL	REE	XRF	T/S	U-Pb Dating
BJD320	BJD320-B	C09-29	477.70	477.90	477.80	260633.31	6944881.34	53.77	N	Y	Y	N
BJD320	BJD320-U	C09-40	824.60	824.80	824.70	260803.02	6944849.26	-246.00	N	N	N	N
BJD328F	BJD328FZ	BJD328FZ	1142.30	1142.70	1142.50	260629.54	6943923.90	-659.62	N	N	N	**Y**
BJD328F	BJD328F-E	C09-26	1083.45	1083.67	1083.56	260630.52	6943929.60	-600.97	Y	Y	Y	N
BJD328F	BJD328F-G	C09-28A	1135.30	1135.60	1135.45	260629.66	6943924.56	-652.61	Y	Y	N	N
BJD328F	BJD328F-G	C09-28B	1135.30	1135.60	1135.45	260629.66	6943924.56	-652.61	Y	Y	N	N
BJD328F	BJD328F-A	C09-36	1030.00	1030.27	1030.14	260631.34	6943935.28	-547.85	N	Y	N	N
BJD332	BJD332Z	BJD332Z	405.95	406.45	406.20	260950.17	6943015.06	117.67	N	N	N	**Y**
BJD332	BJD332Z	BJD332Z	441.70	442.55	442.13	260930.58	6943017.40	87.64	N	N	N	*Y*
BJD332	BJD332-A	C10-124	1374.55	1374.75	1374.65	260462.74	6943128.55	-709.71	Y	Y	N	N
BJD332	BJD332-C	C10-130	1400.15	1400.40	1400.28	260451.23	6943131.85	-732.37	N	Y	N	N
BJD332	BJD332-A	C09-73	382.20	382.40	382.30	260963.03	6943013.42	137.75	N	Y	N	N
BJD332	BJD332-C	C09-74	406.16	406.42	406.29	260950.12	6943015.07	117.59	Y	Y	N	N
BJD332	BJD332-C	C09-74	406.16	406.42	406.29	260950.12	6943015.07	117.59	Y	Y	N	N
BJD332	BJD332-D	C09-75	422.30	422.40	422.35	260941.39	6943016.12	104.15	Y	Y	N	N
BJD332	BJD332-E	C09-76	427.70	427.85	427.78	260938.43	6943016.478	99.62	N	Y	N	N
BJD332	BJD332-F	C09-77A	428.50	428.75	428.63	260937.97	6943016.53	98.91	Y	Y	N	N
BJD332	BJD332-F	C09-77B	428.50	428.75	428.63	260937.97	6943016.53	98.91	N	Y	N	N
BJD332	BJD332-G	C09-78	442.40	442.55	442.48	260930.39	6943017.43	87.35	N	Y	N	N
BJD365A	BJD365A-E	C10-150	1106.15	1106.30	1106.23	260445.65	6943532.35	-609.17	Y	Y	N	N
BJD365A	BJD365A-B	C10-151	1090.60	1090.90	1090.75	260450.35	6943530.87	-594.50	N	Y	N	N
BJD365A	BJD365A-H	C10-154	1111.15	1111.25	1111.20	260444.11	6943532.82	-613.88	N	Y	N	N
BJD406	BJD406-E	C10-103	1395.80	1395.95	1395.88	260474.01	6943053.36	-790.17	Y	Y	Y	N
BJD406	BJD406-F	C10-104	1402.10	1402.25	1402.18	260471.39	6943053.31	-795.90	Y	Y	Y	N
BJD406	BJD406-D	C10-125	1375.95	1376.15	1376.05	260482.17	6943053.60	-772.11	N	Y	N	N
BJD406	BJD406-A	C09-79	306.00	306.30	306.15	260948.10	6943011.83	189.69	Y	Y	N	N
BJD406	BJD406-B	C09-80	327.30	327.63	327.47	260939.44	6943013.25	170.27	N	Y	N	N
BJD406	BJD406-D	C09-81	357.50	357.70	357.60	260926.60	6943015.21	143.07	Y	Y	N	N
BJD406	BJD406-E	C09-82	378.10	378.30	378.20	260917.34	6943016.51	124.72	Y	Y	N	N
BJD406	BJD406-G	C09-83	391.00	391.20	391.10	260911.39	6943017.28	113.30	Y	Y	N	N

Hole ID	Field Sample number	Lab number	From (m)	To (m)	Mid-point (m)	Easting (mE)	Northing (mN)	mRL	REE	XRF	T/S	U-Pb Dating
BJD406	BJD406-G	C10-98	1487.00	1487.25	1487.13	260434.56	6943053.82	-872.45	N	Y	N	N
BJD406	BJD406-A	C10-135	1348.80	1349.10	1348.95	260493.16	6943053.92	-747.34	N	Y	N	N
BJD406	BJD406-B	C10-137	1356.50	1356.70	1356.60	260490.08	6943053.86	-754.34	N	Y	N	N
BJD420	BJD420-D	C10-141	467.30	467.40	467.35	260853.54	6943282.39	73.13	N	Y	N	N
BJD420	BJD420-E	C10-142	471.25	471.45	471.35	260851.36	6943282.17	69.79	N	Y	N	N
BJD438	BJD438-A	C12-186	556.20	556.40	556.30	260962.69	6943684.79	-21.11	N	Y	N	N
BJD439	BJD439-A	C12-185	495.30	495.50	495.40	261001.29	6943536.85	28.79	N	Y	N	N
BJD442C	BJD442C-A	C12-181	565.15	565.35	565.25	260990.29	6944303.01	-42.06	N	Y	N	N
BJD445	BJD445-A	C12-184	774.00	774.20	774.10	260994.04	6944169.83	-180.07	N	Y	Y	N
BJDM002	BJDM002Z	BJDM002Z	833.60	834.45	834.03	260365.14	6944018.10	-256.65	N	N	N	**Y**
BJDM002	BJDM002-G	C09-24	834.60	834.80	834.70	260364.83	6944018.09	-257.25	N	N	Y	N
BJDM002	BJDM002-K	C09-42	960.90	961.10	961.00	260306.20	6944015.00	-369.08	Y	Y	N	N
CME072	CME072-F	C09-37	78.00	78.10	78.05	260740.44	6944647.46	-131.48	Y	Y	N	N
CME090	CME090-F	C09-54	52.00	52.10	52.05	260761.33	6944680.88	-141.64	N	Y	N	N
CME120	CME120-J	C10-100	723.70	723.90	723.80	260890.65	6944487.77	-784.11	N	Y	N	N
CME120	CME120-K	C10-101	737.70	738.00	737.85	260894.62	6944486.39	-797.51	N	Y	Y	N
CME120	CME120-I	C10-118	680.00	680.20	680.10	260877.90	6944491.70	-742.50	N	Y	N	N
CME120	CME120-H	C10-136	637.47	637.64	637.56	260864.80	6944495.37	-702.18	Y	Y	N	N
CME128	CME128-E	C10-109	129.20	129.60	129.40	260421.93	6944316.64	-204.86	Y	Y	Y	N
CME128	CME128-I	C10-113	380.70	380.90	380.80	260191.15	6944289.15	-300.13	Y	Y	Y	N
CME128	CME128-G	C10-119	253.40	253.67	253.54	260309.59	6944300.96	-255.22	N	Y	N	N
CND027	CND027-D	C12-167	393.16	393.38	393.27	261345.85	6944513.56	114.49	N	N	Y	N
CND027	CND027-D	C12-167	393.16	393.38	393.27	261345.85	6944513.56	114.49	N	N	Y	N
CND027	CND027-C	C12-176	375.48	375.68	375.58	261352.97	6944514.36	130.66	N	Y	N	N
CND027M	CND027M-A	C12-182	739.10	739.30	739.20	261193.71	6944499.92	-195.39	N	Y	Y	N
CND029	CND029-A	C12-173	206.26	206.47	206.37	261416.10	6944570.83	289.06	Y	Y	N	N
CND029B	CND029B-B	C12-171	378.36	378.56	378.46	261344.11	6944575.31	132.82	N	Y	N	N
CND029B	CND029B-C	C12-177	622.29	622.50	622.40	261243.18	6944580.77	-89.18	Y	Y	N	N
CND042	CND042-C	C12-164	213.41	213.61	213.51	261398.21	6944757.37	286.31	Y	Y	Y	N
CND042	CND042-B	C12-166	206.57	206.77	206.67	261401.37	6944757.31	292.38	N	Y	N	N

Hole ID	Field Sample number	Lab number	From (m)	To (m)	Mid-point (m)	Easting (mE)	Northing (mN)	mRL	REE	XRF	T/S	U-Pb Dating
CND042	CND042-A	C12-174	193.80	194.00	193.90	261407.27	6944757.19	303.70	N	Y	Y	N
CND042P	CND042P-C	C12-165	806.62	806.88	806.75	261090.44	6944713.12	-214.82	Y	Y	Y	N
CND042P	CND042P-B	C12-170	604.80	605.00	604.90	261214.68	6944741.13	-58.39	N	Y	Y	N
CND042P	CND042P-A	C12-175	505.50	505.75	505.625	261264.55	6944751.34	26.72	N	Y	N	N
CND042R	CND042R-C	C12-156	716.35	716.60	716.475	261188.99	6944758.38	-169.37	N	N	Y	N
CND042R	CND042R-C	C12-156	716.35	716.60	716.475	261188.99	6944758.38	-169.37	N	N	Y	N
CND042R	CND042R-A	C12-157	637.80	638.00	637.90	261216.45	6944750.60	-96.165	N	Y	N	N
CND042R	CND042R-B	C12-159	700.15	700.41	700.28	261194.62	6944756.71	-154.28	Y	Y	N	N
CND042R	CND042R-E	C12-160A	727.26	727.46	727.36	261185.21	6944759.53	-179.52	Y	Y	Y	N
CND042R	CND042R-E	C12-160B	727.26	727.46	727.36	261185.21	6944759.53	-179.52	N	Y	Y	N
CND042R	CND042R-E	C12-160C	727.26	727.46	727.36	261185.21	6944759.53	-179.52	N	Y	Y	N
CND042R	CND042R-E	C12-160D	727.26	727.46	727.36	261185.21	6944759.53	-179.52	N	Y	Y	N
CND042R	CND042R-D	C12-162	728.17	728.46	728.32	261184.88	6944759.63	-180.41	N	Y	Y	N
CND043	CND043-C	C12-172	452.26	452.50	452.38	261308.14	6944891.96	65.26	N	Y	N	N
CND043	CND043-D	C12-178	444.75	444.96	444.86	261310.95	6944891.71	72.23	Y	Y	Y	N
CND043	CND043-E	C12-187	771.75	771.95	771.85	261166.59	6944904.69	-219.83	N	Y	N	N
CND043	CND043-E	C12-187	771.75	771.95	771.85	261166.59	6944904.69	-219.83	N	Y	N	N
CND043D	CND043D-A	C12-161	818.08	818.28	818.18	261184.26	6944873.18	-278.28	Y	Y	N	N
CND043D	CND043D-B	C12-169	776.87	777.08	776.98	261197.87	6944874.91	-239.43	N	Y	Y	N
CND043D	CND043D-B	C12-179	819.65	819.90	819.78	261183.73	6944873.11	-279.78	Y	Y	N	N
CND043D	CND043D-E	C12-180	596.37	596.60	596.49	261257.37	6944883.65	-69.25	N	Y	Y	N
CND052	CND052-E	C12-158	499.28	499.52	499.40	261287.43	6945105.77	-3.60	N	Y	Y	N
CND052	CND052-F	C12-183	788.80	789.00	788.90	261226.08	6945109.99	-286.43	N	Y	N	N
CND053A	CND053A-A	C12-188	947.15	947.35	947.25	261354.72	6945326.71	-378.51	N	Y	N	N
ISD030	ISD30-J	CD08A	46.60	46.80	46.70	260668.52	6944691.53	-40.44	N	Y	Y	N
ISD030	ISD30-J	CD08B	46.60	46.80	46.70	260668.52	6944691.53	-40.44	Y	Y	Y	N
ISD030	ISD30-B	CD11A	9.40	9.60	9.50	260636.78	6944677.37	-27.18	N	N	Y	N
ISD030	ISD30-B	CD11B	9.40	9.60	9.50	260636.78	6944677.37	-27.18	N	N	Y	N
ISD030	ISD30-V	CD14	71.40	71.80	71.60	260689.95	6944700.67	-49.22	N	N	Y	N
ISD030	ISD30-V	CD15	71.40	71.80	71.60	260689.95	6944700.67	-49.22	N	N	Y	N

Hole ID	Field Sample number	Lab number	From (m)	To (m)	Mid-point (m)	Easting (mE)	Northing (mN)	mRL	REE	XRF	T/S	U-Pb Dating
ISD030	ISD30-V	CD16	71.40	71.80	71.60	260689.95	6944700.67	-49.22	N	N	Y	N
ISD030	ISD30-0	CD17	57.40	57.60	57.50	260677.80	6944695.53	-44.25	N	N	Y	N
ISD030	ISD30-0	CD18	57.40	57.60	57.50	260677.80	6944695.53	-44.25	N	Y	Y	N
ISD030	ISD30-W	CD20	73.50	73.70	73.60	260691.68	6944701.39	-49.93	N	Y	Y	N
ISD030	ISD30-U	CD21	68.30	68.80	68.55	260687.32	6944699.56	-48.15	N	N	Y	N
ISD030	ISD30-U	CD22	68.30	68.80	68.55	260687.32	6944699.56	-48.15	N	N	Y	N
ISD030	ISD30-U	CD23	68.30	68.80	68.55	260687.32	6944699.56	-48.15	N	N	Y	N
ISD030	ISD30-D	CD24	15.70	16.10	15.90	260642.22	6944679.82	-29.50	N	Y	Y	N
ISD030	ISD30-D	CD25	15.70	16.10	15.90	260642.22	6944679.82	-29.50	N	Y	Y	N
ISD038	ISD038-S	CD01A	87.65	87.85	87.75	260670.03	6944748.04	-45.24	N	N	Y	N
ISD038	ISD038-S	CD01B	87.65	87.85	87.75	260670.03	6944748.04	-45.24	N	N	Y	N
ISD038	ISD038-I	CD05A	59.90	60.00	59.95	260655.18	6944725.41	-38.93	N	Y	Y	N
ISD038	ISD038-I	CD05B	59.90	60.00	59.95	260655.18	6944725.41	-38.93	N	N	Y	N
ISD038	ISD038-B	CD09	6.30	6.50	6.40	260630.31	6944680.05	-25.13	N	Y	Y	N
ISD038	ISD038-C	CD10A	9.60	9.80	9.70	260631.85	6944682.82	-26.02	N	Y	Y	N
ISD038	ISD038-C	CD10B	9.60	9.80	9.70	260631.85	6944682.82	-26.02	N	Y	Y	N
ISD070	ISD070-N	CD04	68.00	68.15	68.08	260766.22	6944747.20	-83.68	Y	Y	Y	N
ISD070	ISD070-C	CD12	33.00	33.20	33.10	260759.04	6944728.19	-55.22	N	N	Y	N
ISD070	ISD070-C	CD13	33.00	33.20	33.10	260759.04	6944728.19	-55.22	N	N	Y	N
ISD070	ISD070-Z	CD30A	129.50	129.70	129.60	260782.55	6944779.73	-133.26	N	Y	Y	N
ISD070	ISD070-Z	CD30B	129.50	129.70	129.60	260782.55	6944779.73	-133.26	N	Y	Y	N
ISD070	ISD070-G	CD31A	49.25	49.50	49.38	260762.29	6944737.03	-68.49	N	N	Y	N
ISD070	ISD070-G	CD31A	49.25	49.50	49.38	260762.29	6944737.03	-68.49	N	N	Y	N
ISD080	ISD080-A	CD02	1.50	1.70	1.60	260750.95	6944711.44	-29.27	N	Y	Y	N
ISD080	ISD080-FF	CD03	36.85	37.05	36.95	260746.68	6944732.14	-57.60	N	Y	Y	N
ISD080	ISD080-V	CD06A	79.70	79.90	79.80	260742.99	6944756.17	-92.89	N	Y	N	N
ISD080	ISD080-V	CD06B	79.70	79.90	79.80	260742.99	6944756.17	-92.89	N	Y	N	N
ISD080	ISD080-EE	CD07	23.80	24.00	23.90	260748.12	6944724.62	-47.04	N	Y	Y	N
ISD080	ISD080-0	CD19A	52.90	53.20	53.05	260745.15	6944741.21	-70.82	N	Y	Y	N
ISD080	ISD080-0	CD19B	52.90	53.20	53.05	260745.15	6944741.21	-70.82	N	Y	Y	N

Hole ID	Field Sample number	Lab number	From (m)	To (m)	Mid-point (m)	Easting (mE)	Northing (mN)	mRL	REE	XRF	T/S	U-Pb Dating
ISD080	ISD080-F	CD26	13.75	14.00	13.88	260749.34	6944718.75	-39.00	N	N	Y	N
ISD080	ISD080-F	CD27	13.75	14.00	13.88	260749.34	6944718.75	-39.00	N	N	Y	N
ISD080	ISD080-E	CD28	13.50	13.70	13.60	260749.38	6944718.59	-38.79	N	N	Y	N
ISD080	ISD080-E	CD29	13.50	13.70	13.60	260749.38	6944718.59	-38.79	N	N	Y	N
JCD096	JCD096-B	C10-115	492.10	492.46	492.28	260669.84	6944612.27	42.67	N	Y	N	N
JCD096	JCD096-B	C10-115B	492.10	492.46	492.28	260669.84	6944612.27	42.67	Y	Y	N	N
JCD096	JCD096-A	C10-133A	491.15	491.75	491.45	260670.21	6944612.24	43.41	N	Y	N	N
JCD096	JCD096-A	C10-133B	491.15	491.75	491.45	260670.21	6944612.24	43.41	Y	Y	N	N
JCD109	JCD109-F	C10-117A	525.90	526.56	526.23	260648.57	6944649.66	32.46	Y	Y	N	N
JCD109	JCD109-B	C10-120	489.40	489.65	489.53	260668.08	6944651.45	63.50	Y	Y	N	N
JCD109	JCD109-I	C10-91	589.40	589.80	589.60	260614.63	6944646.41	-20.96	N	Y	N	N
JCD109	JCD109-E	C10-130A	524.25	524.45	524.35	260649.57	6944649.75	34.05	Y	Y	N	N
JCD109	JCD109-E	C10-130B	524.25	524.45	524.35	260649.57	6944649.75	34.05	Y	Y	N	N
JCD109	JCD109-C	C10-131A	498.00	498.72	498.36	260663.39	6944651.05	56.02	N	Y	N	N
JCD109	JCD109-C	C10-131B	498.00	498.72	498.36	260663.39	6944651.05	56.02	N	Y	N	N
JCD109	JCD109-D	C10-132	506.10	506.20	506.15	260659.25	6944650.67	49.43	Y	Y	N	N
JCD109	JCD109-A	C10-134	479.66	480.00	479.83	260673.21	6944651.89	71.71	N	Y	N	N
JCD109	JCD109-J	C10-138	643.60	643.80	643.70	260585.27	6944643.67	-66.32	N	Y	N	N
JCD125	JCD125-B	C10-116A	541.65	542.00	541.83	260682.35	6944661.92	12.44	Y	Y	Y	N
JCD125	JCD125-B	C10-116B	541.65	542.00	541.83	260682.35	6944661.92	12.44	Y	Y	Y	N
JCD125	JCD125-E	C10-121	585.10	585.20	585.15	260659.37	6944662.00	-24.29	N	Y	N	N
JCD125	JCD125-F	C10-126	608.35	608.53	608.44	260647.05	6944662.11	-44.06	Y	Y	Y	N
JCD125	JCD125-A	C10-148	506.00	506.20	506.10	260701.56	6944662.00	42.55	Y	Y	N	N
JCD125	JCD125-A	C10-148B	506.00	506.20	506.10	260701.56	6944662.00	42.55	N	Y	N	N
JCD130	JCD130-H	C09-55	637.50	637.60	637.55	260670.61	6944695.32	-64.94	Y	Y	N	N
JCD138	JCD138-A	C09-66	483.60	483.80	483.70	260686.70	6944674.10	60.00	Y	Y	N	N
JCD143	JCD143-J	C09-13	364.17	364.33	364.25	260581.23	6944459.40	149.05	N	Y	N	N
JCD143	JCD143-H	C09-31	296.93	297.17	297.05	260554.10	6944449.96	209.80	Y	Y	Y	N

Appendix 2 - Geochemistry methods and analytical data

A2.1 Sample preparation

Selected core samples were prepared for analysis at the University of Edinburgh. Core samples were cut into small pieces on a diamond-tipped saw and any obvious veins or amygdales were removed. The thin weathered outside edge of the core was removed by grinding on a diamond wheel. This also removed any remaining drilling mud attached to the sample and any core markings/measurements. If desired, core fillets were cut for thin section preparation using a diamond-tipped saw. Veins and undesired parts, such as xenoliths or clasts were removed by trimming the core with a saw. All samples were from holes less than 12 years old and consequently there was very little weathering alteration. All samples were taken from holes below the regolith depth, which typically extends 65 - 85m below the surface.

The cut sample pieces were washed in clean water and dried before being crushed into fragments, ranging from 5 - 15mm in size, in a tungsten carbide jaw crusher. Approximately 50 - 75g of each sample was milled in a tungsten-carbide orbital mill using tungsten-carbide barrels. Due to the quantity of samples, and the coarse grained nature of many of the rocks, it was impractical to use an agate mill due to the longer grinding time required and the agate mill's smaller capacity. Tungsten carbide mills can cause Ta and Co contamination, but these elements were not analysed. However, Nb contamination has also been reported from some tungsten carbide mills (Joron et al., 1980; Hickson and Juras, 1986) and tests using pure vein quartz suggest that different mills cause variable degrees of Nb contamination. Tests on the mill used at the University of Edinburgh by G. Fitton showed that this is <0.2

ppm, which is comparable to the precision of the method used in routine X-ray fluorescence (XRF) analysis (pers comm. Godfrey Fitton, 2013), However, care was taken not to overgrind samples to reduce any possible Nb contamination. Both the crusher and the TEMA mill were thoroughly cleaned between each sample using hot water and acetone solution to avoid sample cross-contamination. The resulting uniform, fine grained powders were then analysed for major and trace elements via XRF at the University of Edinburgh, UK. Rare earth elements were analysed using Inductively Coupled Plasma Mass Spectrometry (ICP-MS) at Scottish Universities Environmental Research Centre (SUERC) in East Kilbride, UK.

A2.2 X-ray Florescence Preparation

XRF spectrometry was used to analyse the whole rock major oxide and trace element concentration in the samples, essentially following the method described by Fitton et al. (1998). Major-element concentrations were determined after fusion with a lithium borate/carbonate flux containing La_2O_3 as a heavy absorber, by a method similar to that developed by Norrish and Hutton (1969). The powdered samples were dried overnight (>12 hours) at 110°C. A nominal, but precisely weighed, 1.0g of each sample was weighed out into Pt5%Au crucible and ignited for 20 minutes at 1100°C. Samples were then removed from the furnace and reweighed after cooling for 10 minutes in a desiccator. The change in weight between the unignited and ignited sample was then used to calculate the percentage loss-on-ignition (LOI %) for each sample. The ignited powders were then mixed with flux (Johnson Matthey Spectroflux 105) in a sample:flux ratio of 1:5, based on the unignited sample mass. Samples were then fused in a muffle furnace, in the same platinum crucibles, for a further 20 minutes. Samples were removed from the furnace, checked to see if the sample had dissolved completely and then left to cool for 10 minutes. If any samples had not fully dissolved they were fused for a further 20 minutes. This occurred occasionally with the most silicic samples, typically the rhyolites. Samples were then reweighed and any flux weight loss was made up with extra flux to within ± 0.0003g of the initially calculated

weight. Each sampled was then fused again over a gas burner and the melt swirled sufficiently to ensure homogeneity. The molten sample was then cast immediately onto a graphite mould on a hot plate at 220^{o}C, where it was flattened into a thin disk using an aluminium plunger. Each disc was left to anneal on the hot plate for five minutes and then cooled before it was labelled and stored in a desiccator.

Trace-element concentrations were determined on pressed-powder samples. 8g (± 0.1g) of powdered sample was weighed into a beaker into which eight drops of binding agent, 2% aqueous solution of polyvinyl alcohol, were added. The sample and the binding agents were thoroughly mixed with a stirring rod until the binding agent was evenly distributed. The sample was transferred into a 40mm diameter cap on a lower tungsten carbide disc within a steel mould. The powder was gently compressed within the aluminium cap using a Perspex rod before a inserting a polished tungsten carbide disc facing downwards onto the powder. A steel plunger was inserted and the die assembly was transferred to an X-Press Spex 3630 hydraulic press to compress the powder. The sample was compressed at a pressure of 0.64 tonnes/cm^2 for two minutes and the pressure then released slowly for 30 seconds before removing the assembly and disc from the press.

The fused and pressed samples were analysed using a PANanalytical PW2404 automatic X-ray Fluorescence Spectrometer with a Rh-anode primary X-ray tube. Corrections for matrix effects on the intensities of major-element lines were made using theoretical alpha coefficients calculated online using the PANanalytical software. The coefficients were calculated to allow for the amount of extra flux replacing volatile components in the sample so that analytical totals should be 100% less the measured LOI. Analytical precision was estimated by making five glass discs and five separate powdered pellets for each of two separate samples from within the Cosmos suite of rocks to text the repeatability of the results (Tables A2.14, A2.15). Percentage error (at 1σ) on major elements for sample repeats were found to be within 1 wt. % of each other, whereas trace element precision sample repeats were found to be within 0.5 - 3ppm of one another (at 1σ). Variability between individual elements was apparent and typically proportional to their concentration, with larger

concentrations showing greater variability (Table. A2.14, A2.15). The accuracy of major and trace elements concentrations of the standards analysed (BHVO-1; BEN; BIR; BCR-1) can be seen in Tables A2.16 and A2.17. Overall 225 samples were analysed for both trace and major elements by XRF spectrometry.

A2.3 ICP-MS Analyses

ICP-MS analyses were undertaken on the same sample powders prepared for XRF analyses. Over 85 Samples were prepared for REE analysis via three acid dissolution, largely following the method of Olive et al. (2001) and then analysed using ICP-MS. These were run in two separate batches.

Between 0.095 and 0.105g of fine powder of each sample was weighed out, along with standards of Columbia River Basalt, BCR-2 (Wilson 1997) into small conical flat-bottomed beakers. 5ml of hydrofluoric acid (HF) and 1ml of 50% HNO_3 was added to each sample. Beakers were covered and placed on a hotplate at 100°C for 24 hours in order to allow the HF to break down the silicate lattice. After 24 hours the lids were removed from the beakers and the samples were left to dry out on the hotplate. Once dry, 1ml of nitric acid was added to each sample beaker and they were returned to the hotplate at 100°C for a further 24 hours. The lids were then removed from the beakers and they were left on the hotplate to dry out once again. Once dry, 1ml of hydrochloric acid was added to each sample and they were placed on the hotplate at 100°C for a third time. After 24 hours the lids were removed from the beakers and the samples were left on the hotplate until very nearly dry, then ~3ml of 5% nitric acid was added to dissolve the sample again. The solution was checked then to ensure that the entire sample had dissolved. The dissolved sample was then transferred into a 100ml conical flask, ensuring the beaker was thoroughly rinsed with 5% HNO_3, which was then used to fill the conical flask to 100ml. The flasks were gently shaken and left overnight. The solution was then transferred into pre-rinsed plastic beakers.

For each sample and standard of BCR-2 , 0.2 ml of internal standard (a mix of In, Ru and Re) was added to a test tube, followed by 1ml of the sample (or standard), followed by 9ml of 5% HNO_3, for a total dilution of the sample of about 10,000. Three elemental standard solutions were also prepared, diluted from an in-house standard 'alpha solution' (a mixture of all the rare earth element and Ba (Olive et al., 2001) and also spiked with 0.2ml of the internal standard. Prior to each analysis run the 'α' solution at different dilutions was used to construct a calibration curve. Calibrations were accepted for correlation coefficients (r) >0.99. Additional elements U, Th, Hf and Pb were analysed for selected samples in a separate run using a different internal standard calibration solution. The samples were then analysed on an Agilent 7500ce Q-ICP-MS at the Scottish Universities Environmental Research Centre (SUERC) in East Kilbride. The ICP-MS was flushed with dilute HNO_3 between each analysis.

Two separate batches of analyses were run. The first batch of results were processed as follows. A sample of BCR-2 was analysed between every five unknown samples. The majority of elements within BCR-2 were normalised to agree with the values of Wilson (1997), although Dy and Er were normalised to the values for BCR-1 as no recommended value is provided by Wilson (1997) for these two elements. The resulting correction factor for each analysis of BCR-2 was then applied to the following five unknown samples. Thus correction factors were applied to individual sets of five unknown samples based on the nearest analysed standard. This allowed for more effective correction of any drift that occurred during the analyses. The average of the BCR-2 standard analyses in the second batch of analyses were normalised to agree with the published values of BCR-2 and this correction factor was subsequently applied to all analyses, following the method of Olive et al. (2001). Estimates of accuracy and precision for ICP-MS analyses can be seen in tables A2.18 and A2.19. The values obtained for La, Ce and Nd from both XRF and ICP-MS analyses have been compared and have been shown in Figure A2.1. There is good consistency in the measured concentration of trace elements between the two analytical methods with R^2 values of ~0.97.

A2.4 Major, trace and rare earth element data

	AM08	AM19	C09-01	C09-02	C09-03	C09-04	C09-05	C09-06	C09-6b	C09-07
SiO_2 (wt%)	75.04	75.97	77.08	74.52	75.43	76.01	81.45	80.90	80.45	78.61
Al_2O_3 (wt%)	12.45	12.45	12.36	12.97	12.29	12.41	11.55	11.56	11.46	12.87
Fe_2O_3 (wt%)	1.41	1.51	1.34	1.40	1.25	1.51	0.58	1.11	1.12	1.15
MnO (wt%)	0.01	0.02	0.01	0.02	0.02	0.01	n.d	0.01	0.01	0.01
MgO (wt%)	0.29	0.22	0.47	0.25	0.24	0.45	0.15	0.29	0.39	0.44
CaO (wt%)	0.53	0.69	0.55	0.75	0.72	1.78	n.d	n.d	0.01	n.d
Na_2O (wt%)	3.38	2.69	4.73	4.55	3.31	3.15	n.d	n.d	n.d	n.d
K_2O (wt%)	4.67	5.42	1.52	3.46	4.52	2.67	3.54	3.81	3.77	4.22
TiO_2 (wt%)	0.12	0.11	0.12	0.12	0.11	0.12	0.11	0.10	0.11	0.12
P_2O_5 (wt%)	0.02	0.01	0.01	0.01	0.01	0.01	0.02	0.01	0.02	0.00
LOI (wt%)	0.66	0.60	0.68	0.76	2.06	0.98	1.66	1.64	0.96	1.86
Total Majors	98.58	99.70	98.87	98.80	99.96	99.10	99.06	99.43	98.31	99.28
Zn (ppm)	11.2	7.8	10.1	8.4	8.0	21.3	3.1	7.5	7.5	8.1
Cu (ppm)	4.0	5.5	3.4	3.6	5.3	4.7	2.7	3.3	3.3	3.3
Ni (ppm)	n.d	n.d	n.d	0.2	n.d	n.d	n.d	n.d	n.d	3.0
Cr (ppm)	-	-	50.9	53.0	52.9	52.7	53.1	51.2	51.2	60.8
V (ppm)	-	-	16.1	15.4	15.3	16.1	16.6	16.6	16.6	17.4
Ba (ppm)	1182.8	1113.2	309.5	600.9	886.7	408.3	283.5	452.2	452.2	450.7
Sc (ppm)	1.5	1.6	4.7	2.7	3.1	0.4	5.5	7.6	7.6	7.3
Nb (ppm)	12.5	12.1	12.9	12.4	11.5	12.4	11.6	11.7	11.7	13.1
Zr (ppm)	154.5	149.3	156.0	151.8	144.9	150.1	136.3	135.4	135.4	152.7
Y (ppm)	29.2	29.4	26.0	32.6	30.8	28.6	22.6	24.4	24.4	28.4
Sr (ppm)	57.7	70.8	57.0	65.2	63.1	56.8	8.7	7.6	7.6	7.2
Rb (ppm)	124.6	134.4	44.1	86.5	114.6	88.4	89.3	110.0	110.0	120.7
Hf (ppm)	-	4.70	-	-	-	-	-	-	-	-
U(ppm)	8.2	7.73	8.2	8.4	8.4	7.7	8.0	7.5	7.5	10.6
Th (ppm)	31.9	29.84	31.4	31.4	30.4	30.5	28.0	28.2	28.2	31.0
Pb (ppm)	19.2	21.55	18.5	26.0	16.0	36.7	10.5	14.4	14.4	19.4
La (ppm)	67.5	66.53	51.7	71.3	58.92	58.68	50.83	55.5	55.5	59.9
Ce (ppm)	105.7	119.89	90.6	113.3	101.65	101.13	88.44	89.5	89.5	98.5
Pr (ppm)	-	12.29	-	-	9.93	9.97	8.70	-	-	-
Nd (ppm)	31.7	39.07	31.7	37.1	31.20	32.03	27.60	31.3	31.3	32.7
Sm (ppm)	-	6.36	-	-	5.18	5.40	4.51	-	-	-
Eu (ppm)	-	0.95	-	-	0.80	0.73	0.47	-	-	-
Gd (ppm)	-	5.95	-	-	5.00	4.84	4.15	-	-	-
Tb (ppm)	-	0.82	-	-	0.68	0.64	0.53	-	-	-
Dy (ppm)	-	4.71	-	-	3.76	3.22	2.63	-	-	-
Ho (ppm)	-	0.94	-	-	0.80	0.64	0.52	-	-	-
Er (ppm)	-	2.85	-	-	2.31	1.73	1.50	-	-	-
Tm (ppm)	-	0.46	-	-	0.36	0.27	0.23	-	-	-
Yb (ppm)	-	2.93	-	-	2.54	1.89	1.64	-	-	-
Lu (ppm)	-	0.44	-	-	0.37	0.29	0.26	-	-	-
Total Majors + Traces	98.76	99.88	98.96	98.94	100.12	99.22	99.14	99.54	98.41	99.39

Table A2.1. Rhyolite compositions. LOI = Loss on ignition; wt% = Weight percent; ppm = Parts per million; n.d = not detected; – denotes element not analysed. Analyses with one decimal place were analysed by XRF whereas analyses with two decimal places were analysed by ICP-MS.

	C09-08	C10-98	C10-153b	C10-154
SiO_2 (wt%)	79.54	78.70	77.01	76.04
Al_2O_3 (wt%)	12.46	12.35	12.71	12.42
Fe_2O_3 (wt%)	0.82	1.65	1.08	1.45
MnO (wt%)	0.00	0.02	0.06	0.02
MgO (wt%)	0.31	1.17	0.86	0.38
CaO (wt%)	n.d	0.66	1.71	0.64
Na_2O (wt%)	n.d	0.25	3.13	3.35
K_2O (wt%)	3.97	3.03	3.14	4.27
TiO_2 (wt%)	0.12	0.11	0.11	0.11
P_2O_5 (wt%)	0.02	0.01	0.01	0.01
LOI (wt%)	1.78	1.91	0.57	0.44
Total Majors	99.02	99.86	100.39	99.14
Zn (ppm)	4.1	12.4	11.6	17.4
Cu (ppm)	3.2	4.1	4.3	10.6
Ni (ppm)	n.d	3.1	0.6	n.d
Cr (ppm)	51.1	n.d	n.d	n.d
V (ppm)	16.4	n.d	n.d	n.d
Ba (ppm)	463.5	302.9	996.6	1116.5
Sc (ppm)	5.7	3.2	2.0	3.0
Nb (ppm)	12.6	11.3	12.5	12.8
Zr (ppm)	148.4	153.4	151.5	154.3
Y (ppm)	26.1	30.4	33.9	30.3
Sr (ppm)	7.9	22.8	47.9	61.5
Rb (ppm)	107.3	130.0	63.5	396.7
Hf (ppm)	-	-	5.01	-
U(ppm)	9.5	-	8.0	8.0
Th (ppm)	30.6	-	30.6	30.8
Pb (ppm)	15.3	-	44.0	15.1
La (ppm)	67.10	66.10	61.31	62.90
Ce (ppm)	105.70	111.50	108.68	99.50
Pr (ppm)	-	-	10.81	-
Nd (ppm)	35.90	35.20	35.02	31.10
Sm (ppm)	-	-	5.69	-
Eu (ppm)	-	-	0.88	-
Gd (ppm)	-	-	5.30	-
Tb (ppm)	-	-	0.76	-
Dy (ppm)	-	-	4.41	-
Ho (ppm)	-	-	0.89	-
Er (ppm)	-	-	2.68	-
Tm (ppm)	-	-	0.45	-
Yb (ppm)	-	-	2.87	-
Lu (ppm)	-	-	0.44	-
Total Majors + Traces	99.14	99.95	100.56	99.34

Table A2.1. Rhyolite compositions continued.

	AM27	AM20	C09-14	C09-15	C09-16	C09-17	C09-20	C09-21	C09-67	C09-68	C09-69
SiO_2 (wt%)	67.69	69.19	73.04	67.71	69.54	73.52	68.17	71.92	71.05	70.23	69.22
Al2O3 (wt%)	14.51	14.43	13.57	15.63	15.41	14.83	15.96	14.20	13.66	13.48	15.12
Fe2O3 (wt%)	3.54	3.81	3.59	4.38	4.81	4.46	4.91	4.57	3.45	3.42	3.99
MnO (wt%)	0.06	0.04	0.02	0.05	0.04	0.04	0.05	0.09	0.06	0.06	0.06
MgO (wt%)	2.21	1.33	2.62	2.70	2.53	1.67	2.66	2.32	2.12	2.19	1.73
CaO (wt%)	4.59	2.63	0.25	2.10	0.20	0.50	0.23	0.08	1.59	1.62	1.10
Na2O (wt%)	1.48	4.55	0.51	0.61	0.29	0.23	0.26	0.11	4.47	4.46	0.86
K2O (wt%)	2.89	1.38	3.52	3.89	4.33	2.80	4.10	3.49	1.28	1.26	3.37
TiO2 (wt%)	0.45	0.39	0.34	0.49	0.46	0.43	0.48	0.39	0.38	0.38	0.44
P2O5 (wt%)	0.21	0.09	0.07	0.11	0.12	0.11	0.11	0.10	0.08	0.09	0.11
LOI (wt%)	1.15	1.02	2.52	2.77	2.40	1.66	2.82	2.19	1.28	1.95	2.47
Total Majors	98.77	98.86	100.06	100.44	100.13	100.25	99.75	99.46	99.42	99.14	98.47
Zn (ppm)	38.8	56.6	24.9	49.9	45.5	59.5	50.6	51.5	32.4	16.4	57.5
Cu (ppm)	4.3	111.3	7.3	3.5	3.7	3.6	5.1	31.5	3.9	5.9	9.2
Ni (ppm)	32.3	10.5	19.6	19.0	10.0	14.4	12.2	26.5	9.3	11.5	23.9
Cr (ppm)	11.3	n.d	68.3	45.5	40.5	56.9	41.9	70.3	n.d	n.d	n.d
V (ppm)	62.5	23.0	51.9	72.6	67.9	65.5	70.0	54.4	47.0	54.4	55.5
Ba (ppm)	390.1	602.9	1049.2	550.1	491.7	464.5	409.2	322.5	429.4	669.3	1057.1
Sc (ppm)	7.9	8.2	17.3	11.3	16.4	16.7	20.0	21.2	5.7	7.9	8.2
Nb (ppm)	5.6	15.9	14.1	10.8	11.1	10.3	11.2	14.7	8.9	9.7	10.4
Zr (ppm)	138.2	242.5	222.9	197.4	188.8	181.3	198.6	235.4	159.5	162.0	183.8
Y (ppm)	12.3	32.7	33.1	20.1	21.2	21.6	26.7	31.5	16.9	20.4	22.7
Sr (ppm)	125.3	101.0	40.4	29.4	11.8	15.6	12.5	17.5	125.2	16.9	47.2
Rb (ppm)	88.2	53.2	264.2	135.2	143.3	72.5	116.1	87.6	45.4	122.8	121.2
Hf (ppm)	-	-	-	-	-	-	-	-	-	-	-
U(ppm)	2.4	6.2	6.2	5.4	5.5	5.5	5.9	8.4	-	4.7	-
Th (ppm)	12.6	25.9	25.2	22.0	20.5	21.1	22.4	25.7	-	19.8	-
Pb (ppm)	22.2	22.5	17.0	22.9	15.6	25.4	11.6	17.8	-	20.9	-
La (ppm)	46.2	87.5	56.38	45.8	39.84	41.93	34.13	67.95	35.0	46.33	44.0
Ce (ppm)	85.7	141.8	104.57	77.5	67.30	69.63	63.40	120.31	61.6	76.08	66.9
Pr (ppm)	-	-	10.98	-	6.72	6.85	5.92	12.31	-	7.60	-
Nd (ppm)	33.1	45.9	36.84	24.2	21.61	21.78	19.12	41.34	22.5	24.61	23.5
Sm (ppm)	-	-	6.35	-	3.78	3.69	3.41	6.95	-	4.32	-
Eu (ppm)	-	-	0.95	-	0.85	0.92	0.70	1.21	-	0.96	-
Gd (ppm)	-	-	6.00	-	3.65	3.59	3.35	6.11	-	4.01	-
Tb (ppm)	-	-	0.80	-	0.45	0.46	0.46	0.78	-	0.51	-
Dy (ppm)	-	-	4.49	-	2.09	2.31	2.54	3.95	-	2.88	-
Ho (ppm)	-	-	0.89	-	0.36	0.44	0.51	0.77	-	0.58	-
Er (ppm)	-	-	2.45	-	0.98	1.17	1.44	1.96	-	1.65	-
Tm (ppm)	-	-	0.37	-	0.14	0.17	0.23	0.30	-	0.26	-
Yb (ppm)	-	-	2.46	-	1.01	1.24	1.61	2.04	-	1.85	-
Lu (ppm)	-	-	0.38	-	0.16	0.19	0.25	0.29	-	0.27	-
Total Majors + Traces	98.88	99.02	100.27	100.58	100.25	100.37	99.86	99.59	99.52	99.28	98.64

Table A2.2 Dacite lava compositions. LOI = Loss on ignition; wt% = Weight percent; ppm = Parts per million; n.d = not detected; – denotes element not analysed. Analyses with one decimal place were analysed by XRF whereas analyses with two decimal places were analysed by ICP-MS.

	C09-70	C09-71	C09-72	C10-103	C10-104	C10-105	C10-106	C10-107	C10-108	C10-109
SiO_2 (wt%)	70.52	68.78	70.77	70.87	69.32	70.00	68.74	69.29	70.00	69.47
Al_2O_3 (wt%)	14.50	14.32	14.30	14.08	14.34	14.43	14.93	14.31	14.27	14.39
Fe_2O_3 (wt%)	3.47	4.31	3.80	3.69	4.95	3.83	4.23	3.96	3.86	4.42
MnO (wt%)	0.05	0.06	0.05	0.05	0.07	0.05	0.05	0.05	0.05	0.08
MgO (wt%)	1.75	2.24	1.83	1.64	2.05	2.03	2.37	2.32	2.20	2.32
CaO (wt%)	1.27	1.15	2.21	1.62	1.63	1.42	1.80	2.20	2.09	1.84
Na_2O (wt%)	2.34	5.06	2.58	0.72	4.87	3.50	4.58	2.82	3.96	3.96
K_2O (wt%)	2.77	1.24	2.50	4.98	0.58	3.22	1.84	2.82	1.70	1.39
TiO_2 (wt%)	0.44	0.45	0.43	0.39	0.44	0.44	0.44	0.45	0.43	0.45
P_2O_5 (wt%)	0.11	0.11	0.10	0.09	0.10	0.10	0.10	0.10	0.10	0.10
LOI (wt%)	1.79	1.15	1.02	1.46	1.54	0.94	0.79	1.23	1.06	1.42
Total Majors	99.02	98.86	99.59	99.60	99.88	99.96	99.88	99.57	99.71	99.85
Zn (ppm)	31.8	32.7	37.3	31.0	58.5	39.0	41.1	42.0	41.1	32.8
Cu (ppm)	2.8	7.5	3.4	253.2	22.0	16.2	8.5	4.0	3.2	11.4
Ni (ppm)	5.6	12.9	6.6	13.0	8.6	12.5	12.9	17.1	9.9	16.6
Cr (ppm)	n.d	n.d	n.d	n.d	n.d	n.d	n.d	n.d	n.d	n.d
V (ppm)	48.7	57.5	49.1	36.3	38.7	40.5	45.6	44.3	38.2	51.4
Ba (ppm)	491.0	325.3	560.0	860.0	516.3	1083.6	622.0	888.0	361.3	712.4
Sc (ppm)	7.8	8.2	7.6	8.1	8.0	9.0	8.9	9.3	8.1	9.7
Nb (ppm)	10.1	9.1	10.0	10.0	10.2	9.6	9.2	9.5	9.7	9.3
Zr (ppm)	183.6	164.1	177.2	151.1	178.5	171.8	163.1	169.8	172.1	168.6
Y (ppm)	20.1	18.1	21.3	20.0	25.6	19.6	20.9	20.7	18.7	19.9
Sr (ppm)	121.3	136.3	85.7	35.6	93.0	80.8	96.9	84.1	68.7	107.8
Rb (ppm)	82.0	49.1	67.6	113.1	24.6	68.8	49.2	102.1	49.6	47.4
Hf (ppm)	-	-	-	-	4.71	-	4.36	-	-	4.83
U(ppm)	4.8	-	-	6.1	5.79	-	5.63	-	-	5.49
Th (ppm)	20.3	-	-	21.1	20.61	-	21.96	-	-	20.13
Pb (ppm)	14.9	-	-	16.8	24.19	-	26.72	-	-	18.33
La (ppm)	36.80	38.7	40.6	42.60	47.28	38.8	42.71	35.3	41.5	38.76
Ce (ppm)	64.60	61.9	64.4	69.80	79.85	62.8	72.34	62.2	70.7	66.46
Pr (ppm)	6.48	-	-	6.77	7.84	-	7.10	-	-	6.67
Nd (ppm)	21.02	23.0	22.5	21.68	25.53	17.5	23.12	19.6	23.2	22.13
Sm (ppm)	3.70	-	-	3.79	4.30	-	3.77	-	-	3.76
Eu (ppm)	0.92	-	-	0.96	1.04	-	0.99	-	-	0.99
Gd (ppm)	3.70	-	-	3.63	4.19	-	3.58	-	-	3.65
Tb (ppm)	0.53	-	-	0.53	0.61	-	0.48	-	-	0.51
Dy (ppm)	3.11	-	-	2.91	3.58	-	2.64	-	-	3.01
Ho (ppm)	0.63	-	-	0.60	0.70	-	0.50	-	-	0.60
Er (ppm)	1.80	-	-	1.70	2.08	-	1.45	-	-	1.78
Tm (ppm)	0.29	-	-	0.26	0.33	-	0.23	-	-	0.29
Yb (ppm)	1.90	-	-	1.81	2.08	-	1.49	-	-	1.85
Lu (ppm)	0.29	-	-	0.28	0.32	-	0.24	-	-	0.29
Total Majors + Traces	99.14	98.96	99.71	99.77	100.00	100.13	100.01	99.72	99.80	99.98

Table A2.2 Dacite lava compositions continued.

	C09-25	C09-26	C09-27	C09-28a	C10-99b	C10-100	C09-28b – Iv xenolith	C10-99 – Iv xenolith	C10-101 – Iv xenolith
SiO_2 (wt%)	71.24	69.70	72.81	69.45	69.19	69.31	55.38	53.69	58.90
Al_2O_3 (wt%)	13.94	13.83	13.56	14.42	14.15	14.41	15.96	16.49	16.02
Fe_2O_3 (wt%)	3.60	3.63	2.48	3.90	4.14	3.79	10.17	9.95	7.61
MnO (wt%)	0.05	0.06	0.04	0.05	0.06	0.06	0.15	0.14	0.10
MgO (wt%)	1.33	1.74	1.41	2.01	2.16	1.50	6.33	7.46	5.04
CaO (wt%)	0.96	0.97	1.02	1.37	1.45	3.10	1.04	1.31	4.99
Na_2O (wt%)	4.69	2.89	3.63	4.52	3.71	4.24	3.07	2.88	2.55
K_2O (wt%)	2.75	5.72	3.94	3.11	3.54	1.45	5.52	5.36	2.73
TiO_2 (wt%)	0.41	0.41	0.33	0.42	0.42	0.51	0.76	0.82	0.78
P_2O_5 (wt%)	0.12	0.10	0.07	0.10	0.10	0.11	0.14	0.14	0.15
LOI (wt%)	1.19	0.89	0.90	0.75	0.72	1.16	1.58	1.54	0.89
Total Majors	100.28	99.93	100.18	100.10	99.64	99.64	100.09	99.80	99.75
Zn (ppm)	33.1	46.8	37.3	36.1	44.6	30.5	114.1	132.4	75.7
Cu (ppm)	18.2	3.4	23.8	3.7	3.9	40.0	4.4	3.8	5.1
Ni (ppm)	4.4	10.9	11.0	10.3	17.6	23.3	91.9	96.1	86.7
Cr (ppm)	43.5	51.7	n.d	n.d	n.d	29.4	183.9	186.8	157.9
V (ppm)	55.7	59.6	30.3	50.6	46.6	68.7	132.9	146.2	147.4
Ba (ppm)	612.5	875.0	993.9	1153.8	1145.9	697.9	886.1	462.6	435.4
Sc (ppm)	10.7	11.1	6.6	6.8	8.4	8.8	24.4	29.8	23.8
Nb (ppm)	9.9	9.0	14.2	9.5	9.4	8.5	5.6	11.3	7.2
Zr (ppm)	183.1	167.0	268.1	168.5	148.8	154.9	102.0	125.7	139.4
Y (ppm)	21.3	19.0	33.0	19.3	21.2	17.6	18.7	17.1	20.6
Sr (ppm)	94.6	87.0	99.9	94.7	95.3	140.4	308.6	66.2	186.5
Rb (ppm)	96.2	109.1	115.2	113.3	94.1	47.0	93.0	221.2	509.0
Hf (ppm)	-	-	-	-	-	-	-	-	-
U(ppm)	5.7	4.9	6.6	5.3	5.7	-	2.1	2.8	-
Th (ppm)	21.2	19.8	26.1	20.3	19.8	-	5.5	6.6	-
Pb (ppm)	14.8	19.3	40.7	16.3	12.7	-	9.0	6.6	-
La (ppm)	42.1	39.84	63.4	43.54	41.10	32.1	28.17	30.06	24.2
Ce (ppm)	63.5	65.81	109.1	72.29	69.74	54.2	52.31	54.12	44.6
Pr (ppm)	-	6.61	-	6.99	6.72	-	5.62	5.64	-
Nd (ppm)	22.5	21.38	38.5	22.07	21.55	17.4	19.73	19.10	17.3
Sm (ppm)	-	3.83	-	3.79	3.84	-	3.87	3.50	-
Eu (ppm)	-	1.02	-	1.09	0.95	-	0.85	0.70	-
Gd (ppm)	-	3.75	-	3.61	3.69	-	3.75	3.51	-
Tb (ppm)	-	0.51	-	0.50	0.53	-	0.53	0.50	-
Dy (ppm)	-	2.77	-	2.73	2.94	-	2.71	2.76	-
Ho (ppm)	-	0.52	-	0.55	0.62	-	0.51	0.58	-
Er (ppm)	-	1.46	-	1.53	1.81	-	1.35	1.57	-
Tm (ppm)	-	0.23	-	0.24	0.27	-	0.19	0.23	-
Yb (ppm)	-	1.57	-	1.64	1.92	-	1.26	1.48	-
Lu (ppm)	-	0.23	-	0.24	0.29	-	0.17	0.22	-
Total Majors + Traces	100.41	100.10	100.38	100.29	99.82	99.77	100.30	99.96	99.94

Table A2.3. Compositions of dacite lava containing intermediate (Iv) xenoliths. LOI = Loss on ignition; wt% = Weight percent; ppm = Parts per million; n.d = not detected; – denotes element not analysed. Analyses with one decimal place were analysed by XRF whereas analyses with two decimal places were analysed by ICP-MS.

	AM03	AM06a	AM26	CD06b	C09-30	C09-31	C09-32	C09-33	C09-35	C09-36
SiO_2 (wt%)	69.41	66.06	67.50	39.78	70.77	73.54	70.16	69.07	68.74	80.03
Al_2O_3 (wt%)	14.12	13.97	13.20	17.72	13.73	13.41	14.47	13.82	15.07	10.02
Fe_2O_3 (wt%)	4.00	5.60	5.77	16.16	3.51	1.98	3.07	3.50	4.82	1.91
MnO (wt%)	0.06	0.09	0.15	0.28	0.11	0.06	0.05	0.08	0.07	0.05
MgO (wt%)	1.66	2.88	0.76	8.24	0.94	0.99	1.74	0.98	2.14	0.50
CaO (wt%)	3.43	3.28	5.67	7.54	1.77	2.21	1.45	2.09	0.56	0.81
Na_2O (wt%)	1.83	0.74	0.20	1.00	3.50	4.06	6.22	3.65	0.38	2.87
K_2O (wt%)	2.87	2.97	1.76	2.75	3.65	2.10	0.78	4.18	5.51	3.13
TiO_2 (wt%)	0.37	0.40	0.41	2.02	0.25	0.29	0.41	0.43	0.45	0.21
P_2O_5 (wt%)	0.08	0.08	0.08	0.48	0.05	0.06	0.08	0.10	0.10	0.04
LOI (wt%)	0.83	2.68	2.45	3.03	1.41	1.16	1.43	0.80	1.88	0.55
Total Majors	98.65	98.75	97.95	98.99	99.69	99.86	99.85	98.69	99.71	100.12
Zn (ppm)	51.9	46.2	127.7	203.1	40.0	37.3	20.3	53.6	82.4	47.3
Cu (ppm)	31.6	4.1	37.8	23	4.8	13.4	15.2	8.7	9.9	109.3
Ni (ppm)	6.4	46.3	n.d	135.8	7.4	4.8	7.2	12.1	23.5	6.7
Cr (ppm)	n.d	n.d	n.d	200.9	n.d	n.d	n.d	n.d	n.d	n.d
V (ppm)	19.7	24.2	n.d	325.3	25.4	24.1	45.7	50.7	64.0	19.0
Ba (ppm)	626.4	1274.7	317.4	1386.3	795.7	777.4	281.8	1164.8	1062.8	1093.5
Sc (ppm)	8.5	8.2	12.8	36.7	6.7	5.8	10.2	7.1	14.5	4.4
Nb (ppm)	14.4	12.6	15.6	5.2	13.5	11.1	14.6	9.7	14.1	10.8
Zr (ppm)	254.2	258.9	275.7	37.1	253.6	247.1	256.4	167.7	255.4	190.3
Y (ppm)	31.4	28.4	40.4	24.3	28.2	24.2	33	18.8	30.5	21.8
Sr (ppm)	95.9	113.1	85.8	129.1	122.3	173.9	114.1	138.7	42.1	71.4
Rb (ppm)	71.7	130.8	91.2	171.4	130	69.7	19.2	94.2	183.2	127.7
Hf (ppm)	-	-	-	-	-	-	-	-	-	-
U(ppm)	5.8	6.1	5.1	0.8	5.8	4.7	6.6	5.5	6.4	4.9
Th (ppm)	26.9	25.6	18.8	n.d	25.3	18.5	28.7	20.6	26.4	20.0
Pb (ppm)	25.5	17	13.3	12.3	18.1	13.7	41.5	31.6	10.8	19.1
La (ppm)	76.7	68.8	59.8	17.2	60.57	49.55	59.99	42.3	62.33	44.4
Ce (ppm)	127	117.4	105.1	37.3	108.98	87.16	111.84	64.0	116.68	75.1
Pr (ppm)	-	-	-	-	11.17	8.93	11.63	-	12.22	-
Nd (ppm)	44.4	40.5	41.1	17.8	37.58	29.88	39.13	20.0	41.24	25.9
Sm (ppm)	-	-	-	-	6.45	5.12	6.93	-	6.99	-
Eu (ppm)	-	-	-	-	1.41	1.65	1.24	-	1.21	-
Gd (ppm)	-	-	-	-	5.88	4.72	6.53	-	6.36	-
Tb (ppm)	-	-	-	-	0.78	0.64	0.93	-	0.85	-
Dy (ppm)	-	-	-	-	4.43	3.74	5.45	-	4.83	-
Ho (ppm)	-	-	-	-	0.94	0.79	1.15	-	1.02	-
Er (ppm)	-	-	-	-	2.60	2.26	3.12	-	2.81	-
Tm (ppm)	-	-	-	-	0.41	0.37	0.47	-	0.45	-
Yb (ppm)	-	-	-	-	2.76	2.45	3.07	-	2.95	-
Lu (ppm)	-	-	-	-	0.41	0.37	0.45	-	0.43	-
Total Majors + Traces	98.81	98.97	98.07	99.27	99.86	100.02	99.97	98.89	99.92	100.31

Table A2.4. Dacite lapilli tuff compositions. LOI = Loss on ignition; wt% = Weight percent; ppm = Parts per million; n.d = not detected; – denotes element not analysed. Analyses with one decimal place were analysed by XRF whereas analyses with two decimal places were analysed by ICP-MS.

	C09-37	C09-38	C09-39	C10-114	C10-126	C10-130	C10-135	C10-136	C10-138
SiO_2 (wt%)	67.30	70.13	65.92	67.84	67.35	71.62	63.79	73.44	72.44
Al_2O_3 (wt%)	14.04	14.71	16.61	14.52	15.14	14.76	14.45	13.46	13.20
Fe_2O_3 (wt%)	5.89	3.77	3.67	5.21	4.00	2.88	5.77	2.42	2.53
MnO (wt%)	0.16	0.05	0.05	0.14	0.07	0.05	0.13	0.05	0.04
MgO (wt%)	1.36	1.56	1.70	1.73	1.58	1.27	2.45	0.72	0.63
CaO (wt%)	3.84	1.33	1.58	3.91	2.72	1.44	4.10	1.00	0.90
Na_2O (wt%)	3.21	5.97	4.78	1.91	4.93	2.04	2.47	4.30	3.04
K_2O (wt%)	2.79	1.00	3.98	2.40	1.66	3.82	4.44	3.05	5.00
TiO_2 (wt%)	0.40	0.41	0.35	0.42	0.77	0.25	0.60	0.22	0.21
P_2O_5 (wt%)	0.09	0.08	0.07	0.07	0.25	0.03	0.15	0.03	0.03
LOI (wt%)	1.02	0.90	0.98	1.24	1.23	1.54	0.58	0.90	0.61
Total Majors	100.09	99.91	99.69	99.38	99.69	99.70	98.93	99.58	98.63
Zn (ppm)	80.3	27.1	26.3	106.7	40.3	42	134.8	25.9	27.7
Cu (ppm)	9.7	47.6	3.7	3.2	22.2	3.5	40.6	5.8	17.3
Ni (ppm)	4.5	10.0	3.8	2.3	24.4	3.8	145	2.9	1.6
Cr (ppm)	n.d	n.d	n.d	n.d	n.d	n.d	16.7	n.d	n.d
V (ppm)	36.1	41.4	33.2	n.d	51.2	5.6	82.4	5.5	2.9
Ba (ppm)	772	188	1258.5	256.9	416.8	1100	933.8	1200.8	1135.9
Sc (ppm)	9.6	10.6	7.2	13.9	13.5	6.9	13.8	6.7	6.9
Nb (ppm)	14.8	15.9	17.6	16.1	12.8	17.0	11.7	15.2	14.8
Zr (ppm)	254.7	268.2	323.1	291	227.3	287.3	184.3	246	241.8
Y (ppm)	28.7	35.7	34.1	41.2	29.3	33.6	27.9	30.6	31
Sr (ppm)	161.3	55.6	77.3	57	145.9	92.1	99.7	92.8	78.5
Rb (ppm)	109.8	24.5	77.1	98.6	65.5	143	214.9	62	119.8
Hf (ppm)	-	-	-	7.09	6.27	7.84	-	7.39	-
U(ppm)	4.9	6.9	8.4	5.14	5.15	8.54	4.5	7.36	6.9
Th (ppm)	23.3	30.7	34.1	19.59	20.00	30.41	18.1	27.58	28.4
Pb (ppm)	13.9	16.2	13.9	19.07	15.30	30.41	63.0	41.54	19.6
La (ppm)	78.70	85.8	70.2	39.89	54.74	75.49	49.4	56.00	63.9
Ce (ppm)	135.27	142.7	119.9	82.96	102.14	141.92	83.0	106.45	105.9
Pr (ppm)	13.59	-	-	9.72	11.00	15.08	-	11.24	-
Nd (ppm)	45.28	53.1	43.6	37.01	38.79	49.61	30.4	38.54	35.5
Sm (ppm)	7.32	-	-	7.20	6.58	8.19	-	6.52	-
Eu (ppm)	1.55	-	-	1.64	1.61	1.48	-	1.18	-
Gd (ppm)	6.72	-	-	6.88	6.04	7.13	-	5.70	-
Tb (ppm)	0.90	-	-	1.06	0.86	0.95	-	0.80	-
Dy (ppm)	4.80	-	-	6.25	4.87	4.92	-	4.38	-
Ho (ppm)	1.01	-	-	1.26	0.96	0.90	-	0.84	-
Er (ppm)	2.84	-	-	3.72	2.78	2.53	-	2.44	-
Tm (ppm)	0.44	-	-	0.59	0.43	0.41	-	0.40	-
Yb (ppm)	3.04	-	-	3.69	2.65	2.57	-	2.52	-
Lu (ppm)	0.46	-	-	0.57	0.40	0.40	-	0.39	-
Total Majors + Traces	100.28	100.01	99.91	99.50	99.83	99.92	99.15	99.78	98.83

Table A2.4. Dacite lapilli tuff compositions continued

	CD10a	C10-116b	C10-131a	C10-132	C10-133b	C10-115	C10-115b	C10-116a	C10-117a	C10-130a	C10-131b	C10-133a
SiO_2 (wt%)	69.66	66.26	60.83	71.13	62.48	53.67	53.68	52.19	53.93	51.96	54.37	54.49
Al2O3 (wt%)	15.33	14.41	16.09	13.14	16.43	14.63	14.59	14.56	14.92	17.77	19.02	14.10
Fe2O3 (wt%)	2.59	5.03	5.58	4.11	5.58	9.66	9.67	10.79	9.99	10.79	7.60	10.17
MnO (wt%)	0.05	0.09	0.11	0.06	0.09	0.18	0.18	0.21	0.17	0.14	0.12	0.17
MgO (wt%)	0.98	2.35	2.47	1.27	2.44	6.10	6.10	6.45	5.90	4.62	3.16	6.21
CaO (wt%)	3.47	2.97	4.41	1.41	2.77	7.84	7.82	5.69	5.45	2.30	4.12	4.94
Na2O (wt%)	4.06	4.57	5.34	5.55	5.85	4.37	4.35	3.43	3.93	4.00	5.38	4.19
K2O (wt%)	1.43	2.15	2.10	0.68	1.78	1.04	1.04	3.64	2.65	5.03	2.79	2.52
TiO2 (wt%)	0.17	0.71	0.85	0.55	0.92	0.99	0.98	1.02	1.07	1.23	0.96	1.02
P2O5 (wt%)	0.09	0.20	0.28	0.14	0.27	0.57	0.57	0.63	0.65	0.30	0.25	0.60
LOI (wt%)	1.25	1.03	0.78	1.14	0.66	0.68	0.72	0.94	0.90	1.03	0.85	0.77
Total Majors	99.08	99.77	98.84	99.18	99.27	99.74	99.71	99.55	99.56	99.18	98.63	99.18
Zn (ppm)	34.9	66.5	106.1	29.0	59.4	120.5	120.5	158.4	124.2	132.3	70.7	127.5
Cu (ppm)	2.9	45.3	5.8	123.0	13.4	4.3	4.3	5.1	4.2	3.8	57.4	3.7
Ni (ppm)	3.8	24.5	22.0	3.1	28.2	182.6	182.6	101.2	146.5	47.8	20.0	80.9
Cr (ppm)	10.9	n.d	n.d	n.d	n.d	502.3	502.3	522.4	535.4	n.d	n.d	471.9
V (ppm)	9.0	33.6	182.8	23.6	112.5	149.3	149.3	149.2	146.8	176.6	77.3	143.7
Ba (ppm)	251.9	1417.2	1510.8	251.4	1267.6	1208.6	1208.6	1858.4	1003.8	2430.7	1044.2	1896.7
Sc (ppm)	6.8	15.9	18.8	10.5	16.5	22.9	22.9	21.0	23.0	26.0	12.9	20.8
Nb (ppm)	9.4	14.2	9.9	9.6	12.6	9.6	9.6	11.0	11.1	13.9	13.0	10.8
Zr (ppm)	267.3	288.0	173.0	159.2	209.7	267.6	267.6	302.3	312.2	226.1	204.5	267.8
Y (ppm)	29.4	32.1	23.1	24.3	28.4	19.5	19.5	22.5	27.3	30.7	28.3	26.5
Sr (ppm)	110.9	280.1	398.2	91.4	246.8	390.2	390.2	287.7	198.9	156.8	210.9	256.4
Rb (ppm)	66.9	53.4	77.1	18.4	51.3	25.3	25.3	97.7	72.5	134.2	44.7	81.1
Hf (ppm)	-	-	-	4.28	-	-	6.24	-	-	5.58	-	-
U(ppm)	7.3	-	3.2	3.79	3.2	-	3.96	-	-	3.25	3.1	3.3
Th (ppm)	31.3	-	11.8	17.15	11.9	-	17.18	-	-	13.43	10.5	14.0
Pb (ppm)	31.1	-	47.8	16.64	24.2	-	30.53	-	-	24.38	36.8	22.2
La (ppm)	78.5	54.54	47.2	30.96	41.71	97.4	85.30	90.91	104.71	53.24	45.9	91.7
Ce (ppm)	132.0	102.07	81.7	66.56	85.65	173.3	169.43	217.96	252.08	103.82	84.1	164.9
Pr (ppm)	-	10.96		7.41	9.47		18.97	18.88	22.28	11.31		
Nd (ppm)	46.5	38.31	26.7	26.25	34.73	62.7	65.24	64.41	77.84	41.34	30.8	63.6
Sm (ppm)	-	7.03	-	4.85	6.25	-	9.19	9.36	11.67	7.30	-	-
Eu (ppm)	-	1.68	-	1.21	1.77	-	2.57	2.67	3.32	1.75	-	-
Gd (ppm)	-	6.55	-	4.50	5.82	-	7.37	7.59	9.30	6.81	-	-
Tb (ppm)	-	0.97	-	0.67	0.83	-	0.81	0.84	1.03	0.94	-	-
Dy (ppm)	-	5.38	-	3.88	4.75	-	3.77	3.85	4.54	5.19	-	-
Ho (ppm)	-	1.10	-	0.77	0.93	-	0.67	0.72	0.83	0.99	-	-
Er (ppm)	-	2.99	-	2.22	2.64	-	1.72	1.83	2.09	2.79	-	-
Tm (ppm)	-	0.44	-	0.35	0.40	-	0.25	0.26	0.29	0.43	-	-
Yb (ppm)	-	2.93	-	2.19	2.45	-	1.55	1.68	1.88	2.56	-	-
Lu (ppm)	-	0.42	-	0.33	0.37	-	0.23	0.24	0.27	0.39	-	-
Total Majors + Traces	99.19	100.03	99.11	99.27	99.50	100.06	100.04	99.95	99.87	99.54	98.82	99.55

Table A2.5. Cosmos Deeps tuff breccia compositions; Left = Felsic matrix. Right = Intermediate clasts. LOI = Loss on ignition; wt% = Weight percent; ppm = Parts per million; n.d = not detected; – denotes element not analysed. Analyses with one decimal place were analysed by XRF whereas analyses with two decimal places were analysed by ICP-MS.

	C09-09	C09-10	C09-11	C10-93	C10-94	C10-95	C10-151	C10-152	C10-153a
SiO_2 (wt%)	59.98	56.14	66.04	62.94	70.16	64.20	71.28	63.80	63.82
Al_2O_3 (wt%)	12.50	13.12	12.66	12.58	13.90	12.95	14.01	12.43	12.75
Fe_2O_3 (wt%)	13.19	16.32	9.24	11.64	4.84	8.94	4.11	10.62	11.18
MnO (wt%)	0.51	0.49	0.31	0.45	0.19	0.25	0.11	0.33	0.42
MgO (wt%)	1.83	3.70	1.28	1.60	0.76	2.66	0.58	1.59	1.98
CaO (wt%)	6.48	6.00	4.71	6.38	4.36	5.85	4.53	4.69	3.84
Na_2O (wt%)	0.41	0.12	0.58	0.69	1.23	0.09	2.09	0.75	1.02
K_2O (wt%)	2.73	1.42	3.09	2.23	3.11	2.03	1.19	2.35	2.96
TiO_2 (wt%)	0.47	0.50	0.42	0.43	0.47	0.39	0.43	0.46	0.47
P_2O_5 (wt%)	0.12	0.12	0.09	0.10	0.10	0.07	0.07	0.11	0.11
LOI (wt%)	0.85	1.53	0.44	0.89	0.86	2.26	0.45	1.54	0.61
Total Majors	99.06	99.45	98.86	99.93	99.97	99.70	98.86	98.67	99.15
Zn (ppm)	105.0	151.3	97.2	104.6	88.4	181.9	85.4	110.2	109.7
Cu (ppm)	14.0	44.5	5.8	6.1	4.5	11.2	41.8	10.6	25.7
Ni (ppm)	7.4	13.4	11.4	9.0	8.4	7.5	1.6	5.4	7.7
Cr (ppm)	43.6	47.7	54.0	n.d	n.d	n.d	n.d	n.d	n.d
V (ppm)	48.5	53.9	44.9	7.7	7.5	n.d	n.d	10.4	10.1
Ba (ppm)	443.3	204.1	375.5	355.9	610.8	205.9	370.3	495.3	512.2
Sc (ppm)	6.5	9.8	13.6	11.3	11.6	15.5	15.3	11.8	11.9
Nb (ppm)	13.2	14.9	13.7	13.4	14.9	15.2	16.3	14.0	13.6
Zr (ppm)	245.3	253.5	243.3	241.7	276.9	260.4	291.2	243.6	247.8
Y (ppm)	35.6	36.5	42.2	40.3	40.9	43.3	41.9	37.6	38.3
Sr (ppm)	54.9	45.8	55.0	73.6	77.5	55.5	67.8	94.7	48.3
Rb (ppm)	88.8	60.9	105.2	64.6	110.0	84.7	73.1	89.3	174.2
Hf (ppm)	-	-	-	5.72	6.68	6.30	-	-	-
U(ppm)	5.0	5.3	4.4	4.34	5.12	4.86	5.2	4.4	4.7
Th (ppm)	18.5	20.7	16	14.40	18.21	16.27	18.6	16.1	16.5
Pb (ppm)	21.6	19.9	22.3	25.13	37.10	30.57	21.6	19.3	30.2
La (ppm)	40.26	46.97	72.6	43.50	39.74	50.88	60.2	49.6	52.5
Ce (ppm)	75.22	86.27	118.5	82.23	77.27	95.78	112	88.1	92.7
Pr (ppm)	8.30	9.47	-	9.18	8.74	10.81	-	-	-
Nd (ppm)	29.91	33.99	46.4	33.88	32.33	38.66	45.6	36.5	38.4
Sm (ppm)	6.00	6.76	-	6.43	6.35	7.31	-	-	-
Eu (ppm)	1.40	1.58	-	1.50	1.45	1.65	-	-	-
Gd (ppm)	5.94	6.43	-	6.25	6.37	7.18	-	-	-
Tb (ppm)	0.90	0.98	-	0.95	1.02	1.08	-	-	-
Dy (ppm)	5.28	5.62	-	5.74	6.44	6.51	-	-	-
Ho (ppm)	1.16	1.21	-	1.17	1.33	1.34	-	-	-
Er (ppm)	3.29	3.43	-	3.44	3.98	4.00	-	-	-
Tm (ppm)	0.50	0.52	-	0.54	0.64	0.64	-	-	-
Yb (ppm)	3.41	3.53	-	3.30	3.93	4.01	-	-	-
Lu (ppm)	0.51	0.52	-	0.50	0.60	0.63	-	-	-
Total Majors + Traces	99.19	99.57	98.99	100.05	100.13	99.82	98.99	98.80	99.30

Table A2.6. Garnet-hornblende felsic schist compositions. LOI = Loss on ignition; wt% = Weight percent; ppm = Parts per million; n.d = not detected; – denotes element not analysed. Analyses with one decimal place were analysed by XRF whereas analyses with two decimal places were analysed by ICP-MS.

	AM06b	AM07	AM09	AM16	AM17	AM25	CD18	CD25	C09-41	C09-43
SiO_2 (wt%)	56.38	54.74	51.00	54.79	57.15	58.70	60.90	56.65	54.27	51.37
Al_2O_3 (wt%)	9.21	15.76	15.91	16.34	16.94	16.05	17.41	17.48	17.80	16.64
Fe_2O_3 (wt%)	10.89	10.90	11.38	9.82	8.78	6.88	4.98	8.09	8.07	11.18
MnO (wt%)	0.26	0.17	0.18	0.11	0.10	0.15	0.04	0.10	0.07	0.24
MgO (wt%)	6.07	4.90	5.39	4.28	4.19	3.96	4.12	3.35	4.59	6.09
CaO (wt%)	14.24	3.54	9.59	7.06	4.30	8.70	3.30	2.55	4.27	5.76
Na_2O (wt%)	0.01	0.89	2.72	0.86	2.93	3.31	4.07	4.88	3.57	3.30
K_2O (wt%)	0.09	4.29	0.59	2.16	2.30	0.12	2.46	4.26	4.17	2.68
TiO_2 (wt%)	0.47	0.97	1.08	0.96	0.99	0.61	0.97	0.82	0.80	1.03
P_2O_5 (wt%)	0.11	0.21	0.21	0.27	0.28	0.09	0.05	0.18	0.22	0.34
LOI (wt%)	1.47	2.33	0.49	1.73	1.46	0.71	0.95	1.00	0.85	0.49
Total Majors	99.20	98.70	98.54	98.38	99.42	99.27	99.26	99.35	98.68	99.11
Zn (ppm)	118.3	107.0	95.9	87.1	80.3	54.1	137.8	98.4	59.2	83.1
Cu (ppm)	31.0	96.8	6.7	64.5	27.2	107.2	15.4	4.9	3.9	53.9
Ni (ppm)	140.1	105.1	154.2	68.8	52.6	92.2	1140.9	34.8	23.0	64.6
Cr (ppm)	106.2	203.5	265.0	121.4	103.9	227.6	n.d	15.2	17.5	115.0
V (ppm)	129.7	217.6	211.0	170.3	159.6	174.3	13.7	115.0	113.3	155.8
Ba (ppm)	12.2	723.9	325.4	617.2	537.3	146.8	823.3	1276.9	683.0	215.7
Sc (ppm)	15.7	30.5	30.4	24.4	23.9	27.2	12.4	17.7	17.8	23.5
Nb (ppm)	4.5	6.2	6.3	10.3	10.9	5.3	16.0	10.8	16.1	10.3
Zr (ppm)	59.9	112.4	113.0	181.0	182.9	92.0	278.8	193.2	297.4	177.0
Y (ppm)	18.6	18.3	22.7	30.3	29.8	17.1	44.8	31.7	31.4	29.3
Sr (ppm)	76.8	103.1	153.7	129.9	88.6	140.8	592.2	127.5	293.2	258.5
Rb (ppm)	1.4	196.4	14.2	90.0	74.9	0.9	59.9	139.2	186.4	15.9
Hf (ppm)	-	-	-	-	-	-	-	-	-	-
U(ppm)	1.3	1.6	1.3	2.0	1.9	1.5	4.4	3.6	5.3	2.1
Th (ppm)	6.2	6.2	6.8	6.5	7.0	6.4	19.4	13.6	23.8	6.9
Pb (ppm)	22.1	19.2	17.1	11.9	14.4	11.7	62.7	28.3	18.0	15.7
La (ppm)	27.7	24.1	29.5	32.9	32.3	19.7	64.9	41.7	73.9	29.67
Ce (ppm)	47.6	44.2	54.8	60.1	59.3	35.3	114.2	73.9	124.4	57.52
Pr (ppm)	-	-	-	-	-	-	-	-	-	6.59
Nd (ppm)	16.9	16.0	20.2	24.2	25.2	15.0	41.2	28.3	48.2	24.58
Sm (ppm)	-	-	-	-	-	-	-	-	-	5.22
Eu (ppm)	-	-	-	-	-	-	-	-	-	1.50
Gd (ppm)	-	-	-	-	-	-	-	-	-	5.28
Tb (ppm)	-	-	-	-	-	-	-	-	-	0.81
Dy (ppm)	-	-	-	-	-	-	-	-	-	4.74
Ho (ppm)	-	-	-	-	-	-	-	-	-	1.01
Er (ppm)	-	-	-	-	-	-	-	-	-	2.82
Tm (ppm)	-	-	-	-	-	-	-	-	-	0.43
Yb (ppm)	-	-	-	-	-	-	-	-	-	2.78
Lu (ppm)	-	-	-	-	-	-	-	-	-	0.40
Total Majors + Traces	99.28	98.91	98.69	98.55	99.57	99.39	99.60	99.57	98.89	99.25

Table A2.7. Andesite lavas, and associated volcaniclastic units, compositions. LOI = Loss on ignition; wt% = Weight percent; ppm = Parts per million; n.d = not detected; – denotes element not analysed. Analyses with one decimal place were analysed by XRF whereas analyses with two decimal places were analysed by ICP-MS.

	C09-44	C09-45	C09-46	C09-47	C09-48	C09-49	C09-54	C09-55	C10-118	C10-119
SiO_2 (wt%)	55.13	50.80	52.13	56.46	57.11	56.41	58.64	58.29	54.42	54.38
Al_2O_3 (wt%)	15.65	14.04	15.39	15.91	15.72	16.17	16.32	15.97	16.78	13.91
Fe_2O_3 (wt%)	9.60	10.71	10.67	9.47	8.98	9.69	7.93	7.75	11.09	11.18
MnO (wt%)	0.15	0.19	0.16	0.17	0.14	0.15	0.12	0.09	0.23	0.17
MgO (wt%)	4.81	7.03	6.67	5.11	4.61	4.18	3.96	4.33	3.65	7.97
CaO (wt%)	8.18	8.26	7.76	5.38	5.20	6.58	4.32	5.04	5.68	5.73
Na_2O (wt%)	3.75	2.63	3.07	3.50	4.61	3.51	5.02	4.56	3.61	4.24
K_2O (wt%)	0.56	2.03	2.56	2.24	1.61	1.64	2.00	2.17	2.42	0.30
TiO_2 (wt%)	0.94	1.10	0.90	1.00	0.90	1.00	0.80	0.80	0.86	1.07
P_2O_5 (wt%)	0.26	0.70	0.21	0.29	0.26	0.29	0.18	0.18	0.24	0.32
LOI (wt%)	1.06	0.91	0.71	0.68	0.63	0.56	0.72	0.70	0.56	0.48
Total Majors	100.10	98.39	100.23	100.21	99.76	100.17	100.00	99.87	99.53	99.74
Zn (ppm)	113.4	107.9	102.5	84.6	73.5	56.7	81.0	74.2	79.8	74.8
Cu (ppm)	4.7	26.5	62.2	38.4	27.4	4.4	24.7	4.3	39.1	10.2
Ni (ppm)	57.8	169.9	165.8	46.2	59.3	45.8	60.6	54.6	24.3	141.6
Cr (ppm)	70.8	618.4	281.6	49.9	98.6	48.1	26.9	18.2	n.d	229.5
V (ppm)	184.7	176.9	172.5	162.8	148.1	160.4	149.1	146.6	167.1	195.8
Ba (ppm)	821.7	1443.3	383.7	448.1	498.6	349.2	705.9	824.5	932.8	45.9
Sc (ppm)	25.2	25.9	26.0	23.3	23.0	22.5	20.1	19.1	16.2	27.6
Nb (ppm)	10.2	9.2	8.5	10.2	10.1	10.5	9.0	9.1	8.5	6.7
Zr (ppm)	177.6	287.3	88.2	177.6	176.2	180.8	144.4	166.1	140.2	122.0
Y (ppm)	29.0	24.4	27.5	28.3	27.8	29.3	26.7	25.4	20.1	22.9
Sr (ppm)	258.4	475.8	232.8	144.7	198.3	390.6	205.7	264.3	241.2	98.4
Rb (ppm)	16.0	57.5	231.6	110.2	54.3	51.9	87.6	58.2	65.7	12.7
Hf (ppm)	-	-	-	-	-	-	-	-	-	-
U(ppm)	0.6	2.6	1.3	1.3	1.9	1.7	-	2.3	-	-
Th (ppm)	2.2	13.2	6.3	6.3	7.4	6.9	-	9.4	-	-
Pb (ppm)	10.8	18.7	34.3	15.6	10.9	14.8	-	13.7	-	-
La (ppm)	28.04	108.1	27.9	28.90	31.80	29.86	29.2	30.61	38.2	24.6
Ce (ppm)	53.64	188.5	44.8	56.62	60.61	58.33	57.1	58.66	71.3	49.3
Pr (ppm)	6.20	-	-	6.55	6.86	6.76	-	6.58	-	-
Nd (ppm)	24.50	71.4	20.3	25.01	25.44	25.46	24.8	24.07	25.9	23.0
Sm (ppm)	4.88	-	-	5.37	5.34	5.40	-	4.98	-	-
Eu (ppm)	1.82	-	-	1.67	1.55	1.61	-	1.37	-	-
Gd (ppm)	4.97	-	-	5.26	5.30	5.47	-	5.02	-	-
Tb (ppm)	0.74	-	-	0.80	0.83	0.85	-	0.76	-	-
Dy (ppm)	4.44	-	-	4.78	4.91	5.13	-	4.41	-	-
Ho (ppm)	0.90	-	-	1.03	1.04	1.09	-	0.94	-	-
Er (ppm)	2.60	-	-	2.86	2.91	3.08	-	2.66	-	-
Tm (ppm)	0.41	-	-	0.42	0.45	0.47	-	0.41	-	-
Yb (ppm)	2.48	-	-	2.74	2.83	2.93	-	2.60	-	-
Lu (ppm)	0.38	-	-	0.40	0.42	0.44	-	0.39	-	-
Total Majors + Traces	100.28	98.77	100.42	100.36	99.92	100.31	100.17	100.05	99.72	99.85

Table A2.7. Andesite lavas, and associated volcaniclastic units compositions, continued.

	C10-120	C10-121	C10-124	C10-125	C10-137	C10-139	C10-140	C10-149
SiO_2 (wt%)	57.25	59.59	56.11	56.80	58.93	46.37	56.73	55.55
Al_2O_3 (wt%)	16.07	16.44	15.95	14.98	16.36	14.50	15.81	17.14
Fe_2O_3 (wt%)	8.66	6.39	9.26	8.09	6.99	14.44	9.53	12.02
MgO (wt%)	5.03	3.69	5.13	6.05	3.90	8.04	4.66	4.10
MnO (wt%)	0.15	0.11	0.17	0.14	0.14	0.39	0.11	0.20
CaO (wt%)	3.63	6.34	4.76	5.50	6.27	8.76	6.38	2.08
Na_2O (wt%)	3.52	4.22	4.22	4.46	3.65	2.17	2.40	0.76
K_2O (wt%)	2.58	1.27	2.16	1.97	1.28	2.06	1.86	4.79
TiO_2 (wt%)	1.03	0.83	0.83	0.72	0.71	1.17	0.93	0.97
P_2O_5 (wt%)	0.24	0.18	0.20	0.14	0.14	0.73	0.26	0.27
LOI (wt%)	1.52	0.59	1.02	0.82	0.75	0.86	0.60	1.70
Total Majors	99.69	99.65	99.80	99.68	99.12	99.48	99.27	99.58
Zn (ppm)	97.8	63.0	105.0	80.5	87.9	136.4	61.0	93.8
Cu (ppm)	25.1	21.0	5.8	195.7	15.6	4.0	14.6	5.9
Ni (ppm)	33.1	52.0	93.5	199.5	122.6	174.0	56.0	56.2
Cr (ppm)	0.3	16.8	80.1	125.6	169.9	613.2	93.0	106.5
V (ppm)	197.5	156.4	161.8	157.5	155.4	175.5	152.4	165.7
Ba (ppm)	1191.4	391.3	1729.5	230.0	192.9	1544.7	239.7	507.0
Sc (ppm)	24.1	21.3	23.0	26.1	24.2	26.1	23.9	28.3
Nb (ppm)	10.5	9.3	8.8	5.9	6.0	9.6	8.3	11.0
Zr (ppm)	131.4	170.9	155.0	86.5	99.6	248.5	170.3	185.1
Y (ppm)	22.6	31.1	23.8	23.6	19.6	22.6	26.6	24.2
Sr (ppm)	198.9	328.5	176.1	112.6	120.0	501.1	158.3	75.4
Rb (ppm)	74.5	38.7	119.5	102.9	57.5	65.8	50.5	166.8
Hf (ppm)	3.30	-	-	-	-	3.96	-	-
U(ppm)	2.38	-	1.7	-	1.6	1.67	1.6	1.9
Th (ppm)	8.55	-	7.6	-	5.3	6.53	5.5	7.6
Pb (ppm)	26.49	-	23.6	-	12.8	11.92	16.7	16.7
La (ppm)	37.54	31.7	27.64	17.1	16.7	93.92	25.3	28.9
Ce (ppm)	70.22	64.2	51.83	38.6	38.0	183.44	54.0	56.1
Pr (ppm)	7.71	-	5.71	-	-	20.91	-	-
Nd (ppm)	28.67	25.6	20.77	16.2	15.5	71.31	25.2	25.0
Sm (ppm)	5.15	-	4.24	-	-	10.47	-	-
Eu (ppm)	1.66	-	1.42	-	-	2.89	-	-
Gd (ppm)	4.85	-	4.17	-	-	8.29	-	-
Tb (ppm)	0.68	-	0.65	-	-	0.90	-	-
Dy (ppm)	3.88	-	3.78	-	-	4.14	-	-
Ho (ppm)	0.76	-	0.78	-	-	0.73	-	-
Er (ppm)	2.18	-	2.31	-	-	1.89	-	-
Tm (ppm)	0.33	-	0.34	-	-	0.27	-	-
Yb (ppm)	2.07	-	2.33	-	-	1.56	-	-
Lu (ppm)	0.32	-	0.33	-	-	0.23	-	-
Total Majors + Traces	99.90	99.79	100.08	99.82	99.24	99.87	99.39	99.73

Table A2.7. Andesite lava, and associated volcaniclastic units, compositions continued.

	C09-42	C09-61	C09-62	C09-63	C09-64	C10-110	C10-112	C10-113	C10-144	C10-145
SiO_2 (wt%)	58.41	55.40	58.11	56.24	59.55	59.61	52.23	59.83	52.41	54.36
Al_2O_3 (wt%)	16.78	16.62	15.37	16.15	15.34	15.47	17.11	15.57	17.33	16.22
Fe_2O_3 (wt%)	7.06	6.78	6.87	7.00	6.44	6.35	8.62	7.36	8.11	7.68
MgO (wt%)	4.35	5.41	5.40	4.75	5.32	5.19	7.00	4.70	2.00	6.31
MnO (wt%)	0.10	0.11	0.10	0.13	0.10	0.09	0.13	0.18	0.09	0.13
CaO (wt%)	9.62	6.47	5.84	8.68	5.91	7.42	6.72	4.64	16.98	7.12
Na_2O (wt%)	2.34	5.52	4.75	4.35	4.34	3.67	4.40	3.44	-0.04	3.72
K_2O (wt%)	0.21	0.35	0.54	0.35	0.33	0.52	0.46	1.38	0.02	0.78
TiO_2 (wt%)	0.61	0.61	0.61	0.60	0.59	0.59	0.77	0.76	0.62	0.80
P_2O_5 (wt%)	0.11	0.12	0.11	0.11	0.11	0.10	0.10	0.14	0.10	0.13
LOI (wt%)	0.64	1.86	1.75	0.86	1.21	0.65	2.21	1.98	2.20	1.54
Total Majors	100.24	99.24	99.45	99.22	99.25	99.65	99.77	99.99	99.80	98.79
Zn (ppm)	58.6	88.6	65.6	56.8	54.6	64.9	79.6	56.9	927.8	74.1
Cu (ppm)	41.8	24.1	73.8	42.7	69.8	49.0	13.0	34.0	185.5	52.4
Ni (ppm)	112.1	100.5	97.0	98.6	103.1	109.3	159.4	81.4	185.4	171.9
Cr (ppm)	249.9	234.4	210.7	226.1	242.8	247.3	360.3	118.6	231.4	335.0
V (ppm)	139.2	144.9	134.6	151.4	140.4	144.2	150.3	151.5	135.2	156.9
Ba (ppm)	48.9	56.4	180.9	68.1	208.8	334.4	101.5	451.6	5.9	222.7
Sc (ppm)	28.3	27.9	28.1	28.1	27.6	28.0	34.7	23.7	20.2	35.2
Nb (ppm)	4.9	5.1	5.2	5.6	5.1	4.9	6.5	8.1	5.2	6.5
Zr (ppm)	92.5	91.6	91.4	89.1	90.3	87.3	117.2	149.2	92.2	123.9
Y (ppm)	17.1	16.6	16.3	15.9	16.3	15.2	19.7	21.5	14.4	22.5
Sr (ppm)	184.3	140.4	159.5	168.6	182.0	142.5	145.3	221.0	375.6	146.4
Rb (ppm)	6.6	19.0	16.7	11.6	12.9	15.2	18.3	149.0	0.1	32.5
Hf (ppm)	2.39	-	-	-	-	-	-	-	-	-
U(ppm)	1.71	1.5	-	1.8	1.6	-	-	-	1.2	2.1
Th (ppm)	6.59	6.5	-	6.6	6.5	-	-	-	3.5	8.5
Pb (ppm)	12.86	11.2	-	9.8	11.4	-	-	-	174.3	13.7
La (ppm)	19.31	17.22	17.7	18.53	18.08	16.0	20.39	27.68	14.9	24.2
Ce (ppm)	36.71	34.01	32.6	35.13	34.97	33.7	39.60	52.36	32.4	48.3
Pr (ppm)	4.08	3.82	-	3.89	3.88	-	4.45	5.77	-	-
Nd (ppm)	15.23	13.94	16.2	14.18	14.17	12.8	16.37	20.79	14.0	22.3
Sm (ppm)	3.01	2.97	-	2.97	2.93	-	3.39	4.18	-	-
Eu (ppm)	0.82	0.67	-	0.84	0.79	-	0.71	0.96	-	-
Gd (ppm)	2.98	2.87	-	2.91	2.94	-	3.45	4.07	-	-
Tb (ppm)	0.45	0.46	-	0.45	0.46	-	0.53	0.60	-	-
Dy (ppm)	2.73	2.78	-	2.65	2.76	-	2.97	3.34	-	-
Ho (ppm)	0.55	0.58	-	0.56	0.58	-	0.66	0.70	-	-
Er (ppm)	1.62	1.63	-	1.55	1.64	-	1.85	1.96	-	-
Tm (ppm)	0.25	0.25	-	0.23	0.23	-	0.28	0.29	-	-
Yb (ppm)	1.55	1.64	-	1.52	1.64	-	1.88	1.95	-	-
Lu (ppm)	0.23	0.24	-	0.22	0.22	-	0.28	0.29	-	-
Total Majors + Traces	100.35	99.35	99.56	99.33	99.37	99.78	99.90	100.15	100.04	98.94

Table A2.8. Intermediate crystal tuff compositions. LOI = Loss on ignition; wt% = Weight percent; ppm = Parts per million; n.d = not detected; – denotes element not analysed. Analyses with one decimal place were analysed by XRF whereas analyses with two decimal places were analysed by ICP-MS.

	C09-23	CO9-79	C12-181	C12-182	C12-184	C12-185	AM18	AM23	C09-58	C09-59	C10-155
SiO_2 (wt%)	72.13	70.33	72.64	72.66	71.03	71.89	70.91	71.61	70.60	70.82	71.42
Al2O3 (wt%)	15.12	15.44	15.14	14.86	15.45	15.21	15.03	15.20	14.75	14.90	15.03
Fe2O3 (wt%)	1.81	1.84	1.52	1.45	1.97	1.79	1.54	1.49	1.29	1.52	1.48
MnO (wt%)	0.03	0.02	0.02	0.02	0.05	0.03	0.02	0.02	0.02	0.01	0.02
MgO (wt%)	1.58	0.63	0.29	0.34	0.49	0.54	0.53	0.64	0.67	0.56	0.63
CaO (wt%)	1.32	2.00	1.82	1.78	1.97	1.73	1.68	1.10	1.26	1.61	1.07
Na2O (wt%)	4.27	4.33	4.63	5.00	4.54	4.04	5.36	7.18	5.45	5.30	5.38
K2O (wt%)	2.31	2.94	3.25	2.71	3.58	3.56	2.86	0.88	3.13	3.04	3.02
TiO2 (wt%)	0.20	0.22	0.20	0.19	0.21	0.21	0.28	0.28	0.27	0.27	0.28
P2O5 (wt%)	0.06	0.07	0.05	0.04	0.05	0.06	0.08	0.09	0.08	0.08	0.07
LOI (wt%)	1.36	1.05	1.12	0.89	0.58	1.06	0.51	0.60	0.85	0.51	0.65
Total Majors	100.18	98.87	100.68	99.95	99.92	100.12	98.79	99.08	98.37	98.62	99.06
Zn (ppm)	16.9	35.3	34.9	30.2	36.6	37.9	49.7	31.0	215.0	52.9	47.4
Cu (ppm)	6.0	3.3	1.4	5.3	2.2	4.6	7.2	8.5	12.5	14.4	9.1
Ni (ppm)	4.4	2.7	8.0	6.2	9.1	7.9	n.d	n.d	1.8	0.2	0.1
Cr (ppm)	57.8	n.d	8.5	8.7	8.7	8.7	n.d	n.d	n.d	n.d	n.d
V (ppm)	32.7	10.5	15.4	14.1	14.3	19.5	14.7	14.0	26.9	28.0	20.0
Ba (ppm)	820.0	1468.8	1360.7	1427.7	1259.6	1150.9	812.8	1193.0	774.5	899.0	863.7
Sc (ppm)	n.d	1.2	1.9	1.8	1.7	1.9	0.3	1.6	1.9	0.5	2.5
Nb (ppm)	3.2	3.7	3.5	3.3	3.5	3.6	2.0	1.8	2.0	1.5	1.9
Zr (ppm)	122.5	132.5	123.6	107.6	126.0	124.9	129.3	133.0	130.1	128.9	133.9
Y (ppm)	4.5	5.3	5.1	5.0	5.0	4.9	3.1	3.3	3.3	3.1	3.2
Sr (ppm)	348.2	449.2	490.8	397.8	476.3	446.6	427.4	548.7	333.5	511.6	351.1
Rb (ppm)	68.8	66.1	67.9	65.8	68.9	108.0	73.7	23.2	86.3	74.4	99.4
Hf (ppm)	-	-	-	-	-	-	-	3.01	-	-	3.30
U(ppm)	2.8	2.9	2.9	3.1	3.2	3.1	4.8	4.9	-	4.5	4.7
Th (ppm)	12.9	15.2	13.3	10.4	14.2	13.2	14.4	14.1	-	13.8	14.2
Pb (ppm)	23.0	29.3	26.9	18.9	29.3	28.4	29.6	37.71	-	28.7	37.17
La (ppm)	30.52	40.09	40	29.2	44.7	33.8	31.2	21.23	25.8	26.38	25.86
Ce (ppm)	54.32	70.24	59.8	46.3	69.3	54.7	50.7	39.16	43.3	45.96	47.28
Pr (ppm)	5.46	7.03	-	-	-	-	-	3.99	-	4.70	4.82
Nd (ppm)	16.85	21.85	17.9	12.2	20.8	15	13.9	13.48	15.7	15.28	16.34
Sm (ppm)	2.38	3.12	-	-	-	-	-	2.04	-	2.38	2.57
Eu (ppm)	0.64	0.81	-	-	-	-	-	0.66	-	0.69	0.75
Gd (ppm)	1.86	2.42	-	-	-	-	-	1.54	-	1.77	1.83
Tb (ppm)	0.19	0.25	-	-	-	-	-	0.15	-	0.18	0.19
Dy (ppm)	0.86	1.07	-	-	-	-	-	0.58	-	0.70	0.77
Ho (ppm)	0.14	0.18	-	-	-	-	-	0.09	-	0.11	0.12
Er (ppm)	0.42	0.47	-	-	-	-	-	0.23	-	0.28	0.28
Tm (ppm)	0.05	0.06	-	-	-	-	-	0.03	-	0.03	0.04
Yb (ppm)	0.40	0.47	-	-	-	-	-	0.19	-	0.24	0.29
Lu (ppm)	0.05	0.06	-	-	-	-	-	0.02	-	0.02	0.04
Total Majors + Traces	100.34	99.11	100.91	100.17	100.14	100.33	98.96	99.29	98.54	98.81	99.22

Table A2.9. Felsic porphyry intrusion compositions; Left = Footwall intrusive porphyry. Right = Hangingwall intrusive porphyry. LOI = Loss on ignition; wt% = Weight percent; ppm = Parts per million; n.d = not detected; – denotes element not analysed. Analyses with one decimal place were analysed by XRF whereas analyses with two decimal places were analysed by ICP-MS.

	C10-111	C10-122	C10-127	C10-128	C10-129	C10-147	CD03	CD04	C09-66	C10-148	C10-148b	C09-60
SiO_2 (wt%)	49.28	49.03	49.15	48.59	50.68	51.39	45.69	48.18	46.14	47.47	46.86	51.85
Al_2O_3 (wt%)	15.60	15.80	16.61	16.10	16.77	14.80	15.39	15.32	15.77	15.56	15.37	4.70
Fe_2O_3 (wt%)	10.89	11.12	10.92	10.09	10.00	12.19	15.17	13.73	14.92	14.93	14.74	10.64
MnO (wt%)	0.17	0.14	0.15	0.15	0.15	0.19	0.20	0.24	0.16	0.18	0.18	0.28
MgO (wt%)	9.93	8.67	8.04	10.52	6.84	7.00	7.65	7.30	6.81	7.00	6.90	17.32
CaO (wt%)	7.59	9.63	11.04	9.28	7.96	8.73	9.30	7.46	9.54	9.00	8.88	10.29
Na_2O (wt%)	2.12	1.67	1.64	2.20	3.44	3.25	2.24	2.64	2.49	2.49	2.45	0.19
K_2O (wt%)	1.16	1.40	0.21	0.38	0.58	0.18	0.82	1.41	0.48	0.42	0.42	0.89
TiO_2 (wt%)	0.78	0.65	0.69	0.67	0.72	0.93	1.51	1.42	1.70	1.56	1.54	0.31
P_2O_5 (wt%)	0.06	0.04	0.06	0.05	0.08	0.09	0.35	0.32	0.44	0.37	0.36	0.04
LOI (wt%)	2.27	1.60	0.85	2.01	1.42	0.67	0.72	1.27	0.58	0.47	0.46	2.50
Total Majors	99.85	99.75	99.36	100.04	98.63	99.41	99.04	99.28	99.03	99.46	98.16	99.00
Zn (ppm)	84.6	102.1	79.7	72.8	73.1	96.0	139.2	101.1	134.8	115.2	115.2	166.0
Cu (ppm)	13.4	95.5	80.6	52.7	101.8	105.8	11.1	99.1	61.0	74.3	74.3	3.6
Ni (ppm)	165.2	166.4	169.9	367.3	85.0	58.9	163.5	149.1	133.3	135.9	135.9	1093.3
Cr (ppm)	291.4	292.0	312.3	426.6	352.7	194.5	241.9	236.1	195.3	206.8	206.8	1631.4
V (ppm)	229.8	218.8	230.7	183.2	196.1	283.7	280.3	259.7	276.7	265.0	265.0	90.1
Ba (ppm)	372.1	239.0	63.2	113.7	144.2	113.1	635.8	927.3	181.6	232.4	232.4	1001.6
Sc (ppm)	39.3	36.1	35.8	28.9	38.5	47.1	30.4	29.2	38.0	33.4	33.4	20.3
Nb (ppm)	2.4	2.3	2.5	2.2	2.9	3.2	3.2	4.5	3.9	3.9	3.9	3.6
Zr (ppm)	48.4	44.9	49.7	41.0	58.6	66.5	42.3	42.9	43.8	51.0	51.0	39.7
Y (ppm)	15.1	13.0	14.7	11.8	16.8	19.5	19.3	21.7	22.4	22.5	22.5	9.7
Sr (ppm)	107.9	71.1	171.9	146.3	217.0	163.6	224.2	280.0	436.2	341.3	341.3	17.0
Rb (ppm)	66.1	40.7	4.7	13.3	31.3	2.9	29.6	76.7	18.2	25.7	25.7	19.0
Hf (ppm)	1.44	1.45	-	-	-	1.69	-	1.03	-	1.27	-	-
U(ppm)	0.38	0.37	-	0.3	-	0.3	0.5	0.7	-	0.4	0.9	-
Th (ppm)	1.48	1.47	-	0.5	-	2.2	0.9	2.2	-	1.68	0.4	-
Pb (ppm)	8.055	8.11	-	5.1	-	5.97	8.9	15.91	-	5.97	4.8	-
La (ppm)	5.19	5.47	7	5.19	4.8	8.25	17.2	20.52	23.99	22.49	20.2	4.1
Ce (ppm)	12.07	11.63	22	11.27	13.8	18.73	32.5	41.93	50.69	48.11	48.5	6.0
Pr (ppm)	1.58	1.47	-	1.44	-	2.34	-	4.93	6.21	5.84	-	-
Nd (ppm)	6.93	6.27	8.3	5.76	7.6	9.94	15.6	19.55	24.63	23.44	23.2	3.1
Sm (ppm)	1.79	1.58	-	1.53	-	2.48	-	3.90	4.79	4.51	-	-
Eu (ppm)	0.91	0.70	-	0.59	-	0.83	-	1.44	1.75	1.58	-	-
Gd (ppm)	2.04	1.78	-	1.80	-	2.69	-	3.96	4.69	4.37	-	-
Tb (ppm)	0.37	0.32	-	0.32	-	0.48	-	0.59	0.69	0.66	-	-
Dy (ppm)	2.41	2.15	-	1.96	-	3.09	-	3.56	3.95	3.87	-	-
Ho (ppm)	0.51	0.46	-	0.43	-	0.65	-	0.71	0.81	0.77	-	-
Er (ppm)	1.51	1.41	-	1.24	-	1.94	-	2.07	2.19	2.17	-	-
Tm (ppm)	0.24	0.23	-	0.19	-	0.31	-	0.32	0.31	0.33	-	-
Yb (ppm)	1.53	1.44	-	1.23	-	1.92	-	1.89	2.05	2.02	-	-
Lu (ppm)	0.23	0.22	-	0.18	-	0.29	-	0.28	0.27	0.30	-	-
Total Majors + Traces	100.00	99.88	99.48	100.19	98.76	99.53	99.23	99.52	99.20	99.62	98.32	99.42

Table A2.10. Mafic intrusions' compositions; Left = Alec Mairs diorite; Middle = Cosmos Deeps dolerite; Right = other small mafic intrusion LOI = Loss on ignition; wt% = Weight percent; ppm = Parts per million; n.d = not detected; – denotes element not analysed. Analyses with one decimal place were analysed by XRF whereas analyses with two decimal places were analysed by ICP-MS..

	C09-74	C09-75	C09-76	C09-77a	C09-77b	C09-78	C09-81	C09-83	C12-157	C12-165	C12-170	C12-177
SiO_2 (wt%)	75.56	74.19	65.10	65.31	80.95	71.14	73.13	59.64	70.67	67.40	72.51	69.55
Al2O3 (wt%)	12.08	13.33	12.12	12.25	10.06	12.29	13.59	18.28	13.23	15.77	12.51	12.71
Fe2O3 (wt%)	1.97	1.59	10.78	11.06	0.86	4.42	2.82	3.98	2.77	2.88	2.43	3.81
MnO (wt%)	0.02	0.03	0.28	0.54	0.09	0.07	0.03	0.05	0.04	0.05	0.04	0.05
MgO (wt%)	1.96	1.66	3.51	3.15	0.19	1.44	2.53	2.82	2.75	0.94	2.54	3.82
CaO (wt%)	0.63	0.70	1.74	1.77	1.51	0.60	0.29	4.03	1.07	3.01	1.79	1.35
Na2O (wt%)	4.61	5.71	1.63	1.73	4.07	2.45	1.59	6.00	3.06	4.46	3.71	2.85
K2O (wt%)	0.88	1.01	2.93	2.81	0.19	5.14	3.04	1.85	4.69	2.87	2.10	3.81
TiO2 (wt%)	0.12	0.20	0.21	0.18	0.11	0.32	0.31	0.65	0.23	0.30	0.21	0.31
P2O5 (wt%)	0.03	0.03	0.03	0.03	0.02	0.08	0.04	0.09	0.04	0.06	0.04	0.05
LOI (wt%)	1.10	0.56	0.87	0.59	0.41	0.71	2.17	0.99	0.64	0.77	1.46	0.92
Total Majors	98.96	99.01	99.19	99.41	98.46	98.65	99.55	98.38	99.19	98.50	99.33	99.23
Zn (ppm)	12.0	10.6	50.6	74.1	n.d	26.1	16.1	25.2	38.1	41.4	28.5	46.8
Cu (ppm)	69.6	5.2	26.7	21.0	11.2	10.4	183.9	2.3	1.8	18.7	5.8	17.6
Ni (ppm)	20.0	3.4	12.2	4.3	n.d	10.4	14.0	118.2	134.1	14.3	116.4	180.6
Cr (ppm)	n.d	n.d	n.d	n.d	n.d	n.d	n.d	n.d	490.7	28.7	273.2	713.6
V (ppm)	n.d	6.5	11.8	6.5	n.d	8.3	33.6	45.1	43.6	48.3	46.1	62.3
Ba (ppm)	172.1	324.0	375.1	454.3	311.3	1111.5	515.3	356.8	1395.5	1062.1	1012.8	1249.2
Sc (ppm)	4.4	6.9	5.9	5.2	1.9	8.8	11.2	7.8	8.6	6.6	8.1	11.0
Nb (ppm)	15.4	18.2	16.8	13.9	13.1	15.6	15.9	17.7	2.6	2.8	2.3	3.3
Zr (ppm)	234.2	252.0	224.6	234.7	204.8	251.7	252.2	677.4	76.1	109.2	66.9	82.8
Y (ppm)	17.7	34.2	36.5	37.1	19.8	34.4	32.4	56.7	6.6	6.8	5.5	7.7
Sr (ppm)	113.2	112.9	103.0	90.1	212.5	76.9	39.8	659.7	305.1	468.4	405.8	234.0
Rb (ppm)	28.8	23.2	68.6	76.1	4.0	56.9	82.1	262.5	131.4	76.3	66.8	108.4
Hf (ppm)	-	-	-	-	-	-	-	-	-	-	-	-
U(ppm)	-	-	-	-	-	-	-	-	2.6	1.8	1.8	2.6
Th (ppm)	-	-	-	-	-	-	-	-	8.4	6.7	5.1	12.7
Pb (ppm)	-	-	-	-	-	-	-	-	26.7	23.2	17.6	20.2
La (ppm)	82.68	68.83	72.3	55.59	49.6	57.9	62.64	71.09	24.6	28.40	16.3	31.99
Ce (ppm)	139.35	121.52	126.5	101.84	93.9	100.0	111.97	121.20	44.3	52.95	32.3	57.74
Pr (ppm)	13.51	12.41	-	10.73	-	-	11.69	11.96		5.55		5.93
Nd (ppm)	43.39	40.51	44.5	36.32	34.8	35.0	39.41	37.90	11.7	19.18	8.0	20.13
Sm (ppm)	6.01	6.89	-	6.67	-	-	7.20	6.42	-	2.96	-	3.02
Eu (ppm)	1.07	1.03	-	1.01	-	-	1.09	0.76	-	0.85	-	0.86
Gd (ppm)	5.03	6.10	-	6.54	-	-	6.88	6.02	-	2.24	-	2.38
Tb (ppm)	0.48	0.77	-	0.98	-	-	0.92	0.79	-	0.26	-	0.28
Dy (ppm)	1.93	4.07	-	5.93	-	-	5.20	4.25	-	1.31	-	1.35
Ho (ppm)	0.37	0.81	-	1.27	-	-	1.09	0.88	-	0.24	-	0.24
Er (ppm)	0.94	2.32	-	3.63	-	-	2.95	2.41	-	0.66	-	0.63
Tm (ppm)	0.18	0.37	-	0.57	-	-	0.47	0.38	-	0.11	-	0.10
Yb (ppm)	1.10	2.64	-	3.88	-	-	3.18	2.69	-	0.66	-	0.63
Lu (ppm)	0.21	0.40	-	0.55	-	-	0.45	0.39	-	0.10	-	0.10
Total Majors + Traces	99.05	99.12	99.31	99.54	98.55	98.83	99.69	98.63	99.46	98.70	99.54	99.52

Table A2.11. Hangingwall felsic sediments; Left = Southern felsic sediments; Right, = Northern Felsic sediments. LOI = Loss on ignition; wt% = Weight percent; ppm = Parts per million; n.d = not detected; – denotes element not analysed. Analyses with one decimal place were analysed by XRF whereas analyses with two decimal places were analysed by ICP-MS.

	CO9-73	CO9-80	C12-159	C12-164	C12-166	C12-171	C12-173	C12-172	C12-175	C12-176	C12-180
SiO_2 (wt%)	49.01	59.80	58.11	62.45	59.53	62.32	61.09	65.58	68.45	72.18	71.28
Al2O3 (wt%)	18.20	15.67	14.72	14.88	15.08	14.81	15.20	13.32	12.25	11.76	11.88
Fe2O3 (wt%)	13.04	8.28	6.69	6.14	7.41	6.81	6.74	5.06	3.97	3.31	3.49
MnO (wt%)	0.17	0.09	0.10	0.08	0.11	0.08	0.09	0.07	0.07	0.05	0.07
MgO (wt%)	5.39	5.15	3.99	3.56	3.92	3.67	3.83	4.15	4.15	3.22	3.70
CaO (wt%)	6.49	7.90	6.53	4.20	5.15	4.13	4.31	2.70	2.94	2.50	2.77
Na2O (wt%)	3.50	3.40	3.27	3.69	3.53	3.02	3.53	3.10	2.91	3.34	3.32
K2O (wt%)	2.62	1.11	2.40	2.18	2.33	2.48	2.66	2.59	2.48	1.79	1.70
TiO2 (wt%)	0.98	0.81	0.88	0.71	0.74	0.71	0.75	0.52	0.31	0.28	0.27
P2O5 (wt%)	0.21	0.20	0.52	0.28	0.34	0.27	0.29	0.16	0.05	0.06	0.04
LOI (wt%)	1.00	0.59	0.99	1.13	1.29	1.00	1.00	0.96	1.51	0.97	0.72
Total Majors	100.61	103.00	98.19	99.30	99.43	99.30	99.49	98.20	99.08	99.46	99.24
Zn (ppm)	80.5	27.4	93.9	80.8	97.9	86.4	90.7	66.7	45.4	35.9	34.3
Cu (ppm)	7.0	3.7	28.8	39.5	40.9	36.3	24.7	13.8	23.5	10.4	27.9
Ni (ppm)	81.5	64.9	106.1	99.0	121.1	104.3	109.8	125.1	197.0	140.4	161.1
Cr (ppm)	93.0	83.3	188.3	178.1	219.2	212.4	193.7	274.1	720.9	330.6	496.7
V (ppm)	146.1	129.9	125.8	116.3	126.2	116.4	122.2	97.5	76.0	64.2	63.0
Ba (ppm)	834.0	224.5	1094.0	985.3	1121.2	989.3	1055.5	864.4	747.9	699.2	759.4
Sc (ppm)	21.5	18.5	15.5	15.5	16.5	17.5	17.1	14.9	12.0	10.3	9.7
Nb (ppm)	9.7	8.4	8.0	5.6	6.3	5.6	5.4	4.1	2.8	2.5	2.6
Zr (ppm)	186.5	149.1	196.4	172.3	182.3	167.2	168.2	119.5	72.1	68.6	67.1
Y (ppm)	21.4	25.6	22.6	17.6	20.7	17.7	19.1	12.8	8.3	7.7	8.9
Sr (ppm)	242.0	233.8	836.2	719.6	727.6	666.5	655.7	340.1	321.7	295.9	336.9
Rb (ppm)	77.1	33.3	69.9	65.5	69.8	112.1	84.1	85.1	68.9	46.9	53.6
Hf (ppm)	-	-	-	-	-	-	-	-	-	-	-
U(ppm)	-	-	3.7	2.8	2.7	2.8	2.4	2.1	3.8	1.3	1.6
Th (ppm)	-	-	15.6	12.7	14.2	11.3	11.8	8.4	7.5	5.1	5.0
Pb (ppm)	-	-	23.1	20.6	20.5	19.3	19.2	18.0	20.2	16.1	18.6
La (ppm)	14.4	26.7	77.46	54.03	71.1	56.6	52.93	41.5	23.2	17.6	16.3
Ce (ppm)	25.1	50.0	164.87	110.54	137.3	105.2	109.18	75.9	40.6	34.3	34.0
Pr (ppm)			20.49	13.33			12.88				
Nd (ppm)	12.3	21.7	77.07	49.03	59.5	47.1	48.87	32.0	13.7	11.8	10.2
Sm (ppm)	-	-	12.74	8.15	-	-	8.17	-	-	-	-
Eu (ppm)	-	-	3.01	1.99	-	-	2.01	-	-	-	-
Gd (ppm)	-	-	9.34	6.15	-	-	6.27	-	-	-	-
Tb (ppm)	-	-	1.02	0.71	-	-	0.75	-	-	-	-
Dy (ppm)	-	-	4.52	3.38	-	-	3.63	-	-	-	-
Ho (ppm)	-	-	0.75	0.59	-	-	0.64	-	-	-	-
Er (ppm)	-	-	1.91	1.57	-	-	1.70	-	-	-	-
Tm (ppm)	-	-	0.27	0.23	-	-	0.26	-	-	-	-
Yb (ppm)	-	-	1.61	1.40	-	-	1.54	-	-	-	-
Lu (ppm)	-	-	0.23	0.21	-	-	0.22	-	-	-	-
Total Majors + Traces	100.79	103.11	98.51	99.58	99.74	99.57	99.77	98.42	99.32	99.64	99.45

Table A2.11. Hangingwall sediments continued; Intermediate Sediments North

	C12-187B	C12-169	C09-82	C12-183	C12-187A	C12-188A
SiO_2 (wt%)	53.43	56.19	51.03	74.87	74.12	75.45
Al_2O_3 (wt%)	14.25	11.07	15.52	12.23	13.77	12.24
Fe_2O_3 (wt%)	12.80	9.26	13.50	2.17	1.93	2.32
MnO (wt%)	0.22	0.18	0.19	0.05	0.04	0.06
MgO (wt%)	5.66	9.53	5.30	1.21	0.74	1.11
CaO (wt%)	9.14	9.24	8.14	5.12	5.54	4.32
Na_2O (wt%)	2.63	1.66	2.58	2.98	3.05	3.33
K_2O (wt%)	0.70	0.69	0.70	0.41	0.21	0.24
TiO_2 (wt%)	1.09	0.50	1.77	0.30	0.24	0.33
P_2O_5 (wt%)	0.11	0.08	0.58	0.09	0.06	0.10
LOI (wt%)	0.57	1.33	0.31	0.64	0.38	0.35
Total Majors	100.60	99.72	99.62	100.07	100.08	99.85
Zn (ppm)	122.6	109.2	107.4	13.7	11.9	22.6
Cu (ppm)	81.2	61.3	61.6	15.2	10.8	10.0
Ni (ppm)	113.9	484.5	93.1	24.9	7.7	28.2
Cr (ppm)	195.3	1094.2	136.1	42.9	9.2	48.4
V (ppm)	310.4	156.1	217.2	40.4	34.4	39.4
Ba (ppm)	309.3	212.7	229.7	150.0	134.0	135.4
Sc (ppm)	46.7	26.8	31.1	2.3	2.5	4.9
Nb (ppm)	3.8	2.6	9.7	4.9	4.6	5.0
Zr (ppm)	77.9	68.0	169.9	134.9	116.7	143.9
Y (ppm)	25.5	13.2	33.1	8.3	7.1	8.8
Sr (ppm)	224.3	166.2	319.6	335.1	282.0	341.3
Rb (ppm)	29.9	51.4	18.7	31.6	12.2	17.3
Hf (ppm)	-	-	-	-	-	-
U(ppm)	0.6	1.2	-	4.1	4.1	4.1
Th (ppm)	0.8	4.6	-	0.0	12.9	18.3
Pb (ppm)	8.4	11.9	-	0.0	11.5	14.1
La (ppm)	4.1	12.5	29.91	46.3	22.9	47.3
Ce (ppm)	15.6	29.4	60.09	78.7	33.4	85.8
Pr (ppm)			7.25			
Nd (ppm)	7.9	12.4	28.30	28.0	14.4	31.6
Sm (ppm)	-	-	6.21	-	-	-
Eu (ppm)	-	-	2.08	-	-	-
Gd (ppm)	-	-	6.42	-	-	-
Tb (ppm)	-	-	0.97	-	-	-
Dy (ppm)	-	-	5.67	-	-	-
Ho (ppm)	-	-	1.21	-	-	-
Er (ppm)	-	-	3.22	-	-	-
Tm (ppm)	-	-	0.47	-	-	-
Yb (ppm)	-	-	3.03	-	-	-
Lu (ppm)	-	-	0.43	-	-	-
Total Majors + Traces	100.76	99.97	99.78	100.17	100.16	99.95

Table A2.11. Hangingwall sediments continued; Left =Mafic sediments; Right = Granite conglomerate clasts.

	C09-19	AMD344D	AMD344E	AMD344F	AMD344G	AMD344H	AMD344I
SiO_2 (wt%)	68.83	63.94	57.39	52.55	55.62	36.67	35.50
Al_2O_3 (wt%)	15.81	15.50	18.96	21.31	19.45	24.89	22.90
Fe_2O_3 (wt%)	4.89	4.33	4.18	4.85	4.18	8.50	9.38
MnO (wt%)	0.05	0.06	0.05	0.07	0.05	0.13	0.13
MgO (wt%)	2.67	3.16	5.23	3.08	3.06	6.63	6.75
CaO (wt%)	0.22	3.72	5.40	9.03	4.14	17.63	17.93
Na_2O (wt%)	0.24	5.90	3.73	1.43	2.12	n.d	n.d
K_2O (wt%)	4.09	1.58	2.99	4.78	8.51	0.60	2.00
TiO_2 (wt%)	0.48	0.48	0.60	0.63	0.60	1.10	0.66
P_2O_5 (wt%)	0.11	0.22	0.28	0.25	0.27	0.25	1.88
LOI (wt%)	0.94	0.46	1.05	1.97	1.46	3.69	3.13
Total Majors	98.34	99.34	99.87	99.95	99.48	99.61	99.96
Zn (ppm)	33.5	43.3	112.8	72.7	50.3	87.4	80.4
Cu (ppm)	9.5	8.1	6.2	11.2	6.6	4.5	4.9
Ni (ppm)	40.6	33.1	43.6	53.9	47.9	94.6	136.1
Cr (ppm)	80.7	41.0	56.7	69.1	61.1	112.1	63.6
V (ppm)	100.3	73.8	72.2	96.1	62.8	166.8	149.7
Ba (ppm)	399.1	416.7	1960.7	4306.6	6430.0	268.9	1075.7
Sc (ppm)	14.8	8.8	12.2	11.8	9.5	20.5	14.9
Nb (ppm)	6.7	5.5	6.6	7.5	6.7	11.6	5.4
Zr (ppm)	176.3	140.3	181.6	188.3	175.0	317.8	245.6
Y (ppm)	14.8	12.4	15.0	15.3	14.8	26.0	18.1
Sr (ppm)	208.1	232.1	530.4	848.1	949.5	2405.5	2446.8
Rb (ppm)	194.8	82.9	217.5	263.2	423.1	49.2	198.6
Hf (ppm)	-	-	-	-	-	-	-
U(ppm)	3.5	2.8	5.2	5.4	4.2	5.5	6.0
Th (ppm)	16.2	13.7	15.6	15.8	16.1	35.9	20.9
Pb (ppm)	31.9	20.6	65.2	74.4	47.8	60.8	59.4
La (ppm)	51.5	49.0	57.3	60.2	53.7	121.9	73.1
Ce (ppm)	97.0	88.7	101.7	92.9	72.8	218.4	128.0
Pr (ppm)	-	-	-	-	-	-	-
Nd (ppm)	40.1	35.3	38.1	29.2	18.3	87.6	48.3
Sm (ppm)	-	-	-	-	-	-	-
Eu (ppm)	-	-	-	-	-	-	-
Gd (ppm)	-	-	-	-	-	-	-
Tb (ppm)	-	-	-	-	-	-	-
Dy (ppm)	-	-	-	-	-	-	-
Ho (ppm)	-	-	-	-	-	-	-
Er (ppm)	-	-	-	-	-	-	-
Tm (ppm)	-	-	-	-	-	-	-
Yb (ppm)	-	-	-	-	-	-	-
Lu (ppm)	-	-	-	-	-	-	-
Total Majors + Traces	98.50	99.47	100.22	100.58	100.32	100.02	100.44

Table A.2.12. Volcanic units along the AM5 "reactivation" contact. LOI = Loss on ignition; wt% = Weight percent; ppm = Parts per million; n.d = not detected; – denotes element not analysed. Analyses with one decimal place were analysed by XRF whereas analyses with two decimal places were analysed by ICP-MS.

	CD08b	C12-158	C12-160A	C12-161	C12-162	C12-178	C12-179
SiO_2 (wt%)	66.58	72.74	76.35	76.56	73.21	72.62	75.71
Al_2O_3 (wt%)	16.54	15.17	14.14	13.96	14.29	14.41	14.30
Fe_2O_3 (wt%)	0.15	0.24	0.81	0.63	1.14	0.71	0.57
MnO (wt%)	0.01	0.06	0.06	0.08	0.63	0.11	0.12
MgO (wt%)	0.07	-0.03	0.02	0.00	-0.01	0.00	0.00
CaO (wt%)	0.35	0.02	0.07	0.33	0.10	0.33	0.27
Na_2O (wt%)	3.87	3.24	3.93	5.43	7.09	4.90	5.40
K_2O (wt%)	8.71	7.41	3.37	2.33	0.55	4.35	2.54
TiO_2 (wt%)	0.01	0.01	0.02	0.02	0.01	0.01	0.02
P_2O_5 (wt%)	0.07	0.01	0.01	0.01	0.01	0.02	0.01
LOI (wt%)	0.77	0.38	0.92	0.44	0.19	0.62	0.47
Total Majors	97.12	99.26	99.70	99.79	97.21	98.07	99.40
Zn (ppm)	3.6	41.9	87.9	43.6	57.6	39.1	53.6
Cu (ppm)	2.0	1.5	1.0	0.1	0.5	1.4	0.3
Ni (ppm)	10.9	3.2	2.3	n.d	3.5	2.8	1.0
Cr (ppm)	n.d	4.5	6.3	1.2	12.1	5.2	4.3
V (ppm)	n.d	2.0	n.d	1.7	2.9	1.9	0.9
Ba (ppm)	135.0	18.6	12.7	11.5	6.7	33.8	16.6
Sc (ppm)	n.d	3.5	3.9	7.9	1.7	0.2	10.0
Nb (ppm)	17.3	30.6	91.4	69.3	92.1	68.0	93.3
Zr (ppm)	6.1	4.1	2.4	19.4	47.7	5.2	18.5
Y (ppm)	9.8	8.6	9.7	57.7	52.2	9.0	55.8
Sr (ppm)	51.5	16.3	10.5	4.8	2.0	18.3	5.3
Rb (ppm)	3981.3	1422.9	1005.6	354.6	130.1	1025.9	405.3
Hf (ppm)	1.90	-	0.48	2.30	-	0.80	1.91
U(ppm)	3.21	2.8	4.07	14.65	16.9	2.50	15.53
Th (ppm)	1.93	n.d	1.84	8.25	3.7	1.56	9.67
Pb (ppm)	56.41	23.6	12.43	38.53	7.2	27.80	31.93
La (ppm)	1.10	0.7	2.03	12.49	4.4	1.50	16.24
Ce (ppm)	2.61	5.3	5.50	34.16	15.8	4.13	45.18
Pr (ppm)	0.30	-	0.73	4.20	-	0.58	5.95
Nd (ppm)	1.01	2.3	2.68	15.32	8.4	2.23	22.26
Sm (ppm)	0.52	-	1.53	5.92	-	1.59	7.88
Eu (ppm)	0.06	-	0.01	0.02	-	0.02	0.01
Gd (ppm)	0.36	-	1.32	5.64	-	1.42	6.08
Tb (ppm)	0.05	-	0.25	1.16	-	0.27	1.15
Dy (ppm)	0.17	-	1.17	6.94	-	1.09	6.68
Ho (ppm)	0.02	-	0.14	1.20	-	0.11	1.12
Er (ppm)	0.07	-	0.32	3.72	-	0.22	3.54
Tm (ppm)	0.01	-	0.06	0.76	-	0.04	0.79
Yb (ppm)	0.09	-	0.46	5.59	-	0.31	6.41
Lu (ppm)	n.d	-	0.06	0.84	-	0.04	0.97
Total Majors + Traces	97.55	99.41	99.83	99.86	97.25	98.20	99.48

Table A2.13. Granite pegmatite compositions. LOI = Loss on ignition; wt% = Weight percent; ppm = Parts per million; n.d = not detected; – denotes element not analysed. Analyses with one decimal place were analysed by XRF whereas analyses with two decimal places were analysed by ICP-MS.

A2.5 XRF accuracy and precision

	CD09	CD09 DUP1	CD09 DUP2	CD09 DUP3	CD09 DUP4	CD09 Mean	1σ	relative 1σ error (%)
SiO_2 (wt%)	63.24	63.34	63.18	63.43	63.09	63.26	0.13	0.21
Al_2O_3 (wt%)	16.06	16.09	16.04	16.16	16.02	16.07	0.05	0.34
Fe_2O_3 (wt%)	6.12	6.14	6.14	6.13	6.14	6.13	0.01	0.15
MnO (wt%)	0.10	0.10	0.10	0.10	0.10	0.10	0.00	1.08
MgO (wt%)	1.79	1.76	1.77	1.76	1.78	1.77	0.01	0.74
CaO (wt%)	2.42	2.42	2.41	2.42	2.40	2.41	0.01	0.37
Na_2O (wt%)	5.69	5.71	5.76	5.74	5.72	5.72	0.03	0.47
K_2O (wt%)	2.03	2.05	2.04	2.04	2.03	2.04	0.01	0.33
TiO_2 (wt%)	0.86	0.86	0.86	0.86	0.86	0.86	0.00	0.11
P_2O_5 (wt%)	0.28	0.28	0.29	0.29	0.29	0.28	0.00	1.07
LOI (wt%)	0.76	0.54	0.51	0.54	0.65	0.60	0.10	17.05
Total Majors	99.35	99.29	99.10	99.46	99.08	99.25	0.17	0.17
Zn (ppm)	60.0	59.2	59.3	59.7	60.4	59.7	0.5	0.9
Cu (ppm)	9.5	9.8	9.8	10.1	9.8	9.8	0.2	2.2
Ni (ppm)	2.3	1.8	1.8	4.1	3.6	2.7	1.1	39.2
V (ppm)	48.2	49.1	50.9	51.0	50.2	49.9	1.2	2.4
Ba (ppm)	533.6	536.5	533.7	536.0	540.0	536.0	2.6	0.5
Sc (ppm)	12.5	12.5	13.1	13.5	13.4	13.0	0.5	3.7
Nb (ppm)	13.5	13.5	13.5	13.5	13.4	13.5	n.d	0.4
Zr (ppm)	245.3	244.9	244.7	244.7	244.9	244.9	0.2	0.1
Y (ppm)	31.9	31.8	31.7	31.8	32.0	31.8	0.1	0.4
Sr (ppm)	144.9	145.5	145.3	145.5	145.0	145.2	0.3	0.2
Rb (ppm)	79.9	80.0	79.8	79.6	79.4	79.7	0.2	0.3
U(ppm)	5.1	5.1	5.0	5.1	5.0	5.1	0.1	1.1
Th (ppm)	19.8	19.8	19.9	19.8	20.0	19.9	0.1	0.5
Pb (ppm)	13.6	13.4	13.4	13.5	13.3	13.4	0.1	0.9
La (ppm)	61.7	63.2	61.6	60.5	60.4	61.5	1.1	1.9
Ce (ppm)	113.5	115.5	113.8	114.2	114.2	114.2	0.8	0.7
Nd (ppm)	41.4	43.3	41.0	43.9	42.1	42.3	1.2	2.9
Total Traces	1436.7	1444.9	1438.3	1446.5	1447.1	1442.7	4.8	0.33
Total Majors + Traces	99.49	99.43	99.24	99.61	99.22	99.40	0.17	0.17

Table A2.14. Repeat analyses of sample CD09 (Felsic volcanic unit) to show the typical precision of XRF analyses. Note that elements with low concentrations have a higher standard deviations, but this is a function of the concentration some elements being close to the detection limit (e.g., Ni). Note Cr was not detected in any of the samples so this element has been omitted from the table. Loss On Ignition (LOI) shows a higher deviation as this is measured separately during preparation and typically cannot be measured with as much accuracy or repeatability.

	C12-160A	C12-160B	C12-160C	C12-160D	C12-160 Mean	1σ	relative 1σ error (%)
SiO_2 (wt%)	76.35	76.20	75.97	76.27	76.20	0.16	0.22
Al_2O_3 (wt%)	14.14	14.05	14.03	14.19	14.10	0.08	0.54
Fe_2O_3 (wt%)	0.81	0.79	0.81	0.82	0.81	0.01	1.56
MnO (wt%)	0.06	0.06	0.06	0.06	0.06	0.00	1.58
MgO (wt%)	0.02	0.01	0.03	0.03	0.02	0.01	42.60
CaO (wt%)	0.07	0.08	0.07	0.08	0.08	0.01	7.70
Na_2O (wt%)	3.93	3.94	3.89	3.94	3.93	0.02	0.61
K_2O (wt%)	3.37	3.36	3.35	3.36	3.36	0.01	0.30
TiO_2 (wt%)	0.02	0.02	0.02	0.02	0.02	0.00	7.45
P_2O_5 (wt%)	0.01	0.01	0.01	0.01	0.01	0.00	4.45
LOI (wt%)	0.92	0.80	0.78	0.71	0.80	0.09	10.68
Total Majors	99.70	99.32	99.02	99.50	99.38	0.29	0.29
Zn (ppm)	87.9	81.4	85.6	84.0	84.7	2.7	3.3
Cu (ppm)	1.0	1.3	0.5	0.6	0.9	0.4	44.0
Ni (ppm)	2.3	7.5	1.6	1.6	3.3	2.9	88.8
Cr (ppm)	6.3	23.9	2.2	1.8	8.6	10.4	244.1
V (ppm)	n.d	2.5	0.8	2.6	2.0	1.0	51.5
Ba (ppm)	12.7	11.7	12.0	10.8	11.8	0.8	6.8
Sc (ppm)	3.9	3.7	4.0	4.1	3.9	0.2	4.4
Nb (ppm)	91.4	86.5	85.7	84.9	87.1	2.9	3.4
Zr (ppm)	2.4	2.5	2.6	2.4	2.5	0.1	4.0
Y (ppm)	9.7	9.2	9.6	10.2	9.7	0.4	4.2
Sr (ppm)	10.5	10.6	10.6	10.4	10.5	0.1	0.9
Rb (ppm)	1005.6	1011.5	1010.2	1008.7	1009.0	2.5	0.3
U(ppm)	4.0	4.0	4.1	4.1	4.1	0.1	1.5
Th (ppm)	3.9	4.1	4.2	4.1	4.1	0.1	3.1
Pb (ppm)	8.0	8.3	8.2	8.4	8.2	0.2	2.1
La (ppm)	n.d	n.d	2.2	2.1	2.2	0.1	3.3
Ce (ppm)	3.8	5.2	6.6	6.7	5.6	1.4	24.5
Nd (ppm)	2.3	3.6	2.2	3.4	2.9	0.7	25.3
Total Traces	1255.7	1277.5	1252.9	1250.9	1259.3	12.3	1.0
Total Majors + Traces	99.83	99.45	99.14	99.62	99.51	0.29	0.29

Table A2.15 Repeat analysis of sample C10-160 (granite pegmatite) to show the typical precision of the XRF analyses. Note that low concentrations of specific elements appear to have higher standard deviations but this is a function of the concentration of that element being close to the detection limit (e.g. MgO, CaO, Ce, and Nd). Cr values are very wide ranging, possibly reflecting the fact that Cr may not be correctly calibrated for silicic rocks. This is not important as the Cr values have not been utilised in geochemical analysis of the Cosmos succession. LOI shows a higher deviation as this is measured directly during preparation and typically cannot be measured with as much accuracy or precision.

A2.6 XRF standards accuracy and uncertainty

	Govindaraju (1994)	Edinburgh Average 2004-2011	Average 2009-mid 2012	1σ on average
SiO_2 (wt%)	49.940	50.233	50.244	0.404
Al_2O_3 (wt%)	13.800	13.693	13.752	0.167
Fe_2O_3 (wt%)	12.230	12.368	12.343	0.061
MnO (wt%)	0.168	0.170	0.173	0.003
MgO (wt%)	7.230	7.181	7.186	0.091
CaO (wt%)	11.400	11.446	11.408	0.106
Na_2O (wt%)	2.260	2.467	2.339	0.266
K_2O (wt%)	0.520	0.527	0.528	0.006
TiO_2 (wt%)	2.710	2.726	2.718	0.021
P_2O_5 (wt%)	0.273	0.292	0.288	0.016
		n=136	n=26	

Table A2.16. Major element concentrations for sample USGS reference standard BHVO-1 on the PANanalytical PW2404 automatic X-ray fluorescence spectrometer showing the averages obtained on the machine over seven years. Also show is the average of the BHVO-1 standards over the duration of batches of analyses of the Cosmos samples.

A2.6.1 Standards used for major and trace element analysis

The following standards were used during XRF analyses

BHVO-1 = Basalt, Hawaiian Volcanic Observatory

BCR-1 = Columbia River Basalt

BCR-2 = Columbia River Basalt

BEN = Basalt from d'Essey-la-Coté

BIR = Icelandic Basalt

	BCR-1 Published Values	BCR-2009 Average	BCR-1 2009 1σ	BCR-1 relative 1□ error (%)	BEN Published Values	BEN-2009 Average	BEN-2009 1σ	BEN relative 1□ error (%)	BHVO-1 Published Values	BHVO-1 Average	BHVO-1-2009 1σ	BVHO-1 relative 1□ error (%)	BIR-1 Published Values	BIR-2009 Average	BIR-2009 1σ	BIR-1 relative 1□ error (%)
Zn (ppm)	129.50	127.30	1.15	0.91	120.00	126.43	0.15	0.12	105.00	103.80	0.26	0.25	71.00	67.97	0.21	0.31
Cu (ppm)	19.00	19.53	0.35	1.80	72.00	73.73	0.15	0.21	136.00	136.20	0.26	0.19	126.00	123.17	0.12	0.09
Ni (ppm)	13.00	12.50	0.30	2.40	267.00	271.83	1.25	0.46	121.00	116.43	0.42	0.36	166.00	151.03	1.36	0.90
V (ppm)	407.00	414.63	1.59	0.38	235.00	260.23	1.79	0.69	317.00	327.73	0.72	0.22	313.00	311.37	0.46	0.15
Ba (ppm)	681.00	691.60	1.57	0.23	1025.00	1037.27	5.36	0.52	139.00	141.13	0.31	0.22	7.00	17.27	2.75	15.95
Sc (ppm)	32.60	34.73	1.03	2.95	-	22.50	1.11	4.95	31.80	33.97	0.57	1.67	44.00	41.73	0.42	1.00
Nb (ppm)	14.00	12.75	0.07	0.55	105.00	117.37	0.42	0.35	19.80	19.50	0.10	0.51	0.60	0.63	0.06	9.12
Zr (ppm)	190.00	192.33	1.02	0.53	260.00	273.60	0.82	0.30	182.00	175.80	0.40	0.23	15.50	17.40	0.20	1.15
Y (ppm)	38.00	38.17	0.25	0.66	30.00	29.87	0.21	0.70	27.60	27.47	0.21	0.76	16.00	16.43	0.25	1.53
Sr (ppm)	330.00	333.80	1.04	0.31	1370.00	1388.00	4.85	0.35	403.00	392.87	0.32	0.08	108.00	109.47	0.25	0.23
Rb (ppm)	47.20	47.77	0.15	0.32	47.00	47.93	0.38	0.79	11.00	9.57	0.15	1.60	0.25	0.43	0.23	53.29
U(ppm)	1.80	1.67	0.06	3.46	2.40	2.30	0.10	4.35	0.40	0.53	0.31	57.28	0.00	n.d	n.d	n.d
Th (ppm)	5.98	7.17	0.15	2.13	10.40	12.67	0.15	1.21	1.08	0.60	0.26	44.10	0.03	n.d	n.d	n.d
Pb (ppm)	13.60	14.67	0.21	1.42	4.00	4.23	0.40	9.55	2.60	2.20	0.26	12.03	3.00	3.43	0.12	3.36
La (ppm)	24.90	25.43	0.70	2.76	82.00	86.87	0.59	0.67	15.80	11.60	0.75	6.51	0.62	n.d	n.d	n.d
Ce (ppm)	53.70	51.97	0.64	1.22	152.00	153.77	1.70	1.11	39.00	37.73	0.57	1.51	1.95	0.80	0.66	81.97
Nd (ppm)	28.80	30.13	0.64	2.11	67.00	68.00	0.40	0.59	25.20	27.50	0.96	3.51	2.50	4.23	0.42	9.83
		n=3				n=3				n=3				n=3		

Table A2.17. Estimates of accuracy and precision based on repeated analysis of USGS and CRPG international reference standards. Published values from Govindaraju (1994).

A2.7 Accuracy and uncertainty for ICP-MS measurements

	BCR-2 (2012)a	BCR-2 (2012)b	BCR-2 (2012)c	BCR-2 (2012)d	BCR-2 (2012)e	BCR-2 (2012)f	Mean	1σ	relative 1σ error (%)
Hf (ppm)	5.13	5.03	5.09	5.17	5.16	5.19	5.13	0.06	1.11
Pb (ppm)	13.72	13.38	14.29	13.90	13.78	16.16	14.21	1.00	6.21
Th (ppm)	6.18	6.03	6.05	6.13	6.10	6.11	6.10	0.05	0.88
U (ppm)	1.81	1.77	1.77	1.78	1.78	1.78	1.78	0.02	0.91
La (ppm)	24.88	24.78	24.77	24.77	24.71	24.58	24.75	0.10	0.39
Ce (ppm)	53.65	53.61	53.38	53.38	53.50	52.75	53.38	0.33	0.63
Pr (ppm)	6.83	6.82	6.85	6.85	6.85	6.80	6.83	0.02	0.29
Nd (ppm)	28.90	28.92	28.93	28.93	28.82	28.68	28.86	0.10	0.35
Sm (ppm)	6.61	6.59	6.64	6.64	6.62	6.59	6.61	0.02	0.34
Eu (ppm)	1.94	1.94	1.96	1.96	1.93	1.92	1.94	0.01	0.64
Gd (ppm)	6.65	6.63	6.61	6.61	6.61	6.52	6.61	0.04	0.67
Tb (ppm)	1.04	1.04	1.03	1.03	1.04	1.03	1.04	0.00	0.45
Dy (ppm)	6.32	6.36	6.37	6.37	6.31	6.29	6.34	0.04	0.59
Ho (ppm)	1.26	1.26	1.26	1.26	1.26	1.24	1.26	0.01	0.61
Er (ppm)	3.63	3.64	3.64	3.64	3.63	3.58	3.63	0.02	0.66
Tm (ppm)	0.56	0.56	0.56	0.56	0.56	0.55	0.56	0.00	0.74
Yb (ppm)	3.38	3.37	3.34	3.34	3.31	3.32	3.34	0.03	0.77
Lu (ppm)	0.50	0.50	0.50	0.50	0.51	0.50	0.50	0.00	0.37

Table A2.18. Precision estimates for trace and rare element concentrations in USGS international standards BCR-2 measured by ICP-MS at SUERC.

	Certified value	Mean BCR-2 (2012)	Difference	% Difference
La (ppm)	25.00	24.75	0.25	1.01
Ce (ppm)	53.00	53.38	-0.38	-0.71
Pr (ppm)	6.80	6.83	-0.03	-0.51
Nd (ppm)	28.00	28.86	-0.86	-3.09
Sm (ppm)	6.70	6.61	0.09	1.32
Eu (ppm)	2.00	1.94	0.06	2.86
Gd (ppm)	6.80	6.61	0.19	2.85
Tb (ppm)	1.07	1.04	0.03	3.00
Dy (ppm)	6.34*	6.34	0.00	0.05
Ho (ppm)	1.33	1.26	0.07	5.40
Er (ppm)	3.63*	3.63	0.00	0.02
Tm (ppm)	0.54	0.56	-0.02	-3.46
Yb (ppm)	3.50	3.34	0.16	4.51
Lu (ppm)	0.51	0.50	0.01	1.40
		n=6		

Table A2.19. Accuracy estimates for rare element concentrations in USGS international standards BCR-2 measured by ICP-MS at SUERC compared with the published values of Wilson (1997) (*samples corrected to the published values for BCR-1 as no published value is given for BCR-2 by Wilson (1997)).

A2.8 Comparison of trace element concentrations obtained from ICP-MS and XRF

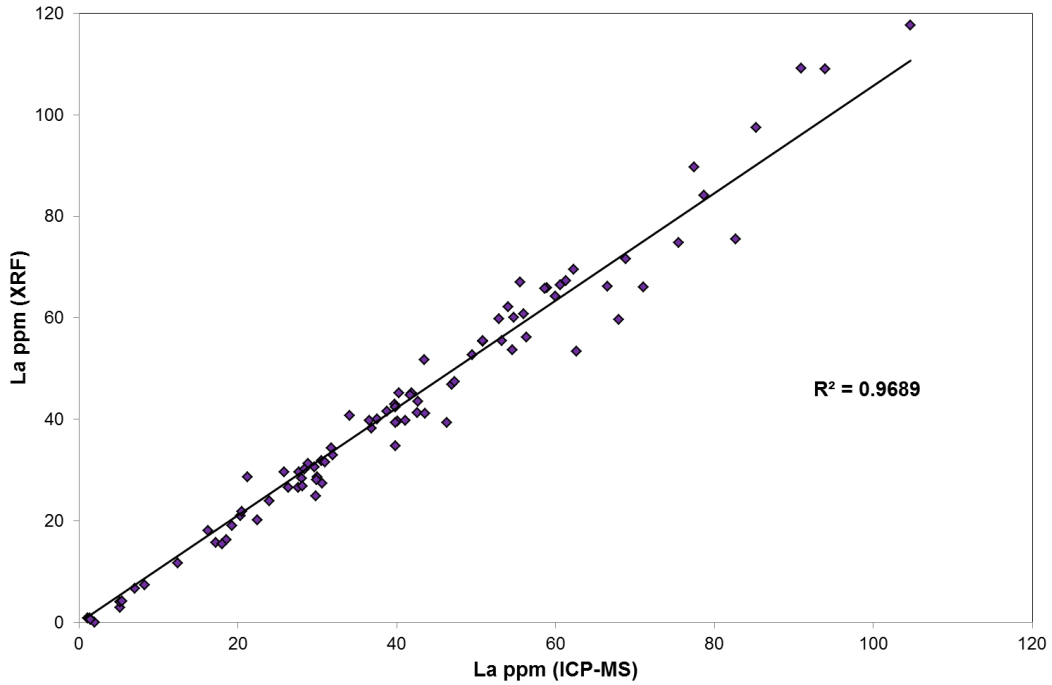

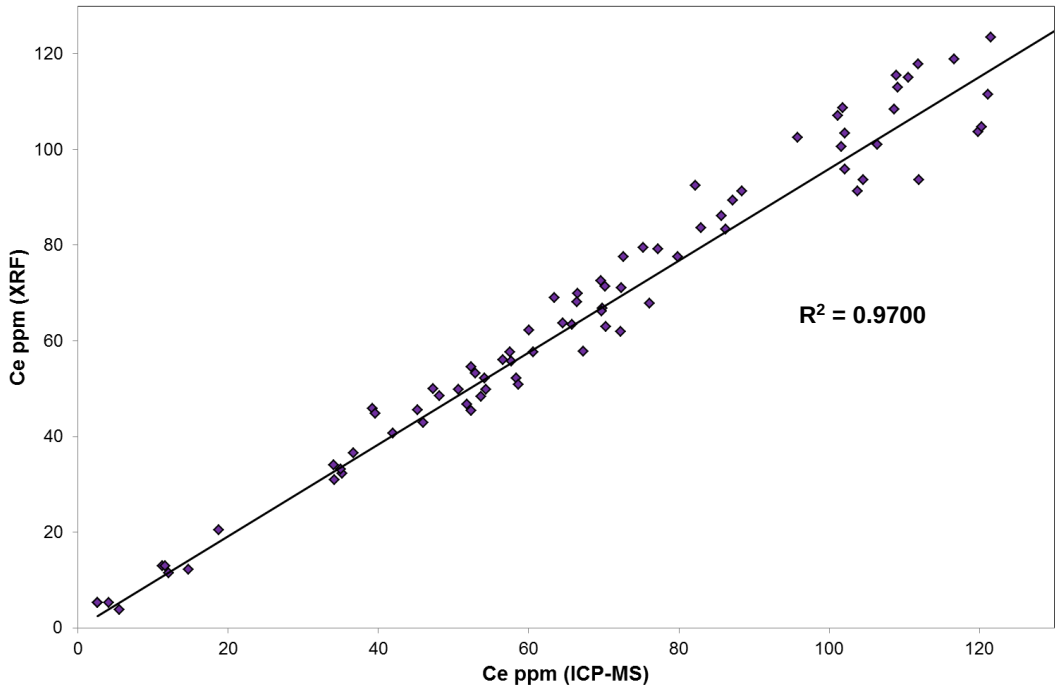

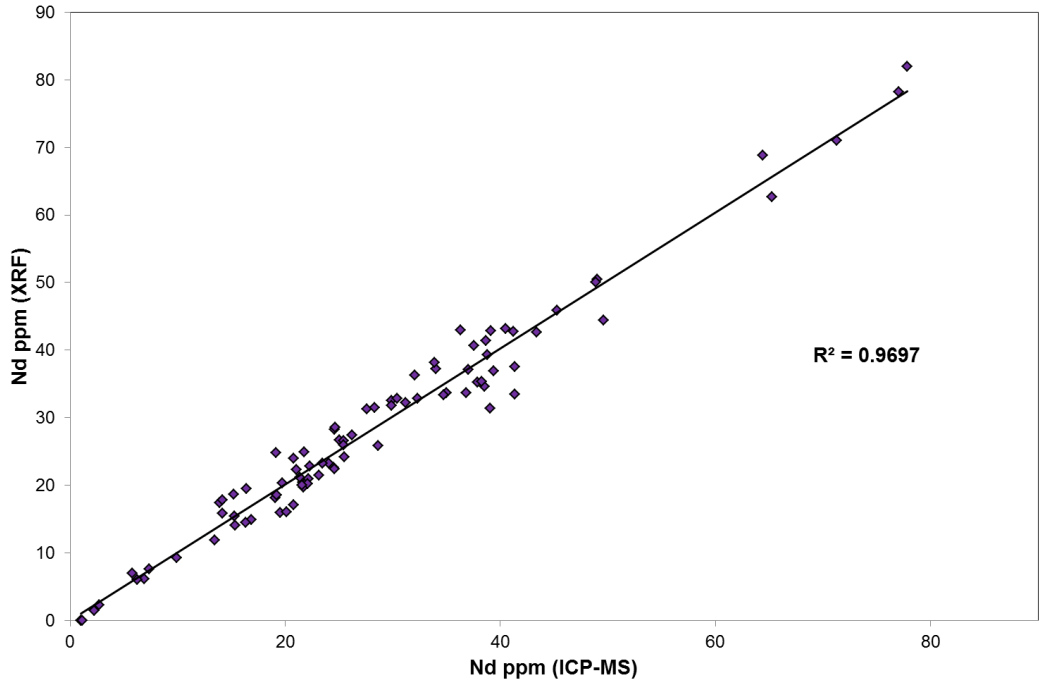

Figure A2.1 Comparison of La, Ce and Nd (ppm) concentrations obtained for the same powdered samples via XRF and ICP-MS. Highlighting the good correlation between the values obtained from the two separate analytical techniques.

A2.9 References

Fitton, J. G., Saunders, A. D., Larsen, L. M., Hardarson, B. S., Norry, M. J., 1998. Volcanic rocks from the southeast Greenland margin at 63°N: composition, petrogenesis and mantle sources. In: Saunders, A.D., Larsen, H.C., Wise, S.H. (Eds.) Proceedings of the Ocean Drilling Program Scientific Results, 152. College Station, TX: Ocean Drilling Program, pp. 331–350.

Govindaraju, K., 1994, Compilation of working values and sample descriptions for 383 geostandards: Geostandard Newsletters 18, 1-158.

Hickson, C. J., Juras, S.J., 1986. Sample contamination by grinding. Canadian Mineralogist 24(3), 585-9.

Joron, J. L., Briqueu, L., Bougault, H., Treuil, M., 1980. 30. East Pacific Rise, Galapagos spreading centre and Siqueiros fracture zone, Deep Sea drilling Project Leg 54: Hydromagmaphile elements – A comparison with the North Atlantic.

Norrish, K., Hutton, J. T., 1969. An accurate X-ray spectrographic method for the analysis of a wide range of geological samples. Geochimica et Cosmochimica Acta 33, 431−453.

Olive, V., Ellam, R. M., and Wilson, L., 2001, A Protocol for the Determination of the Rare Earth Elements at Picomole Level in Rocks by ICP-MS: Results on Geological Reference Materials USGS PCC-1 and DTS-1: Geostandards Newsletter, 25 (2-3), 219-228.

Wilson, S. A., 1997. The collection, preparation, and testing of USGS reference material BCR-2, Columbia River, Basalt: U.S. Geological Survey Open-File Report 98-xxx.A

Appendix 3 - Garnet-Biotite Geothermometry

A3.1 Electron Micro-Probe Analysis (EMPA) methodology for garnet-biotite geothermometry

Garnet-biotite geothermometry was undertaken on several samples from within the Cosmos stratigraphic sequence to estimate the peak metamorphic temperature for the region. Samples were chosen from several different footwall volcanic lithologies that were composed of garnet and biotite-rich metamorphic mineral assemblages. Petrography was undertaken, prior to EMPA, on individual samples to locate suitable areas for analysis. The timing relationships between the growth of garnet porphyroblasts and biotite matrix crystals was assessed to confirm that the two minerals represented an equilibrium mineral assemblage without significant retrogression. Chemical equilibrium was assumed when biotite and garnet crystals were in contact with one another throughout the sample. Any samples that petrography revealed had experienced strong retrograde metamorphism, typified by the retrogression of biotite to chlorite, particularly along garnet rims, were not analysed.

Electron micro-probe analysis was carried out on six garnet-biotite bearing samples from within the stratigraphic footwall on a Cameca SX100 electron probe at the University of Edinburgh using Wavelength Dispersive Spectrometry. Thin sections of the five samples were cleaned in DI water and petroleum spirit and in an ultrasonic bath prior to carbon coating. Analyses of major and trace elements (Na, Mg, Al, Si, Fe, Ca, Mn, K, Ti, Cr, Ni for garnet and Na, Mg, Al, Si, K, Fe, F, Cl, Ca, Ti, Cr, Mn, Ni for biotite) were made for garnet-biotite mineral pairs from a number of pre-selected locations within each sample. An 15keV energy and a beam current of 10nA

was used for major elements (in sequence; Na, Mg, Al, Fe, Ca, Mn, Si) and 100nA for minor elements (in sequence; K, Ti, Cr, Ni). Several different beam configurations were tested for biotite analyses. For biotite analyses, a smaller beam size and current were used. A 15keV energy and a beam current of 1nA was used for major analyses (in sequence; Na, Mg, Al, Si, K, Fe) and a current of 60nA used for minor elements (in sequence; F, Cl, Ca, Ti, Cr, Mn, Ni). Analysis locations were selected using secondary electron imaging and analyses were made away from visible fractures and inclusions. At least two individual measurements were made within 10 - 20μm of each other at each location. This was to ensure that adjacent analyses gave consistent results and that the area of crystal being analysed was not affected by imperfections at the surface such as inclusions, fracturing or mineral alteration. Pairs of analyses from the same location that were inconsistent were discarded. Peak counting times were 20s on major elements and 30s on minor elements and 3s on the background. For all elements the Kα line was measured.

Secondary mineral standards were analysed routinely throughout analytical sessions and at the beginning and end of individual manual and automated sessions to ensure that the instrument was producing consistent results. NBS 30 was used as the biotite standard and an in-house garnet standard (see section A3.2) was used. For instrument calibration the standards used were jadeite for Na, spinel for Mg and Al, orthoclase for K, wollastonite for Si and Ca, synthetic fayalite for Fe, Durango apatite for P, rutile for Ti, $RbMnF_3$ for F, NaCl for Cl and pure metals for Mn, Cr, and Ni. Data reduction was carried out in Cameca's PeakSight software. Totals which were outside the range of 99 – 101% were discarded for garnet analyses, whilst biotite analyses were found to vary much more between individual samples. Of the three samples found to provide suitable consistent estimates of peak metamorphic temperature, based on constraints from metamorphic mineral assemblages, the biotite totals ranged from approximately 95 – 98 wt% in sample BJD102B, between approximately 91.5 – 94.5 wt% in sample BJD312HB and between 91.5 – 95.5. wt% in sample AMD310Q. This likely reflects the variable water content held within the biotite lattice (typically 4 - 5% (Deer et al., 1992), as well as the possibility of the presence of unanalysed minor phases such as Ba, Rb, Li or the presence of some Fe as

Fe_2O_3 (biotite can contain up to 1.5 – 3.5 wt% Fe_2O_3; Deer et al., 1992). It could also reflect an increased water content within the crystal lattice due to minor alteration of the biotite crystals to clay. Analyses outside these values were discarded from garnet-biotite geothermometry calculations.

A3.2 Estimate of accuracy and uncertainty of EMPA analyses

Major element	**Block 8 Garnet** Determined value from UoE (wt%)	**Block 8 Garnet** Average ADJ analyses (wt%)	1σ	%σ	Difference	% Difference
SiO_2	37.03	36.39	0.50	1.38	-0.64	-1.76
Al_2O_3	21.08	21.23	0.15	0.72	0.15	0.71
FeO	34.30	33.67	0.77	2.28	-0.63	-1.87
MgO	2.23	2.12	0.14	6.63	-0.11	-5.19
CaO	1.88	1.98	0.08	3.91	0.10	5.05
Na_2O	0.02	0.02	0.01	49.02	-	-
K_2O	0.00	0.00	-	-	-	-
TiO_2	0.00	0.00	-	-	-	-
MnO	4.43	4.73	0.80	16.95	0.3	6.34
Cr_2O_3	0.00	0.00	0.01	-	-	-
NiO	0.01	0.00	-	-	-0.01	-
Total	101.01	100.14			-0.87	-0.87
		n = 56				

Table A3.1. Accuracy and uncertainty estimates for EMPA in-house Block 8 garnet standard analyses. The percentage accuracy on major elements analyses, to the University of Edinburgh determined value, is typically between ± 0.7 - <7%, while repeat analyses for this data set are generally within 0.2 – 1.6 wt% (2σ) of the average obtained across the data set as a whole.

	NBS 30 - Biotite Determined value from UoE	**NBS 30 - Biotite** Average ADJ analyses	1σ	%σ	Difference	% Difference
SiO_2	34.80	35.98	0.98	2.72	-1.18	-3.28
Al_2O_3	14.93	15.78	0.42	2.69	-0.85	-5.39
FeO	20.24	20.39	0.86	4.21	-0.15	-0.74
MgO	9.92	9.87	0.36	3.67	0.05	0.05
CaO	0.05	0.01	0.01	-	0.04	400.00
Na_2O	0.16	0.14	0.04	30.66	0.02	14.29
K_2O	9.10	8.29	0.59	7.15	0.81	9.77
TiO_2	3.23	3.22	0.16	4.90	0.01	0.31
MnO	0.23	0.21	0.02	8.96	0.02	9.52
Cr_2O_3	-	0.01	0.01	-	-	-
NiO	-	0.00	0.01	-	-	-
F	-	0.17	0.02	11.31	-	-
Cl	-	0.06	0.01	10.29	-	-
Total		94.15	2.20	2.34	-	-
		n = 56				

Table A3.2. Accuracy and uncertainty estimates for EMPA analyses of NBS 30 biotite. – denotes not analysed/not applicable. The percentage difference on major elements analyses, to the University of Edinburgh determined value, is typically between ± 0.05 - <10%, if CaO and Na_2O are discounted due to their low concentrations. Repeat analyses for this data set are generally within 0.2 – 2 wt% (2σ) of the average obtained across the data set as a whole.

A.3.3 Summary of samples selected for garnet-biotite geothermometry

(Next page)

Table A3.3. Descriptions and core photos of the six samples selected for garnet-biotite geothermometry. BJD050L was not used for garnet-biotite geothermometry as it did not provide sufficient biotite analyses.

Sample	Interpreted Lithology	Core photo	Interpretation of timing of Garnet growth	Thin section example
BJD102B	Intermediate volcaniclastic unit		Syn-tectonic, but late stage, garnets – aligned inclusion trails in garnet and biotite fabric.	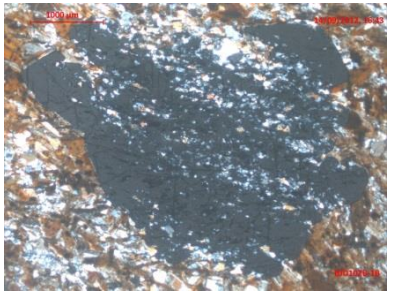
AMD310Q	Crenulated and strongly sericite replaced felsic schist		Syn-tectonic garnets – spiralling S-shaped inclusions within garnets porphyroblasts that are also wrapped by fabric. Sample contains andalusite.	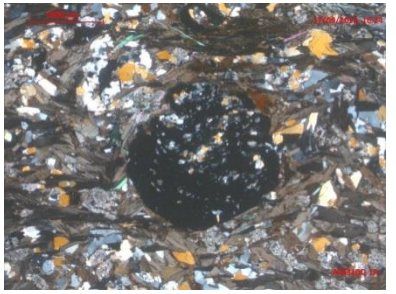
BJD312HB	Andesitic mafic-phyric lava		Syn-tectonic, but probably late stage garnets - fabric wraps large garnets. Garnet and biotite grew in equilibrium but core of garnet unlikely to have equilibrated with biotite matrix due to garnets being ~10mm in diameter.	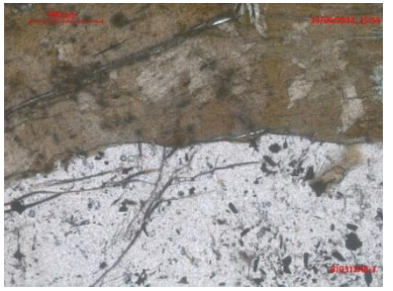

Sample	Interpreted Lithology	Core photo	Interpretation of timing of Garnet growth	Thin section example
AMD139B	Dacite lapilli tuff	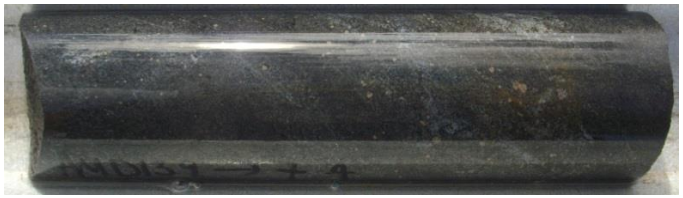	Syn-tectonic, but possibly late stage small and abundant garnet porphyroblasts. Fabric wraps garnets and biotite content much greater than garnet therefore minerals will be in equilibrium.	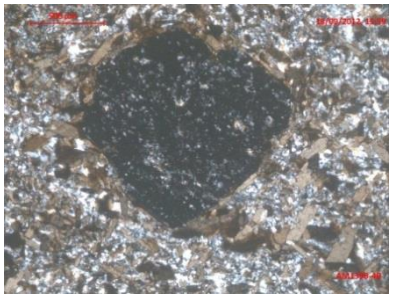
CD06	Intermediate garnet-amphibole schist	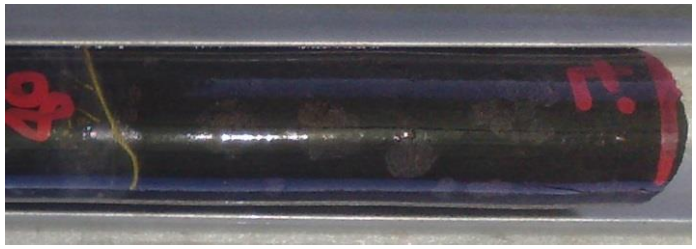	Post-tectonic garnets? Possible truncation of biotite fabric by large garnets whose cores are unlikely to have re-equilibrated with matrix. Minor chlorite along garnet rims suggests some retrogression of biotite.	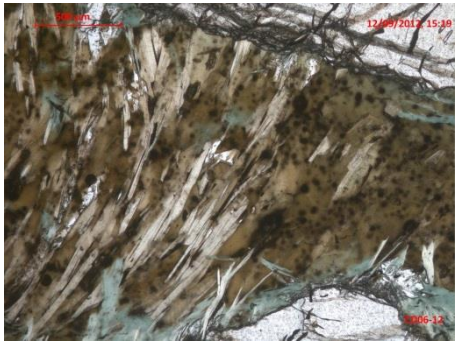

BJD050L	Garnet bearing mafic-phyric intermediate volcanic	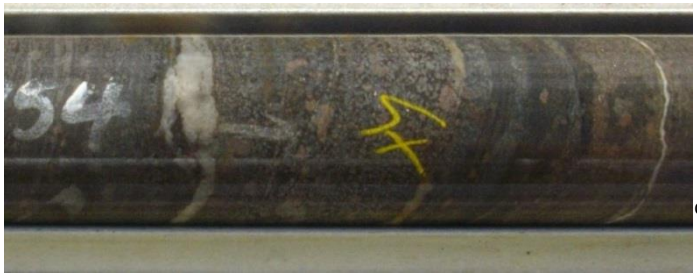	Garnets are likely post-tectonic as the fabric does not bend around the porphyroblasts and inclusions within garnet are aligned with inclusion trails outside the garnet porphyroblasts. Sample did not provide sufficient biotite analyses to allow it to be used in geothermometry calculations but significantly contained the amphibole gedrite, which places a minimum metamorphic temperature of ~525°C on the succession	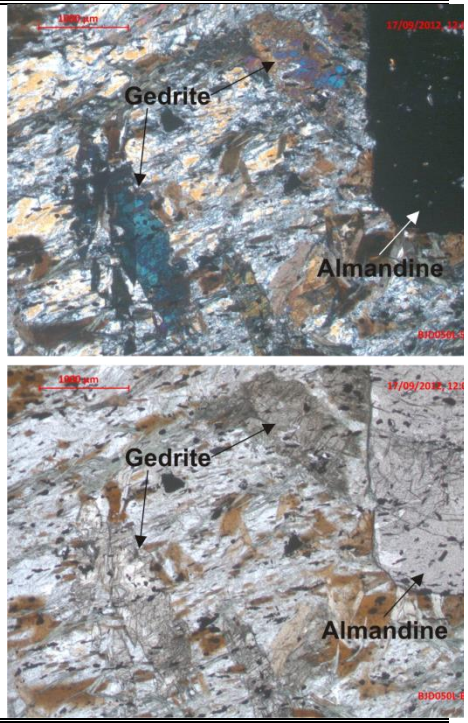

A3.4 Garnet-biotite equations

$X_{Mg(grt)F\&S}$ =	Mg/(Mg+Fe)
$X_{Mg(grt)P\&L}$	Mg/(Mg+Fe+Mn)
$X_{Mg(bt)F\&S}$	Mg/(Mg+Fe)
$X_{Mg(bt)P\&L}$	Mg/(Mg+Fe+Mn)
$X_{Ca(grt)F\&S}$	Ca/(Ca+Mg+Fe+Mn)
$X_{Mn(grt)F\&S}$	Mn/(Ca+Mg+Fe+Mn)
$K_{dF\&S}$	$(Mg/Fe)_{grt}/(Mg/Fe)_{bt}$
Log $K_{dF\&S}$	$\ln(((1-X_{Mg(grt)F\&S}/XMg_{(grt)F\&S})*(XMg_{(bt)F\&S}/(1-XMg_{(bt)F\&S})))$
Log $K_{dP\&L}$	$\ln(((1-X_{Mg(grt)P\&L}/XMg_{(grt)P\&L})*(XMg_{(bt)P\&L}/(1-XMg_{(bt)P\&L})))$

Table A3.4. Table of equations used in this study. F & S = Ferry and Spear (1978). P & L = Perchuk and Lavrent'eva (1983). grt = garnet; bt = biotite

Calibration	Year	Abbrevi-tion	Equation
Ferry and Spear	1978	FS	$T\ (°C)= \{((((12454+(57*P(kbar)))/(4.662+(5.961*(\ln K_{dF\&S})))\}-273$
Lavrent'eva and Perchuk	1981	PL81	$T\ (°C) = \{(3720+(2871*X_{Ca(grt)})+(38*P(kbar)))/(2.868+\ln K_{dF\&S}+(0.65*X_{Ca(grt)}))\}-273$
Pigage and Greenwood	1982	PG	$T\ (°C) = \{((2089+(9.560001*P(kbar))+(1586*X_{Ca(grt)}+(1308*X_{Mn(grt)}))/(0.78158+\ln K_{dF\&S}))\}-273$
Thompson	1976	Th	$T\ (°C) = \{(2740+23.4*P(kbar))/(1.56+\ln K_{dF\&S})\}-273$
Holdaway and Lee	1977	HL	$T\ (°C) = \{(3095+(0.0124*1000*P(kbar)))/(\ln K_{dF\&S}+1.978)\} - 273$
Perchuk and Lavrent'eva	1983	PL83A	$T\ (°C) = \{(7834.7+0.0246*(P(kbar)-6000))/(5.699-((8.31414/4.184)*\ln K_{dF\&S}))\}-273$
Perchuk and Lavrent'eva	1983	PL83B	$T\ (°C) = \{(7834.7+0.0246*(P(kbar)-6000))/(((8.31414/4.184)*\ln K_{dP\&L})+5.699)\}-273$

Table A3.5. Equations for the seven calibrations of the garnet-biotite geothermometer used in this study

A3.5 Sample BJD102B

Sample	Core /Rim	Average Almandine %	Average Grossular %	Average Pyrope %	Average Spessartine %	Average Gro + Spess %	Average Garnet composition
BJD102B	Average Core	67.41	6.97	9.75	15.87	22.84	$Alm_{67}Gro_7Py_{10}Sp_{16}$
BJD102B	Average Rim	72.15	6.86	11.72	9.27	16.13	$Alm_{72}Gro_7Py_{12}Sp_9$

Table A3.6 Average composition of garnet within BJD102B

Table A3.7. BJD102B Analyses of garnet chosen for geothermometry in this study. Cationic proportions of garnets are recalculated on the basis of 24 oxygens, anhydrous conditions. * denotes sample not used in average geothermometry calculation

Sample Name	Core/Rim	Garnet Number	Na_2O	K_2O	MgO	CaO	MnO	FeO	NiO	Al_2O_3	Cr_2O_3	SiO_2	TiO_2	Total	Na	K	Mg	Ca	Mn	Fe	Ni	Al	Cr	Si	Ti	Total	XMg(Gt) (Mg/Mg+Fe)	XCa(Gt) Ca/Ca+Mg+Fe+Mn	XMn(Gt) Mn/Ca+Mg+Fe+Mn
5/1 09 Oct	Rim	Garnet 1	0.00	0.01	2.86	2.28	4.23	32.84	0.00	21.31	0.00	36.56	0.02	100.12	0.00	0.00	0.69	0.39	0.58	4.44	0.00	4.06	0.00	5.91	0.00	16.07	0.134	0.065	0.095
6/1 09 Oct	Rim	Garnet 1	0.01	0.01	2.78	2.31	4.27	33.35	0.02	21.29	0.01	36.74	0.02	100.80	0.00	0.00	0.67	0.40	0.58	4.48	0.00	4.03	0.00	5.91	0.00	16.08	0.129	0.065	0.095
7/1 09 Oct	Rim	Garnet 1	0.01	0.00	2.92	2.28	4.23	32.70	0.00	21.28	0.02	36.17	0.03	99.65	0.00	0.00	0.71	0.40	0.58	4.44	0.00	4.07	0.00	5.87	0.00	16.09	0.137	0.065	0.095
8/1 09 Oct	Rim	Garnet 1	0.02	0.00	2.90	2.36	4.25	33.09	0.02	21.16	0.02	36.51	0.04	100.38	0.01	0.00	0.70	0.41	0.58	4.47	0.00	4.03	0.00	5.89	0.00	16.09	0.135	0.066	0.094
1/1 09 Oct	Rim	Garnet 1	0.00	0.00	3.00	2.43	3.83	33.09	0.00	21.19	0.04	36.67	0.03	100.28	0.00	0.00	0.72	0.42	0.52	4.46	0.00	4.03	0.01	5.91	0.00	16.07	0.139	0.068	0.085
2/1 09 Oct	Rim	Garnet 1	0.01	0.00	2.96	2.34	3.77	32.78	0.00	21.15	0.03	36.74	0.03	99.80	0.00	0.00	0.71	0.41	0.52	4.43	0.00	4.03	0.00	5.94	0.00	16.04	0.139	0.067	0.085
25/1 10 Oct	Rim	Garnet 2	0.01	0.00	2.99	2.42	3.93	33.04	0.00	21.29	0.05	37.00	0.02	100.76	0.00	0.00	0.72	0.42	0.53	4.43	0.00	4.02	0.01	5.93	0.00	16.06	0.139	0.068	0.088
26/1 10 Oct	Rim	Garnet 2	0.02	0.01	2.98	2.41	3.71	32.69	0.00	21.33	0.04	37.27	0.02	100.47	0.01	0.00	0.71	0.41	0.50	4.38	0.00	4.03	0.01	5.97	0.00	16.02	0.140	0.069	0.084
59/1 10 Oct	Rim	Garnet 3	0.02	0.00	3.01	2.32	3.96	33.12	0.00	21.55	0.00	36.66	0.01	100.65	0.01	0.00	0.72	0.40	0.54	4.45	0.00	4.08	0.00	5.89	0.00	16.08	0.140	0.065	0.088
60/1 10 Oct	Rim	Garnet 3	0.01	0.00	3.00	2.37	4.17	32.54	0.01	21.45	0.01	37.09	0.02	100.66	0.00	0.00	0.72	0.41	0.57	4.36	0.00	4.05	0.00	5.94	0.00	16.04	0.141	0.067	0.093
49/1 10 Oct	Rim	Garnet 3	0.01	0.00	2.99	2.40	3.85	33.07	0.00	21.41	0.02	37.07	0.03	100.85	0.00	0.00	0.71	0.41	0.52	4.43	0.00	4.04	0.00	5.93	0.00	16.05	0.139	0.068	0.086
50/1 10 Oct	Rim	Garnet 3	0.00	0.00	2.94	2.29	3.82	32.92	0.00	21.31	0.01	37.20	0.01	100.49	0.00	0.00	0.70	0.39	0.52	4.41	0.00	4.03	0.00	5.96	0.00	16.02	0.137	0.065	0.086
15/1 09 Oct	Rim	Garnet 4	0.02	0.02	2.61	2.43	4.25	32.61	0.00	21.36	0.02	37.06	0.02	100.38	0.01	0.00	0.63	0.42	0.58	4.38	0.00	4.05	0.00	5.96	0.00	16.02	0.125	0.070	0.096
16/1 09 Oct	Rim	Garnet 4	0.02	0.02	2.65	2.40	4.22	32.67	0.00	21.29	0.03	37.22	0.02	100.54	0.01	0.00	0.63	0.41	0.57	4.38	0.00	4.03	0.00	5.97	0.00	16.02	0.126	0.069	0.095
9/1 09 Oct	Core	Garnet 1	0.02	0.00	2.12	2.42	8.29	28.79	0.01	21.03	0.02	36.81	0.51	100.01	0.01	0.00	0.51	0.42	1.14	3.89	0.00	4.01	0.00	5.95	0.06	15.99	0.116	0.070	0.191
10/1 09 Oct	Core	Garnet 1	0.02	0.00	2.20	2.33	8.48	29.34	0.00	20.98	0.02	36.88	0.10	100.37	0.01	0.00	0.53	0.40	1.16	3.96	0.00	3.99	0.00	5.96	0.01	16.04	0.118	0.067	0.192
11/1 09 Oct	Core	Garnet 1	0.01	0.00	2.33	2.40	7.64	29.54	0.02	21.20	0.01	36.19	0.14	99.47	0.00	0.00	0.57	0.42	1.05	4.02	0.00	4.07	0.00	5.90	0.02	16.05	0.123	0.069	0.174
12/1 09 Oct	Core	Garnet 1	0.00	0.00	2.30	2.62	7.62	30.35	0.00	21.20	0.00	36.85	0.05	101.00	0.00	0.00	0.55	0.45	1.04	4.08	0.00	4.02	0.00	5.92	0.01	16.07	0.119	0.074	0.169
19/1 09 Oct	Core	Garnet 1	0.02	0.00	2.34	2.47	7.72	29.99	0.00	21.02	0.02	37.11	0.17	100.87	0.01	0.00	0.56	0.43	1.05	4.03	0.00	3.98	0.00	5.96	0.02	16.03	0.122	0.070	0.173
29/1 10 Oct	Core	Garnet 2	0.01	0.00	2.53	2.44	5.59	31.22	0.01	21.19	0.03	37.13	0.10	100.27	0.00	0.00	0.61	0.42	0.76	4.20	0.00	4.02	0.00	5.97	0.01	16.00	0.126	0.070	0.127
30/1 10 Oct	Core	Garnet 2	0.00	0.00	2.52	2.28	5.77	31.84	0.00	21.15	0.05	36.95	0.10	100.65	0.00	0.00	0.60	0.39	0.79	4.28	0.00	4.01	0.01	5.94	0.01	16.04	0.124	0.065	0.130
55/1 10 Oct	Core	Garnet 3	0.01	0.00	2.25	2.49	8.11	29.78	0.00	21.19	0.00	36.57	0.12	100.52	0.00	0.00	0.54	0.43	1.11	4.02	0.00	4.03	0.00	5.91	0.02	16.06	0.119	0.070	0.182

Sample Name	Core/Rim	Garnet Number	Na_2O	K_2O	MgO	CaO	MnO	FeO	NiO	Al_2O_3	Cr_2O_3	SiO_2	TiO_2	Total	Na	K	Mg	Ca	Mn	Fe	Ni	Al	Cr	Si	Ti	Total	**XMg(Gt)** (Mg/Mg+Fe)	**XCa(Gt)** Ca/Ca+Mg+Fe+Mn	**XMn(Gt)** Mn/Ca+Mg+Fe+Mn
56/1 10 Oct	Core	Garnet 3	0.02	0.00	2.19	2.32	8.20	29.44	0.00	21.09	0.03	36.64	0.15	100.07	0.01	0.00	0.53	0.40	1.13	3.99	0.00	4.03	0.00	5.94	0.02	16.03	0.117	0.067	0.186
58/1 10 Oct	Core	Garnet 3	0.02	0.01	2.25	2.36	8.13	29.66	0.00	21.38	0.02	36.45	0.14	100.41	0.01	0.00	0.54	0.41	1.11	4.01	0.00	4.07	0.00	5.89	0.02	16.06	0.119	0.067	0.183
13/1 09 Oct	Core	Garnet 4	0.00	0.00	2.98	2.34	3.72	33.16	0.00	21.44	0.03	36.85	0.02	100.55	0.00	0.00	0.71	0.40	0.51	4.45	0.00	4.06	0.00	5.92	0.00	16.05	0.138	0.066	0.083
14/1 09 Oct	Core	Garnet 4	0.02	0.00	2.96	2.34	3.75	32.65	0.01	21.36	0.02	37.33	0.02	100.46	0.01	0.00	0.71	0.40	0.51	4.37	0.00	4.03	0.00	5.98	0.00	16.01	0.139	0.067	0.085
3/1 09 Oct*	Rim	Garnet 1	0.00	0.02	2.74	2.47	4.31	32.70	0.01	21.44	0.01	35.96	0.02	99.67	0.00	0.00	0.66	0.43	0.59	4.45	0.00	4.11	0.00	5.85	0.00	16.10	0.130	0.070	0.097
4/1 09 Oct*	Rim	Garnet 1	0.00	0.02	2.44	3.03	4.82	32.11	0.00	20.97	0.02	36.40	0.03	99.83	0.00	0.01	0.59	0.53	0.66	4.36	0.00	4.01	0.00	5.91	0.00	16.08	0.119	0.086	0.108

Table A3.8. Analyses of biotite chosen for geothermometry in BJD102B. Cationic proportions of biotite are recalculated on the basis of 22 oxygens, anhydrous conditions. Close denotes biotite analysis within ~2mm of garnet rim; Far denotes matrix biotite analysis >>2mm from garnet porphyroblasts. – denotes element not analysed. Note little difference in composition was found between biotite analyses throughout the sample.

Sample Number	Associated Garnet	Far/Close?	Cl	F	Na_2O	K_2O	MgO	CaO	MnO	FeO	NiO	Al_2O_3	Cr_2O_3	SiO_2	TiO_2	Total	Si	Ti	Al	Fe^{2+}	Mn	Mg	Ca	Na	K	Total	Mg/Mg+Fe
1/1 09 Oct	Garnet 1	Close	-	0.09	0.13	8.70	11.13	0.12	0.13	22.17	0.02	16.74	0.03	35.19	1.73	96.18	5.39	0.20	3.02	2.84	0.02	2.54	0.02	0.04	1.70	15.76	0.472
2/1 09 Oct	Garnet 1	Close	-	0.12	0.09	9.09	10.98	0.11	0.13	21.94	0.03	16.82	0.05	35.30	1.80	96.44	5.40	0.21	3.03	2.80	0.02	2.50	0.02	0.03	1.77	15.77	0.471
1/1 22 Oct	Garnet 1	Close	0.07	0.00	0.36	8.68	11.00	0.05	0.08	20.99	0.03	18.02	0.01	36.42	1.85	97.56	5.43	0.21	3.17	2.62	0.01	2.45	0.01	0.10	1.65	15.65	0.483
2/1 22 Oct	Garnet 1	Close	0.06	0.00	0.31	8.68	10.90	0.05	0.09	21.20	0.02	17.71	0.03	36.65	1.81	97.50	5.47	0.20	3.12	2.65	0.01	2.43	0.01	0.09	1.65	15.63	0.478
3/1 22 Oct	Garnet 1	Close	0.09	0.00	0.31	8.30	11.04	0.04	0.12	21.11	0.02	17.96	0.02	36.80	1.82	97.64	5.47	0.20	3.15	2.62	0.02	2.45	0.01	0.09	1.57	15.58	0.482
4/1 22 Oct	Garnet 1	Close	0.06	0.00	0.32	8.72	11.07	0.02	0.11	21.03	0.01	17.86	0.04	35.70	1.86	96.81	5.38	0.21	3.17	2.65	0.01	2.49	0.00	0.09	1.68	15.70	0.484
5/1 22 Oct	Garnet 1	Close	0.08	0.00	0.34	8.68	10.62	0.03	0.14	21.93	0.03	18.52	0.04	36.00	1.84	98.27	5.36	0.21	3.25	2.73	0.02	2.36	0.00	0.10	1.65	15.68	0.463
21/1 22 Oct	Garnet 2	Close	0.09	0.00	0.06	8.51	10.90	0.04	0.10	21.26	0.04	17.62	0.04	35.39	1.95	96.01	5.39	0.22	3.16	2.71	0.01	2.47	0.01	0.02	1.65	15.64	0.478
22/1 22 Oct	Garnet 2	Close	0.09	0.01	0.25	8.22	10.42	0.02	0.13	20.54	0.03	18.29	0.03	36.85	1.92	96.78	5.50	0.22	3.22	2.57	0.02	2.32	0.00	0.07	1.57	15.49	0.475

Sample Number	Associated Garnet	Far/Close?	Cl	F	Na_2O	K_2O	MgO	CaO	MnO	FeO	NiO	Al_2O_3	Cr_2O_3	SiO_2	TiO_2	Total	Si	Ti	Al	Fe^{2+}	Mn	Mg	Ca	Na	K	Total	Mg/Mg+Fe
23/1 22 Oct	Garnet 2	Close	0.04	0.00	0.25	7.80	10.55	0.03	0.12	20.11	0.03	17.60	0.00	37.25	1.99	95.77	5.59	0.22	3.11	2.53	0.02	2.36	0.00	0.07	1.49	15.41	0.483
24/1 22 Oct	Garnet 2	Close	0.10	0.00	0.39	7.74	10.92	0.02	0.12	20.80	0.02	18.30	0.03	36.41	1.92	96.78	5.44	0.22	3.22	2.60	0.02	2.43	0.00	0.11	1.48	15.52	0.483
25/1 22 Oct	Garnet 2	Close	0.06	0.00	0.26	8.37	10.37	0.02	0.13	20.37	0.01	18.22	0.02	37.15	1.90	96.89	5.54	0.21	3.20	2.54	0.02	2.30	0.00	0.08	1.59	15.48	0.476
15/1 22 Oct	Garnet 3	Close	0.07	0.00	0.31	8.69	10.74	0.02	0.11	20.98	0.01	17.23	0.02	35.21	1.85	95.24	5.41	0.21	3.12	2.70	0.01	2.46	0.00	0.09	1.70	15.71	0.477
16/1 22 Oct	Garnet 3	Close	0.08	0.01	0.26	8.35	10.74	0.01	0.11	20.24	0.02	17.72	0.01	36.40	1.82	95.75	5.50	0.21	3.16	2.56	0.01	2.42	0.00	0.08	1.61	15.55	0.486
17/1 22 Oct	Garnet 3	Close	0.12	0.01	0.21	8.08	10.85	0.02	0.13	21.44	0.03	17.65	0.00	35.20	1.84	95.57	5.38	0.21	3.18	2.74	0.02	2.47	0.00	0.06	1.58	15.64	0.474
20/1 22 Oct	Garnet 2	Close	0.09	0.01	0.29	8.41	10.78	0.02	0.11	20.26	0.02	17.91	0.02	36.41	1.87	96.18	5.48	0.21	3.18	2.55	0.01	2.42	0.00	0.08	1.62	15.56	0.487
17/1 09 Oct	Garnet 4	Close	-	0.09	0.28	8.56	11.12	0.05	0.13	21.00	0.00	18.50	0.04	36.60	1.71	98.08	5.42	0.19	3.23	2.60	0.02	2.45	0.01	0.08	1.62	15.62	0.486
20/1 09 Oct	Garnet 4	Close	-	0.05	0.31	9.02	10.94	0.05	0.12	20.26	0.02	18.21	0.05	36.96	1.74	97.72	5.48	0.19	3.18	2.51	0.02	2.42	0.01	0.09	1.71	15.62	0.490
23/1 09 Oct	Garnet 4	Close	-	0.10	0.34	9.03	11.10	0.04	0.10	20.46	0.01	18.31	0.03	36.71	1.76	97.99	5.44	0.20	3.20	2.54	0.01	2.45	0.01	0.10	1.71	15.66	0.492
21/1 09 Oct	Garnet 4	Far	-	0.10	0.33	9.24	11.17	0.02	0.11	20.45	0.00	18.43	0.04	36.83	1.78	98.50	5.44	0.20	3.21	2.52	0.01	2.46	0.00	0.09	1.74	15.68	0.493
22/1 09 Oct	Garnet 4	Far	-	0.09	0.31	9.14	11.08	0.04	0.11	20.57	0.02	17.97	0.03	36.55	1.76	97.69	5.45	0.20	3.16	2.57	0.01	2.46	0.01	0.09	1.74	15.69	0.490
6/1 22 Oct	Garnet 1 & 2	Far	0.09	0.01	0.31	8.58	10.70	0.12	0.13	20.64	0.01	18.68	0.01	36.09	1.82	97.21	5.39	0.20	3.29	2.58	0.02	2.38	0.02	0.09	1.64	15.62	0.480
7/1 22 Oct	Garnet 1 & 2	Far	0.07	0.01	0.19	7.92	10.56	0.11	0.14	21.49	0.02	18.15	0.01	35.19	1.91	95.77	5.36	0.22	3.26	2.74	0.02	2.40	0.02	0.06	1.54	15.59	0.467
8/1 22 Oct	Garnet 1 & 2	Far	0.08	0.00	0.31	8.83	10.91	0.02	0.11	19.94	0.03	17.54	0.02	35.50	1.93	95.24	5.43	0.22	3.16	2.55	0.01	2.49	0.00	0.09	1.72	15.68	0.494
9/1 22 Oct	Garnet 1 & 2	Far	0.09	0.01	0.32	8.88	10.77	0.02	0.11	21.20	0.02	17.75	0.01	36.00	1.92	97.09	5.42	0.22	3.15	2.67	0.01	2.42	0.00	0.09	1.71	15.69	0.475
11/1 22 Oct	Garnet 1 & 2	Far	0.08	0.00	0.44	8.61	10.72	0.01	0.12	20.32	0.03	18.12	0.00	35.78	1.92	96.16	5.41	0.22	3.23	2.57	0.02	2.42	0.00	0.13	1.66	15.65	0.485
12/1 22 Oct	Garnet 1 & 2	Far	0.05	0.00	0.28	8.54	10.92	0.03	0.12	20.66	0.03	17.49	0.07	37.15	1.88	97.21	5.54	0.21	3.07	2.58	0.02	2.43	0.00	0.08	1.62	15.56	0.485
14/1 22 Oct	Garnet 1 & 2	Far	0.08	0.01	0.31	8.71	10.95	0.03	0.11	20.27	0.00	17.86	0.09	36.07	1.94	96.42	5.44	0.22	3.17	2.55	0.01	2.46	0.00	0.09	1.67	15.64	0.491
18/1 22 Oct	Garnet 3	Far	0.06	0.01	0.41	8.53	10.52	0.03	0.12	20.30	0.00	17.58	0.01	36.60	1.87	96.04	5.53	0.21	3.13	2.56	0.02	2.37	0.00	0.12	1.64	15.58	0.480
19/1 22 Oct	Garnet 3	Far	0.08	0.00	0.38	8.22	10.90	0.04	0.13	20.13	0.02	18.26	0.01	35.74	1.90	95.81	5.40	0.22	3.25	2.55	0.02	2.46	0.01	0.11	1.59	15.60	0.491

Table A3.9. (Previous page) Molar fractions of garnet and biotite pairs chosen for geothermometry in sample BJD102B. Molar fraction equations are from Ferry and Spear (1978) (=FS) and Perchuk and Lavrent'eva (1983) (=P&L83B). Distribution coefficients (Kd) and temperatures (T in°C) are calculated using the calibrations of Ferry and Spear (1978) (T(FS)), Lavrent'eva and Perchuk (1981) (T(PL81)), Pigage and Greenwood (1980) (T(PG)), Thompson (1976) (T(Th)), Holdaway and Lee (1977) (T(HL)) and Perchuk and Lavrent'eva (1983) (T(PL83A)) and (T(PL83B)).

Sample Pair	Garnet Sample	Biotite sample	Gt/Bt Pairing	XMg(grt)	XMg(grt) P&L83B	XCa(grt)	XMn(grt)	XMg(Bt)	XMg(Bt) P&L 83	Pressure (kbar)	log Kd	Log Kd P & L 83	T(FS)	T(PL81)	T(PG)	T(Th)	T(HL)	T(PL) 83A	T(PL) 83B
Garnet 1 Pair A	5/1 09 Oct	1/1 09 Oct	Rim/Close	0.1343	0.1206	0.0646	0.0950	0.4723	0.4708	2.5	1.7527	1.8694	561	585	650	572	565	571	559
Garnet 1 Pair B	6/1 09 Oct	2/1 09 Oct	Rim/Close	0.1292	0.1161	0.0650	0.0948	0.4715	0.4700	2.5	1.7941	1.9100	547	578	635	561	556	563	552
Garnet 1 Pair C	7/1 09 Oct	1/1 22 Oct	Rim/Close	0.1373	0.1234	0.0648	0.0951	0.4830	0.4820	2.5	1.7695	1.8890	555	582	644	568	561	568	555
Garnet 1 Pair D	8/1 09 Oct	2/1 22 Oct	Rim/Close	0.1350	0.1213	0.0665	0.0944	0.4782	0.4771	2.5	1.7703	1.8883	555	583	645	567	561	568	556
Garnet 1 Pair E	7/1 09 Oct	3/1 22 Oct	Rim/Close	0.1373	0.1234	0.0648	0.0951	0.4825	0.4810	2.5	1.7674	1.8850	556	582	645	568	562	568	556
Garnet 1 Pair F	8/1 09 Oct	3/1 22 Oct	Rim/Close	0.1350	0.1213	0.0665	0.0944	0.4825	0.4810	2.5	1.7873	1.9038	549	580	639	563	557	565	553
Garnet 1 Pair G	1/1 09 Oct	4/1 22 Oct	Rim/Close	0.1393	0.1266	0.0684	0.0854	0.4841	0.4828	2.5	1.7572	1.8628	559	586	646	571	564	570	560
Garnet 1 Pair H	2/1 09 Oct	4/1 22 Oct	Rim/Close	0.1386	0.1260	0.0668	0.0851	0.4841	0.4828	2.5	1.7632	1.8681	557	584	643	569	563	569	559
Garnet 1 Pair I	9/1 09 Oct	21/1 09 Oct	Core/Far	0.1158	0.0921	0.0705	0.1905	0.4933	0.4920	2.5	2.0058	2.2562	485	544	615	512	512	527	496
Garnet 1 Pair J	10/1 09 Oct	22/1 09 Oct	Core/Far	0.1181	0.0939	0.0667	0.1916	0.4898	0.4885	2.5	1.9696	2.2211	495	548	625	520	519	533	501
Garnet 1 Pair K	11/1 09 Oct	8/1 22 Oct	Core/Far	0.1231	0.1001	0.0690	0.1739	0.4937	0.4924	2.5	1.9382	2.1653	504	554	628	527	525	538	510
Garnet 1 Pair L	12/1 09 Oct	11/1 22 Oct	Core/Far	0.1188	0.0971	0.0739	0.1695	0.4846	0.4832	2.5	1.9425	2.1630	503	556	627	526	524	538	510
Garnet 1 Pair M	19/1 09 Oct	12/1 22 Oct	Core/Far	0.1222	0.0995	0.0702	0.1731	0.4851	0.4837	2.5	1.9117	2.1375	511	559	637	533	531	543	514
Garnet 1 Pair N	19/1 09 Oct	14/1 22 Oct	Core/Far	0.1222	0.0995	0.0702	0.1731	0.4906	0.4892	2.5	1.9335	2.1597	505	556	630	528	526	539	510
Garnet 2 Pair A	25/1 10 Oct	21/1 22 Oct	Rim/Close	0.1390	0.1259	0.0681	0.0877	0.4775	0.4763	2.5	1.7334	1.8425	567	590	656	577	569	574	564
Garnet 2 Pair B	26/1 10 Oct	22/1 22 Oct	Rim/Close	0.1397	0.1271	0.0688	0.0839	0.4749	0.4733	2.5	1.7171	1.8196	573	594	660	581	573	577	568
Garnet 2 Pair C	25/1 10 Oct	23/1 22 Oct	Rim/Close	0.1390	0.1259	0.0681	0.0877	0.4832	0.4817	2.5	1.7564	1.8642	559	586	647	571	564	570	560

Sample Pair	Garnet Sample	Biotite sample	Gt/Bt Pairing	XMg(grt)	XMg(grt) P&L83B	XCa(grt)	XMn(grt)	XMg(Bt)	XMg(Bt) P&L 83	Pressure (Kbar)	log Kd	Log Kd P & L 83	T(FS)	T(PL81)	T(PG)	T(Th)	T(HL)	T(PL83A)	T(PL83B)
Garnet 2 Pair D	26/1 10 Oct	24/1 22 Oct	Rim/Close	0.1397	0.1271	0.0688	0.0839	0.4834	0.4820	2.5	1.7514	1.8545	561	587	648	572	565	571	562
Garnet 2 Pair E	25/1 10 Oct	25/1 22 Oct	Rim/Close	0.1390	0.1259	0.0681	0.0877	0.4757	0.4741	2.5	1.7263	1.8337	569	592	658	579	571	576	565
Garnet 2 Pair F	26/1 10 Oct	25/1 22 Oct	Rim/Close	0.1397	0.1271	0.0688	0.0839	0.4868	0.4741	2.5	1.7648	1.8231	557	585	643	569	562	569	567
Garnet 2 Pair G	29/1 10 Oct	8/1 22 Oct	Core/Far	0.1261	0.1088	0.0703	0.1271	0.4937	0.4924	2.5	1.9112	2.0721	512	560	615	533	531	543	524
Garnet 2 Pair H	30/1 10 Oct	11/1 22 Oct	Core/Far	0.1236	0.1065	0.0648	0.1297	0.4846	0.4832	2.5	1.8974	2.0601	516	559	617	536	534	545	526
Garnet 2 Pair I	29/1 10 Oct	12/1 22 Oct	Core/Far	0.1261	0.1088	0.0703	0.1271	0.4851	0.4837	2.5	1.8766	2.0373	522	566	626	541	538	549	530
Garnet 2 Pair J	30/1 10 Oct	14/1 22 Oct	Core/Far	0.1236	0.1065	0.0648	0.1297	0.4906	0.4892	2.5	1.9211	2.0843	509	555	610	531	529	541	522
Garnet 2 Pair K	29/1 10 Oct	18/1 22 Oct	Core/Far	0.1261	0.1088	0.0703	0.1271	0.4802	0.4787	2.5	1.8569	2.0174	528	569	633	546	542	552	533
Garnet 2 Pair L	30/1 10 Oct	19/1 22 Oct	Core/Far	0.1236	0.1065	0.0648	0.1297	0.4912	0.4895	2.5	1.9234	2.0856	508	555	609	530	528	541	522
Garnet 3 Pair A	59/1 10 Oct	15/1 22 Oct	Rim/Close	0.1395	0.1264	0.0654	0.0881	0.4771	0.4758	2.5	1.7278	1.8367	569	590	656	578	571	575	565
Garnet 3 Pair B	60/1 10 Oct	16/1 22 Oct	Rim/Close	0.1410	0.1269	0.0674	0.0935	0.4861	0.4847	2.5	1.7514	1.8679	561	587	652	572	565	571	559
Garnet 3 Pair C	49/1 10 Oct	17/1 22 Oct	Rim/Close	0.1388	0.1260	0.0679	0.0858	0.4743	0.4727	2.5	1.7225	1.8277	571	592	659	580	572	576	566
Garnet 3 Pair D	50/1 10 Oct	15/1 22 Oct	Rim/Close	0.1372	0.1246	0.0654	0.0859	0.4771	0.4758	2.5	1.7468	1.8525	563	586	648	573	566	572	562
Garnet 3 Pair D	55/1 10 Oct	18/1 22 Oct	Core/Far	0.1187	0.0955	0.0704	0.1818	0.4802	0.4787	2.5	1.9252	2.1629	508	557	637	530	528	541	510
Garnet 3 Pair E	56/1 10 Oct	19/1 22 Oct	Core/Far	0.1169	0.0936	0.0665	0.1861	0.4912	0.4895	2.5	1.9868	2.2287	490	545	616	516	515	530	500
Garnet 3 Pair F	58/1 10 Oct	18/1 22 Oct	Core/Far	0.1189	0.0956	0.0674	0.1832	0.4802	0.4787	2.5	1.9233	2.1622	508	556	636	530	528	541	510
Garnet 4 Pairs A	15/1 09 Oct	17/1 09 Oct	Rim/Close	0.1248	0.1119	0.0696	0.0964	0.4856	0.4840	2.5	1.8900	2.0078	518	563	606	538	535	547	535
Garnet 4 Pairs B	16/1 09 Oct	20/1 09 Oct	Rim/Close	0.1263	0.1134	0.0686	0.0955	0.4905	0.4890	2.5	1.8955	2.0123	516	561	604	537	534	546	534
Garnet 4 Pairs C	15/1 09 Oct	23/1 09 Oct	Rim/Close	0.1248	0.1119	0.0696	0.0964	0.4916	0.4904	2.5	1.9143	2.0334	511	559	598	532	530	542	531
Garnet 4 Pairs D	13/1 09 Oct	21/1 09 Oct	Core/Far	0.1379	0.1256	0.0664	0.0832	0.4933	0.4920	2.5	1.8063	1.9083	543	576	626	558	553	561	552
Garnet 4 Pairs E	14/1 09 Oct	22/1 09 Oct	Core/Far	0.1390	0.1264	0.0671	0.0848	0.4898	0.4885	2.5	1.7827	1.8872	551	581	636	564	558	565	556

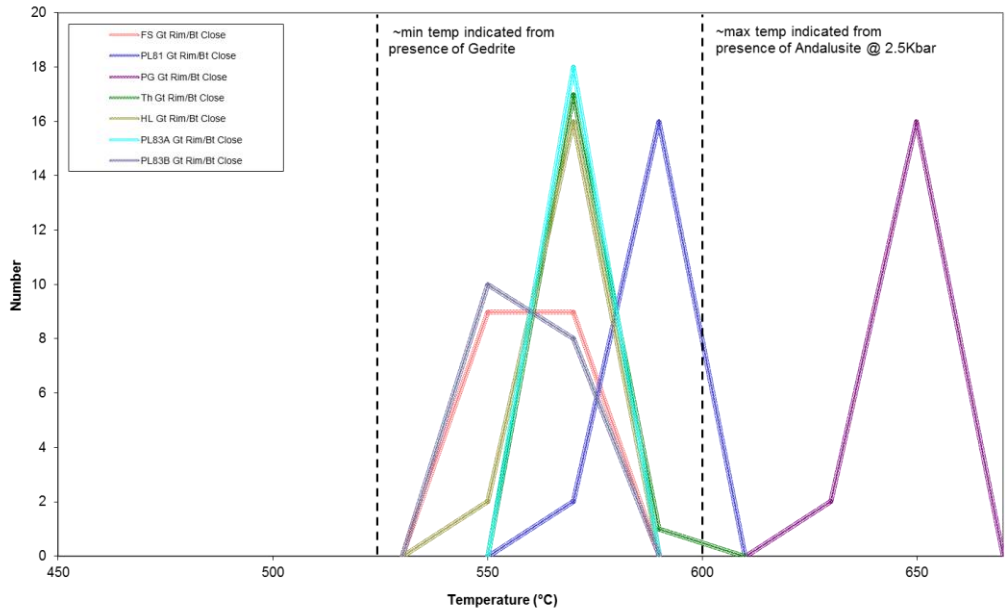

Figure A3.1 Histogram of all rim garnet-biotite close pairs for BJD102B. Histogram bin width = 20°C, n = 18.

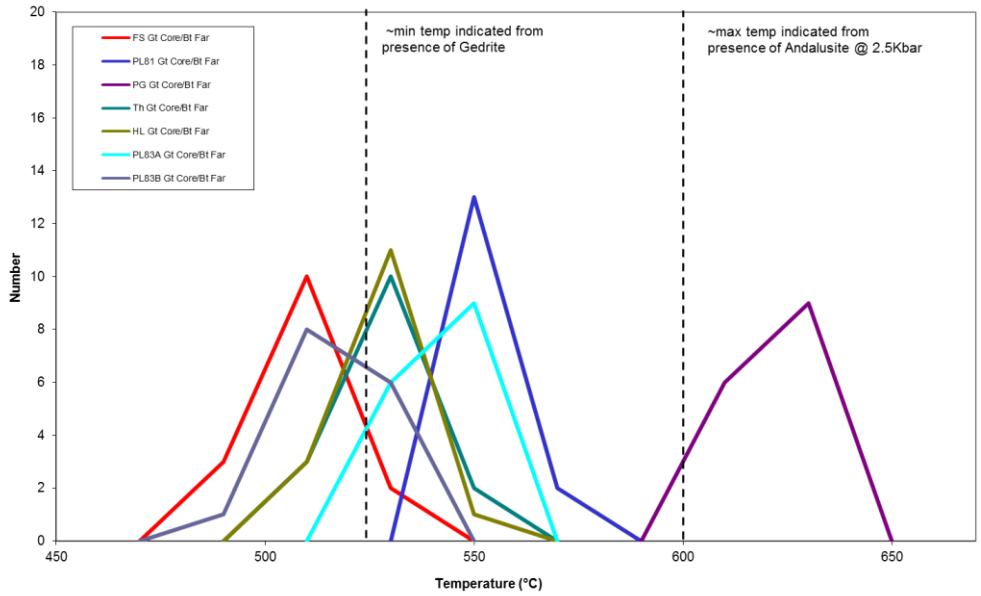

Figure A3.2 Histogram of all core garnet-biotite far pairs for BJD102B. Histogram bin width = 20°C, n = 15.

A3.6 Sample AMD310Q

Sample	Core /Rim	Average Almandine %	Average Grossular %	Average Pyrope %	Average Spessartine %	Average Gro + Spess %	Average Garnet composition
AMD310Q	All	75.85	5.64	8.45	10.07	15.71	$Alm_{76}Gro_{6}Py_{8}Sp_{10}$

Table A3.10. Average composition of garnet within AMD310Q.

Table A3.11. AMD310Q - Analyses of garnet chosen for geothermometry in this study. Cationic proportions of garnets are recalculated on the basis of 24 oxygens, anhydrous conditions.

Sample Name	Core/ Rim	Garnet Number	Na_2O	K_2O	MgO	CaO	MnO	FeO	NiO	Al_2O_3	Cr_2O_3	SiO_2	TiO_2	Total	Na	K	Mg	Ca	Mn	Fe	Al	Cr	Si	Ti	Total	**XMg(Gt)** (Mg/Mg+Fe)	**XCa(Gt)** Ca/Ca+Mg+Fe+Mn	**XMn(Gt)** Mn/Ca+Mg+Fe+Mn
1 / 1 24 Oct	Rim	Garnet 2	0.00	0.00	2.05	1.64	4.49	34.13	0.00	20.99	0.01	36.60	0.01	99.91	0.00	0.00	0.50	0.29	0.62	4.64	4.03	0.00	5.96	0.00	16.03	0.097	0.047	0.102
2 / 1 24 Oct	Rim	Garnet 2	0.03	0.00	2.07	1.66	4.55	34.31	0.00	21.13	0.02	36.89	0.00	100.66	0.01	0.00	0.50	0.29	0.62	4.63	4.02	0.00	5.96	0.00	16.03	0.097	0.048	0.103
5 / 1 24 Oct	Rim	Garnet 3	0.02	0.00	1.95	1.70	4.71	33.74	0.00	21.03	0.00	37.09	0.01	100.24	0.01	0.00	0.47	0.29	0.65	4.57	4.01	0.00	6.00	0.00	16.00	0.093	0.049	0.108
6 / 1 24 Oct	Rim	Garnet 3	0.02	0.00	1.97	1.73	4.56	33.96	0.00	20.87	0.01	36.93	0.00	100.06	0.01	0.00	0.48	0.30	0.63	4.61	3.99	0.00	6.00	0.00	16.01	0.094	0.050	0.104
11 / 1 24 Oct	Rim	Garnet 5	0.01	0.00	2.01	1.75	4.59	33.82	0.00	21.11	0.01	36.67	0.01	99.99	0.00	0.00	0.49	0.30	0.63	4.59	4.04	0.00	5.96	0.00	16.02	0.096	0.051	0.105
12 / 1 24 Oct	Rim	Garnet 5	0.00	0.00	1.96	1.64	4.80	33.99	0.00	21.03	0.01	36.55	0.01	100.00	0.00	0.00	0.48	0.29	0.66	4.63	4.03	0.00	5.95	0.00	16.03	0.093	0.047	0.109
15 / 1 24 Oct	Rim	Garnet 6	0.01	0.00	2.01	1.59	4.61	33.97	0.00	21.20	0.00	37.26	0.00	100.64	0.00	0.00	0.48	0.27	0.63	4.58	4.02	0.00	6.00	0.00	15.99	0.095	0.046	0.105
16 / 1 24 Oct	Rim	Garnet 6	0.02	0.00	2.05	1.65	4.73	33.97	0.00	21.14	0.02	36.93	0.00	100.52	0.01	0.00	0.49	0.29	0.65	4.59	4.03	0.00	5.97	0.00	16.02	0.097	0.047	0.108
3 / 1 11 Oct	Rim	Garnet 1	0.00	0.00	2.19	1.67	4.53	34.33	0.00	21.34	0.00	36.50	0.01	100.58	0.00	0.00	0.53	0.29	0.62	4.64	4.07	0.00	5.91	0.00	16.06	0.102	0.048	0.102
5 / 1 11 Oct	Rim	Garnet 1	0.02	0.00	1.88	1.66	5.10	34.19	0.00	21.13	0.00	36.30	0.01	100.31	0.01	0.00	0.46	0.29	0.70	4.65	4.05	0.00	5.91	0.00	16.07	0.089	0.048	0.115
18 / 1 11 Oct	Rim	Garnet 1	0.02	0.01	1.81	1.63	5.05	33.74	0.00	21.26	0.00	36.37	0.01	99.91	0.01	0.00	0.44	0.28	0.70	4.60	4.08	0.00	5.93	0.00	16.04	0.088	0.047	0.116
19 / 1 11 Oct	Rim	Garnet 1	0.01	0.01	2.06	1.74	4.76	34.04	0.00	21.24	0.02	37.08	0.01	100.96	0.00	0.00	0.49	0.30	0.65	4.58	4.03	0.00	5.97	0.00	16.02	0.097	0.050	0.108
3 / 1 24 Oct	Core	Garnet 2	0.00	0.01	2.09	2.01	4.40	33.54	0.00	20.90	0.01	37.07	0.02	100.05	0.00	0.00	0.50	0.35	0.60	4.54	3.99	0.00	6.00	0.00	16.00	0.100	0.058	0.101
4 / 1 24 Oct	Core	Garnet 2	0.02	0.00	2.04	2.05	4.26	33.84	0.00	21.04	0.02	36.97	0.01	100.26	0.01	0.00	0.49	0.36	0.58	4.58	4.01	0.00	5.98	0.00	16.01	0.097	0.059	0.097
7 / 1 24 Oct	Core	Garnet 3	0.04	0.00	2.17	1.96	3.93	34.25	0.01	21.00	0.02	36.86	0.01	100.25	0.01	0.00	0.52	0.34	0.54	4.64	4.01	0.00	5.97	0.00	16.03	0.101	0.056	0.089
8 / 1 24 Oct	Core	Garnet 3	0.01	0.00	2.21	1.92	4.06	34.07	0.00	21.12	0.01	36.89	0.02	100.31	0.00	0.00	0.53	0.33	0.56	4.61	4.02	0.00	5.96	0.00	16.02	0.104	0.055	0.092
9 / 1 24 Oct	Core	Garnet 5	0.01	0.00	2.06	2.02	4.52	33.90	0.02	20.96	0.10	36.92	0.03	100.53	0.00	0.00	0.50	0.35	0.62	4.58	3.99	0.01	5.97	0.00	16.03	0.098	0.058	0.102
10 / 1 24 Oct	Core	Garnet 5	0.02	0.00	2.04	1.92	4.66	33.80	0.00	20.78	0.12	37.34	0.05	100.73	0.01	0.00	0.49	0.33	0.64	4.55	3.95	0.02	6.02	0.01	16.00	0.097	0.055	0.106
13 / 1 24 Oct	Core	Garnet 6	0.02	0.00	2.07	1.90	4.38	33.67	0.01	21.04	0.03	37.10	0.06	100.28	0.01	0.00	0.50	0.33	0.60	4.55	4.01	0.00	5.99	0.01	16.00	0.099	0.055	0.100
14 / 1 24 Oct	Core	Garnet 6	0.01	0.00	2.12	1.93	4.43	34.11	0.00	21.08	0.02	36.99	0.05	100.74	0.00	0.00	0.51	0.33	0.60	4.60	4.01	0.00	5.96	0.01	16.03	0.100	0.055	0.100
1 / 1 11 Oct	Core	Garnet 1	0.02	0.00	2.09	1.87	4.89	33.71	0.00	21.08	0.03	37.15	0.04	100.88	0.01	0.00	0.50	0.32	0.67	4.54	4.00	0.00	5.98	0.01	16.02	0.100	0.053	0.111
2 / 1 11 Oct	Core	Garnet 1	0.01	0.00	2.11	1.92	4.54	33.90	0.00	21.09	0.02	37.12	0.02	100.73	0.00	0.00	0.51	0.33	0.62	4.57	4.01	0.00	5.98	0.00	16.02	0.100	0.055	0.103

Table A3.12. AMD310Q Analyses of biotite chosen for geothermometry in this study. Cationic proportions of biotite are recalculated on the basis of 22 oxygens, anhydrous conditions.

Sample Number	Associated Garnet	Far/Close?	Cl	F	Na_2O	K_2O	MgO	CaO	MnO	FeO	NiO	Al_2O_3	Cr_2O_3	SiO_2	TiO_2	Total	Si	Ti	Al	Fe^{2+}	Mn	Mg	Ca	Na	K	Total	Mg/Mg+Fe
13 / 1 23 Oct	Garnet 1	Close	0.01	0.06	0.08	7.60	6.97	0.09	0.14	23.04	0.01	19.39	0.02	33.45	2.11	92.95	5.29	0.25	3.61	3.05	0.02	1.64	0.02	0.02	1.53	15.43	0.350
14 / 1 23 Oct	Garnet 1	Close	0.00	0.10	0.09	7.82	6.76	0.03	0.15	22.16	0.01	19.22	0.02	33.39	2.01	91.75	5.34	0.24	3.62	2.96	0.02	1.61	0.01	0.03	1.59	15.42	0.352
16 / 1 23 Oct	Garnet 1	Close	0.01	0.09	0.14	8.05	7.58	0.02	0.11	21.87	0.01	19.08	0.02	34.63	1.90	93.50	5.41	0.22	3.51	2.86	0.01	1.77	0.00	0.04	1.60	15.43	0.382
18 / 1 23 Oct	Garnet 1	Close	0.01	0.09	0.10	7.78	7.08	0.02	0.15	21.61	n.d	19.50	0.02	34.54	1.85	92.74	5.42	0.22	3.61	2.84	0.02	1.66	0.00	0.03	1.56	15.35	0.369
19 / 1 23 Oct	Garnet 1	Close	0.00	0.04	0.12	7.72	7.15	0.02	0.11	22.04	n.d	19.12	0.00	33.96	1.76	92.05	5.39	0.21	3.58	2.93	0.01	1.69	0.00	0.04	1.56	15.41	0.366
20 / 1 23 Oct	Garnet 1	Close	0.01	0.07	0.07	8.48	7.37	0.06	0.13	21.69	n.d	19.28	0.03	34.57	1.51	93.27	5.42	0.18	3.56	2.84	0.02	1.72	0.01	0.02	1.70	15.48	0.377
21 / 1 23 Oct	Garnet 1	Close	0.01	0.05	0.10	7.97	7.06	0.10	0.17	21.41	0.01	19.83	0.03	34.46	1.47	92.66	5.41	0.17	3.67	2.81	0.02	1.65	0.02	0.03	1.60	15.39	0.370
4 / 1 11 Oct	Garnet 1	Close	0.00	0.08	0.04	8.74	7.33	0.06	0.12	23.11	0.01	19.51	0.01	34.55	1.98	95.56	5.33	0.23	3.55	2.98	0.02	1.69	0.01	0.01	1.72	15.53	0.361
6 / 1 11 Oct	Garnet 1	Close	0.00	0.08	0.08	8.62	7.43	0.03	0.13	23.13	0.01	19.78	0.02	34.11	2.03	95.45	5.27	0.24	3.60	2.99	0.02	1.71	0.00	0.02	1.70	15.55	0.364
1 / 1 23 Oct	Garnet 2	Close	0.01	0.04	0.08	8.57	7.18	0.01	0.11	23.00	0.03	18.55	0.03	34.71	1.90	94.21	5.43	0.22	3.42	3.01	0.01	1.67	0.00	0.02	1.71	15.50	0.358
2 / 1 23 Oct	Garnet 2	Close	0.00	0.06	0.11	8.23	6.84	0.01	0.11	22.47	0.01	19.54	0.04	33.67	1.89	93.00	5.32	0.22	3.64	2.97	0.01	1.61	0.00	0.03	1.66	15.48	0.352
3 / 1 23 Oct	Garnet 2	Close	0.01	0.04	0.11	8.21	6.86	0.01	0.15	22.15	0.01	19.15	0.01	34.11	1.80	92.63	5.40	0.21	3.57	2.93	0.02	1.62	0.00	0.03	1.66	15.45	0.356
4 / 1 23 Oct	Garnet 2	Close	0.00	0.07	0.00	8.00	6.66	0.04	0.16	23.43	0.02	19.05	0.04	33.50	1.81	92.78	5.33	0.22	3.57	3.12	0.02	1.58	0.01	0.00	1.62	15.48	0.336
7 / 1 23 Oct	Garnet 2	Close	0.00	0.06	0.19	8.00	7.24	0.02	0.12	21.75	0.03	19.50	0.03	35.19	1.91	94.04	5.45	0.22	3.56	2.82	0.02	1.67	0.00	0.06	1.58	15.37	0.372
9 / 1 23 Oct	Garnet 2	Close	0.00	0.07	0.06	8.21	7.05	0.02	0.16	21.90	0.00	18.62	0.02	34.85	1.96	92.93	5.48	0.23	3.45	2.88	0.02	1.65	0.00	0.02	1.65	15.39	0.365
10 / 1 23 Oct	Garnet 3	Close	0.01	0.10	0.08	7.72	7.28	0.02	0.15	24.70	0.00	19.24	0.01	33.78	1.83	94.92	5.27	0.21	3.54	3.22	0.02	1.69	0.00	0.02	1.54	15.53	0.344
11 / 1 23 Oct	Garnet 3	Close	0.00	0.07	0.01	7.93	7.01	0.02	0.14	22.98	0.01	19.27	0.03	33.44	1.85	92.76	5.31	0.22	3.60	3.05	0.02	1.66	0.00	0.00	1.61	15.47	0.352
12 / 1 23 Oct	Garnet 3	Close	0.01	0.07	0.01	7.60	7.53	0.02	0.11	23.46	0.01	19.02	0.02	32.40	1.81	92.04	5.20	0.22	3.60	3.15	0.01	1.80	0.00	0.00	1.56	15.56	0.364
22 / 1 23 Oct	None	Far	0.00	0.03	0.23	7.96	7.14	0.02	0.12	22.37	0.04	19.78	0.02	34.00	1.91	93.62	5.32	0.22	3.65	2.93	0.02	1.67	0.00	0.07	1.59	15.46	0.363
23 / 1 23 Oct	None	Far	0.01	0.06	0.25	7.42	6.94	0.02	0.13	22.16	0.03	18.90	0.02	33.80	1.92	91.66	5.39	0.23	3.55	2.96	0.02	1.65	0.00	0.08	1.51	15.39	0.358

Sample Number	Associated Garnet	Far/Close?	Cl	F	Na_2O	K_2O	MgO	CaO	MnO	FeO	NiO	Al_2O_3	Cr_2O_3	SiO_2	TiO_2	Total	Si	Ti	Al	Fe^{2+}	Mn	Mg	Ca	Na	K	Total	Mg/Mg+Fe
24 / 1 23 Oct	None	Far	0.00	0.07	0.25	7.74	7.34	0.02	0.12	22.16	0.01	20.02	0.03	34.74	1.95	94.45	5.36	0.23	3.64	2.86	0.02	1.69	0.00	0.07	1.52	15.39	0.371
33 / 1 23 Oct	None	Far	0.00	0.05	0.09	6.73	7.73	0.01	0.12	24.33	0.01	18.74	0.02	32.61	1.91	92.36	5.21	0.23	3.53	3.25	0.02	1.84	0.00	0.03	1.37	15.49	0.362
34 / 1 23 Oct	None	Far	0.01	0.07	0.10	8.17	7.23	0.01	0.13	22.19	0.02	19.08	0.02	33.74	1.93	92.70	5.34	0.23	3.56	2.94	0.02	1.71	0.00	0.03	1.65	15.48	0.367
35 / 1 23 Oct	None	Far	0.00	0.06	0.08	7.75	7.24	0.03	0.13	22.88	0.00	19.85	0.04	33.70	1.92	93.68	5.28	0.23	3.66	3.00	0.02	1.69	0.01	0.02	1.55	15.45	0.361
36 / 1 23 Oct	None	Far	0.01	0.08	0.18	7.96	7.12	0.02	0.13	21.89	0.04	19.48	0.03	34.03	1.76	92.74	5.37	0.21	3.62	2.89	0.02	1.67	0.00	0.06	1.60	15.44	0.367
37 / 1 23 Oct	None	Far	0.00	0.06	0.24	7.67	7.29	0.01	0.11	22.46	0.01	18.91	0.02	34.61	1.81	93.20	5.43	0.21	3.50	2.95	0.01	1.70	0.00	0.07	1.53	15.41	0.367
38 / 1 23 Oct	None	Far	0.00	0.05	0.21	7.64	7.48	0.02	0.13	22.41	0.00	19.58	0.04	34.24	1.75	93.53	5.35	0.21	3.60	2.93	0.02	1.74	0.00	0.06	1.52	15.44	0.373
39 / 1 23 Oct	None	Far	0.01	0.04	0.21	7.61	7.12	0.02	0.14	21.84	0.02	18.76	0.03	34.51	1.94	92.26	5.45	0.23	3.49	2.89	0.02	1.68	0.00	0.06	1.53	15.37	0.368
40 / 1 23 Oct	None	Far	0.01	0.04	0.22	7.47	6.95	0.03	0.12	21.43	0.02	19.33	0.03	33.79	1.90	91.33	5.39	0.23	3.63	2.86	0.02	1.65	0.01	0.07	1.52	15.36	0.366
41 / 1 23 Oct	None	Far	0.00	0.10	0.17	7.86	7.05	0.02	0.15	21.87	0.01	18.98	0.03	33.50	1.99	91.73	5.35	0.24	3.57	2.92	0.02	1.68	0.00	0.05	1.60	15.45	0.365
42 / 1 23 Oct	None	Far	0.00	0.08	0.17	7.68	7.13	0.02	0.14	22.14	n.d	19.58	0.02	33.97	1.60	92.53	5.36	0.19	3.64	2.92	0.02	1.68	0.00	0.05	1.55	15.42	0.365
43 / 1 23 Oct	None	Far	0.01	0.09	0.15	7.93	7.32	0.02	0.12	21.88	-0.01	18.99	0.03	34.75	1.57	92.85	5.46	0.19	3.52	2.88	0.02	1.71	0.00	0.05	1.59	15.41	0.374
44 / 1 23 Oct	None	Far	0.01	0.07	0.13	7.98	7.27	0.02	0.12	22.21	0.01	19.69	0.02	34.19	1.60	93.32	5.36	0.19	3.64	2.91	0.02	1.70	0.00	0.04	1.60	15.45	0.368

Table A3.13. Molar fractions of garnet and biotite pairs chosen for geothermometry in sample AMD310Q. Molar fraction equations are from Ferry and Spear (1978) (=FS) and Perchuk and Lavrent'eva (1983) (=P&L83B). Distribution coefficients (Kd) and temperatures (T in°C) are calculated using the calibrations of Ferry and Spear (1978) (T(FS)), Lavrent'eva and Perchuk (1981) (T(PL81)), Pigage and Greenwood (1980) (T(PG)), Thompson (1976) (T(Th)), Holdaway and Lee (1977) (T(HL)) and Perchuk and Lavrent'eva (1983) (T(PL83A)) and (T(PL83B)).

Sample Pair	Garnet Sample	Biotite sample	XMg(grt)	XMg(grt) P&L83B	XCa(grt)	XMn(grt)	XMg(Bt)	XMg(Bt) P&L 83	Pressure (kbar)	log Kd	Log Kd P & L 83	T(FS)	T(PL81)	T(PG)	T(Th)	T(HL)	T(PL) 83A	T(PL) 83B
Garnet 1 A	3 / 1 11 Oct	13 / 1 23/10/12	0.1023	0.0913	0.0477	0.1019	0.3588	0.3489	2.5	1.5920	1.6740	617	607	705	615	603	601	595

Sample Pair	Garnet Sample	Biotite sample	XMg(grt)	XMg(grt) P&L83B	XCa(grt)	XMn(grt)	XMg(Bt)	XMg(Bt) P&L 83	Pressure (kbar)	log Kd	Log Kd P & L 83	T(FS)	T(PL81)	T(PG)	T(Th)	T(HL)	T(PL) 83A	T(PL) 83B
Garnet 1 B	5 / 1 11 Oct	14 / 1 23/10/12	0.0894	0.0786	0.0475	0.1152	0.3522	0.3507	2.5	1.7111	1.8451	575	584	665	583	574	579	563
Garnet 1 C	18 / 1 11 Oct	16 / 1 23/10/12	0.0875	0.0769	0.0472	0.1158	0.3819	0.3807	2.5	1.8626	1.9986	526	557	612	545	541	551	537
Garnet 1 D	19 / 1 11 Oct	18 / 1 23/10/12	0.0974	0.0863	0.0497	0.1076	0.3687	0.3671	2.5	1.6889	1.8142	582	589	671	588	579	583	569
Garnet 1 E	3 / 1 11 Oct	19 / 1 23/10/12	0.1023	0.0913	0.0477	0.1019	0.3664	0.3652	2.5	1.6246	1.7449	605	601	692	606	595	595	582
Garnet 1 F	5 / 1 11 Oct	20 / 1 23/10/12	0.0894	0.0786	0.0475	0.1152	0.3772	0.3758	2.5	1.8190	1.9537	539	565	626	555	550	559	544
Garnet 1 G	18 / 1 11 Oct	21 / 1 23/10/12	0.0875	0.0769	0.0472	0.1158	0.3702	0.3683	2.5	1.8127	1.9459	541	565	629	557	552	560	546
Garnet 1 H	19 / 1 11 Oct	4 / 1 11 Oct	0.0974	0.0863	0.0497	0.1076	0.3612	0.3600	2.5	1.6565	1.7836	594	596	684	597	587	589	574
Garnet 1 I	3 / 1 11 Oct	6 / 1 11 Oct	0.1023	0.0913	0.0477	0.1019	0.3641	0.3628	2.5	1.6148	1.7344	609	603	696	608	597	597	584
Garnet 2 A	1 / 1 24 Oct	1 / 1 23/10/12	0.0967	0.0863	0.0473	0.1023	0.3575	0.3564	2.5	1.6481	1.7684	597	596	683	599	589	590	577
Garnet 2 B	2 / 1 24 Oct	2 / 1 23/10/12	0.0971	0.0866	0.0475	0.1030	0.3518	0.3506	2.5	1.6185	1.7396	607	602	695	607	596	596	583
Garnet 2 C	1 / 1 24 Oct	3 / 1 23/10/12	0.0967	0.0863	0.0473	0.1023	0.3557	0.3541	2.5	1.6402	1.7585	599	597	686	601	591	592	579
Garnet 2 D	2 / 1 24 Oct	7 / 1 23/10/12	0.0971	0.0866	0.0475	0.1030	0.3724	0.3711	2.5	1.7079	1.8283	576	585	660	583	575	579	566
Garnet 2 E	1 / 1 24 Oct	9 / 1 23/10/12	0.0967	0.0863	0.0473	0.1023	0.3646	0.3629	2.5	1.6789	1.7966	586	590	671	591	582	585	572
Garnet 3 A	5 / 1 24 Oct	10 / 1 23/10/12	0.0934	0.0828	0.0493	0.1080	0.3444	0.3430	2.5	1.6292	1.7553	603	601	694	604	594	594	580
Garnet 3 B	6 / 1 24 Oct	11 / 1 23/10/12	0.0937	0.0834	0.0500	0.1042	0.3522	0.3508	2.5	1.6599	1.7812	592	595	681	596	586	588	575
Garnet 3 C	6 / 1 24 Oct	12 / 1 23/10/12	0.0937	0.0834	0.0500	0.1042	0.3639	0.3628	2.5	1.7107	1.8335	575	585	661	583	574	579	565
Garnet 5 A	11 / 1 24 Oct	13 / 1 23/10/12	0.0958	0.0852	0.0506	0.1050	0.3503	0.3489	2.5	1.6273	1.7500	604	602	694	605	594	594	581
Garnet 5 B	12 / 1 24 Oct	14 / 1 23/10/12	0.0932	0.0825	0.0473	0.1094	0.3522	0.3507	2.5	1.6659	1.7927	590	593	679	595	585	587	573
Garnet 5 C	11 / 1 24 Oct	16 / 1 23/10/12	0.0958	0.0852	0.0506	0.1050	0.3819	0.3807	2.5	1.7633	1.8870	557	576	643	569	563	569	556
Garnet 5 D	12 / 1 24 Oct	18 / 1 23/10/12	0.0932	0.0825	0.0473	0.1094	0.3687	0.3671	2.5	1.7372	1.8639	566	579	652	576	568	574	560

Sample Pair	Garnet Sample	Biotite sample	XMg(grt)	XMg(grt) P&L83B	XCa(grt)	XMn(grt)	XMg(Bt)	XMg(Bt) P&L 83	Pressure (kbar)	log Kd	Log Kd P & L 83	T(FS)	T(PL81)	T(PG)	T(Th)	T(HL)	T(PL) 83A	T(PL) 83B
Garnet 5 E	11 / 1 24 Oct	19 / 1 23/10/12	0.0958	0.0852	0.0506	0.1050	0.3664	0.3652	2.5	1.6972	1.8209	579	588	667	586	578	581	568
Garnet 5 F	12 / 1 24 Oct	20 / 1 23/10/12	0.0932	0.0825	0.0473	0.1094	0.3772	0.3758	2.5	1.7737	1.9013	554	573	639	566	560	567	553
Garnet 5 G	11 / 1 24 Oct	21 / 1 23/10/12	0.0958	0.0852	0.0506	0.1050	0.3702	0.3683	2.5	1.7135	1.8343	574	585	661	582	574	578	565
Garnet 5 H	12 / 1 24 Oct	4 / 1 11 Oct	0.0932	0.0825	0.0473	0.1094	0.3612	0.3600	2.5	1.7048	1.8333	577	585	664	584	576	580	565
Garnet 5 I	12 / 1 24 Oct	6 / 1 11 Oct	0.0932	0.0825	0.0473	0.1094	0.3641	0.3628	2.5	1.7175	1.8455	572	583	660	581	573	577	563
Garnet 6 A	15 / 1 24 Oct	13 / 1 23/10/12	0.0954	0.0849	0.0460	0.1055	0.3503	0.3489	2.5	1.6317	1.7544	602	598	690	604	593	594	580
Garnet 6 B	16 / 1 24 Oct	14 / 1 23/10/12	0.0971	0.0862	0.0475	0.1076	0.3522	0.3507	2.5	1.6204	1.7455	607	601	697	607	596	596	582
Garnet 6 C	15 / 1 24 Oct	16 / 1 23/10/12	0.0954	0.0849	0.0460	0.1055	0.3819	0.3807	2.5	1.7677	1.8914	556	573	639	568	562	568	555
Garnet 6 D	16 / 1 24 Oct	18 / 1 23/10/12	0.0971	0.0862	0.0475	0.1076	0.3687	0.3671	2.5	1.6918	1.8167	581	588	669	588	579	582	568
Garnet 6 E	15 / 1 24 Oct	19 / 1 23/10/12	0.0954	0.0849	0.0460	0.1055	0.3664	0.3652	2.5	1.7016	1.8253	578	585	663	585	577	580	567
Garnet 6 F	16 / 1 24 Oct	20 / 1 23/10/12	0.0971	0.0862	0.0475	0.1076	0.3772	0.3758	2.5	1.7282	1.8541	569	581	655	578	570	575	562
Garnet 6 G	15 / 1 24 Oct	21 / 1 23/10/12	0.0954	0.0849	0.0460	0.1055	0.3702	0.3683	2.5	1.7179	1.8387	572	582	657	581	573	577	564
Garnet 6 H	16 / 1 24 Oct	4 / 1 11 Oct	0.0971	0.0862	0.0475	0.1076	0.3612	0.3600	2.5	1.6593	1.7860	593	594	681	596	586	588	574
Garnet 6 I	16 / 1 24 Oct	6 / 1 11 Oct	0.0971	0.0862	0.0475	0.1076	0.3641	0.3628	2.5	1.6720	1.7983	588	591	676	593	583	586	572
Garnet 1 Pair A	1 / 1 11 Oct	38 / 1 23 Oct	0.0996	0.0880	0.0534	0.1105	0.3730	0.3717	2.5	1.6820	1.8131	585	593	678	590	581	584	569
Garnet 1 Pair B	2 / 1 11 Oct	39 / 1 23 Oct	0.0998	0.0889	0.0550	0.1029	0.3675	0.3660	2.5	1.6571	1.7779	593	598	684	597	587	589	576
Garnet 2 Pair A	3 / 1 24 Oct	22 / 1 23 Oct	0.1000	0.0893	0.0581	0.1006	0.3626	0.3614	2.5	1.6336	1.7529	602	604	695	603	593	593	580
Garnet 2 Pair B	4 / 1 24 Oct	23 / 1 23 Oct	0.0970	0.0870	0.0591	0.0971	0.3583	0.3569	2.5	1.6477	1.7618	597	602	688	599	589	591	579
Garnet 3 Pair A	7 / 1 24 Oct	24 / 1 23 Oct	0.1015	0.0919	0.0563	0.0892	0.3712	0.3700	2.5	1.6540	1.7585	594	599	679	598	588	589	579
Garnet 3 Pair B	8 / 1 24 Oct	33 / 1 23 Oct	0.1036	0.0935	0.0552	0.0922	0.3616	0.3604	2.5	1.5888	1.6978	618	611	706	616	603	602	591
Garnet 5 Pair A	9 / 1 24 Oct	34 / 1 23 Oct	0.0977	0.0871	0.0578	0.1023	0.3674	0.3660	2.5	1.6793	1.8001	586	595	677	591	582	585	571

Sample Pair	Garnet Sample	Biotite sample	XMg(grt)	XMg(grt) P&L83B	XCa(grt)	XMn(grt)	XMg(Bt)	XMg(Bt) P&L 83	Pressure (kbar)	log Kd	Log Kd P & L 83	T(FS)	T(PL81)	T(PG)	T(Th)	T(HL)	T(PL) 83A	T(PL) 83B
Garnet 5 Pair B	10 / 1 24 Oct	35 / 1 23 Oct	0.0971	0.0863	0.0551	0.1058	0.3606	0.3593	2.5	1.6569	1.7818	593	598	686	597	587	589	575
Garnet 6 Pair A	13 / 1 24 Oct	36 / 1 23 Oct	0.0988	0.0883	0.0550	0.1003	0.3670	0.3656	2.5	1.6659	1.7837	590	596	680	595	585	587	574
Garnet 6 Pair B	14 / 1 24 Oct	37 / 1 23 Oct	0.0997	0.0892	0.0551	0.1000	0.3665	0.3654	2.5	1.6529	1.7716	595	599	685	598	588	590	577
Garnet 1 Pair C	1 / 1 11 Oct	40 / 1 23 Oct	0.0996	0.0880	0.0534	0.1105	0.3663	0.3650	2.5	1.6532	1.7845	595	598	689	598	588	589	574
Garnet 1 Pair D	2 / 1 11 Oct	41 / 1 23 Oct	0.0998	0.0889	0.0550	0.1029	0.3649	0.3633	2.5	1.6458	1.7662	597	600	689	600	590	591	578
Garnet 2 Pair C	3 / 1 24 Oct	42 / 1 23 Oct	0.1000	0.0893	0.0581	0.1006	0.3647	0.3632	2.5	1.6425	1.7609	599	602	691	601	590	592	579
Garnet 2 Pair D	4 / 1 24 Oct	43 / 1 23 Oct	0.0970	0.0870	0.0591	0.0971	0.3736	0.3723	2.5	1.7137	1.8282	574	589	662	582	574	578	566
Garnet 3 Pair C	7 / 1 24 Oct	44 / 1 23 Oct	0.1015	0.0919	0.0563	0.0892	0.3685	0.3672	2.5	1.6422	1.7467	599	602	684	601	590	592	581

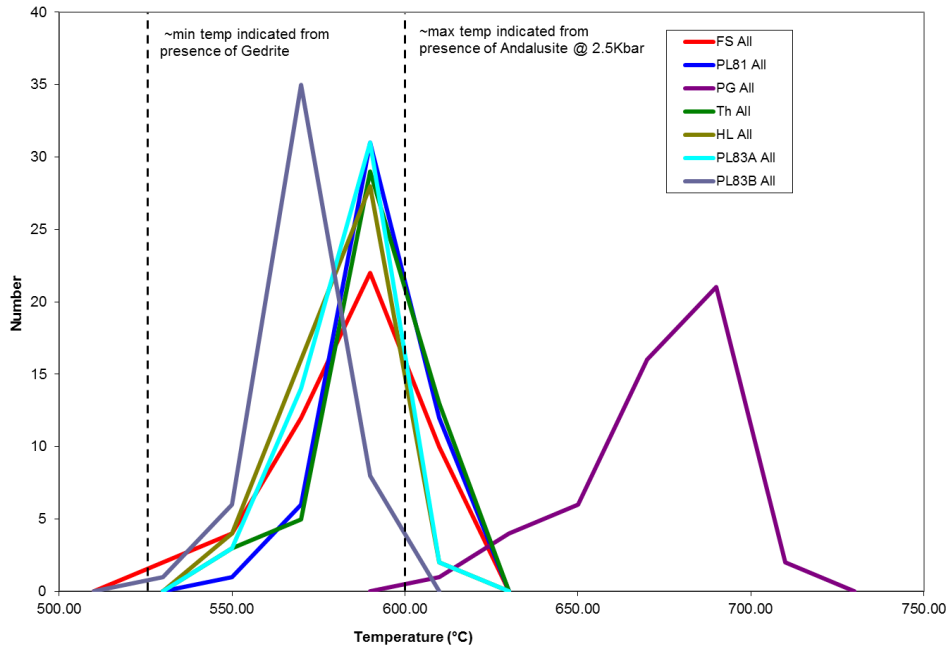

Figure A3.3. Histogram of all garnet-biotite pairs in AMD310Q. Histogram bin width = 20°C, n = 50

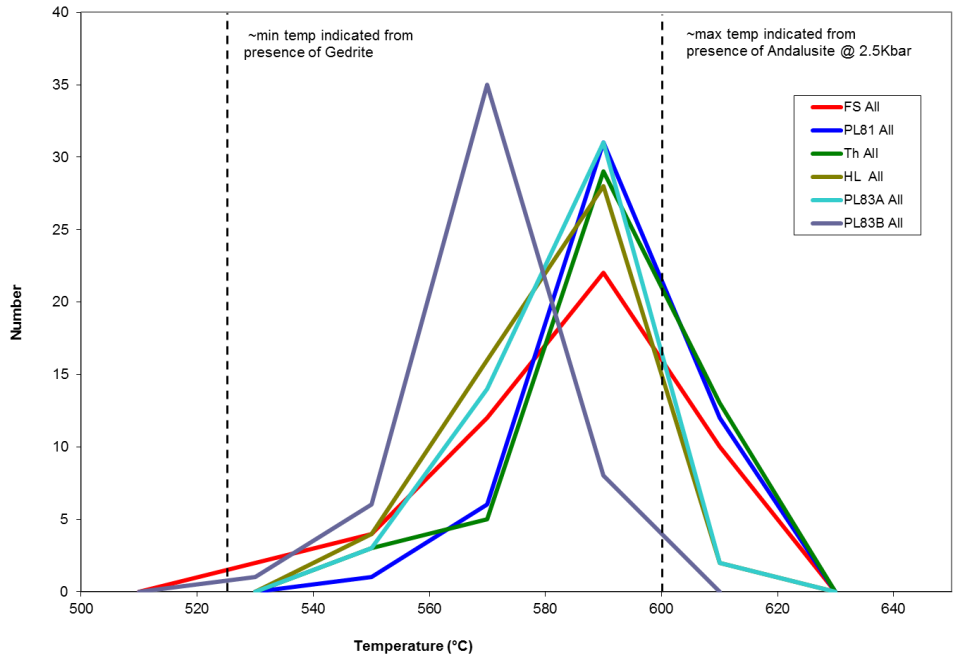

Figure A3.4. Histogram of all garnet-biotite pairs in AMD310Q, as above with PG calibration removed. The Ca and Mn correction of the PG calibration results in a temperature estimate that is not compatible with the metamorphic mineral assemblage or other geothermometry calibrations so has been removed. Histogram bin width = 20°C, n = 50.

A3.7 Sample BJD312HB

Sample	Core /Rim	Average Almandine %	Average Grossular %	Average Pyrope %	Average Spessartine %	Average Gro + Spess %	Average Garnet composition
BJD312HB	Core	61.07	8.57	8.09	22.27	30.84	$Alm_{61}Gro_{9}Py_{8}Sp_{22}$
BJD312HB	Rim	73.36	5.97	12.06	8.61	14.58	$Alm_{73}Gro_{6}Py_{12}Sp_{9}$

Table A3.14. Average composition of garnet within BJD312HB.

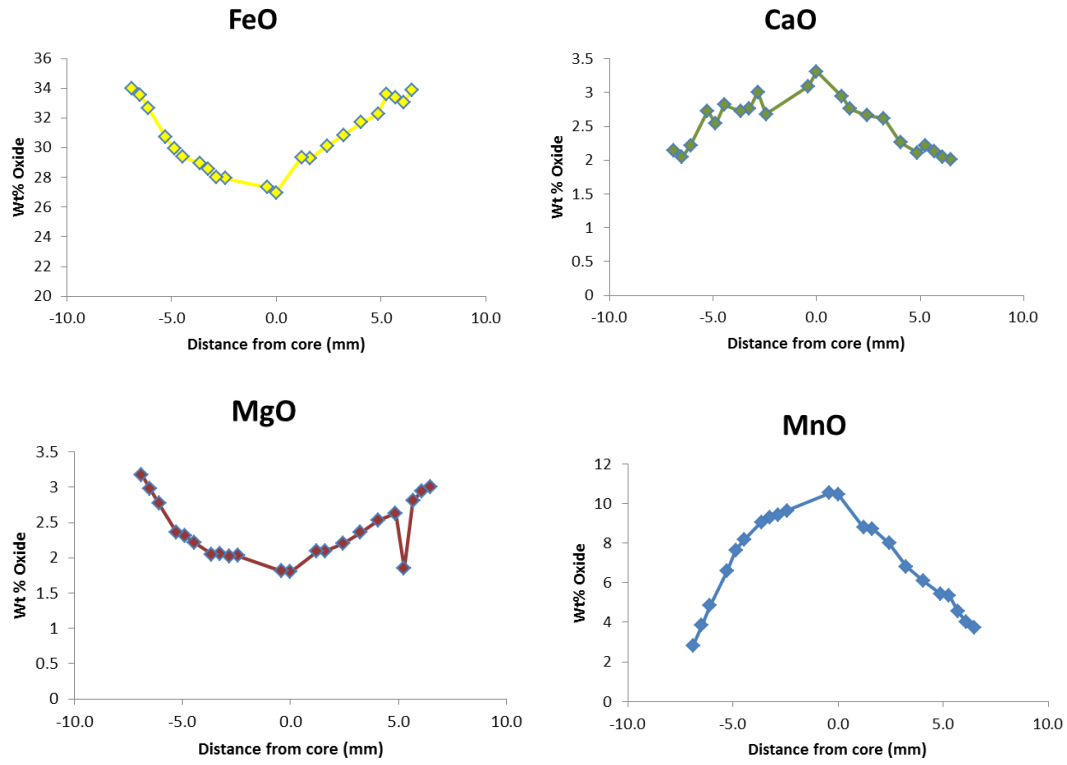

Figure A3.5. Results of a transect across Garnet 1 in sample BJD312HB, showing the typical normal compositional zoning. The core of garnet 1 can be seen to be more Mn-rich and poorer in Fe and Mg. Analyses were automated across the centre of the garnet porphyroblast and taken every 0.4mm. Analyses were omitted if they deviated more than ±1% from 100% or if they had a major element composition that was inconsistent with that of garnet (i.e., the analysis was of a mineral inclusion within the garnet such as quartz).

Table A3.15. BJD312HB: Analyses of garnet chosen for geothermometry in this study. Cationic proportions of garnets are recalculated on the basis of 24 oxygens, anhydrous conditions.

Sample Name	Core/Rim	Garnet Number	Na_2O	K_2O	MgO	CaO	MnO	FeO	NiO	Al_2O_3	Cr_2O_3	SiO_2	TiO_2	Total	Na	K	Mg	Ca	Mn	Fe	Al	Si	Ti	Total	XMg(Gt) (Mg/Mg+Fe)	XCa(Gt) Ca/Ca+Mg+ Fe+Mn	XMn(Gt) Mn/Ca+Mg+ Fe+Mn
21 / 1 10 Oct	Core	Garnet 1	0.00	0.00	2.02	2.51	9.83	28.36	0.00	21.22	0.01	36.57	0.24	100.76	0.00	0.00	0.49	0.43	1.34	3.83	4.04	5.90	0.03	16.05	0.113	0.071	0.221
22 / 1 10 Oct	Core	Garnet 1	0.00	0.00	1.96	2.65	9.63	28.42	0.00	21.32	0.00	35.92	0.25	100.15	0.00	0.00	0.48	0.46	1.33	3.87	4.09	5.84	0.03	16.09	0.109	0.075	0.216
46 / 1 10 Oct	Core	Garnet 1	0.00	0.00	1.79	2.86	10.80	27.11	0.00	21.10	0.01	36.41	0.23	100.32	0.00	0.00	0.43	0.50	1.48	3.68	4.03	5.90	0.03	16.05	0.105	0.082	0.243
47 / 1 10 Oct	Core	Garnet 1	0.01	0.00	1.80	3.05	10.80	27.51	0.00	21.17	0.00	36.47	0.13	100.94	0.00	0.00	0.43	0.53	1.48	3.71	4.03	5.89	0.02	16.08	0.104	0.086	0.240
48 / 1 10 Oct	Core	Garnet 1	0.00	0.00	1.76	3.06	10.55	27.07	0.00	21.17	0.01	36.31	0.13	100.07	0.00	0.00	0.43	0.53	1.45	3.68	4.05	5.90	0.02	16.06	0.104	0.088	0.239
35 / 1 10 Oct	Core	Garnet 2	0.01	0.00	2.11	2.75	8.95	29.20	0.00	21.06	0.00	36.63	0.12	100.83	0.00	0.00	0.51	0.48	1.22	3.94	4.00	5.91	0.01	16.08	0.114	0.077	0.199
36 / 1 10 Oct	Core	Garnet 2	0.00	0.00	2.04	2.85	8.85	29.00	0.00	21.31	0.00	36.27	0.14	100.47	0.00	0.00	0.49	0.49	1.21	3.93	4.07	5.87	0.02	16.08	0.112	0.081	0.198
37 / 1 10 Oct	Core	Garnet 2	0.00	0.00	2.14	2.89	8.11	28.89	0.00	20.88	0.01	37.00	0.11	100.03	0.00	0.00	0.52	0.50	1.11	3.91	3.98	5.98	0.01	16.01	0.116	0.083	0.184
38 / 1 10 Oct	Core	Garnet 2	0.00	0.00	2.14	2.96	7.83	29.65	0.00	21.13	0.01	36.96	0.09	100.77	0.00	0.00	0.51	0.51	1.07	3.99	4.01	5.95	0.01	16.04	0.114	0.084	0.176
1 / 14 9 Oct	Core	Garnet 1	0.00	0.00	2.10	2.76	8.73	29.29	0.00	21.27	0.01	34.90	0.14	99.21	0.00	0.00	0.52	0.49	1.22	4.04	4.13	5.75	0.02	16.16	0.113	0.078	0.195
1 / 15 9 Oct	Core	Garnet 1	0.00	0.00	2.09	2.94	8.80	29.37	0.00	21.20	0.01	35.75	0.12	100.28	0.00	0.00	0.51	0.51	1.21	4.00	4.07	5.82	0.02	16.13	0.112	0.082	0.195
1 / 22 9 Oct	Core	Garnet 1	0.00	0.00	1.80	3.31	10.48	26.98	0.00	20.95	0.01	35.33	0.20	99.08	0.00	0.00	0.44	0.59	1.46	3.72	4.07	5.82	0.03	16.12	0.106	0.094	0.236
1 / 23 9 Oct	Core	Garnet 1	0.00	0.00	1.81	3.09	10.53	27.34	0.00	21.18	0.01	35.12	0.11	99.19	0.00	0.00	0.45	0.55	1.47	3.77	4.11	5.79	0.01	16.14	0.106	0.088	0.236
39 / 1 10 Oct	Rim	Garnet 2	0.02	0.01	2.97	2.01	3.42	33.95	0.00	21.40	0.01	36.08	0.04	99.91	0.01	0.00	0.72	0.35	0.47	4.61	4.09	5.85	0.01	16.10	0.135	0.057	0.077
40 / 1 10 Oct	Rim	Garnet 2	0.01	0.01	2.95	2.08	3.51	34.22	0.00	21.34	n.d	36.13	0.04	100.29	0.00	0.00	0.71	0.36	0.48	4.63	4.07	5.85	0.01	16.12	0.133	0.058	0.078
37 / 1 10 Oct	Rim	Garnet 2	0.00	0.00	2.94	1.82	3.24	34.41	0.02	21.28	0.02	36.70	0.04	100.46	0.00	0.00	0.71	0.31	0.44	4.64	4.04	5.91	0.00	16.06	0.132	0.051	0.072
38 / 1 10 Oct	Rim	Garnet 2	0.00	0.00	2.98	1.84	3.14	34.60	0.00	21.48	0.01	36.51	0.04	100.61	0.00	0.00	0.72	0.32	0.43	4.66	4.08	5.88	0.00	16.08	0.133	0.052	0.070
1 / 2 9 Oct	Rim	Garnet 1	0.02	0.00	3.00	2.01	3.71	33.92	0.00	21.60	0.01	36.38	0.03	100.69	0.01	0.00	0.72	0.35	0.51	4.57	4.10	5.85	0.00	16.10	0.136	0.056	0.082
1 / 3 9 Oct	Rim	Garnet 1	0.00	0.00	2.94	2.05	4.02	33.08	0.00	21.29	0.01	36.76	0.11	100.28	0.00	0.00	0.71	0.35	0.55	4.46	4.04	5.92	0.01	16.04	0.137	0.058	0.090

Sample Name	Core/Rim	Garnet Number	Na_2O	K_2O	MgO	CaO	MnO	FeO	NiO	Al_2O_3	Cr_2O_3	SiO_2	TiO_2	Total	Na	K	Mg	Ca	Mn	Fe	Al	Si	Ti	Total	XMg(Gt) (Mg/Mg+Fe)	XCa(Gt) Ca/Ca+Mg +Fe+Mn	XMn(Gt) Mn/Ca+Mg +Fe+Mn
1 / 4 9 Oct	Rim	Garnet 1	0.02	0.00	2.81	2.13	4.57	33.39	0.00	21.26	0.02	36.70	0.06	100.96	0.01	0.00	0.67	0.37	0.62	4.49	4.03	5.90	0.01	16.09	0.130	0.060	0.101
1 / 37 9 Oct	Rim	Garnet 1	0.01	0.00	2.77	2.22	4.85	32.68	0.00	21.09	0.01	36.49	0.10	100.22	0.00	0.00	0.67	0.39	0.66	4.42	4.02	5.90	0.01	16.08	0.131	0.063	0.108
1 / 38 9 Oct	Rim	Garnet 1	0.01	0.00	2.98	2.04	3.84	33.58	0.00	21.00	0.01	36.28	0.09	99.83	0.00	0.00	0.72	0.36	0.53	4.56	4.02	5.89	0.01	16.09	0.137	0.058	0.086
1 / 39 9 Oct	Rim	Garnet 1	0.01	0.00	3.18	2.14	2.81	34.02	0.00	21.30	0.01	36.47	0.05	100.01	0.00	0.00	0.77	0.37	0.38	4.60	4.06	5.89	0.01	16.08	0.143	0.061	0.063

Table A3.16. BJD312HB: Analyses of biotite chosen for geothermometry in this study. Cationic proportions of biotite are recalculated on the basis of 22 oxygens, anhydrous conditions.

Sample Number	Associated Garnet	Far/Close?	Cl	F	Na_2O	K_2O	MgO	CaO	MnO	FeO	NiO	Al_2O_3	Cr_2O_3	SiO_2	TiO_2	Total	Si	Ti	Al	Fe^{2+}	Mn	Mg	Ca	Na	K	Total	Mg/Mg+Fe
49 / 1 22 Oct	Garnet 2	Close	0.17	0.01	0.12	7.97	10.52	0.02	0.08	19.34	0.00	18.68	0.00	35.38	0.26	92.55	5.51	0.03	3.43	2.52	0.01	2.44	0.00	0.04	1.58	15.56	0.492
51 / 1 22 Oct	Garnet 2	Close	0.11	0.02	0.17	7.96	10.55	0.02	0.13	19.82	0.04	18.88	0.00	35.38	0.24	93.31	5.47	0.03	3.44	2.56	0.02	2.43	0.00	0.05	1.57	15.59	0.487
52 / 1 22 Oct	Garnet 2	Close	0.15	0.02	0.14	7.71	10.53	0.01	0.13	19.67	0.03	18.64	0.01	34.63	0.71	92.37	5.42	0.08	3.44	2.57	0.02	2.46	0.00	0.04	1.54	15.57	0.488
53 / 1 22 Oct	Garnet 2	Close	0.13	0.02	0.16	8.16	10.06	0.02	0.13	19.53	0.01	19.12	0.01	35.19	0.73	93.27	5.45	0.09	3.49	2.53	0.02	2.32	0.00	0.05	1.61	15.55	0.479
54 / 1 22 Oct	Garnet 2	Close	0.15	0.01	0.16	8.17	9.79	0.01	0.12	19.05	0.04	18.33	0.01	35.53	0.81	92.19	5.56	0.10	3.38	2.49	0.02	2.28	0.00	0.05	1.63	15.50	0.478
55 / 1 22 Oct	Garnet 2	Close	0.07	0.01	0.14	8.30	9.96	0.03	0.16	19.13	0.06	18.29	0.02	34.15	1.08	91.42	5.42	0.13	3.42	2.54	0.02	2.35	0.01	0.04	1.68	15.61	0.481
56 / 1 22 Oct	Garnet 2	Close	0.11	0.01	0.21	8.24	10.21	0.01	0.10	19.26	0.04	19.82	0.01	34.85	1.06	93.94	5.35	0.12	3.59	2.47	0.01	2.34	0.00	0.06	1.61	15.57	0.486
57 / 1 22 Oct	Garnet 2	Close	0.15	0.01	0.11	6.69	11.27	0.02	0.19	20.50	0.04	19.38	0.03	33.08	1.00	92.47	5.18	0.12	3.58	2.69	0.03	2.63	0.00	0.03	1.34	15.60	0.495
58 / 1 22 Oct	Garnet 2	Close	0.16	0.01	0.22	8.31	10.11	0.02	0.10	19.15	0.04	19.07	0.01	34.29	1.13	92.62	5.36	0.13	3.51	2.50	0.01	2.36	0.00	0.07	1.66	15.61	0.485
63 / 1 22 Oct	Garnet 1	Close	0.09	0.02	0.11	8.21	9.75	0.04	0.15	19.90	0.06	19.06	0.01	34.38	1.36	93.13	5.36	0.16	3.50	2.59	0.02	2.26	0.01	0.03	1.63	15.57	0.466
64 / 1 22 Oct	Garnet 1	Close	0.12	0.02	0.21	7.87	9.79	0.05	0.14	19.58	0.05	19.01	0.01	34.24	1.39	92.47	5.36	0.16	3.51	2.56	0.02	2.28	0.01	0.06	1.57	15.54	0.471
65 / 1 22 Oct	Garnet 1	Close	0.12	0.01	0.21	7.83	9.56	0.01	0.15	19.54	0.05	19.11	0.01	34.87	1.46	92.94	5.42	0.17	3.50	2.54	0.02	2.21	0.00	0.06	1.55	15.47	0.466

Sample Number	Associated Garnet	Far/Close?	Cl	F	Na_2O	K_2O	MgO	CaO	MnO	FeO	NiO	Al_2O_3	Cr_2O_3	SiO_2	TiO_2	Total	Si	Ti	Al	Fe^{2+}	Mn	Mg	Ca	Na	K	Total	Mg/Mg+Fe
67 / 1 22 Oct	Garnet 1	Close	0.10	0.02	0.15	8.05	9.91	0.03	0.13	19.80	0.07	19.76	0.01	34.04	1.20	93.27	5.29	0.14	3.62	2.57	0.02	2.30	0.00	0.05	1.60	15.58	0.472
68 / 1 22 Oct	Garnet 1	Close	0.09	0.02	0.16	8.31	9.74	0.02	0.12	19.45	0.05	18.90	0.02	33.47	1.23	91.60	5.31	0.15	3.54	2.58	0.02	2.30	0.00	0.05	1.68	15.64	0.472
69 / 1 22 Oct	Garnet 1	Close	0.10	0.01	0.17	8.00	9.79	0.02	0.14	19.68	0.05	18.79	0.00	34.38	1.25	92.39	5.39	0.15	3.47	2.58	0.02	2.29	0.00	0.05	1.60	15.55	0.470
59 / 1 22 Oct	None	Far	0.13	0.01	0.11	8.22	9.90	0.03	0.11	19.21	0.06	19.08	0.01	34.33	1.24	92.45	5.37	0.15	3.52	2.51	0.01	2.31	0.01	0.03	1.64	15.56	0.479
60 / 1 22 Oct	None	Far	0.08	0.02	0.25	8.47	9.91	0.02	0.11	20.43	0.06	18.51	-0.01	34.68	1.28	93.82	5.39	0.15	3.39	2.65	0.01	2.30	0.00	0.08	1.68	15.65	0.464
61 / 1 22 Oct	None	Far	0.08	0.02	0.16	7.96	9.78	0.03	0.17	19.46	0.09	19.05	0.01	34.48	1.32	92.60	5.38	0.16	3.51	2.54	0.02	2.28	0.01	0.05	1.59	15.52	0.473
62 / 1 22 Oct	None	Far	0.15	0.01	0.20	8.36	9.64	0.03	0.11	19.25	0.07	18.41	0.00	34.39	1.24	91.87	5.43	0.15	3.43	2.54	0.01	2.27	0.01	0.06	1.68	15.58	0.472
46 / 1 22 Oct	None	Far	0.10	0.01	0.12	8.12	10.05	0.03	0.13	19.79	0.05	18.29	0.02	35.10	1.43	93.25	5.45	0.17	3.35	2.57	0.02	2.33	0.00	0.04	1.61	15.53	0.475
47 / 1 22 Oct	None	Far	0.12	0.01	0.15	8.36	10.03	0.03	0.14	19.84	0.05	19.10	0.01	34.87	1.42	94.14	5.37	0.16	3.47	2.56	0.02	2.30	0.00	0.04	1.64	15.57	0.474
48 / 1 22 Oct	None	Far	0.13	0.01	0.18	7.98	9.97	0.03	0.13	18.65	0.06	19.33	0.01	35.23	1.44	93.18	5.43	0.17	3.51	2.40	0.02	2.29	0.00	0.05	1.57	15.46	0.488

Table A3.17. Molar fractions of garnet and biotite pairs chosen for geothermometry in sample BJD312HB. Molar fraction equations are from Ferry and Spear (1978) (=FS) and Perchuk and Lavrent'eva (1983) (=P&L83B). Distribution coefficients (Kd) and temperatures (T in°C) are calculated using the calibrations of Ferry and Spear (1978) (T(FS)), Lavrent'eva and Perchuk (1981) (T(PL81)), Pigage and Greenwood (1980) (T(PG)), Thompson (1976) (T(Th)), Holdaway and Lee (1977) (T(HL)) and Perchuk and Lavrent'eva (1983) (T(PL83A)) and (T(PL83B)).

Sample Pair	Garnet Sample	Biotite sample	XMg(grt)	XMg(grt) P&L83B	XCa(grt)	XMn(grt)	XMg(Bt)	XMg(Bt) P&L 83	Pressure (kbar)	log Kd	Log Kd P & L 83	T(FS)	T(PL81)	T(PG)	T(Th)	T(HL)	T(PL) 83A	T(PL) 83B
Garnet 1 Rim/Close Pair A	1 / 2 9 Oct	63 / 1 22 Oct	0.1361	0.1242	0.0564	0.0823	0.4662	0.4643	2.5	1.7129	1.8102	574	588	653	582	574	571	570
Garnet 1 Rim/Close Pair B	1 / 3 9 Oct	64 / 1 22 Oct	0.1368	0.1236	0.0584	0.0904	0.4713	0.4695	2.5	1.7273	1.8361	569	587	653	578	571	569	565
Garnet 1 Rim/Close Pair C	1 / 4 9 Oct	65 / 1 22 Oct	0.1305	0.1164	0.0597	0.1010	0.4658	0.4639	2.5	1.7601	1.8820	558	581	648	570	563	563	557
Garnet 1 Rim/Close Pair D	1 / 37 9 Oct	69 / 1 22 Oct	0.1315	0.1163	0.0627	0.1082	0.4700	0.4682	2.5	1.7679	1.9007	556	581	650	568	562	561	553
Garnet 1 Rim/Close Pair E	1 / 38 9 Oct	67 / 1 22 Oct	0.1365	0.1241	0.0577	0.0856	0.4715	0.4699	2.5	1.7303	1.8333	568	586	649	578	570	568	565

Sample Pair	Garnet Sample	Biotite sample	XMg(grt)	XMg(grt) P&L83B	XCa(grt)	XMn(grt)	XMg(Bt)	XMg(Bt) P&L 83	Pressure (kbar)	log Kd	Log Kd P & L 83	T(FS)	T(PL81)	T(PG)	T(Th)	T(HL)	T(PL) 83A	T(PL) 83B
Garnet 1 Rim/Close Pair F	1 / 39 9 Oct	68 / 1 22 Oct	0.1430	0.1335	0.0606	0.0628	0.4716	0.4701	2.5	1.6769	1.7509	586	597	659	592	582	578	581
Garnet 1 Core/Far Pair A	21 / 1 10 Oct	59 / 1 22 Oct	0.1125	0.0858	0.0713	0.2207	0.4788	0.4774	2.5	1.9806	2.2758	492	548	637	517	517	525	493
Garnet 1 Core/Far Pair B	22 / 1 10 Oct	60 / 1 22 Oct	0.1094	0.0838	0.0754	0.2164	0.4637	0.4624	2.5	1.9510	2.2405	500	555	648	524	523	530	498
Garnet 1 Core/Far Pair C	46 / 1 10 Oct	61 / 1 22 Oct	0.1054	0.0774	0.0816	0.2434	0.4725	0.4703	2.5	2.0289	2.3588	479	545	638	507	507	517	480
Garnet 1 Core/Far Pair D	47 / 1 10 Oct	62 / 1 22 Oct	0.1042	0.0768	0.0858	0.2401	0.4716	0.4702	2.5	2.0379	2.3669	476	546	636	505	505	516	479
Garnet 1 Core/Far Pair E	48 / 1 10 Oct	46 / 1 22 Oct	0.1036	0.0765	0.0875	0.2385	0.4751	0.4735	2.5	2.0585	2.3846	471	543	630	500	501	512	477
Garnet 1 Core/Far Pair F	1 / 14 9 Oct	47 / 1 22 Oct	0.1133	0.0894	0.0779	0.1947	0.4740	0.4722	2.5	1.9533	2.2100	500	556	638	524	522	529	503
Garnet 1 Core/Far Pair G	1 / 15 9 Oct	48 / 1 22 Oct	0.1124	0.0885	0.0824	0.1947	0.4879	0.4862	2.5	2.0185	2.2765	482	547	619	509	509	519	492
Garnet 1 Core/Far Pair H	1 / 22 9 Oct	61 / 1 22 Oct	0.1065	0.0788	0.0942	0.2355	0.4725	0.4703	2.5	2.0171	2.3400	482	553	645	509	509	519	483
Garnet 1 Core/Far Pair I	1 / 23 9 Oct	46 / 1 22 Oct	0.1056	0.0783	0.0875	0.2359	0.4751	0.4735	2.5	2.0367	2.3592	477	547	635	505	506	516	480
Garnet 2 Rim/Close Pair A	39 / 1 10 Oct	49 / 1 22 Oct	0.1347	0.1238	0.0568	0.0765	0.4923	0.4912	2.5	1.8290	1.9220	536	567	609	553	548	551	550
Garnet 2 Rim/Close Pair B	40 / 1 10 Oct	51 / 1 22 Oct	0.1332	0.1222	0.0582	0.0778	0.4869	0.4852	2.5	1.8201	1.9123	539	570	614	555	550	552	551
Garnet 2 Rim/Close Pair C	37 / 1 10 Oct	52 / 1 22 Oct	0.1322	0.1221	0.0515	0.0725	0.4883	0.4866	2.5	1.8352	1.9196	534	564	602	551	547	550	550
Garnet 2 Rim/Close Pair D	38 / 1 10 Oct	53 / 1 22 Oct	0.1330	0.1232	0.0520	0.0701	0.4787	0.4770	2.5	1.7889	1.8703	549	572	617	563	557	558	559
Garnet 2 Rim/Close Pair E	39 / 1 10 Oct	54 / 1 22 Oct	0.1347	0.1238	0.0568	0.0765	0.4781	0.4765	2.5	1.7722	1.8630	554	578	629	567	561	561	560
Garnet 2 Rim/Close Pair F	40 / 1 10 Oct	55 / 1 22 Oct	0.1332	0.1222	0.0582	0.0778	0.4814	0.4792	2.5	1.7980	1.8884	546	574	621	560	555	556	556
Garnet 2 Rim/Close Pair G	37 / 1 10 Oct	56 / 1 22 Oct	0.1322	0.1163	0.0515	0.0725	0.4858	0.4845	2.5	1.8254	1.9662	537	565	605	554	549	551	542
Garnet 2 Rim/Close Pair H	38 / 1 10 Oct	57 / 1 22 Oct	0.1330	0.1241	0.0520	0.0701	0.4949	0.4926	2.5	1.8540	1.9244	529	561	595	547	543	546	549
Garnet 2 Rim/Close Pair I	39 / 1 10 Oct	58 / 1 22 Oct	0.1347	0.1335	0.0568	0.0765	0.4848	0.4835	2.5	1.7991	1.8047	546	573	619	560	555	556	571
Garnet 2 Core/Far Pair A	35 / 1 10 Oct	59 / 1 22 Oct	0.1142	0.0896	0.0773	0.1990	0.4788	0.4774	2.5	1.9636	2.2282	497	554	636	521	520	528	500
Garnet 2 Core/Far Pair B	36 / 1 10 Oct	60 / 1 22 Oct	0.1116	0.0875	0.0806	0.1980	0.4637	0.4624	2.5	1.9295	2.1933	506	561	649	529	527	533	505

Sample Pair	Garnet Sample	Biotite sample	XMg(grt)	XMg(grt) P&L83B	XCa(grt)	XMn(grt)	XMg(Bt)	XMg(Bt) P&L 83	Pressure	log Kd	Log Kd P & L 83	T(FS)	T(PL81)	T(PG)	T(Th)	T(HL)	T(PL) 83A	T(PL) 83B
Garnet 2 Core/Far Pair C	37 / 1 10 Oct	61 / 1 22 Oct	0.1165	0.0931	0.0830	0.1841	0.4725	0.4703	2.5	1.9164	2.1578	510	565	648	532	530	536	511
Garnet 2 Core/Far Pair D	38 / 1 10 Oct	62 / 1 22 Oct	0.1138	0.0920	0.0839	0.1756	0.4716	0.4702	2.5	1.9392	2.1705	504	561	637	527	525	532	509
Garnet 2 Core/Far Pair E	35 / 1 10 Oct	46 / 1 22 Oct	0.1142	0.0896	0.0773	0.1990	0.4751	0.4735	2.5	1.9489	2.2126	501	556	641	525	523	530	502
Garnet 2 Core/Far Pair F	36 / 1 10 Oct	47 / 1 22 Oct	0.1116	0.0875	0.0806	0.1980	0.4740	0.4722	2.5	1.9708	2.2329	495	554	635	520	519	526	499
Garnet 2 Core/Far Pair G	37 / 1 10 Oct	48 / 1 22 Oct	0.1165	0.0931	0.0830	0.1841	0.4879	0.4862	2.5	1.9781	2.2214	493	554	628	518	517	525	501
Garnet 2 Core/Far Pair H	38 / 1 10 Oct	46 / 1 22 Oct	0.1138	0.0920	0.0839	0.1756	0.4740	0.4735	2.5	1.9486	2.1836	501	560	634	525	523	530	507

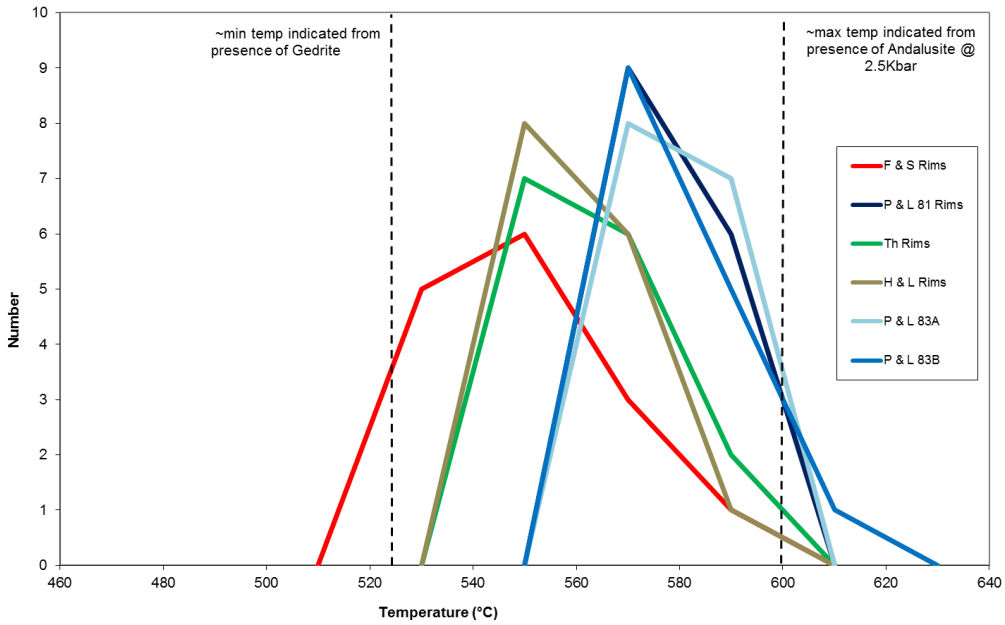

Figure A3.6. Histogram of all rim garnet-biotite close pairs in BJD312HB. Histogram bin width = 20°C, n = 15.

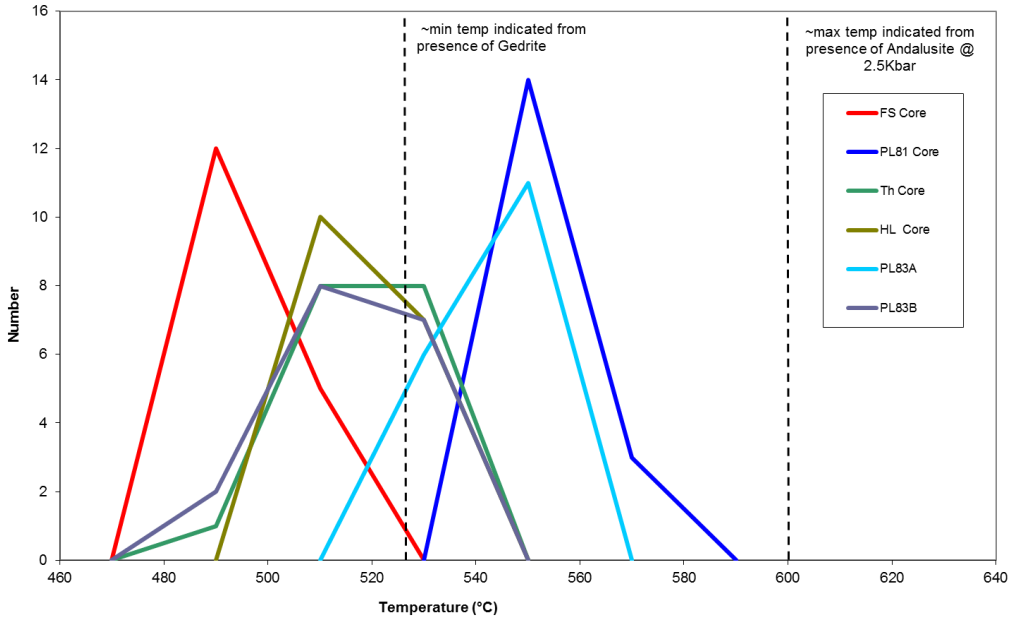

Figure A3.7. Histogram of all core garnet-biotite far pairs in BJD312HB. The Ca and Mn correction of the PG calibration results in a temperature estimate that is not compatible with the metamorphic mineral assemblages or the other geothermometry calibrations, so this calibration is not shown. Histogram bin width = 20°C, n = 17.

A3.8 Sample AMD139B

Sample	Core /Rim	Average Almandine %	Average Grossular %	Average Pyrope %	Average Spessartine %	Average Gro + Spess %	Average Garnet composition
AMD139B	All	46.37	20.71	2.83	30.09	50.80	$Alm_{46}Gro_{20}Py_{3}Sp_{30}$

Table A3.18 Average composition of garnet within AMD139B. Note the high grossular and spessartine contents.

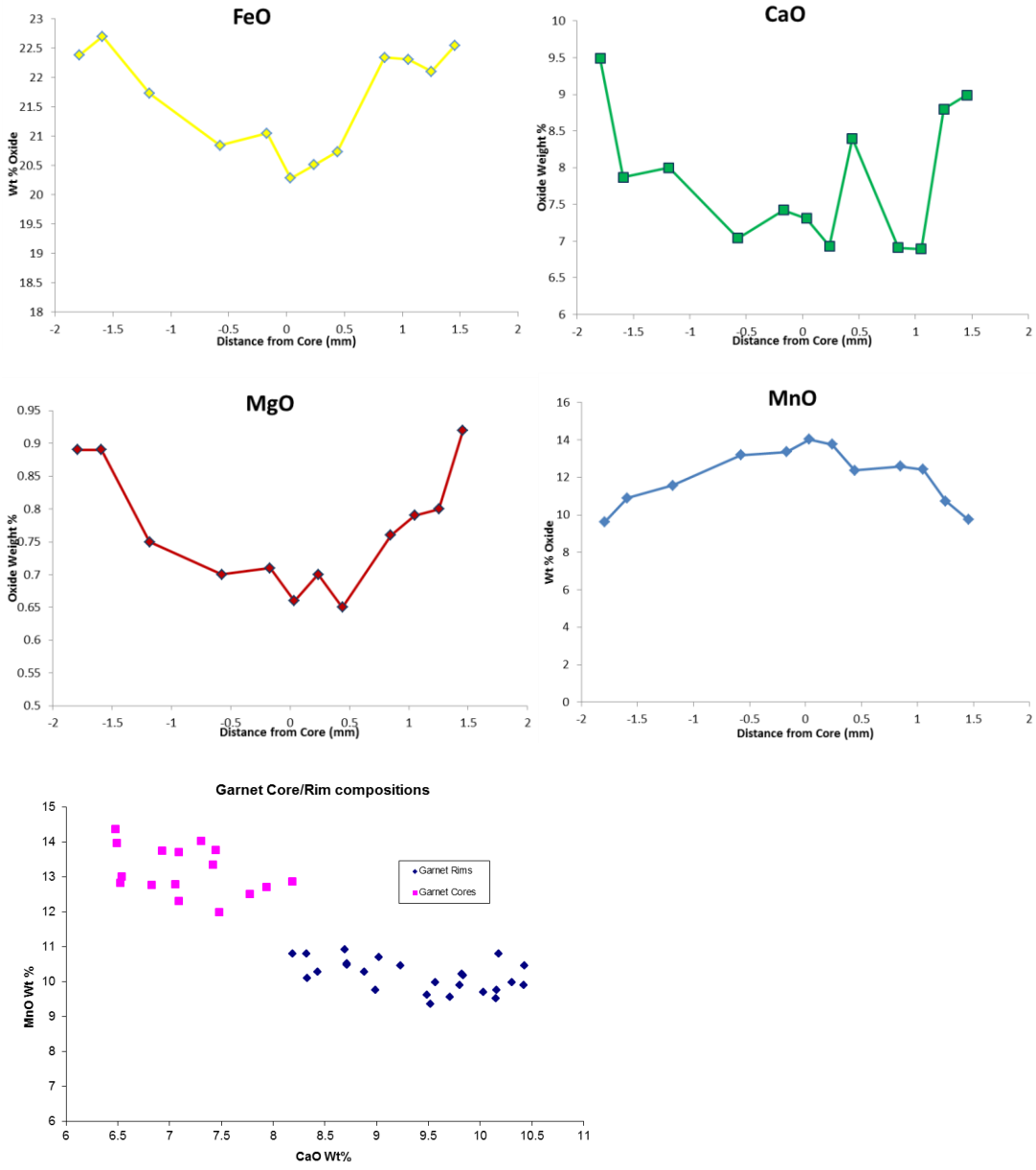

Figure A3.8. (Previous page). Results of a transect across Garnet 2 in sample AMD139B, showing the typical normal compositional zoning. The core of garnet one can be seen to be more Mn-rich and poorer in Fe, Ca, and Mg. Analyses were automated across the centre of the garnet porphyroblast and taken every 0.2mm. Analyses were omitted if the total deviated more than ± 1% from 100% or if they had a major element composition inconsistent with that of garnet (i.e., the analysis was of a mineral inclusion within the garnet such as quartz). In comparison to other samples, the garnets within AMD139 have a much higher Ca and Mn content and a very low Mg content. Therefore the estimates of Mg/Fe equilibration temperatures are unlikely to produce realistic indications of temperature because of the low concentration of Mg. Minor elements in garnet, including Mn and Ca, are not accounted for in the Fe-Mg ideal mixing assumed in (T(FS)), (T(PL81)), (T(Th)) and (T(HL)) calibrations (e.g., Chuming and Yusheng, 1999).

Table A3.19. AMD139B: Analyses of garnet chosen for geothermometry in this study. Cationic proportions of garnets are recalculated on the basis of 24 oxygens, anhydrous conditions.

Sample Name	Core/Rim	Garnet Number	Na_2O	K_2O	MgO	CaO	MnO	FeO	NiO	Al_2O_3	Cr_2O_3	SiO_2	TiO_2	Total	Na	K	Mg	Ca	Mn	Fe	Al	Si	Ti	Total	XMg(Gt) (Mg/Mg+Fe)	XCa(Gt) Ca/Ca+Mg+Fe+Mn	XMn(Gt) Mn/Ca+Mg+Fe+Mn
1/1 11 Oct	Rim	Garnet 1	0.00	0.00	0.80	8.19	10.79	23.01	0.00	20.81	0.00	37.02	0.14	100.77	0.00	0.00	0.19	1.41	1.47	3.09	3.94	5.95	0.02	16.07	0.448	0.229	0.238
2/1 11 Oct	Rim	Garnet 1	0.01	0.00	0.70	10.18	10.78	21.05	0.00	21.24	0.00	36.91	0.10	100.96	0.00	0.00	0.17	1.74	1.46	2.81	4.00	5.90	0.01	16.09	0.489	0.282	0.236
1 / 1 Night 11 Oct	Rim	Garnet 2	0.00	0.00	0.72	10.31	9.97	21.65	0.00	21.13	0.00	37.08	0.07	100.95	0.00	0.00	0.17	1.76	1.35	2.89	3.98	5.92	0.01	16.08	0.440	0.286	0.218
2 / 1 Night 11 Oct	Rim	Garnet 2	0.00	0.00	0.72	10.43	10.44	21.00	0.01	21.04	0.00	37.26	0.08	100.99	0.00	0.00	0.17	1.78	1.41	2.80	3.96	5.94	0.01	16.07	0.474	0.289	0.229
7 / 1 Night 11 Oct	Rim	Garnet 2	0.02	0.00	0.79	9.23	10.45	21.96	0.01	21.05	0.00	36.72	0.08	100.31	0.01	0.00	0.19	1.59	1.43	2.96	3.99	5.91	0.01	16.09	0.453	0.258	0.231
8 / 1 Night 11 Oct	Rim	Garnet 2	0.00	0.00	0.74	9.02	10.68	22.13	0.00	21.10	0.00	36.89	0.05	100.61	0.00	0.00	0.18	1.55	1.45	2.97	3.99	5.92	0.01	16.08	0.461	0.252	0.236
43 / 1 23 Oct	Rim	Garnet 2	0.01	0.00	0.67	8.69	10.90	21.50	0.00	20.76	0.01	37.64	0.04	100.23	0.00	0.00	0.16	1.49	1.48	2.88	3.93	6.04	0.00	15.99	0.486	0.248	0.246
44 / 1 23 Oct	Rim	Garnet 2	0.02	0.00	0.70	8.88	10.27	21.41	0.00	20.95	0.01	37.62	0.05	99.91	0.01	0.00	0.17	1.53	1.40	2.87	3.96	6.04	0.01	15.98	0.459	0.256	0.234
1 / 1 12 Oct	Rim	Garnet 2	0.01	0.01	0.92	8.99	9.74	22.55	0.00	21.26	0.01	37.21	0.02	100.72	0.00	0.00	0.22	1.54	1.32	3.01	4.01	5.95	0.00	16.05	0.408	0.253	0.217
17 / 1 12 Oct	Rim	Garnet 2	0.00	0.01	0.89	9.49	9.60	22.38	0.00	21.06	0.00	36.66	0.06	100.15	0.00	0.00	0.21	1.64	1.31	3.02	4.00	5.91	0.01	16.09	0.405	0.265	0.212
1 / 1 2 12 Oct	Rim	Garnet 2	0.00	0.00	0.79	10.15	9.50	21.49	0.01	21.20	0.01	37.23	0.06	100.45	0.00	0.00	0.19	1.74	1.29	2.87	3.99	5.95	0.01	16.04	0.420	0.286	0.211
2 / 1 2 12 Oct	Rim	Garnet 2	0.01	0.00	0.80	8.32	10.79	22.39	0.00	20.72	0.00	37.34	0.13	100.50	0.00	0.00	0.19	1.43	1.47	3.01	3.92	6.00	0.02	16.03	0.459	0.235	0.241
21 / 1 Night 11 Oct	Rim	Garnet 3	0.00	0.02	0.86	8.71	10.50	22.27	0.00	21.03	0.00	36.85	0.04	100.28	0.00	0.00	0.21	1.50	1.43	3.00	3.99	5.93	0.01	16.07	0.447	0.245	0.233
22 / 1 Night 11 Oct	Rim	Garnet 3	0.00	0.01	0.89	8.33	10.08	22.34	0.00	21.00	0.01	37.34	0.04	100.02	0.00	0.00	0.21	1.43	1.37	3.00	3.98	6.00	0.01	16.01	0.427	0.238	0.228
27 / 1 Night 11 Oct	Rim	Garnet 3	0.02	0.01	0.83	10.03	9.69	21.53	0.00	20.87	0.00	37.38	0.09	100.43	0.01	0.00	0.20	1.72	1.31	2.88	3.94	5.98	0.01	16.04	0.427	0.281	0.215
28 / 1 Night 11 Oct	Rim	Garnet 3	0.01	0.00	0.74	10.42	9.88	21.23	0.00	21.08	0.00	37.28	0.08	100.71	0.00	0.00	0.18	1.78	1.34	2.83	3.97	5.95	0.01	16.06	0.444	0.291	0.218
16 / 1 23 Oct	Rim	Garnet 4	0.02	0.01	0.72	9.57	9.97	21.54	0.00	20.81	0.00	37.53	0.05	100.22	0.01	0.00	0.17	1.64	1.35	2.89	3.93	6.02	0.01	16.02	0.442	0.271	0.223

Sample Name	Core/Rim	Garnet Number	Na_2O	K_2O	MgO	CaO	MnO	FeO	NiO	Al_2O_3	Cr_2O_3	SiO_2	TiO_2	Total	Na	K	Mg	Ca	Mn	Fe	Al	Si	Ti	Total	XMg(Gt) (Mg/Mg+Fe)	XCa(Gt) Ca/Ca+Mg+Fe+Mn	XMn(Gt) Mn/Ca+Mg+Fe+Mn
17 / 1 23 Oct	Rim	Garnet 4	0.01	0.02	0.79	9.52	9.34	22.06	0.00	20.71	0.00	37.78	0.04	100.26	0.00	0.00	0.19	1.63	1.27	2.95	3.91	6.05	0.00	16.00	0.403	0.270	0.210
18 / 1 23 Oct	Rim	Garnet 4	0.00	0.02	0.77	9.71	9.54	21.61	0.00	20.74	0.00	37.47	0.06	99.90	0.00	0.00	0.18	1.67	1.30	2.90	3.93	6.02	0.01	16.01	0.420	0.276	0.214
24 / 1 23 Oct	Rim	Garnet 4	0.02	0.00	0.75	9.80	9.88	21.75	0.00	20.95	0.00	37.41	0.04	100.60	0.01	0.00	0.18	1.68	1.34	2.91	3.95	5.98	0.00	16.04	0.433	0.275	0.219
25 / 1 23 Oct	Rim	Garnet 4	0.00	0.00	0.65	10.16	9.74	21.13	0.01	20.85	0.00	37.59	0.05	100.18	0.00	0.00	0.16	1.74	1.32	2.83	3.93	6.02	0.01	16.01	0.443	0.288	0.218
4 / 1 23 Oct	Rim	Garnet 7	0.00	0.01	0.68	9.82	10.20	21.31	0.00	20.75	0.00	37.46	0.06	100.29	0.00	0.00	0.16	1.69	1.39	2.86	3.92	6.01	0.01	16.03	0.459	0.277	0.227
5 / 1 23 Oct	Rim	Garnet 7	0.00	0.00	0.68	9.84	10.17	21.21	0.00	20.76	0.01	37.33	0.06	100.06	0.00	0.00	0.16	1.69	1.38	2.85	3.93	6.00	0.01	16.03	0.459	0.278	0.227
38 / 1 23 Oct	Rim	Unknown	0.00	0.00	0.77	8.71	10.47	22.27	0.01	20.91	0.00	37.60	0.04	100.78	0.00	0.00	0.18	1.49	1.42	2.98	3.94	6.01	0.00	16.01	0.449	0.246	0.234
39 / 1 23 Oct	Rim	Unknown	0.00	0.00	0.79	8.43	10.27	22.13	0.01	20.71	0.00	37.50	0.04	99.88	0.00	0.00	0.19	1.45	1.40	2.98	3.93	6.04	0.00	15.99	0.442	0.241	0.232
5/1 11 Oct	Core	Garnet 1	0.01	0.00	0.77	7.78	12.50	21.55	0.00	20.65	0.00	36.60	0.22	100.09	0.00	0.00	0.19	1.35	1.72	2.92	3.94	5.93	0.03	16.07	0.552	0.219	0.278
6/1 11 Oct	Core	Garnet 1	0.01	0.00	0.76	6.83	12.77	22.44	0.00	20.85	0.00	36.88	0.25	100.79	0.00	0.00	0.18	1.18	1.74	3.02	3.96	5.94	0.03	16.06	0.543	0.192	0.284
7 / 1 12 Oct	Core	Garnet 2	0.04	0.01	0.70	6.93	13.75	20.51	0.00	20.59	0.01	36.19	0.46	99.19	0.01	0.00	0.17	1.21	1.91	2.80	3.97	5.92	0.06	16.05	0.640	0.199	0.313
8 / 1 12 Oct	Core	Garnet 2	0.01	0.00	0.66	7.31	14.03	20.28	0.00	20.87	0.00	36.70	0.25	100.11	0.00	0.00	0.16	1.27	1.92	2.74	3.98	5.94	0.03	16.04	0.662	0.208	0.316
9 / 1 12 Oct	Core	Garnet 2	0.03	0.00	0.71	7.42	13.35	21.05	0.00	20.84	0.01	36.51	0.33	100.25	0.01	0.00	0.17	1.29	1.83	2.85	3.97	5.91	0.04	16.07	0.606	0.210	0.298
6 / 1 2 12 Oct	Core	Garnet 2	0.03	0.00	0.76	7.94	12.71	21.03	0.00	21.06	0.00	37.11	0.20	100.84	0.01	0.00	0.18	1.36	1.73	2.82	3.98	5.95	0.02	16.05	0.575	0.224	0.283
8 / 1 2 12 Oct	Core	Garnet 2	0.01	0.00	0.66	8.19	12.86	20.62	0.01	20.65	0.00	37.09	0.19	100.28	0.00	0.00	0.16	1.41	1.76	2.78	3.92	5.98	0.02	16.04	0.598	0.232	0.287
9 / 1 2 12 Oct	Core	Garnet 2	0.15	0.04	0.42	7.06	12.79	18.75	0.00	23.33	0.00	37.01	0.13	99.68	0.05	0.01	0.10	1.21	1.73	2.50	4.39	5.91	0.02	15.91	0.665	0.218	0.312
3 / 1 Night 11 Oct	Core	Garnet 2	0.03	0.00	0.67	6.49	13.96	20.75	0.01	20.64	0.01	36.36	0.28	99.21	0.01	0.00	0.16	1.14	1.93	2.84	3.98	5.94	0.04	16.04	0.644	0.187	0.318
4 / 1 Night 11 Oct	Core	Garnet 2	0.03	0.00	0.68	6.48	14.37	20.85	0.00	20.80	0.00	36.23	0.39	99.84	0.01	0.00	0.17	1.13	1.98	2.84	3.99	5.90	0.05	16.06	0.659	0.185	0.324
5 / 1 Night 11 Oct	Core	Garnet 2	0.03	0.00	0.70	7.09	13.70	20.57	0.00	20.75	0.00	36.80	0.53	100.18	0.01	0.00	0.17	1.23	1.88	2.78	3.95	5.95	0.06	16.02	0.636	0.203	0.310

Sample Name	Core/Rim	Garnet Number	Na_2O	K_2O	MgO	CaO	MnO	FeO	NiO	Al_2O_3	Cr_2O_3	SiO_2	TiO_2	Total	Na	K	Mg	Ca	Mn	Fe	Al	Si	Ti	Total	XMg(Gt) (Mg/Mg+Fe)	XCa(Gt) Ca/Ca+Mg+Fe+ Mn	XMn(Gt) Mn/Ca+Mg+Fe+ Mn
6 / 1 Night 11 Oct	Core	Garnet 2	0.00	0.00	0.69	7.45	13.76	20.65	0.00	20.81	0.02	36.82	0.37	100.57	0.00	0.00	0.17	1.29	1.88	2.78	3.95	5.93	0.04	16.05	0.637	0.210	0.307
19 / 1 Night 11 Oct	Core	Garnet 3	0.03	0.00	0.87	7.09	12.30	22.38	0.00	20.92	0.01	36.95	0.27	100.83	0.01	0.00	0.21	1.22	1.67	3.01	3.96	5.94	0.03	16.05	0.520	0.200	0.274
20 / 1 Night 11 Oct	Core	Garnet 3	0.01	0.00	0.82	7.48	11.98	22.47	0.00	20.88	0.01	37.07	0.26	100.98	0.00	0.00	0.20	1.29	1.63	3.01	3.95	5.95	0.03	16.05	0.507	0.210	0.266
19 / 1 23 Oct	Core	Garnet 4	0.01	0.00	0.70	6.53	12.83	22.04	0.00	20.21	0.01	37.46	0.37	100.16	0.00	0.00	0.17	1.13	1.76	2.98	3.85	6.05	0.04	15.98	0.558	0.187	0.291
20 / 1 23 Oct	Core	Garnet 4	0.02	0.00	0.69	6.54	13.00	22.15	0.00	20.26	0.01	37.56	0.32	100.55	0.01	0.00	0.17	1.13	1.77	2.98	3.85	6.05	0.04	15.99	0.563	0.187	0.293

Table A3.20. AMD139B: Analyses of biotite chosen for geothermometry in this study. Cationic proportions of biotite are recalculated on the basis of 22 oxygens, anhydrous conditions – denotes not analysed.

Sample Number	Associated Garnet	Far/Close?	Cl	F	Na_2O	K_2O	MgO	CaO	MnO	FeO	NiO	Al_2O_3	Cr_2O_3	SiO_2	TiO_2	Total	Si	Ti	Al	Fe^{2+}	Mn	Mg	Ca	Na	K	Total	Mg/Mg+Fe
9 / 1 11 Oct	Garnet 1	Close	-	0.14	0.04	8.93	7.51	0.08	0.45	24.71	0.00	16.78	0.01	35.74	2.14	96.52	5.52	0.25	3.05	3.19	0.06	1.73	0.01	0.01	1.76	15.59	0.351
10 / 1 11 Oct	Garnet 1	Close	-	0.15	0.05	8.71	7.34	0.12	0.47	25.72	0.00	16.87	0.00	35.15	2.29	96.89	5.44	0.27	3.08	3.33	0.06	1.69	0.02	0.02	1.72	**15.62**	0.337
31 / 1 23 Oct	Garnet 1	Close	0.01	0.15	0.07	8.42	7.00	0.03	0.46	23.17	0.01	16.90	0.01	34.68	1.82	92.73	5.54	0.22	3.18	3.10	0.06	1.67	0.01	0.02	1.72	15.52	0.350
32 / 1 23 Oct	Garnet 1	Close	0.01	0.12	0.00	7.91	6.93	0.05	0.44	23.46	0.00	16.10	0.00	35.31	1.77	92.10	5.66	0.21	3.04	3.15	0.06	1.66	0.01	0.00	1.62	15.41	0.345
33 / 1 23 Oct	Garnet 1	Close	0.00	0.11	0.00	8.32	7.02	0.06	0.42	23.53	0.03	16.85	0.00	35.72	1.78	93.84	5.62	0.21	3.13	3.10	0.06	1.65	0.01	0.00	1.67	15.44	0.347
35 / 1 23 Oct	Garnet 1	Close	0.01	0.13	0.11	8.10	7.23	0.04	0.45	24.05	0.00	16.68	0.01	35.79	1.77	94.37	5.61	0.21	3.08	3.15	0.06	1.69	0.01	0.03	1.62	15.47	0.349
37 / 1 23 Oct	Garnet 1	Close	0.01	0.11	0.00	7.45	7.15	0.10	0.53	24.50	0.01	16.13	0.00	33.75	1.65	91.40	5.50	0.20	3.10	3.34	0.07	1.74	0.02	0.00	1.55	15.52	0.342
40 / 1 23 Oct	Garnet 2	Close	0.01	0.13	0.05	7.42	7.27	0.07	0.46	24.31	0.00	16.60	0.00	34.58	1.70	92.60	5.53	0.20	3.13	3.25	0.06	1.73	0.01	0.02	1.51	15.46	0.348

Sample Number	Associated Garnet	Far/Close?	Cl	F	Na_2O	K_2O	MgO	CaO	MnO	FeO	NiO	Al_2O_3	Cr_2O_3	SiO_2	TiO_2	Total	Si	Ti	Al	Fe^{2+}	Mn	Mg	Ca	Na	K	Total	Mg/Mg+Fe
42 / 1 23 Oct	Garnet 2	Close	0.01	0.13	n.d	7.71	6.88	0.04	0.55	23.44	0.00	16.49	0.00	34.25	1.90	91.40	5.55	0.23	3.15	3.18	0.08	1.66	0.01	n.d	1.59	15.44	0.343
9 / 1 Night 11 Oct	Garnet 2	Close	-	0.13	0.04	9.18	7.32	0.10	0.45	24.98	0.01	17.75	0.00	35.66	2.28	97.89	5.44	0.26	3.19	3.18	0.06	1.66	0.02	0.01	1.79	15.61	0.343
11 / 1 Night 11 Oct	Garnet 2	Close	-	0.16	0.09	9.01	7.40	0.10	0.45	25.24	0.00	17.33	0.00	36.28	2.37	98.42	5.50	0.27	3.09	3.20	0.06	1.67	0.02	0.03	1.74	15.57	0.343
23 / 1 Night 11 Oct	Garnet 3	Close	-	0.13	0.09	9.11	7.70	0.02	0.45	24.99	0.00	17.32	0.01	35.61	2.02	97.44	5.46	0.23	3.13	3.20	0.06	1.76	0.00	0.03	1.78	15.65	0.355
24 / 1 Night 11 Oct	Garnet 3	Close	-	0.13	0.07	8.96	7.60	0.02	0.47	25.11	0.00	17.34	0.00	35.46	1.97	97.13	5.45	0.23	3.14	3.23	0.06	1.74	0.00	0.02	1.76	15.64	0.350
12 / 1 23 Oct	Garnet 4	Close	0.01	0.13	0.17	8.32	6.98	0.06	0.40	23.97	0.02	16.50	0.01	35.13	2.10	93.78	5.56	0.25	3.08	3.17	0.05	1.65	0.01	0.05	1.68	15.51	0.342
13 / 1 23 Oct	Garnet 4	Close	0.01	0.14	0.13	7.90	6.74	0.04	0.42	22.69	0.01	16.21	0.01	35.55	2.05	91.92	5.69	0.25	3.06	3.04	0.06	1.61	0.01	0.04	1.61	15.36	0.346
14 / 1 23 Oct	Garnet 4	Close	0.01	0.10	0.13	8.07	7.06	0.05	0.47	22.85	0.00	17.02	0.00	34.94	2.09	92.79	5.55	0.25	3.19	3.04	0.06	1.67	0.01	0.04	1.64	15.44	0.355
15 / 1 23 Oct	Garnet 4	Close	0.01	0.15	0.11	8.06	7.02	0.08	0.45	23.16	0.01	16.74	0.00	34.44	2.06	92.30	5.53	0.25	3.17	3.11	0.06	1.68	0.01	0.03	1.65	15.49	0.351
21 / 1 23 Oct	Garnet 4	Close	0.01	0.15	0.07	8.06	7.04	0.02	0.43	24.58	0.01	16.65	0.00	35.87	1.91	94.80	5.61	0.22	3.07	3.21	0.06	1.64	0.00	0.02	1.61	15.45	0.338
1 / 1 Day 23 Oct	Garnet 5	Close	0.01	0.13	0.12	8.29	7.36	0.02	0.41	23.86	0.00	17.10	0.01	34.31	2.00	93.60	5.45	0.24	3.20	3.17	0.06	1.74	0.00	0.04	1.68	15.57	0.355
2 / 1 Day 23 Oct	Garnet 5	Close	0.01	0.16	0.06	8.00	7.13	0.01	0.43	24.70	0.01	16.76	0.00	34.42	2.08	93.77	5.47	0.25	3.14	3.28	0.06	1.69	0.00	0.02	1.62	15.53	0.340
3 / 1 Day 23 Oct	Garnet 5	Close	0.01	0.12	0.12	8.03	7.11	0.03	0.42	22.90	0.00	17.27	0.00	34.44	2.04	92.49	5.50	0.24	3.25	3.06	0.06	1.69	0.01	0.04	1.64	15.47	0.356
4 / 1 Day 23 Oct	Garnet 5	Close	0.01	0.13	0.05	8.16	7.25	0.02	0.44	24.15	0.00	16.70	0.00	33.81	2.06	92.79	5.43	0.25	3.16	3.25	0.06	1.74	0.00	0.02	1.67	15.58	0.349
1 / 1 23 Oct	Garnet 7	Close	0.01	0.14	0.03	8.09	6.98	0.03	0.42	23.94	0.03	16.37	0.00	35.80	1.70	93.54	5.66	0.20	3.05	3.17	0.06	1.65	0.01	0.01	1.63	15.43	0.342
2 / 1 23 Oct	Garnet 7	Close	0.01	0.14	0.12	8.16	7.13	0.03	0.42	24.07	0.00	16.61	0.01	35.45	1.67	93.81	5.60	0.20	3.09	3.18	0.06	1.68	0.01	0.04	1.64	15.49	0.346
3 / 1 23 Oct	Garnet 7	Close	0.01	0.14	0.16	8.05	7.18	0.02	0.44	23.06	0.00	16.71	0.00	35.03	1.63	92.44	5.60	0.20	3.15	3.08	0.06	1.71	0.00	0.05	1.64	15.48	0.357
9 / 1 23 Oct	Garnet 4?	Inclusion	0.00	0.11	0.11	8.26	7.04	0.03	0.41	23.68	0.00	16.64	0.00	34.99	2.00	93.28	5.56	0.24	3.12	3.15	0.06	1.67	0.01	0.03	1.67	15.50	0.346
10 / 1 23 Oct	Garnet 4?	Inclusion	0.01	0.12	0.08	7.86	7.13	0.02	0.43	23.83	0.00	16.68	0.01	35.21	2.06	93.43	5.57	0.25	3.11	3.15	0.06	1.68	0.00	0.02	1.59	15.43	0.348
11 / 1 23 Oct	Garnet 4?	Inclusion	0.00	0.09	0.05	7.89	7.19	0.02	0.45	24.32	0.00	16.27	0.00	35.08	2.03	93.40	5.57	0.24	3.05	3.23	0.06	1.70	0.00	0.02	1.60	15.47	0.345
6 / 1 23 Oct	None	Far	0.01	0.16	0.14	7.94	6.98	0.05	0.38	23.83	0.00	16.21	0.00	35.64	2.13	93.47	5.64	0.25	3.02	3.15	0.05	1.65	0.01	0.04	1.60	15.42	0.343
7 / 1 23 Oct	None	Far	0.01	0.16	0.10	8.03	6.89	0.05	0.41	24.37	0.00	16.83	0.00	35.66	2.14	94.65	5.58	0.25	3.10	3.19	0.05	1.61	0.01	0.03	1.60	15.43	0.335
8 / 1 23 Oct	None	Far	0.01	0.10	0.18	8.23	6.98	0.05	0.37	24.26	0.00	16.80	0.02	35.13	2.07	94.20	5.54	0.25	3.12	3.20	0.05	1.64	0.01	0.06	1.65	15.51	0.339

Sample Number	Associated Garnet	Far/Close?	Cl	F	Na_2O	K_2O	MgO	CaO	MnO	FeO	NiO	Al_2O_3	Cr_2O_3	SiO_2	TiO_2	Total	Si	Ti	Al	Fe^{2+}	Mn	Mg	Ca	Na	K	Total	Mg/Mg+Fe
45 / 1 23 Oct	None	Far	0.01	0.10	0.10	7.78	6.76	0.08	0.47	23.95	0.01	16.57	0.00	35.54	1.78	93.16	5.64	0.21	3.10	3.18	0.06	1.60	0.01	0.03	1.57	15.40	0.335
46 / 1 23 Oct	None	Far	0.02	0.15	0.07	7.84	6.70	0.06	0.45	24.14	0.01	16.49	0.02	35.31	1.60	92.87	5.63	0.19	3.10	3.22	0.06	1.59	0.01	0.02	1.60	15.43	0.331
48 / 1 23 Oct	None	Far	0.00	0.14	0.07	8.36	7.17	0.04	0.45	25.18	0.00	16.99	0.00	36.07	1.52	96.00	5.59	0.18	3.10	3.26	0.06	1.66	0.01	0.02	1.65	15.52	0.337
50 / 1 23 Oct	None	Far	0.01	0.14	0.18	8.24	6.94	0.03	0.41	23.64	0.00	17.65	0.00	36.84	1.68	95.76	5.65	0.19	3.19	3.03	0.05	1.59	0.00	0.05	1.61	15.39	0.344
51 / 1 23 Oct	None	Far	0.01	0.13	0.09	8.12	6.96	0.02	0.39	24.29	0.00	16.79	0.02	34.97	1.73	93.52	5.55	0.21	3.14	3.23	0.05	1.65	0.00	0.03	1.64	15.50	0.338
52 / 1 23 Oct	None	Far	0.01	0.12	0.04	7.73	6.79	0.02	0.44	23.86	0.00	16.81	0.01	35.50	1.72	93.05	5.63	0.21	3.14	3.16	0.06	1.60	0.00	0.01	1.56	15.38	0.337
53 / 1 23 Oct	None	Far	0.02	0.10	0.09	8.31	7.05	0.03	0.43	23.10	0.00	16.96	0.00	34.80	1.74	92.61	5.56	0.21	3.19	3.08	0.06	1.68	0.01	0.03	1.69	15.50	0.352
54 / 1 23 Oct	None	Far	0.01	0.15	0.04	7.96	6.74	0.03	0.45	23.79	0.02	16.38	0.00	35.41	1.80	92.78	5.65	0.22	3.08	3.17	0.06	1.60	0.01	0.01	1.62	15.41	0.336
55 / 1 23 Oct	None	Far	0.00	0.16	0.03	7.94	6.96	0.03	0.46	24.62	0.00	17.21	0.01	34.86	1.79	94.07	5.50	0.21	3.20	3.25	0.06	1.64	0.01	0.01	1.60	15.49	0.335
56 / 1 23 Oct	None	Far	0.00	0.13	0.05	8.18	6.82	0.03	0.44	24.56	0.00	16.60	0.00	35.33	1.81	93.96	5.59	0.22	3.09	3.25	0.06	1.61	0.01	0.02	1.65	15.48	0.331

Table A3.21. Molar fractions of garnet and biotite pairs chosen for geothermometry in sample AMD139B. Molar fraction equations are from Ferry and Spear (1978) (=FS) and Perchuk and Lavrent'eva (1983) (=P&L83B). Distribution coefficients (Kd) and temperatures (T in°C) are calculated using the calibrations of Ferry and Spear (1978) (T(FS)), Lavrent'eva and Perchuk (1981) (T(PL81)), Pigage and Greenwood (1980) (T(PG)), Thompson (1976) (T(Th)), Holdaway and Lee (1977) (T(HL)) and Perchuk and Lavrent'eva (1983) (T(PL83A)) and (T(PL83B)).

Sample	Garnet Sample	Biotite sample	Gt/Bt Pairing	XMg(grt)	XMg(grt) P&L83B	XCa(grt)	XMn(grt)	XMg(Bt)	XMg(Bt) P&L 83	Pressure (kbar)	log Kd	Log Kd P & L 83	T(FS)	T(PL81)	T(PG)	T(Th)	T(HL)	T(PL) 83A	T(PL) 83B
Garnet 1 Pair A	1/1 11 Oct	9 / 1 11 Oct	Rim/Close	0.0582	0.0402	0.2289	0.2384	0.3514	0.3472	2.5	2.1711	2.5416	443	589	671	477	480	501	455
Garnet 1 Pair B	2/1 11 Oct	10 / 1 11 Oct	Rim/Close	0.0557	0.0374	0.2822	0.2359	0.3372	0.3331	2.5	2.1541	2.5534	447	615	704	480	484	503	453
Garnet 1 Pair C	1/1 11 Oct	31 / 1 23 Oct	Rim/Close	0.0582	0.0402	0.2289	0.2384	0.3500	0.3455	2.5	2.1651	2.5340	444	590	673	478	482	502	456
Garnet 1 Pair D	2/1 11 Oct	32 / 1 23 Oct	Rim/Close	0.0557	0.0374	0.2822	0.2359	0.3449	0.3407	2.5	2.1886	2.5874	438	610	693	474	477	498	448

Sample	Garnet Sample	Biotite sample	Gt/Bt Pairing	XMg(grt)	XMg(grt) P&L83B	XCa(grt)	XMn(grt)	XMg(Bt)	XMg(Bt) P&L 83	Pressure	log Kd	Log Kd P & L 83	T(FS)	T(PL81)	T(PG)	T(Th)	T(HL)	T(PL) 83A	T(PL) 83B
Garnet 1 Pair E	1/1 11 Oct	33 / 1 23 Oct	Rim/Close	0.0582	0.0402	0.2289	0.2384	0.3472	0.3431	2.5	2.1525	2.5234	447	592	677	481	484	504	457
Garnet 1 Pair F	2/1 11 Oct	35 / 1 23 Oct	Rim/Close	0.0557	0.0374	0.2822	0.2359	0.3489	0.3447	2.5	2.2062	2.6050	434	607	687	470	474	495	446
Garnet 1 Pair G	1/1 11 Oct	37 / 1 23 Oct	Rim/Close	0.0582	0.0402	0.2289	0.2384	0.3422	0.3373	2.5	2.1305	2.4976	453	596	684	485	488	507	461
Garnet 1 Pair H	5/1 11 Oct	8 / 1 23 Oct	Core/Far	0.0599	0.0386	0.2189	0.2779	0.3390	0.3356	2.5	2.0859	2.5326	464	599	712	495	496	514	456
Garnet 1 Pair I	6/1 11 Oct	45 / 1 23 Oct	Core/Far	0.0574	0.0372	0.1923	0.2844	0.3347	0.3304	2.5	2.1118	2.5473	457	582	691	489	491	510	454
Garnet 1 Pair J	5/1 11 Oct	48 / 1 23 Oct	Core/Far	0.0599	0.0386	0.2189	0.2779	0.3367	0.3327	2.5	2.0755	2.5196	466	601	715	497	498	516	458
Garnet 1 Pair K	6/1 11 Oct	51 / 1 23 Oct	Core/Far	0.0574	0.0372	0.1923	0.2844	0.3381	0.3345	2.5	2.1269	2.5659	453	580	686	486	489	508	451
Garnet 1 Pair L	5/1 11 Oct	55 / 1 23 Oct	Core/Far	0.0599	0.0386	0.2189	0.2779	0.3351	0.3309	2.5	2.0683	2.5116	468	602	718	498	500	517	459
Garnet 2 Pair A	1 / 1 Night 11 Oct	9 / 1 Night 11 Oct	Rim/Close	0.0562	0.0390	0.2855	0.2185	0.3431	0.3391	2.5	2.1724	2.5373	442	614	692	477	480	501	455
Garnet 2 Pair B	2 / 1 Night 11 Oct	11 / 1 Night 11 Oct	Rim/Close	0.0575	0.0390	0.2892	0.2287	0.3432	0.3392	2.5	2.1472	2.5370	448	620	707	482	485	505	455
Garnet 2 Pair C	7 / 1 Night 11 Oct	9 / 1 Night 11 Oct	Rim/Close	0.0601	0.0413	0.2584	0.2313	0.3431	0.3391	2.5	2.1008	2.4762	460	614	707	491	493	512	464
Garnet 2 Pair D	8 / 1 Night 11 Oct	11 / 1 Night 11 Oct	Rim/Close	0.0565	0.0387	0.2521	0.2361	0.3432	0.3392	2.5	2.1660	2.5462	444	600	684	478	481	502	454
Garnet 2 Pair E	43 / 1 23 Oct	42 / 1 23 Oct	Rim/Close	0.0526	0.0354	0.2481	0.2460	0.3435	0.3382	2.5	2.2427	2.6336	426	586	662	463	468	490	442
Garnet 2 Pair F	44 / 1 23 Oct	40 / 1 23 Oct	Rim/Close	0.0551	0.0377	0.2560	0.2341	0.3477	0.3434	2.5	2.2134	2.5904	432	594	670	469	473	494	448
Garnet 2 Pair G	1 / 1 12 Oct	9 / 1 Night 11 Oct	Rim/Close	0.0677	0.0481	0.2528	0.2165	0.3431	0.3391	2.5	1.9725	2.3174	494	634	743	519	518	533	486
Garnet 2 Pair H	2 / 1 12 Oct	11 / 1 Night 11 Oct	Rim/Close	0.0605	0.0414	0.2469	0.2378	0.3432	0.3392	2.5	2.0933	2.4750	462	610	706	493	495	513	464
Garnet 2 Pair I	17 / 1 12 Oct	40 / 1 23 Oct	Rim/Close	0.0663	0.0472	0.2651	0.2120	0.3477	0.3434	2.5	2.0163	2.3579	482	632	732	510	510	525	480
Garnet 2 Pair J	16 / 1 12 Oct	42 / 1 23 Oct	Rim/Close	0.0653	0.0449	0.2221	0.2430	0.3435	0.3382	2.5	2.0133	2.3860	483	613	723	510	510	526	476
Garnet 2 Pair K	13 / 1 2 12 Oct	9 / 1 Night 11 Oct	Rim/Close	0.0603	0.0368	0.2056	0.3101	0.3431	0.3391	2.5	2.0966	2.5981	461	591	715	492	494	512	447
Garnet 2 Pair L	14 / 1 2 12 Oct	11 / 1 Night 11 Oct	Rim/Close	0.0648	0.0427	0.2124	0.2689	0.3432	0.3392	2.5	2.0202	2.4433	481	607	727	509	509	525	468

Sample	Garnet Sample	Biotite sample	Gt/Bt Pairing	XMg(grt)	XMg(grt) P&L83B	XCa(grt)	XMn(grt)	XMg(Bt)	XMg(Bt) P&L 83	Pressure (kbar)	log Kd	Log Kd P & L 83	T(FS)	T(PL81)	T(PG)	T(Th)	T(HL)	T(PL) 83A	T(PL) 83B
Garnet 2 Pair M	1 / 1 2 12 Oct	40 / 1 23 Oct	Rim/Close	0.0617	0.0434	0.2856	0.2114	0.3477	0.3434	2.5	2.0926	2.4437	462	628	716	493	495	513	468
Garnet 2 Pair N	2 / 1 2 12 Oct	42 / 1 23 Oct	Rim/Close	0.0597	0.0409	0.2349	0.2406	0.3435	0.3382	2.5	2.1086	2.4825	458	602	696	490	492	511	463
Garnet 2 Pair N	3 / 1 Night 11 Oct	8 / 1 23 Oct	Core/Far	0.0546	0.0332	0.1873	0.3183	0.3390	0.3356	2.5	2.1829	2.6870	440	568	680	475	478	499	435
Garnet 2 Pair O	4 / 1 Night 11 Oct	45 / 1 23 Oct	Core/Far	0.0552	0.0333	0.1848	0.3239	0.3347	0.3304	2.5	2.1523	2.6620	447	572	691	481	484	504	439
Garnet 2 Pair P	5 / 1 Night 11 Oct	48 / 1 23 Oct	Core/Far	0.0573	0.0350	0.2028	0.3099	0.3367	0.3327	2.5	2.1222	2.6198	455	585	705	487	489	508	444
Garnet 2 Pair Q	6 / 1 Night 11 Oct	51 / 1 23 Oct	Core/Far	0.0560	0.0342	0.2104	0.3073	0.3381	0.3345	2.5	2.1535	2.6531	447	584	698	481	484	504	440
Garnet 2 Pair R	7 / 1 12 Oct	55 / 1 23 Oct	Core/Far	0.0575	0.0350	0.1992	0.3126	0.3351	0.3309	2.5	2.1118	2.6115	457	586	708	489	491	510	445
Garnet 2 Pair S	8 / 1 12 Oct	8 / 1 23 Oct	Core/Far	0.0548	0.0330	0.2078	0.3155	0.3390	0.3356	2.5	2.1805	2.6961	440	578	691	475	479	499	434
Garnet 2 Pair T	9 / 1 12 Oct	45 / 1 23 Oct	Core/Far	0.0566	0.0353	0.2096	0.2983	0.3347	0.3304	2.5	2.1258	2.6024	454	588	702	486	489	508	446
Garnet 2 Pair V	8 / 1 2 12 Oct	51 / 1 23 Oct	Core/Far	0.0538	0.0337	0.2316	0.2874	0.3381	0.3327	2.5	2.1954	2.6607	437	586	686	472	476	497	439
Garnet 3 Pair A	21 / 1 Night 11 Oct	23 / 1 Night 11 Oct	Rim/Close	0.0643	0.0444	0.2446	0.2334	0.3545	0.3504	2.5	2.0783	2.4508	466	612	708	496	498	515	467
Garnet 3 Pair B	22 / 1 Night 11 Oct	24 / 1 Night 11 Oct	Rim/Close	0.0660	0.0462	0.2382	0.2279	0.3504	0.3462	2.5	2.0334	2.3910	478	617	718	506	506	523	476
Garnet 3 Pair C	27 / 1 Night 11 Oct	23 / 1 Night 11 Oct	Rim/Close	0.0640	0.0449	0.2815	0.2149	0.3545	0.3504	2.5	2.0835	2.4409	464	627	718	495	497	515	469
Garnet 3 Pair D	28 / 1 Night 11 Oct	24 / 1 Night 11 Oct	Rim/Close	0.0582	0.0403	0.2908	0.2181	0.3504	0.3462	2.5	2.1676	2.5350	443	617	697	478	481	501	455
Garnet 3 Pair E	19 / 1 Night 11 Oct	8 / 1 23 Oct	Core/Far	0.0650	0.0427	0.1996	0.2739	0.3390	0.3356	2.5	1.9990	2.4261	487	605	730	513	513	528	471
Garnet 3 Pair F	20 / 1 Night 11 Oct	45 / 1 23 Oct	Core/Far	0.0608	0.0403	0.2101	0.2658	0.3347	0.3304	2.5	2.0511	2.4631	473	601	713	502	503	520	465
Garnet 4 Pair A	16 / 1 23 Oct	12 / 1 23 Oct	Rim/Close	0.0562	0.0390	0.2714	0.2235	0.3417	0.3379	2.5	2.1647	2.5323	444	609	689	478	482	502	456
Garnet 4 Pair B	17 / 1 23 Oct	13 / 1 23 Oct	Rim/Close	0.0600	0.0428	0.2703	0.2096	0.3462	0.3420	2.5	2.1156	2.4539	456	617	699	488	491	509	467
Garnet 4 Pair C	18 / 1 23 Oct	14 / 1 23 Oct	Rim/Close	0.0597	0.0420	0.2759	0.2143	0.3552	0.3504	2.5	2.1600	2.5090	445	612	689	479	482	503	459

Sample	Garnet Sample	Biotite sample	Gt/Bt Pairing	XMg(grt)	XMg(grt) P&L83B	XCa(grt)	XMn(grt)	XMg(Bt)	XMg(Bt) P&L 83	Pressure (kbar)	log Kd	Log Kd P & L 83	T(FS)	T(PL81)	T(PG)	T(Th)	T(HL)	T(PL) 83A	T(PL) 83B
Garnet 4 Pair D	24 / 1 23 Oct	15 / 1 23 Oct	Rim/Close	0.0579	0.0404	0.2750	0.2192	0.3508	0.3464	2.5	2.1736	2.5326	442	609	687	477	480	500	456
Garnet 4 Pair E	25 / 1 23 Oct	21 / 1 23 Oct	Rim/Close	0.0520	0.0360	0.2882	0.2184	0.3380	0.3341	2.5	2.2312	2.5967	428	605	675	465	470	492	447
Garnet 4 Pair F	19 / 1 23 Oct	8 / 1 23 Oct	Core/Far	0.0536	0.0344	0.1874	0.2910	0.3390	0.3356	2.5	2.2038	2.6519	435	565	662	471	475	496	440
Garnet 4 Pair G	20 / 1 23 Oct	45 / 1 23 Oct	Core/Far	0.0526	0.0337	0.1865	0.2931	0.3347	0.3304	2.5	2.2040	2.6508	435	565	662	470	474	496	440
Garnet 4 Pair H	19 / 1 23 Oct	48 / 1 23 Oct	Core/Far	0.0536	0.0344	0.1874	0.2910	0.3367	0.3327	2.5	2.1934	2.6389	437	567	665	473	476	497	442
Garnet 4 Pair D	20 / 1 23 Oct	51 / 1 23 Oct	Core/Far	0.0526	0.0337	0.1865	0.2931	0.3381	0.3345	2.5	2.2190	2.6694	431	562	657	468	472	494	438
Garnet 4 Pair E	19 / 1 23 Oct	55 / 1 23 Oct	Core/Far	0.0536	0.0344	0.1874	0.2910	0.3351	0.3309	2.5	2.1862	2.6309	439	568	667	474	478	499	443
Garnet 7 Pair A	4 / 1 23 Oct	8 / 1 23 Oct	Rim/Close	0.0538	0.0369	0.2769	0.2274	0.3390	0.3356	2.5	2.1991	2.5790	436	606	683	471	475	497	450
Garnet 7 Pair B	5 / 1 23 Oct	45 / 1 23 Oct	Rim/Close	0.0541	0.0370	0.2781	0.2272	0.3347	0.3304	2.5	2.1752	2.5513	442	610	691	476	480	500	453
Garnet 7 Pair C	4 / 1 23 Oct	48 / 1 23 Oct	Rim/Close	0.0538	0.0369	0.2769	0.2274	0.3367	0.3327	2.5	2.1887	2.5660	438	607	686	474	477	498	451
Garnet 7 Pair D	5 / 1 23 Oct	51 / 1 23 Oct	Rim/Close	0.0541	0.0370	0.2781	0.2272	0.3381	0.3345	2.5	2.1902	2.5700	438	608	686	473	477	498	451
Garnet 7 Pair E	4 / 1 23 Oct	55 / 1 23 Oct	Rim/Close	0.0538	0.0369	0.2769	0.2274	0.3351	0.3309	2.5	2.1815	2.5580	440	609	689	475	479	499	452

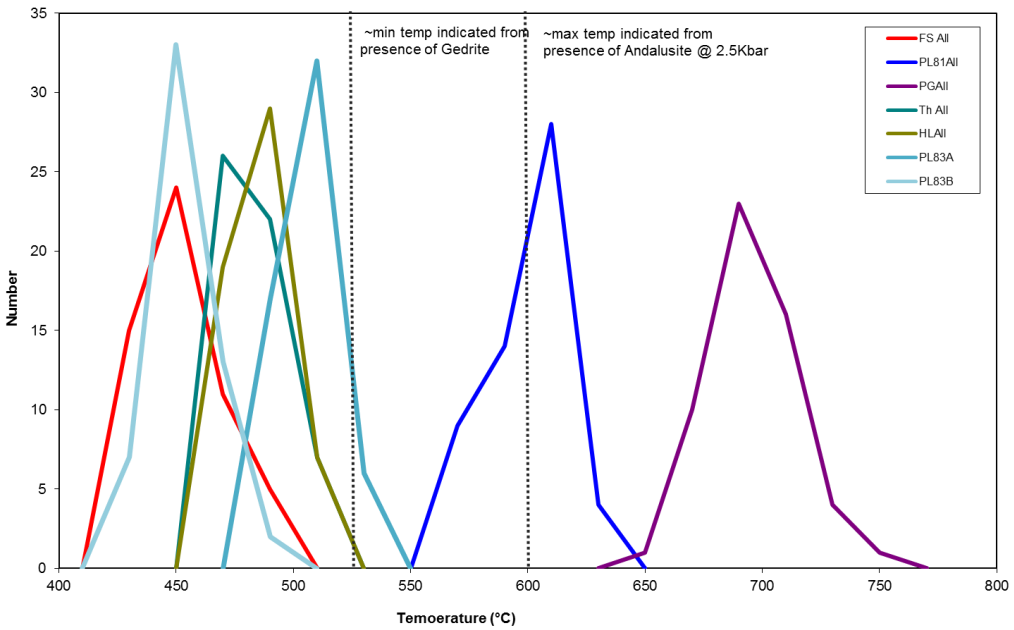

Figure A.9. Histogram of all garnet-biotite pairs in sample AMD139B. Histogram bin width = 20°C, n = 55. The estimated temperatures provided by all geothermometers are inconsistent with the metamorphic mineral assemblages as well as estimates between different calibrations varying by up to 350°C. The high Ca and Mn content, and low Mg, content of the garnets results in underestimates of the equilibrium temperature for calibrations that do not correct for the concentration of these elements, while the PG calibration overestimates the likely peak metamorphic temperature by >100°C . Consequently this sample has not been used for the peak metamorphic temperature estimate in Chapter 2 due to the high spessartine and grossular content of the garnets within the sample.

.

A3.9 Sample CD06

Hole ID/Sample	Core /Rim	Average Almandine %	Average Grossular %	Average Pyrope %	Average Spessartine %	Average Gro + Spess %	Average Garnet composition
ISD080/CD06	Core	61.78	7.51	4.87	25.84	33.35	$Alm_{62}Gro_{8}Py_{5}Sp_{26}$
ISD080/CD06	Rim	82.92	2.94	13.19	0.95	3.89	$Alm_{83}Gro_{3}Py_{13}Sp_{1}$

Table A3.22. Average composition of garnet within CD06. Note the high grossular and spessartine contents.

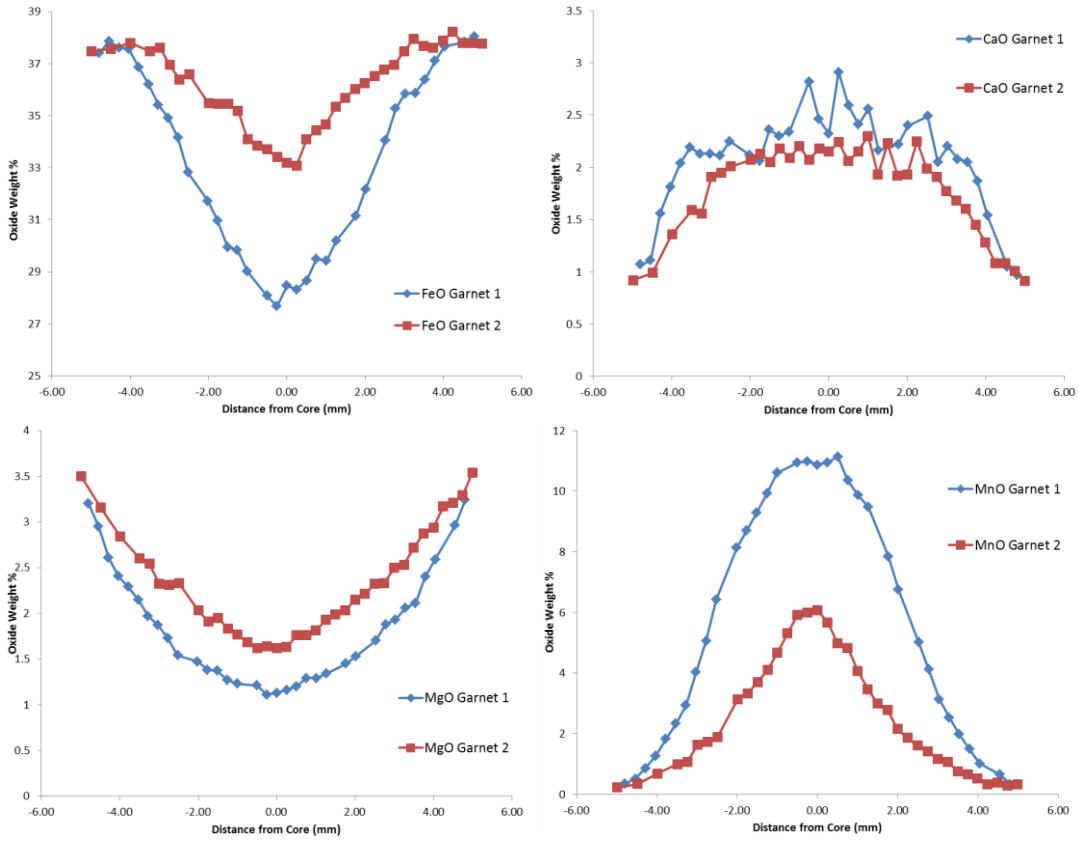

Figure A3.10. Results of a transect across 2 large garnets within sample CD06, showing the typical normal compositional zoning. The core of garnet 1 can be seen to be more Mn and Ca-rich and poorer in Fe and Mg. Analyses were automated across the centre of the garnet porphyroblast and taken every 0.25mm. Analyses were omitted if the total deviated more than ± 1% from 100% or if they had a major element composition that inconsistent with that of garnet (i.e. the analysis was richer in silica than established garnet compositions).

.

Table A3.23. CD06: Analyses of garnet chosen for geothermometry in this study. Cationic proportions of garnets are recalculated on the basis of 24 oxygens, respectively, anhydrous conditions.

Sample Name	Core/Rim	Garnet Number	Na_2O	K_2O	MgO	CaO	MnO	FeO	NiO	Al_2O_3	Cr_2O_3	SiO_2	TiO_2	Total	Na	K	Mg	Ca	Mn	Fe	Al	Si	Ti	Total	XMg(Gt) (Mg/Mg+Fe)	XCa(Gt) Ca/Ca+Mg+Fe+Mn	XMn(Gt) Mn/Ca+Mg+Fe+Mn
1 / 1 10 Oct	Rim	Garnet 1	0.01	0.00	3.50	0.79	0.28	37.64	0.01	21.48	0.00	37.01	0.00	100.73	0.00	0.00	0.84	0.14	0.04	5.04	4.06	5.93	0.00	16.04	0.142	0.022	0.006
2 / 1 10 Oct	Rim	Garnet 1	0.01	0.00	3.46	0.87	0.39	37.58	0.00	21.30	0.00	36.53	0.00	100.15	0.00	0.00	0.83	0.15	0.05	5.08	4.06	5.90	0.00	16.07	0.141	0.025	0.009
1 / 2 10 Oct	Rim	Garnet 1	0.00	0.00	3.20	1.07	0.35	37.40	0.00	21.50	0.00	36.51	0.02	100.06	0.00	0.00	0.77	0.19	0.05	5.05	4.09	5.90	0.00	16.05	0.132	0.031	0.008
1 / 3 10 Oct	Rim	Garnet 1	0.01	0.01	2.95	1.11	0.50	37.86	0.00	21.36	0.00	37.05	0.07	100.91	0.00	0.00	0.71	0.19	0.07	5.08	4.04	5.94	0.01	16.03	0.122	0.032	0.011
1 / 39 10 Oct	Rim	Garnet 1	0.01	0.00	2.96	1.05	0.65	37.83	0.00	21.20	0.00	36.86	0.09	100.64	0.00	0.00	0.71	0.18	0.09	5.09	4.02	5.94	0.01	16.04	0.122	0.030	0.015
1 / 40 10 Oct	Rim	Garnet 1	0.02	0.00	3.24	0.97	0.33	38.03	0.01	21.36	0.00	36.90	0.01	100.86	0.01	0.00	0.77	0.17	0.04	5.10	4.04	5.92	0.00	16.06	0.132	0.027	0.007
1 / 1 10 Oct	Rim	Garnet 1	0.01	0.00	3.60	0.88	0.41	37.70	0.00	21.49	0.01	36.77	0.01	100.87	0.00	0.00	0.86	0.15	0.06	5.05	4.06	5.89	0.00	16.08	0.145	0.025	0.009
2 / 1 10 Oct	Rim	Garnet 1	0.02	0.00	3.55	0.87	0.36	37.61	0.00	21.61	0.00	36.63	0.00	100.66	0.01	0.00	0.85	0.15	0.05	5.05	4.09	5.88	0.00	16.08	0.144	0.025	0.008
9 / 1 10 Oct	Rim	Garnet 1	0.02	0.00	2.88	1.20	0.46	37.96	0.00	21.15	0.00	37.21	0.04	100.92	0.01	0.00	0.69	0.21	0.06	5.09	4.00	5.97	0.01	16.03	0.119	0.034	0.010
10 / 1 10 Oct	Rim	Garnet 1	0.00	0.00	2.88	1.05	0.47	38.07	0.01	21.31	0.00	37.23	0.02	101.04	0.00	0.00	0.69	0.18	0.06	5.10	4.02	5.96	0.00	16.02	0.119	0.030	0.011
12 / 1 10 Oct	Rim	Garnet 1	0.02	0.00	3.50	0.89	0.29	37.90	0.00	21.60	0.00	36.86	0.00	101.06	0.01	0.00	0.83	0.15	0.04	5.07	4.07	5.90	0.00	16.07	0.141	0.025	0.006
13 / 1 10 Oct	Rim	Garnet 1	0.00	0.00	3.49	0.96	0.30	37.69	0.00	21.47	0.00	36.77	0.01	100.69	0.00	0.00	0.84	0.17	0.04	5.06	4.06	5.90	0.00	16.07	0.142	0.027	0.007
19 / 1 10 Oct	Rim	Garnet 2	0.00	0.00	3.59	0.86	0.26	37.82	0.00	21.40	0.01	36.41	0.01	100.37	0.00	0.00	0.86	0.15	0.04	5.10	4.07	5.87	0.00	16.09	0.145	0.024	0.006
20 / 1 10 Oct	Rim	Garnet 2	0.00	0.00	3.57	0.85	0.25	37.83	0.01	21.43	0.01	36.50	0.01	100.48	0.00	0.00	0.86	0.15	0.03	5.10	4.07	5.88	0.00	16.09	0.144	0.024	0.006
23 / 1 10 Oct	Rim	Garnet 2	0.00	0.01	2.84	1.37	0.60	37.49	0.00	21.10	0.00	36.49	0.03	99.93	0.00	0.00	0.69	0.24	0.08	5.09	4.04	5.92	0.00	16.06	0.119	0.039	0.013
24 / 1 10 Oct	Rim	Garnet 2	0.02	0.00	2.94	1.38	0.52	37.55	0.00	21.18	0.00	36.90	0.04	100.55	0.01	0.00	0.71	0.24	0.07	5.06	4.02	5.94	0.01	16.05	0.123	0.039	0.012
27 / 1 10 Oct	Rim	Garnet 2	0.01	0.01	3.32	0.79	0.43	37.95	0.00	21.32	0.00	35.95	0.01	99.79	0.00	0.00	0.81	0.14	0.06	5.16	4.09	5.85	0.00	16.11	0.135	0.022	0.010
28 / 1 10 Oct	Rim	Garnet 2	0.01	0.02	3.31	0.79	0.28	37.70	0.01	21.36	0.00	36.14	0.02	99.63	0.00	0.00	0.80	0.14	0.04	5.13	4.09	5.88	0.00	16.08	0.135	0.022	0.006
31 / 1 10 Oct	Rim	Garnet 2	0.00	0.00	3.34	0.78	0.38	37.70	0.00	21.44	0.00	36.52	0.02	100.19	0.00	0.00	0.81	0.14	0.05	5.09	4.08	5.90	0.00	16.06	0.137	0.022	0.008
32 / 1 10 Oct	Rim	Garnet 2	0.00	0.00	3.43	0.85	0.32	37.92	0.00	21.52	0.00	36.82	0.01	100.87	0.00	0.00	0.82	0.15	0.04	5.08	4.07	5.90	0.00	16.06	0.139	0.024	0.007
33 / 1 10 Oct	Rim	Garnet 2	0.01	0.00	3.36	0.93	0.36	37.99	0.00	21.63	0.00	36.51	0.02	100.80	0.00	0.00	0.81	0.16	0.05	5.10	4.10	5.87	0.00	16.09	0.136	0.026	0.008
34 / 1 10 Oct	Rim	Garnet 2	0.00	0.01	3.29	0.86	0.37	38.03	0.00	21.50	0.00	36.16	0.02	100.26	0.00	0.00	0.80	0.15	0.05	5.15	4.10	5.85	0.00	16.10	0.134	0.024	0.008

Sample Name	Core/Rim	Garnet Number	Na_2O	K_2O	MgO	CaO	MnO	FeO	NiO	Al_2O_3	Cr_2O_3	SiO_2	TiO_2	Total	Na	K	Mg	Ca	Mn	Fe	Al	Si	Ti	Total	**XMg(Gt)** (Mg/Mg+Fe)	**XCa(Gt)** Ca/Ca+Mg+Fe+Mn	**XMn(Gt)** Mn/Ca+Mg+Fe+Mn
2 / 1 10 Oct	Rim	Garnet 2	0.00	0.00	3.50	0.92	0.22	37.46	0.00	21.51	0.01	37.08	0.01	100.70	0.00	0.00	0.84	0.16	0.03	5.02	4.06	5.94	0.00	16.03	0.143	0.026	0.005
2 / 3 10 Oct	Rim	Garnet 2	0.00	0.00	3.16	0.99	0.34	37.57	0.00	21.35	-0.01	36.54	0.01	99.97	0.00	0.00	0.76	0.17	0.05	5.09	4.07	5.91	0.00	16.05	0.130	0.028	0.008
2 / 39 10 Oct	Rim	Garnet 2	0.01	0.00	3.21	1.08	0.38	37.79	0.00	21.63	0.00	36.37	0.03	100.49	0.00	0.00	0.77	0.19	0.05	5.09	4.11	5.86	0.00	16.08	0.131	0.031	0.009
2 / 40 10 Oct	Rim	Garnet 2	0.00	0.00	3.29	1.01	0.28	37.78	0.00	21.39	0.00	36.69	0.02	100.47	0.00	0.00	0.79	0.18	0.04	5.09	4.06	5.91	0.00	16.06	0.134	0.029	0.006
2 / 41 10 Oct	Rim	Garnet 2	0.00	0.00	3.54	0.91	0.32	37.76	0.00	21.56	0.01	36.82	0.01	100.94	0.00	0.00	0.85	0.16	0.04	5.06	4.07	5.90	0.00	16.07	0.143	0.025	0.007
1 / 19 10 Oct	Core	Garnet 1	0.01	0.00	1.21	2.82	10.93	28.08	0.00	20.96	0.00	35.56	0.22	99.79	0.00	0.00	0.30	0.50	1.52	3.86	4.06	5.84	0.03	16.10	0.071	0.080	0.246
1 / 20 10 Oct	Core	Garnet 1	0.01	0.00	1.11	2.46	10.98	27.67	0.01	20.19	0.00	36.35	0.24	99.00	0.00	0.00	0.27	0.43	1.54	3.82	3.93	6.00	0.03	16.01	0.067	0.072	0.253
1 / 21 10 Oct	Core	Garnet 1	0.00	0.00	1.13	2.32	10.87	28.46	0.02	20.08	0.00	34.34	3.69	100.92	0.00	0.00	0.28	0.41	1.50	3.89	3.87	5.61	0.45	16.00	0.066	0.067	0.248
1 /22 10 Oct	Core	Garnet 1	0.00	0.00	1.16	2.91	10.94	28.31	0.00	20.85	0.01	35.39	0.20	99.76	0.00	0.00	0.28	0.51	1.53	3.90	4.05	5.83	0.03	16.12	0.068	0.082	0.245
1 / 23 10 Oct	Core	Garnet 1	0.02	0.00	1.20	2.59	11.14	28.65	0.00	20.77	0.00	35.44	0.20	100.02	0.01	0.00	0.30	0.46	1.55	3.94	4.03	5.83	0.03	16.14	0.070	0.073	0.249
6 / 1 10 Oct	Core	Garnet 1	0.01	0.00	1.27	2.36	10.78	28.68	0.00	20.78	0.00	35.44	0.20	99.54	0.01	0.00	0.31	0.42	1.51	3.96	4.04	5.85	0.03	16.11	0.073	0.067	0.243
7 / 1 10 Oct	Core	Garnet 1	0.02	0.00	1.17	2.41	11.29	28.19	0.00	20.94	0.00	36.60	0.16	100.79	0.01	0.00	0.28	0.42	1.55	3.82	4.00	5.94	0.02	16.05	0.069	0.069	0.255
8 / 1 10 Oct	Core	Garnet 1	0.00	0.00	1.19	2.40	11.30	28.79	0.00	20.96	0.00	36.27	0.16	101.08	0.00	0.00	0.29	0.42	1.55	3.91	4.01	5.89	0.02	16.09	0.069	0.068	0.252
2 / 19 10 Oct	Core	Garnet 2	0.00	0.00	1.62	2.07	5.92	33.70	0.00	21.04	0.00	36.13	0.08	100.57	0.00	0.00	0.39	0.36	0.82	4.59	4.04	5.88	0.01	16.09	0.079	0.059	0.133
2 / 20 10 Oct	Core	Garnet 2	0.00	0.00	1.64	2.18	6.00	33.41	0.00	21.08	0.01	36.46	0.08	100.87	0.00	0.00	0.40	0.38	0.82	4.53	4.03	5.91	0.01	16.07	0.080	0.062	0.135
2 / 21 10 Oct	Core	Garnet 2	0.02	0.00	1.62	2.15	6.06	33.19	0.01	20.97	0.01	35.88	0.05	99.96	0.01	0.00	0.40	0.38	0.84	4.55	4.05	5.88	0.01	16.10	0.080	0.061	0.137
2 / 22 10 Oct	Core	Garnet 2	0.04	0.00	1.63	2.24	5.66	33.07	0.00	21.04	0.00	35.56	0.10	99.34	0.01	0.00	0.40	0.40	0.79	4.55	4.08	5.85	0.01	16.10	0.081	0.064	0.129

Table A3.24. CD06: Analyses of biotite chosen for geothermometry in this study. Cationic proportions of biotite are recalculated on the basis of 22 oxygens, anhydrous conditions. – denotes not analysed

Sample Number	Associated Garnet	Far/Close?	Cl	F	Na_2O	K_2O	MgO	CaO	MnO	FeO	NiO	Al_2O_3	Cr_2O_3	SiO_2	TiO_2	Total	Si	Ti	Al	Fe^{2+}	Mn	Mg	Ca	Na	K	Total	Mg/Mg+Fe
3 / 1 10 Oct	Close	Garnet 1	-	0.08	0.04	5.04	11.82	0.02	0.09	27.35	0.07	18.34	0.00	32.24	0.56	95.62	5.01	0.07	3.36	3.55	0.01	2.74	0.00	0.01	1.00	15.75	0.435
4 / 1 10 Oct	Close	Garnet 1	-	0.11	0.15	8.67	10.02	0.05	0.03	22.90	0.08	18.36	0.01	35.44	0.86	96.69	5.40	0.10	3.29	2.92	0.00	2.27	0.01	0.04	1.68	15.72	0.438
3 / 1 11 Oct	Close	Garnet 1	-	0.11	0.06	7.91	10.63	0.04	0.07	24.53	0.07	18.88	0.01	34.83	0.46	97.58	5.27	0.05	3.37	3.11	0.01	2.40	0.01	0.02	1.53	15.76	0.436
4 / 1 11 Oct	Close	Garnet 1	-	0.08	0.09	8.81	9.94	0.06	0.06	23.29	0.08	18.61	0.00	35.79	0.72	97.53	5.41	0.08	3.31	2.94	0.01	2.24	0.01	0.03	1.70	15.72	0.432
2 / 1 22 Oct	Close	Garnet 1	0.03	0.10	0.25	7.95	9.79	0.04	0.02	23.13	0.07	18.38	0.01	34.91	0.74	95.42	5.38	0.09	3.34	2.98	0.00	2.25	0.01	0.07	1.56	15.68	0.430
3 / 1 22 Oct	Close	Garnet 1	0.03	0.14	0.09	8.30	9.92	0.02	0.02	22.54	0.09	18.60	0.00	34.86	0.59	95.20	5.38	0.07	3.38	2.91	0.00	2.28	0.00	0.03	1.63	15.69	0.440
4 / 1 22 Oct	Close	Garnet 1	0.04	0.10	0.10	8.55	9.66	0.07	0.04	21.76	0.09	17.99	0.00	34.70	0.86	93.94	5.42	0.10	3.31	2.84	0.01	2.25	0.01	0.03	1.70	15.69	0.442
6 / 1 22 Oct	Close	Garnet 1	0.04	0.05	0.08	8.04	9.57	0.04	0.06	22.33	0.11	17.28	0.00	34.88	0.93	93.42	5.48	0.11	3.20	2.94	0.01	2.24	0.01	0.02	1.61	15.62	0.433
31 / 1 22 B Oct	Close	Garnet 1	0.04	0.11	0.07	8.01	9.51	0.03	0.02	22.30	0.08	17.83	0.00	34.14	0.86	93.00	5.40	0.10	3.32	2.95	0.00	2.24	0.01	0.02	1.62	15.66	0.432
32 / 1 22 B Oct	Close	Garnet 1	0.03	0.07	0.22	8.24	9.74	0.05	0.02	22.42	0.06	17.52	0.00	35.23	0.85	94.46	5.48	0.10	3.21	2.91	0.00	2.26	0.01	0.07	1.63	15.67	0.436
8 / 1 22 Oct	Close	Garnet 2	0.03	0.09	0.22	8.17	9.81	0.02	0.04	23.30	0.08	18.57	0.00	35.35	0.87	96.56	5.38	0.10	3.33	2.97	0.01	2.23	0.00	0.06	1.59	15.68	0.429
9 / 1 22 Oct	Close	Garnet 2	0.03	0.08	0.22	8.17	9.77	0.01	0.04	24.13	0.05	17.85	0.00	34.66	0.89	95.89	5.35	0.10	3.25	3.12	0.01	2.25	0.00	0.07	1.61	15.76	0.419
9 / 1 22 B Oct	Close	Garnet 3	0.03	0.06	0.18	8.45	9.94	0.00	0.05	22.53	0.09	18.90	0.02	34.98	0.79	96.02	5.35	0.09	3.41	2.88	0.01	2.27	0.00	0.05	1.65	15.71	0.440
10 / 1 22 B Oct	Close	Garnet 3	0.03	0.06	0.42	7.96	10.07	0.01	0.03	22.73	0.08	17.84	0.00	35.86	0.76	95.86	5.48	0.09	3.21	2.91	0.00	2.29	0.00	0.12	1.55	15.66	0.441
12 / 1 22 B Oct	Close	Garnet 3	0.04	0.09	0.12	8.62	10.04	0.04	0.04	23.04	0.09	17.76	0.02	35.44	0.59	95.93	5.45	0.07	3.22	2.96	0.01	2.30	0.01	0.04	1.69	15.74	0.437
13 / 1 22 B Oct	Close	Garnet 3	0.05	0.11	0.07	6.93	10.92	0.02	0.06	24.97	0.07	17.42	0.02	34.50	0.46	95.60	5.34	0.05	3.18	3.23	0.01	2.52	0.00	0.02	1.37	15.72	0.438
14 / 1 22 B Oct	Close	Garnet 3	0.04	0.08	0.08	7.97	9.99	0.02	0.04	22.79	0.06	18.58	0.02	35.17	0.42	95.25	5.41	0.05	3.37	2.93	0.01	2.29	0.00	0.02	1.56	15.65	0.439
17 / 1 22 B Oct	Close	Garnet 3	0.04	0.10	0.13	8.09	9.89	0.05	0.05	23.82	0.08	18.00	0.01	35.23	0.59	96.08	5.41	0.07	3.26	3.06	0.01	2.26	0.01	0.04	1.59	15.70	0.425
18 / 1 22 B Oct	Close	Garnet 3	0.04	0.07	0.09	7.83	9.81	0.05	0.04	22.97	0.06	17.87	0.03	36.15	0.69	95.72	5.52	0.08	3.22	2.94	0.01	2.23	0.01	0.03	1.53	15.56	0.432
38 / 1 22 B Oct	Far	Garnet 1 & 7	0.04	0.13	0.18	8.12	10.31	0.03	0.05	23.48	0.06	17.39	0.00	35.63	0.78	96.20	5.46	0.09	3.14	3.01	0.01	2.35	0.00	0.05	1.59	15.70	0.439
39 / 1 22 B Oct	Far	Garnet 1 & 8	0.04	0.12	0.25	7.78	10.02	0.02	0.05	23.18	0.08	18.18	0.01	34.12	0.78	94.61	5.32	0.09	3.34	3.02	0.01	2.33	0.00	0.08	1.55	15.73	0.435

Sample Number	Associated Garnet	Far/Close?	Cl	F	Na_2O	K_2O	MgO	CaO	MnO	FeO	NiO	Al_2O_3	Cr_2O_3	SiO_2	TiO_2	Total	Si	Ti	Al	Fe^{2+}	Mn	Mg	Ca	Na	K	Total	Mg/Mg+Fe
10 / 1 22 Oct	Far	None	0.04	0.11	0.14	8.11	10.09	0.01	0.03	22.29	0.08	17.94	0.00	34.96	0.77	94.55	5.42	0.09	3.28	2.89	0.00	2.33	0.00	0.04	1.60	15.67	0.447
11 / 1 22 Oct	Far	None	0.03	0.11	0.13	7.94	10.10	0.01	0.04	22.10	0.09	18.36	0.00	35.04	0.77	94.74	5.41	0.09	3.34	2.85	0.01	2.33	0.00	0.04	1.56	15.63	0.449
12 / 1 22 Oct	Far	None	0.03	0.11	0.11	8.23	10.20	0.02	0.02	22.48	0.08	18.46	0.00	34.66	0.76	95.16	5.35	0.09	3.36	2.90	0.00	2.35	0.00	0.03	1.62	15.71	0.447
13 / 1 22 Oct	Far	None	0.04	0.12	0.17	8.04	9.80	0.02	0.03	22.64	0.10	18.23	0.00	34.50	0.73	94.41	5.37	0.09	3.35	2.95	0.00	2.28	0.00	0.05	1.60	15.69	0.436
14 / 1 22 Oct	Far	None	0.04	0.12	0.14	7.90	10.04	0.02	0.04	23.00	0.09	17.86	0.00	33.96	0.72	93.93	5.34	0.09	3.31	3.02	0.01	2.35	0.00	0.04	1.58	15.74	0.438
17 / 1 22 Oct	Far	None	0.04	0.08	0.23	8.18	9.82	0.05	0.03	22.49	0.06	18.20	0.00	35.66	0.94	95.78	5.45	0.11	3.28	2.88	0.00	2.24	0.01	0.07	1.60	15.63	0.438
18 / 1 22 Oct	Far	None	0.04	0.11	0.07	7.77	9.89	0.04	0.02	23.27	0.06	17.86	0.00	34.02	0.93	94.10	5.33	0.11	3.30	3.05	0.00	2.31	0.01	0.02	1.55	15.69	0.431
1 / 1 22 B Oct	Far	None	0.04	0.11	0.18	8.18	10.02	0.04	0.04	22.79	0.09	17.63	0.00	35.46	0.98	95.55	5.45	0.11	3.20	2.93	0.01	2.30	0.01	0.05	1.61	15.66	0.439
2 / 1 22 B Oct	Far	None	0.03	0.12	0.24	8.28	9.78	0.03	0.02	23.42	0.06	18.93	0.00	35.47	0.95	97.32	5.36	0.11	3.37	2.96	0.00	2.20	0.00	0.07	1.60	15.68	0.427
3 / 1 22 B Oct	Far	None	0.04	0.08	0.27	8.09	9.81	0.03	0.05	23.15	0.08	18.33	0.00	36.24	0.96	97.13	5.47	0.11	3.26	2.92	0.01	2.21	0.00	0.08	1.56	15.61	0.430
4 / 1 22 B Oct	Far	None	0.04	0.08	0.19	8.79	9.35	0.03	0.02	22.19	0.07	17.70	0.00	35.71	1.00	95.19	5.51	0.12	3.22	2.86	0.00	2.15	0.00	0.06	1.73	15.66	0.429
5 / 1 22 B Oct	Far	None	0.04	0.06	0.13	8.09	9.60	0.02	0.01	22.90	0.05	17.86	0.01	36.75	0.89	96.41	5.57	0.10	3.19	2.90	0.00	2.17	0.00	0.04	1.56	15.54	0.428
7 / 1 22 B Oct	Far	None	0.03	0.07	0.18	8.31	9.75	0.01	0.03	22.95	0.07	18.14	0.01	35.97	0.89	96.42	5.47	0.10	3.25	2.92	0.00	2.21	0.00	0.05	1.61	15.63	0.431
19 / 1 22 B Oct	Far	None	0.04	0.10	0.20	7.93	9.87	0.10	0.03	22.96	0.06	17.94	0.01	35.07	0.92	95.23	5.41	0.11	3.26	2.96	0.00	2.27	0.02	0.06	1.56	15.66	0.434
20 / 1 22 B Oct	Far	None	0.04	0.10	0.21	7.83	9.87	0.06	0.06	22.53	0.09	17.93	0.00	35.44	0.90	95.06	5.46	0.10	3.26	2.90	0.01	2.27	0.01	0.06	1.54	15.61	0.438
22 / 1 22 B Oct	Far	None	0.04	0.08	0.26	7.98	9.77	0.08	0.03	23.53	0.04	18.21	0.00	34.77	0.88	95.68	5.36	0.10	3.31	3.03	0.00	2.24	0.01	0.08	1.57	15.71	0.425
23 / 1 22 B Oct	Far	None	0.04	0.12	0.29	8.08	9.74	0.07	0.06	23.24	0.06	17.55	0.00	35.72	0.93	95.89	5.48	0.11	3.17	2.98	0.01	2.23	0.01	0.09	1.58	15.66	0.428
26 / 1 22 B Oct	Far	None	0.04	0.07	0.06	6.98	10.64	0.06	0.03	24.62	0.05	17.70	0.00	33.83	0.90	94.99	5.27	0.11	3.25	3.20	0.00	2.47	0.01	0.02	1.39	15.71	0.435
27 / 1 22 B Oct	Far	None	0.04	0.07	0.06	7.47	10.18	0.05	0.08	24.42	0.05	17.96	0.01	34.17	0.85	95.42	5.30	0.10	3.28	3.17	0.01	2.35	0.01	0.02	1.48	15.71	0.426

Table A3.25. Molar fractions of garnet and biotite pairs chosen for geothermometry in sample CD06. Molar fraction equations are from Ferry and Spear (1978) (=FS) and Perchuk and Lavrent'eva (1983) (=P&L83B). Distribution coefficients (Kd) and temperatures (T in°C) are calculated using the calibrations of Ferry and Spear (1978) (T(FS)), Lavrent'eva and Perchuk (1981) (=T(PL81)), Pigage and Greenwood (1980) (=T(PG)), Thompson (1976) (T(Th)), Holdaway and Lee (1977) (T(HL)) and Perchuk and Lavrent'eva (1983) (T(PL83A)) and (T(PL83B)).

Sample	Garnet Sample	Biotite sample	Gt/Bt Pairing	XMg(grt)	XMg(grt) P&L83B	XCa(grt)	XMn(grt)	XMg(Bt)	XMg(Bt) P&L 83	Pressure (kbar)	log Kd	Log Kd P & L 83	T(FS)	T(PL81)	T(PG)	T(Th)	T(HL)	T(PL) 83A	T(PL) 83B
Garnet 1 Pair A	1 / 1 10 Oct	3 / 1 10 Oct	Rim/Close	0.1422	0.1413	0.0225	0.0063	0.4351	0.4343	2.5	1.5361	1.5402	639	605	658	631	617	612	622
Garnet 1 Pair B	2 / 1 10 Oct	4 / 1 10 Oct	Rim/Close	0.1411	0.1398	0.0245	0.0087	0.4382	0.4379	2.5	1.5577	1.5668	630	602	652	625	611	608	616
Garnet 1 Pair C	1 / 2 10 Oct	3 / 1 11 Oct	Rim/Close	0.1323	0.1312	0.0307	0.0079	0.4358	0.4351	2.5	1.6230	1.6295	606	592	630	606	595	595	604
Garnet 1 Pair D	1 / 3 10 Oct	4 / 1 11 Oct	Rim/Close	0.1219	0.1205	0.0316	0.0113	0.4321	0.4314	2.5	1.7009	1.7116	578	578	604	585	577	580	588
Garnet 1 Pair G	1 / 39 10 Oct	4 / 1 22 Oct	Rim/Close	0.1223	0.1205	0.0296	0.0147	0.4418	0.4283	2.5	1.7365	1.6991	566	570	592	576	569	574	590
Garnet 1 Pair H	1 / 40 10 Oct	6 / 1 22 Oct	Rim/Close	0.1317	0.1307	0.0273	0.0072	0.4331	0.4188	2.5	1.6168	1.5668	608	592	630	608	597	596	616
Garnet 1 Pair I	1 / 1 10 Oct	3 / 1 10 Oct	Rim/Close	0.1454	0.1441	0.0247	0.0090	0.4351	0.4343	2.5	1.5101	1.5176	649	611	671	639	623	618	626
Garnet 1 Pair J	2 / 1 10 Oct	4 / 1 10 Oct	Rim/Close	0.1439	0.1427	0.0246	0.0080	0.4382	0.4379	2.5	1.5346	1.5429	639	606	661	631	617	613	621
Garnet 1 Pair K	9 / 1 10 Oct	3 / 1 11 Oct	Rim/Close	0.1192	0.1179	0.0342	0.0102	0.4358	0.4351	2.5	1.7420	1.7512	564	572	591	575	567	573	580
Garnet 1 Pair L	10 / 1 10 Oct	4 / 1 11 Oct	Rim/Close	0.1187	0.1174	0.0299	0.0106	0.4321	0.4314	2.5	1.7311	1.7409	568	572	592	577	570	575	582
Garnet 1 Pair M	12 / 1 10 Oct	2 / 1 22 Oct	Rim/Close	0.1413	0.1403	0.0251	0.0064	0.4300	0.4298	2.5	1.5231	1.5299	644	609	665	635	620	615	624
Garnet 1 Pair N	13 / 1 10 Oct	3 / 1 22 Oct	Rim/Close	0.1416	0.1407	0.0270	0.0067	0.4396	0.4394	2.5	1.5590	1.5662	630	603	652	624	611	608	617
Garnet 2 Pair A	19 / 1 10 Oct	9 / 1 22 Oct	Rim/Close	0.1448	0.1440	0.0242	0.0059	0.4402	0.4397	2.5	1.5354	1.5402	639	606	659	631	617	613	622
Garnet 2 Pair B	20 / 1 10 Oct	10 / 1 22 Oct	Rim/Close	0.1441	0.1433	0.0238	0.0055	0.4413	0.4409	2.5	1.5453	1.5506	635	604	654	628	614	611	620
Garnet 2 Pair C	23 / 1 10 Oct	12 / 1 22 Oct	Rim/Close	0.1188	0.1171	0.0392	0.0135	0.4372	0.4367	2.5	1.7512	1.7654	561	573	593	572	565	571	578
Garnet 2 Pair D	24 / 1 10 Oct	13 / 1 22 Oct	Rim/Close	0.1225	0.1210	0.0394	0.0117	0.4381	0.4375	2.5	1.7197	1.7312	572	578	603	580	572	577	584
Garnet 2 Pair E	27 / 1 10 Oct	14 / 1 22 Oct	Rim/Close	0.1350	0.1337	0.0222	0.0096	0.4386	0.4382	2.5	1.6105	1.6201	610	590	630	610	598	598	606
Garnet 2 Pair F	28 / 1 10 Oct	17 / 1 22 Oct	Rim/Close	0.1353	0.1345	0.0225	0.0062	0.4253	0.4248	2.5	1.5538	1.5591	632	601	650	626	612	609	618
Garnet 2 Pair G	31 / 1 10 Oct	18 / 1 22 Oct	Rim/Close	0.1365	0.1354	0.0224	0.0084	0.4322	0.4318	2.5	1.5716	1.5799	625	598	645	621	608	605	614
Garnet 2 Pair H	32 / 1 10 Oct	9 / 1 22 Oct	Rim/Close	0.1389	0.1379	0.0238	0.0072	0.4402	0.4397	2.5	1.5843	1.5907	620	596	640	617	605	603	612

Sample	Garnet Sample	Biotite sample	Gt/Bt Pairing	XMg(grt)	XMg(grt) P&L83B	XCa(grt)	XMn(grt)	XMg(Bt)	XMg(Bt) P&L 83	Pressure (kbar)	log Kd	Log Kd P & L 83	T(FS)	T(PL81)	T(PG)	T(Th)	T(HL)	T(PL) 83A	T(PL) 83B
Garnet 2 Pair I	33 / 1 10 Oct	10 / 1 22 Oct	Rim/Close	0.1362	0.1351	0.0260	0.0078	0.4413	0.4409	2.5	1.6109	1.6189	610	592	632	610	598	598	606
Garnet 2 Pair J	34 / 1 10 Oct	12 / 1 22 Oct	Rim/Close	0.1338	0.1327	0.0243	0.0083	0.4372	0.4367	2.5	1.6150	1.6231	609	590	629	608	597	597	605
Garnet 2 Pair K	2 / 1 10 Oct	13 / 1 22 Oct	Rim/Close	0.1427	0.1420	0.0263	0.0048	0.4381	0.4375	2.5	1.5437	1.5471	636	605	656	629	615	611	620
Garnet 2 Pair L	2 / 3 10 Oct	14 / 1 22 Oct	Rim/Close	0.1303	0.1293	0.0284	0.0077	0.4386	0.4382	2.5	1.6514	1.6588	595	586	618	598	588	590	598
Garnet 2 Pair M	2 / 39 10 Oct	17 / 1 22 Oct	Rim/Close	0.1315	0.1303	0.0306	0.0087	0.4253	0.4248	2.5	1.5872	1.5954	619	599	644	616	604	602	611
Garnet 2 Pair N	2 / 40 10 Oct	18 / 1 22 Oct	Rim/Close	0.1343	0.1334	0.0287	0.0062	0.4322	0.4318	2.5	1.5909	1.5966	617	597	640	615	603	602	610
Garnet 2 Pair O	2 / 41 10 Oct	9 / 1 22 Oct	Rim/Close	0.1432	0.1422	0.0254	0.0071	0.4402	0.4397	2.5	1.5488	1.5550	634	604	655	627	613	610	619
Garnet 1 Pair O	1 / 19 10 Oct	38 / 1 22 Oct	Core/Far	0.0715	0.0523	0.0804	0.2464	0.4391	0.4385	2.5	2.3192	2.6494	408	499	553	448	454	479	440
Garnet 1 Pair P	1 / 20 10 Oct	39 / 1 22 Oct	Core/Far	0.0670	0.0487	0.0716	0.2533	0.4352	0.4347	2.5	2.3734	2.7093	397	487	538	438	445	471	433
Garnet 1 Pair Q	1 / 21 10 Oct	10 / 1 22 Oct	Core/Far	0.0663	0.0487	0.0667	0.2477	0.4466	0.4462	2.5	2.4307	2.7564	385	477	519	428	436	463	427
Garnet 1 Pair R	1 /22 10 Oct	11 / 1 22 Oct	Core/Far	0.0679	0.0497	0.0824	0.2453	0.4489	0.4485	2.5	2.4145	2.7430	388	486	529	431	439	465	428
Garnet 1 Pair S	1 / 23 10 Oct	12 / 1 22 Oct	Core/Far	0.0696	0.0510	0.0732	0.2485	0.4472	0.4469	2.5	2.3800	2.7112	395	487	535	437	444	470	432
Garnet 1 Pair T	6 / 1 10 Oct	13 / 1 22 Oct	Core/Far	0.0733	0.0542	0.0673	0.2432	0.4355	0.4352	2.5	2.2777	2.5989	418	499	557	456	462	485	447
Garnet 1 Pair U	7 / 1 10 Oct	14 / 1 22 Oct	Core/Far	0.0689	0.0500	0.0691	0.2553	0.4376	0.4372	2.5	2.3527	2.6916	401	489	543	442	449	474	435
Garnet 1 Pair V	8 / 1 10 Oct	17 / 1 22 Oct	Core/Far	0.0686	0.0501	0.0678	0.2518	0.4377	0.4373	2.5	2.3575	2.6907	400	488	539	441	448	473	435
Garnet 1 Pair W	1 / 19 10 Oct	18 / 1 22 Oct	Core/Far	0.0715	0.0523	0.0804	0.2464	0.4310	0.4308	2.5	2.2866	2.6181	416	504	562	455	460	483	444
Garnet 1 Pair X	1 / 20 10 Oct	1 / 1 22 Oct	Core/Far	0.0670	0.0487	0.0716	0.2533	0.4394	0.4389	2.5	2.3904	2.7266	393	485	533	435	443	469	430
Garnet 1 Pair Y	1 / 21 10 Oct	2 / 1 22 Oct	Core/Far	0.0663	0.0487	0.0667	0.2477	0.4267	0.4265	2.5	2.3500	2.6762	402	488	539	443	449	474	437
Garnet 1 Pair Z	1 /22 10 Oct	3 / 1 22 Oct	Core/Far	0.0679	0.0497	0.0824	0.2453	0.4303	0.4298	2.5	2.3390	2.6671	404	497	549	445	451	476	438
Garnet 1 Pair AA	1 / 23 10 Oct	4 / 1 22 Oct	Core/Far	0.0696	0.0510	0.0732	0.2485	0.4289	0.4287	2.5	2.3060	2.6371	411	498	554	451	457	481	442
Garnet 1 Pair BB	6 / 1 10 Oct	5 / 1 22 Oct	Core/Far	0.0733	0.0542	0.0673	0.2432	0.4277	0.4276	2.5	2.2457	2.5678	425	504	565	462	467	490	451
Garnet 1 Pair CC	7 / 1 10 Oct	7 / 1 22 Oct	Core/Far	0.0689	0.0500	0.0691	0.2553	0.4309	0.4306	2.5	2.3256	2.6649	407	493	550	447	453	478	438

Sample	Garnet Sample	Biotite sample	Gt/Bt Pairing	XMg(grt)	XMg(grt) P&L83B	XCa(grt)	XMn(grt)	XMg(Bt)	XMg(Bt) P&L 83	Pressure (kbar)	log Kd	Log Kd P & L 83	T(FS)	T(PL81)	T(PG)	T(Th)	T(HL)	T(PL) 83A	T(PL) 83B
Garnet 1 Pair DD	8 / 1 10 Oct	19 / 1 22 Oct	Core/Far	0.0686	0.0501	0.0678	0.2518	0.4338	0.4335	2.5	2.3419	2.6751	403	490	543	444	451	475	437
Garnet 1 Pair EE	1 / 19 10 Oct	20 / 1 22 Oct	Core/Far	0.0715	0.0523	0.0804	0.2464	0.4385	0.4378	2.5	2.3169	2.6465	409	500	554	449	455	479	441
Garnet 1 Pair FF	1 / 20 10 Oct	22 / 1 22 Oct	Core/Far	0.0670	0.0487	0.0716	0.2533	0.4253	0.4250	2.5	2.3332	2.6699	405	493	548	446	452	477	438
Garnet 1 Pair GG	1 / 21 10 Oct	23 / 1 22 Oct	Core/Far	0.0663	0.0487	0.0667	0.2477	0.4276	0.4270	2.5	2.3537	2.6781	401	488	538	442	449	474	437
Garnet 1 Pair HH	1 /22 10 Oct	26 / 1 22 Oct	Core/Far	0.0679	0.0497	0.0824	0.2453	0.4351	0.4348	2.5	2.3586	2.6877	400	494	544	441	448	473	435
Garnet 1 Pair II	1 / 23 10 Oct	27 / 1 22 Oct	Core/Far	0.0696	0.0510	0.0732	0.2485	0.4263	0.4255	2.5	2.2953	2.6240	414	499	557	453	459	482	444
Garnet 2 Pair P	2 / 19 10 Oct	38 / 1 22 Oct	Core/Far	0.0791	0.0679	0.0586	0.1326	0.4391	0.4385	2.5	2.2101	2.3718	433	506	522	469	473	495	478
Garnet 2 Pair Q	2 / 20 10 Oct	39 / 1 22 Oct	Core/Far	0.0804	0.0689	0.0617	0.1345	0.4352	0.4347	2.5	2.1760	2.3410	441	512	534	476	480	500	483
Garnet 2 Pair R	2 / 21 10 Oct	10 / 1 22 Oct	Core/Far	0.0800	0.0683	0.0614	0.1365	0.4466	0.4462	2.5	2.2284	2.3968	429	504	521	466	470	492	475
Garnet 2 Pair S	2 / 22 10 Oct	11 / 1 22 Oct	Core/Far	0.0809	0.0698	0.0644	0.1285	0.4489	0.4485	2.5	2.2246	2.3826	430	506	520	466	471	493	477
Garnet 2 Pair T	2 / 23 10 Oct	12 / 1 22 Oct	Core/Far	0.0842	0.0742	0.0589	0.1122	0.4472	0.4469	2.5	2.1746	2.3115	442	511	523	476	480	500	487
Garnet 2 Pair U	2 / 19 10 Oct	13 / 1 22 Oct	Core/Far	0.0791	0.0679	0.0586	0.1326	0.4355	0.4352	2.5	2.1958	2.3583	437	508	526	472	476	497	480
Garnet 2 Pair V	2 / 20 10 Oct	14 / 1 22 Oct	Core/Far	0.0804	0.0689	0.0617	0.1345	0.4376	0.4372	2.5	2.1858	2.3512	439	511	531	474	478	499	481
Garnet 2 Pair W	2 / 21 10 Oct	17 / 1 22 Oct	Core/Far	0.0800	0.0683	0.0614	0.1365	0.4377	0.4373	2.5	2.1923	2.3607	437	510	530	473	477	498	480
Garnet 2 Pair X	2 / 22 10 Oct	18 / 1 22 Oct	Core/Far	0.0809	0.0698	0.0644	0.1285	0.4310	0.4308	2.5	2.1520	2.3109	447	517	539	481	484	504	487
Garnet 2 Pair Y	2 / 23 10 Oct	1 / 1 22 Oct	Core/Far	0.0842	0.0742	0.0589	0.1122	0.4394	0.4389	2.5	2.1431	2.2791	449	516	532	483	486	505	492
Garnet 2 Pair Z	2 / 19 10 Oct	2 / 1 22 Oct	Core/Far	0.0791	0.0679	0.0586	0.1326	0.4267	0.4265	2.5	2.1599	2.3228	445	513	536	479	482	503	486
Garnet 2 Pair AA	2 / 20 10 Oct	3 / 1 22 Oct	Core/Far	0.0804	0.0689	0.0617	0.1345	0.4303	0.4298	2.5	2.1561	2.3211	446	515	539	480	483	503	486
Garnet 2 Pair BB	2 / 21 10 Oct	4 / 1 22 Oct	Core/Far	0.0800	0.0683	0.0614	0.1365	0.4289	0.4287	2.5	2.1567	2.3255	446	515	540	480	483	503	485
Garnet 2 Pair CC	2 / 22 10 Oct	5 / 1 22 Oct	Core/Far	0.0809	0.0698	0.0644	0.1285	0.4277	0.4276	2.5	2.1383	2.2976	451	519	543	484	486	506	489
Garnet 2 Pair DD	2 / 23 10 Oct	7 / 1 22 Oct	Core/Far	0.0842	0.0742	0.0589	0.1122	0.4309	0.4306	2.5	2.1088	2.2453	458	521	541	490	492	511	497
Garnet 2 Pair EE	2 / 19 10 Oct	19 / 1 22 Oct	Core/Far	0.0791	0.0679	0.0586	0.1326	0.4338	0.4335	2.5	2.1889	2.3514	438	509	528	473	477	498	481
Garnet 2 Pair FF	2 / 20 10 Oct	20 / 1 22 Oct	Core/Far	0.0804	0.0689	0.0617	0.1345	0.4385	0.4378	2.5	2.1893	2.3538	438	510	530	473	477	498	481

Sample	Garnet Sample	Biotite sample	Gt/Bt Pairing	XMg(grt)	XMg(grt) P&L83B	XCa(grt)	XMn(grt)	XMg(Bt)	XMg(Bt) P&L 83	Pressure (kbar)	log Kd	Log Kd P & L 83	T(FS)	T(PL81)	T(PG)	T(Th)	T(HL)	T(PL) 83A	T(PL) 83B
Garnet 2 Pair GG	2 / 21 10 Oct	22 / 1 22 Oct	Core/Far	0.0800	0.0683	0.0614	0.1365	0.4253	0.4250	2.5	2.1420	2.3105	450	517	544	483	486	505	487
Garnet 2 Pair HH	2 / 22 10 Oct	23 / 1 22 Oct	Core/Far	0.0809	0.0698	0.0644	0.1285	0.4276	0.4270	2.5	2.1380	2.2952	451	519	543	484	486	506	490
Garnet 2 Pair II	2 / 23 10 Oct	26 / 1 22 Oct	Core/Far	0.0842	0.0742	0.0589	0.1122	0.4351	0.4348	2.5	2.1259	2.2625	454	519	536	486	489	508	495
Garnet 2 Pair JJ	2 / 19 10 Oct	27 / 1 22 Oct	Core/Far	0.0791	0.0679	0.0586	0.1326	0.4263	0.4255	2.5	2.1581	2.3187	446	514	536	480	483	503	486

.

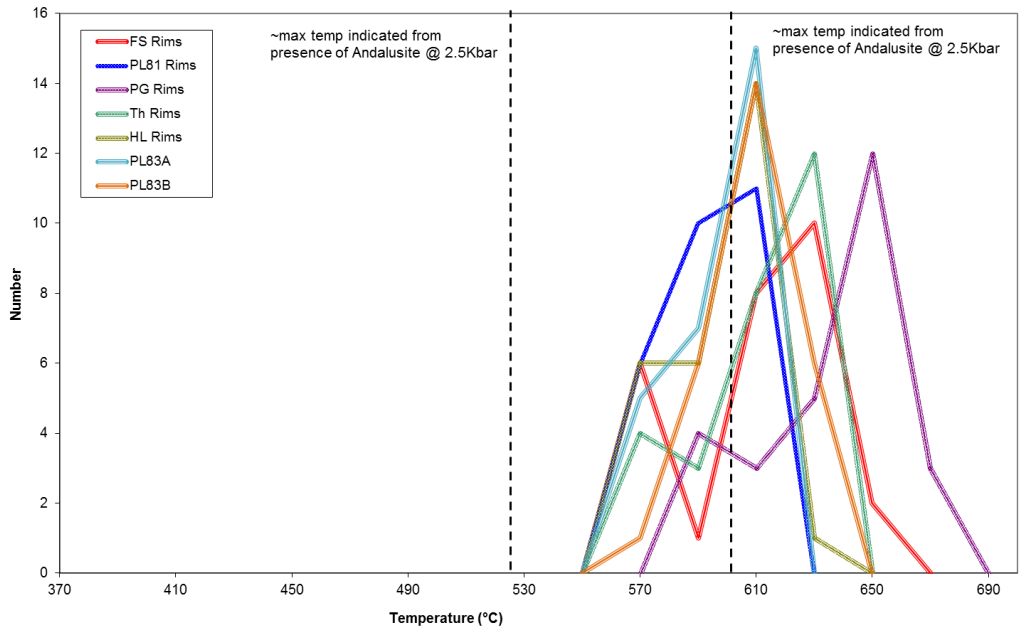

Figure A3.11. Histogram of all rim garnet-biotite close pairs in sample CD06. The rim temperatures estimated by all calibrations appears to slightly overestimate the peak metamorphic temperature. The equilibrium of Mg and Fe may have been affected by the presence of retrograde chlorite. Histogram bin width = 20°C, n = 27.

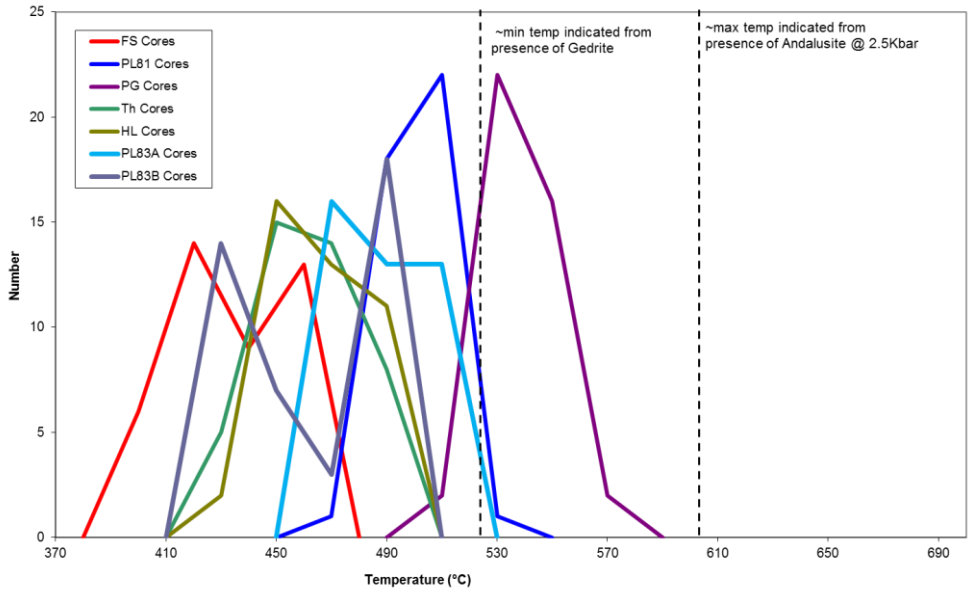

Figure A3.12. Histogram of all core garnet-biotite far pairs in sample CD06. Low Mg content of the cores of the garnet porphyroblasts, combined with high spessartine content results in a temperature estimate that is too low and not compatible with the metamorphic mineral assemblages. The strong compositional zoning of the garnets results in a very broad variation in peak metamorphic temperature estimates between garnet core and rims, although the biotite composition appears to be relatively uniform throughout the sample. The cores of the large garnets are unlikely to have equilibrated with the matrix biotite while the rims of the garnets may have been affected by re-equilibration with retrograde chlorite. Consequently this sample has not been used for the peak metamorphic temperature estimate in Chapter 2. Histogram bin width = 20°C, n = 42

Sample	Core /Rim	Garnet composition	Average XMg(Gt)	Average XCa (Gt)	Average XMn (Gt)	Average XMg (Bt)	Log KD	AverageT(F &S)	2σ T(F & S)	AverageT(P & L 81)	2σ T(P & L 81)	AverageT(P & G)	2σ T(P & G)	Average T(Th)	2σ T(Th)	Average T(H & L)	2σ T(H & L)	Average T (P & L 83A)	2σT(P & L 83A)	Average T (P & L 83B)	2σT(P & L 83B)
BJD102B	Core	$Alm_{67}Gro_{7}Py_{10}Sp_{16}$	0.1216	0.0687	0.1595	0.4876	1.9282	507	22	556	14	624	20	529	18	527	16	540	13	515	23
BJD102B	Rim	$Alm_{72}Gro_{7}Py_{12}Sp_{9}$	0.1377	0.0669	0.0893	0.4797	1.7533	561	14	586	9	649	14	572	11	565	10	571	8	560	10
AMD310Q	All	$Alm_{76}Gro_{6}Py_{8}Sp_{10}$	0.0966	0.0504	0.1048	0.3648	1.6816	585	39	591	23	673	42	591	30	581	26	584	21	571	23
BJD312H-B	Core	$Alm_{61}Gro_{9}Py_{8}Sp_{22}$	0.1109	0.0820	0.2079	0.4747	1.9810	492	24	553	13	637	15	517	19	517	17	525	14	495	23
BJD312H-B	Rim	$Alm_{73}Gro_{6}Py_{12}Sp_{9}$	0.1344	0.0566	0.0800	0.4792	1.7798	552	33	576	21	628	44	565	26	559	23	559	18	559	20
AMD139B	All	$Alm_{46}Gro_{20}Py_{3}Sp_{30}$	0.0579	0.2385	0.2543	0.3419	2.1366	451	32	599	36	695	39	484	26	487	24	506	20	454	23
CD06	Core	$Alm_{62}Gro_{8}Py_{5}Sp_{26}$	0.0749	0.0669	0.1889	0.4347	2.2546	424	43	503	24	539	23	461	36	466	33	488	28	461	49
CD06	Rim	$Alm_{83}Gro_{3}Py_{13}Sp_{1}$	0.1344	0.0274	0.0084	0.4360	1.6071	612	55	594	25	635	49	611	41	599	36	599	29	608	30

Table A3.26. Average temperature estimates (°C) obtained from the five samples using seven different geothermometry calibrations, including errors for each calibration at 2σ.

Sample	Core /Rim	Average (PL81)	Average T(Th)	2σ T(PL81)	2σ T(Th)	T (Th) Mean - 2σ	T (Th) Mean + 2σ	T (Th) Lowest Temp Pair	T (Th) Highest Temp Pair	T (PL81) Mean - 2σ	T (PL81) Mean + 2σ	T (PL81) Lowest Temp Pair	T (PL81) Highest Temp Pair
BJD102B	Core	556	529	14	18	512	547	512	546	542	569	544	569
BJD102B	Rim	586	572	9	11	561	583	561	581	577	595	578	594
AMD310Q	All	591	591	23	30	560	621	557	616	568	614	565	611
BJD312HB	Core	553	517	13	19	498	537	500	532	540	566	543	565
BJD312HB	Rim	576	565	21	26	539	591	547	592	555	597	561	597
AMD139B	*All*	*599*	*484*	*36*	*26*	*458*	*511*	*463*	*519*	*563*	*635*	*562*	*634*
CD06	*Core*	*503*	*461*	*24*	*36*	*425*	*498*	*428*	*490*	*479*	*527*	*477*	*521*
CD06	*Rim*	*594*	*611*	*25*	*41*	*570*	*653*	*572*	*639*	*569*	*619*	*570*	*611*

Table A3.27. Temperature estimates (°C) of the two most consistent calibrations, PL81 and Th, across samples BJD102B, AMD310Q and BJD312HB, which are used in Chapter 2. The estimates for AMD139B and CD06 have not been used in Chapter 2 because their garnet compositions and the presence of minor retrograde chlorite result in temperature estimates that are less robust than the other three samples, as discussed above. The 2σ errors are shown above and below the mean temperature as well as the highest and lowest individual estimate obtained from individual garnet-biotite pairs.

.

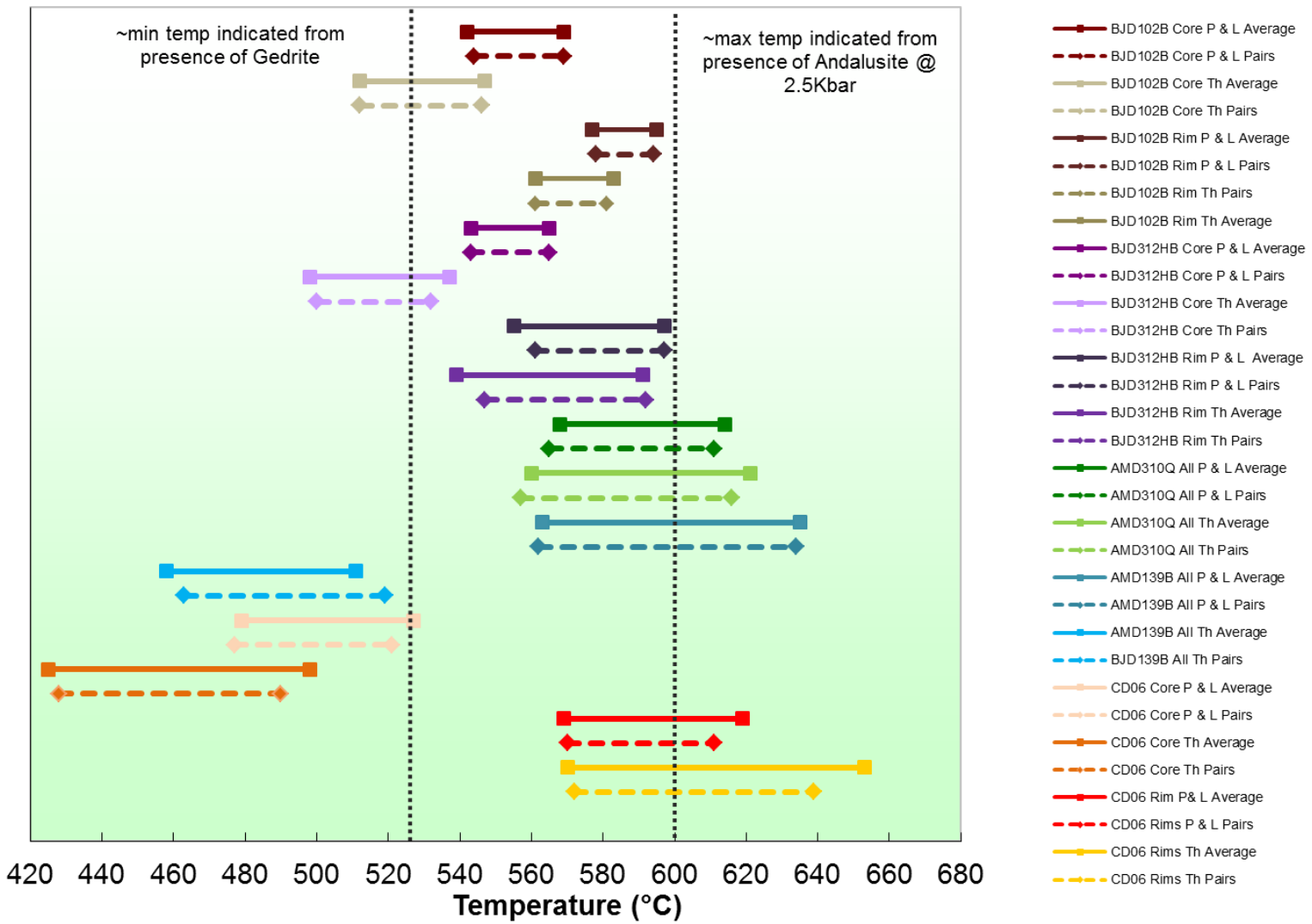

Figure A3.13. Showing the range of peak metamorphic temperature estimates obtained from all samples. The estimates from BJD102B, BJD312HB and AM310Q are consistent with a peak metamorphic temperature of ~560-580°C (see Chapter 2). (Th = Thompson 1976; P & L = Lavrent'eva and Perchuk, 1981)

A3.10 References

Chuming, W., Yusheng, P., 1991. Reviews in Garnet-Biotite Geothermometer: Its Versions, Inherent Problems of Accuracy and Precision, and Perspective for Further Research. Chinese Journal of Geochemistry 18 (1), 55 – 61.

Deer, W. A., Howie, R. A., Zussman, J. 1992. An introduction to the rock-forming minerals. Second Edition. Longman Scientific and Technical, Harlow, UK, pp. 285.

Ferry, J.M., Spear, F.S., 1978. Experimental calibration of the partitioning of Fe and Mg between biotite and garnet. Contributions to Mineralogy and Petrology 66, 113-117.

Holdaway, M. J., Lee, S. M., 1977, Fe-Mg cordierite stability in high grade pelitic rocks based on experimental, theoretical, and natural observations: Contributions to Mineralogy and Petrology 63, 175- 198.

Lavrent'eva, I. V., Perchuk, L. L., 1981. Phase correspondence in the system biotite-garnet: Experimental data. In Dokl. Akad. Nauk USSR, 260, 731-734.

Perchuk L. L., Lavrent'eva I. V., 1983. Experimental investigation of exchange equilibria in the system cordierite-garnet-biotite. In; Saxena SK (Ed.) Kinetics and equilibrium in mineral reactions. Springer, Berlin Heidelberg New York, pp199-239.

Pigage, L. C., Greenwood, H. J., 1982. Internally consistent estimates of pressure and temperature; the staurolite problem. American Journal of Science 282(7), 943-969.

Thompson, A. B., 1976. Mineral reactions in pelitic rocks; II, Calculation of some PTX (Fe-Mg) phase relations. American Journal of Science 276(4), 425-454.

Appendix 4 - Cross sections and Level plans

A4.1 Level Plans

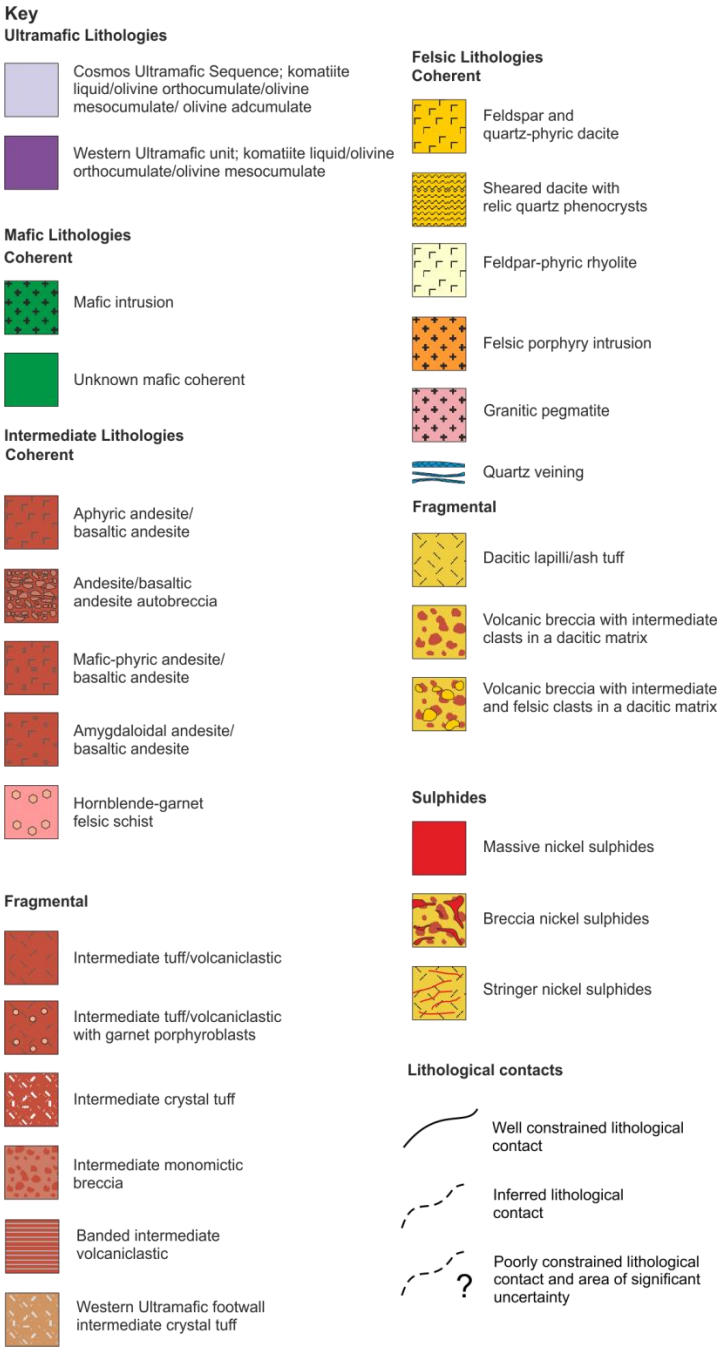

A4.1 Lithological key for level plans.

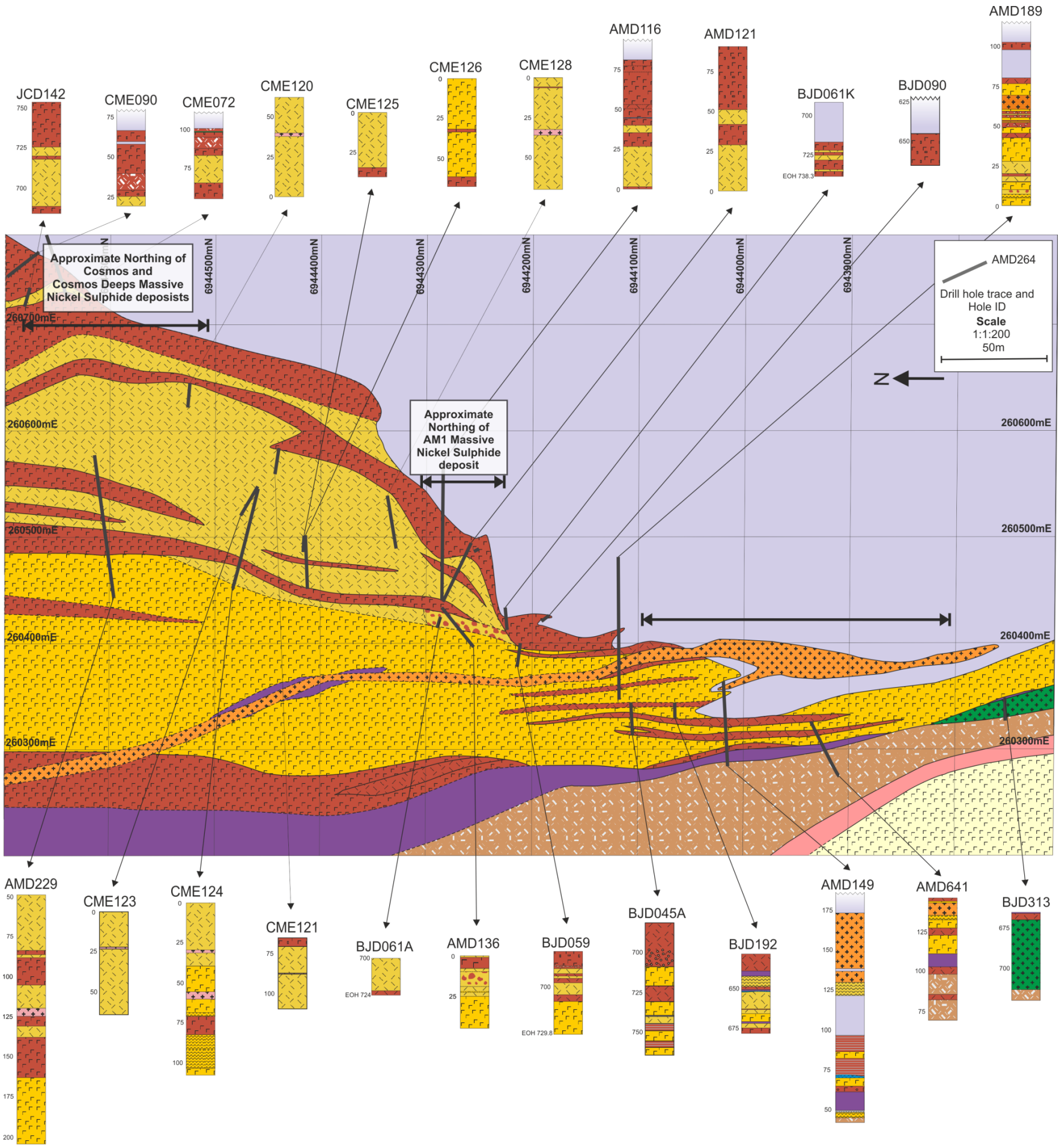

Figure A4.2. Level plan at the -150mRL (-150m bsl) ± 25m showing the lithological correlations of the footwall succession to the Cosmos Ultramafic Sequence and the holes used to construct the level plan.

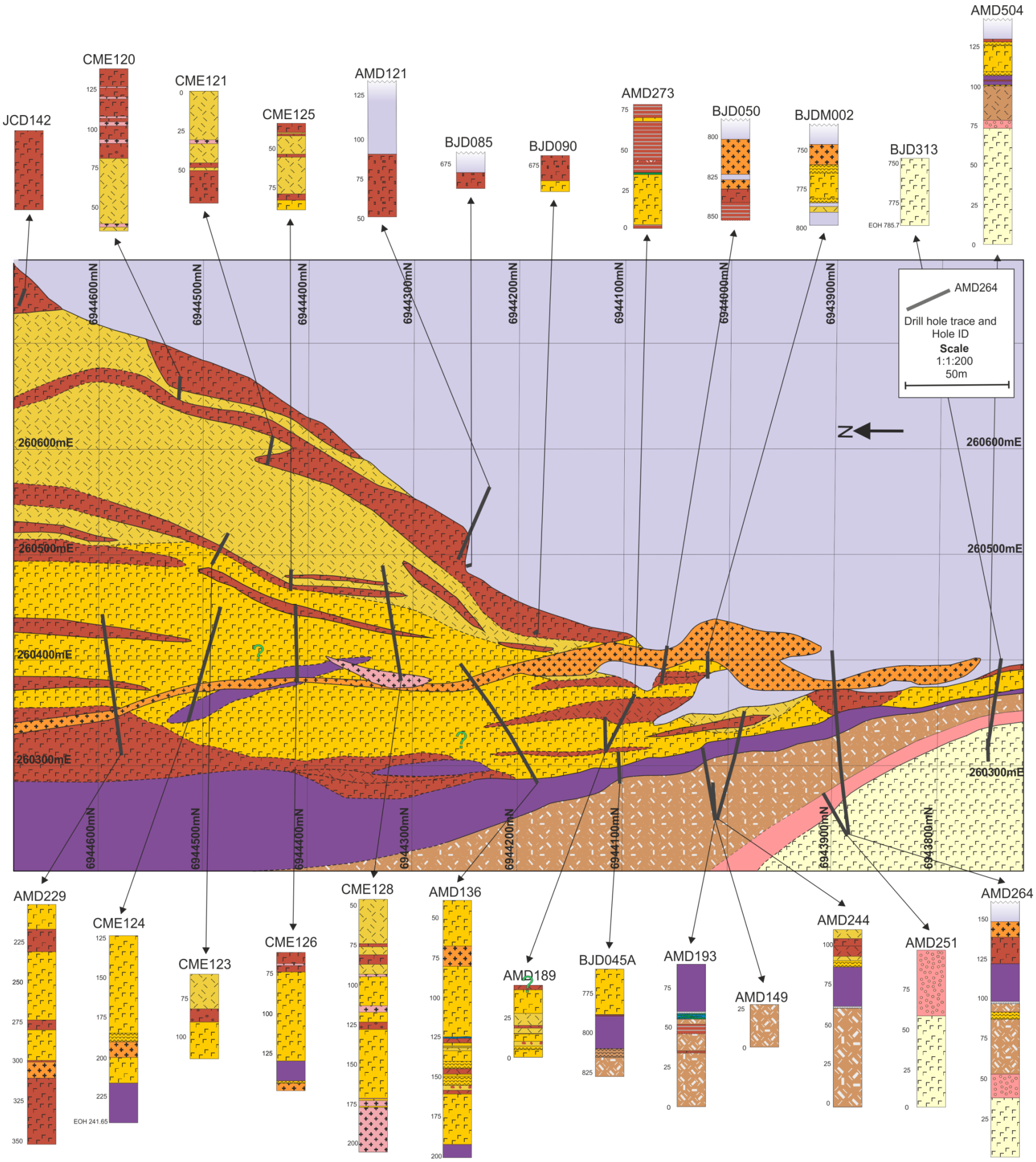

Figure A4.3. Level plan at the -200mRL (-200m bsl) ± 25m showing the lithological correlations of the footwall succession to the Cosmos Ultramafic Sequence and the holes used to construct the level plan

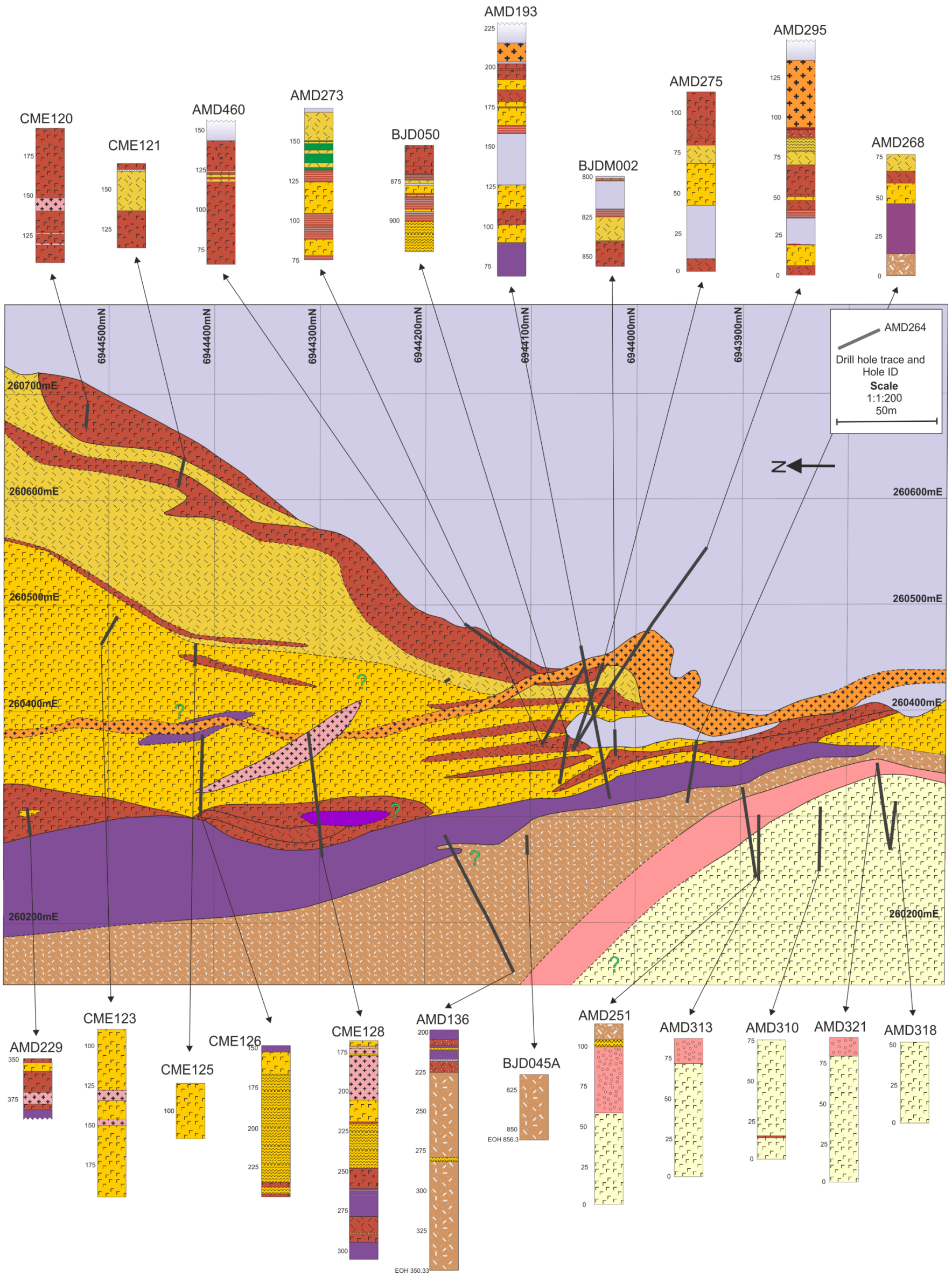

Figure A4.4. Level plan at the -250mRL (250m bsl) ± 25m showing the lithological correlations of the footwall succession to the Cosmos Ultramafic Sequence and the holes used to construct the level plan

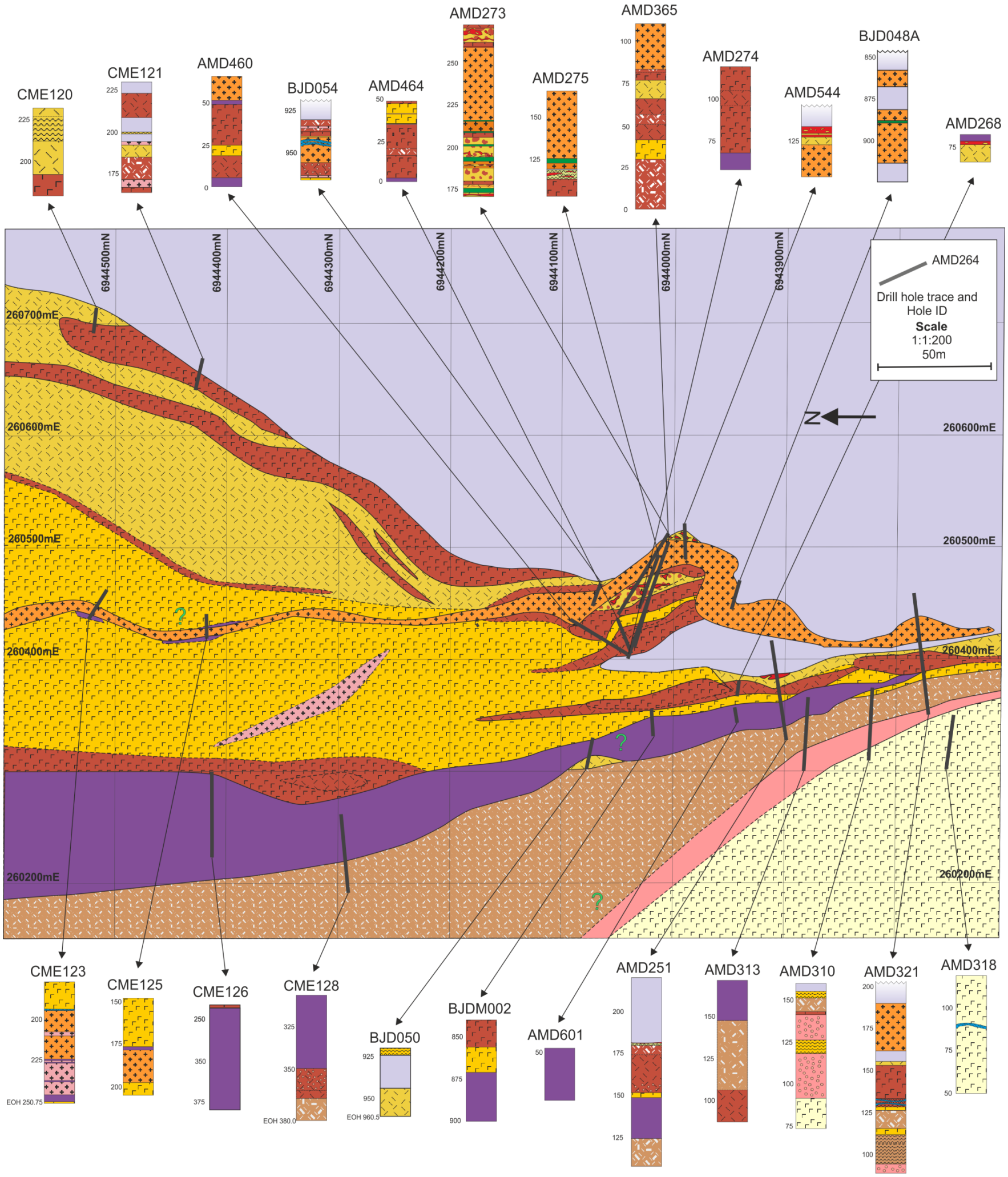

Figure A4.5. Level plan at the -300mRL (-300m bsl) ± 25m showing the lithological correlations of the footwall succession to the Cosmos Ultramafic Sequence and the holes used to construct the level plan

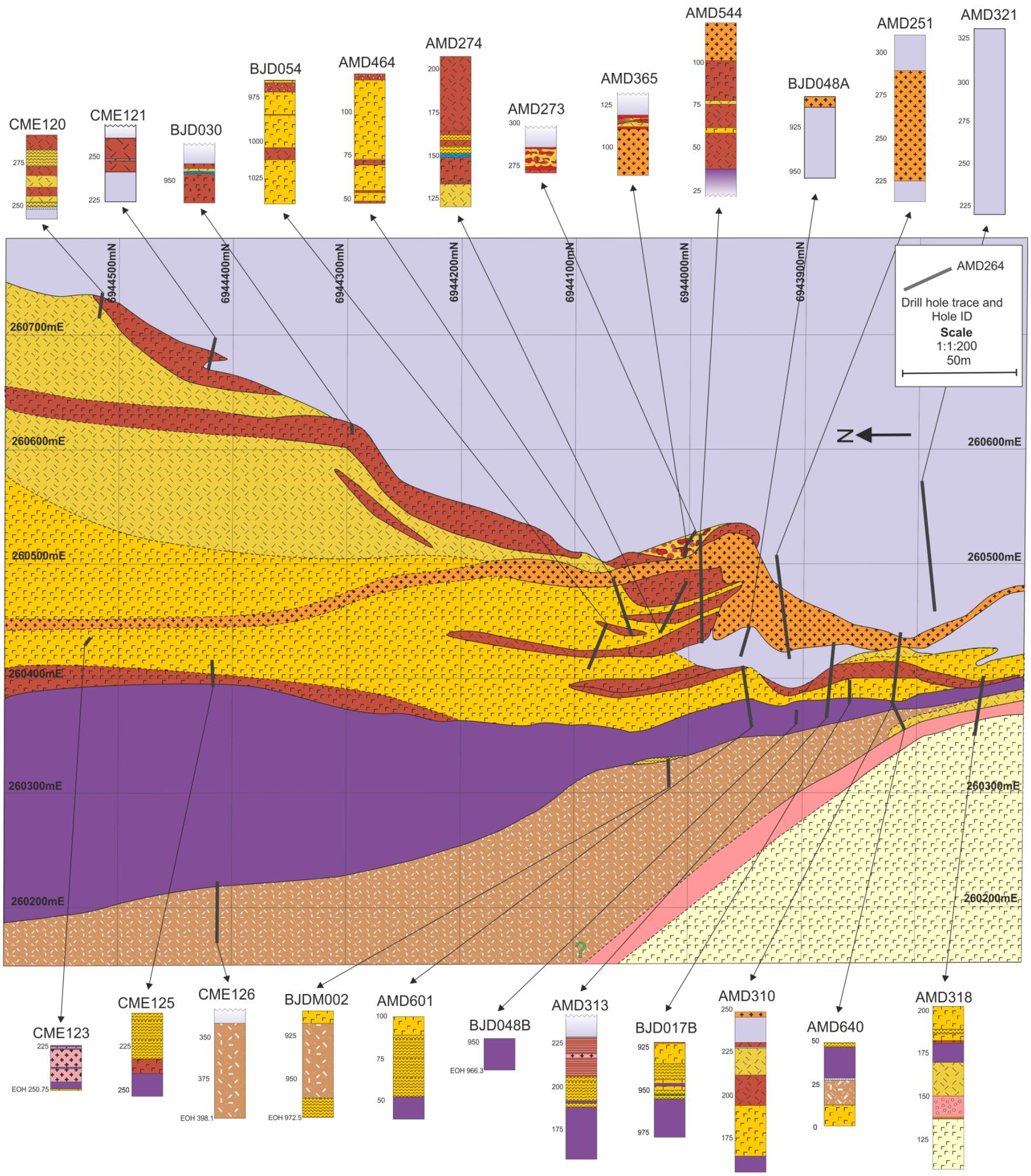

Figure A4.6 Level plan at the -350mRL (150m bsl) ± 25m showing the lithological correlations of the footwall succession to the Cosmos Ultramafic Sequence and the holes used to construct the level plan

A4.2 Cross-Sections

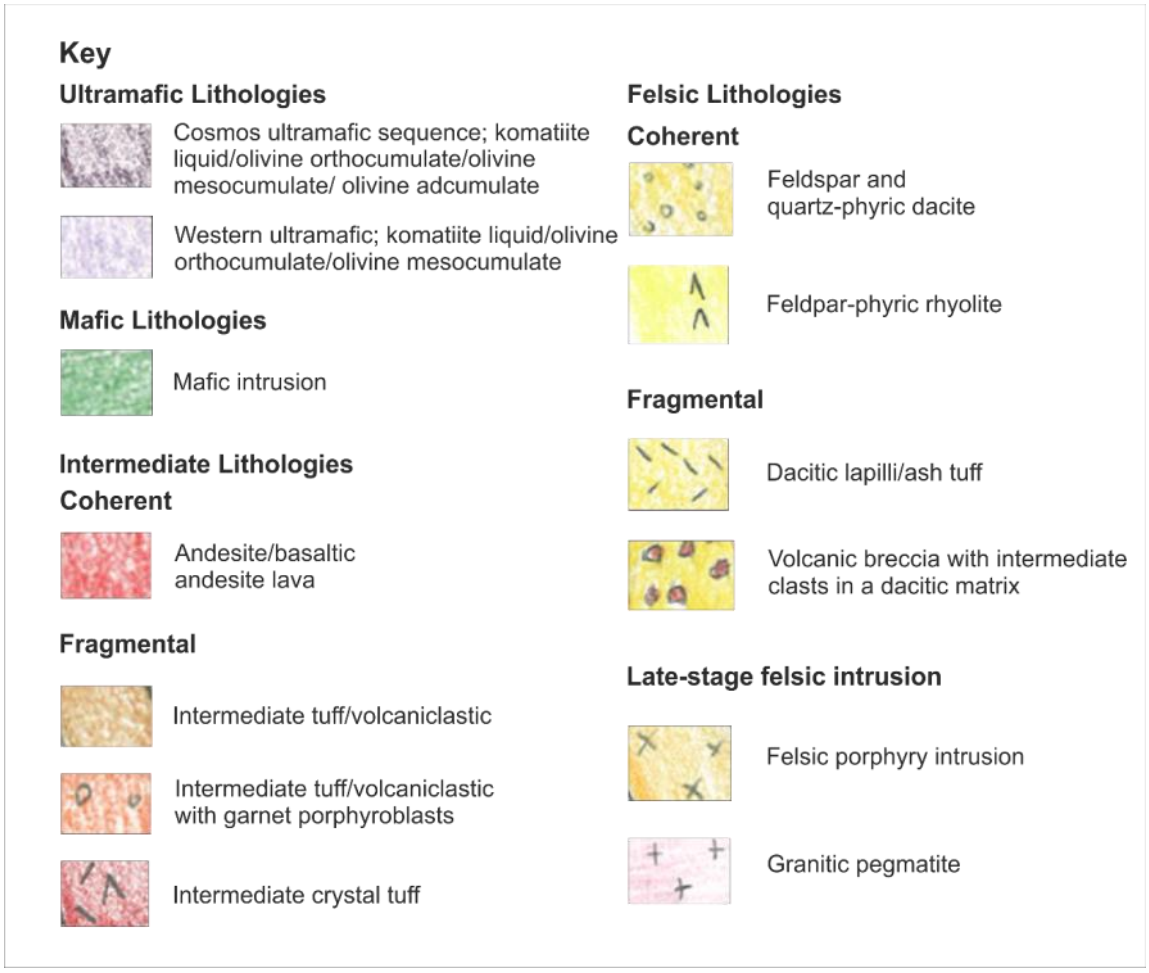

Figure A4.7. Lithological key for interpreted cross sections. Note that these cross-sections are the originals, constructed in the field; therefore lithological interpretations may have been modified during further data processing. A3 PDF files of all cross-sections can be found on the attached CD.

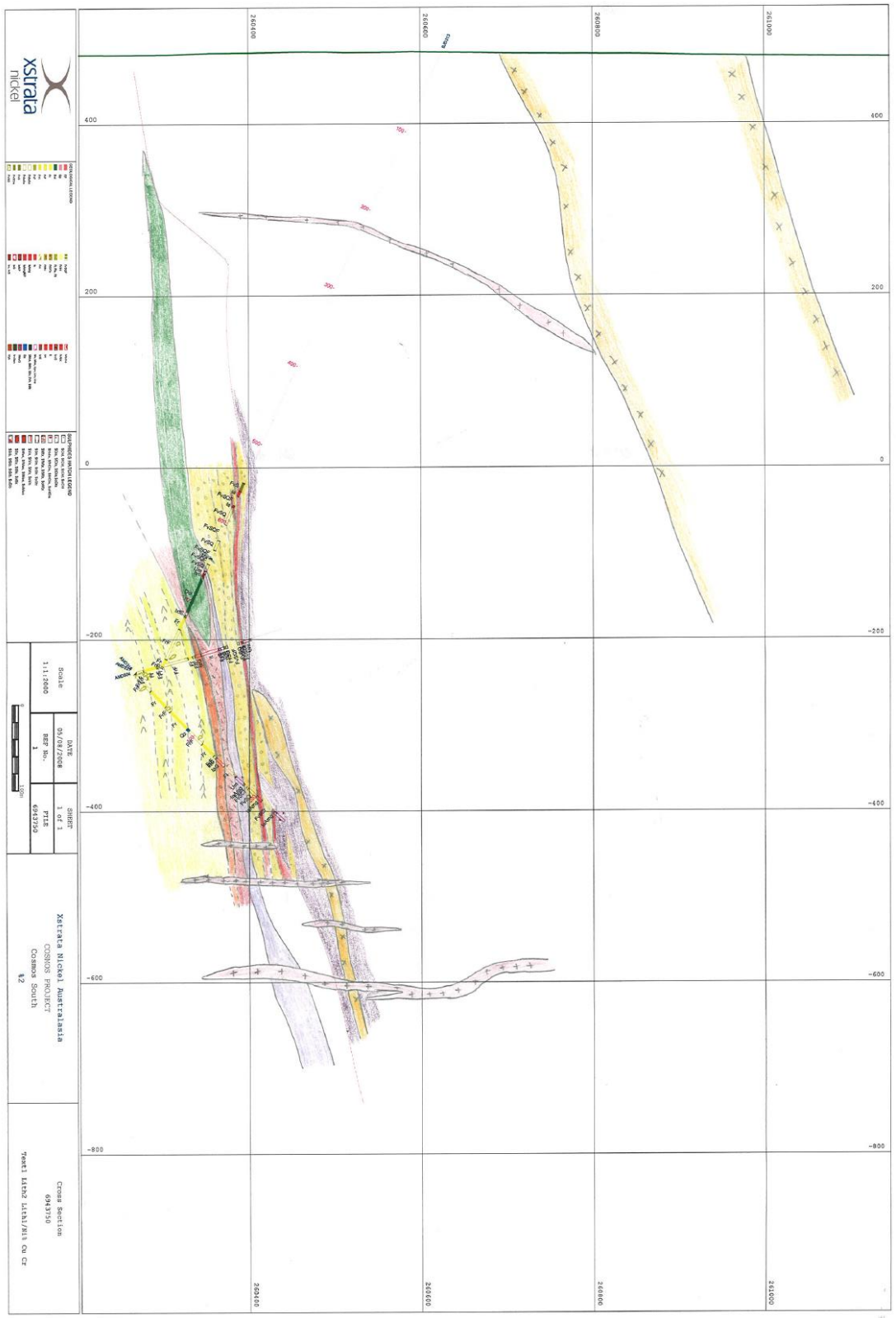

Figure A4.8. 6943750mN (±12.5m) cross section of the North Cosmos region

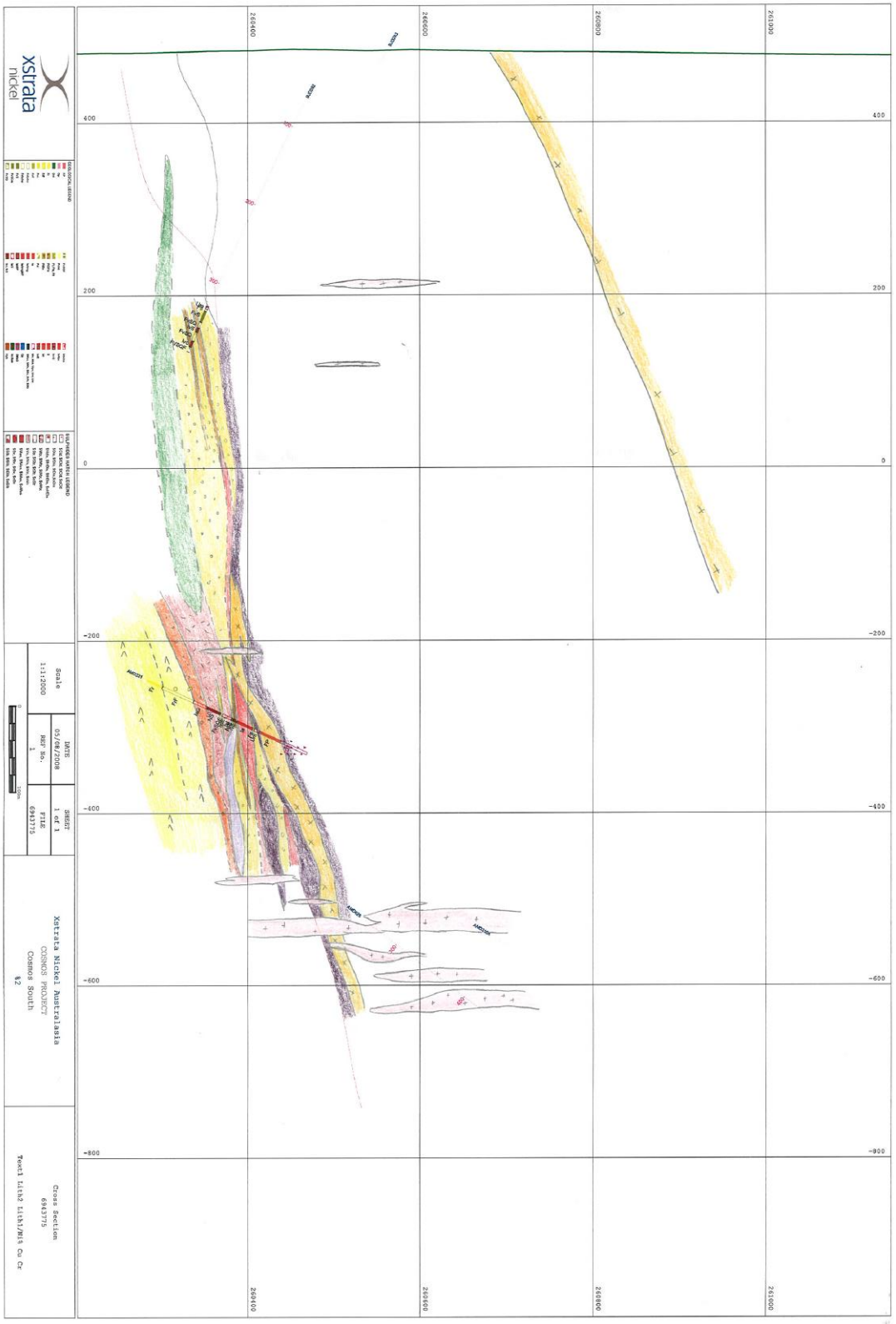

Figure A4.9. 6943775mN (±12.5m) cross section of the North Cosmos region.

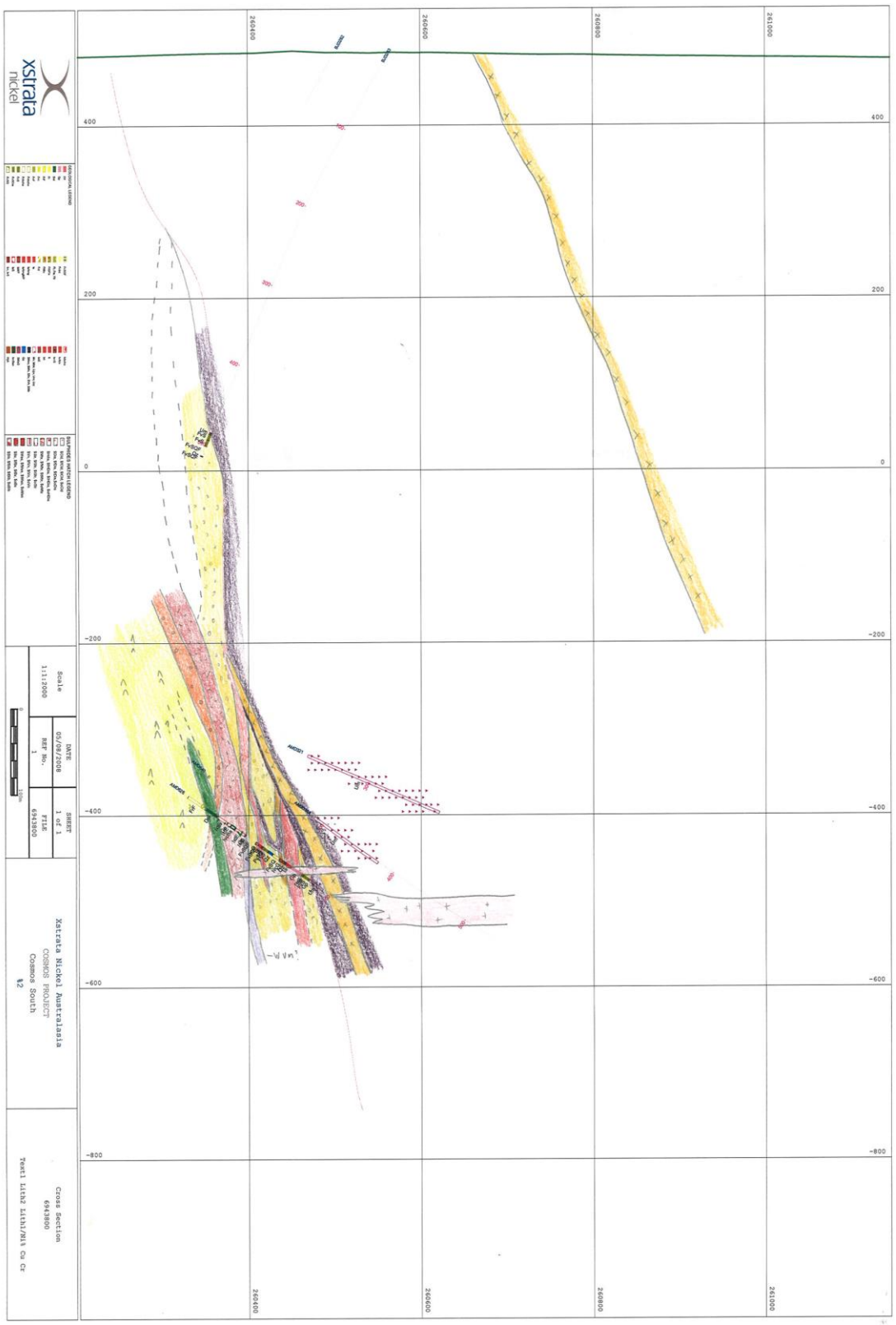

Figure A4.10. 6943800mN (±12.5m) cross section of the North Cosmos region.

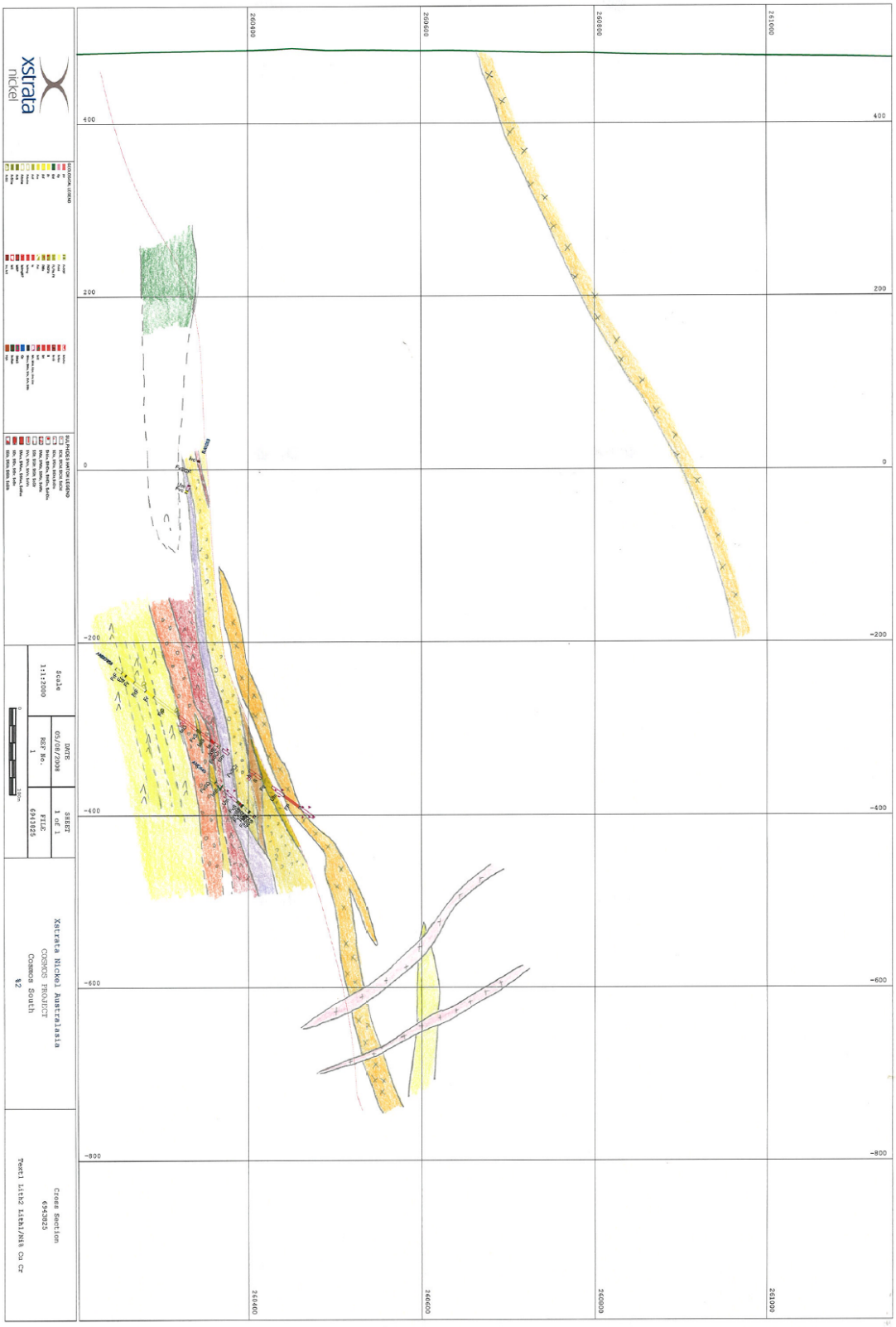

Figure A4.11. 6943825mN (±12.5m) cross section of the North Cosmos region.

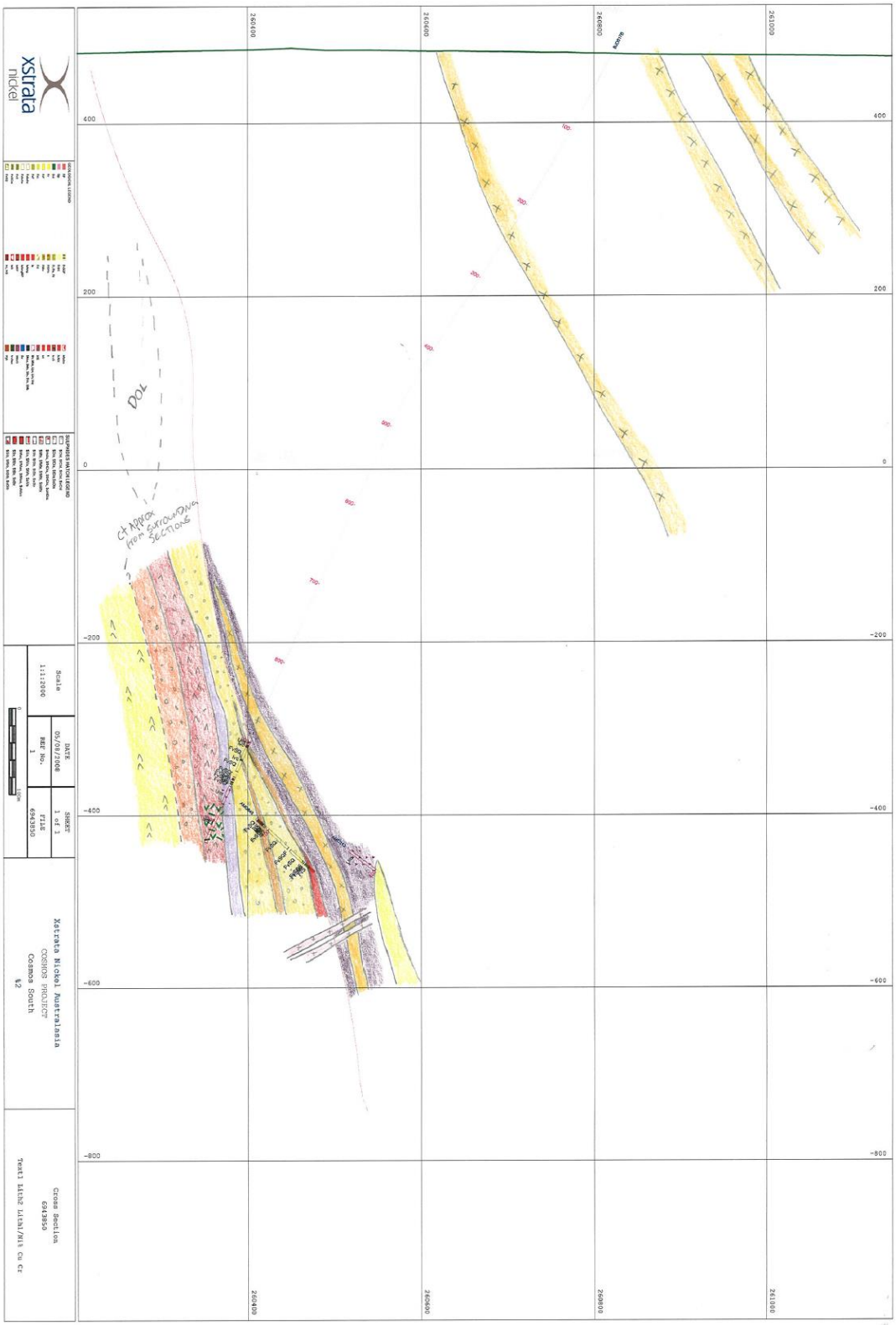

Figure A4.12. 6943850mN (±12.5m) cross section of the North Cosmos region.

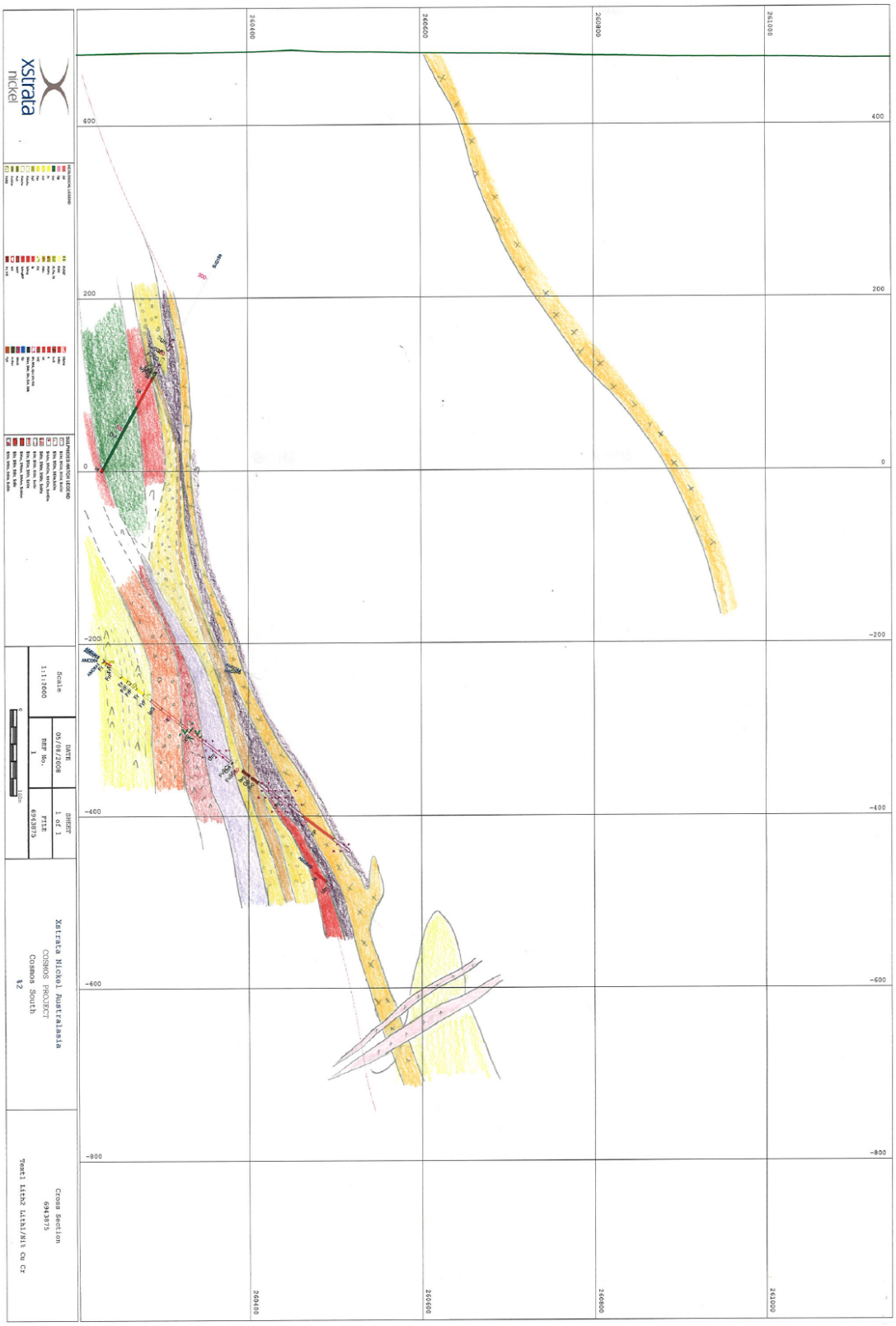

Figure A4.13. 6943875mN (±12.5m) cross section of the North Cosmos region.

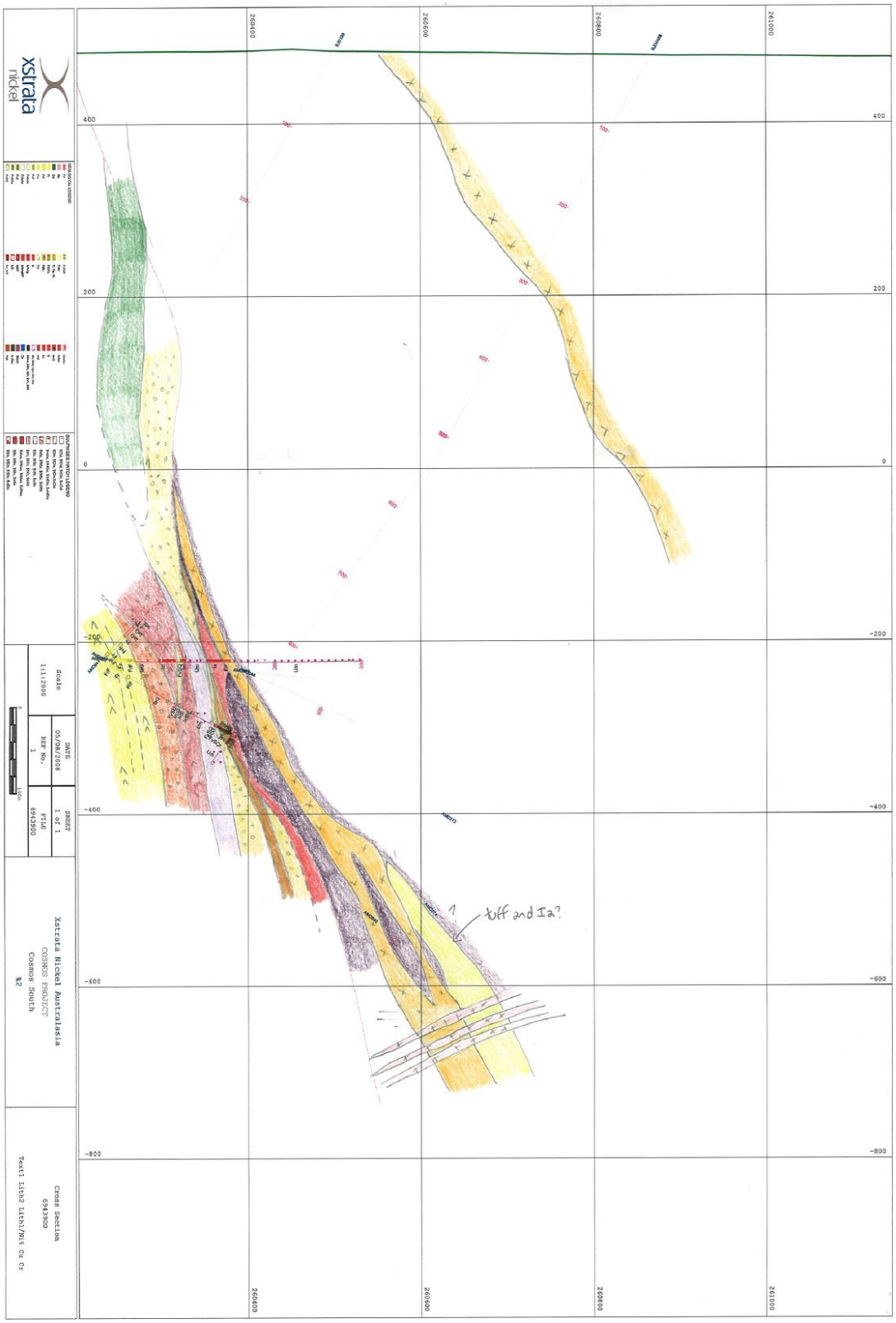

Figure A4.14. 6943900mN (±12.5m) cross section of the North Cosmos region.

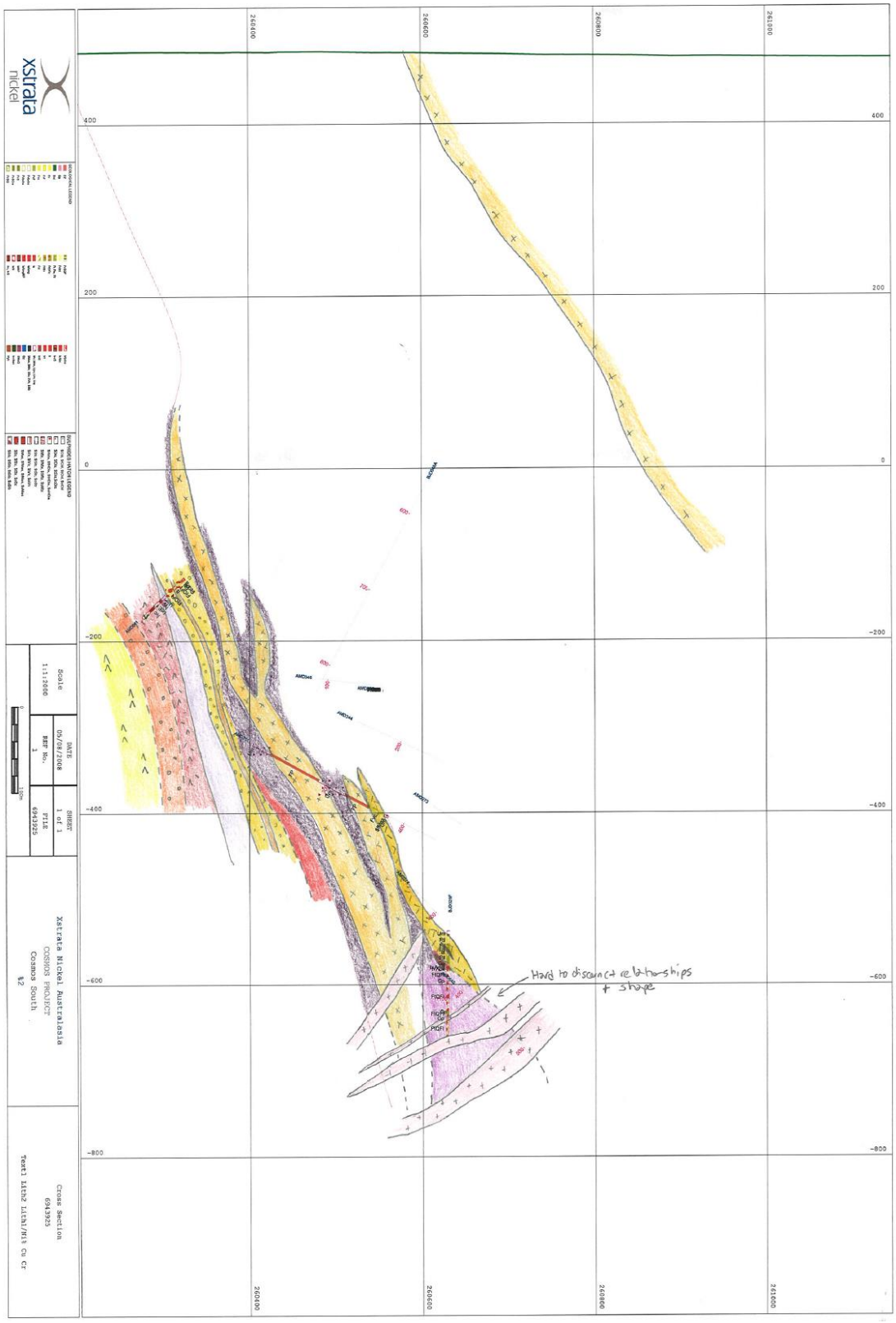

Figure A4.15. 6943925mN (±12.5m) cross section of the North Cosmos region.

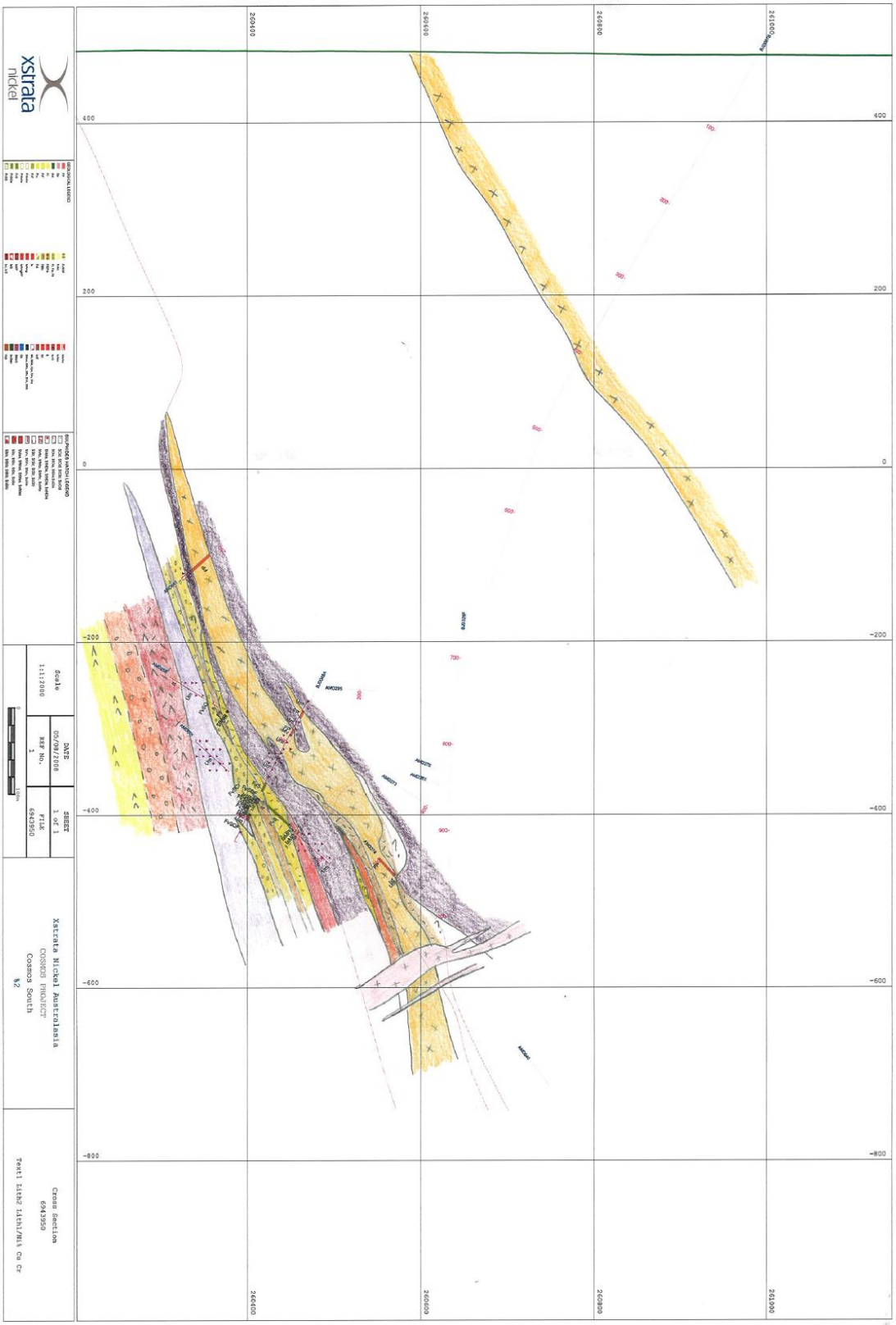

Figure A4.16. 6943950mN (±12.5m) cross section of the North Cosmos region.

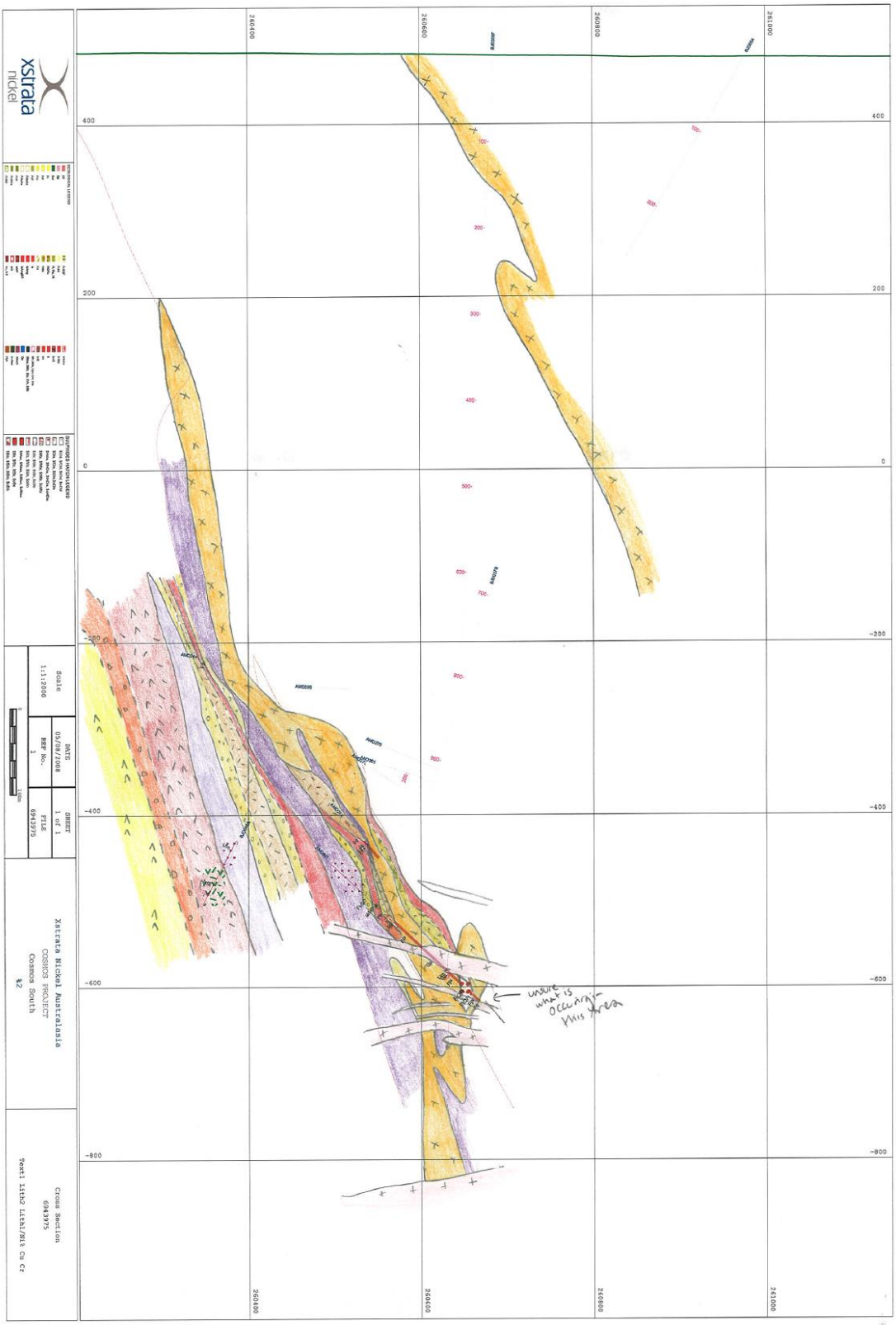

Figure A4.17. 6943975mN (±12.5m) cross section of the North Cosmos region.

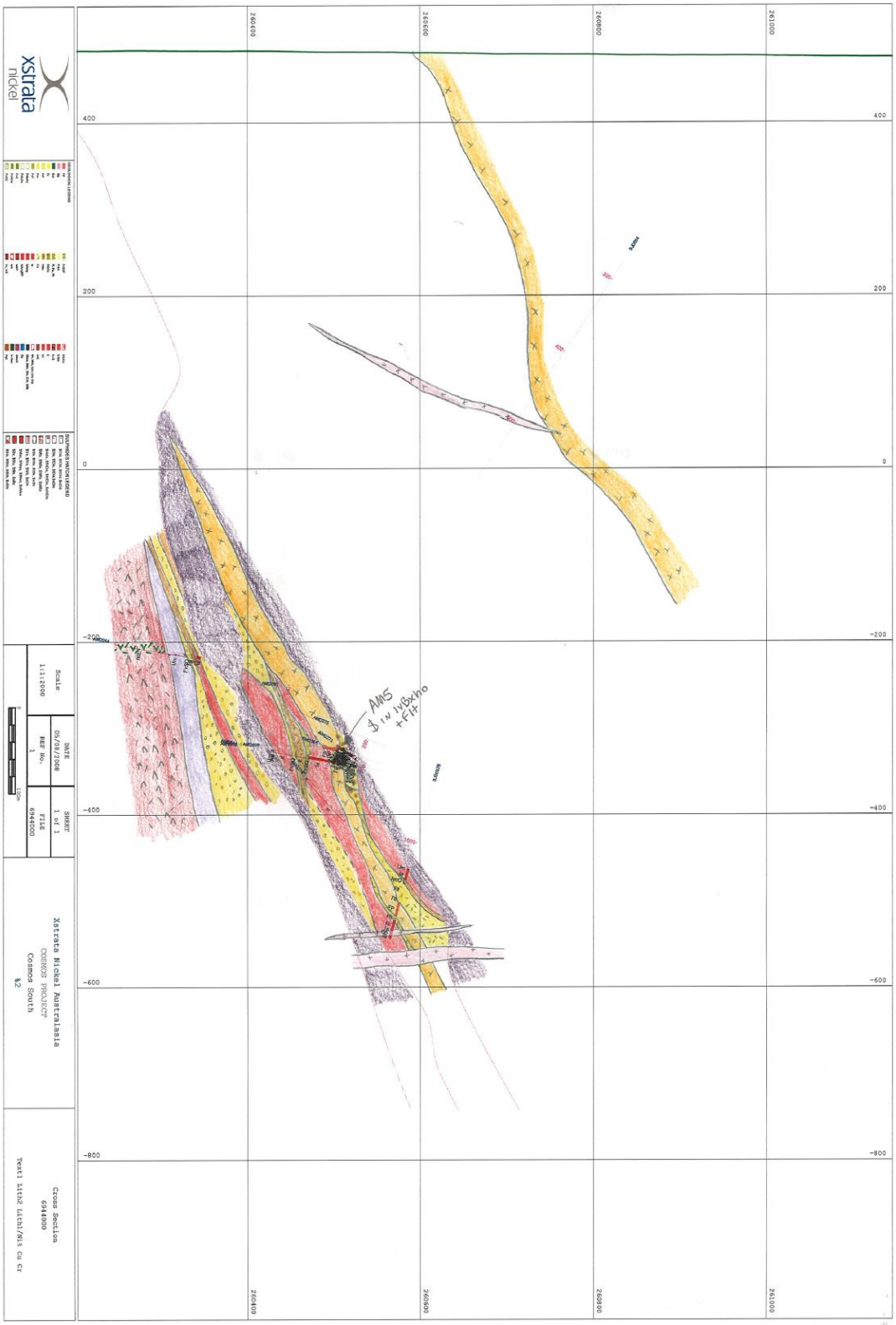

Figure A4.18. 6944000mN (±12.5m) cross section of the North Cosmos region.

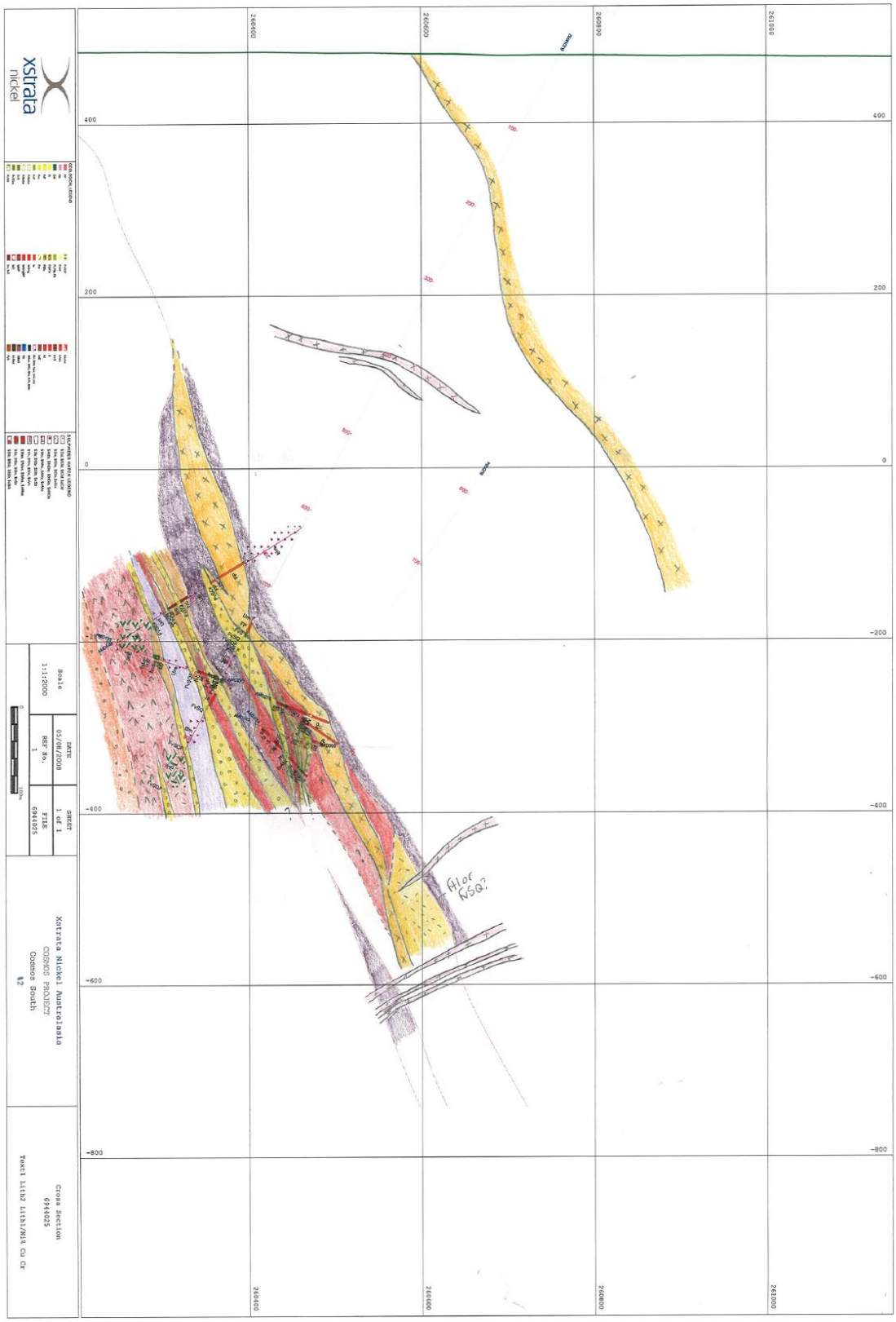

Figure. A4.19. 6944025mN (±12.5m) cross section of the North Cosmos region.

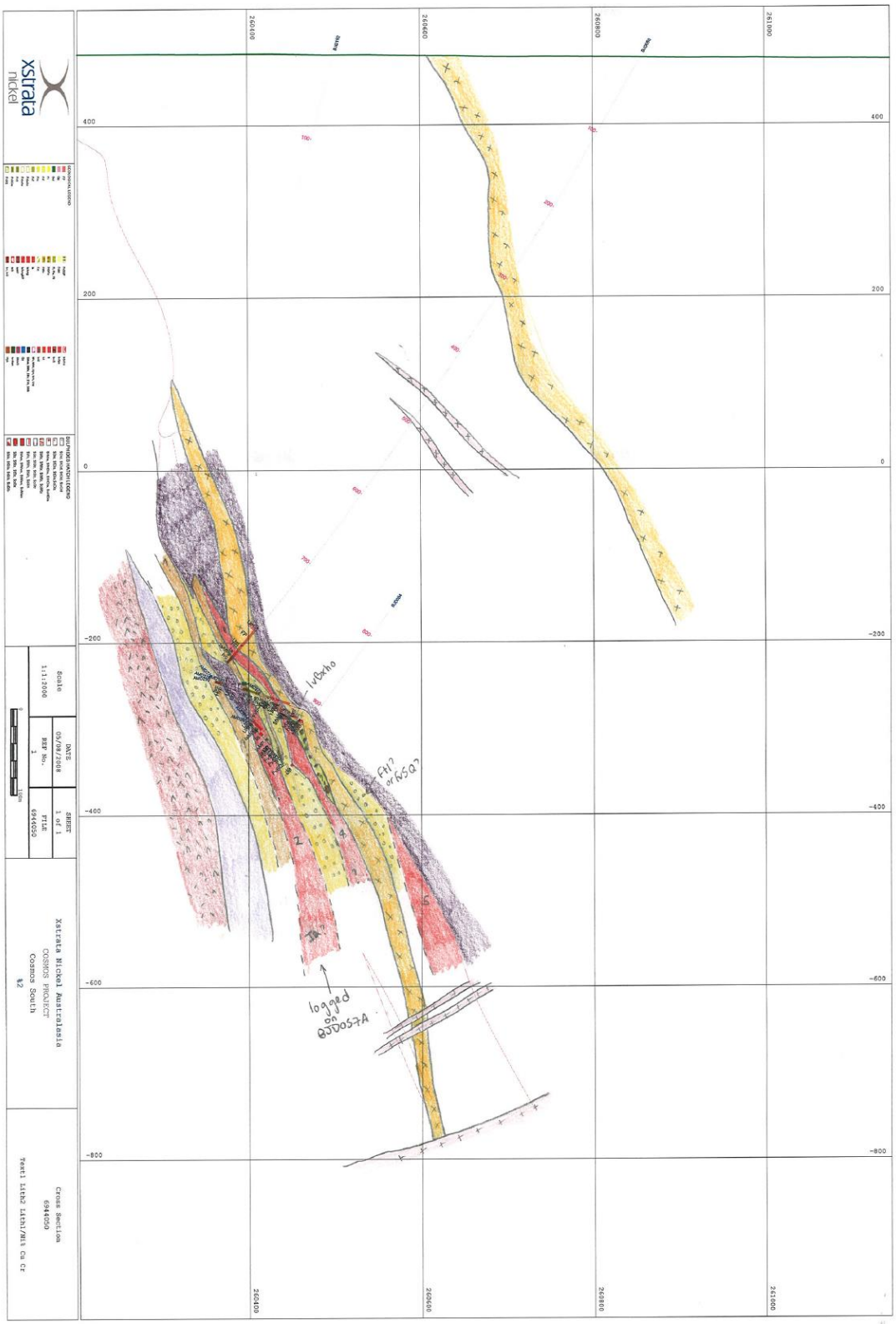

Figure A4.20. 6944050mN (±12.5m) cross section of the North Cosmos region.

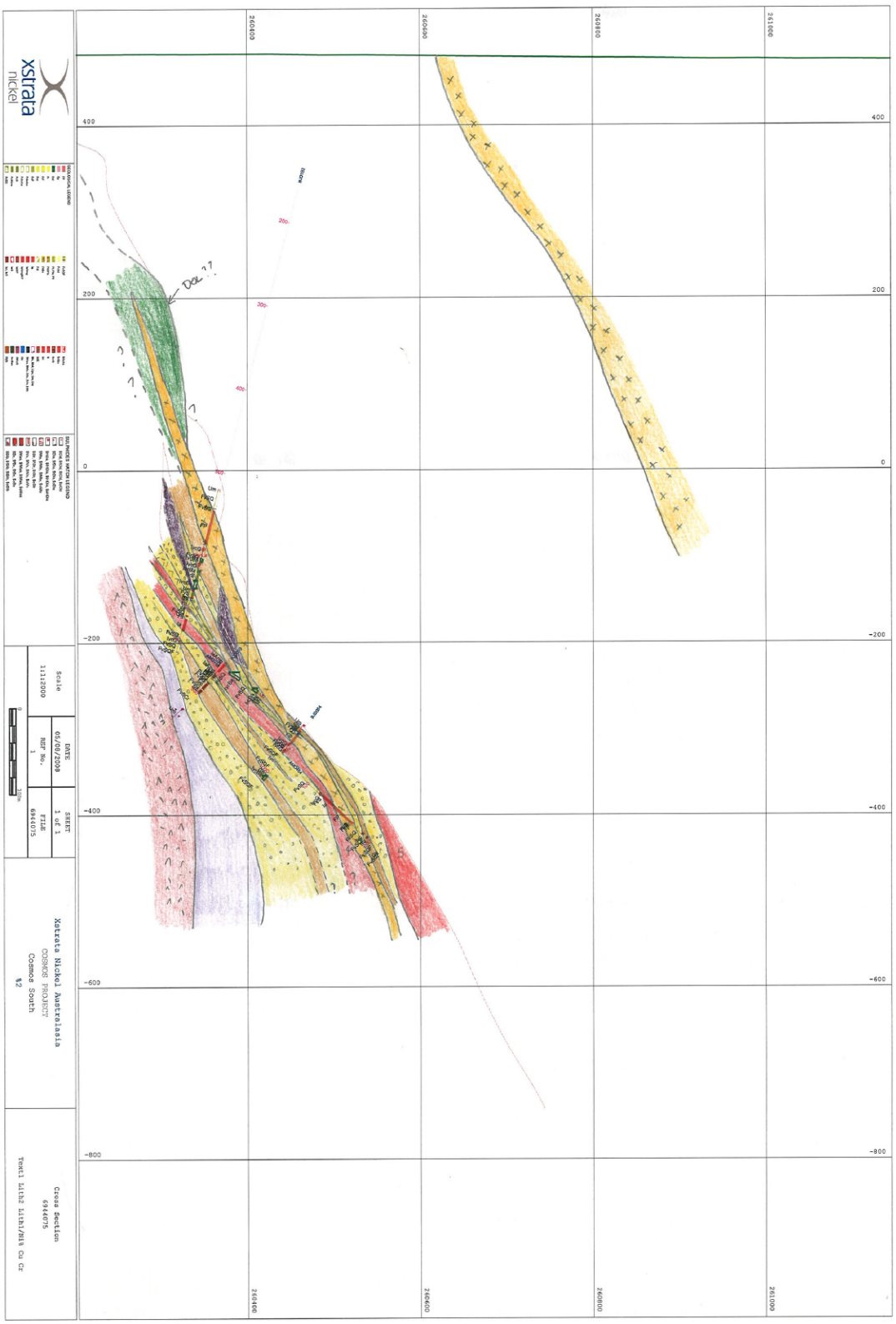

Figure A4.21. 6944075mN (±12.5m) cross section of the North Cosmos region.

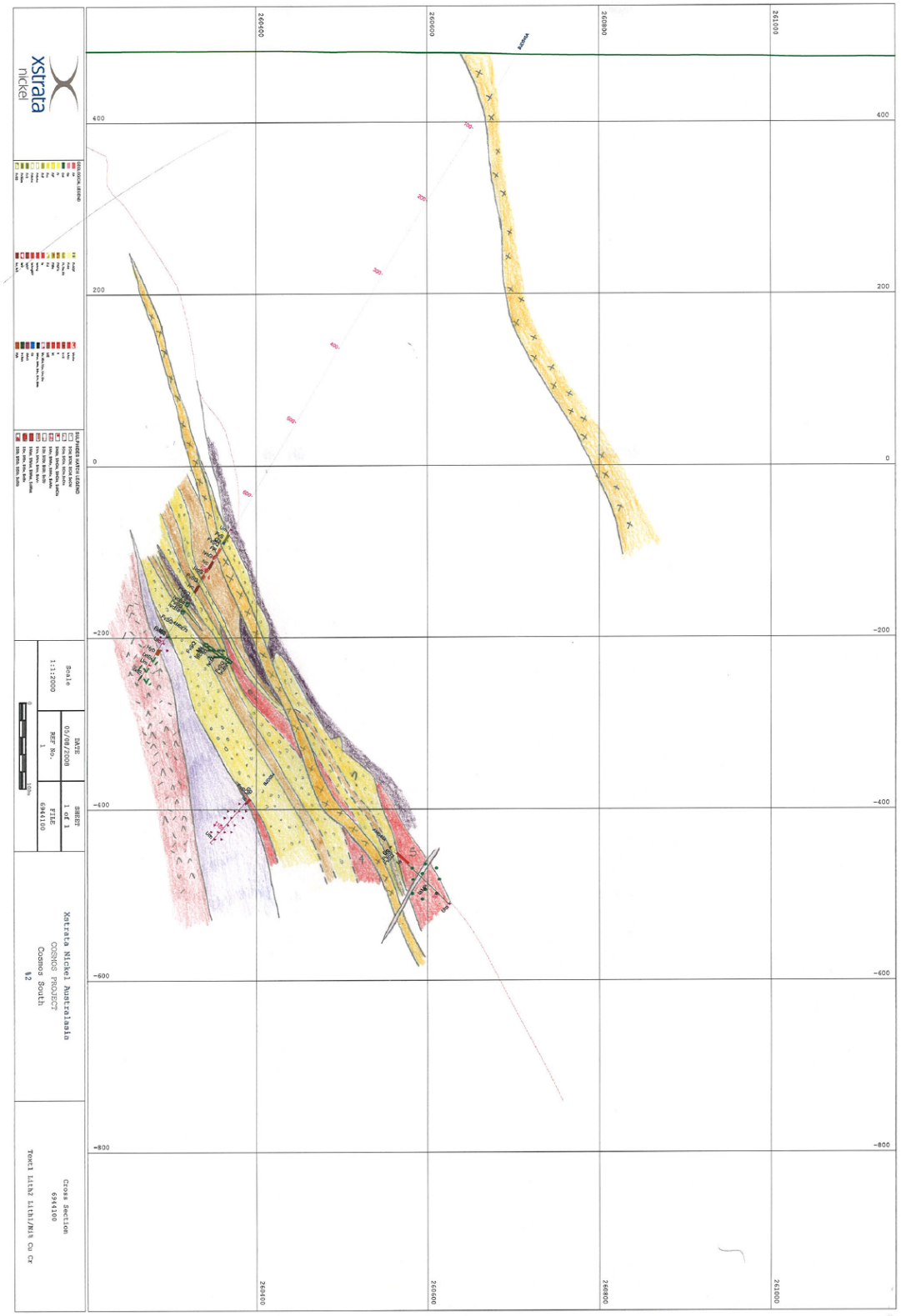

Figure A4.22. 6944100mN (±12.5m) cross section of the North Cosmos region.

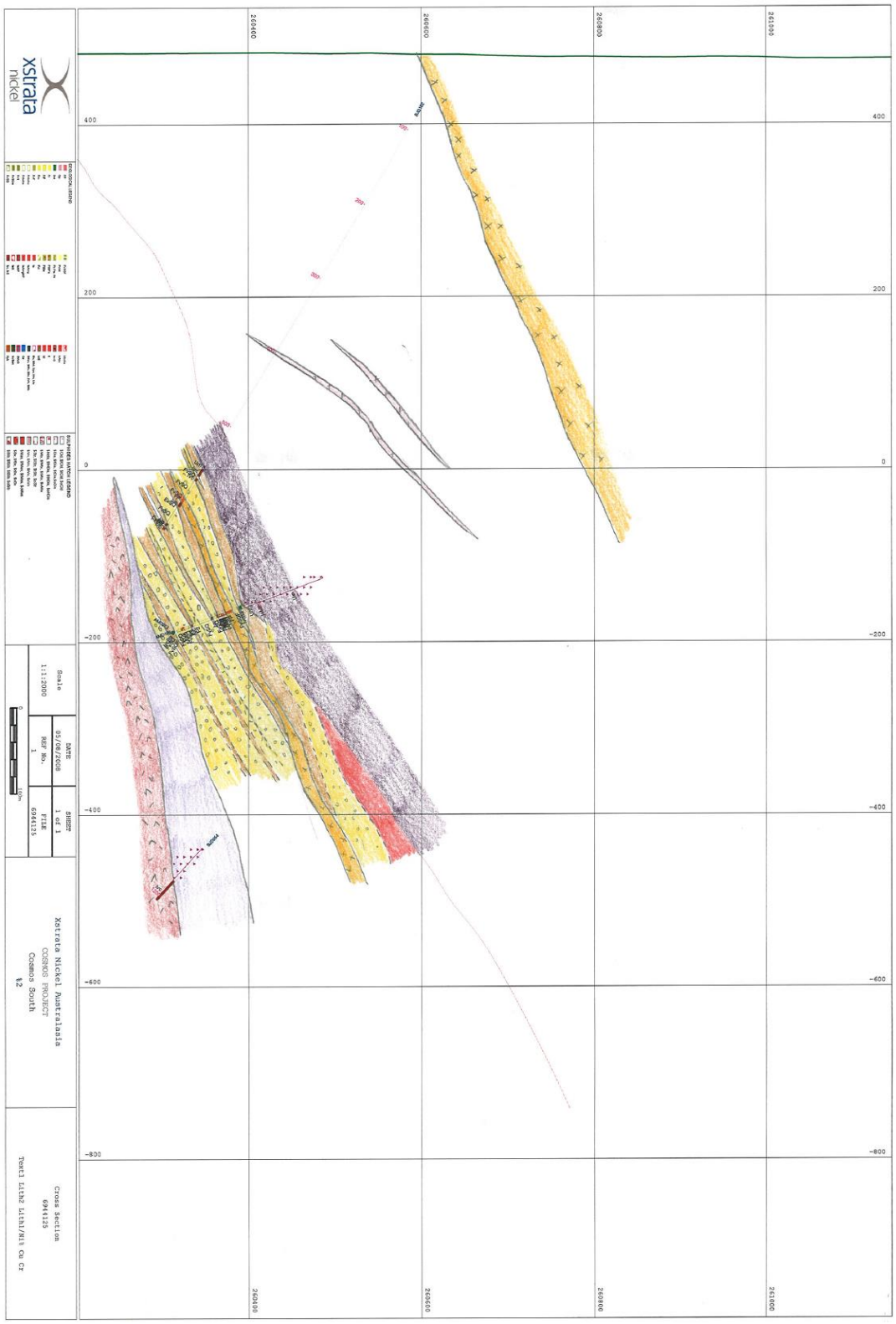

Figure A4.23. 6944125mN (±12.5m) cross section of the North Cosmos region.

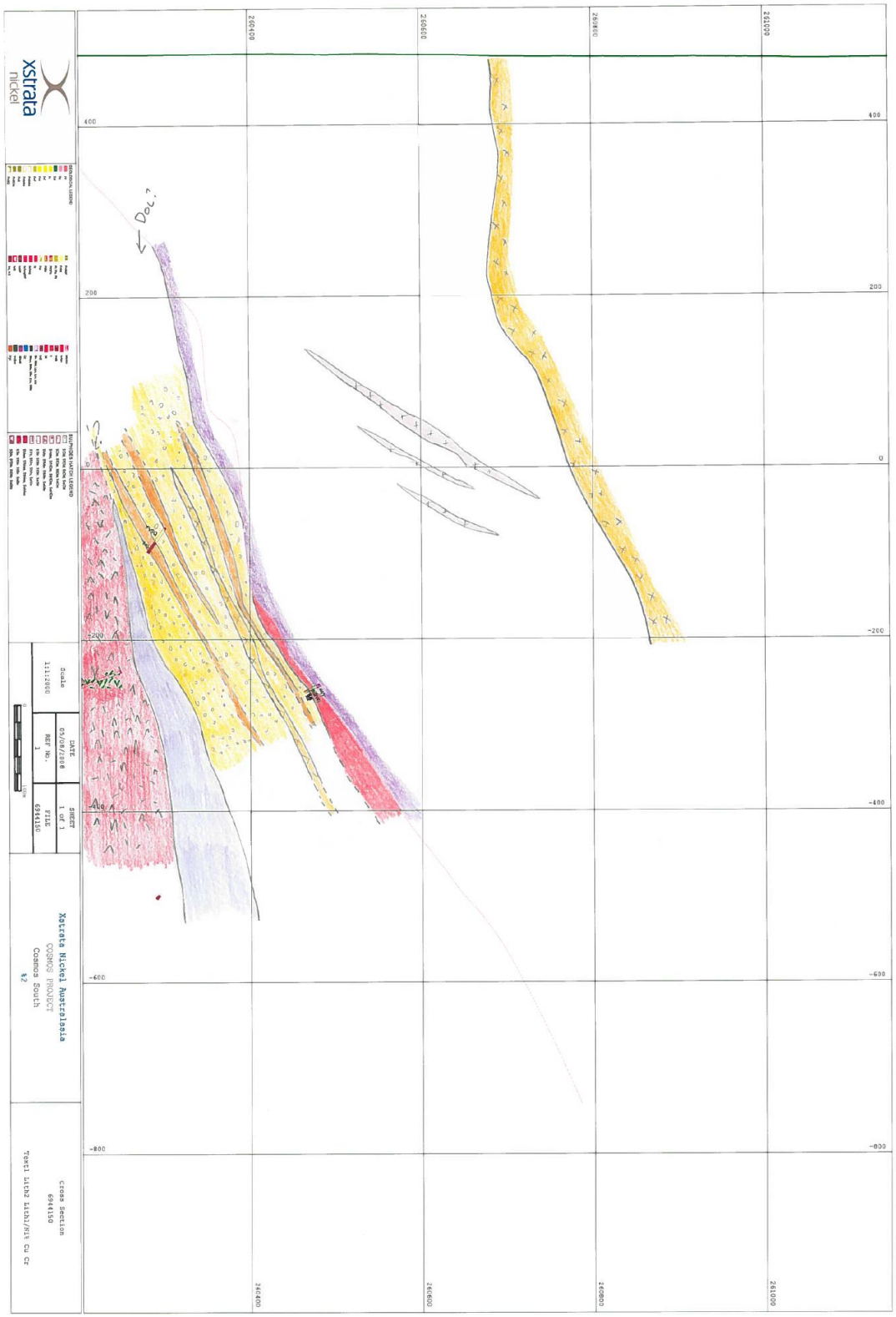

Figure A4.24. 6944150mN (±12.5m) cross section of the North Cosmos region.

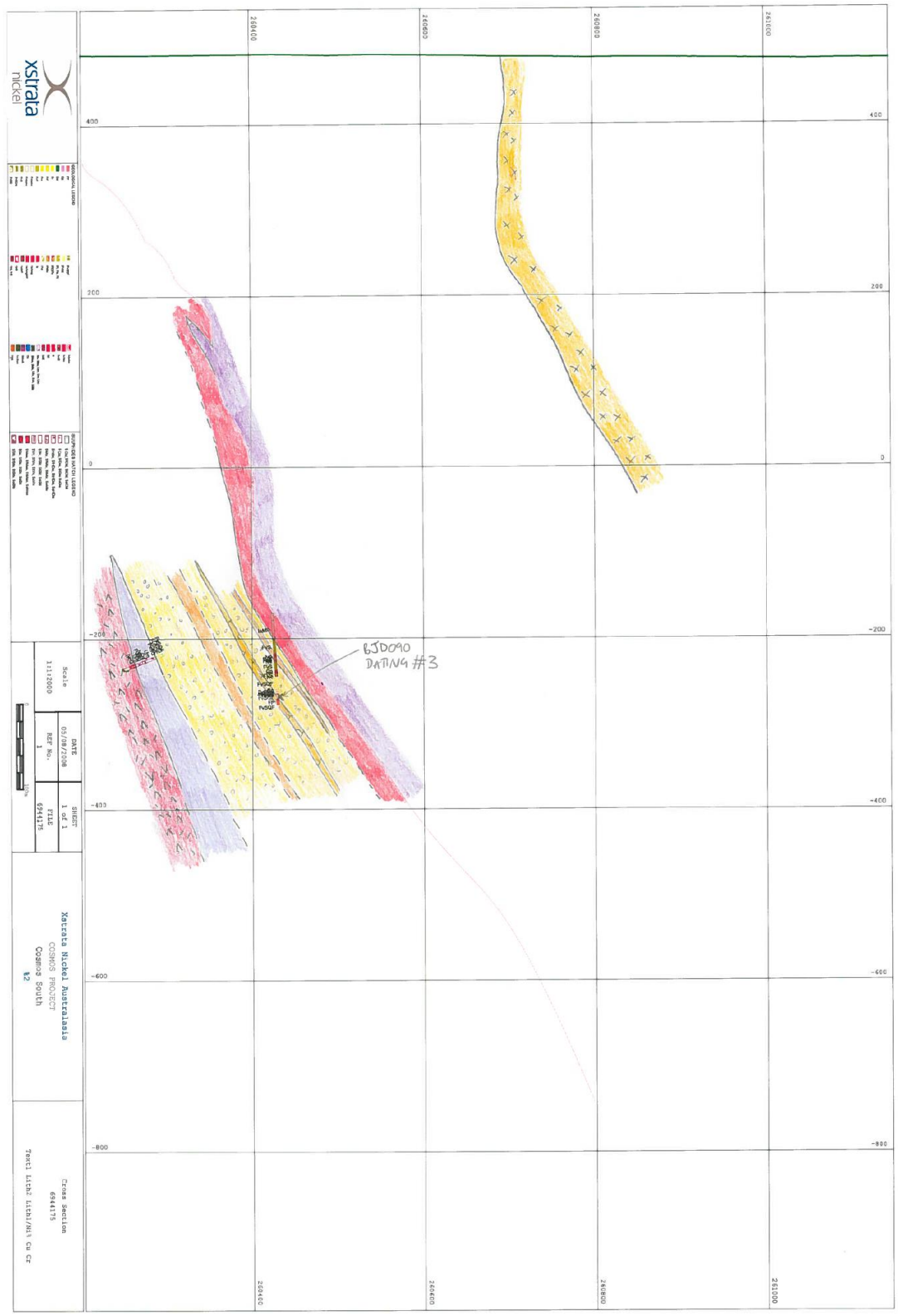

Figure A4.25. 6944175mN (±12.5m) cross section of the North Cosmos region.

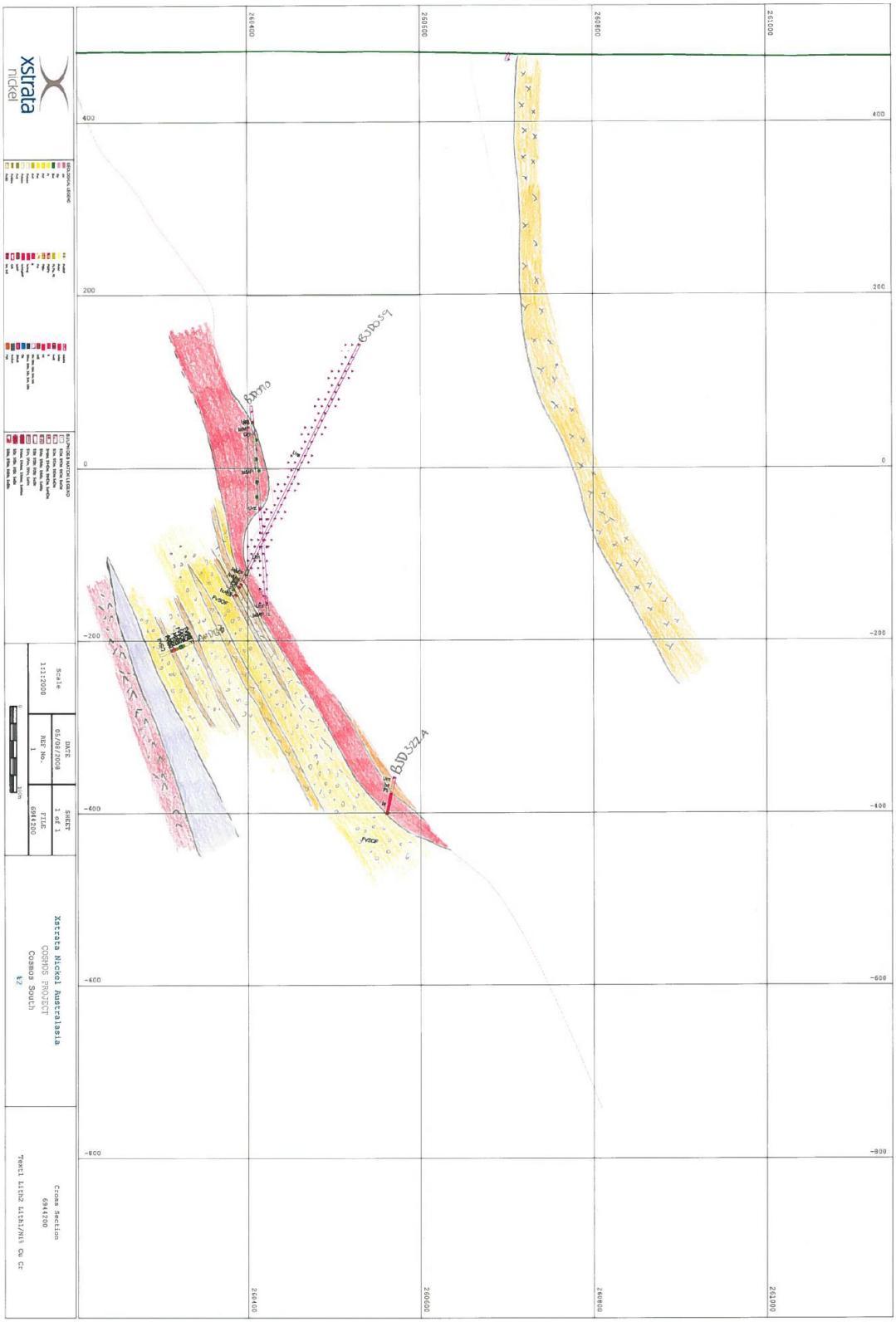

Figure A4.26. 6944200mN (±12.5m) cross section of the North Cosmos region.

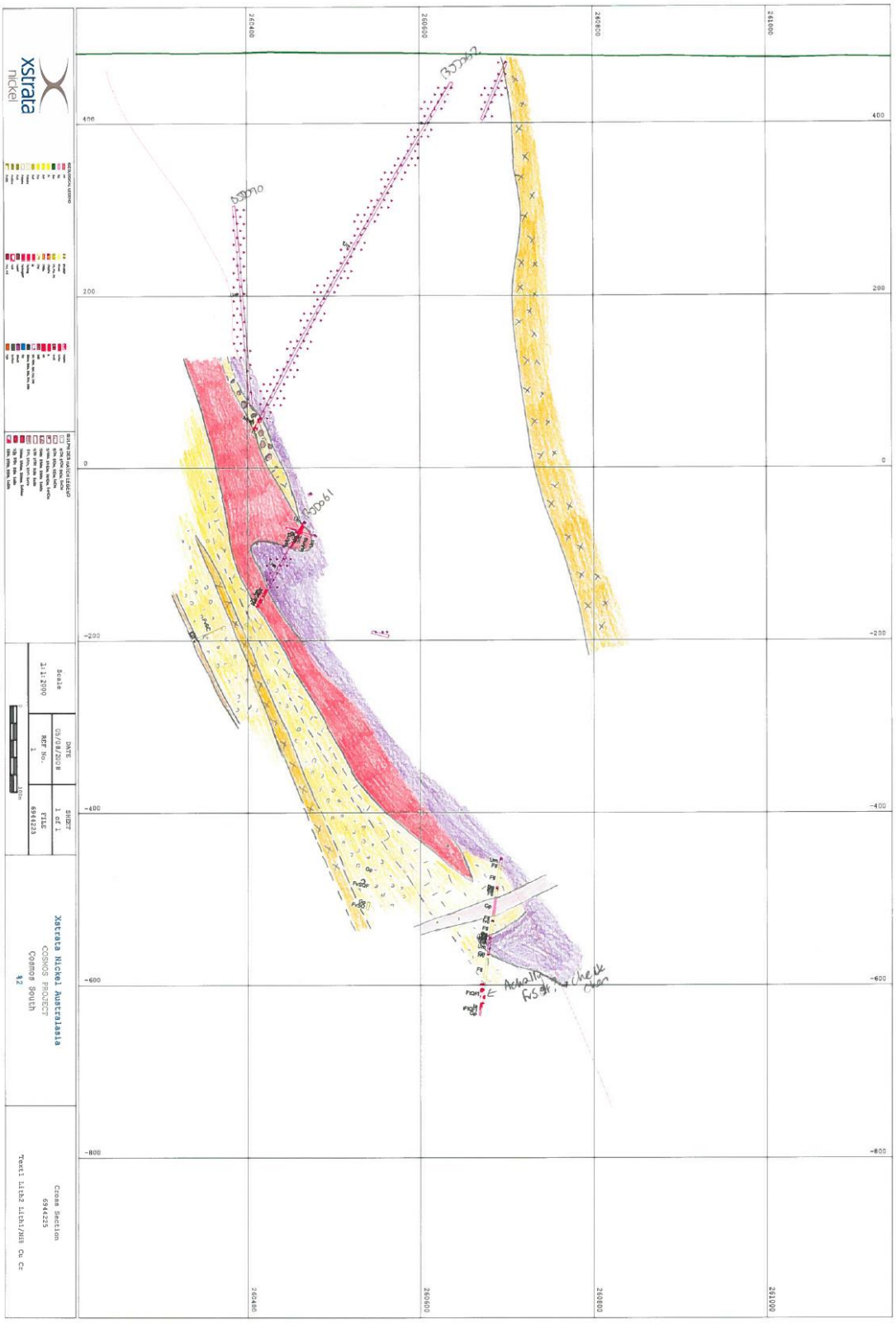

Figure A4.27. 6944225mN (±12.5m) cross section of the North Cosmos region.

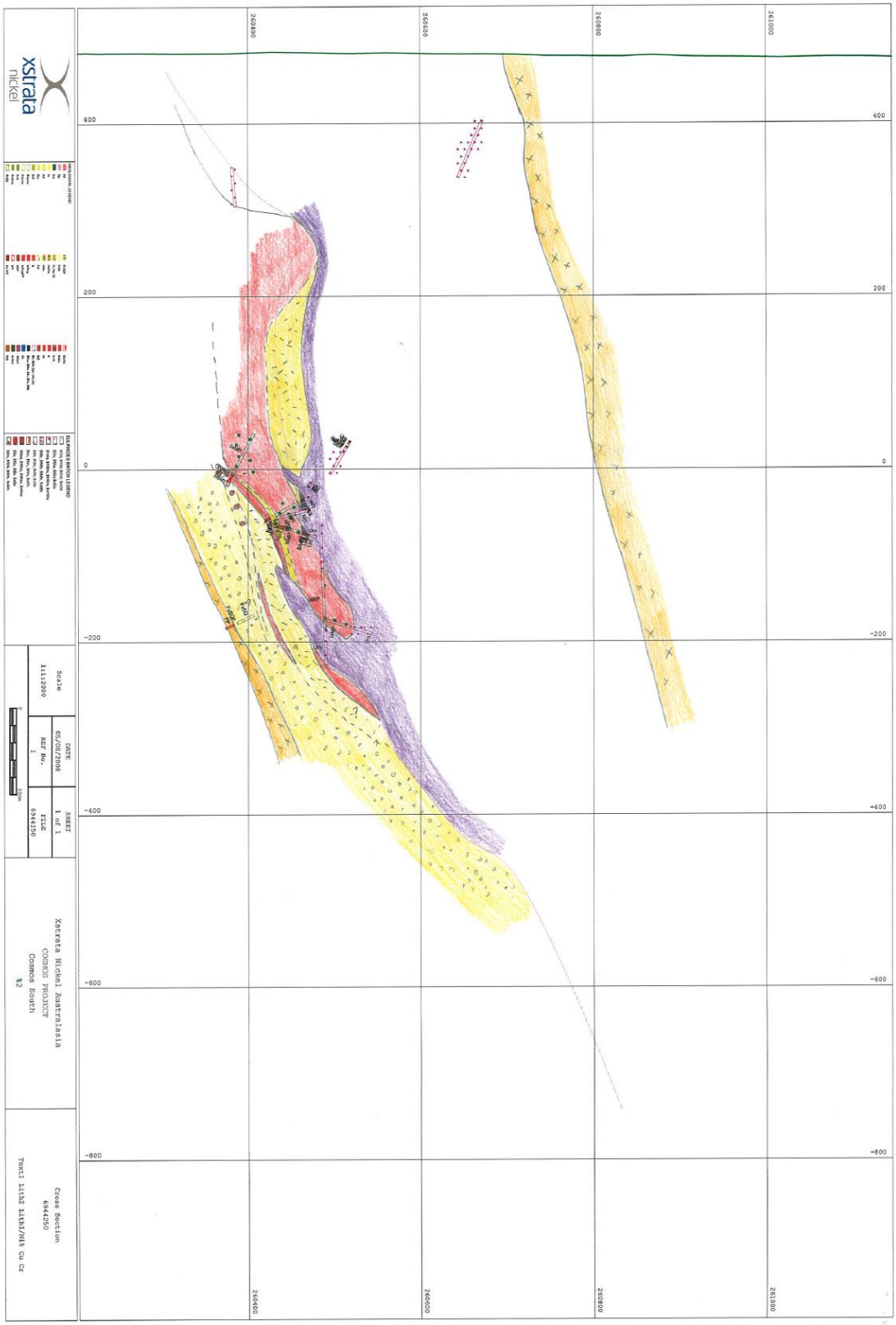

Figure A4.28. 6944250mN (±12.5m) cross section of the North Cosmos region.

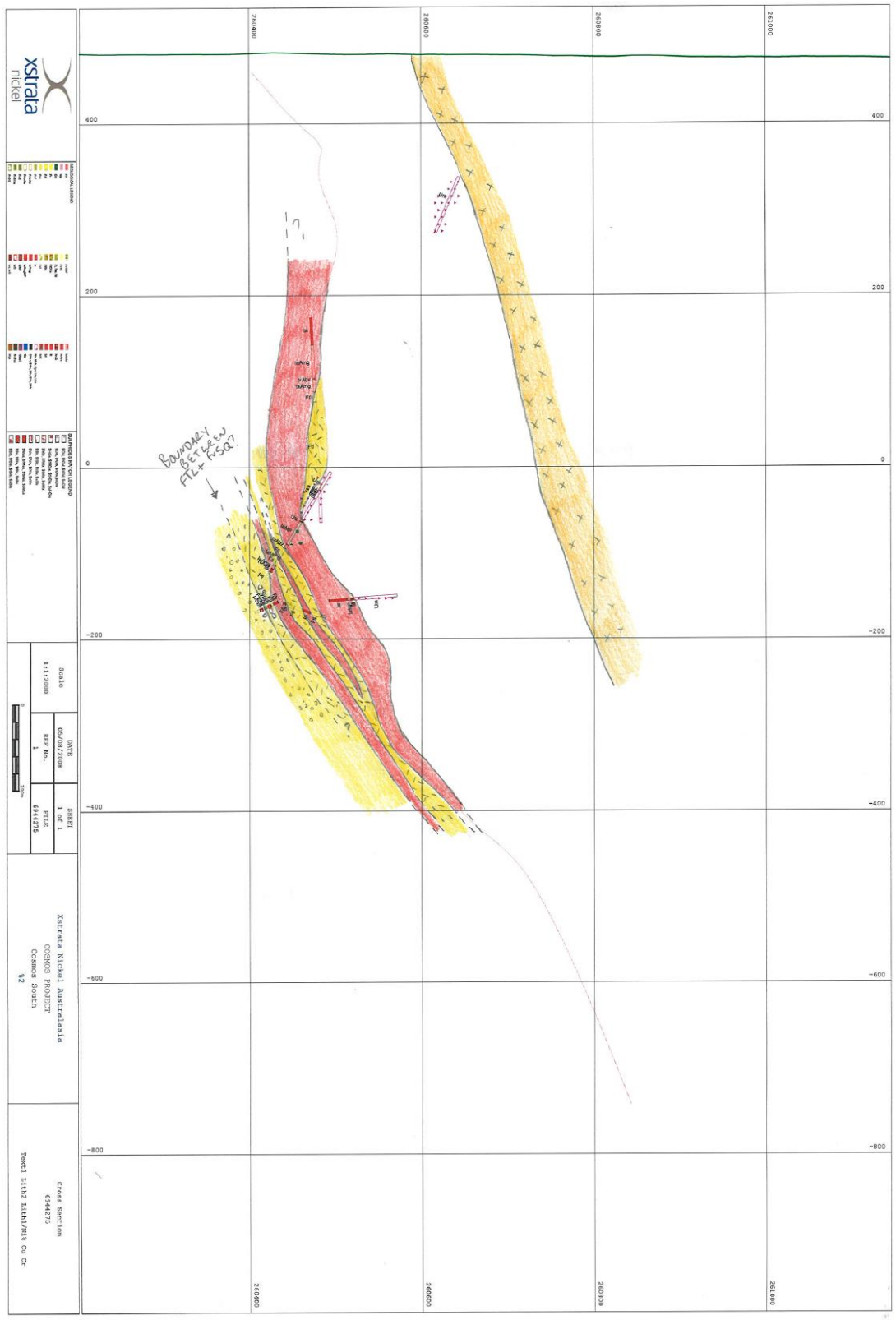

Figure A4.29. 6944275mN (±12.5m) cross section of the North Cosmos region.

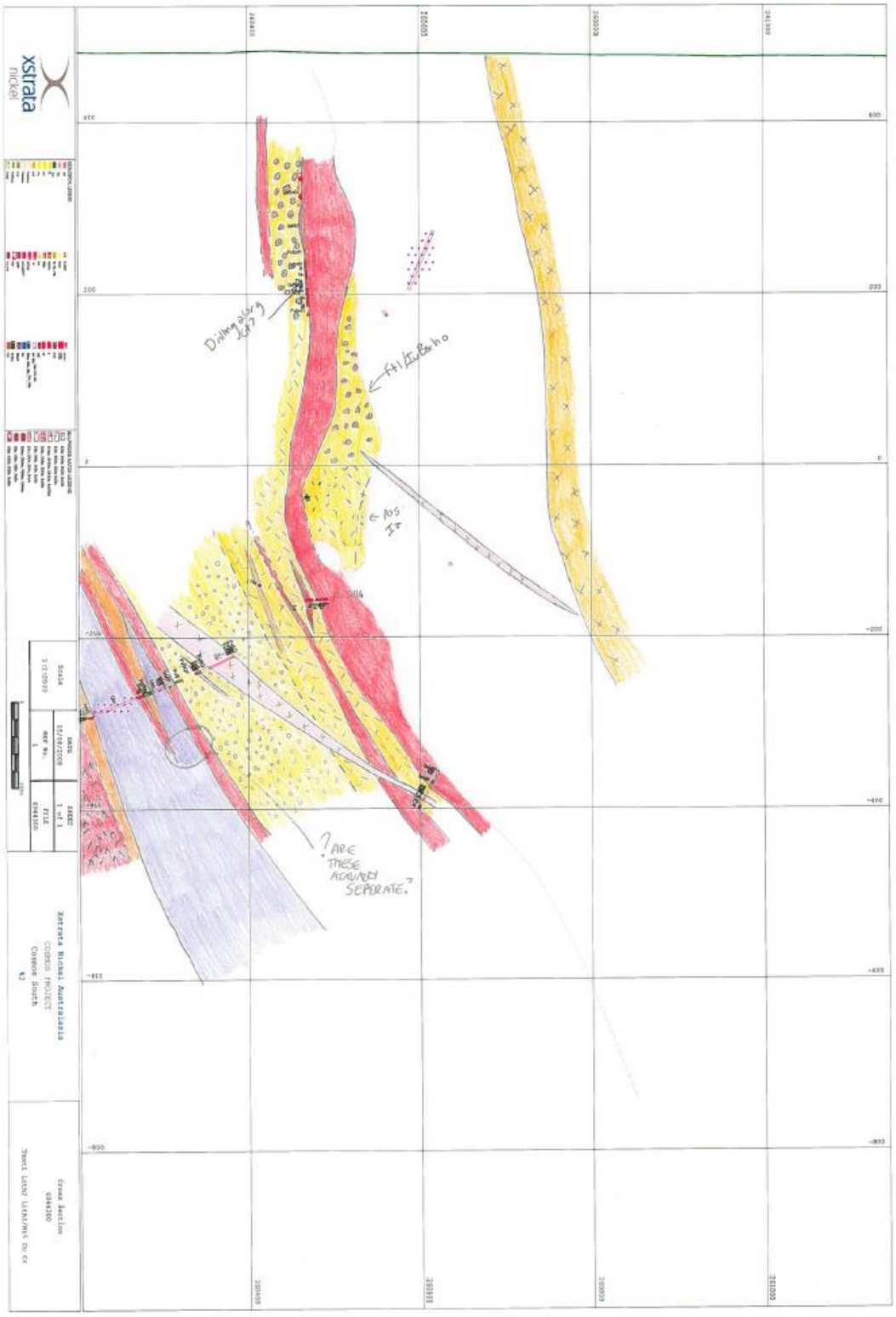

Figure A4.30. 6944300mN (±12.5m) cross section of the North Cosmos region.

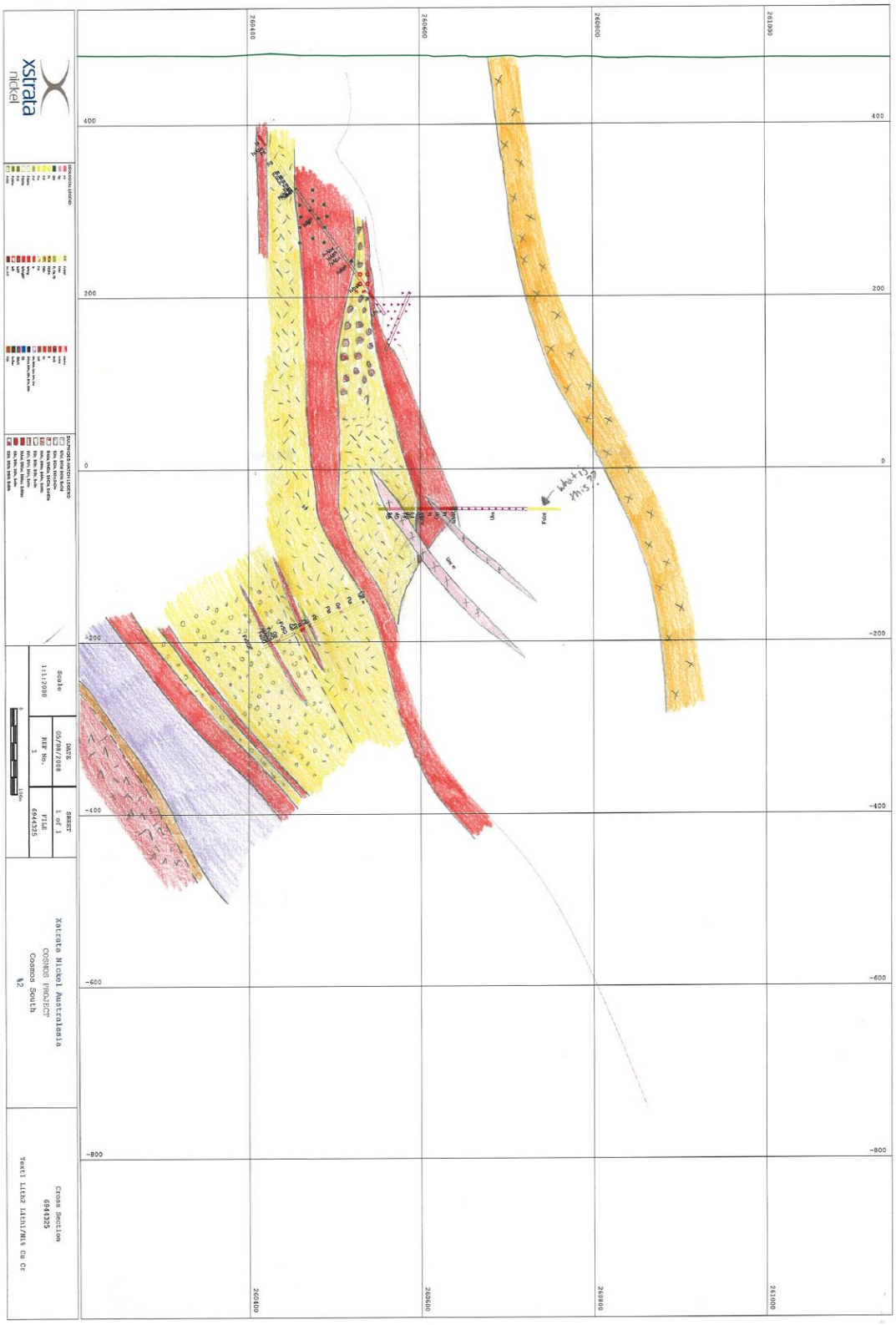

Figure. A4.31. 6944325mN (±12.5m) cross section of the North Cosmos region.

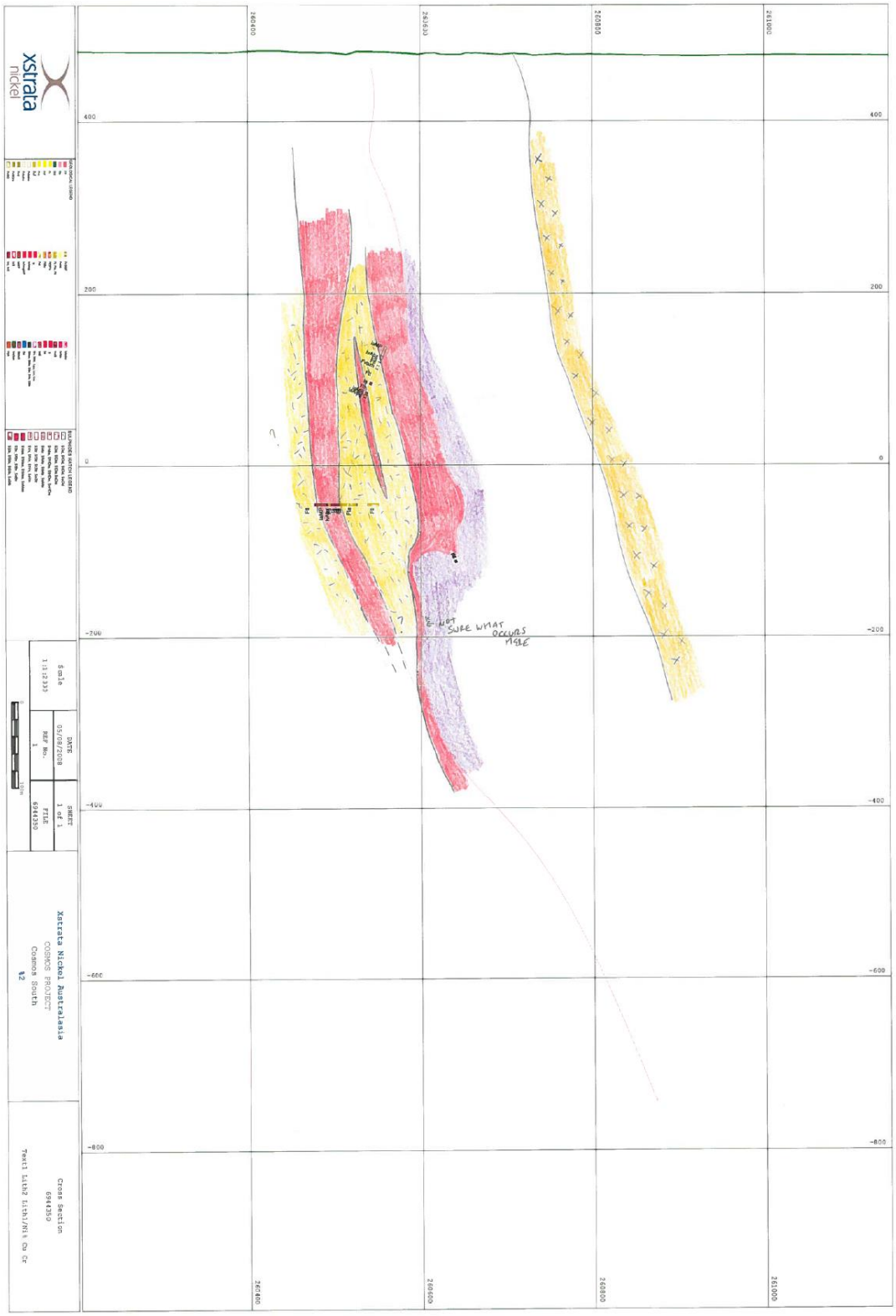

Figure A4.32. 6944350mN (±12.5m) cross section of the North Cosmos region.

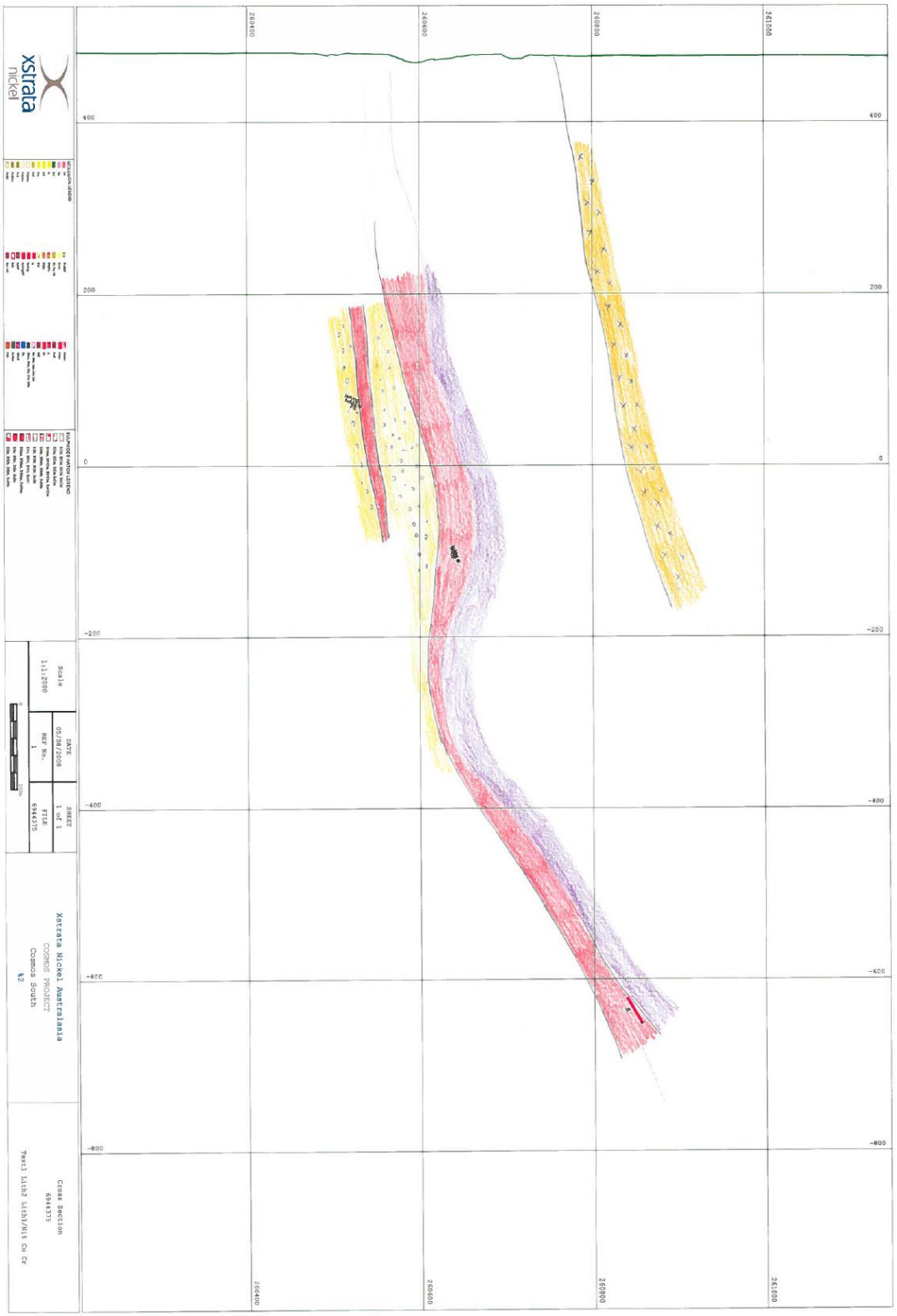

Figure A4.33. 6944375mN (±12.5m) cross section of the North Cosmos region.

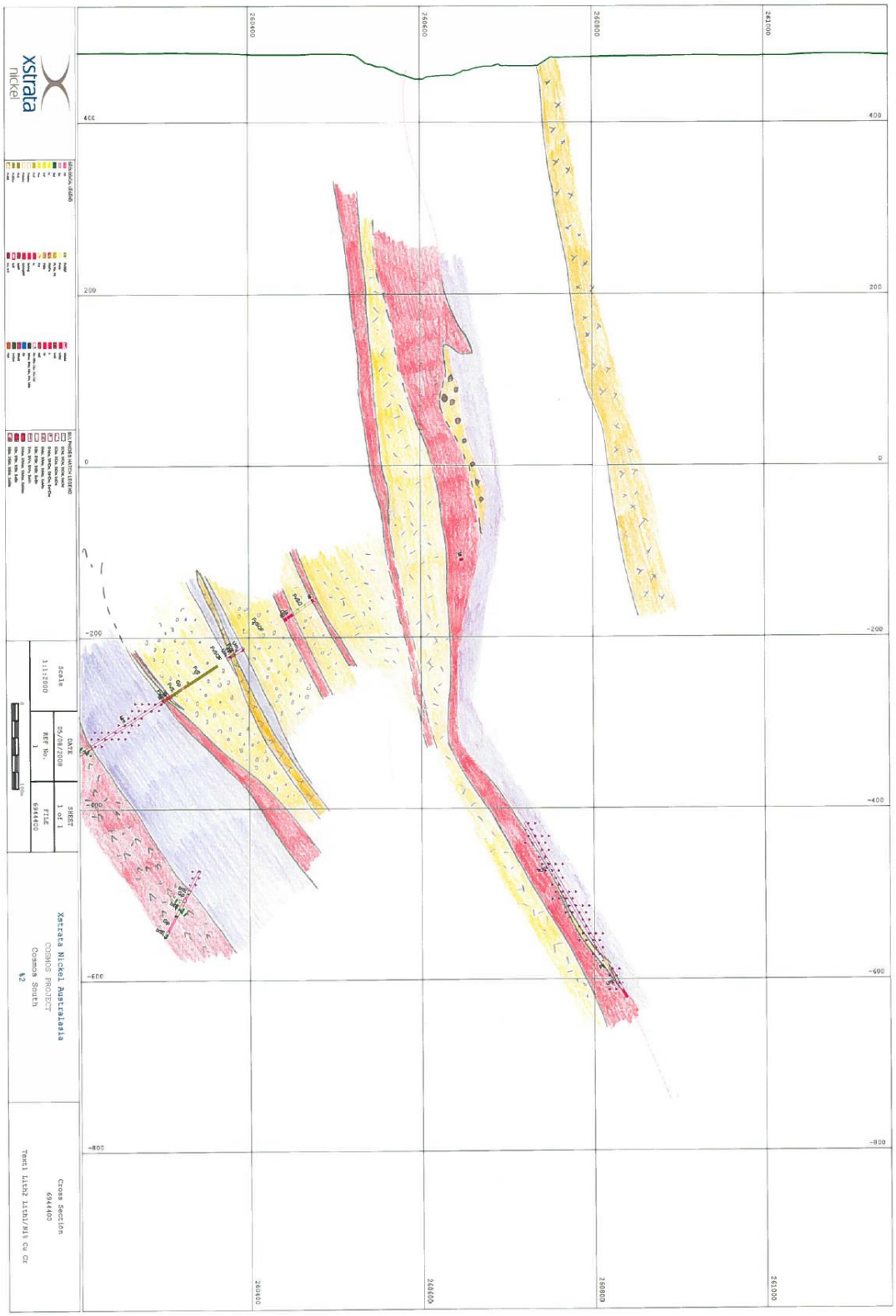

Figure A4.34. 6944400mN (±12.5m) cross section of the North Cosmos region.

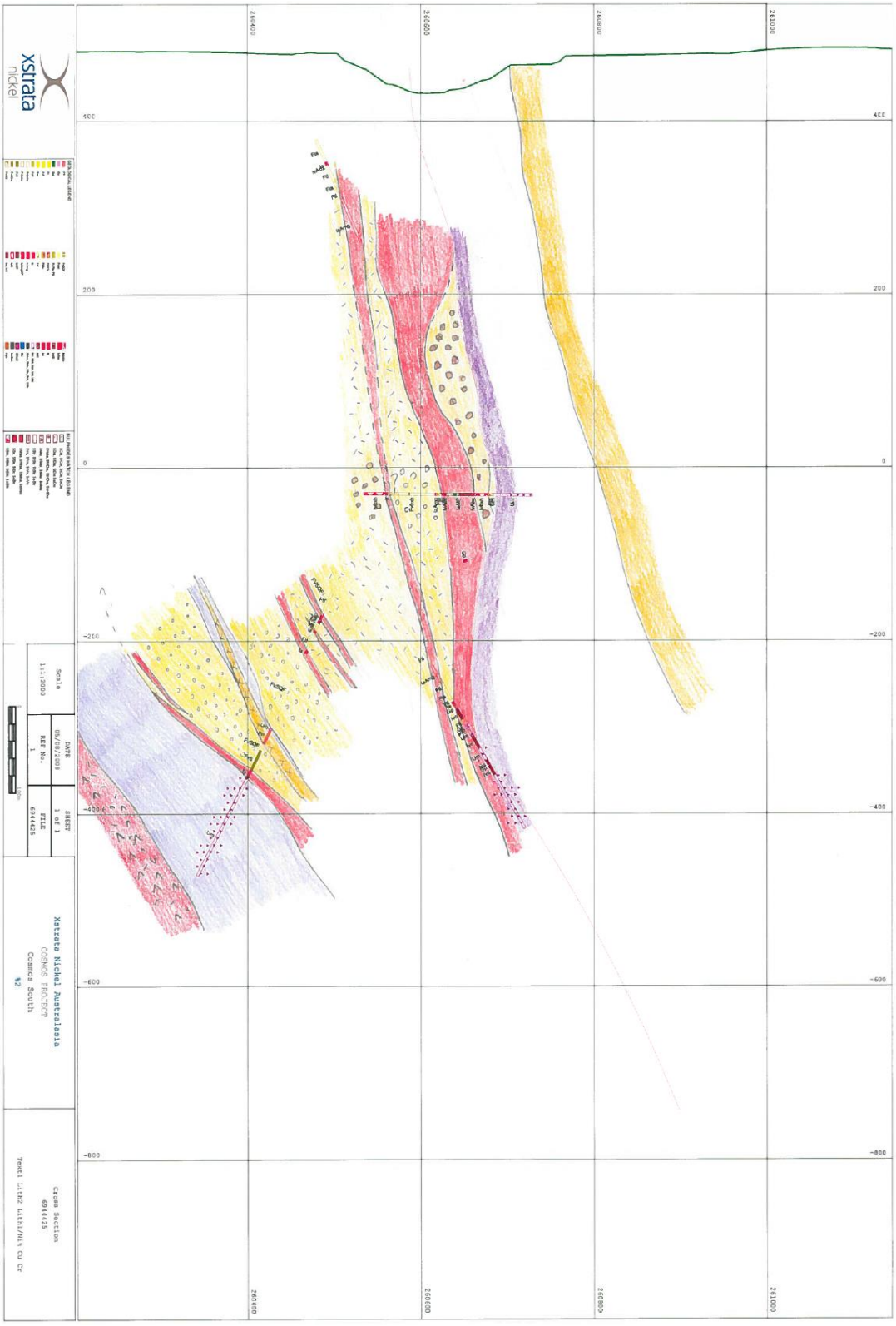

Figure A4.35. 6944425mN (±12.5m) cross section of the North Cosmos region.

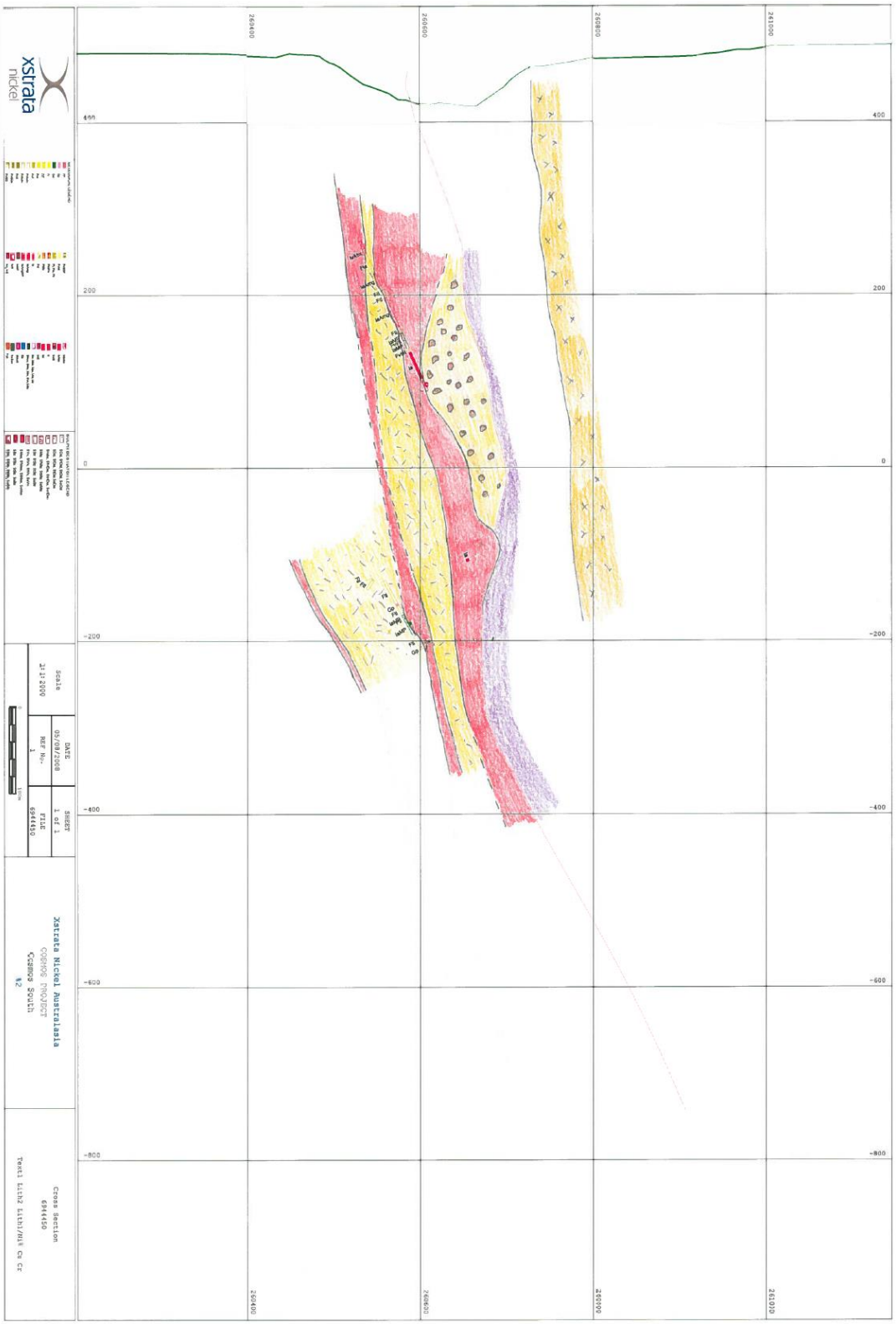

Figure A4.36. 6944450mN (±12.5m) cross section of the North Cosmos region.

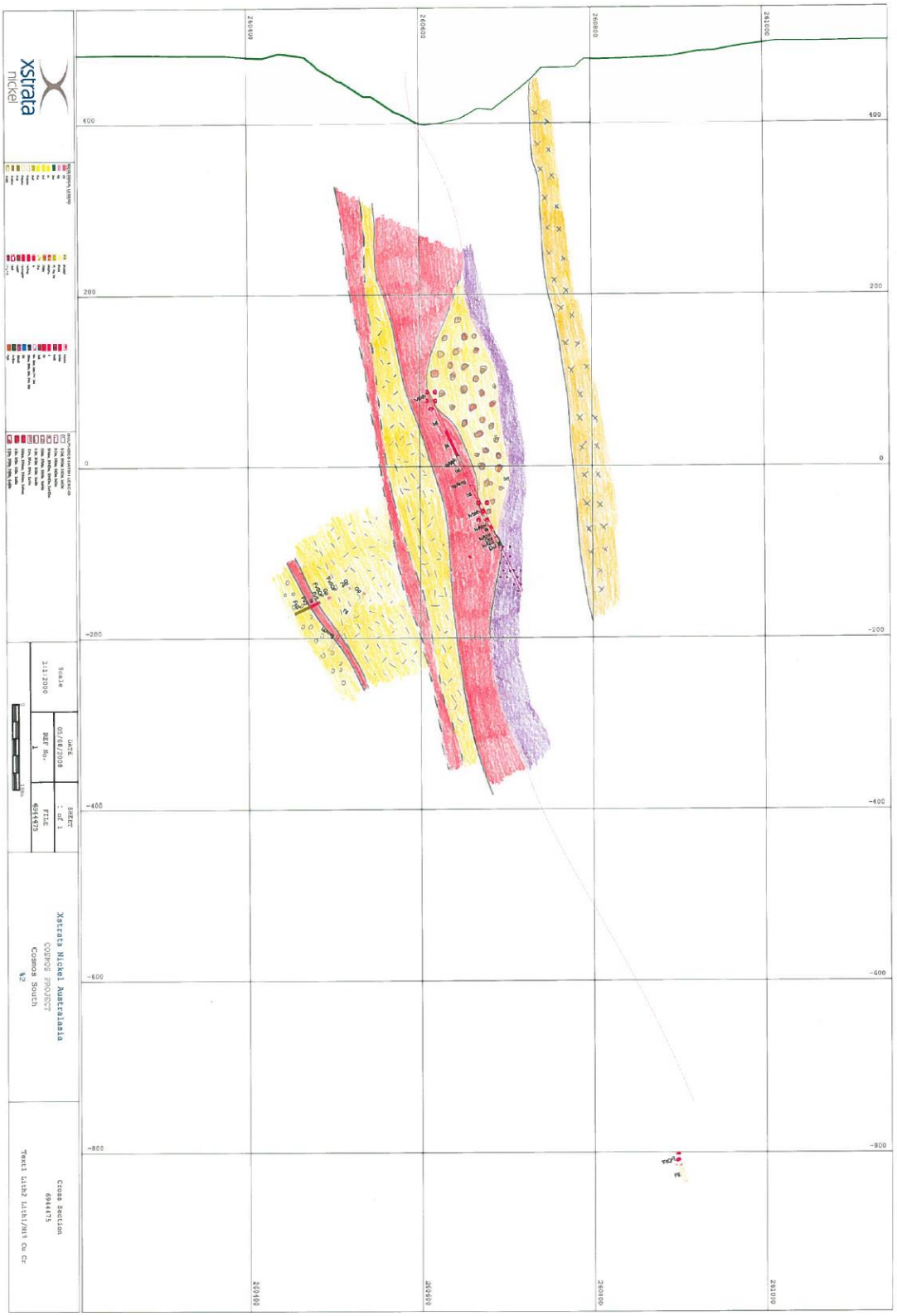

Figure A4.37. 6944475mN (±12.5m) cross section of the North Cosmos region.

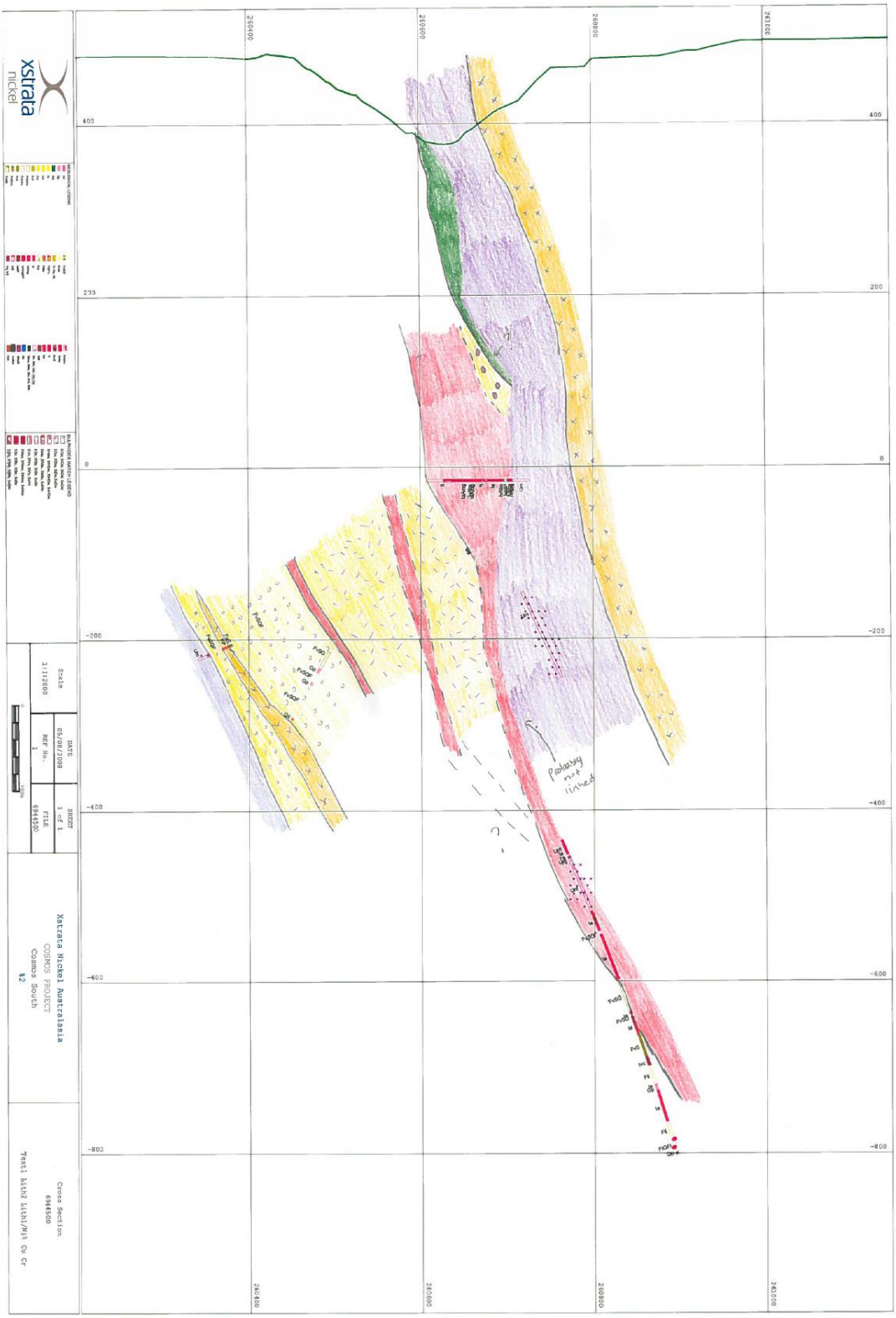

Figure A4.38. 6944500mN (±12.5m) cross section of the North Cosmos region.

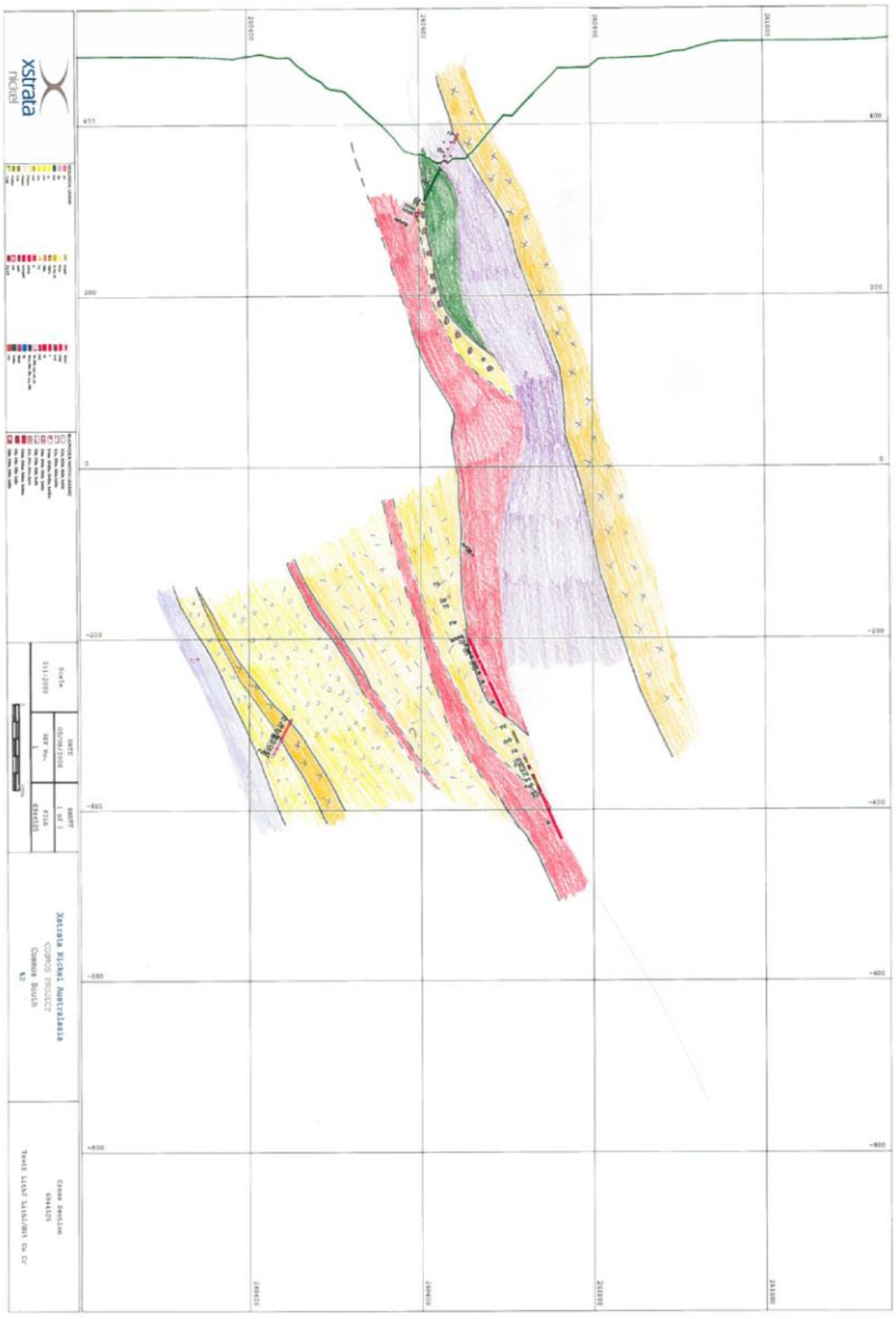

Figure A4.39. 6944525mN (±12.5m) cross section of the North Cosmos region.

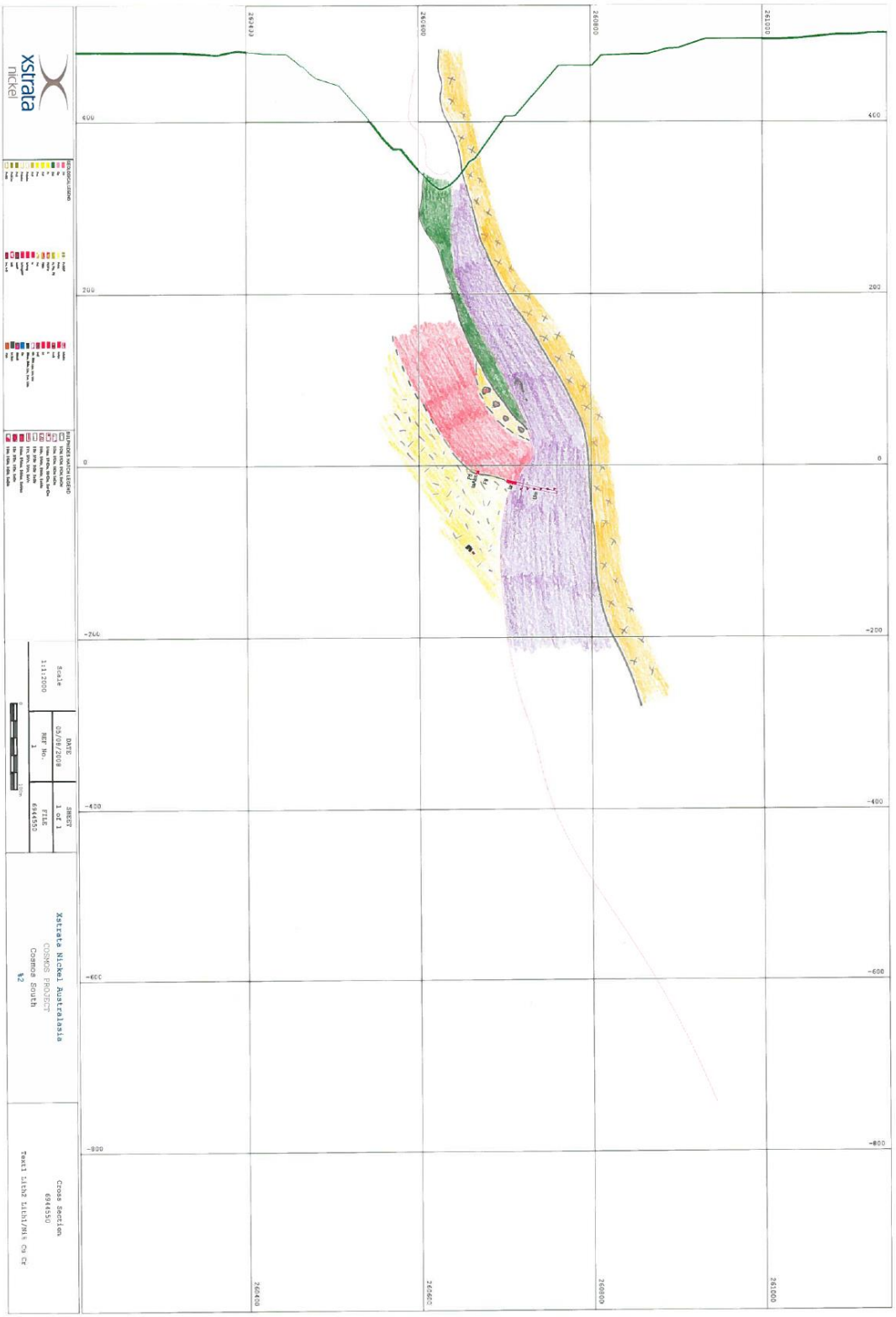

Figure A4.40. 6944550mN (±12.5m) cross section of the North Cosmos region.

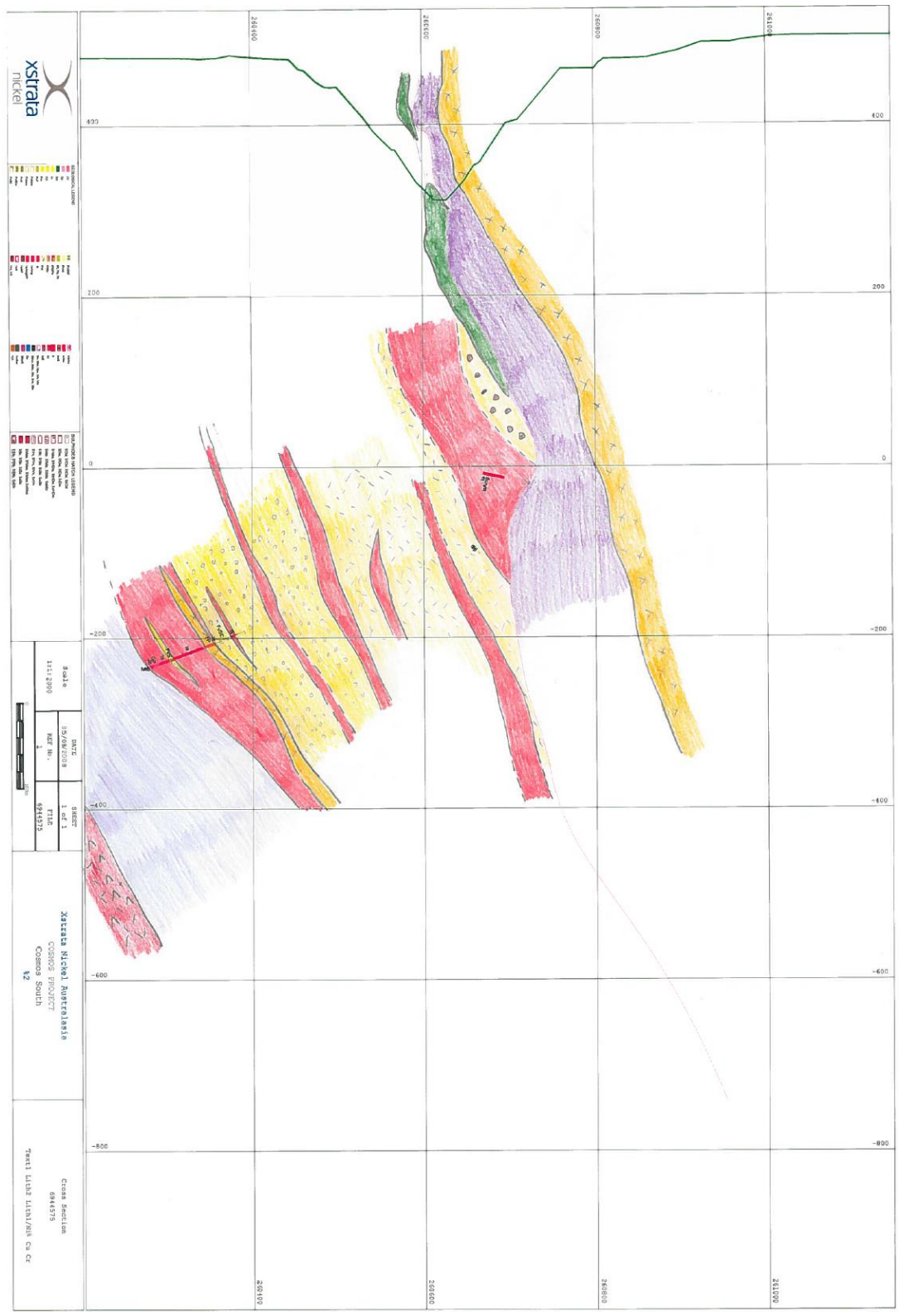

Figure A4.41. 6944575mN (±12.5m) cross section of the North Cosmos region.

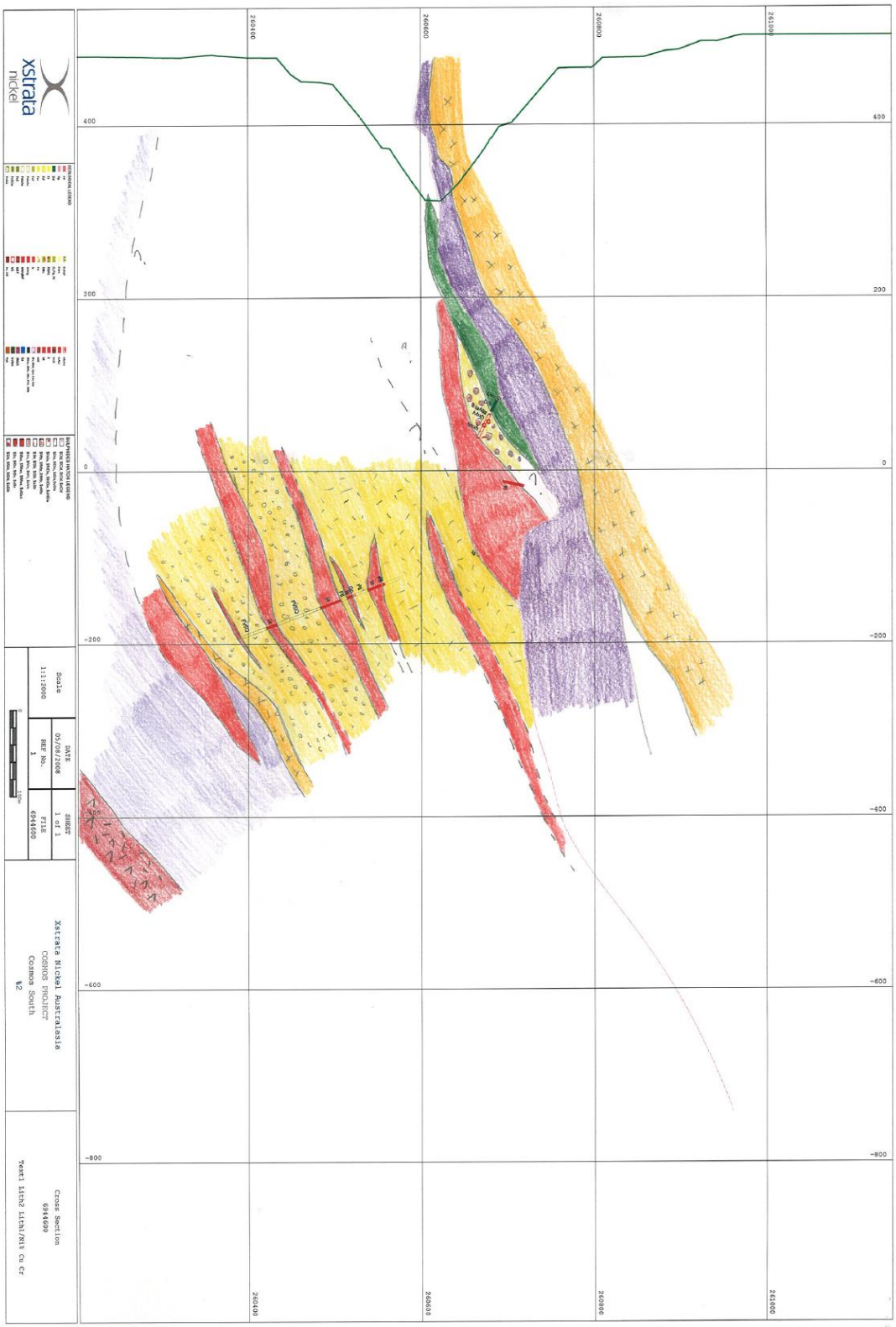

Figure A4.42. 6944600mN (±12.5m) cross section of the North Cosmos region.

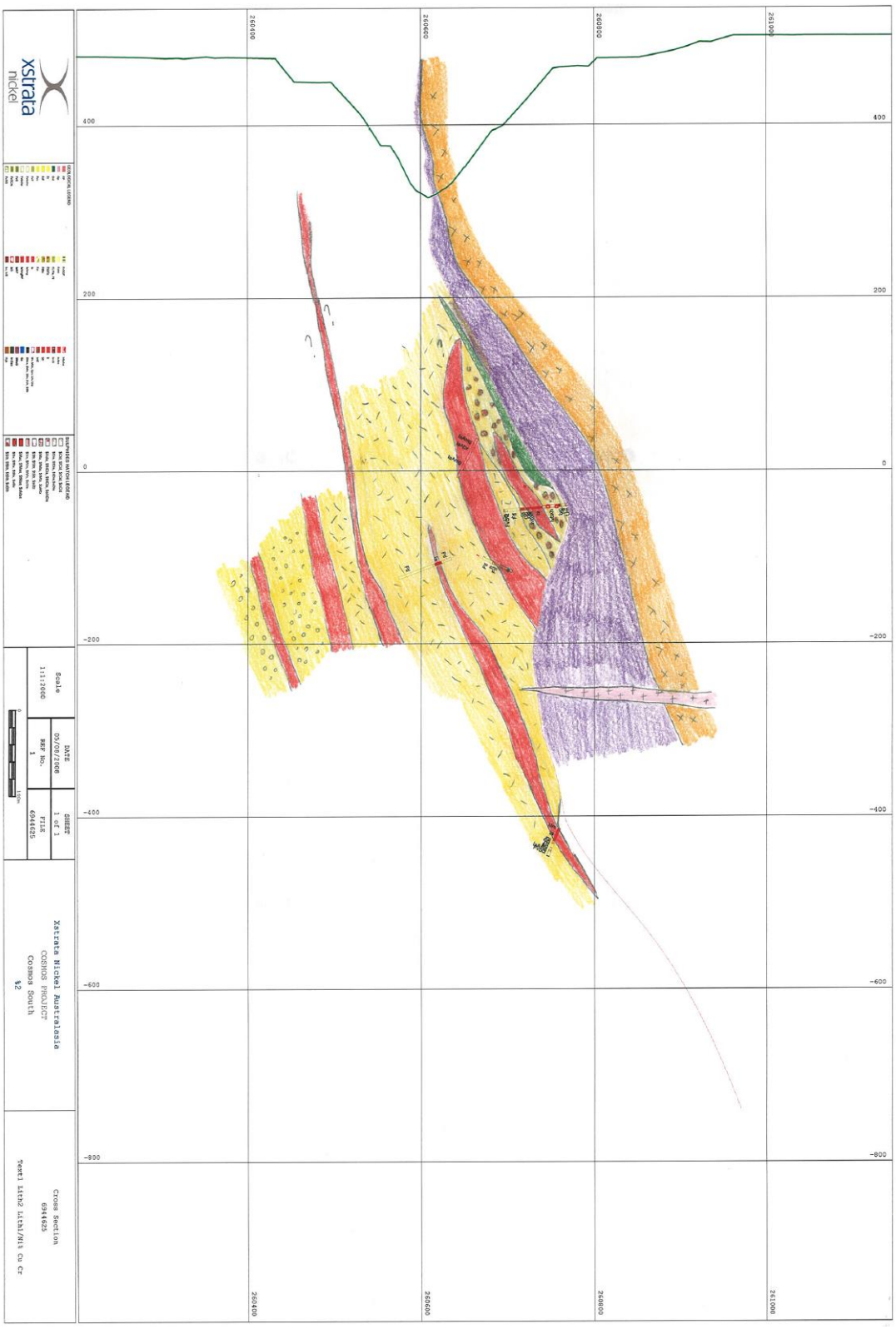

Figure A4.43. 6944625mN (±12.5m) cross section of the North Cosmos region.

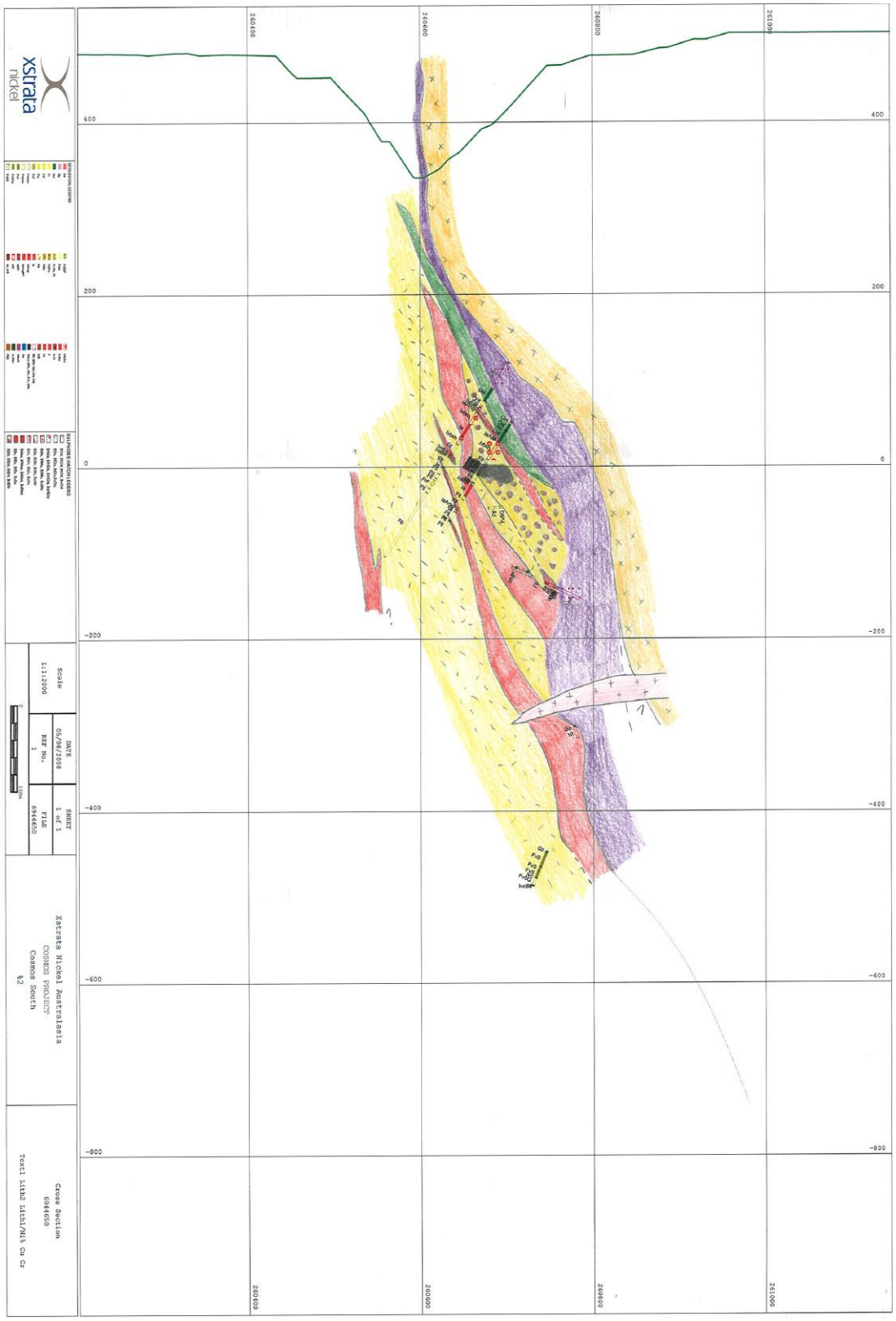

Figure A4.44. 6944650mN (±12.5m) cross section of the North Cosmos region.

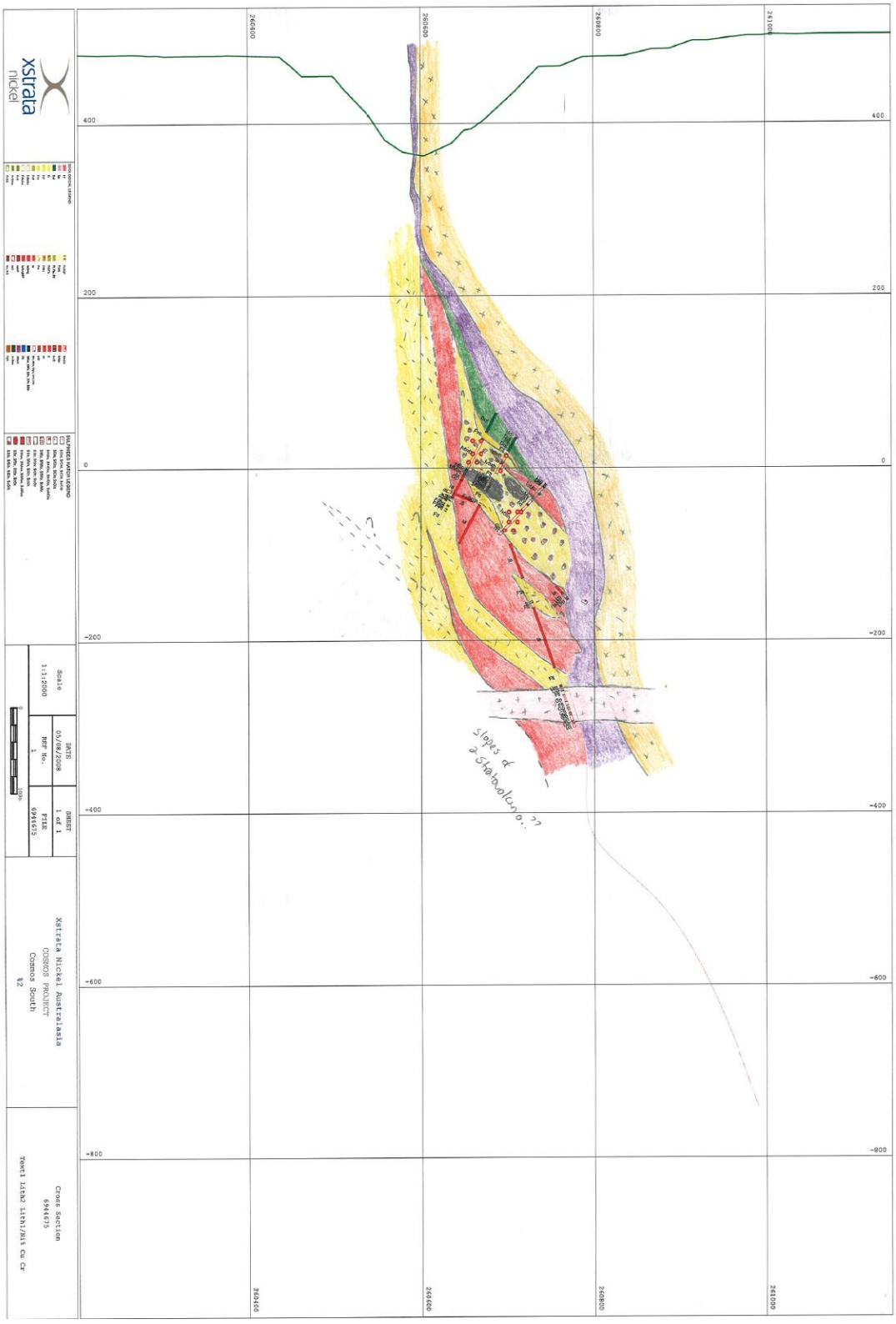

Figure A4.45. 6944675mN (±12.5m) cross section of the North Cosmos region.

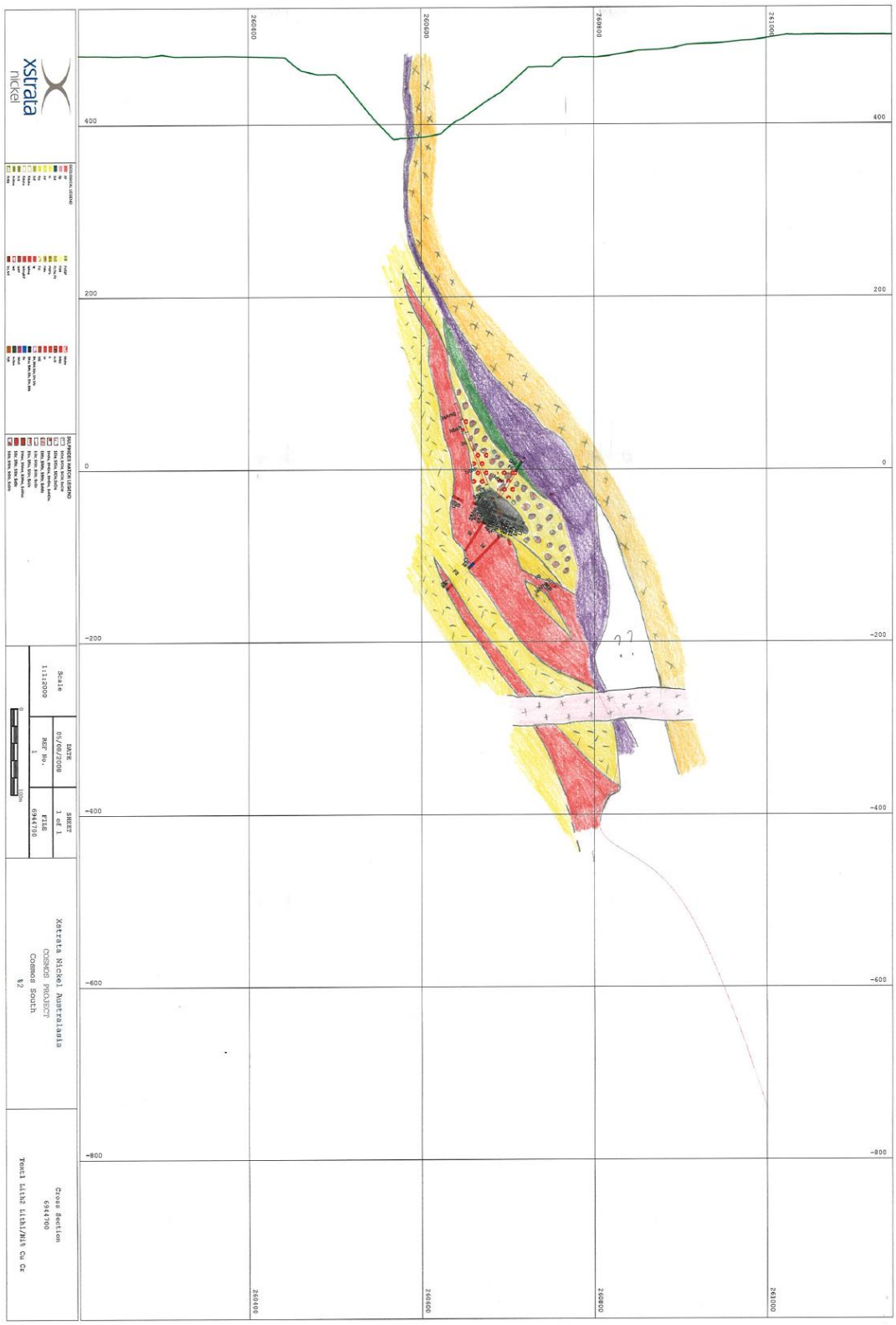

Figure A4.46. 6944700mN (±12.5m) cross section of the North Cosmos region.

Appendix 5- Grain size classification schemes

A5.1 Grain size terminology for pyroclastic, coherent volcanic and sedimentary rocks

Grain Size	Primary volcaniclastic deposit		Sedimentary deposit		Coherent volcanic rocks
(mm)	Unconsolidated	Lithified	Unconsolidated	Lithified	Crystal size nomenclature
< 0.0625	Extremely fine ash	Extremely fine tuff	Clay	Clay	Microlites
0.0625 - 0.125	Very fine ash	Very fine tuff	Very fine sand	Very fine sandstone	Fine crystals
0.125 - 0.250	Fine ash	Fine tuff	Fine sand	Fine sandstone	Fine crystals
0.25 - 0.50	Medium ash	Medium tuff	Medium sand	Medium sandstone	Medium crystals
0.5 - 1.0	Coarse ash	Coarse tuff	Coarse sand	Coarse sandstone	Coarse crystals
1 - 2	Very coarse ash	Very coarse tuff	Coarse sand	Coarse sandstone	Very coarse crystals
2 - 4	Fine lapilli	Fine lapilli-tuff	Granule	Grit, granule conglomerate	Extremely coarse crystals
4 - 8	Medium lapilli	Medium lapilli-tuff	Pebble	Pebble conglomerate	Large crystals
8-16	Medium lapilli	Medium lapilli-tuff	Pebble	Pebble conglomerate	Very large crystals
16 - 32	Coarse lapilli	Coarse lapilli-tuff	Cobble	Cobble conglomerate	Extremely large crystals
32 - 64	Coarse lapilli	Coarse lapilli-tuff	Cobble	Cobble conglomerate	Extraordinarily large crystals (e.g. spinifex, pegmatite crystals)
> 64	Block/bomb	Breccia	Boulder	Boulder conglomerate	Extraordinarily large crystals (e.g. spinifex, pegmatite crystals)

Table A5.1 Grain size terms for primary volcaniclastic rocks, sedimentary rocks and coherent volcanic rocks. Grain size nomenclature is copied from White and Houghton (2006) who modified the ash and lapilli grain size ranges from Fisher (1961) to match and include the subdivisions within the sand and gravel ranges given by Wentworth (1922). Grain size nomenclature for coherent rocks has been modified from Cas et al., (2008), who derived the nomenclature in part from McArthur et al. (1998).

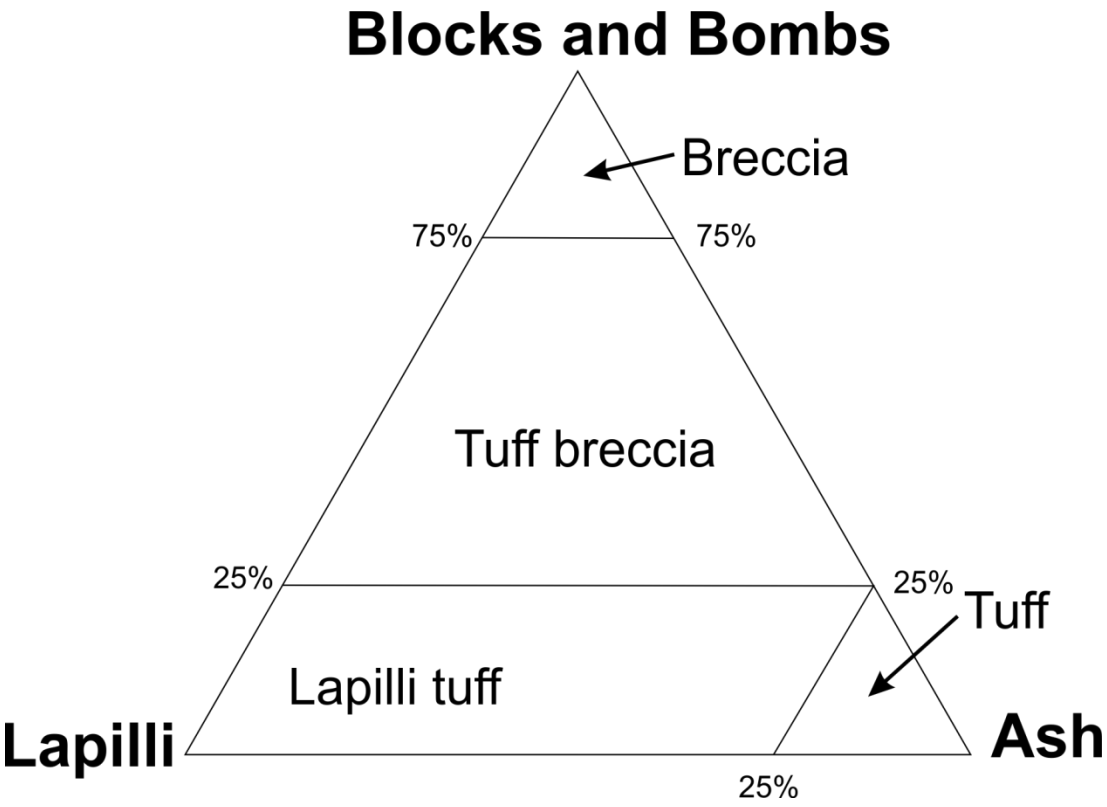

Figure A5.1. Grain-size ternary diagram from naming primary volcaniclastic rocks after Fisher (1961) following Schmid (1981) with the removal of lapillistone (modified after White and Houghton, 2006).

A5.2 References

Cas, R. A. F., Porritt, L., Pittari, A., Hayman, P., 2008. A new approach to kimberlite facies terminology using a revised general approach to the nomenclature of all volcanic rocks and deposits: descriptive to genetic. Journal of Volcanology and Geothermal Research 174(1), 226-240.

Fisher, R. V., 1961. Proposed classification of volcaniclastic sediments and rocks. Geological Society of America Bulletin 72, 1409-1414.

McArthur, A. N., Cas, R. A. F., Orton, G. 1998. Distribution and significance of crystalline, perlitic and vesicular textures in the Ordovician Garth Tuff (Wales. Bulletin of Volcanology 60, 260–285.

Schmid, R., 1981, Descriptive nomenclature and classification of pyroclastic rocks and fragments: Recommendations of the IUGS Subcommission on the Systematics of Igneous Rocks. Geology 9, 41–43.

Wentworth, C. K., 1922, A scale of grade and class terms for clastic sediments: The Journal of Geology 30, 377–392.

White, J. D. L., Houghton, B. F., 2006. Primary volcaniclastic rocks. Geology 34(8), 677-680.

Appendix 6- Ion microprobe analysis methods for U-Pb

A6.1 Methods

U-Pb zircon dating has been undertaken on samples collected from various lithologies and stratigraphic positions within the Cosmos succession. Overall fourteen samples were selected for analysis; five had no or very poor zircon yield; Samples 6.BJD085 (granitic pegmatite) and 8.AMD264 (rhyolite lava) were highly silicic and could have experienced zircon removal by fractional crystallisation prior to emplacement. Samples 5.BJD048A (intermediate crystal tuff) and Sample 11.BJD085 (basaltic andesite lava) were too mafic in composition to have zircon as a liquidus phase. Sample 13.BJD332 contained very few zircons amongst abundant sulphide. Thus, these five samples could not be used for dating and were excluded from the study. The nine remaining zircon-bearing samples were analysed for U-Pb. These consisted of two dacitic lapilli tuffs (1.BJD085 and 2.BJDM002), two dacitic lavas (3.BJD090 and 10.BJD328F), two felsic porphyritic intrusions (4.AMD273 and 9.BJD320), a felsic schist (14.AMD313), a hangingwall volcanically-derived sediment (12.BJD332) and a coherent dacite from the AM5 “reactivation” contact (7.AMD346).

Approximately 2kg of each of the 14 samples was sent away for zircon separation at Geotrack International in Melbourne. Samples were crushed in a jaw crusher and milled using a disc pulveriser to disaggregate the rock rather than crush the constituent mineral grains. Fine material was then removed by hand washing prior to heavy mineral separation. Frantz isodynamic magnetic separators and heavy liquid mineral separations were used to separate mineral grains by gravity and magnetic

susceptibility. From each sample three vials were returned containing a zircon concentrate, zircon fraction and apatite fraction. The zircon fraction consisted of zircons with densities >3.3 g/cc^3 and magnetic character, while the zircon concentrate consisted of zircons with densities >3.3 g/cc^3 and non-magnetic character. The latter separate was usually a more pure non-magnetic separate and zircons from this fraction were preferentially selected for mounting. However, the 'zircon fraction' was also used if zircons in a particular sample were found to be magnetic and thus preferentially concentrated in the magnetic 'zircon fraction' or if the concentration of zircons in the concentrate was particularly low.

Zircons from each sample separate were hand-picked and mounted in epoxy. Individual grains were positioned sequentially in rows around a central row of the zircon standards, either 91500 (^{206}Pb/^{238}U age - 1062.5 Ma (Wiedenbeck et al., 1995) or GJ-1 (^{206}Pb/^{238}U age – 600.4 Ma (Jackson et al., 2004). The mounts were then polished to expose the zircon interiors.

The characteristic features of individual zircons were mapped using backscattered electrons on a Philips XL30CP Scanning electron microscope (SEM). Backscattered electron imaging was used instead of cathodoluminescence (CL) imaging as many of the zircons did not exhibit strong luminescence in CL and the compositional zoning within zircons was not always immediately visible. These mineral-maps were utilised to select zircons of a suitable size and morphology for analysis. The mounts were then gold-coated and selected zircons were analysed by SIMS (secondary ionising mass spectrometry) on a Cameca 1270 Ion microprobe for U-Pb. In total two mounts were analysed, encompassing analysis of nearly 150 zircons from nine separate samples.

In each session, standards were analysed at the beginning and the end as well as between every 3 - 5 analyses of unknowns. Individual sessions lasted 5 to >24 hours, depending on the beam conditions and analyses required in each session, with each analysis of an individual zircon grain taking ~30 minutes. A new session was commenced every time there was a change in conditions, such as a major variation in the beam current, or once a new set of analyses commenced from a different sample.

Only standards analysed in a specific session were used in correcting the data obtained from the unknowns. Pb yield was enhanced by flooding the surface with oxygen (~ a factor of two increase in Pb intensity). A ~ 5nA $16O_2^-$ primary beam of 22KeV net impact energy, using Köhler illumination, gave a flat bottomed pit of approximately 30μm diameter. Surface contamination around the pit was removed by a 2 minutes 15μm^2 raster pre-sputter prior to each analysis.

Processing of raw data is as follows. A correction was applied for common Pb, ^{204}Pb. A correction for dead time was applied (electronically set 51 nanoseconds). 20 analytical cycles were measured for each sample; the first five were not used in any subsequent data processing. The analysed Uranium content for each sample is based on the Uranium content of 91500, which is taken to be 81 ppm. The Uranium content was based on the UO_2/Zr_2O_2 ratio, measured in 91500. One mount contained only GJ1 and no 91500 thus the standard Uranium analysis was measured off mount on 91500, prior to the start of the session. The precise U/Pb ratio was corrected for changes in instrumental conditions using ln($^{206}Pb/^{238}U$) vs. ln($^{238}UO2/^{238}UO$) and a slope factor of 2.6 (Kelly et al., 2008) and either 91500 of GJ-1 standards to derive the U/Pb yields.

A6.2 References

Jackson, S. E, Pearson, N. J., Griffin, W. L., Belousova, E. A., 2004. The application of laser ablation-inductively coupled plasma-mass spectrometry to in situ U–Pb zircon geochronology. Chemical Geology 211, 47–69.

Kelly, N. M., Hinton, R. W., Harley, S. L., Appleby, S. K., 2008. New SIMS U-Pb zircon ages from the Langavat Belt, South Harris, NW Scotland: implications for the Lewisian Terrane mode. Journal of the Geological Society, 165, 967-981.

Wiedenbeck, M., Alle, P., Corfu, F., Griffin, W.L, Meier, M., Oberli, F, Von Quadt, A., Roddick, J.C., Spiegel, W., 1995. Three natural zircon standards for U–Th–Pb, Lu–Hf, trace element and REE analyses, Geostandards Newsletter 19, 1–24.